Open Research Online

The Volcanic Evolution of Syrtis Major Planum, Mars

Thesis

Version: Version of Record

oro.open.ac.uk

The Volcanic Evolution of Syrtis Major Planum, Mars

Peter Fawdon

Msci

31th March 2016

A thesis submitted to The Open University in the subject of Physical Sciences for the degree of

Doctor of Philosophy

Department of Physical Sciences

The Open University

Abstract

This thesis explores the geological history of the Syrtis Major Planum volcanic province on Mars. The primary aims are (i) to differentiate the various units that make up the lava plain of Syrtis Major Planum, (ii) to investigate the formation of the central caldera complex, and (iii) to understand how the volcanic architecture has evolved over time in the regional contex.

The methodology applied is that of planetary geological mapping using remote sensing data. Two new morpho-stratigraphic maps of Syrtis Major Planum have been produced. Map 1, a 1: 2,000,000 scale map, uses 100 m/pixel THEMIS data as the base layer, and draws on 6 m/pixel CTX data to provide additional information. Map 2 is a 1:250,000 scale map of the Nili Patera caldera and uses base layer mosaics of CTX data and CTX Digital Terrain Models.

The mapping shows that there were two major phases of magmatism at Syrtis Major. The first phase (~3.6 Ga – ~3.2 Ga) consisted of tube-fed lava plains interleaved with giant (>300 km) tabular lava flows emplaced from the centre of the planum. By the end of this phase, a fractionally crystallised magma reservoir, partially melting the hydrated sediments of the underlying Noachian highlands, had developed. The eruptive products of this magma reservoir include an ignimbrite, now exposed in Nili Patera. The second phase of magmatism (~2.7 Ga - ~2.2 Ga) consisted of temporally sporadic volcanism, spatially concentrated in the central caldera complex, and includes two examples of high-silica lava units. These derived from partial melting of the fractionally crystallised magma reservoir in the presence of hydrothermal fluids.

The evolution of lava emplacement style and composition over time is best explained by the interaction between the waxing to waning stages of a mantle plume with the underlying Noachian terrain. This interaction led to the distinctive morphology of the volcanic shield, the explosive formation of the calderas, and the unusual compositions found within the central caldera complex. The volcanism of Syrtis Major is therefore defined both by the epoch in which it occurred, and the composition of the crust in which it formed.

Acknowledgments

Table of contents

List of figures

Chapter 5

Chapter 7

List of tables

List of equations

List of abbreviations

Abbreviation	Full wording
CTX	*Context Camera*
CHVP	*Circum-Helas Volcanic Province*
Ga	*Giga anum, 1 Billion year*
HiRISE	*High Resolution Imaging Science Experiment*
HRSC	*High Resolution Stereo Camera*
ISIS	*Integrated Software for Images and Spectrometers*
MEX	*Mars Express*
MGS	*Mars Global Surveyor*
MOC	*Mars Orbital Camera*
MOLA	*Mars Orbital Laser Altimeter*
SMCCC	*Syrtis Major Central Caldera Complex*
SMP	*Syrtis Major Planum*
MRO	*Mars Reconnaissance Orbiter*
NEFZ	*North East Fissure Zone*
SCFZ	*Southern Crypto fissure zone*
THEMIS	*Thermal Emission Imaging System*
TES	*Thermal Emission Spectrometer*
GIS	*Grographic Information Systems*

Chapter 1: Introduction

1.1 Introduction

Syrtis Major Planum is a Hesperian-aged, volcanic plains volcano covering ~3 % of the martian

surface (Figure 1.1). Syrtis Major Planum is located on the edge of the Noachian highlands, on the

rim of the Isidis basin [*Meyer and Grolier*, 1977a; *Scott and Carr*, 1978; *Plescia and Saunders*,

1979; *Schaber*, 1982; *Greeley and Guest*, 1987a; *Tanaka, et al.*, 2014a; *Tanaka et al.*, 2014b]. It

consists of a gently sloping 'shield' of lava plains 1100 km wide, and estimated to have a mean

thickness of only 500 m [*Hiesinger and Head*, 2004]. At the center of the lava plain is the central

caldera complex. This consists of a depression 200 km × 400 km in extent, the floor of which is

over a kilometre below the elevation of the surrounding planum. Within the central caldera

complex are two calderas, Nili Patera and Meroe Patera. In this thesis I will investigate the

evolution of the entire planum and the sequence of events that have led to the central caldera

complex as we see it today.

Syrtis Major Planum was emplaced in the Hesperian, towards the end of a period of critical

environmental change on Mars. During this time, the eruption styles of Mars' major volcanic

edifices changed from producing flat, plains-style volcanoes, to forming steeper-sided, highland

Patera volcanoes. During this time, there was an exponential decrease in the production of new

crust [*Grott et al.*, 2012; *Baratoux et al.*, 2013]. This was a time of either widespread highland

glaciation [*Fastook and Head*, 2015] or a warmer and wetter climate on ancient Mars; either way

it was during this time that's Mars lost this highland ice and/or last remnants of any global oceans

[*Di Achille and Hynek*, 2010]. Consequently, this is a fascinating time in Mars' geological history,

because of the many fundamental changes that were taking place.
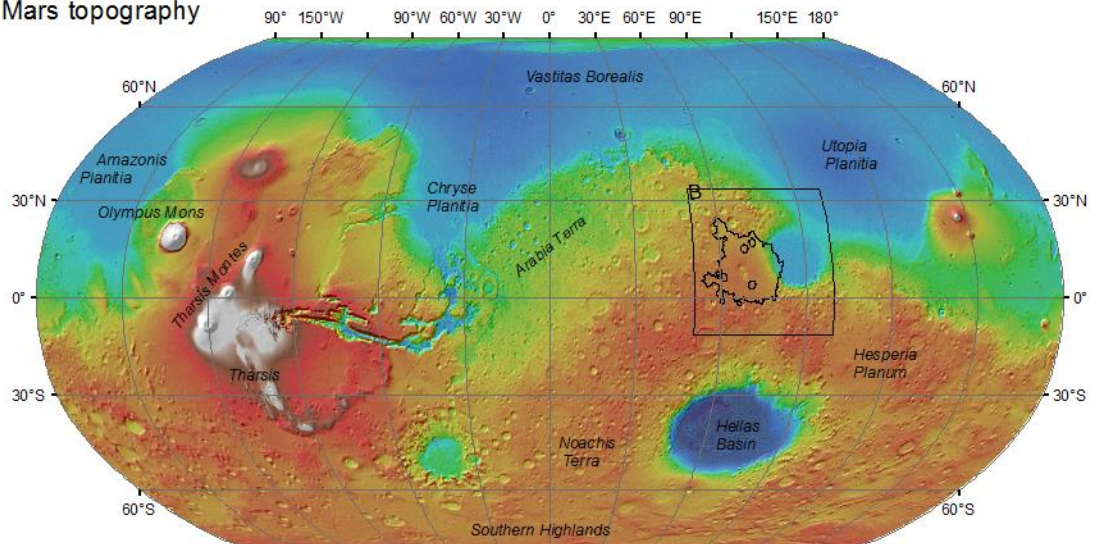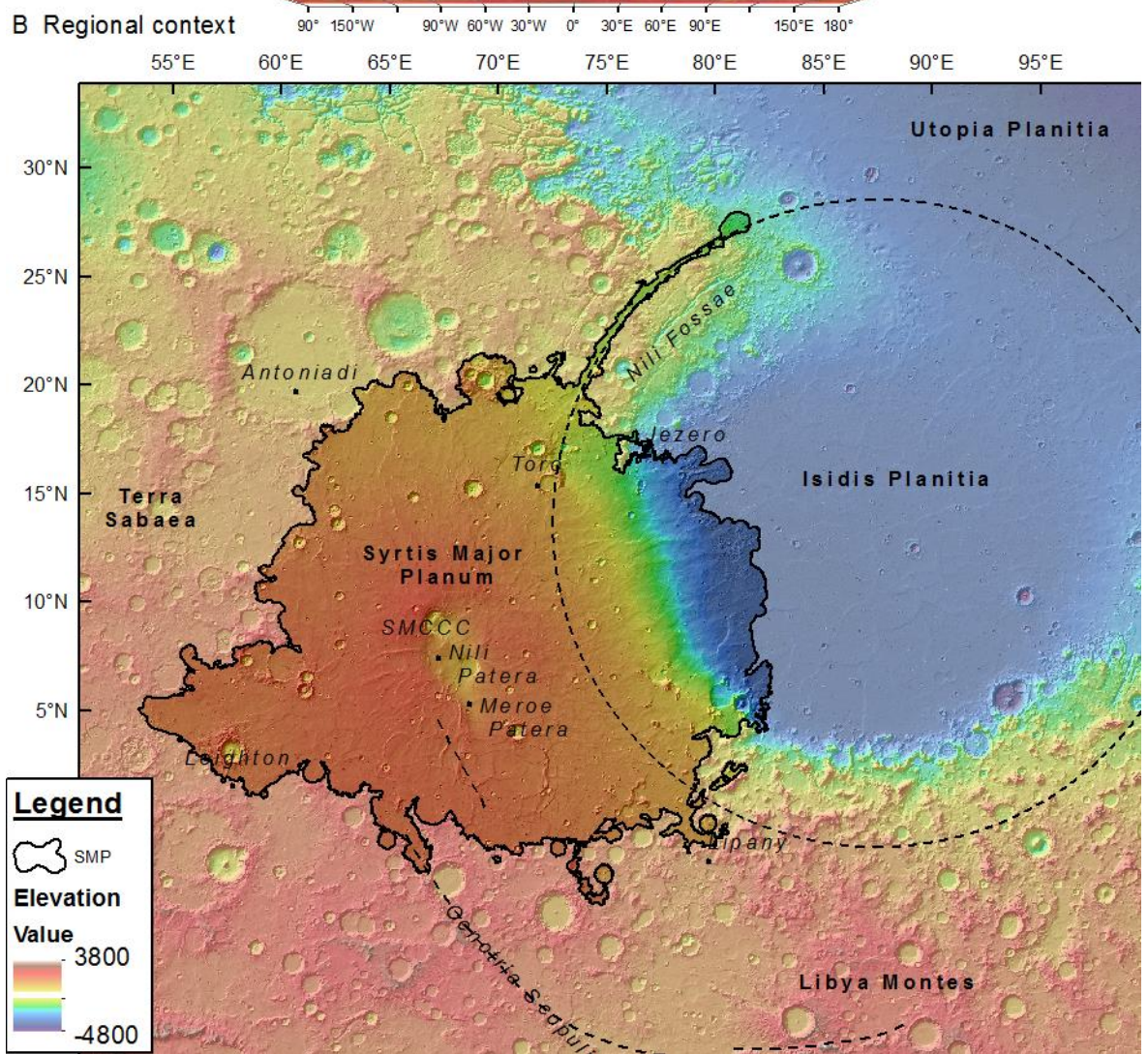
Figure 1.1

The regional context of Syrtis Major Planum on Mars. The unshaded regions shows Syrtis Major Planum. Dotted lines show the arc of Nili fossae, the Isidis basin rim and the Oenotria Scopuli fault zone. MOLA elevation shaded outside Syrtis Major Planum to highlight the Planum.

Syrtis Major Planum is important because it represents the best-exposed example of Hesperian plains volcanism on Mars. Additionally, areas around Syrtis Major contain abundant clays, carbonates [*Ehlmann et al.*, 2008], and serpentinite [*Ehlmann et al.*, 2010; *Ehlmann and Mustard*, 2012] dating from the possibly more habitable Noachian period of martian history. These materials are targets for the NASA 2020 Rover, making sites that contain them leading candidates for the final destination of the mission. Such materials may have also influenced the development of Syrtis Major, as it has been emplaced through and onto these terrains, possibly providing a source of heat to sustain a niche of subsurface habitability.

Because of the strong winds and low levels of surface dust over the planum, there has been a significant number of studies of the region that utilise reflectance spectrum data. These show that Syrtis Major Planum hosts the most diverse range of mineral compositions on the otherwise basaltic planet. The plains of the volcano are basaltic to basaltic komatiite [*Rampey and Harvey*, 2012], but within the structurally unique central caldera complex [*Plescia*, 2004] there is evidence for more evolved, dacitic lava compositions [*Christensen et al.*, 2005]. There are also mounds of silica here, interpreted to be hydrothermal deposits directly associated with volcanic heat sources [*Skok et al.*, 2010a].

These and many other individual locations associated with Syrtis Major have been studied in detail (chapter 2.3). However, since the Viking era [*Schaber*, 1982] and the well documented Mars Global Surveyor data analysis [*Hiesinger and Head*, 2004], there has been no detailed study drawing on the currently available high resolution data sets from Mars Odyssey [*Saunders et al.*, 2004], Mars Express [*Schmidt*, 2001] and Mars Reconnaissance Orbiter [*Zurek and Smrekar*, 2007]. This study puts all these important discoveries in context with the volcanological perspective on the formation of Syrtis Major Planum, and builds a holistic understanding of how the Planum has evolved.

1.2 Aims and Objectives

1.2.1 Aims

The aim of this thesis is to understand the formation and development of Syrtis Major Planum. The primary concern is how the volcanic plains of Syrtis Major Planum developed and, within that, to articulate the story of caldera development in the centre of the planum. Secondly, the thesis is concerned with how Syrtis Major Planum fits into the global and regional geological histories, and to what extent developing an understanding of this planum can aid our understanding of both other martian volcanic plains volcanoes, and large igneous provinces on Earth.

1.2.2 Objectives

To achieve the aims stated above I identified the following objectives:

(1) Create a map of Syrtis Major Planum in which the lava shield is divided on a morphological basis. This will identify the different styles of volcanic activity at Syrtis Major Planum, and address the distribution of volcanism across the planum. To complete this objective I will draw on terrestrial analogues, mainly the Afar region of Ethiopia, to make comparative studies in a volcanic desert environment on Earth.

(2) Develop a stratigraphy using both the map (objective 1) and impact crater size-frequency statistics obtained for various units within the map area. This is needed to identify the timing of the sequence of events forming Syrtis Major Planum, and to understand how the planum has developed relative to other events in martian history.

(3) Create 1 or more, high resolution maps to understand the magmatic and tectonic development of Nili Patera, Mereo Patera and the central caldera complex. This objective uses higher resolution basemaps to study how these areas, known to host a range of scientifically important locations, (e.g. Christensen et al. [2005] and Skok et al. [2010a]) fit into the development of the whole planum.

1.2.3 Methodology

To complete these objectives, I will employ a geomorphological approach, with a focus on documenting the volcanic landforms to understand the geology of Syrtis Major Planum. Geomorphology is the process whereby the shape and appearance of the landscape are examined to de-convolve the range and influence of the different process that has created the landscape.

To do this effectively, many data sets and many different ways of looking at the landforms are employed. From these different perspectives, a working hypothesis is developed, which is tested by exploring further whilst collecting more data. With this data, the current working hypothesis is reevaluated and then altered if needed. To help understand the processes that formed the landscape, planetary geomorphology uses terrestrial analogue landforms. The logic of this is that if known landforms (e.g. hummocky ground on a 5-10 m length scale), known contexts (e.g. slopes on the side of a volcano) and known processes (e.g. inflation of lava lobes) are compared to similar landforms in similar contexts on Mars, then a similar process can be inferred.

From the available data and analogues, the most consilient lines of evidence are drawn together to make the best working hypothesis and the most parsimonious solution for how the landform evolved in the landscape. The greatest challenge to this methodology is convergence of form. This occurs when two (or more) landforms look similar, but are formed by different processes. For example, layering in an outcrop could have formed through sedimentary or volcanic processes, yet it is hard to distinguish this without in-situ observations. To mitigate against this, many lines of evidence must be drawn together and the context of a landform with others in the landscape considered. However, in many cases more than one good working hypothesis must be considered valid (although one might be preferred) until new information is available. In the far future, perhaps in-situ studies will validate or refute the hypotheses developed in this thesis, but in the meantime, the conclusions I come to here reflect the parsimonious synthesis of observations and interpretations available for Syrtis Major Planum.

1.3 Thesis Structure

This thesis is structured around the results drawn from the mapping efforts that are shown as map sheets 1 and 2. **Chapter 1** provides an introduction and outlines the science questions. In **Chapter 2,** background information is presented pertinent to the three thematic chapters which present the main results of the thesis. This chapter provides an overview of volcanism on Mars, details previous studies, and summarises the key Syrtis Major Planum studies made to date. It goes on to describe elements of physical volcanology relevant to the interpretation of the observations of Syrtis Major Planum. **Chapter 3** describes the data and methods used to compile the two map sheets and the three thematic chapters.

Chapters 4, 5 and 6 are the "results" chapters. **Chapter 4** describes and discusses elements from map sheet 1 relevant to the changes in style and distribution of volcanically emplaced surfaces across Syrtis Major Planum. The results of this chapter build a stratigraphy of the volcanic architecture of Syrtis Major Planum. Chapters 5 and 6 are concerned with Nili Patera and Meroe Patera respectively. **Chapter 5** presents the geological history of Nili Patera. This chapter was published as an article in the peer-reviewed "Journal of Geophysical Research (planets)" and draws on map sheet 2. **Chapter 6** presents the geological history of Meroe Patera. It draws on the mapping of map sheet 1 and the published interpretations from Nili Patera to understand the development of Meroe Patera and its relationship with the central caldera complex.

The results of chapters 4, 5 and 6 are each discussed within the context of those chapters. **Chapter 7** connects the results from these three chapters by considering their implications with respect to one another. This chapter draws together the stratigraphy detailed in chapters 4, 5 and 6, along with the non-volcanic elements on map sheet 1, to summarise the geological history of Syrtis Major Planum. The key conclusions of this thesis are presented in **Chapter 8,** alongside a summary of the work that has been completed, and a final section outlining further avenues of investigation that could be undertaken to build on the work performed here.

Chapter 2: Background

2.1 Introduction, volcanoes and Mars

This background chapter is divided into three sections. Section 2.1 briefly introduces volcanism on terrestrial planets and the early evolution of the martian crust, and I review the impact of the martian environment on volcanism and on the composition of martian magmas. In Section 2.2 I review volcanism on Mars and the different styles of volcanic activity through time. Finally, in section 2.3 I review in detail the previous work carried out on, and pertaining to, the evolution of Syrtis Major Planum.

2.1.1 Volcanoes and terrestrial planets

Fundamentally, a volcano is a surface expression of heat advection through a planetary crust. During the process of planetary accretion, radiogenic and gravitational potential energy is concentrated within a planet. This concentration of energy then equilibrates with interplanetary space through the lifetime of the planet. Once a solid crust has formed, heat transfer through that crust becomes limited to locations where, through various processes, low-density molten rock breaks though the crust. Once on the surface the molten rock cools to a solid, forming a new patch of crust and transferring the energy it carried into space. Evidence for this process has been observed on all terrestrial planets as well as on many smaller planetary bodies in the Solar System. Whilst the fundamental driving forces remain the same for all planetary bodies, the volcanism expressed on each differs as a reflection of that planet's properties: fundamentally this is how much heat it has to lose, i.e. how massive the planet is, which is proportional to the cube of its radius and its initial inventory of radiogenic elements which depends on its early accretion history.
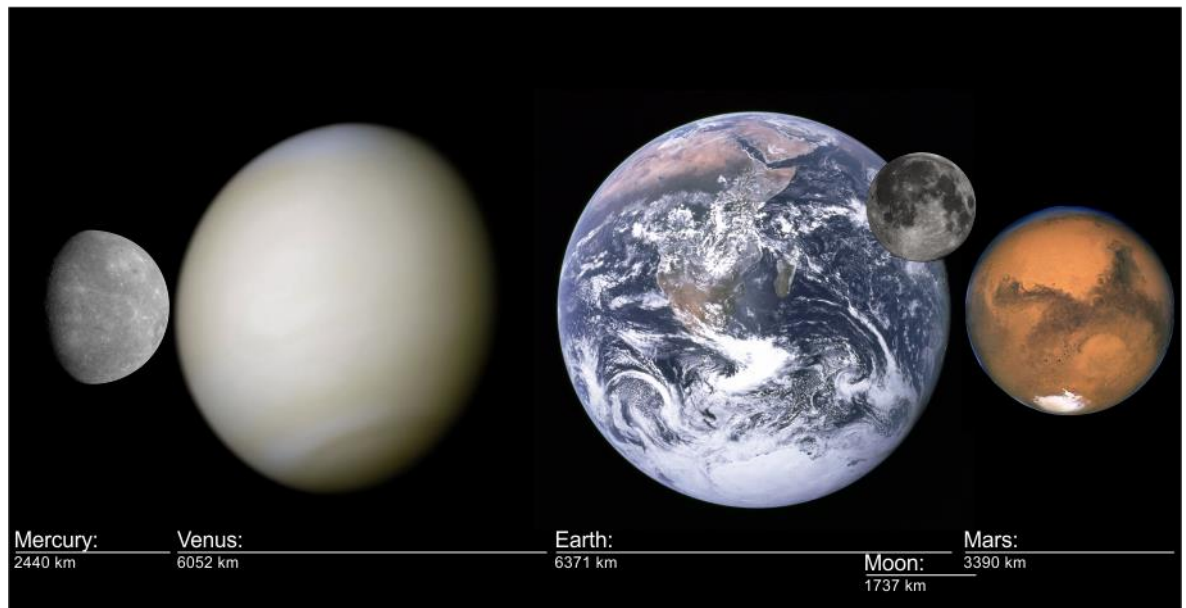
Figure 2.1

A size comparison of silicate planetary bodies in the inner Solar System: Mercury; WAC mosaic from 2009:(https://commons.wikimedia.org/wiki/File:MESSENGER_first_photo_of_unseen_side_of_mercury.jpg); *Venus; real colour from Mariner 10 in 1974* (http://www.astrosurf.com/nunes/explor/explor_m10.htm); *Earth seen by Apollo 17 in 1972* (http://grin.hq.nasa.gov/ABSTRACTS/GPN-2000-001138.html); *the full Moon in 2010* (https://commons.wikimedia.org/wiki/File:FullMoon2010.jpg); *and Mars in 2003 from the Hubble Space Telescope* (http://hubblesite.org/newscenter/archive/releases/2005/34/image/j/).

Small bodies such as Mercury and the Moon (Figure 2.1) had a smaller gross initial internal heat budget than Earth or Venus and have cooled to the point where there are no longer any major volcanic events. There were massive extrusive events early in their history, followed by minor explosive volcanism [*Schultz and Spudis*, 1983; *Thomas et al.*, 2014]. On larger bodies such as Venus, Earth and Mars (Figure 2.1) there is a sufficiently large internal heat budget for the surface of the planet to maintain volcanism until relatively recently [*Wilson*, 2009]. For Earth, the crust is continually recycled through plate tectonics [*Tuzo*, 1963], which efficiently advects heat to the surface. The majority of well-preserved volcanic structures are related to this process and do not record the majority of the planet's history. On Venus there appears to be a 'one plate, stagnant lid' regime [*Solomatov and Moresi*, 1997; *Breuer and Spohn*, 2003]. Here, however, the entire surface has been, or still is, episodically resurfaced [*Strom et al.*, 1994], and only the most recent volcanic processes are preserved. Mars, however, is of an intermediate size (Figure 2.1). It is large enough to have maintained volcanism throughout most of its history [*Carr*, 1973; *Greeley*

and Spudis, 1981; *Carr and Head*, 2010; *Tanaka et al.*, 2014b] but lacks sufficient internal heat to have resurfaced its entire surface. Consequently, Mars preserves a range of volcanic structures charting a greater range of planetary thermal evolution than either the smaller moons or larger terrestrial planets.

2.1.2 Early evolution of the martian crust

The crust of Mars (like that of Earth) is dominated by a bimodal elevation distribution caused by a structure known as the crustal dichotomy [*Hartmann*, 1973; *Smith and Zuber*, 1996]. Mars is divided into the southern highlands and the northern lowlands (Figure 2.2). The crust of the southern highlands is thicker and older, hosting numerous impact craters of all sizes, whereas that of the northern lowlands is thinner and the surface is younger with significantly fewer impact craters [*Smith and Zuber*, 1996; *Zuber et al.*, 2000; *Neumann et al.*, 2004; *Wieczorek and Zuber*, 2004; *Tanaka et al.*, 2014b]. The boundary between these areas is not as sharply defined [*Frey et al.*, 1998], nor as well understood, as the crustal dichotomy of Earth. The dichotomy on Earth is a division between the thick, high-standing continental crust, and the thin, low-lying oceanic crust caused by an endogenic process – the cycling of tectonic plates [*Tuzo Wilson*, 1963]. On Mars, however, the bimodal distribution is less distinct or well defined and its origin is not clear [*McGill*, 2000; *Zuber et al.*, 2000; *Carr and Head*, 2010]. There are competing hypotheses for the genesis of the crustal dichotomy.

Figure 2.2 (opposite)

*The planet Mars: (a) seen in visible Viking mosaic; (b) martian topography gridded from the MOLA instrument [*Smith et al.*, 2001] blue is low and red and brown is high elevations; and (c) geological map of Mars, 2014 [*Tanaka, et al.*, 2014a].*

A Viking
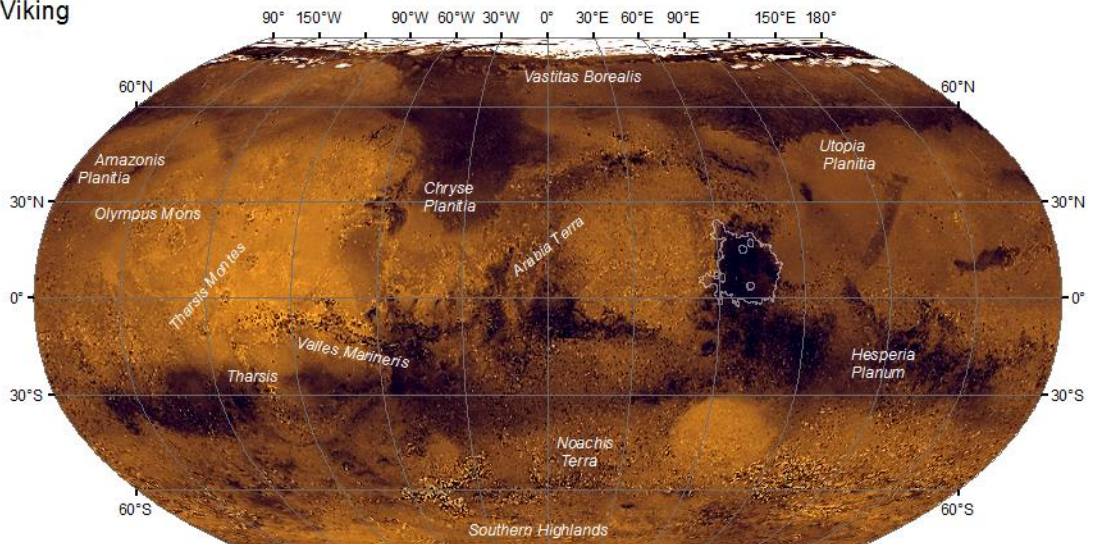
B MOLA topography
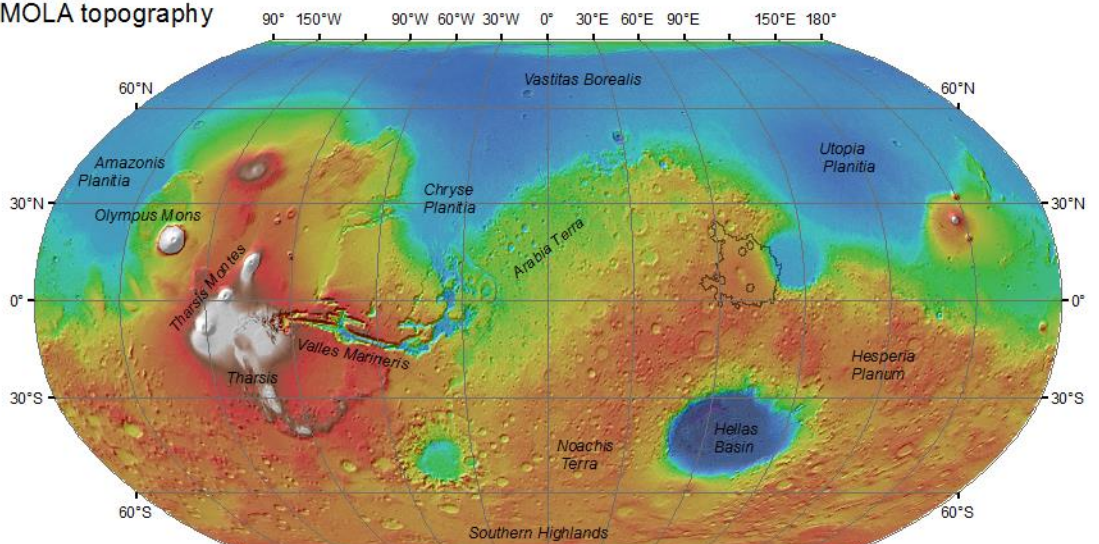
C 2014 Geology
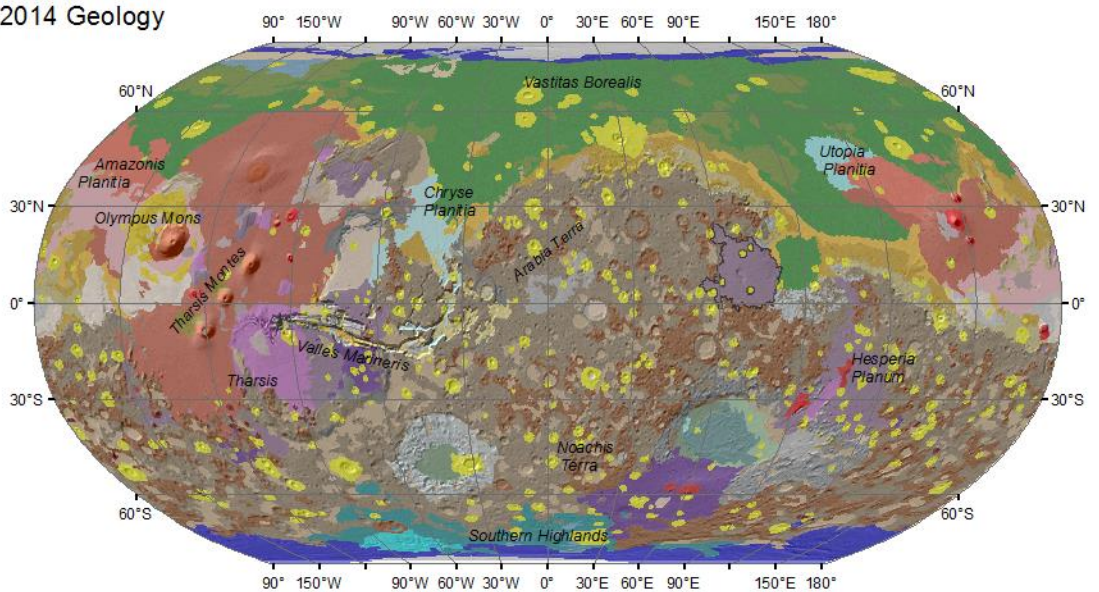
Firstly, an endogenic origin has been suggested [*Spohn and Schubert*, 1983; *McGill and Dimitriou*, 1990; *Zhong and Zuber*, 2001], in which the martian mantle was a single convection cell, stripping material from the underside of the northern lowlands and underplating the southern highlands. Here, the dichotomy has also been considered in terms of putative plate tectonics [e.g. Sleep, [1994], although this is not plausable because Noachian aged deposits underly the surface of the amazonian northern plains precluding recycleing of oceanic crust.

The second hypothesis for the genesis of the Martian crustal dichotomy is an exogenic process, such as a giant impact event or a series of giant impact events [*Wilhelms and Squyres*, 1984; *Frey and Schultz*, 1988; *McGill and Dimitriou*, 1990; *Andrews-Hanna et al.*, 2008]. In this case, one (or more) giant impact events, early in the planet's history, evacuated significant volumes of material from what is now the northern hemisphere, with subsequent gravitational collapse forming a thinner, low-lying crust. This is supported by the geometry of the dichotomy fitting to a number of circular structures and gravity data showing an area of thinned crust under the northern part of the Tharsis rise completing the circular outlines and regions of thinned crust caused by hypothetical impact basin formation.

Although the second of these hypotheses appears most consistent with the evidence, and whilst the evidence for postulated plate tectonic is not compelling, the evolution of the Martian interior has driven the surface volcanism. Furthermore, the interaction between melting in the mantle and the crust after the dichotomy and other basin-forming impacts has moderated the surface expression of mantle melting, producs the range and distribution of volcanism we can observe today (Figures 2.3 and 2.4).
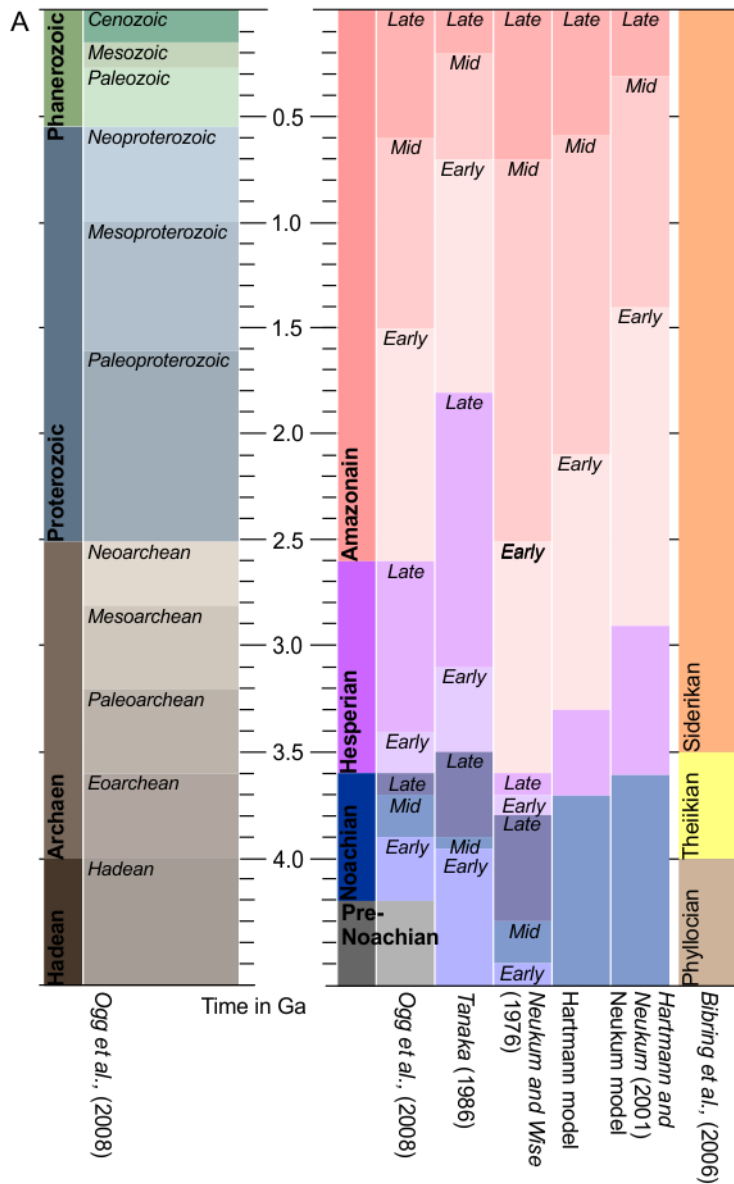
Figure 2.3

Figure showing a comparison between the terrestrial geological timescale (a) and times scales for Mars by different authors adapted from Van Gasselts and Neukum [2011]. (b) is a schematic showing geological activity as a function of time on Mars; adapted from Carr and Head [2010]. This history shows the major surface modification processes and their relative intensity with time.
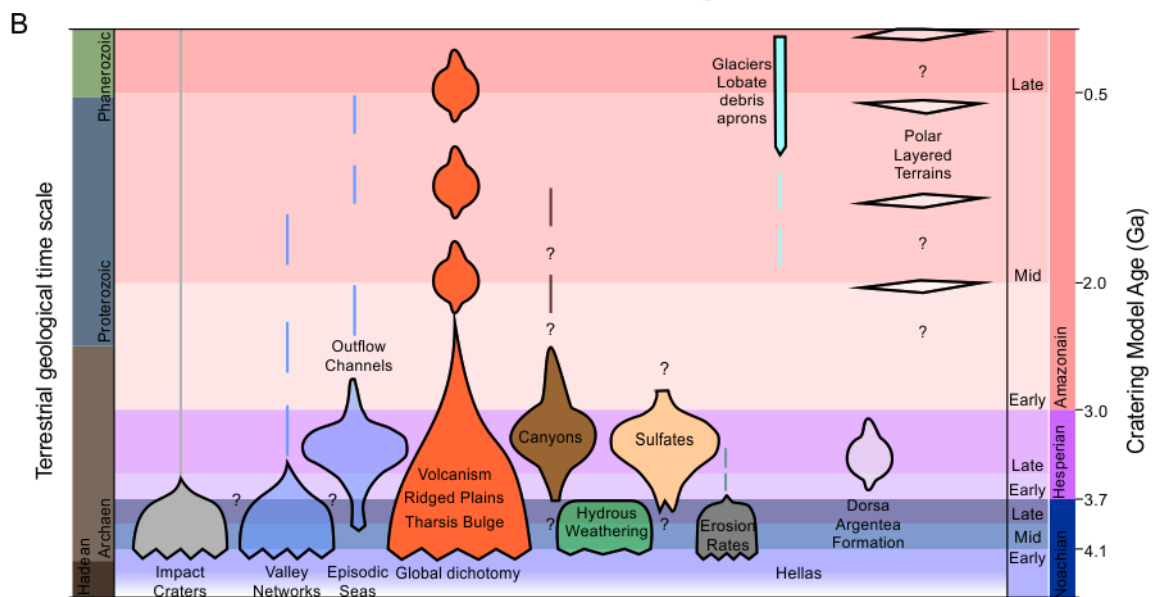
2.1.3 Physical volcanology on Mars

The environment of Mars is different from that of Earth; consequently, so too is the surface expression of volcanism. The two most important factors that result in the differences in volcanic processes and landforms between Earth and Mars are the lower gravity and lower atmospheric pressure of Mars. The theoretical implications of the change in these parameters between Earth and Mars are discussed in detail in Wilson and Head [1994; and references therein]. Here, the major implications are summarised (Table 2.1).

The gravity on Mars (~3.7 m s^{-2}) is only 38 % of that of the Earth (~9.8 ms^{-2}). Because of this, gravity-driven processes (such as buoyancy) operate less strongly on Mars. This means that a larger density contrast is needed to have the same uplift force on Mars compared to Earth. It also means that the Martian lithospheric density profile increases with depth more slowly than on Earth. The result of these two factors is that when melt successfully ascends and erupts on Mars, it will have formed a larger diapir and formed magma reservoirs at deeper depths (because neutral buoyancy is deeper) than on Earth. Consequently, when these larger and deeper bodies do erupt they form dikes and vents increased in width relative to the theoretical same melt body in the terrestrial environment. When magma does reach the surface, however, the surface textures of lava flows will not be significantly affected [as noted by Wilson and Head, 1994], and neither will the rate of cooling. However, because of the enhanced dyke width and effusion rates, a cooling-limited lava flow could extend an estimated six times further before freezing. Furthermore, supply-limited flows are more likely because magma reservoirs, although larger, will drain faster.

Table 2.1 The effect of the Martian environment on volcanism.

Global parameters	Magnitude compared to Earth	Factor
Gravity	lower	0.38
Atmospheric pressure	much lower	
Buoyancy forces	slower	
Density profile	shallower	
Process/Landform	**Magnitude compared to Earth**	**Factor**
Magma storage		
Diapir	larger	
Magma reservoir	deeper	x4
Dikes	wider	x2
Magma ascent		
Effusion rate	higher	x5
Feeder dikes and vents	wider	
Volatile nucleation	deeper	
Magma disruption	deeper	
Lava flows		
Flow cooling rate	no change	
Surface textures	no change	
Cooling-limited flows	longer	x6
Explosive eruptions		
Grain size distribution	finer grained	x10
Plinian cloud, height	higher	x5
Plinian cloud, shape	the same	
Height/deposit size ratio	the same	
Strombolian/Hawaiian cones	wider spread of fine particals	
Cone, deposits	broader	
Cone, width	wider	x2
Cone, height	lower	0.25
Cone, central craters	wider	x5
Fountain-feeding pyroclastic flow	higher	>2x
Eruption speed	greater	x1.5
Explosive deposits		
Pyroclastic flows	more likely	
flow distance	further	~3x
Fall deposit, grain size	finer	100x
Fall deposit, size	wider	
Basaltic Plinian eruptions	more common	

The second factor is the reduced atmospheric pressure (although it should be noted that the atmosphere of Mars may have been denser in the past [*Carr and Head*, 2010]). The result of this, combined with the shallower density profile, is that the nucleation of volatiles dissolved in the magma will happen at a deeper depth on Mars than it would on Earth. Furthermore, the fragmentation of magma is enhanced when it reaches the surface, resulting in smaller particles. Because of these factors, [*Wilson and Head*, 1994] consider explosive eruptions more likely on Mars and in particular note that basaltic Plinian eruptions, rare on Earth, should have been relatively common on Mars. Wilson and Head [1994] also find the height of pyroclastic fountains and Plinian eruptions to be two and five times higher respectively. During these eruptions, they find the grain size distribution to be an order of magnitude smaller. The smaller particle are more mobile in the atmosphere and this will result in deposits spread over a significantly larger area, and fractionated such that fall deposits may have a grain size distribution with a mean two orders of magnitude smaller than that commonly found on Earth.

2.2 The volcanoes of Mars

Volcanism and volcanic surfaces on Mars are distributed widely across the surface and occurred throughout the history of the planet (Figures 2.4 and 2.5). There is a huge range in size of volcanic constructs, from the largest volcano in the Solar System (by height), Olympus Mons, and (by volume, Alba Mons (Figures 2.4c and 2.7) to sub-kilometre cones [*Carr et al.*, 1977; *Frey and Jarosewich*, 1982; *Hodges and Moore*, 1994; *Plescia*, 2004]. The style and distribution of volcanism have changed with time [*Carr*, 1973; *Carr et al.*, 1977; *Greeley and Spudis*, 1981; *Plescia*, 2004; *Werner*, 2009; *Carr and Head*, 2010] from wide flat edifices in the Noachian-Hesperian to steeper and more spatially concentrated shield volcanoes in the Amazonian.

Here I have broadly divided volcanoes on Mars into the following categories and follow the classification of Greeley and Spudis [1981].:

- **Plains-forming volcanoes** with both simple (Hesperia Planum) and complex (many, Tharsis) flow fields (Figure 2.6a and b). These are perhaps most similar to Syrtis Major Planum.

- **Central volcanoes**. This category includes large shields (Arsia Mons), smaller domes (Tharsis Tholus) and Highland Patera (e.g. Tyrrhena Patera; Figure 2.6c, d and 2.7a).

- **Small-scale volcanoes**. Not widely observed until the advent of higher-resolution data sets.

2.2.1 Plains-forming volcanism (Noachian–Hesperian)

The earliest phases of volcanism, after the stabilisation of the crust and the formation of the Hellas basin, (~4.0–3.6 Ga) were (i) around the rim of the Hellas basin in the areas known as the Circum-Hellas Volcanic Province (CHVP) [*Werner*, 2009; *Williams et al.*, 2009a] and (ii) in the Tharsis area [*Peterson*, 1978; *Werner*, 2009; *Xiao et al.*, 2012; *Rogers and Nazarian*, 2013].

2.2.1.1 Malea Planum

The earliest plains-forming volcanoes clearly exposed (i.e. not buried by later Tharsis deposits) are in Malea Planum. Malea Planum is the older part of the CHVP, located on the southwest rim of Hellas. The Planum consists of the Peneus Patera, Malea Patera, Pityusa Patera (Figure 2.4a) and Amphitrites Patera, although this last example is younger, and more like a highland patera. The three older paterae of Malea Planum are flat caldera-like depressions. These paterae lack positive-relief edifices and only have a weak gravity anomaly [*Williams et al.*, 2009a]. Surrounding these paterae is a flat plain. This totally obscures the rim of the Hellas impact structure [*Head and Pratt*, 2001] to its north, and is itself obscured by polar deposits to the south. The flat, caldera-like paterae of Malea Planum are dated to ~3.8 Ga in the late Noachian, whilst Amphitrites Patera is younger, dated to ~3.6 Ga, although these dates are within error of each other [*Williams et al.*, 2010b]. It was also at this time that Malea Planum plains formed (3.4–3.6 Ga), as did Hesperia

Planum (~3.4–3.6 Ga), a volcanic plains region to the east of Hellas, Promethei Terra (3.5–3.7 Ga), and the eastern Hellas basin floor (3.6–3.8 Ga) [*Williams et al.*, 2010b].

These regions show contemporaneity with smaller volcanic structures that support their volcanic origin, although in many regions small-scale volcanic structures are not observed, leading to interpretation as being formed of 'simple' rather than 'complex' flows in volcanic plains [*Greeley and Spudis*, 1981]. In Malea Planum, small-scale volcanic structures are observed, so this region is a 'complex flows' volcanic plains example [*Greeley and Spudis*, 1981; *Hiesinger and Head*, 2004]. Williams et al., [2009] suggests that Malea and Pityusa Patera (and possibly Peneus) and associated plains are equivalent to terrestrial giant calderas (e.g. Yellowstone). These paterae erupted large volumes of volcanic materials over a wide area suggests volcanic products as low viscosity lava flows [*Rampey and Harvey*, 2012] or ignimbrites [*Williams et al.*, 2009a]. The edifices most closely associated with the plains volcanism are ~1000 km across with only ~1 km of relief, except where they impinge on the Isidis basin floor [*Hiesinger and Head*, 2004; *Plescia*, 2004].

Figure 2.4 (opposite)

Areas of Mars mapped as volcanic in origin by Tanaka et al. [2014a]. Noachian volcanic units (>3.7 Ga): Noachian volcanic edifice unit (Nve), and the Late Noachian volcanic unit (lNv) . Hesperian volcanic units (3.7 Ga–3 Ga); Hesperian volcanic edifice unit (Hve), Early Hesperian volcanic unit (eHv), and the Late hesperian volcanic units (lHv)Amazonian volcanic units including large volcanic plains dated as Amazonian/Hesperian(<3 Ga); Amazonian volcanic edifice (Ave), Amazonian and Hesperian volcanic Unit (AHv), Amazonian volcanic unit (Av), and the Late Amazonian volcanic unit (lAv).
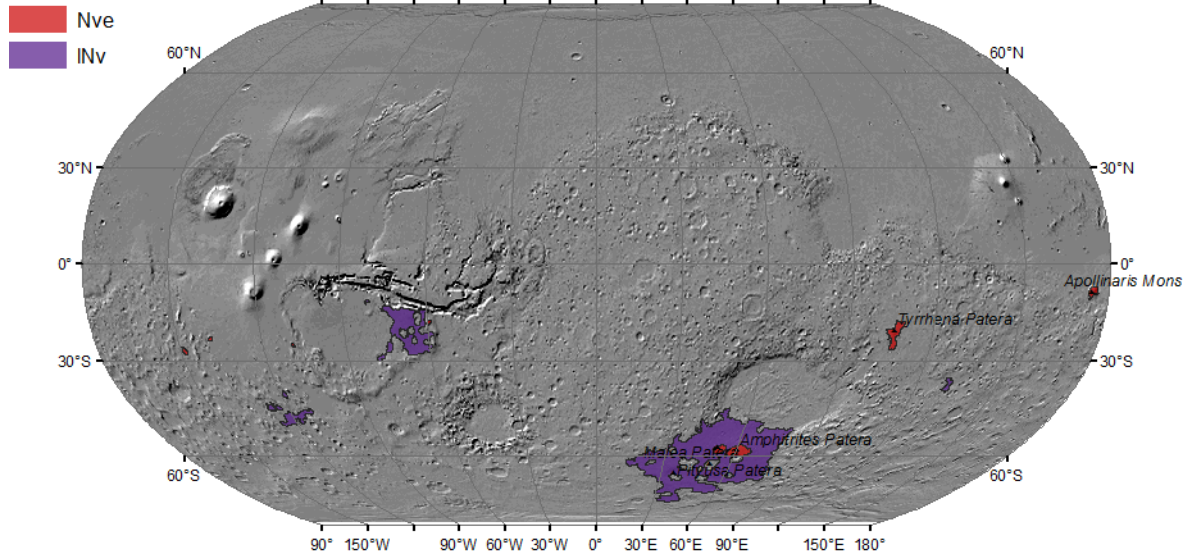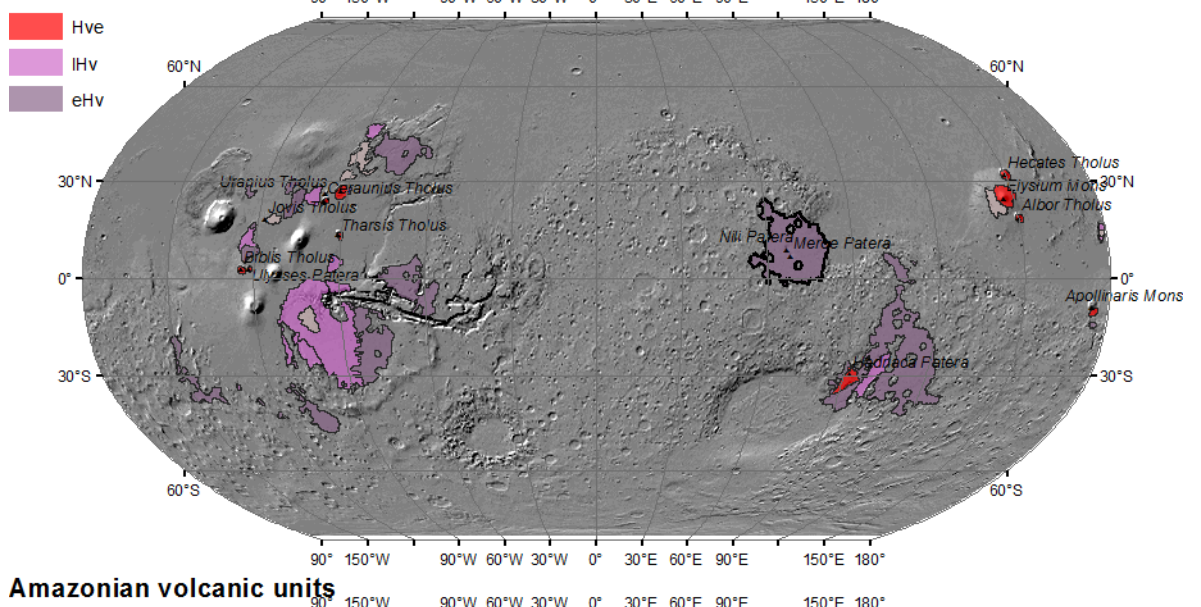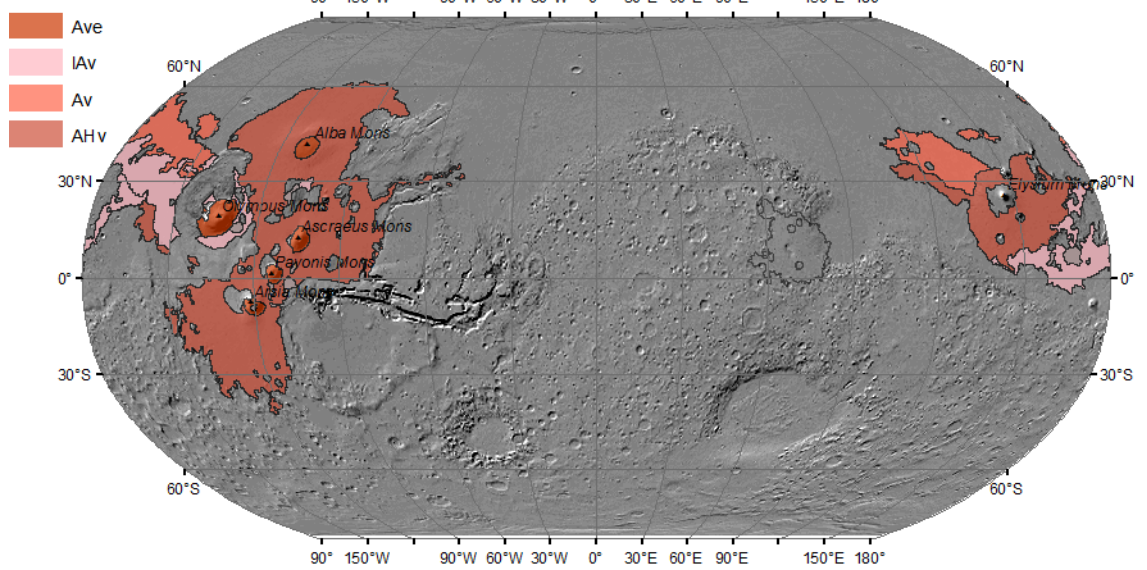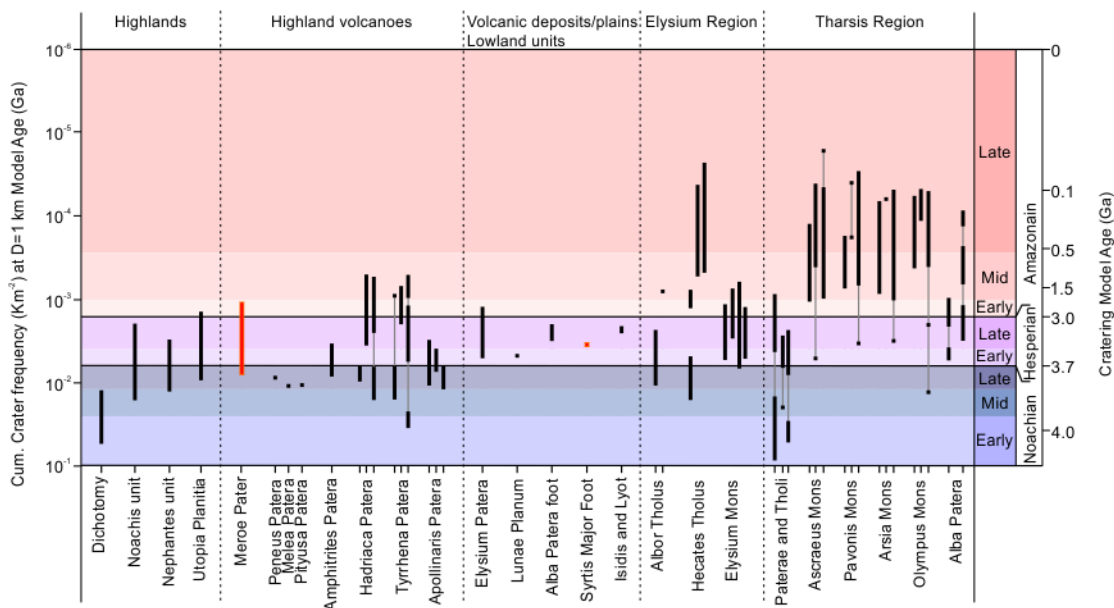
Figure 2.5

*A summary of crater frequencies (left-hand scale) and derived model ages (right-hand scale) for most of the volcanic constructs on Mars and key plains units. Adapted from Werner et al. [2009]. Age ranges marked in **red** directly relate to Syrtis Major Planum.*

2.2.1.2 Hesperia Planum

To the northeast of Hellas is Hesperia Planum (Figure 2.6b). This area is the type locality for the start of the Hesperian period (3.7 Ga). This planum is considered to be formed of flood lavas [*Greeley and Spudis*, 1981; *Ivanov et al.*, 2005]. However, more recent high-resolution images open the possibility of a layered sedimentary component of lacustrine or ignimbrite origin [*Gregg and de Silva*, 2009]. The volume of the Hesperia Planum is comparable to the Columbia River basalt group [*Ivanov et al.*, 2005] and it is cross-cut by numerous patterns of wrinkle ridge structures [*Carr*, 1973; *Greeley and Spudis*, 1981; *Plescia and Golombek*, 1986; *Raitala*, 1988]. At Hesperia Planum, the ridges reflect crustal shortening, most probably of coherent lava over a substrate with less internal strength [*Raitala*, 1988]. On the Planum, and other similar volcanic plains, circular ridge patterns have been related to thin deposits of lava draping the buried rims of impact craters. The older parts of the ridge pattern reflect shortening on regional crustal faults, reactivated in the ridged surface of the Planum. The more recent ridge patterns found parallel or perpendicular to the boundaries of the Planum are a response to a decrease in internal volume in and under the Planum [*Raitala*, 1988]. In summary, Hesperia Planum shares many features with

the volcanic plains of Syrtis Major Planum so interpretations about Syrtis Major volcanic plains

have a bearing on the formation of Hesperia Planum.
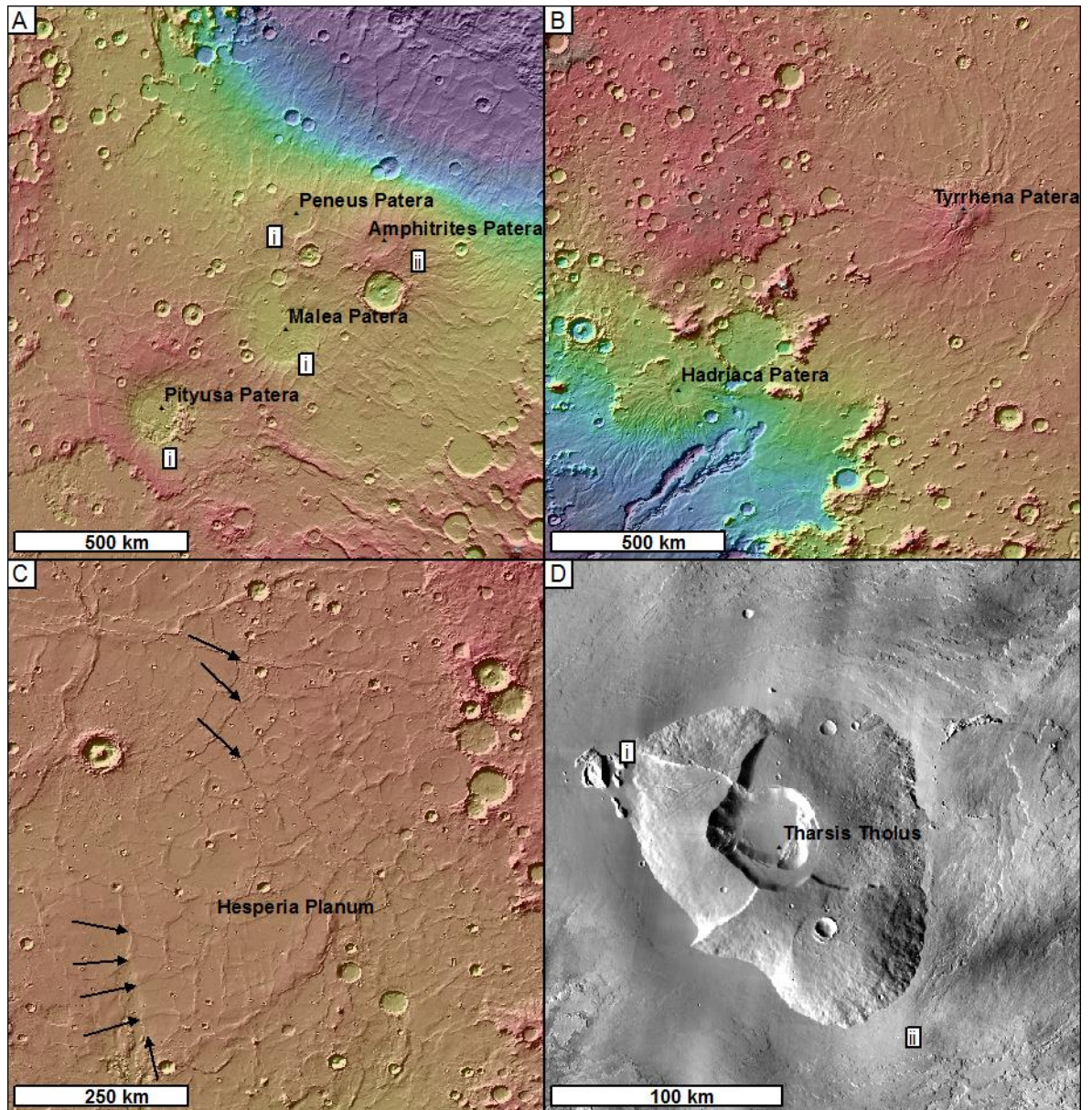
Figure 2.6 (opposite)

Different types of volcano on Mars. (a) Malea Planum southwest of the Hellas basin showing the transition from (i) flat caldera-like edifices to (ii) highland patera (colourised MOLA hill-shade). (b) Highland patera volcanoes (colourised MOLA hill-shade). (c) Hesperia Planum; arrows point to wrinkle ridges (colourised MOLA hill-shade). (d) The 'Dome' Tharsis Tholus a small central volcano (THEMIS daytime mosaic).

2.2.1.3 Syrtis Major Planum

Syrtis Major Planum fits into the global stratigraphy in the early to mid-Hesperian (Figures 2.2, and 2.3) [*Schaber*, 1982; *Hiesinger and Head*, 2004]. Syrtis Major Planum is made up of a wide, low-relief plain and a central caldera depression hosting two calderas, Nili Patera and Meroe Patera [*Schaber*, 1982; *Hiesinger and Head*, 2004]. Topographically, Syrtis Major Planum is most similar to the late Noachian edifices to the south west of the Hellas basin (Figure 2.6a) [*Plescia*, 2004; *Williams et al.*, 2009a], but has a diverse range of igneous compositions not seen at any other edifice on Mars (e.g. Mustard et al., [1993], Christensen et al., [2005] Wray et al., [2013]).

2.2.1.4 Changes in edifice style

After the plains-forming patera in the west of Malea Planum, there was a subtle shift in the style of emplacement of volcanic centres. There was a progression to an edifice-building, highland patera style. These youger edifices include Amphitrite Patera on the eastern Hellas rim, Tyrrhena Patera and Hadriaca Patera to the east of Hellas and Apollinaris Patera south of Elysium Planitia (Section 2.2.2.1; Figures 2.4b and2.6c).

The highland patera edifices in the CHVP also host evidence of more friable, less consolidated deposits. This is expressed by channelling and other erosional features in the flanks of the edifices [*Greeley and Crown*, 1990; *Crown et al.*, 1992; *Crown and Greeley*, 1993; *Gregg and Farley*, 2006; *Williams et al.*, 2007]. Also, the surface of the eastern-most part of Malea Planum paterae where Amphitrites Patera and Peneus Patera occur, is dominated by scalloped and pitted terrain, suggesting the whole of the Malea Planum has been subjected to cryotic processes and has a high ice content [*Williams et al.*, 2010a]. This in turn suggests that alteast the uppermost few metres of the surface are not solid bedrock. However, Malea Patera and Pityusa Patera have no channelled flanks, no scalloped and pitted terrain, and lack the 'softened' appearance of their surfaces. This morphology is indicative of a surface made of a stronger and less erodible material [*Williams et al.*, 2009a]. This again shows the progression with time and space from 'simple flows' volcanic plains to the highland patera style volcanoes.

2.2.2 Central volcanoes (Hesperian–Amazonian)

2.2.2.1 Highland paterae

Highland paterae are ash shield volcanoes [*Greeley and Spudis*, 1981] which are found in the southern highlands of Mars. They formed in the Hesperian (Figures 2, 4 and 5) in association with volcanic plains [*Carr*, 1973; *Greeley and Spudis*, 1981; *Greeley and Crown*, 1990; *Crown and Greeley*, 1993]. Highland paterae are hundreds of kilometres in diameter but only have a few (1–3) km of relief [*Plescia*, 2004]. Positive gravity anomalies are found at Tyrrhena, Hadriaca, and Amphitrites Paterae, perhaps indicative of dense magma bodies below the surface differentiating them from older edifices [*Williams et al.*, 2009a]. Tyrrhena and Hadriaca Paterae have low slopes, well-channelled flanks, and smooth caldera floors (at tens of metres/pixel scale), indicative of volcanoes formed from poorly consolidated pyroclastic deposits that have been modified by fluvial and aeolian erosion and deposition [*Gregg and Farley*, 2006]. Modelling work investigating the possible origin of volatiles needed to generate pyroclastic deposits [*Greeley and Crown*, 1990; *Crown and Greeley*, 1993] support groundwater interaction with magma as a driving force for the construction of the edifice.

2.2.2.2 Domes

The next youngest type of volcanic construct have been referred to as **domes** [*Greeley and Spudis*, 1981; *Plescia*, 2004]. These are relatively small [*Greeley and Spudis*, 1981; *Plescia*, 2004], central-vent volcanoes formed in the Hesperian and part of the Amazonian (Figures 2.4 to 2.7) [*Plescia and Saunders*, 1979; *Plescia*, 1994; *Werner*, 2009]. These volcanoes are found in and around the Tharsis region and on the flanks of Elysium Mons. They are around 100 km in diameter and have a few (2–5) km of relief [*Plescia*, 2004].

In both the Tharsis and Elysium regions, these volcanoes are partially buried by later emplacement of volcanic plains and by more recent flows from larger volcanoes. Domes have a range of morphologies with various degrees of complexity. Jovis Tholus is the simplest, consisting of a cone-like form with a central caldera. Ulysses Patera has a giant caldera and a line of small

cones, suggesting a high volatile content in the later stages of formation. Biblis Patera has nested calderas and flank vents from concentric fissures [*Plescia*, 1994]. Tharsis Tholus has the oldest and most complex history, including multiple collapse and regrowth phases from 3.4 to 1.9 Ga [*Plescia*, 2003; *Platz et al.*, 2011]. Despite the differences in history between individual domes, they are generally interpreted to be effusive basaltic constructs.

On the other hand, Ceraunius Tholus, Uranius Tholus, Uranius Patera, and Hecates Tholus share many characteristics with terrestrial composite shields, rather than purely effusive basaltic edifices [*Reimers and Komar*, 1979]. Like giant shields, they have a large caldera diameter relative to their size suggesting that they possessed magma chambers within the edifice at a height above the ground level of the surrounding region. Domes only differ from giant shields in that they are significantly smaller (Figures 2.6d and 2.7a) and, given terrestrial eruption rates, might take 10^4 to 10^5 years to form [*Plescia*, 1994].

2.2.2.3 Giant shield volcanoes (Amazonian)

Giant shield volcanoes are the largest volcanic constructs on Mars and are some of the largest in the Solar System. These volcanoes are cone-shaped piles of basaltic lava with a caldera (or multipel calderas) at their summits. Giant shield volcanoes are hundreds of kilometres in diameter and many (8–21) kilometres high [*Plescia*, 2004]. They are found in the following settings ordered by decreasing age:

(i) Alba Mons is a special case of a central volcano [*Greeley and Spudis*, 1981]. It has an extremely low relief of 5 km for its width of over 1000 km. The volcano is formed of a lower shield with flanks dissected by N–S trending graben. There is also a wide summit plateau, an upper, summit shield, and a caldera complex partially overlain by the later part of the upper shield. In addition to this, there are aprons lava flows from fissure zones on the east and west flanks, although these are much less steep than the lava aprons on Tharsis Montes. The eastern apron is cross-cut by the N–S trending graben whilst the western one overlies them [*Plescia*, 2004].

(ii) The Tharsis Montes comprises three giant shield volcanoes in the Tharsis region. They lie in a line striking northeast–southwest and are spaced ~700 km apart. The most northeastern is Ascraeus Mons; this is the largest and tallest. Pavonis Mons lies in the middle, and Arsia Mons is to the southwest. Arsia Mons has the largest flank apron [*Carr et al.*, 1977; *Plescia and Saunders*, 1979; *Greeley and Spudis*, 1981; *Neukum and Hiller*, 1981; *Bleacher et al.*, 2007b]. Each volcano is made up of a central caldera, flank regions, apron regions (Figure 2.7a), which are also aligned with the NE–SW trend, and small vent fields. The volcanic features of each shield volcano all share a common magma source and each shield volcano exhibits the same change in dominant eruption location, a switch from flank building to lava apron building after a hiatus [*Wilson et al.*, 2001; *Bleacher et al.*, 2007b]. On the main flanks, channel-fed flows overlie tube-fed flows, suggesting a change from stable, long-lived eruptions to shorter duration eruptions [*Bleacher et al.*, 2007b]. From SW to NE the median slope increases, as does the number of small vents there and the abundance of tube fed flows. In contrast lava apron volcumes and rift apron elevation decreaces [*Bleacher et al.*, 2007b] from SW to NE, although on each volcano the maximum elevation of the rift apron is the same [*Plescia*, 2004]. These spatial trends probably follow the development of the magma supply in giant shield volcanoes.

(iii) Olympus Mons is the largest central volcano in the Solar System [*Wilson*, 2009]. It is roughly symmetrical (~840 km x 640 km at its base) and stands 22 km above the surrounding plains [*Carr et al.*, 1977; *Plescia*, 2004]. The total volume is comparable to the entire Hawaiian–Emperor seamount chain [*Bargar and Jackson*, 1974]. The volcano has been active in the last 0.5 Ga [*Werner*, 2009] and activity in the six nested calderas dates to 420–140 Ma [*Robbins et al.*, 2011]. The most recent activity, although minor in scale, occurred on the flanks and may have been as recent as ~25-40 Ma [*Basilevsky et al.*, 2006]. Tube-fed flows are most common beyond the basal scarp (Figure 2.7b), switching to channel-fed flows in younger areas [*Bleacher et al.*, 2007a] (Figures 2.4, 2.5). This change from tube to channel fed flows follows a similar trend to the

Tharsis Montes [*Bleacher et al.*, 2007b] and to Hawaiian shields, where magma supply rate decreases with age [*Bleacher et al.*, 2007a].

The northwest and southeastern flanks of Olympus Mons have pronounced basal scarps [*Carr et al.*, 1977]. These extend to an area 1000 km to the north of the volcano and 600 km to the southeast, and consist of wide lobate areas, 0.5–1.5 km thick [*Plescia*, 2004], of curvilinear ridged terrain. These features have been ascribed to catastrophic mass movement, lubricated by ice and volatiles, after the collapse of the lower part of the Olympus Mons edifice [*Francis and Wadge*, 1983; *Tanaka*, 1985; *McGovern et al.*, 2004].

(iv) The Elysium volcanic province is the second largest volcanic province on Mars and is centred around the giant shield Elysium Mons [*Carr*, 1973; *Carr et al.*, 1977; *Greeley and Spudis*, 1981; *Greeley and Guest*, 1987a]. Elysium Mons is 375 km in diameter with a summit elevation of ~14 km [*Plescia*, 2004]. Although Elysium Mons is generally similar to other giant shields [*Greeley and Spudis*, 1981] its flanks have steeper slopes [*Kallianpur and Mouginis-Mark*, 2001] and the caldera is small relative to the size of the edifice [*Mouginis-Mark et al.*, 1984; *Crumpler et al.*, 1996]. The morphology (although not size) has been likened to the Tibesti volcano (Sahara, North africa) [*Malin*, 1977]. Lava flow activity at Elysium Mons ranges from 3.4 Ga to 60 Ma in age, with a peak at 2.2 Ga [*Platz and Michael*, 2011] the summit area was emplaced by the late Hesperian (Figures 2.4 and 2.5) but the flanks have been active into the Amazonian [*Greeley and Spudis*, 1981]. In addition to tube and channel flows with properties similar to those of Tharsis Montes [*Pasckert et al.*, 2012],the flanks of Elysium Mons also host at least 41 sinuous channels [*Wilson and Mouginis-Mark*, 2001]. These channels appear to represent a combination of collapsed tube-features and channels apparently eroded either thermally or mechanically by turbulent, low-viscosity lavas [*Wilson and Mouginis-Mark*, 2001].
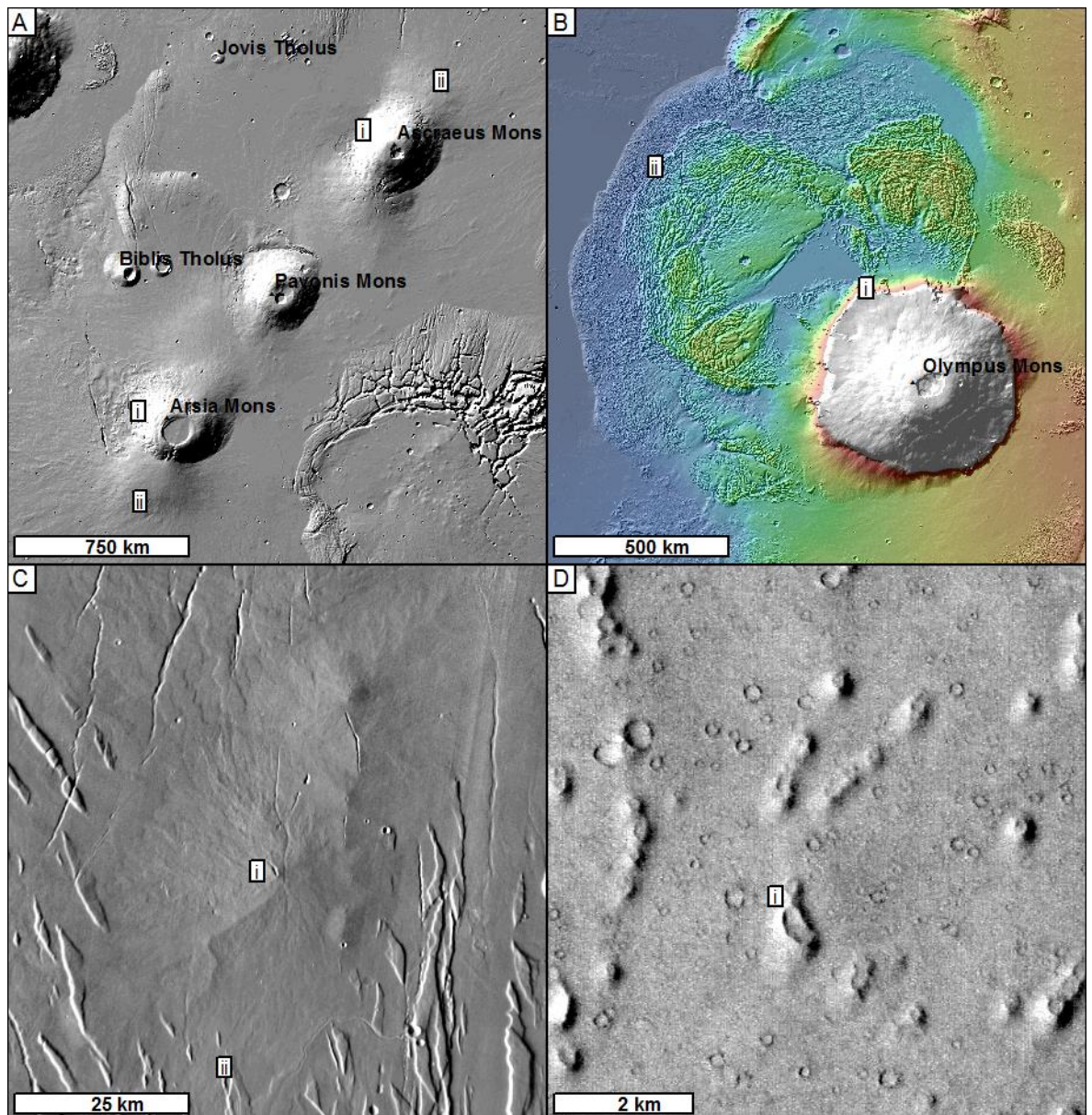
Figure 2.7

Different volcano types on Mars. (a) Tharsis giant shield volcanoes showing the location of (i) shields, and (ii) rift aprons (MOLA hill-shade). (b) Olympus Mons showing (i) the basal scarp and (ii) collapse aureole (colourised MOLA hill-shade). (c) Small shield in the Tharsis region showing (i) the small fissure at the summit and (ii) where the flanks have embayed the faulted basement (THEMIS daytime mosaic). (d) Small (i) cones on the floor of Isidis Planitia (HRSC H5216_0000_ND4).

Whilst giant shield volcanos are arguably some of the most obvious volcanic constructs on Mars, and bear little topographic similarity to Syrtis Major Planum, their age means that the detailed morphology of their lava flows are clearer than older volcanic areas. As a result, the volcanic features seen on giant shield volcanos provide an excellent comparison for understanding and interpreting the volcanic features of Syrtis Major Planum.

2.2.3 Small-scale and very recent volcanism (Amazonian?)

2.2.3.1 Small volcanoes

Small volcanoes predominantly include flank vents on larger volcanoes [*Mouginis-Mark and Christensen*, 2005] and low shields building up volcanic plains units [*Hauber et al.*, 2009]. These volcanoes are tens of kilometres in diameter and only tens of metres high, with small caldera-like pits in their often elongate summits. These edifices are dominantly found in the Tharsis and Elysium plains.

There is little evidence for these features in terrains dated to before the Amazonian, but this may be sampling bias, because the areas in which small volcanoes are known to have formed have been extensively resurfaced [*Tanaka, et al.*, 2014a]. Nevertheless, many small volcanoes are only a few hundreds to tens of Ma old [*Berman and Hartmann*, 2002; *Neukum et al.*, 2004b; *Hauber et al.*, 2011].

In addition to small volcanoes in established volcanic provinces, there is at least one instance of a small edifice in the southern highlands (dated to the middle Amazonian) [*Brož et al.*, 2015]. The morphology of this edifice is most simply explained by a more evolved, silica-rich composition [*Brož et al.*, 2015]. This inferred composition, as well as the cone's location away from any other volcanic province, is in contrast to the recent small-scale volcanism associated with large volcanic centres [*Hauber et al.*, 2011].

Finally, as well as these Amazonian examples of small volcanic edifices, there are also a few 'small' Noachian volcanoes in the highland area around the south pole, These have been dated to >4.0 Ga [*Xiao et al.*, 2012]. Although it is not clear if any identifying volcanic morphologies would have survived the Late Heavy Bombardment and thus these features may actually be younger. These small volcanoes therefore possibly represent smaller-scale and widely distributed activity associated with the large Tharsis-volcano and CHVP plains emplacement.

Although the major volcanic edifices are considered to reflect deep-seated mantle plumes, the recent and small-scale volcanism runs counter to the thick contemporary lithosphere predicted by this idea and, to some extent, demonstrated by gravity data [*Zuber et al.*, 2000]. An alternative mechanism to generate these small-scale areas of melt is localised radiogenic heating in the thickened crust of these large provinces [*Schumacher and Breuer*, 2007] but their origin is still unclear.

2.2.3.2 Small cones

The smallest (probable) volcanic structures on Mars are the thousands of small cones found across parts of the northern plains in areas such as Acidalia Planitia, Cydonia Mensae, Utopia Planitia and Isidis Planitia (Figure 2.2) [*Frey et al.*, 1979; *Wood*, 1979; *Frey and Jarosewich*, 1982; *Grizzaffi and Schultz*, 1989; *Hodges and Moore*, 1994; *Tanaka*, 1997; *Lanagan et al.*, 2001; *Bridges et al.*, 2003; *Farrand et al.*, 2005; *Lanz et al.*, 2010; *Ivanov et al.*, 2012]. These cones are typically 200–500 m across, <50 m high [*Farrand et al.*, 2005], and often occur in curvilinear chains.

No single origin for these cones can be proposed and there are several processes which have been proposed for their formation in various contexts. These include: monogenetic cinder cones, [e.g. *Wood* [1979], similar to terrestrial rift volcanism [*Lanz et al.*, 2010], and rootless cones or pseudocraters, [e.g. *Frey and Jaroewich* [1982] and *Fagents* et al., [2002], considering the examples in Isidis Planitia (Figure 2.7d) that are similar to Icelandic examples [e.g.*Thorarinsson* [1953]. In addition to the magmatic origin, non-magmatic origins such as mud volcanoes [e.g. *Tanaka* [1997; 2003]] and pingos [e.g. *Lucchitta* [1981] have also been proposed.

Although no small volcanic constructs have been reported to exist on Syrtis Major Planum, investigation into the formation of the small cones in Isidis Planitia is important to understand the development of Syrtis Major Planum and the environmental conditions into which it was emplaced. For example, if these cones are associated with periglacial or icy regolith processes it suggests that there has been significant amount of water in the vicinity of Syrtis Major Planum.

However, if they are simply small monogenetic volcanos then they might or might not be related to volcanism at Syrtis Major Planum at all.

2.3 Syrtis Major Planum

Here, I begin with an overview of the mapping history of Syrtis Major Planum, summarising what was known about Syrtis Major Planum at the time of writing. I review Planum-wide studies, and summarise smaller-scale, local studies on and around Syrtis Major Planum made using higher-resolution datasets.

Syrtis Major Planum (Figure 2.8) was the first feature documented on the surface of another planet, illustrated on 28 November 1659 by Christiaan Huygens [*Sheehan*, 1996a]. The Planum was initially referred to as 'The Hourglass Sea' but the area became known as Syrtis Major after Giovanni Schiaparelli mapped it during a close approach in 1877 [*Sheehan*, 1996b]. Since the dawn of the space age and mapping from orbit, the Syrtis Major quadrangle was mapped by Meyer and Grolier [1977] and then included in the Scott and Carr [1978] 'Geologic map of Mars'. These works interpreted Syrtis Major to be ridged plains, probably basaltic lava flows.

It was not until Schaber [1982] re-evaluated the physiographic setting using terrestrial radar data that Syrtis Major Planum was identified as a 'planum' (plateau) rather than as 'planitia' (low plains). Schaber [*Schaber*, 1982] also positively identified the central caldera complex containing two summit calderas. Viking data showed areas of bright material in Nili Patera and 'lava tubes' at Meroe Patera. On the flanks, Schaber observed further lava tubes, lava channels and fissures, in addition to the Luna mare-like wrinkle ridges previously identified. These observations confirmed the interpretation that Syrtis Major Planum was a low-relief volcanic structure. This interpretation was included in the Greeley and Guest [*Greeley and Guest*, 1987a] map produced at the end of the Viking era. The interpretations of the mapping effort have changed little, with Tanaka et al. [2014a] describing the area of Syrtis Major as: *'Early Hesperian volcanic' (eHv) with 'Planar deposits meters to tens of meters thick and tens to hundreds of kilometres across; lobate scarps common. Variable daytime IR brightness in places. Hundreds of meters or more total thickness'*

and interpreting these features to be: *'Flood lavas, undifferentiated, sourced from regional fissure and vent systems. Tectonically contracted'*.
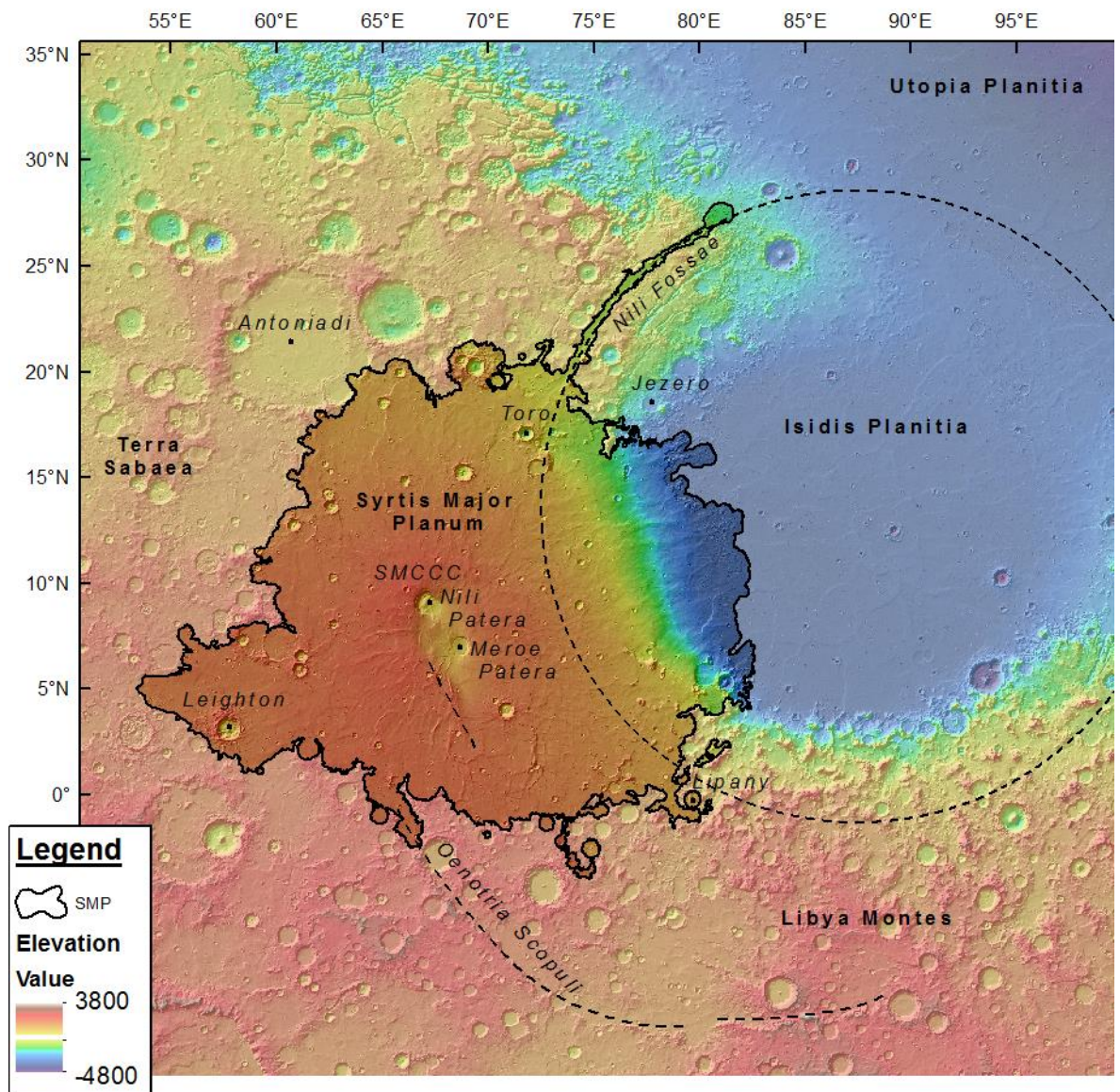
Figure 2.8

The regional context of Syrtis Major Planum.

2.3.1 Physiography

The physical parameters of Syrtis Major Planum, as observed by the MOLA instrument and products derived from those data [*Hiesinger and Head*, 2004], are summarised in Table 2.2. Syrtis Major Planum is relatively flat compared to most other martian volcanoes [*Plescia*, 2004]. The majority of the edifice on the southern highland west of the Isidis basin has less than a kilometre of relief. The area impinging into Isidis basin, however, gives the edifice up to 4 km of relief and the steepest slopes over a baseline of hundreds of kilometres. The contact with highland terrain in the north is lower than the contact in the south and the slopes over the radius of the Planum are significantly shallower in the south than in the north [*Hiesinger and Head*, 2004]. To the west, slopes are of an intermediate value (Table 2.2). These slopes reflect the topographic trends in the surrounding highlands. This, coupled with the impingement into the Isidis basin, suggest that Planum-wide slopes are a reflection of regional topography and that the Planum is lying flat upon the underlying highland terrain.

The centre of Syrtis Major Planum is dominated by the Syrtis Major Central Caldera Complex (SMCCC). This elliptical depression, into which are set the two calderas Nili Patera and Meroe Patera, is depressed by approximately 700 m relative to the surrounding Planum. The eastern side of the SMCCC has a shallower slope than that on the western side. From the south-western corner of the SMCCC is a break in slope with approximately 1 km of relief striking south-southeast [*Plescia*, 2004]. Syrtis Major Planum has a similar distribution of slopes at different wavelengths to other volcanic provinces [*Kreslavsky and Head*, 2000], but significantly different from that of surfaces dominated by sedimentary processes, such as Utopia Planitia.

Table 2.2 *Physiography of Syrtis Major Planum.*

Parameter	Value
Dimensions	
Diameter	*1200 km*
Central caldera complex	*190 km x 400 km*
Nili Patera	*40 km x 60 km*
Meroe Patera	*40 km x 50 km*
Elevation	
Highest point	*2300 m*
Lowest point	*−3950 m*
Northern boundary	*−300 m to 700 m*
Southern boundary	*800 m to 1800 m*
Central caldera complex	*~700 m deep*
Nili Patera caldera floor	*~0 m*
Meroe Patera caldera floor	*~200 m*
Slopes	
Northern flank	*~ 0.13°*
Southern flank	*~0.02°*
Western flank	*~0.08°*
Eastern flank (into Isidis)	*~0.40°*

2.3.2 Composition

The composition of Syrtis Major Planum has been a subject of considerable investigation. It is an area of low dust cover and, consequently, reflectance spectrum data from the bedrock are of good quality and apparently unobscured by coatings of dust [*Ody et al.*, 2012]. The Planum-wide infrared spectral and thermal data have been extensively interrogated. These studies have produced a range of model compositions for different parts of the Planum ranging from komatiite lavas [*Reyes and Christensen*, 1994] to crustal granites [*Bandfield*, 2006].

The first spectral data of Syrtis Major Planum were interpreted to show a composition of augite pyroxene with minor amounts of olivine [*Mustard et al.*, 1993]. These same data have also been interpreted to show an ultramafic komatiite or basaltic komatiite composition [*Reyes and Christensen*, 1994]. This composition suggests high quantities of MgO in the surface rocks. On Earth, rocks with these compositions have high crystallisation temperatures, which suggest very high eruption temperatures and low-viscosity lava flows.

Data from the Thermal Emission Spectrometer (TES) [*Christensen et al.*, 2001] aboard Mars Global Surveyor (MGS [*Albee et al.*, 2001]) showed the model surface spectra to be type I,

basaltic in the central area and type II, andesitic in the west and north of the Planum [*Bandfield et al.*, 2000]. This east–west variation [*Mustard et al.*, 1990] was first attributed to variation between bedrock and debris, with more dust in some places than others [*Mustard et al.*, 1993]. Poulet et al. [2003], however, found that the type 1 terrain in west Syrtis Major Planum is actually best fitted by a combination of sand grains covered in oxides and 50–60 % pyroxenes. The andesitic composition can also be interpreted to be basalt with a large glass component, or a weathering effect [*Noble and Pieters*, 2001], This is also considered to correlate with the Syrtis patterns of aeolian dust mixing by *Poulet et al.*, [2003] and *Hiesinger and Head*, [2004].

TES data of Syrtis Major Planum were also interpreted as mixtures of high-calcium pyroxene (HCP, interpreted to be clino-pyroxene) and low-calcium pyroxene (LCP, interpreted to be ortho-pyroxene) [*Mustard et al.*, 1997]. It is on the basis of these compositional interpretations that Mustard et al. [*Mustard et al.*, 1997] inferred that the mantle of Mars must have become depleted in aluminium by 3 Ga (to match recent compositions dated to 180 Ma). This transition is also repeated in thermodynamic compositional modelling of melting of a possible martian mantle [*Baratoux et al.*, 2013]. This composition, a mixture of HCP and LCP with minor amounts of olivine, was also found by the **O**bservatoire pour la **M**inéralogie, l'**E**au, les **G**laces et l'**A**ctivité (OMEGA) [*Bibring et al.,* 2005; *Clenet et al.*, 2013] instrument on the ESA spacecraft, Mars Express, although Clenet et al. [2013] later revised this interpretation to increace the amount of olivine, particularly in mixtures with the two pyroxenes. This follows the global trend of HCP dominating low-albedo Hesperian volcanic regions compared to LCP which dominates older Noachian cratered terrains (also reported in small quantities in Syrtis Major Planum although the spatial distribution is not explained).

From the OMEGA compositional data, Clenet et al. [2013] found that there is heterogeneity in the terrains surrounding Syrtis Major Planum and variations in olivine, HCP and LCP mixtures across Syrtis Major Planum as a result of igneous processes. The authors go on to infer that this shows a range of crystallisation temperatures/compositions, concluding that, although there was

no link between the spectral observations and morphology observed, this demonstrates either (1) differentiation from a common parent melt or (2) progressive evolution of the mantle source composition/temperature. Finally, Clenet et al. [2013] concluded that olivine in the centre of the Planum results from a late-stage phase of high temperature volcanism high in MgO.

In addition to these compositional models for the surface of Syrtis Major Planum, there have been local studies indicating significantly more silica-rich compositions [*Christensen et al.*, 2005; *Bandfield*, 2006; *Skok et al.*, 2010a; *Wray et al.*, 2013]. The observations directly associated with volcanic units are located in Nili Patera, the northern-most of the two calderas in the SMCCC (Figure 2.8). Here, a bright region of material has been interpreted to contain a large felsic component [*Wray et al.*, 2013], and an adjacent lava flow is found to be have a dacitic composition [*Christensen et al.*, 2005]. The felsic composition is modelled as having <5 % of mafic minerals as any higher fraction would mask the spectral response of the felsic component [*Cheek et al.*, 2013; *Wray et al.*, 2013]. Initially, it was argued that this, and the associated surface texture, was suggestive of an exposed pluton [*Wray et al.*, 2013]. However, an extrusive formation following low-pressure partial melting of the presumed martian mantle composition is also consistent with this spectra [*Horgan*, 2013; *Rogers and Nekvasil*, 2015] and Clenet et al. [*Clenet et al.*, 2013] found this area to have the highest olivine content in their spectral modelling from OMEGA data.

Whilst the compositions of the lavas are crucial for the understanding of the evolution of Syrtis Major Planum, little connection has been made between planum-wide studies and geomorphological evidence. Clenet et al. [2013] allude to a relationship between their modelled mineral distributions and geomorphic features, refuting the interpretation that the apparent differences between the east and west of the planum are related to aeolian mixing processes [*Poulet et al.*, 2003]. In chapter 7 I will discuss whether the relationships between spectrally inferred composition, volcanic geomorphology, and evidence for aeolian process have any meaningful correlation.

2.3.3 Volcanology and tectonics

2.3.3.1 Volcanology

The volcanology of Syrtis Major Planum has been characterised as a 'low-relief shield volcano' [*Schaber*, 1982]. On the basis of the available Viking data [*Carr et al.*, 1976], which ranged from 300 to 21 metres per pixel, Schaber [1982] identified at least two eruptive stages in the construction of the Planum. The first stage noted was a ridged-plains unit constructed on underlying ancient, cratered plains. The second stage consisted of long narrow lava flows emplaced outwards from the two calderas. Within the latter phase of construction, lava tubes or channels can be seen radiating from the calderas. Nili Patera and Meroe Patera; lava flow fronts are reported north of the calderas, and a putative collapsed tube was identified descending into Isidis Plantia. However, no such flow fronts are seen in the ridged-plains phase [*Schaber*, 1982]. Rampey and Harvey [2012] drew on these results and the review of MGS data [*Hiesinger and Head*, 2004], along with compositional observations (Section 2.3.2) and volcanology of Arnus Vallis [*Rampey and Harvey*, 2008] to propose a magmatic evolution for the Planum. In their scheme, Rampey and Harvey [2012] suggest that Syrtis Major Planum was initially emplaced by voluminous and low-viscosity basaltic/komatiitic magmas, an interpretation whereby the two observed pyroxene compositions are consistent [*Rampey and Harvey*, 2012]. They go on to propose that later flows erupted at a lower temperature, richer in feldspar, and that numerous thin flows eventually superposed many of the earlier ones. Furthermore, Rampey and Harvey [2012] compare the setting of Syrtis Major Planum, with the CHVP [*Plescia*, 2004; *Williams et al.*, 2009a] and suggest that there is a common method of magma emplacement and evolution between the Hesperian plains volcanoes on the periphery of giant impact basins [*Rampey and Harvey*, 2012].

2.3.3.2 Thickness and volume

The volume of Syrtis Major Planum has been estimated to be 2×10^5 km^3 [*Schaber*, 1982] and between 1.6×10^5 and 3.3×10^5 km^3 [*Hiesinger and Head*, 2004]. A consequence of this large volume is that, if the erupted basalt had 1 wt.% H_2O, then the eruptions would have outgassed a 3 cm deep global equivalent layer of water [*Craddock*, 1994].

Estimates for the volume of Syrtis Major Planum are based on estimates of the thickness of the lavas and the diameter of 1100 km. There are various estimates of the thickness of lava at Syrtis Major Planum (Table 2.3). The smallest, and probably most reliable, of these estimates is drawn from MOLA profile data, and is only ~500 m [*Hiesinger and Head*, 2004]. The largest estimates of 1–5 km [*Wichman and Schultz*, 1988] assume the lavas have buried remnants of the Isidis rim, which was eroded either prior to, or by, Syrtis Major Planum lava emplacement – a proposition supported by the allegedly erosional power of high temperature, fluid lava emplacement [*Rampey and Harvey*, 2008, 2012] and/or other mechanisms [*Hiesinger and Head*, 2004] as discussed in Section 2.3.5.1.

Table 2.3 *Estimation of Syrtis Major Planum lava thickness*

Thickness (Km)	Method	Author(s)
0.5	Radar	[Schaber, *1982]*
<0.6 (in ghost crater areas)	Ghost crater rim diameter and heights	[Hiesinger and Head, *2004]*
>0.6 (no ghost craters)	Ghost crater rim diameter and heights	[Hiesinger and Head, *2004]*
0.5	MOLA profiles	[Hiesinger and Head, *2004]*
0.9	Ridge spacing	[Saunders et al., *1981]*
1–2	Assuming burial of Isidis rim	[Wichman and Schultz, *1988]*
2.5 maximum	Assuming burial of Isidis rim	[Wichman and Schultz, *1988]*

2.3.4 Tectonics, gravity and demagnetisation

2.3.4.1 Wrinkle ridges

The surface of Syrtis Major Planum is cross-cut by complex patterns of ridges (illustrated in Figure 2.9) [*Greeley and Spudis*, 1981; *Wichman and Schultz*, 1988; *Raitala and Kauhanen*, 1989; *Watters*, 1993; *Hiesinger and Head*, 2004]. Generally, these ridges are interpreted to be 'wrinkle

ridges' [*Schaber*, 1982; *Raitala and Kauhanen*, 1989; *Hiesinger and Head*, 2004], although they have also been tentatively interpreted as flow fronts or lava channels [*Hiesinger and Head*, 2004]. Wrinkle ridges are broad arch structures, a few kilometres wide, often with a superposed ridge [*Golombek*, 1985; *Watters*, 1993, 2004; *Schultz*, 2000]. Wrinkle ridges were first identified in smooth volcanic plains units on the Moon, Mars, and Mercury [*Solomon and Head*, 1980; *Watters*, 1988]. However, terrestrial examples [*Plescia and Golombek*, 1986] show that these structures are not unique to volcanic surfaces. Wrinkle ridges are interpreted to be compressional folds forming an asymmetric antiform over thrust faults in the bedrock [*Golombek*, 1985; *Plescia and Golombek*, 1986; *Raitala*, 1988; *Watters*, 1993; *Schultz*, 2000].

The landform of a wrinkle ridge does not appear to be unique to a single process. Wrinkle ridges have been associated with a dislocation between stronger upper layers and weaker lower layers [*Golombek*, 1985], where the best fit to the broad arch and superposed ridge cross-section is a fault that flattens out at a décollement [*Watters*, 2004]. Examples of such internal strength contrasts include a mega regolith (Moon and Mars) [*Golombek*, 1985], ice-rich layers inferred from the correlation between fluidised ejecta craters and ridges plains [*Mangold et al.*, 1998], or other zones of crustal weakness such as inter-bedded evaporite zones [*Stone*, 1993]. However, modelling of wrinkle ridges has also shown that the faults may be tens of kilometres deep and that the ridge spacing is proportional to the depth to a deep brittle to ductile transition zone [*Golombek et al.*, 2001; *Montési and Zuber*, 2003]. Terrestrial examples reveal that these land forms occur in a variety of settings and a variety of material competencies and are all low-angle reverse faults [*Plescia and Golombek*, 1986]. In either case, wrinkle ridges, along with lobate scarps and high-relief ridges, are all identified to be caused by crustal shortening as a response to local-scale compressive stresses [*Watters*, 1993; *Schultz*, 2000].
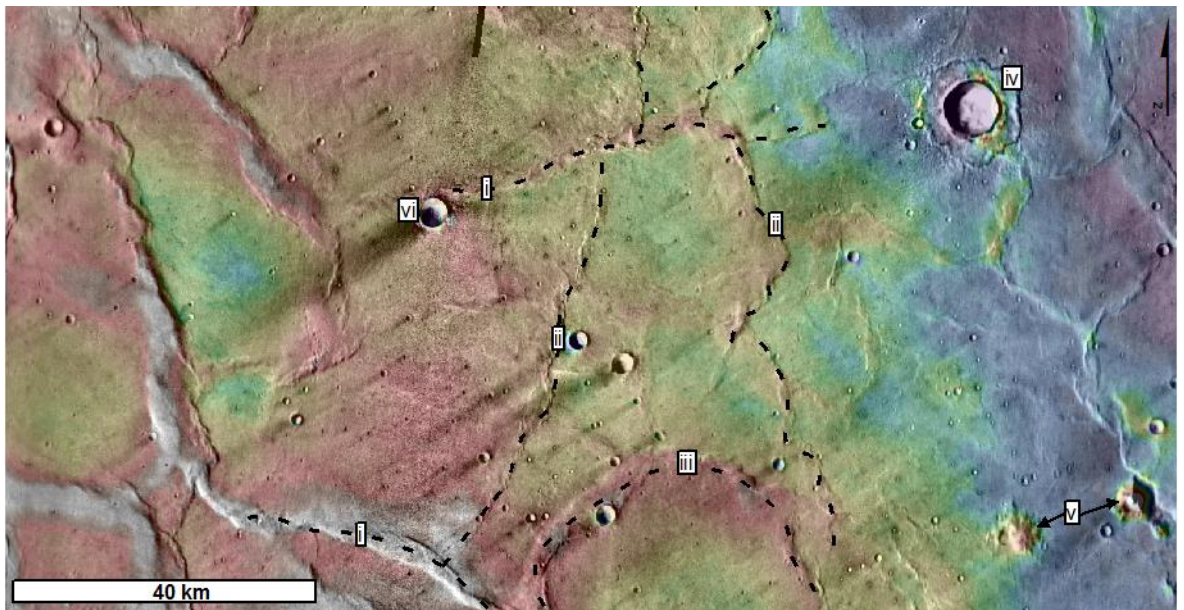
Figure 2.9

Examples of wrinkle ridges East-Southeast of the central caldera complex. this shows examples from the patterns of ridges described in Hiesinger and Head [2004] (i) radial ridges, seen here running ~ East-West, (ii) concentric ridges, seen here running ~ North-South) and (ii) ridges that are in a circular pattern outlining 'ghost craters' [Cruikshank et al., 1973]. MOLA topography across the area shows the relief across the ridges (blue is low). Several additional features, common to Syrtis Major Planum can be seen in this area (iv) an impact crater with lobate inner ejecta blanket [Barlow et al., 2000], (v) knobs of pre cratered highland terrain protruding through the Syrtis Major Planum lava shield, (vi) a wind streak associated with a small crater, which appears dark in the Themis daytime base layer, trending South-West.

The patterns of wrinkle ridges on Syrtis Major Planum identified in Viking data [*Raitala and Kauhanen*, 1989] are reported to consist of two orientation sets, but, when examined in the hill-shade model from the MOLA gridded data, three sets of ridges are visible [*Hiesinger and Head*, 2004]. MOLA data (Figure 2.9 and Figure 9 from Hiesinger and Head [*Hiesinger and Head*, 2004]) show ridges that are (i) radial and (ii) concentric to the central caldera complex, as well as (iii) circular ridges with no such orientation preference. In contrast, the interpretation from the Viking data [*Raitala and Kauhanen*, 1989] showed just two patterns: ridges striking north–south in the northwest, and ridges striking northwest–southeast in the southeast.

[*Raitala and Kauhanen*, 1989] suggested that a combination of external forces (from the development of regional tectonic systems such as Oenotria Scopulus) and gravitational loading might have caused the compressional ridges. The authors concluded that because the N–S ridges parallel to the Isidis basin are also parallel to tensional features associated with the Isidis basin

the loads of Syrtis Major Planum and the Isidis basin floor have acted together on the lithosphere. [*Raitala and Kauhanen*, 1989] also noted that in the central zone down-sag loading of the caldera complex dominates the region ridge patterns. [*Raitala and Kauhanen*, 1989] considered that this down-sag is caused by a decrease in dynamic support from the upper asthenosphere as a cooling magma body dragged the central area of the Planum down to create the SMCCC volcano tectonic depression.

Hiesinger and Head [*Hiesinger and Head*, 2004] find that ridges radial to the central caldera complex are dominant in the northern sectors, whereas ridges that are concentric to the central caldera complex are dominant in the southeast sector of the Planum. Also, closer to the SMCCC, ridges are more likely to be concentric than further away, where ridges are more likely to have a radial orientation. In the south and east these are more arcuate ridges, concentric to the SMCCC, and are interpreted to be related to gravitational sector collapse and sliding towards the southeast [*Hiesinger and Head*, 2004].

The circular wrinkle-ridge patterns [*Hiesinger and Head*, 2004] are interpreted to be the result of loading over buried impact craters (ghost craters; further examples in Figure 3.4). Circular ridges, or ghost craters [*Cruikshank et al.*, 1973], are more numerous in the southeast sector than in the central or the north-western sectors. Estimation of lava thickness [*Hiesinger et al.*, 2002] based on the relationship between buried rim height and diameter of the flooded craters [*DeHon and Waskom*, 1976; *Garvin et al.*, 2002] shows that there is <600 m of lava in regions where circular ridges occur and >600 m of lava where there are no circular ridges [*Hiesinger and Head*, 2004].

The patterns of wrinkle ridges on Syrtis Major Planum date from the later volcanic period of the Planum [*Schaber*, 1982; *Raitala and Kauhanen*, 1989; *Hiesinger and Head*, 2004]. Like Hesperia Planum, (figures 2.2b, 2.3b and 2.6c) the wrinkle ridges on Syrtis Major Planum (outside the SMCCC) appear to be expressions of external stresses interacting with the volcanic plains

[*Raitala*, 1988]. The peak of activity was in Hesperian-aged materials, in accordance with global observations of ridge formation [*Watters*, 1993; *Anderson et al.*, 2008].

2.3.4.2 Magma chambers

At the centre of Syrtis Major Planum is the Syrtis Major Central Caldera Complex (SMCCC), an elliptical region of ~100 km x 200 km, elongated approximately north–south and tangential to the Isidis basin (Figure 2.8) [*Schaber*, 1982; *Raitala and Kauhanen*, 1989; *Crumpler et al.*, 1996; *Hiesinger and Head*, 2004; *Plescia*, 2004]. Within this volcano tectonic depression are set the two calderas Nili Patera and Meroe Patera. The central caldera region is depressed ~700 m below the elevation of the surrounding planum whilst Nili Patera reaches a maximum depth of 1800 m below the surrounding planum [*Hiesinger and Head*, 2004; *Plescia*, 2004]. The development of this depression is key to understanding the evolution of Syrtis Major Planum.

The Syrtis Major Planum gravity data (Figure 2.10) show, the trivial mass contribution of Syrtis Major Planum to the crustal load [*Kiefer*, 2004], resulting in the majority of the Planum being indistinguishable from the surrounding highlands in terms of gravity anomaly and crustal thickness [*Zuber et al.*, 2000]. However, there is a positive free air gravity anomaly with a peak of 126 mGal located over Nili Patera (Figure 2.10) [*Kiefer*, 2004]. Modelling of the subsurface load required to produce this anomaly suggests it has a mass of ~10^{18} kg, about 30 % of the whole volcano [*Kiefer*, 2004]. Kiefer [*Kiefer*, 2004] reports that this buried load would be distributed in two buried cylindrical regions with radii of ~150–175 km. It has also been suggested that this anomaly represents a buried magma body with a thickness of between 2.8 km and 3.6 km, depending on dominant minerology (olivine or pyroxene) [*Kiefer*, 2004]. Although this is based on the best reasonable assumptions about the elastic thickness of the Hesperian lithosphere, the radius, depth and density contrasts are not well constrained.

As the mass of this modelled magma body is ~30 % of the whole edifice mass, it is too large to be a single intrusion [*Wilson and Head*, 1994; *Kiefer*, 2004]. Importantly, the ~10 % change in volume on solidification of such a body would only account for 300–400 m of surface depression

[*Kiefer*, 2004]. However, the depths of the central caldera complex and both local calderas are greater than this. The observed depths in the SMCCC must have resulted from collapse/subsidence following the eruption of material onto the surface, leaving dense cumulates behind [*Kiefer*, 2004].

Interrogation of the orbital magnetic data and subsequent thermal magnetic modelling of the observed subsurface demagnetisation [*Lillis et al.*, 2015] show the areal extent and volume of intrusive magmatism beneath the volcano. The size of the modelled intrusions is dependent on several uncertainties:

(i) The thickness of the magnetised layer

(ii) Saturation of the crustal replacement (over 50 % crustal replacement causes total demagnetisation, therefore this is a minimum intrusive volume)

(iii) The assumed dominant magnetic mineral.

The result of this modelling best-fits a dog-bone-shaped intrusion in which the northern and southern ends are cylinders of 400– 500 km in diameter. These are connected by a central portion which is 150–200 km in width and extends under the SMCCC.
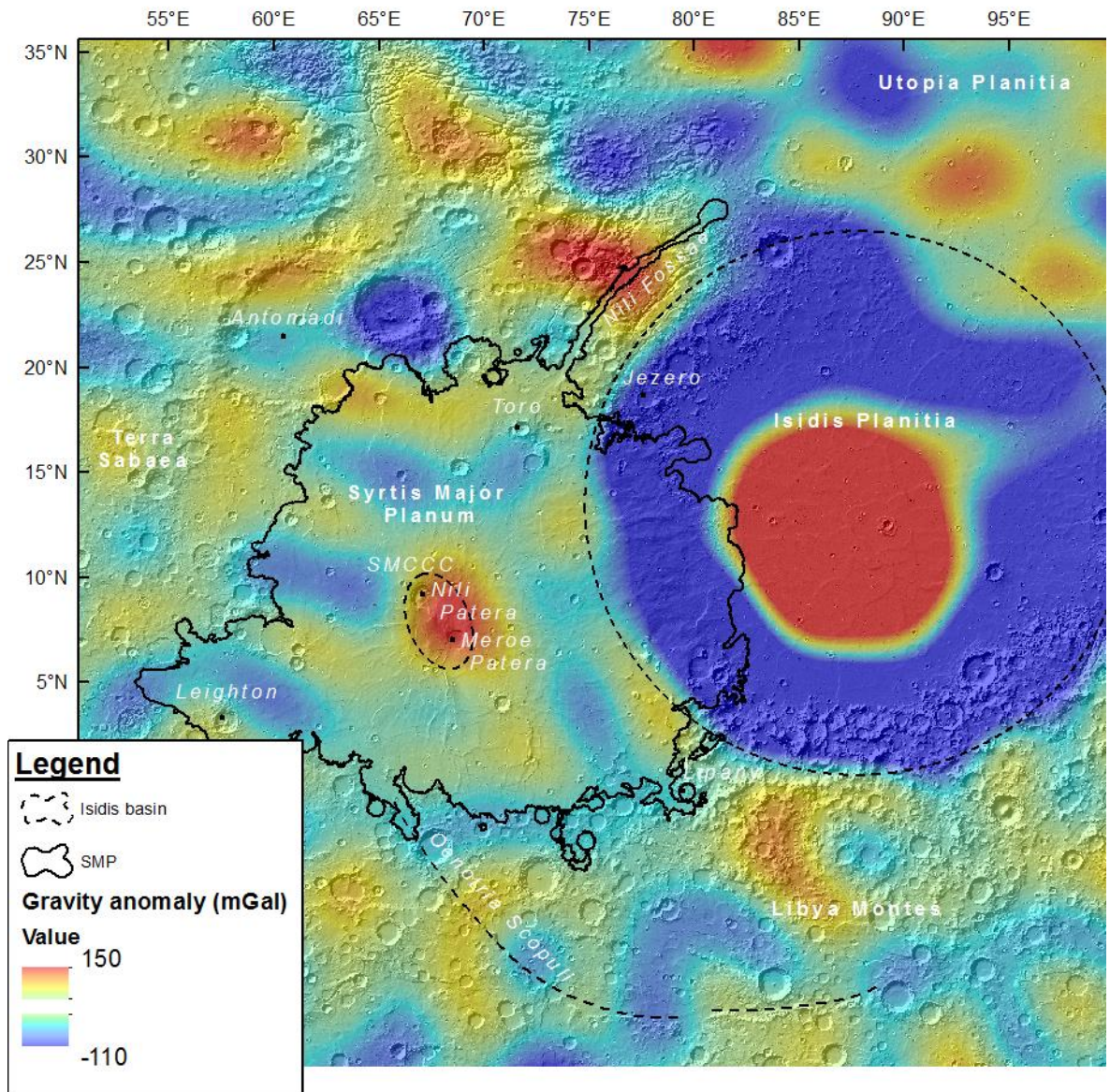
Figure 2.10

A map of the gravity anomaly over the Syrtis Major region [Lemoine et al., 2001]. This shows the gravity 'high' coincident with the Syrtis Major Central caldera complex and the extreme gravity anomaly centred in the floor of the Isidis basin which is thought to result from impact induced crustal thinning [Zuber et al., 2000; Neumann et al., 2004].

This intrusive activity modelled from crustal demagnetisation [*Lillis et al.*, 2015] and the free air gravity anomaly [*Kiefer*, 2004] has implications for the geological history of Syrtis Major Planum: Firstly, the geophysical signatures of subsurface magmatic activity are localised (a few 100 km) relative to the 1100 km diameter of Syrtis Major Planum. Therefore, to cause this demagnetisation, and to collect sufficient dense crystal cumulates to cause the observed gravity anomaly, most of the magma that erupted to form Syrtis Major Planum must have gone through

this now-frozen part of the plumbing system [*Kiefer*, 2004; *Lillis et al.*, 2015]. This subsurface behaviour is consistent with melt derived from the mantle sustained in one location though out the history of Syrtis Major Planum.

Furthermore, a dense cumulate residue in the crust (implied by gravity data) is consistent with silicic magma being removed from a crystalline mush during fractional crystallisation in an extensive igneous system and/or partial melting of the crust. These processes are also consistent with the petrological diversity observed at the surface [*Mustard et al.*, 1993; *Reyes and Christensen*, 1994; *Christensen et al.*, 2005; *Clenet et al.*, 2013; *Wray et al.*, 2013; *Rogers and Nekvasil*, 2015].

Finally, the best fit shape for the intrusive demagnetisation is elongated tangential to Isidis, in accordance to the regional tectonic setting locally related to the Isidis basin (e.g. Nili fossae) or related to regional tectonism (e.g. Oenotria Scopulus [*Raitala and Kauhanen*, 1989]). This suggests a rift-like origin for magma ascent and that comparable processes may have operated in the Circum-Hellas Volcanic Province [*Lillis et al.*, 2015].

2.3.5 Regional context

The regional context of Syrtis Major Planum (Figure 2.8) is important to understand where the Planum fits into the geological history of Mars. In this section I outline observations pertaining to the areas of Mars directly connected to Syrtis Major Planum, and therefore influencing (or being influenced by) its emplacement and development .

2.3.5.1 East: Isidis Planitia

To the East of Syrtis Major Planum is Isidis Planitia (Figure 2.8), a Noachian-aged impact basin [*Schultz and Frey*, 1990; *Ivanov and Head*, 2003; *Ivanov et al.*, 2012; *Tanaka et al.*, 2014b]. Lava flows from Syrtis Major Planum have buried the western rim of Isidis and flowed down to the basin floor. Where Syrtis Major Planum covers the rim of Isidis, the rim appears to be unusually smooth and low, although there is considerable range in what could be considered the 'normal'

Isidis rim topography [*Hiesinger and Head*, 2004]. In their review of MGS data, Hiesinger and Head [*Hiesinger and Head*, 2004] discuss in detail the ways to explain the interaction between the emplacement of Syrtis Major Planum and the pre-Syrtis western Isidis rim. Hiesinger and Head [*Hiesinger and Head*, 2004] simulated the topography using MOLA tracks from other relevant Isidis rim sections (i.e. not the boundary with Utopia Planitia) and looked at what the coverage of Syrtis Major Planum lava should be for a minimum likely rim elevation (comparable to the north-eastern Syrtis/northwest Isidis rim area) and a maximum likely rim height (comparable to the south-eastern Isidis rim). They found that 75 % of the rim would be buried in the maximal case and 60 % should be covered in the minimal case. However, suitably significant massifs are not observed protruding through the lavas in the relevant area of Syrtis Major Planum to support this hypothesis. Therefore, the authors conclude that either the rim never existed (unlikely) or that it has been lowered in some way, for which they suggest five possible scenarios:

In the first two scenarios, the pre-existing topography of the rim was catastrophically eroded by the release of volatiles due to either solely intrusive or both intrusive <u>and</u> extrusive emplacement of Syrtis Major magmas. Pre-existing volatiles (water and ice), interacting with magma, allowed the Noachian crust (impact mega breccia) to be disrupted and transported into the local sink of the Isidis basin floor [*Tanaka et al.*, 2001, 2002]. However, this source of basin fill is inconsistent with TES results [*Bridges et al.*, 2003], and others propose different sources for the Isidis fill [*Ivanov et al.*, 2012]. In the third scenario, graben formation (similar to that seen at Nili Fossae; Figure 3.7) took place prior to the formation of Syrtis Major Planum, lowering the Isidis rim. The lowered rim was then buried by lavas. The fourth scenario involves loading of the Isidis rim by the emplacement of Syrtis Major Planum lavas. This load then caused fault propagation in the rim of Isidis. The subsequent slumping of the rim was then buried by later Syrtis Major Planum lavas. In the final scenario, Syrtis Major Planum is thicker than estimated and it buried the rim more deeply to the level observed today – explaining the lack of rim-material showing through the lavas.
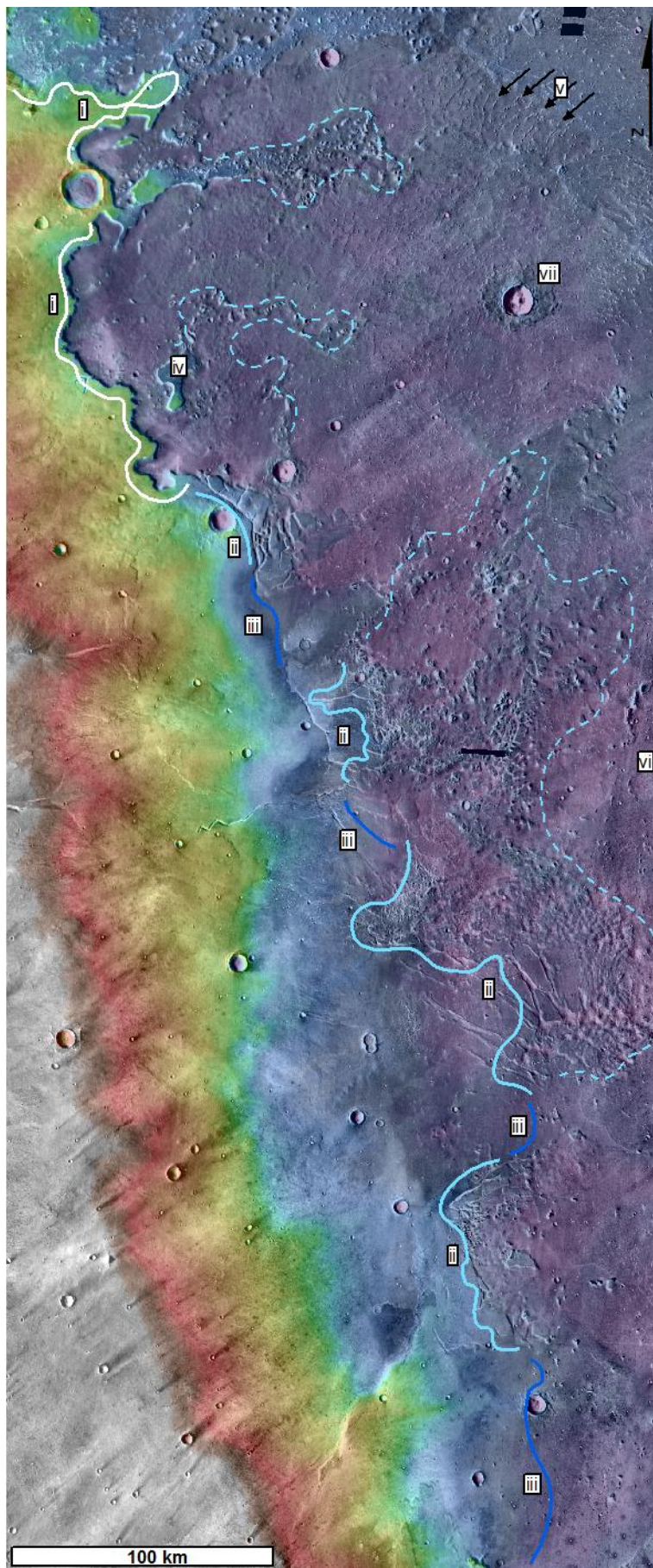
Figure 2.11

The boundary between lava plain of Syrtis Major Planum (west) and the floor of the Isidis Planitia (East) shown here in the daytime Themis base layer overlain by MOLA topography (where Blue is low). This shows the three main morphologies of the boundary. The first (i) is the 500m high scarp in the northern part of the boundary, lined on the upslope Syrtis Major Planum side in white. The second (ii) is areas where the smooth lavas are disintegrating (light blue solid line) and transitioning into chaotic and knobbly terrain (light blue dashed line). The third (iii) (Dark Blue) is areas where the smooth slope of the Syrtis Major Planum transitions into the Isidis basin Floor materials (dark blue lines). Additionally there are examples of other important features (iv) outliers of Syrtis Major Planum where the connection to the planum has been eroded away, (v) alignments of small cones, just visible at this scale (comparable to those shown in figure 2.8), (vi) An impact crater on the floor of Isidis flooded by superposing material (no circular wrinkle ridge is formed in this case), and (vii) a small impact crater with lobate ejecta commonly seen as indicative of a substrate rich in ice.

The boundary between the Syrtis Major Planum lavas and the Vastitas Borealis formation on the floor of the Isidis basin takes a variety of forms [*Schaber*, 1982; *Ivanov and Head*, 2003; *Hiesinger and Head*, 2004; *Ivanov et al.*, 2012]. The northern part of the boundary (Figure 2.11) is a cliff, 500 m high, with a series of knobs and mesas also present. These mesas are isolated from the Isidis basin floor and get progressively smaller with distance from Syrtis Major Planum. To the south there is a smooth plain sloping into the basin floor. This is broken up by a series of cross-cutting graben. Further from the Syrtis Major Planum, these graben become wider and transition into rectilinear knobs and mesas [*Ivanov and Head*, 2003].

There are several mechanisms by which this topography may have formed. Firstly, lavas of Syrtis Major Planum might have superposed a volatile-rich layer of friable material that has been subsequently degraded, causing the collapse of the volcanic overburden to form the current 'chaotic' terrain [*Ivanov and Head*, 2003; *Ivanov et al.*, 2012]. Secondly, water ponded in Isidis may have undermined the edge of the lavas to create the cliff [*Craddock*, 1994] and the outlying mesas and knobs. Thirdly, the cliff (Figure 2.11) may have formed abutted to a natural barrier that has subsequently been removed, such as an ice sheet. Such an ice body was suggested by Skok and Mustard [*Skok and Mustard*, 2014] to explain a disparity between the rim height and channel outlet height of a small basin also closely associated with related cliffs on the north-eastern edge of Syrtis Major Planum. Although glaciation has been reported to have been involved in the development of the Isidis basin between 3.1 and 3.41 Ga [*Ivanov et al.*, 2012], it is considered to have primarily developed in the southern Libya Montes region (Figure 2.8) rather than the north-eastern Syrtis area [*Bridges et al.*, 2003; *Ivanov et al.*, 2012; *Bishop et al.*, 2013].

Given the currently available information I favour disintegration of ice rich regolith developing the 'chaos like' terrain and increasing ice content in the northern part where scarp development is most progressed. Although it is not clear how this fits in with the geological story of the Northeast Syrtis region and the rest of Isidis Planitia, there is scope for further detailed study in this area.

2.3.5.2 The Noachian crust under and around Syrtis Major Planum

Syrtis Major Planum is adjacent to, and directly south of, the Nili Fossae and the northeast Syrtis region. This area has one of the best mineralogically expressed cross-sections on Mars. Its compositional stratigraphy starts with the Isidis impact and records Noachian–Hesperian transitions through changing volcanic processes and styles of aqueous alteration and ends with the emplacement of Syrtis Major Planum lavas [*Ehlmann and Mustard*, 2012]. Directly beneath the northeastern Syrtis Major lava flows is a layered box-work of polyhydrated jarosite ridges, above a layered sequence of clay–carbonate–sulphate-bearing units [*Ehlmann and Mustard*, 2012]. In addition, there are also major exposures of olivine-rich terrain [*Mustard et al.*, 2005], found in conjunction with serpentine deposits [*Ehlmann et al.*, 2010]. The serpentine deposits exposed on the surface show that, although it may not be a contemporary process, the conditions for serpentinisation have existed in the past [*Ehlmann et al.*, 2010].

Serpentinisation is an astrobiologically important process (e.g *Schulte et al.* [2006] and Lane [*Lane*, 2010] and references herein). It is important in this context because the environment in which serpentinisation occurs is a reducing environment in which complex organic molecules are not destroyed (oxidised). Furthermore, high rates of serpentinisation in the early history of Earth are thought to have produced suitable thermal and proton gradients key to all biological processes. Also, the structure of secondary mineralisation provides a substrate conducive to the concentrations of pre-organic molecules (e.g *Schulte et al.* [2006] and Lane [*Lane*, 2010] and references herein).

There are several lines of evidence that the terrains with this diverse astrobiologically significant suite of minerals extend under the lavas of Syrtis Major Planum. Firstly, global maps of clay spectra [*Carter et al.*, 2015] show numerous instances, both north and south of Syrtis Major Planum, of deposits rich in clay minerals. These are often weathering sequence of kaolin clays transitioning down though magnesium-rich and then iron-rich clays. Such sequences are best

characterised in Mawrth Vallis in the north of Arabai Terra (Figure 2.2) [*Bibring et al.*, 2006; *Loizeau et al.*, 2007; *Michalski and Noe Dobrea*, 2007; *Wray et al.*, 2010].

Secondly, impact craters provide samples of the subsurface below Syrtis Major Planum. Spectrally there are two types of crater ejecta composition [*Baratoux et al.*, 2007; *Skok et al.*, 2010b]. The first type are systematically younger, dominated by high-calcium pyroxene and distinct from the surface of Syrtis Major Planum [*Skok et al.*, 2010b]. These craters form a temporally continuous population at 2 Ga (isochron: Hartmann [*Hartmann*, 2005]) and are spatially random [*Skok et al.*, 2010b]. The second type is older and have a composition with both high, and low-calcium pyroxene [*Baratoux et al.*, 2007] and are less distinguishable from the surface of Syrtis Major Planum [*Skok et al.*, 2010b]. The younger spectrally distinct type [*Baratoux et al.*, 2007; *Skok et al.*, 2010b] is made from rock-forming minerals and excavated materials. This ejecta represents the true composition of Syrtis Major Planum [*Skok et al.*, 2010b].

The spectra for the type 1 ejecta change with radius. There is a maximum in HCP/LCP abundance at ~1.2–3 crater radii. This suggests that material excavated from a few hundred metres below the surface adds a significant LCP component to the ejecta [*Baratoux et al.*, 2007]. Baratoux et al. [*Baratoux et al.*, 2007] interpret this to represent the maximum thickness of the lavas in an impact site. Below this point, the HCP/LCP decreases, so the impact has sampled either more ancient compositions from early in the history of Syrtis Major Planum, or excavated the underlying Noachian crust. The older type of ejecta is less distinct from the surface of Syrtis Major Planum and has been affected by long-term weathering. These craters show alteration by environmental conditions that no longer existed at the time when the craters with spectrally distinct ejecta were emplaced [*Skok et al.*, 2010b].

In addition to the ejecta, the central peak regions of impact craters also sample the deep subsurface. In Toro crater (Figure 2.8) there is an impact-induced hydrothermal system which shows geomorphic indicators of volatile release and liquid flow alongside a hydrated phase in the central uplift complex [*Marzo et al.*, 2010]. This suite of minerals is analogous to clay carbonate

hydrothermal weathering in Australia [*Brown et al.*, 2010], supporting the interpretation of hydrothermal activity associated with crater peaks in the Syrtis Major Planum area. Crustal carbonates are exposed in the central peak of Leighton crater (Figure 2.8), southwest of Syrtis Major Planum [*Michalski and Niles*, 2010]. Through comparison of cross-sections between Nili Fossae [*Mustard et al.*, 2009] and Toro crater (Figure 2.8), Marzo et al., [*Marzo et al.*, 2010] show that these areas share a common phyllosilicate-bearing breccia overlain by minerals that suggest a subsequent pulse of alteration. Also, in Antoniadi crater (Figure 2.8), and in the central mounds of two smaller craters close to it, are silica deposits [*Bandfield*, 2006]. These surfaces are consistent with quartz and feldspar, and could be alteration products or basement materials pre-dating Syrtis Major Planum [*Smith and Bandfield*, 2012].

Finally, there is evidence for these ancient processes and subsurface deposits on the surface of Syrtis Major Planum itself. Glotch and Rogers [*Glotch and Rogers*, 2013] find some evidence for carbonate decomposition products in the kilometre-scale TES data. They attribute this to either the interaction between lava and subsurface carbonates, or perhaps even exotic carbonate magma. Mounds of silica are also observed in Nili Patera [*Skok et al.*, 2010a]. Here, however, these deposits cannot be associated with impact-induced hydrothermal activity and thus are interpreted to be volcanic hydrothermal deposits instead [*Skok et al.*, 2010a].

2.3.6 Age of Syrtis Major Planum

Many studies have included dating of all [*Tanaka*, 1986; *Greeley and Guest*, 1987a; *Hiesinger and Head*, 2004], or parts [*Baratoux et al.*, 2005; *Werner*, 2009; *Skok et al.*, 2010b; *Robbins et al.*, 2011; *Ivanov et al.*, 2012; *Bishop et al.*, 2013; *Bamberg et al.*, 2014; *Platz et al.*, 2014; *Skok and Mustard*, 2014; *Warner et al.*, 2015], of Syrtis Major Planum. Some authors [*Tanaka*, 1986; *Greeley and Guest*, 1987a; *Hiesinger and Head*, 2004; *Warner et al.*, 2015] present these data in terms of a normalised density of craters larger than a specified size (e.g. 1, 5, or 10 km) per $10^6 \, km^2$. These are known as N(1), N(5) or N(10) values [*Arvidson et al.*, 1979]. This method is good for comparing different studies. However, other dating studies are also reported mainly in

terms of their stratigraphic position in the contemporary divisions and understanding of Martian history [*Condit*, 1978; *Arvidson et al.*, 1979; *Neukum and Hiller*, 1981; *Scott et al.*, 1986; *Tanaka*, 1986; *Strom et al.*, 1992; *Tanaka et al.*, 1992; *Hartmann*, 1999, 2005; *Werner*, 2005; *Werner and Tanaka*, 2011; *Platz et al.*, 2013a].
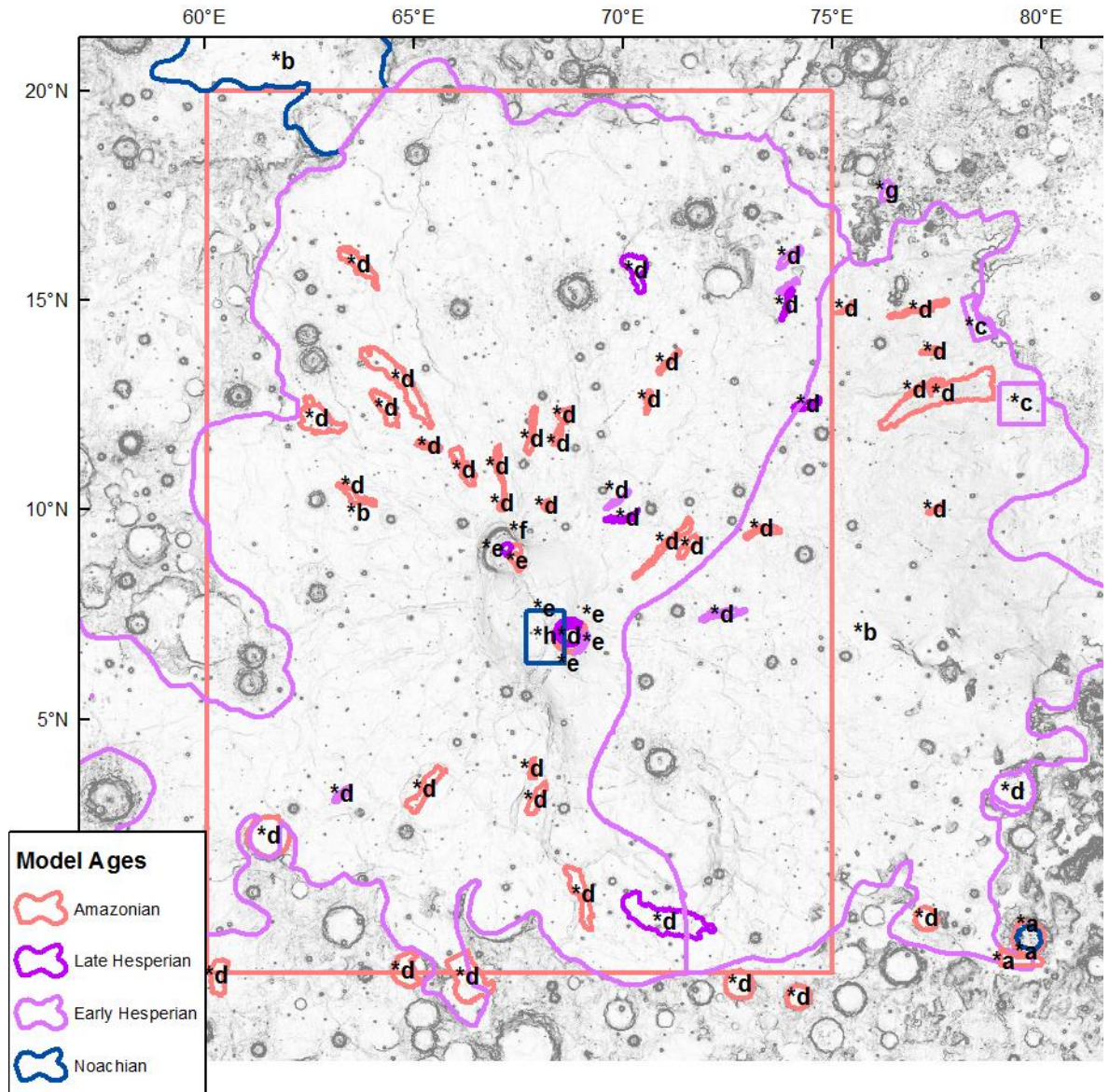
Figure 2.12

The distribution of areas where crater count data and absolute model ages have been obtained across Syrtis Major Planum. Key to references: (a) Bamberg et al. [Bamberg et al., 2014], (b) Hiesinger and Head [Hiesinger and Head, 2004], (c) Ivanov et al. [Ivanov et al., 2012], (d) Platz et al. [Platz et al., 2014], (e) Robbins et al. [Robbins et al., 2011], (f) Skok et al. [Skok et al., 2010b], (g) Skok and Mustard [Skok and Mustard, 2014], (h) Warner [2015], (i) Werner [Werner, 2009]. The ages for these areas are summarised in Table 2.4.

In addition, some studies [*Hiesinger and Head*, 2004; *Werner*, 2009; *Robbins et al.*, 2011; *Ivanov et al.*, 2012; *Bamberg et al.*, 2014; *Platz et al.*, 2014; *Warner et al.*, 2015] report absolute model ages and have plotted these in a variety of different styles based on either the chronology and production functions of Hartmann or Neukum [*Hartmann and Neukum*, 2001a; *Hartmann*, 2005].

Table 2.4 Summarises all the available model age data for Syrtis Major Planum and Figure 2.12 shows the distribution of the areas dated. These reported ages apparently show ages for different parts of the Planum ranging from the earliest Hesperian (~3.7 Ga) well into the Amazonian (~0.8 Ga). The distribution of these ages shows two clusters; one around ~3.5 Ga in the Hesperian and one around ~2 Ga in the early Amazonian (figure 2.13b). Although the range and distribution of model ages might be considered evidence for the evolution of the Planum, care must be taken to consider the validity of each date in terms of the number of craters counted, the area in which they are counted and the data from which the count data are taken. This is best discussed by Warner [2015] who, as part of a larger study into the minimum effective area for crater count data collection, studied an area of northern Syrtis Major Planum. In this study, Warner [*Warner et al.*, 2015] conducted crater counts for 100 adjacent boxes, each 100 km^2 in area. These adjacent areas produced a randomly distributed range of ages covering ~2.05 Ga (3.51 Ga–1.46 Ga, mean 2.63 Ga) for craters >200 m in diameter and an age range covering ~0.74 Ga (3.98 Ga–3.24 Ga, mean 3.55 Ga) for craters >500 m. This range and disparity of ages for adjacent areas that have experienced the same erosional history since their contemporaneous emplacement, highlights the caution that must be taken when considering crater counts from 'small' areas.

A **Model Age and Minuimum Counted Crater Diameter**

- ● Model age (Ga) D > 200
- ● Model age (Ga) D > 500
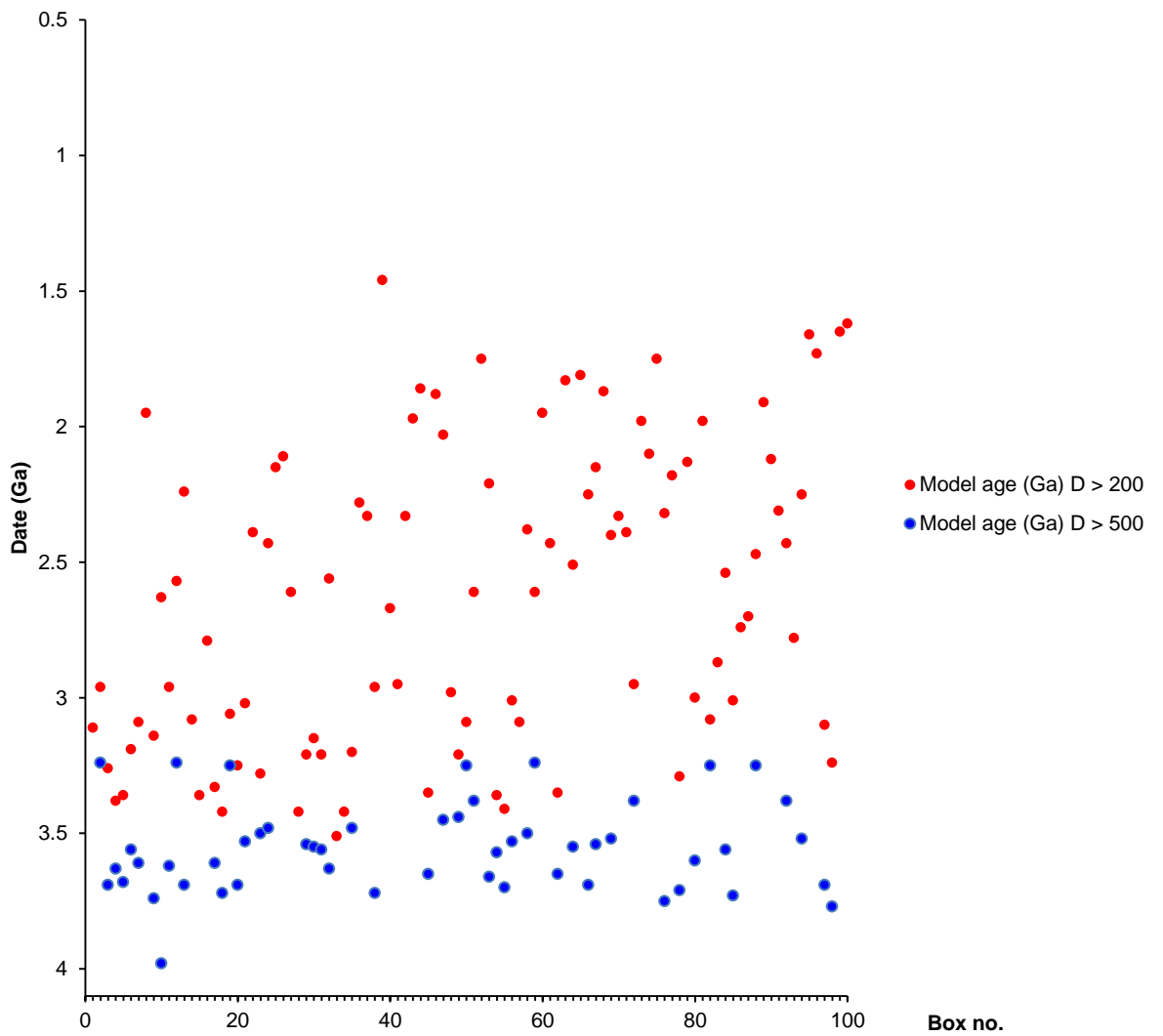
Model ages of Syrtis Major Planum (count area >10³ km²)

- ■ ~Amazonian
- ■ ~Hesperian
- ■ Noachian
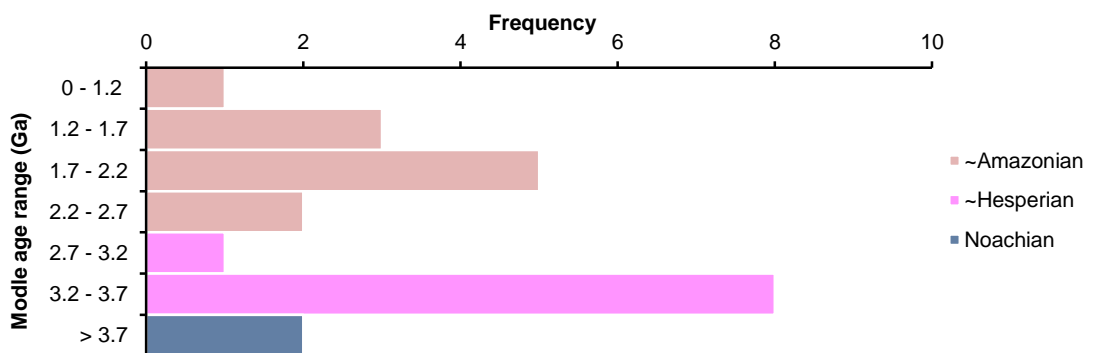
Figure 2.13

(a) The distribution of ages for 100 boxes 100 km² in area on northern Syrtis Major Planum [from Warner et al., 2015]. (b) Histogram showing published model ages for Syrtis major planum with count areas over 1000 km²

Table 2.4 Published dates for Syrtis Major Planum.

Area	Age (Ga)	Area (km^2)	Reference
	Amazonian		
Lava flow 39	0.84	160	[*Platz et al.*, 2014]
Lava flow 32	0.97	1019	[*Platz et al.*, 2014]
Lava flow 29	1.30	139	[*Platz et al.*, 2014]
Lava flow 14	1.38	462	[*Platz et al.*, 2014]
Meroe Patera	1.40	87	[*Robbins et al.*, 2011]
Lava flow 31	1.52	569	[*Platz et al.*, 2014]
Lava flow 21	1.54	831	[*Platz et al.*, 2014]
Lava flow 8	1.57	92	[*Platz et al.*, 2014]
Nili Patera	1.61	297	[*Robbins et al.*, 2011]
Lava flow 54	1.63	4704	[*Platz et al.*, 2014]
Lava flow 11	1.64	227	[*Platz et al.*, 2014]
Lava flow 59	1.64	2585	[*Platz et al.*, 2014]
Lava flow 53	1.66	1289	[*Platz et al.*, 2014]
Lava flow 71	1.77	308	[*Platz et al.*, 2014]
Lava flow 18	1.79	690	[*Platz et al.*, 2014]
Lava flow 12	1.80	185	[*Platz et al.*, 2014]
Lava flow 70	1.80	2598	[*Platz et al.*, 2014]
Lava flow 60	1.81	845	[*Platz et al.*, 2014]
Lava flow 27	1.83	182	[*Platz et al.*, 2014]
Lava flow 24	1.88	762	[*Platz et al.*, 2014]
Lava flow 16	1.91	123	[*Platz et al.*, 2014]
Lava flow 45	1.92	1003	[*Platz et al.*, 2014]
Lava flow 72	1.92	1238	[*Platz et al.*, 2014]
Lava flow 41	2.00	1283	[*Platz et al.*, 2014]
Nili Patera	2.04	174	[*Robbins et al.*, 2011]
Meroe Patera	2.05	71	[*Robbins et al.*, 2011]
Lava flow 58	2.06	113	[*Platz et al.*, 2014]
Lava flow 36	2.11	103	[*Platz et al.*, 2014]
Lava flow 10	2.11	351	[*Platz et al.*, 2014]
Lava flow 3	2.12	418	[*Platz et al.*, 2014]
Lava flow 61	2.13	1241	[*Platz et al.*, 2014]
Lava flow 19	2.22	2488	[*Platz et al.*, 2014]
Lipany floor	2.42	761	[*Bamberg et al.*, 2014]
Lava flow 52	2.42	799	[*Platz et al.*, 2014]
Lava flow 23	2.42	1661	[*Platz et al.*, 2014]
Lava flow 68	2.48	896	[*Platz et al.*, 2014]
Lava flow 15	2.51	236	[*Platz et al.*, 2014]
Lava flow 1	2.54	187	[*Platz et al.*, 2014]
Lava flow 42	2.58	350	[*Platz et al.*, 2014]
Lava flow 62	2.61	198	[*Platz et al.*, 2014])
Syrtis Major >0.2 km	2.63	8453	[*Warner et al.*, 2015]*
Lipany plains	2.84	794	[*Bamberg et al.*, 2014]

Lava flow 5	2.89	411	[*Platz et al.*, 2014]
Hesperian			
Lava flow 63	2.94	273	[*Platz et al.*, 2014]
Meroe Patera	2.95	252	[*Robbins et al.*, 2011]
Meroe Patera	2.95	516	[*Robbins et al.*, 2011]
Nili Patera	3.02	148	[*Robbins et al.*, 2011]
Meroe Patera	3.03	198	[*Robbins et al.*, 2011]
Lava flow 30	3.10	317	[*Platz et al.*, 2014]
Lava flow 2	3.12	996	[*Platz et al.*, 2014]
Lava flow 38	3.17	214	[*Platz et al.*, 2014]
Lava flow 69	3.28	3757	[*Platz et al.*, 2014]
Lava flow 46	3.31	203	[*Platz et al.*, 2014]
Lava flow 56	3.38	2922	[*Platz et al.*, 2014]
Lava flow 37	3.41	195	[*Platz et al.*, 2014]
Northern Lava	3.41	303	[*Skok and Mustard*, 2014]
Lava flow 66	3.41	479	[*Platz et al.*, 2014]
Isidis Boundary 2	3.46	3562	[*Ivanov et al.*, 2012]
Eastern SMP	3.50	466069	[*Hiesinger and Head*, 2004]
Lava flow 64	3.51	154	[*Platz et al.*, 2014]
Syrtis Major >0.5 km	3.55	8453	[*Warner et al.*, 2015]*
Western SMP	3.60	872913	[*Hiesinger and Head*, 2004]
Meroe Patera	3.63	206	[*Robbins et al.*, 2011]
Lava flow 33	3.63	380	[*Platz et al.*, 2014]
Isidis boundary 1	3.67	1425	[*Ivanov et al.*, 2012]
Antoniadi	3.70	71015	[*Hiesinger and Head*, 2004]
Noachian			
Meroe Patera	3.73	4021	[*Werner*, 2009]
Lipany fractured	3.95	875	[*Bamberg et al.*, 2014]
Syrtis Major >1.0 km	3.98	8453	[*Warner et al.*, 2015]*

The crater count model ages published for the formation of surface units on Syrtis Major Planum. Production function, number of craters, and production or chronology function were not available for most dates. Dividing lines represent the Amazonian (0–2.9 Ga), Hesperian (2.9–3.7 Ga) and Noachian (3.7–4.1 Ga)*

*Except for the ages published in Warner et al. [2015] which are populations of craters with different minimum sizes in the same area taken to investigate the validity of the crater count method.

2.4 Conclusions

To date, the main themes of research in the area of Syrtis Major Planum have been (i) how Syrtis Major Planum fits into regional sites of astrobiological importance [*Mustard et al.*, 2009; *Skok et al.*, 2010a; *Ehlmann and Mustard*, 2012], (ii) the mineralogical diversity of Syrtis Major Planum [*Mustard et al.*, 1993; *Reyes and Christensen*, 1994; *Skok et al.*, 2010b; *Clenet et al.*, 2013; *Wray et al.*, 2013] and (iii) geomorphology summaries of Viking and Mars Global datasets [*Schaber*, 1982; *Hiesinger and Head*, 2004]. These avenues of research all develop the story of how the Planum developed relative to Noachian/Hesperian highland volcanoes, Amazonian giant shield volcanoes, and terrestrial large igneous provinces, and where Syrtis Major Planum fits into the evolution of Mars as a whole in terms of its magmatic story and its influence on the regional and global environment.

Much of this research has been facilitated by the minimal surface dust cover across Syrtis Major Planum (*Szwast et al.,* 2006), which affords spectral investigation and a window into the composition of martian surface rocks. Whilst this thesis does not contest compositional interpretations of spectral data used to develop ideas about the evolution of Syrtis Major Planum I will critically assess the relevance of these ideas relative to the observed geomorphology and volcanology.

This background chapter highlights what is known about Syrtis Major Planum. Using this understanding as a starting point, this thesis draws on the wealth of new data from MEX and MRO, to investigate in detail the volcanic geomorphology of Syrtis Major Planum. Taking this approach, I attempt to understand the volcanic evolution of the planum and the central caldera complex, and present a planum-wide map that can be used as basis for further studies into the many unanswered questions pertaining to Syrtis Major Planum.

Chapter 3: Methods

The purpose of this chapter is to show the data and methods employed in making Map sheet 1, a geomorphological map of Syrtis Major Planum, focusing on the differentiation of volcanic surface textures presented at 1: 2,000,000, and Map sheet 2, a Geological map of the Nili Patera caldera, presented at 1:250,000. This chapter details which data are used (Table 3.1) and how the data are interpreted to obtain new scientific conclusions. It then goes on to discuss the mapping strategies employed for Map sheets 1 and 2, and outline the data and protocols used for crater counting model age estimation. Finally, I briefly discuss the field experience (Table 3.2) gained during the project and which terrestrial remote sensing data (Table 3.3) have been used to compliment this in shaping my understanding and interpretations of volcanic landforms.

3.1 Data

Martian remote sensing data come from a series of spacecraft launched over the last 50 years [*Williams*, 2001]. Of these, data from orbiters has built the largest data sets of the planet's surface falling into three timeframes of exploration, each showing an increease in the resolution of the data.

Table 3.1: *Instrument specifications for data used. Data types that were not used in this project is shown faded.*

Instrument	bands	Wavelengths	Pixel size/pacing	Foot print (width)	Usage	Source
Thermal data products						
Themis IR						
	1	678 nm	100 m	8.4 km		
	2	678 nm	100 m	8.4 km	One mineral correlation	ASU[1]
	3	793 nm	100 m	8.4 km		
	4	856 nm	100 m	8.4 km	One mineral correlation	ASU[1]
	5	935 nm	100 m	8.4 km		
	6	1221 nm	100 m	8.4 km	One mineral correlation	ASU[1]
	7	1104 nm	100 m	8.4 km		
	8	1179 nm	100 m	8.4 km		
	9	2557 nm	100 m	8.4 km (Global mosaic)	Base layer Geomorphology (day and night time)	USGS[2]
	10	1488 nm	100 m	8.4 km		
Visible data products						
HRSC						
	Stereo 1	500 – 800 nm	12.5 -100 m	50 – 80 km		
	Stereo 1	500 – 800 nm	12.5 -100 m	50 – 80 km		
	Super resolution camera	500 – 800 nm	12.5 -100 m	50 – 80 km		
	Panchromatic	500 – 800 nm	12.5 -100 m	50 – 80 km	Pan sharpening/ Geomorphology	FUB[3]
	NIR	1000 – 1200 nm	25 -100 m	50 – 80 km		
	Red	700 – 800 nm	25 - 100 m	50 – 80 km	RGB composite	FUB[3]
	Green	500 – 600 nm	25 - 100 m	50 – 80 km	RGB composite	FUB[3]
	blue	400 – 500 nm	25 - 100 m	50 – 80 km	RGB composite	FUB[3]
CTX	Panchromatic	500 – 800 nm	6 m	26.5 km	Geomorphology/ Nili Patera base layer	ASU[4]
HiRISE						
	Red	400 – 600 nm	0.25 - 1 m	5 km	Geomorphology	ASU[5]
	Blue-Green	550 – 850 nm	0.25 - 1 m	1.2 km		
	NIR	800 – 1,000 nm	0.25 - 1 m	1.2 km		

Topographic data sets

MOLA points	~300m spacing along track		PDS	PDS[6]
MOLA (gridded elevation)	~463 m (128 pixels per degree)	Global mosaic	USGS	USGS[7]
MOLA (gridded hill shade)	~463 m (128 pixels per degree)	Global mosaic	USGS	USGS[7]
HRSC DTM	~50 - 100 m			FUB[3]
CTX DTM	~20 m			I made
HiRISE DTM	~1 m			ASU[5]/I made

[1] *Arizona State University* http://viewer.mars.asu.edu/viewer/themis#T=0

[2] *United States geological Survey (USGS)(1)* http://astrogeology.usgs.gov/maps/mars-themis-derived-global-thermal-inertia-mosaic

[3] *Freie University Berlin (FUB)* http://maps.planet.fu-berlin.de/

[4] *Arizona State University (ASU)* http://viewer.mars.asu.edu/viewer/ctx#T=0

[5] *Arizona State University (ASU)* http://viewer.mars.asu.edu/viewer/hirise#T=0

[6] *Planetary Data Service (PDS) University of Washington St Lewis* http://ode.rsl.wustl.edu/mars/dataPointSearch.aspx

[7] *United States geological Survey (USGS)* http://astrogeology.usgs.gov/search/details/Mars/GlobalSurveyor/MOLA/Mars_MGS_MOLA_DEM_mosaic_global_463m/cub

Whilst this project draws on all the available data, the primary data sources are detailed in table 3.1. These data are subdivided here into the following categories: (i) **'Thermal'** data: this is infrared data drawn from the THermal EMission Imaging System (THEMIS) camera on the Mars Odyssey mission [*Christensen et al.*, 2004; *Saunders et al.*, 2004], (ii) **'Visible'** data: this data is from instruments that are sensitive to the visible part of the spectra. Whilst this includes data from the Viking [*Snyder*, 1977] , Mars Global Surveyor [*Albee et al.*, 2001] and Mars Odyssey [*Saunders et al.*, 2004] spacecraft, I have primarily relied on High Resolution Stereo Camera (HRSC) [*Neukum et al.*, 2004a] data from Mars Express [*Schmidt*, 2001] and the ConTeXt Camera (CTX) [*Malin et al.*, 2007] and Hi Resolution Imaging Science Experiment (HiRISE) [*McEwen et al.*, 2007] on Mars Reconnaissance Orbiter. (iii) **'Topographic'** data are data that show the elevation of terrain. This is measured either in terms of the distance from the surface to the spacecraft, such as in the Mars Orbital Laser Altimeter (MOLA; *Smith et al.*, 2001] or, as in the case of HRSC,

CTX and HiRISE Digital Terrain Model's (DTM), using photogrammetry from two visible images looking at the terrain from different angles.

I have used a simple cylindrical projection for data imported into the Geographic Information Systems (GIS) environment (ArcGIS) with the Mars2000 spheroid. This projection has been chosen because Syrtis Major Planum is close to the equator. Data imported into ArcGIS are re-projected 'on the fly', so data with various projections systems can be used easily, although this is not needed with most data products.

3.1.1 Thermal data

The project makes extensive use of data products from the THermal EMission Imaging System (THEMIS) camera on the Mars Odyssey mission [*Christensen et al.*, 2004; *Saunders et al.*, 2004]. The global THEMIS day, and night-time mosaics (Figure 3.1) distributed by the United States Geological Survey, USGS, (http://astrogeology.usgs.gov/search/details/Mars/Odyssey/THEMIS-Global-Thermal-Inertia-Mosaic/Quantitative-32-Bit/THEMIS_TI_Mosaic_Quant_00N060E_100mpp/cub) [*Fergason et al.*, 2006; *Christensen et al.*, 2013] are used as a base layer for my geological/geomorphological interpretations. Multi-band THEMIS data (Table 3.1) are used in Chapter 6: *Meroe Patera*. The THEMIS daytime mosaic provides data regarding the reflectance of the surface in THEMIS band 9 (1257 nm) at 16:00 in the martian afternoon. The pixels are ~100 x 100 m in size. The analysis of these data is drawn from the literature [*Christensen et al.*, 2005] and is generally made qualitatively from products available from the USGS. It was considered reasonable to draw on qualitative data because quantitative analysis that explains these qualitative differences could be referenced thus justifying the comparisons made.
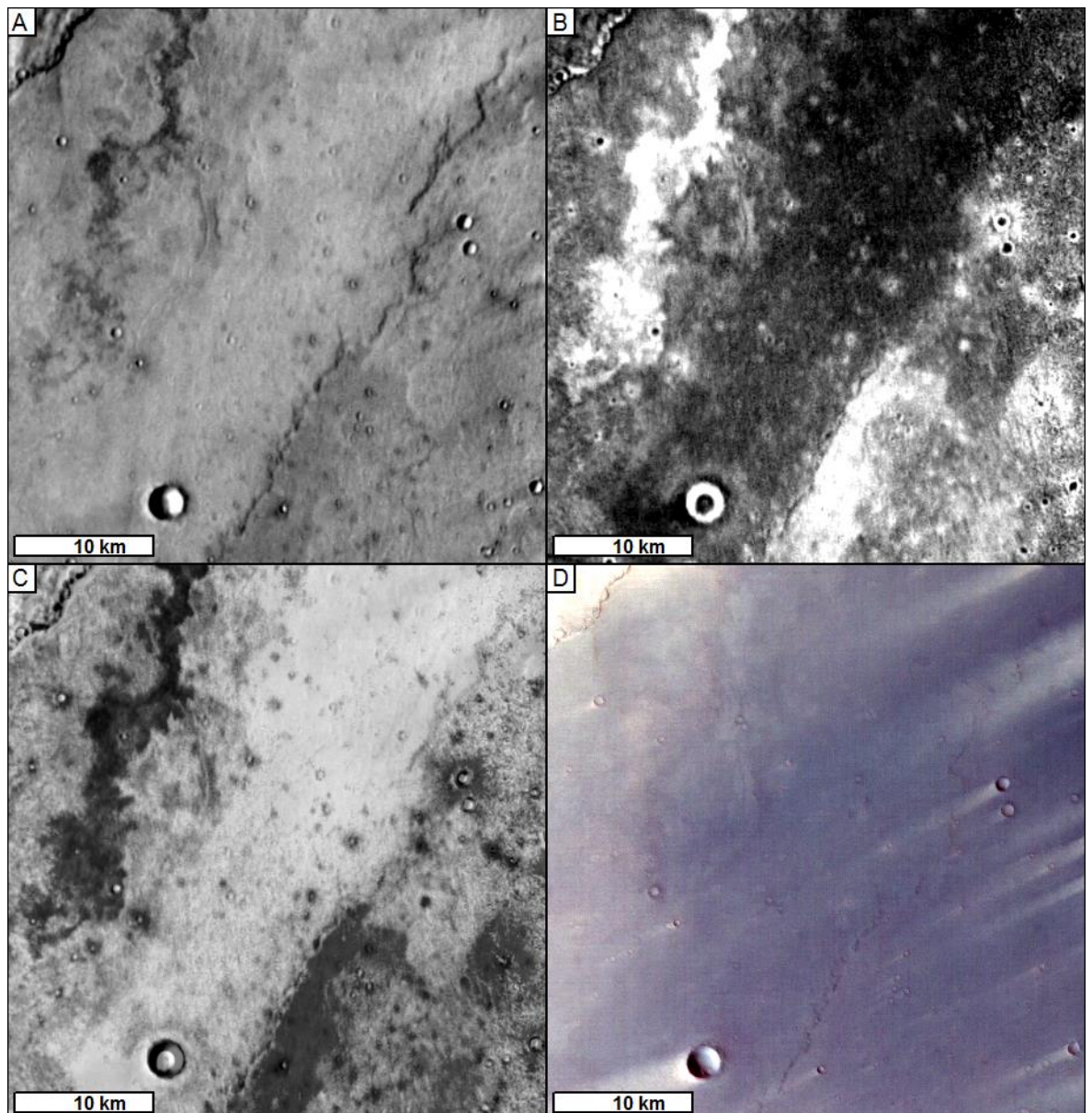
Figure 3.1:

An example of THEMIS data used as the base layer for the Map Sheet 1. (a) Daytime THEMIS. (b) Night-time THEMIS of the same area. (c) THEMIS daytime data overlain by a translucent night-time THEMIS data with an inverted grey scale. (d) HRSC data of the same area.

Materials that *reflect* electromagnetic radiation at this wavelength appear bright and materials that adsorb this wavelength appear darker. Materials that are darker and bluer on the surface of Mars (such as lava) appear to be darker in this data product, whereas materials that are lighter or redder (e.g., Fe^{3+} oxide on sand) appear to be lighter. The THEMIS night-time data global mosaic shows the emission from the surface in THEMIS band 9 (1257 nm) at 04:00 in the martian night. Materials that have a high thermal conductivity and a low thermal inertia (such as sand

dunes) appear darker, whereas materials with low thermal conductivity and high thermal inertia (such as exposed bedrock) appear brighter.

A number of factors can affect the thermal inertia of a material on the 100 m scale of a THEMIS pixel. Consolidated material (indurated or cemented sandstones) or material where there is a low porosity (fine-grained, indurated materials) and solid rocks (such as the core of lava flow or less degraded smoother surfaces, such as preserved ropey surfaces of a pāhoehoe lava flow) will retain heat from the day and therefore be brighter than other surrounding materials during the night-time. Conversely, materials that change temperature more with diurnal cycles – either due to a physical property of the material or because of increased communicability with the atmosphere facilitated by a high porosity (e.g., unconsolidated sand, rubbly crusts of lava flows, scoria, uncemented sediments, impact ejecta) – will appear darker in night-time thermal inertia maps. It is important to consider that the 8-bit value of each THEMIS pixel is the average reflectivity/emissivity at this wavelength for everything in a $100 \, \text{m} \times 100 \, \text{m}$ area. In this study area, there is the potential for a great diversity in the thermal properties of surface material. This is particularly true for volcanic terrains with lava flows of different emplacement styles and states of degradation. Hence, there are likely to be differing proportions of high and low thermal inertia materials at the surface at all scales. Whilst this presents a significant challenge it can be overcome by drawing on higher resolution visible datasets.

To help in identifying volcanic units, I have used a novel (previously unreported) combination of night-time and daytime THEMIS data. I combine the daytime THEMIS mosaic with a semi-transparent night-time mosaic with an inverted grey scale. This juxtaposing of data shows where there is a correlation between low daytime values and high night-time values, a correlation indicative of a fresher bedrock surface (Figure 3.1c). Consequently, it is easier to define boundaries and to investigate areas that are otherwise hard to decipher (Figure 3.1d). This technique also helps to remove the effects of of slope and shadow from night-and daytime data.

3.1.2 Visible data

I have used three sources of visible data: **Con**te**x**t camera [*Malin et al.*, 2007], the High Resolution Stereo Camera (**HRSC**) [*Neukum et al.*, 2004a], and **Hi**gh **R**esolution Imaging **S**cience **E**xperiment [*McEwen et al.*, 2007]. The specification for these are found in Table 3.1 and data coverage is shown in Figure 3.2

3.1.2.1 HRSC

At the start of the project, I used the available (Figure 3.2a) **H**igh **R**esolution **S**tereo **C**amera (**HRSC**) [*Neukum et al.*, 2004a] as the detail component to supplement the THEMIS daytime base layer. The HRSC camera is on the Mars Express (MEX) spacecraft [*Schmidt*, 2001] in orbit since 2003. The camera consists of a nadir-pointing camera with panchromatic, Infrared (IR), Red, Green and Blue (RGB) detectors. It also has forward and backward pointing cameras providing stereo data for Digital Terrain Model (DTM) production, and a super resolution camera (SRC).

HRSC nadir products (12.5 – 25 m/pixel) were initially used to add detail for identification of volcanic features below the scale of the THEMIS base layer; i.e., to help differentiate surface textures. However, I found that HRSC data does not have sufficient resolution, and is often too noisy, to permit the required investigation at the scale of surface textures of the different volcanic units. Consequently, CTX data, although sparse in the plains area (Figure 3.2c), became the primary visible-type data used to provide the information required to make a determination about the surface structure of areas identified in THEMIS data. By the end of the project, CTX images covered a large proportion of the area being investigated. As such, there was no significant spatial-resolution limit on the interpretations made (Figure 3.2d).
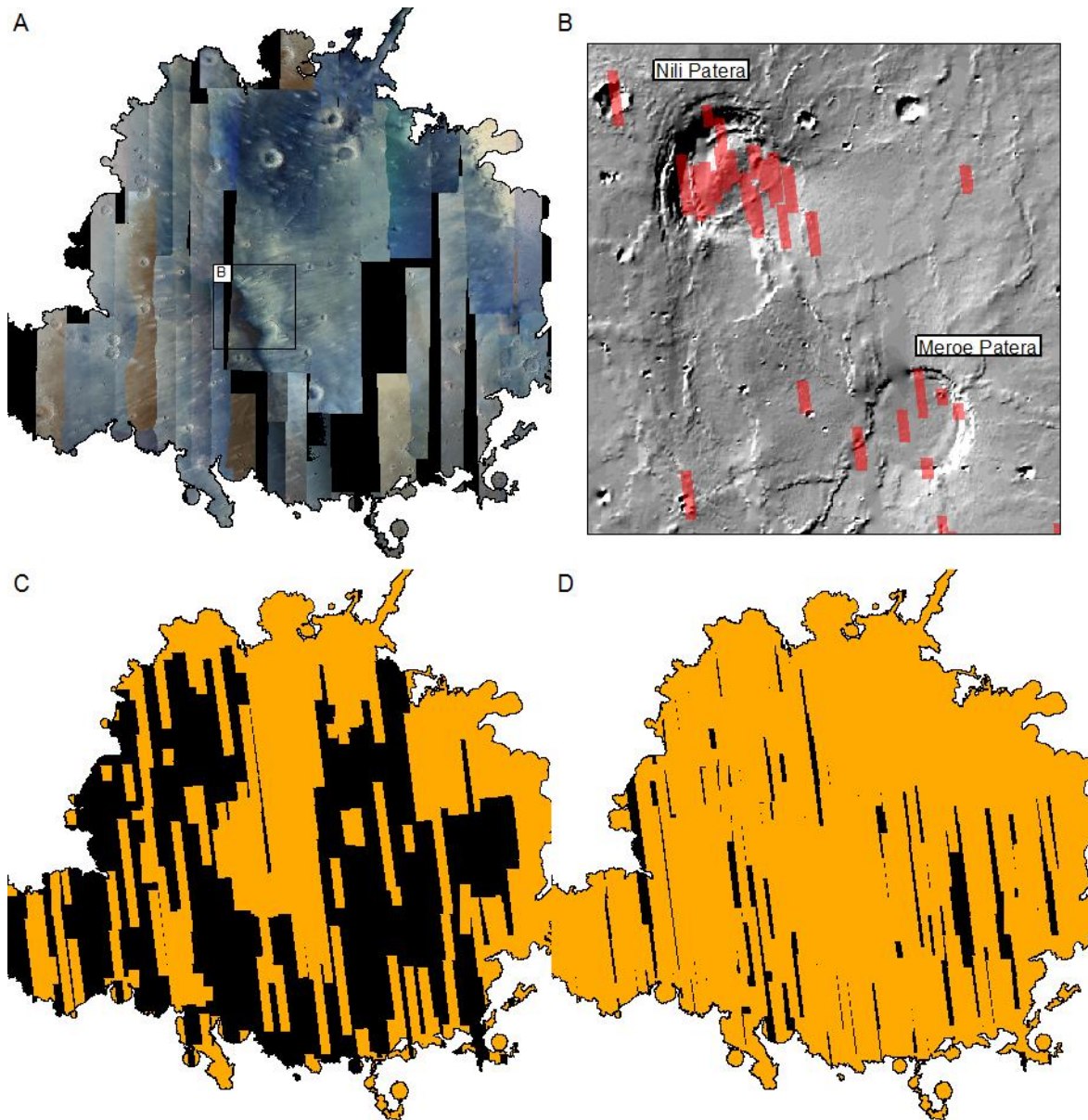
Figure 3.2:

Coverage of data used for the project. (a) A mosaic of HRSC colour data coverage. (b) The HiRISE image coverage of Nili Patera and Meroe Patera in the central caldera complex. (c) The availability of CTX data (Orange) at the start of the mapping effort in February 2012. (d) The CTX data coverage at the end of the mapping effort in June 2015. Black shows data gaps.

HRSC was still used to provide colour information to the CTX and HRSC nadir data. The red, green blue (RGB) colour components (e.g. h1089_0000_re3, h1098_0000_gr3 and h1089_0000_bl3) were composited using tools within ESRI ArcGIS 10.1 software. These were then pan-sharpened using the nadir product (e.g. h1098_0000_nd3; Chapter 5.2.3.1), again within ArcGIS 10.1. In places, the RGB colour composite data has then been geo-referenced to the CTX

data and then pan-sharpened using CTX images. These data provide (RGB) colour to help visually characterise units and highlight outliers of the underlying Noachian highlands.

3.1.2.2 CTX

Con**TeX**t Camera (**CTX**) [*Malin et al.*, 2007] data have been increasingly drawn on through the project as the coverage increased (Figure 3.2). CTX data (Table 3.1) are of a high enough resolution (6 m/pixel) that it is feasible for an area the size of Syrtis Major Planum to present a map at 1: 2,000,000. These data have been used to differentiate between geological units and to investigate the high-resolution surface texture of units and features. This dataset has proved essential when differentiating and interpreting differing styles of volcanism across the Syrtis Major Planum.

3.1.2.3 HiRISE

High **R**esolution **I**maging **S**cience **E**xperiment images were not used for mapping and compiling Map Sheet 1 because they cover an insignificant proportion of the volcanic plains. Where available, though, I have used them extensively to "calibrate" landforms and surface textures at the metre-scale with patterns and textures observed in lower-resolution CTX and HRSC images. All HiRISE images publicly available at the time of writing were imported into the GIS and examined as part of creating Map Sheet 2 and to study the areas around Nili and Meroe Patera in Chapters 5 and 6 (Figure 3.2). I also studied HiRISE DTMs DTEEC_017762_1890_018039_1890_A01 and DTEED_013582_1890_020940_1890_A01

(hirise.lpl.arizona.edu/dtm/dtm.php?ID=ESP_013582_1895*,*

http://hirise.lpl.arizona.edu/dtm/dtm.php?ID=ESP_017762_1890) and a DTM I created from stereo pair ESP_035247_1890 and ESP_035537_1890 using SocetSet software. HiRISE data do not provide complete coverage of the mapped area, but do add detailed textural information to units mapped in CTX.

3.1.3 Topographic data

Mars **O**rbital **L**aser **A**ltimeter (**MOLA;** *Smith et al.,* 2001]) data from the Mars Global Surveyor mission [*Albee et al.*, 2001] are used extensively in the project and come in two forms: point elevation data and gridded raster data.
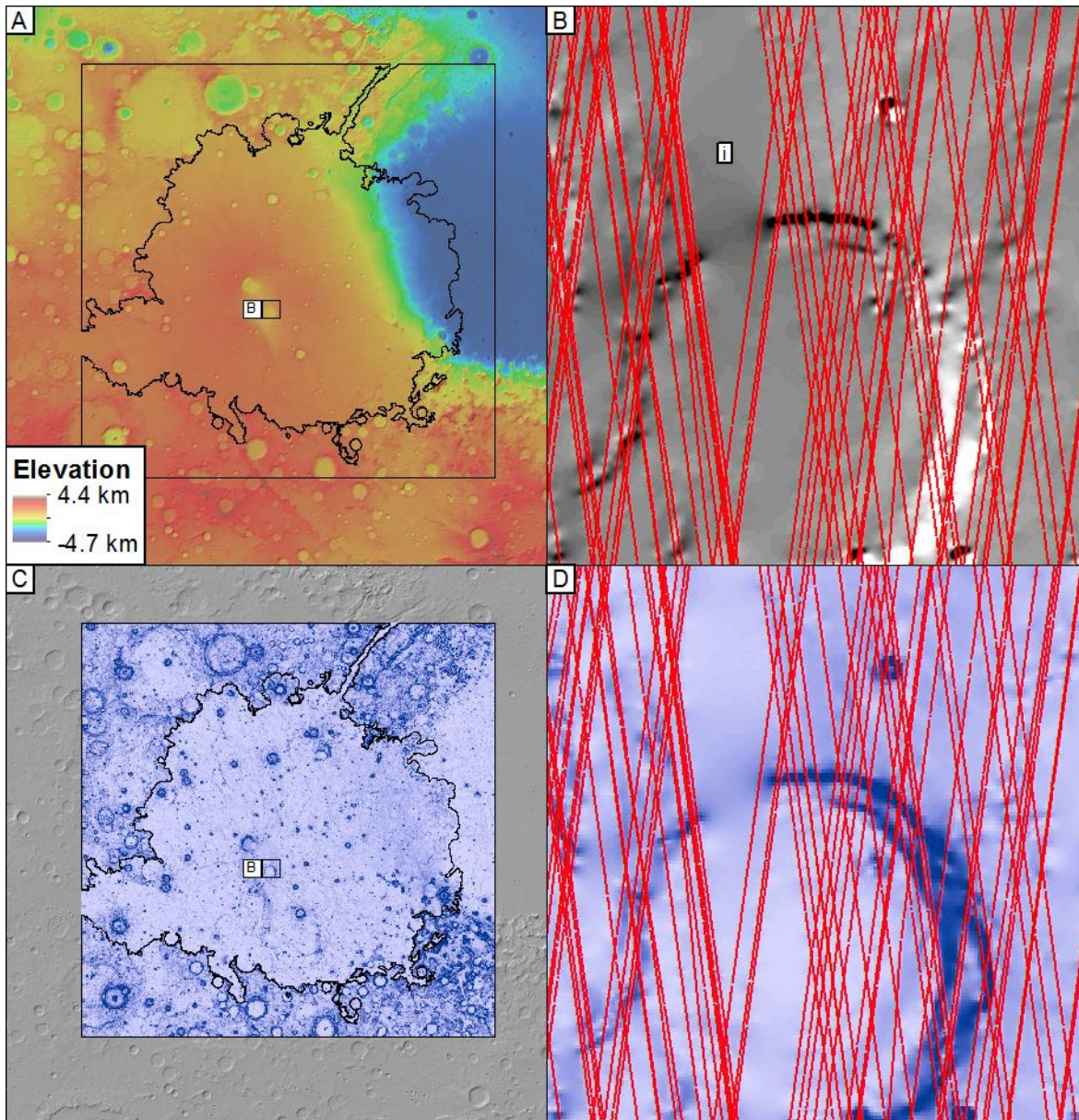
Figure 3.3:

*A sample of the MOLA data used in the mapping. (a) MOLA data gridded at 512 pixels per degree in the region of Mars around Syrtis Major Planum. The **black** lines show the total extent of the mapping area and the extent of Syrtis Major Planum. (b) MOLA point data overlying the gridded MOLA hill-shade product at the northern rim of Meroe Patera. This shows (i) the east–west sparsity of points and the resulting artefacts in the hill-shade product formed during gridding interpolation. (c) The slope map of gridded MOLA data in the mapping area. The smooth extent of the Planum is highlighted by the lack of more steeply sloping. (d) MOLA point data overlying the gridded MOLA slope map product at the northern rim of Meroe Patera.(darker blue = steeper)*

3.1.3.1 MOLA point data

There are approximately 8.5×10^6 MOLA points in the mapped area. MOLA points have an along-track spacing of ~300 m, and a vertical accuracy of ±0.37 m [*Smith et al.*, 2001]. Throughout the project I have used MOLA point data to measure profiles where features are too small (less than ~500 m wide measuring North-South or less than the local East-West track spacing) to be accurately represented in the gridded data. This is only possible where the track of MOLA points (~North – ~South) is approximately perpendicular to the orientation of a feature (i.e., an East – West trending feature). For features in this orientation there is a point every 300 meters. However, across the track, spacing of the points is dependent on the frequency of tracks in the area, and this frequency varies from place to place. Figure 3.3c shows the example of Mero Patera; here profiles taken along the track, where there are tracks, capture the topography of the caldera rim whereas transects extracted in and East-West orientation encounter data gaps, such as area (i) in Figure 3.3c.

3.1.3.2 MOLA gridded data

The gridded MOLA data is an interpolated raster product with a pixel size of 128 pixels per degree, which equates to ~463 m per pixel in the projected co-ordinate system. Due to the spacing of orbital tracks of the MGS spacecraft close to the equator, there are often gaps of more than the gridded MOLA pixel size between MOLA tracks. This results in areas where interpolation means that the raster has no real information. This means that the gridded data have a variable longitudinal accuracy and features below this resolution can be poorly represented in the gridded data. For example, an impact crater may appear to be a small mound in the gridded data where the orbital track has only captured the elevated crater rim, rather than crater floor. However, provided the user is aware of such caveats, the gridded data is still a valuable and convenient product.

Using the MOLA gridded elevation data across Syrtis Major Planum (Figure 3.3) slope maps (Figure 3.3c), (calculated using the mean slope in a 3 × 3 moving window as standard for

ArcMap 10.1) shows the slopes at a baseline of ~1300 m. These, and combinations of these have been used throughout this study.

3.1.3.3 CTX photogrammetry

I generated a digital elevation model (DEM) using the method of Kirk et al. [2008] from two CTX [*Malin et al.*, 2007] images (D10_031182_1435_XI_36S185W and D09_030892_1435_XI_36S185W). This method uses public-domain **I**ntegrated **S**oftware for **I**mages and **S**pectrometers (**ISIS**) software to pre-process the raw experimental data records (EDRs) before processing in SocetSet®, a commercially available photogrammetry suite (http://www.socetset.com). During the processing in SocetSet®, I controlled the DTMs using MOLA track data, thus allowing me to correlate elevations between topographic data sets of different scales. The output from SocetSet® was an 18 metre per pixel (mpp) DTM resolving topography of ~50–60 m and an orthorectifed CTX image (from D09_030892_1435_XI_36S185W) at 6 m/pixel. Although no calculations are done from CTX DTMs, so knowledge of vertical accuracy is not essential, the precision of elevation values in the DTM can be estimated based on viewing geometry and pixel scale. For example, image D10_031182_1435_XI_36S185W (5.44 mpp, emission angle 15.14°) and D09_030892_1435_XI_36S185W (5.28 mpp, emission angle 12.12°) have a 3.02° stereoscopic convergence angle. Assuming 0.2 pixel matching error, the vertical precision is estimated to be approximately 28.73 m [cf. *Kirk et al.*, 2003, 2008]. As shown in the worked example, the Expected vertical Precision (EP) of a single stereo pair is estimated as:

Eq. 1.

$$EP = \Delta p \; IFOV / (parallax/height)$$

Where: IFOV is the instantaneous field of view of the image pixels in metres on the ground. If two images of differing IFOV are paired, the RMS of their IFOV values is used; e.g. $IFOV = 7.58 = \sqrt{(5.44^2 + 5.28^2)}$.

The parallax/height ratio is calculated from the three-dimensional intersection geometry but reduces to tan(e) for an image with emission angle e paired with a nadir image; e.g. parallax/height = tan(e) = 0.0527 (e = 3.02 = 15.14 − 12.12). Δp is the RMS stereo matching error in pixel units. 0.2 pixel is often used as a rule of thumb [Cook et al., 1996] and confirmed with our matching software for several other planetary image data sets [*Kirk et al.*, 1999; *Howington-Kraus et al.*, 2002]; e.g. Δp = 0.2. The pixel matching error is influenced by signal-to-noise ratio, scene contrast and differences in illumination between images. Pattern noise can also be introduced by the automatic terrain extraction algorithm, especially in areas of low correlation. These can be identified as patches of 'triangles' in the hill-shade model in areas of poor correlation (e.g. smooth, low contrast slopes and along shadows).

3.1.4 GIS techniques

Throughout the project I have used a range of GIS techniques. The principal of the most common are outlined here

Gridded data is a raster representation of point data where the value of each cell in the raster is generated from the value of the point data or an interpolation between 2 or more points.

Geo-referencing is adjusting the position of an image in the co-ordinate system of mars so features in the image match the position of features in the base map. This was done where there is a discrepancy between image location data from images from different sensors

A **hill shade** model is a grey scale representation of a surface showing the degree of illumination across the slopes of the surface from a defined light source. In this project we have used the default illumination position of azimuth of 135° and altitude of 45°.

RGB compositing is the process of combining three images (usually the Red Green and Blue components of a cooler scene) in one data product with three bands

Pan-sharpening is the process of increasing the resolution of cooler data with a higher resolution panchromatic image by averaging the pixel values between the high and low resolution data sets across in each of the three bands of the cooler data to create a new colure data product with the resolution of the higher result ion panchromatic data

A **Slope map** is a map of the slope between each pixel of a DTM and the surrounding pixels, where this is used the algorithm for calculating the slope map is discussed.

3.2 Maps

For this thesis I have compiled two maps. The first, Map Sheet 1, is a map of the whole of Syrtis Major Planum, on which I identify and map the distribution of different styles of volcanic surfaces to understand the volcanic history of the whole Planum. The second, Map Sheet 2, is a larger scale map of the Nili Patera caldera at the centre of Syrtis Major Planum. This map focuses on differentiating volcanic surfaces and their stratigraphic relations to reconstruct the geological history of the caldera.

3.2.1 Map sheet 1: Syrtis Major Planum

The main map drawn up in this project is Map sheet 1: (Geological map of Syrtis Major Planum: Mars). This map uses the THEMIS daytime mosaic as a base layer, with CTX used to help develop interpretations of the mapped units. The Map covers an area of 3.16×10^6 km^2 presented at a scale of 1: 2,000,000. Map sheet 1 is a thematic map aimed at understanding the different styles of volcanism across the Planum, based mainly on topographic features and surface textures. As such, it is mainly a geomorphological map denoting various geomorphological units. The map differs from planetary mapping guidelines [*K.L. Tanaka*, 2010] in that it specifically endeavours to investigate, and thus subdivide, the volcanic plains of Syrtis Major Planum into groups of areas with similar volcanic morphologies. For Map Sheet 1 I defined a unit as a surface area that, after the context of that area has been considered, has a similar surface appearance in visible or THEMS IR data. This includes albedo, texture and smaller-scale landforms. Within each unit are elements of that unit. Each element is an identifiable instance or inferred instance of the surface

type described for that unit (e.g. an individual lava flow in the late Hesperian volcanic flow unit). The mapping of groups may identify individual flow fields (where numerous successive lava flows can be attributed to a single eruption; Self et al. 1998). The aim of the mapping is not to identify every lava flow event, but rather to identify apparently genetically similar groups of volcanic deposits.

The boundaries between groups were digitised with a vertex spacing of ~200 m at a scale of 1:60,000 - 1: 100,000. This scale for digitisation was chosen because it is the maximum level of zoom for the resolution of the 100 m/pixel base map. This vertex spacing was chosen so lines will appear smooth at the scale of map presentation (1: 2,000,000) but also (made possible because this is a digital map) the line will remain smooth when zoomed in 10 times (1: 200,000) which is the maximum reasonable scale to view the 100 m/pixel base layer THEMIS mosaic. This is important because it is not possible to display all the relevant relationship and detail required to investigate the volcanic history (which occurs over scales of 10's of meters) across an area ~1000 km across on a reasonable sized piece of paper. Boundaries between units are classified as certain, approximate, inferred or gradational. For a certain boundary, I have assumed that the boundary is within 200 m (2 THEMIS pixels) of the digitised line. For an approximate boundary, the boundary lies within 1000 m (10 pixels), but it is not clear exactly where it is. An inferred boundary is reported when logically there must be a division in this area, but where there is little evidence for exactly where the boundary should be, and where there is no evidence that the boundary is gradational. A gradational boundary divides elements of the mapped groups where, at the scale of digitisation, the units appear to fade into each other but where the two different elements can only be clearly distinguished at a distance >> 1km from the boundary.

Impact craters have been mapped where they are sufficiently large to have continuous ejecta, appear in the MOLA hill-shade data product, or intersect and obscure a boundary.

3.2.1.1 Digitisation method

High-resolution data sets are needed to meet the objectives (Chapter 1.2), however, it was not feasible to map at this resolution across the whole of Syrtis Major Planum in the timescale of this research. The locations of features are identified and mapped in the THEMIS data but their detailed structure was studied in the CTX. CTX data are required (6 m per pixel) for decision making and to identify many key features in the structures and surfaces of lava flows (such as small ridges and pits) of the order of tens of metres across. This detail is required to explain trends seen in the THEMIS data which alone would not allow us to answer the science questions. To identify and digitise every potential unit as seen in CTX data would be an impossibly large task, which is why I have digitised groups of morphologically similar surfaces even when they could be subdivided, for example into individual flows [*K.L. Tanaka*, 2010].

Throughout this project I have used 3D visualisation to help understand the topographic relationships of the different volcanic surfaces of Syrtis Major Planum (Figure 3.4). To do this I have used ArcScene and Geovisionary™. Both these programs allow me to overlay THEMIS HRSC and CTX data over sections of the MOLA gridded DTM, or CTX HRSC and HiRISE DTMs. ArcScene is a standard part of the ArcGiS package and was used to view small areas and thematic cut-outs section of Syrtis Major Planum. The Geovisionary™ is a 3D visualization environment developed by the British Geological Survey specifically for visualizing large 3D data sets (such a HiRISE DTM or a 1000 km x 1000km section of MOLA data). Geovisonary™ allows for various image overlays whilst freely changing the view perspective and vertical exaggeration on the fly and is fully interactive with ArcGIS 10.1. This allowed unit and contact mapping to be performed in 3D. Whilst this was not used for all boundaries, these techniques add invaluable perspective on subtle topographic trends and relationships (Figure 3.4).
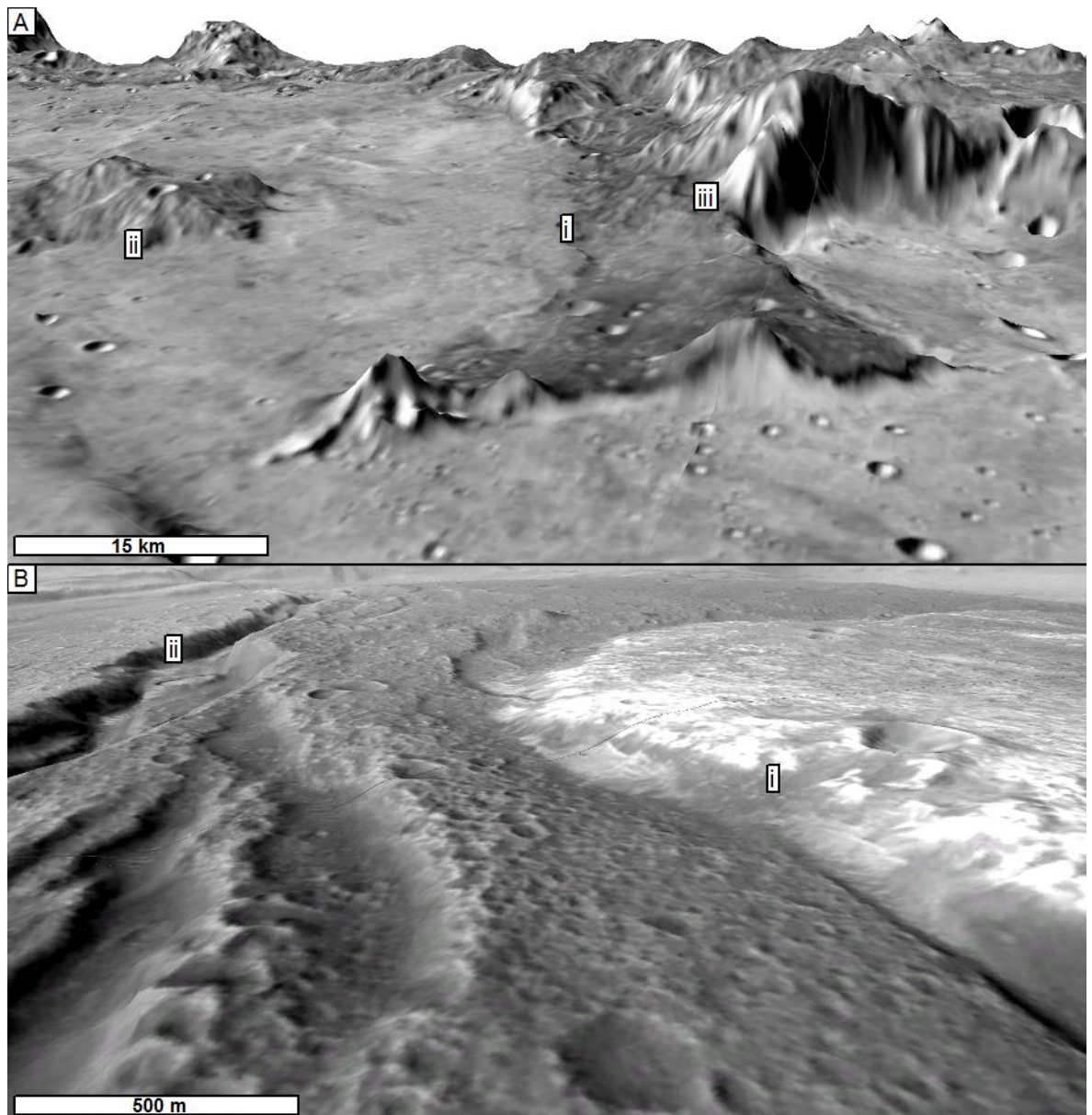
Figure 3.4

These are two examples of data visualised in 3D. (a) Visualised in ArcScene is from the northern edge of Syrtis major Planum, looking west, showing (i) the edge of Syrtis Major Planum lava units superposing the underlying highlnd material which appears dark in the Themis daytime data. (ii) Highland material sticking though the lava plain and (iii) the slopeing highland plain slope ing down to the location (i).(b) Visualised in Geovisionary™, this view is from the Nili Patera caldera (Chapter 5) and looks North from the centre of the caldera showing (i) a bright lava unit superposing faults and (ii) the graben which runs along the axis of the dome on the caldera floor.

This thesis is focused on the volcanic processes of Syrtis Major Planum and how they have changed with time, rather than the seeking to explain the sequence of every lava flow, or the details of all other processes affecting the Planum throughout its history (such as fluvial erosion or the development of Nili Fossae). Surfaces not directly of volcanic origin, whilst interesting in their own right, are described and interpreted on Map Sheet 1, but no further discussion as to their

origin is attempted: the aim was to map in detail the relevant components of the study area, rather than synoptically map every unit within a defined area.

Because Syrtis Major Planum has been well studied, and its volcanic origin established e.g. [*Schaber*, 1982], it is therefore reasonable to begin with a volcanic origin as a working hypothesis to explain most of the observed morphology. From this simple starting point, the subtleties in the appearances of the various different lava flows have been teased out.

3.2.1.2 Simplified instances of the map

In addition to Map Sheet 1, I have created a simplified version of the map which amalgamates all the mapped groups into six top-level formations: 'Highlands, 'Volcanic plains', two groups of 'lava flow', 'the central caldera complex', and 'Isidis Planitia'. The simplified map of Syrtis Major Planum (shown in Figure 4.2) has been used to show the general location of major volcanic groups. This simplified map interpolates boundaries across areas covered by other processes (such as impact ejecta). This makes the simplified map suitable for presenting subsets of more detailed data (e.g. Figure 4.5) and for extracting crater data from the Robbins catalogue [*Robbins and Hynek*, 2012a]. The formally mapped boundaries are inappropriate for this because they specifically include impact craters' ejecta in the study areas.

3.2.2 Map Sheet 2: Nili Patera

The second map presented in this thesis is Mthe map of Nili Patera map sheet 2. This map is presented here at a scale of 1: 250,000. The map is based on three CTX DTMs and ortho-photos. The approach to mapping for the Nili Patera (Map Sheet 2) is a traditional one, using identification of units based on their visible surface morphology, day and night thermal response, texture, stratigraphic relations and, where available, reflectance spectral responses in the visible to IR. The locations of boundaries were identified at this scale and digitisation was performed with a vertex every 10 m on the ground. Boundaries are classified as certain, approximate, inferred or gradational in a similar way to Map Sheet 1 (Section 3.2.1).

Map Sheet 2 is the basis for Chapter 5: The geological history of Nili Patera. In Chapter 6: Meroe Patera and the Syrtis Major central caldera complex, an extract of map sheet 1 is presented at a smaller scale (1: 250,000, the same as Map Sheet 2). The digitisation here derives from the larger mapping effort presented as map sheet 1. However, the colour scheme and units have been taken from Map Sheet 2 to facilitate a clear comparison between the Nili and Meroe Patera, as well as to differentiate this mapping, where additional detail from HiRISE and CTX has been considered, from that presented in Map Sheet 1.

3.3 Crater counting

To evaluate the age of surfaces I have used impact crater size frequency distribution statistics [*Hartmann*, 1977; *Tanaka*, 1986; *Hartmann and Neukum*, 2001b; *Werner and Tanaka*, 2011]. Data for these analyses were collected in two ways:

- For crater counts of large areas, crater locations and diameters were collected from a database of all Martian craters <1 km in diameter [*Robbins and Hynek*, 2012a, 2012b].

- I performed crater counting myself using HRSC and CTX data in smaller areas where the stratigraphy is well defined.

These result are presented though the thesis as well as being collated with an expanded description of the methord and underlying asumptions in appendix 1

3.3.1 Crater counts assimilated from database

To evaluate the age of large areas of Syrtis Major, crater location (latitude, longitude) and diameter (km) were extracted from the Robbins database [*Robbins and Hynek*, 2012a]. This database contains >300 000 martian craters larger than 1 km. From this, I extracted all (10,200) craters in the study area; Figure 3.5). Those that were within the boundary of Syrtis Major (as defined by the simplified map of volcanic groups (Figures; 3.5, 4.1 and 4.19) were assessed in order to identify and remove any ghost craters [*Cruikshank et al.*, 1973] from the data. 'Ghost craters' are identified where, at the level of the THEMIS 100 m/pixel base layer, I can see that the

present-day surface formed *after* the impact crater and the centre point of the crater is outside

the Noachian highlands. This includes craters where there is only a circular wrinkle ridge to

identify the rim (Figure 3.5) or where the crater is in highland terrain, but has been embayed by

material associated with Syrtis Major Planum or the material coating the floor of the Isidis basin.

107 ghost craters have been identified. The filtered data set of 10,093 craters was subdivided by

unit in the simplified map. The results of these data are presented in Section 4.2.3.1.
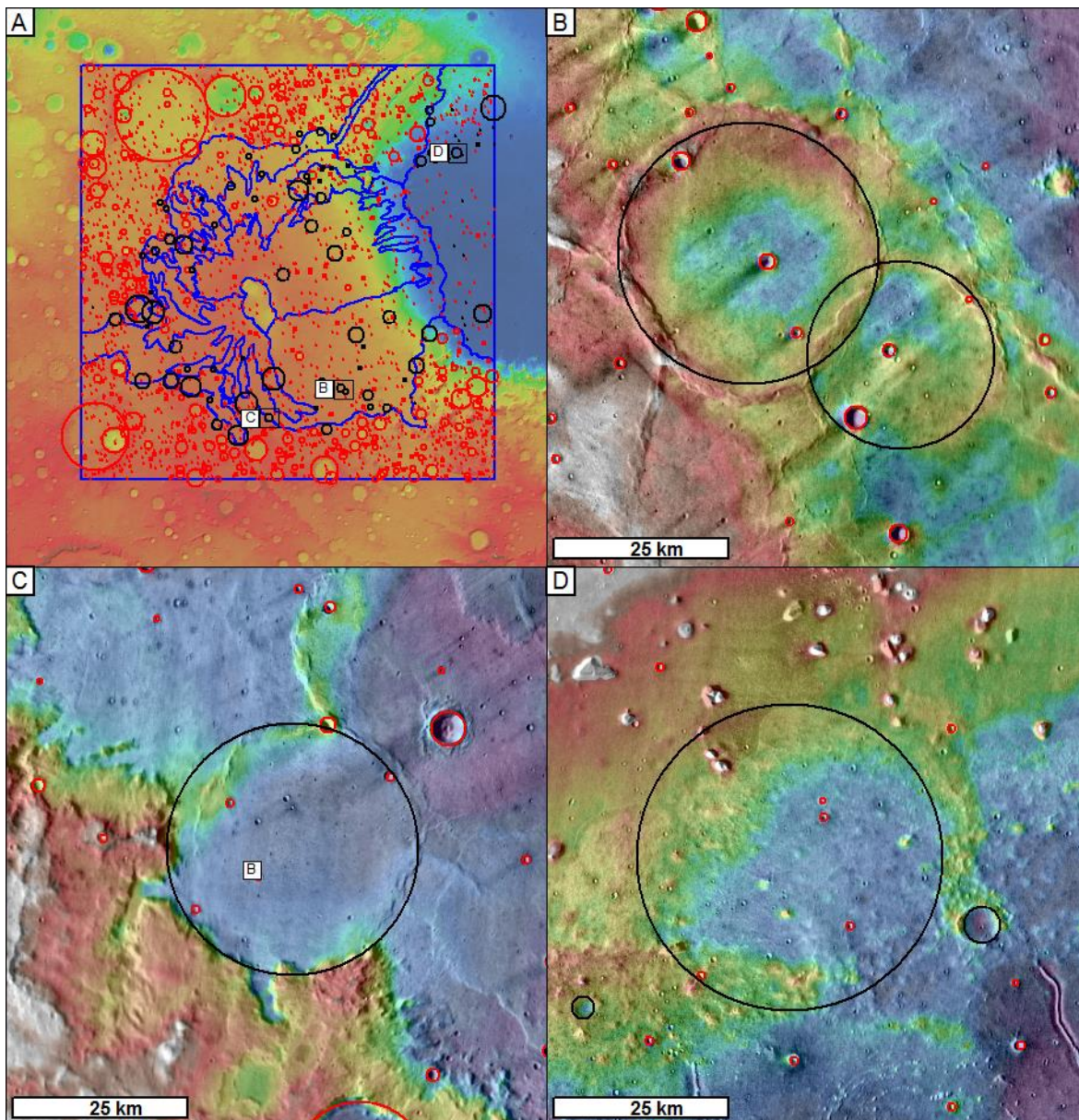
Figure 3.5:

(a) The craters extracted from the Robbins [Robbins and Hynek, 2012a] crater database used in Chapter 4. Red *circles are the (10,093) craters included in the count areas (*blue *lines show simplified map units),* **Black** *circles are (107) ghost craters included in the Robbins database but filtered from the data because they pre-date the surfaces I am investigating. Examples of ghost*

craters were excluded from all counts made to investigate the emplacement age of Syrtis Major Planum. (b) ghost craters only identifiable by wrinkle ridges tracing the rim. (c) A crater in the Noachian highlands embayed by material associated with Syrtis Major lavas. (d) Ghost impact crater on the floor of Isidis Planitia.

3.3.2 Crater counts conducted for the project

I conducted crater counts in 16 areas across Syrtis Major. Impact craters were identified visually in HRSC, CTX or HiRISE images as appropriate to the scale of the unit, group or area and digitised in ArcGIS using the three-point digitisation method in the CraterTools software package [*Kneissl et al.*, 2011a], guided by the methodologies of Platz et al. [2013] and Tanaka et al. [2014a]. Units were crater-counted after they had been identified stratigraphically. Care was taken not to count craters embayed by the units being examined. Craters in all states of degradation were counted to sample formation age rather than a resurfacing age created when smaller craters in the population are in filled and larger ones partially in filled. Only units where there was no significant evidence of crater modification, ongoing erosion, or other resurfacing processes were deemed suitable for crater counting. I have endeavoured to only count units where there is stratigraphic evidence to validate crater count statistics, such as a unit underling or overlying impact ejecta.

3.3.3 Model ages

To determine crater retention model ages, I used the CraterStats software package [*Michael and Neukum*, 2010]. I considered the whole cumulative population and then fitted ages using the Hartman [*Hartmann and Werner*, 2010] production and chronology function to the steepest part of the slope. For consistency between units, I endeavoured to use the same crater size bins for units counted on directly comparable data for determination of model ages. Crater size-frequency model ages are summarised in Tables 4.4, 4.5 and 5.1. Additionally, I note the conclusions of Warner et al. [2015] (Section 2.3.6) appreciating the implications for the validity (or lack thereof) of crater count-derived model ages made using areas <1000 km^2. It should also be noted that these are only model crater-retention ages; absolute formation ages can only be calculated through sample analyses.

3.4 Field work

As part of this investigation I have done field work to help improve my ability to recognise volcanic terrain in remote sensing data. I have studied volcanic structures in the field and in corresponding remote sensing data to compare to my interpretations of the orbital images of Mars. This forms a crucial part of the mapping approach. For this, I have visited the following locations (with highlights pertaining to Syrtis Major Planum noted).

In the Manda Harrao rift segment in Afar, Ethiopia I observed how the predominantly páhoehoe landscape formed from successive small flow units. This is a good martian analogue because it is an arid desert environment with a very small amount of vegetation. I examined the landscape both in plan-view and in cross-sections through successive ('A'ā and pāhoehoe) lava flows afforded by the pervasive extensional faulting of the rift. This was relevant to understanding the lava plains (such as the early Hesperian volcanic plains unit Chapter 4) and how aeolian sand in fills and changes the appearance of the Pāhoehoe landscape. It was also instructive for understanding how the 3D architecture of lava flows, and the flow fields they compose, build up to construct the landscape.

On Mt. Etna, Sicily I was involved in a long standing GPS and precise levelling campaign [*Murray*, 2013] monitoring deformation over the last 40 years. During this study I observed 'a'ā lava flow channels, and the development of lava flow architecture on a steeper edifice. This was relevant to the understanding of 'a'ā flows in general and specifically to the features I ended up mapping as "Late Hesperian volcanic flow unit". This field study also demonstrated to me how scoria can mask flow structures.

In Iceland I observed the relationship between two small cones, 'a'ā channels, their transition into digitate pāhoehoe lobes, and the interactions between flows and the topography of remnant hyaloclastite ridges. This was interesting in terms of the topography at the boundary between Syrtis Major Planum lavas and the upstanding highland terrain. I observed the Krafla fissure vents associated with the 1975 - 1984 "Krafla fires" [*Opheim and Gudmundsson*, 1989], the topography

of the vent system and the onlapping relationships between vent proximal deposits and lava flows from different phases of the eruption [*Harris et al.*, 2000]. This is relevant to understanding the ridges and pits and channels on the flanks of Syrtis Major Planum.

On Lanzarote I also observed open channels that fed the rapidly emplaced slabby Pāhoehoe in the Timanfaya national park [*Solana et al.*, 2004]. I also observed lava tubes and channels and assessed how visible such features would be in remote sensing data of various resolutions. These observations were also important for interpreting the rough lava surfaces as well as channels and chains of pits on Syrtis Major Planum.

On Oahu, Hawaii, I studied the network of dykes in the plumbing system of the Ko'olau Range volcano, where exposed by catastrophic flank collapse [*Moore et al.*, 1994]. This was important in terms of understanding Syrtis Major Planum as it gave a more detailed appreciation of how the magma is fed to the surface.

Finally, on Hawaii, I drew on the 'Geologic Guide To The Island Of Hawaii: A Field Guide for Comparative Planetary Geology [*Greeley*, 1974]. Here I observed smooth platy and ridged surfaces of pāhoehoe lava flows and the transition from a'ā to pāhoehoe, as well as the topographic effect on that transition that are important for my interpretation of volcanic trends on Syrtis Major Planum. Observing the vent and vent proximal landforms of pit craters and drained lava lakes on the ground, and comparing this to LiDAR data, has been important in my interpretation of vent and pit features in the central caldera complex of Syrtis Major.

3.4.5 Application of field data

Volcanic landforms appear very different in remote sensing data to when studied in the field [*Tanaka et al.*, 2009]. To combat this I looked at data from the analogue locations described above throughout the project. In particular, I have noted that even when looking at landforms formed by the same processes (such as a Pāhohoe flow), the environmental context of the landscape can act to produce variations in how the features generated by that process appear

both on the ground, and in remote sensing data. Therefore, by studying a range of terrestrial volcanic environments as examples, I have developed my expertise and build my experience in interpreting remote sensing data of volcanic landforms on Mars.

Comparison with terrestrial examples and corresponding remote sensing data has been invaluable whilst going through the process of identifying volcanic landforms at Syrtis Major Planum. Throughout the project I have found comparable terrestrial landforms and then observed how those volcanic landforms appear on the ground, while considering the variations in appearance in terrestrial and planetary remote sensing data. This process has been important for me to appreciate the ways that many processes can form what appear to be similar landforms (equifinality). Conversely, it has helped me to recognise landforms and, considering the context, be able to understand the variety of process that may have produced them. Specific reference is made to these analogue sites in the discussion sections of Chapters 4, 5, 6, and 7 and in the overall discussion of Syrtis Major Planum within the context of martian volcanology and geological history.

Chapter 4: Planum Building flows

4.1 Introduction

This chapter investigates the volcanic units that make up the bulk of Syrtis Major Planum. Of the units mapped in Map Sheet 1 (1: 2,000,000), this chapter is primarily concerned with the Volcanic plains formation (The Early Hesperian volcanic plains unit; eHvp and Volcanic plains group on linear rises; eHvr), The Planum building lava flow formation (Hesperian fissure field unit; Hff, Giant flow group; Hvp, and the Late Hesperian volcanic flow unit; lHvf), and the Late stage volcanic formation (The Amazonian/Hesperian dark plains unit; AHdp, Amazonian dark ridge unit; Adr, and unique examples of themrally distinct materials, Amazonain volcanic field units; Avf). The other groups included on Map Sheet 1, whilst important in the history of Syrtis Major Planum, are not considered in this chapter.

Previous work on Syrtis Major Planum has identified features of lava flow fields and effusive volcanic activity [*Carr*, 1973; *Meyer and Grolier*, 1977b; *Schaber*, 1982; *Raitala and Kauhanen*, 1989; *Ivanov and Head*, 2003; *Hiesinger and Head*, 2004; *Werner*, 2009; *Rampey and Harvey*, 2012; *Platz et al.*, 2014]. However, these authors did not specifically investigate the morphology or distribution of volcanic features other than to suggest that the relatively flat planum could be formed from the superposition of thin low viscosity flows [*Rampey and Harvey*, 2012]. This interpretation is supported by the compositional interpretation of spectral data, which suggest that the mineralogy of Syrtis Major Planum is dominated by a two pyroxene mineralogy and that this best fits a highly mafic lava such as komatiite [*Mustard et al.*, 1993, 2005; *Reyes and Christensen*, 1994; *Clenet et al.*, 2013].

In addition to this hypothesis for the early volcanic character of the planum, it has been noted that areas further away from the central caldera complex are more degraded and parts of the lava

plain are inconsistent with effusion coming only from a central point [*Hiesinger and Head*, 2004]. However, whilst this degradation suggests that edges are older than the middle of Syrtis major Planum, recent crater count model ages indicate that spatially disparate parts of the planum may be significantly younger [*Platz et al.*, 2014a] than the early Hesperian age (3.4 Ga to 3.7 Ga) defined for the planum from global mapping and stratigraphy [*Meyer and Grolier*, 1977b; *Greeley and Guest*, 1987b; *Tanaka, et al.*, 2014a; *Tanaka et al.*, 2014b].

In this chapter, the components of the volcanic groups that make up the majority of Syrtis Major Planum are described and the morphologies of lava flows and lava flow features within them are interpreted to understand the volcanic history of the whole planum. The relative stratigraphy of lava flows and volcanic vents is achieved based on mapping. The occurrences of linear and point volcanic features found in each of the planum building groups of Syrtis Major Planum are compiled with spatial and temporal distributions of the flow groups and used to support interpretations of volcanism during the major constructive phase of Syrtis Major Planum's history.

The following observation section section presents descriptions and examples of the features and groups that make up the bulk of Syrtis Major Planum. These are mapped on Map Sheet 1 (Figure 4.1).
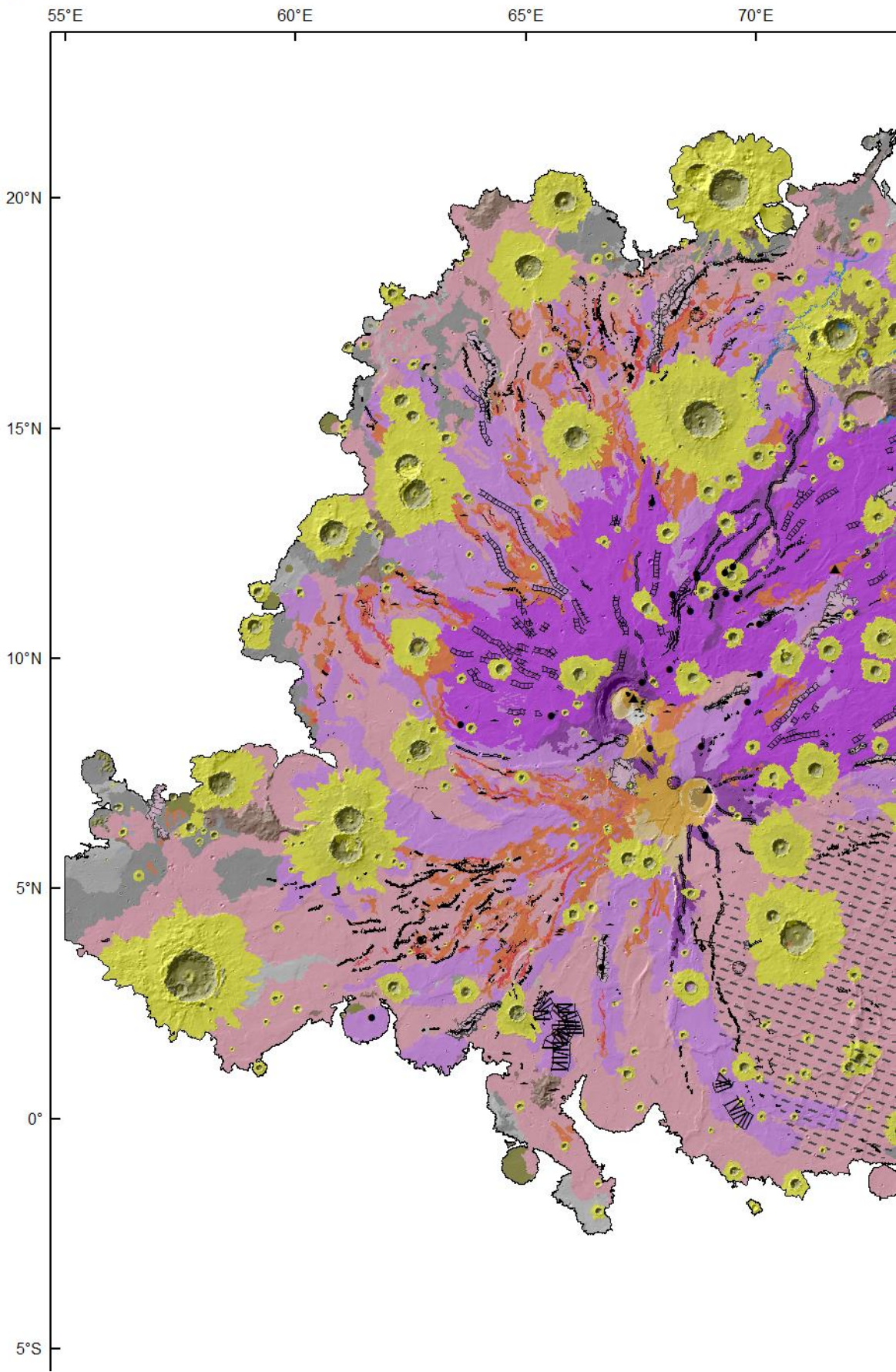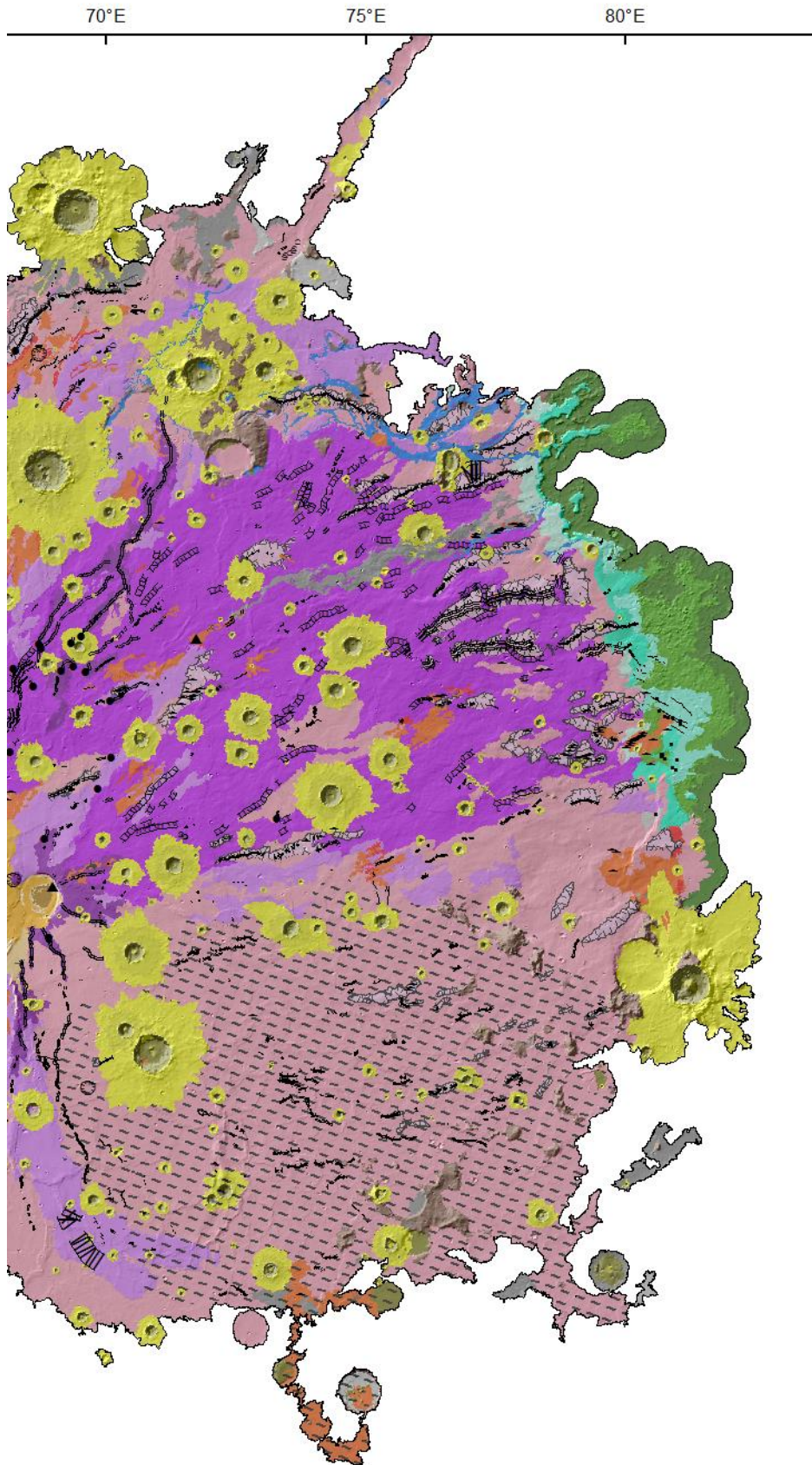
Figure 4.1

(a). An overview of Map sheet 1. (b) and (c) (on the following pages show a summary table of symbols and tables of units as seen on Map sheet 1 and used in simplified maps throughout this chapter.

B

4.2 Observations of Volcanic features

Across Syrtis Major Planum I have identified features best represented by points and lines. These have a common scheme throughout the planum-building volcanic groups. The full symbology for all classes of features described here is displayed in Map Sheet 1 and a simplified symbology is presented in figures 4.1 and 4.2. This has been done to make the representation of features simpler whilst still conveying the important information. Section 4.2.1 discribes linear and point features associated with volcanic processes. Generally, the linear features include various linearly aligned pits, single and paired parallel ridges, channels and fissures. These are interpreted as drained channels, lava levees, and as volcanic vents. Point features have positive or negative relief and are noteworthy for their potential to be volcanic vents.

C **Map Units**

Impact materials
E	Ejecta (all)

Surficial and Isidis basin formation
Sim	Smooth infilling unit
lHkp	Late Hesperian Knobbed plains unit
lHhf	Late Hesperian Hummocky field unit
lHLPd	Late Hesperian Lower Planum dark unit
lHLPb	Late Hesperian Lower Planum bright unit
lHLPt	late Hesperian Lower Planum transitional unit
lHLPh	late Hesperian Lower Planum hummocky unit
Rmf	Ridged mantling field

Late Stage Volcanic formation
Adr	Amazonian dark ridge unit
Ahdp	Amazonian/Hesperian dark plains unit
Avf	Amazonian volcanic field units

SMCCC Formation
Alv$_{(n/m)}$	Amazonian late volcanic units (Nili/Meroe)
Abcv$_{(n)}$	Amazonian bright caldera volcanic units (Nili)
Aev$_{(n/m)}$	Amazonian early volcanic units (Nili/Meroe)
lHuCf$_{(n/m)}$	late Hesperian upper Caldera floor (Nili/Meroe)
lHlCf$_{(n/m)}$	late Hesperian lower Caldera floor (Nili/Meroe)

Planum Building Flow Formation
Hff	Hesperian fissure field unit
lHvf	late Hesperian volcanic flow unit
Hvp	Hesperian volcanic plateau unit

Volcanic Plains Formation
eHvp	early Hesperian volcanic plains unit
eHvr	early Hesperian volcanic ridge unit

Pre-planum basal materials
Nhfr	Noachian Hesperian flat topped ridges
Nup	Noachian upper plains unit
Nlp	Noachian lower plains unit
Nbp	Noachian bright plains unit
Ncf	Noachian crater fill unit
Nhm	Noachian Highland massifs

Simple Map Units

⊢──	(subsumed into underlying group)
⬛	Area of the Isidis Basin floor units
──	(subsumed into underlying group)
──	(subsumed into underlying group)
🟧	Syrtis Major Central Caldera Complex
🟪	Area of the late Hesperian volcanic flow unit
🟪	Area of the Hesperian volcanic plateau unit
🟥	Area of the early Hesperian volcanic plains units
🟫	Cratered highland terrain

103

Surface	Area Km²	Area %	Elevation μ (m)	Elevation σ (m)	Range (m)	Max. (m)	Min. (m)	Slope μ (°)	Slope σ (°)	Thermal inertia μ (Jm⁻²K⁻¹s⁻½)	Thermal inertia σ (Jm⁻²K⁻¹s⁻½)
Impact ejecta	-	-	-	-	-	-	-	1.89	2.26	265.96	76.87
Isidis basin floor	-	-	-3628.74	411.10	3488	-1574	-5062	1.01	2.05	337.12	136.57
Adr	11321.70	1.1	1148.57	1258.58	5928	2142	-3786	0.48	0.39	273.99	61.62
Tdv	62981.84	6.2	1134.98	1288.04	6112	2191	-3921	0.63	0.70	266.13	57.02
lHvf	221885.60	21.8	551.33	1396.04	5982	2247	-3735	0.76	0.73	241.72	53.49
Hff	20874.43	2.1	1347.67	809.83	5980	2231	-3749	1.52	2.24	243.05	49.78
Gfg	167401.80	16.5	1353.77	1172.98	6180	2202	-3978	0.65	0.84	236.12	47.35
eHvr	40506.79	4.0	-749.68	1763.82	5899	2128	-3771	0.97	0.72	278.94	61.11
eHvp	491195.80	48.3	895.65	1396.04	5982	2247	-3735	0.73	1.03	268.16	59.19
Cratered Highlands	-	-	806.16	544.11	4976	2253	-2723	2.80	3.38	345.51	150.25

Table 4.1

*Topographic and thermal properties the Planum building groups of Syrtis Major Planum. The reported area percentages are of total areas covered by lava, excluding areas identified as impact ejecta. Elevation and slope are derived from Gridded MOLA data. Slope calculations use mean slope in a 3x3 pixel moving window on a grid spacing of ~463 m giving a baseline length of 654 m. Thermal inertia is Extracted from the Quantitative THEMIS Thermal inertia mosaic (*http://astrogeology.usgs.gov/search/details/ Mars/Odyssey/THEMIS-Global-Thermal-Inertia-Mosaic/Quantitative-32-Bit/THEMIS_TI_Mosaic_Quant_00N060E_100 mpp/cub*; [Christensen et al., 2013]. Data was extracted using the 'Zonal statistics as Table' tool Arc 10.1.(ESRI, 2011) In addition to Planum building volcanic groups data from the Cratered highland terrain (Cht), the floor of the Isidis basin and single lobe ejecta blanketsalso reported here.*

A
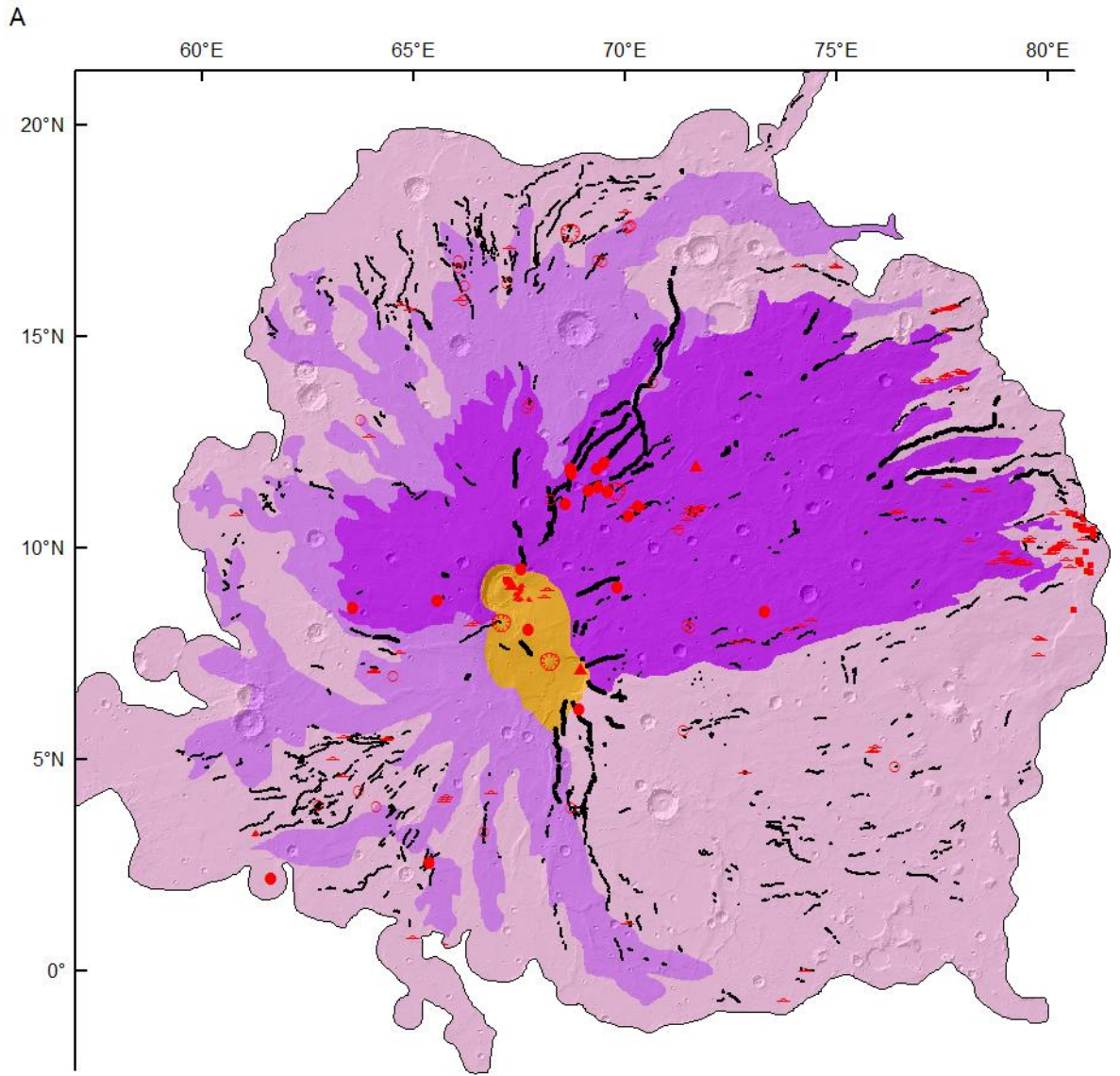
Legend

Vent classes

▲ Large conical mound

⌒ Low circular mound

■ Flat topped mound

▴ Tiny rubbly mound

● Large linear pits

○ Small pits

⊛ Wide flat bottemd pit

Volcanic channels and ridges

━━ Major

── Minor

Simple Map Groups

Central Caldera Complex

Area of the late Hesperian volcanic flow unit (lHvf)

Area of the Hesperian volcanic plateau unit (Hvp)

Area of the early Hesperian volcanic plains group (eHvp)

B
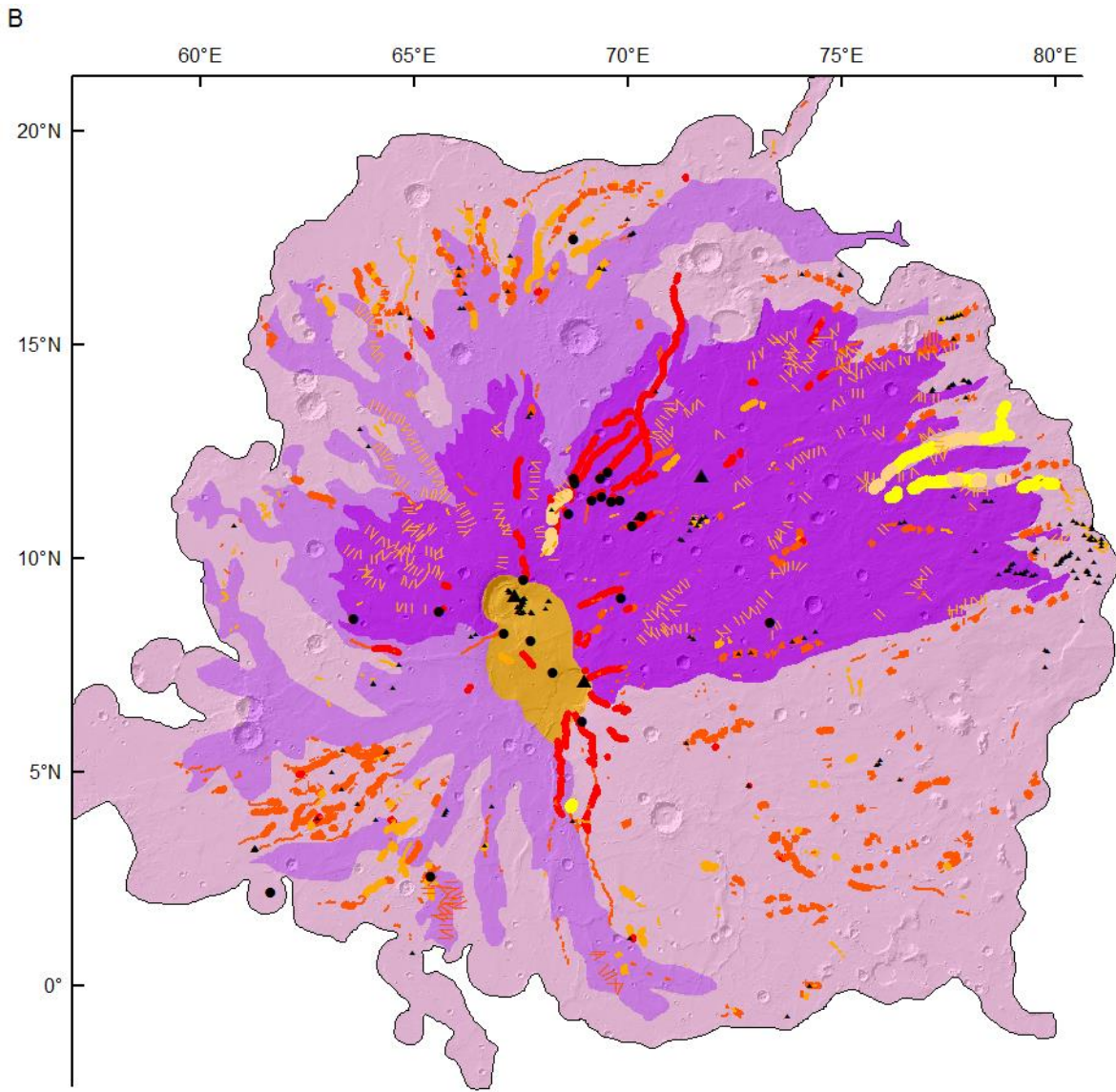
Legend

Linear volcanic feature class

- ▬ Mega channel (on a mound)
- ▬ Rectangular ridge (on a mound)
- ▬ Major channel/rill
- — Narrow linear depression, continuous
- ▬ Narrow linear depression, continuous on a mound
- - - - Narrow linear depression, discontinuous
- ▬ ▬ Narrow linear depression, discontinuous, on a mound
- — Narrow linear ridge, continuous
- ▬ Narrow linear ridge, continuous, on a mound
- - - - Narrow linear ridge, discontinuous
- ▬ ▬ Narrow linear ridge, discontinuous, on a mound

- |||||||| Wide channel

- |||||||| Medial channel

Simple Map Groups

- ▨ Area of the Central Caldera Complex
- ▨ Area of the late Hesperian volcanic flow unit (lHvf)
- ▨ Area of the Hesperian volcanic plateau unit (Hvp)
- ▨ Area of the early Hesperian volcanic plains (eHvp)

Vent classes

- ● Major pit
- ▲ Major cone
- ▴ Minor pits, cones and sheilds

106

Figure 4.2

A summary map of the major planum building volcanic groups showing (a) the distribution of the important classes of point volcanic features with two summary classes of channel and ridge features. (b) The distribution of 13 classes of linear volcanic ridges and channels with three summary classes of vent features

4.2.1 Point features

I catalogued seven classes of volcanic point features across Syrtis Major Planum (Figure 4.3). They

are referred to as "point features" as they can only be marked as "points" on any map of small-

enough scale to encompass the whole planum (such as Map Sheet 1; 1:2,000,000). These features

are split into those with positive and negative relief. Following the identification of these features

a working hypothesis that they represent vent features was considered appropriate and they have

been classifed as such.

Positive relief features;
- *Large conical mounds*
- *Low circular mounds*
- *Flat topped mounds*
- *Tiny rubbly mounds*

Negative relief features;
- *Large linear pits*
- *Small pits*
- *Wide flat bottomed pits*
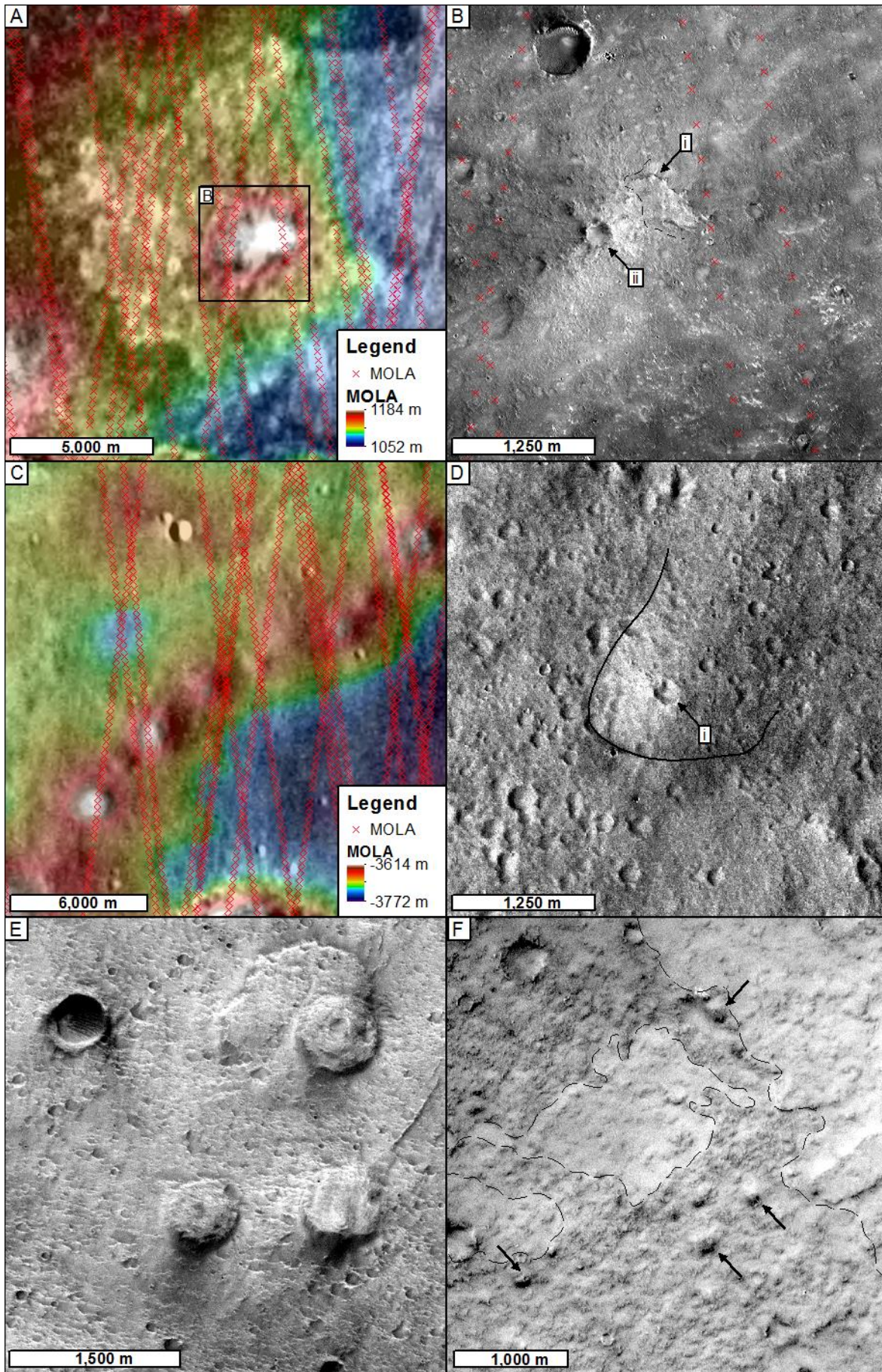
Seven different classes of point feature found across Syrtis Major Planum are interpreted to be volcanic vents. The large conical mound on the eastern flank of Syrtis Major Planum shown in (a) Night time THEMIS data overlain with gridded and Point MOLA data. (b) Shows the morphology of the flat topped section; (i) and (ii) show overlying peak and summit crater (HiRISE ESP_032135_1920). (c) A chain of low circular mounds close to the edge of the Isidis basin shown in Themis day with overlain gridded and Point MOLA data. (d) An individual small shield in CTX data. (e) 'Flat top mound' type cones close to the boundary between Syrtis Major Planum and the floor of the Isidis basin. (f) Small tumulus style cones (arrows) seen in the darker flow unit overlying the smoother brighter volcanic plains material.

4.2.1.1 Positive relief features

4.2.1.1.1 Large conical mounds

Large conical mounds are the largest cone shaped features on Syrtis Major Planum. There are three features in this class, each of which has a unique morphology. Nili Tholus (Figure 6.12c), and a smaller cone in Meroe Patera (Figure 7.26f), are found in the central caldera complex and are discussed further in later chapters. The third example is east of the central caldera complex (Figures 4.3a and b; Section 4.3.8). MOLA point profiles across the flank of this cone suggest that it is at least 80 m high through extrapolation of the flank slopes the summit is estimated to have been at least ~100 m high; It is ~4 km across at its base. CTX and HiRISE data show at least two stages of development: a steep edged, flat topped section overlain by a more conical section with what appears to be a summit crater.

4.2.1.1.2 Small sheilds

Figure 4.3c and d show small shields. These are hard to identify in visual images but have distinct topographic signatures where sampled by MOLA track data. I define small shields as typically 2- 3 km across and 10 – 20 m high. They have gently sloping flanks, and commonly have craters at their summits. Low circular mounds commonly occur in chains perpendicular to the circumference of the Isidis basin, but also occur elsewhere across Syrtis Major Planum.

4.2.1.1.3 Flat-topped mound

Flat-topped mounds between 0.5 km and 1 km in diameter and 30 m to 50 m high are also identified. Although there are some examples of flat topped mounds in Nili Patera (Figures 4.12a

and 5.11a in Chapter 5), most examples are found in the lowest elevation parts of Syrtis Major, at the boundary with the Isidis Basin (e.g., Figure 4.3e). These examples have steep flanks and small pits or craters at their summit. Flat-topped mounds appear associated with the flat-topped ridges, which are described in section 4.3.5). These cones have a strong morphological similarity to cones found in linear chains across the floor of the Isidis basin (Section 2.3.2.2).

4.2.1.1.4 rubbly knobs

The smallest cones have been called rubbly knobs. These features are only observed in a cluster at the southern edge of Syrtis Major in what appears to be a minor flow overlying older volcanic plains unit material (Figure 4.3f) and Nili Patera (Figure 5.13a). Cones of this size are generally below the resolution of the planum-wide mapping effort and MOLA data. However, cones in these locations are sufficiently distinct to identify reliably. Cones of this style are also discussed in sections 5.2.5.3 and 6.3.4.4 (Figure 6.27).

4.2.1.2 Negative relief features

4.2.1.2.1 Large linear pits

The largest Negative relief features are large linear pits (Figures 4.4 a-d). These probable vents occur around the SMCCC and in an area to the north of it. These features range from 5 – 10 km in length and 0.5 – 1 km in width. They are therefore large enough to be mapped on Map Sheet 1 (Figure 4.13). The larger of these vents (Figure 4.4a) have straighter sides compared to smaller examples (Figure 4.4c, d), which appear to have formed from a line of coalesced collapse pits. Large linear pits are often, but not exclusively, associated with the head regions of lava channel features (Figure; 6.28f). The largest linear pits are associated with major channels and smaller large linear pits are associated with long linear depressions. The relationship between large linear pits, channels and tectonic structures at Nili and Meroe Patera shows that vents of this style predate the for mationa of the Calderas section 6.3.1.1.

4.2.1.2.2 Small pits

Small pits (figure 4.4e) are rare across Syrtis Major Planum: The few examples of these features have proportions similar to the individual segments of the smaller large linear pits. No MOLA track points intersect with the floor of a small pit meaning their depths remain unknown.

4.2.1.2.3 Wide flat bottomed pits

There are two examples of wide flat-bottomed pits on Syrtis Major Planum. The first of these, north-west of Meroe Patera, is described in detail in Section 6.3.1.1 where comparison is drawn with terrestrial examples. The second of these shown in Figure 5.4f is located south west of Nili Patera. This wide flat-bottomed pit is significantly shallower (only 20 m deep compared to ~45 m) but is associated with a minor linear depression (Figure 5.5b). Stratigraphically, this example predates the collapse of SMCCC associating its genesis in time with large linear pits, which also had lava channels.
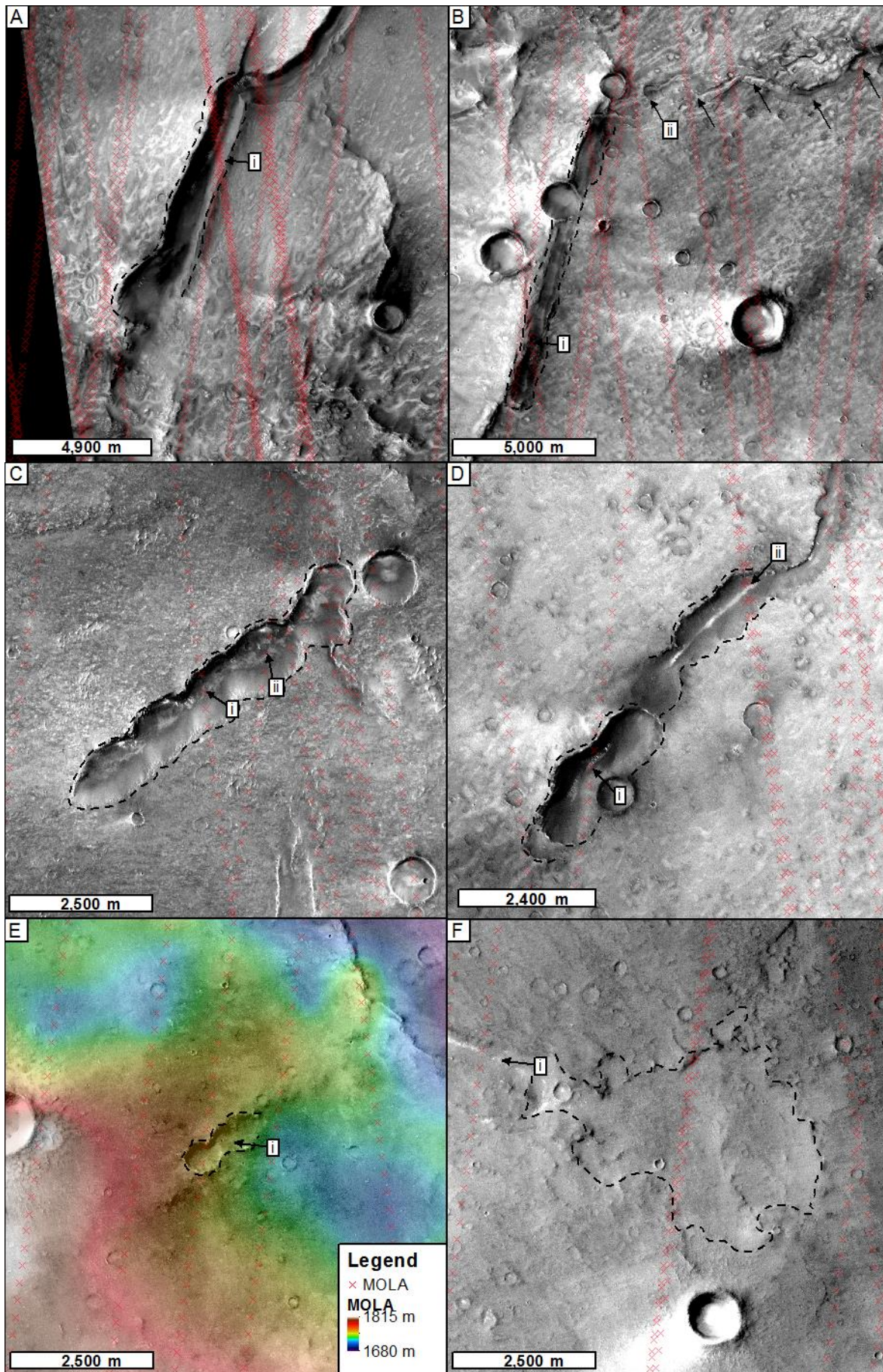
Figure 4.4

*Large linear pits. (a) a large linear pits at the head of Arnus Vallis [Rampey and Harvey, 2008] a known major channel shown in Figure 4.5c. Arnus Vallis [Rampey and Harvey, 2008] is 1.5 km wide 150 m deep (at the point lablled i) and at least 93 km long. (b) Long linear pit ~ 0.6 x 10.5 km and 40 m deep (at the point i) leading to a minor linear depression at (ii). (c) Isolated fissure pit to the west of Nili Patera with distinctive arcuate rim segments; ~ 0.9 km x 6.4 km, 50 m and 70 m deep at (i) and (ii) respectivly. (d) Smaller large linear pit made of two segments ~ 0.75 x 2.6 km and 90 m deep at (i) and ~ 0.75 km x 3 km and 40 m deep at (ii). (e) Small isolated pit ~20 m deep. (f) Shallow (20 m deep) flat bottomed pit crater leading to a minor linear depression (i) south west of Nili Patera. Lines of red (**X**) crosses show MOLA point data from which relief data was measured.*

4.2.2 Linear vent and transport features

I have identified 13 types of linear volcanic-related features across Syrtis Major Planum

(Figure 4.5, and Map Sheet 1).

Major channels
- *Mega channel*
- *Rectangular section ridge*
- *Major channels*

Minor linear depressions and ridges
- *Long narrow linear depressions (continuous or discontinuous on and off mounds)*
- *Long narrow ridges (continuous or discontinuous on and off mounds)*

Wide medial channels
- *Wide channels*
- Medial channels

4.2.2.1 Major channels

The major occurrences of Mega channels are on the slope down into the Isidis basin. Here,

these channels are located at the top of large, trapezoidal sectioned linear mounds or rises of up

to 400 m (Figure 4.5a). The source regions for these channels are buried by later flows.

Downstream, these channels convert into a rectangular section ridge (Figure 4.5b) atop mounds

before fanning out, narrowing and trending into a major channel/rill. They then become a

continuous linear depression on a mound before being overlain by Isidis boundary formation

related materials (Map Sheet 1). There is one segment of square section channel north of the

central caldera complex, both ends of which are buried by later deposits.

Major channels (Figure 4.5c) are dominantly located in the north of Syrtis Major Planum trending

northwards from a group of large linear pits. They are large enough to be identified in THEMIS

data (300 – 500 m wide). While these are similar in appearance to sinuous rilles on the moon [*Hulme*, 1982], they are smaller and appear to be less sinuous. Major channels trend down slope and some contribute to a larger channel, although they do not form a contributory network. The channels narrow downstream and often trend to long narrow linear depressions.

Figure 4.5 (a – c, Opposite)

*This figure (split over the next few pages) illustrates the 13 types of linear feature relating to volcanic process found across Syrtis Major planum divided in to four major classes. Major channels and ridges: (a). Mega channels; wide channels perched along the ridges of wide mounds impinging into the Isidis basin (THEMIS with gridded MOLA overlay). (b) Rectangular section ridges; Flat topped segments raised section along the axis of wide mounds impinging into the Isidis basin (THEMIS with gridded MOLA overlay). (c). Major channels/rill; Luna rill style channels, Arnus Vallis [*Rampey and Harvey, 2008*] seen here in CTX image P18_007978_1938_XN_13N289W).*
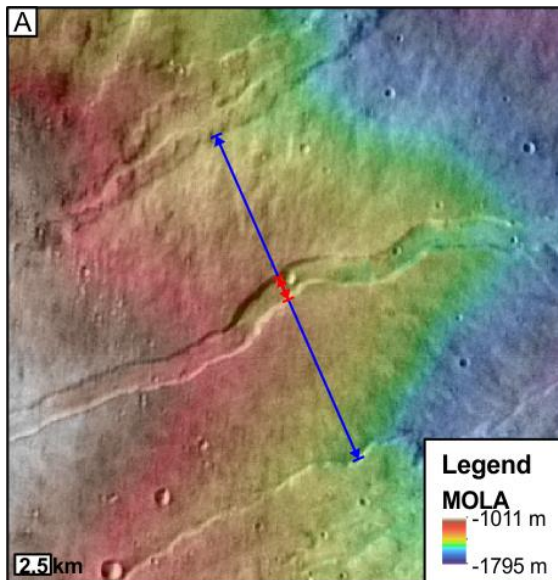
Major channels and ridges

Mega channel
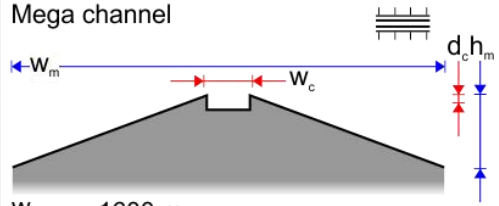
w_c = ~ 1600 m
d_c = ~ 50 m
w_m = ~ 20000 m
h_m = ~ 400 m
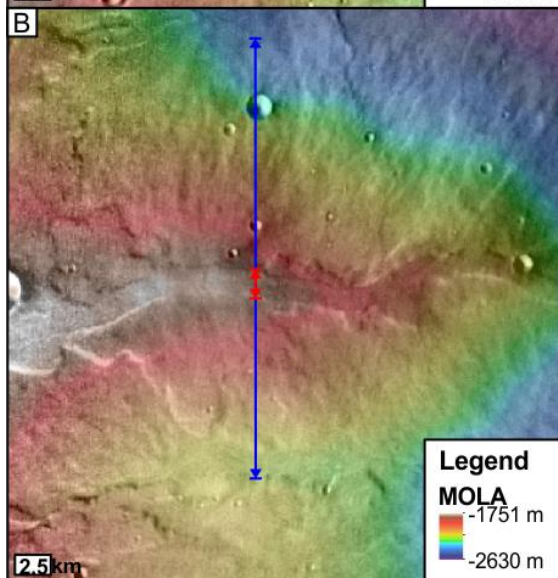
Rectangular section ridges
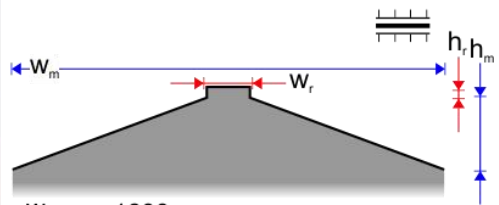
w_c = ~ 1600 m m
h_r = ~ 40 m
w_m = ~ 20000 m
h_m = ~ 400 m
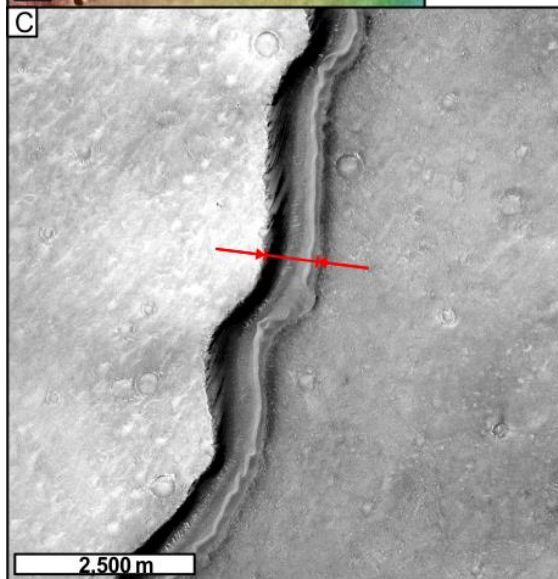
Major channel/Rill
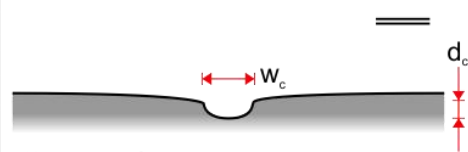
w_c = ~750 m
d_c = 50 - 100 m

4.2.2.2 Long linear depressions and ridges

Long narrow linear depressions cannot be consistently identified in THEMIS (100 m/pixel) data and require CTX (6 m/pixel) resolution imagery to identify them. Generally, long narrow linear depressions trend away from the central caldera complex and occur in the early Hesperian volcanic plains unit (eHvp; Figure 4.2b). These can be continuous (Figure 4.5d) or discontinuous (Figure 4.5e).

Continuous examples are often related to large linear pits, or are sub parallel to, and associated with, major channels. The channels in this class have a consistent width, and trend down slope, except where modified by later tectonic wrinkle ridge activity. They often trend into discontinuous channels, and discontinuous and continuous ridges. Long narrow linear depressions can occur both along the axis of low mounds and in areas of flat-lying volcanic terrain.

Long discontinuous channels (Figure 4.5e) are similar to long continuous channels except that the channel is formed of a series of circular to elongate pit or channel segments. These commonly occur along the crest of low mounds associated with the eHvr and Hff units (Figure 4.5f and e). The channels in this class never appear to crosscut other volcanic architecture as erosional features and do not have any evidence for dendritic contributory upstream segments. They are indicative of constructional features.

Long narrow ridge features can be continuous (Figure 4.5k) or discontinuous (Figure 4.5j) ridges that either occurs on flat terrain or along the axis of low mounds (Figure 4.5h and i). These ridges occur in the same trends as long narrow linear depressions. Although not clearly identifiable in THEMIS data, long narrow ridges can be seen clearly in CTX data.

Minor linear depressions and ridges

Long narrow linear depression (continuous)

w_c = 200 - 250 m
d_c = ~5 - 10 m

Long narrow linear depression (discontinuous)

w_c = <250 m
d_c = ~5 - 10 m
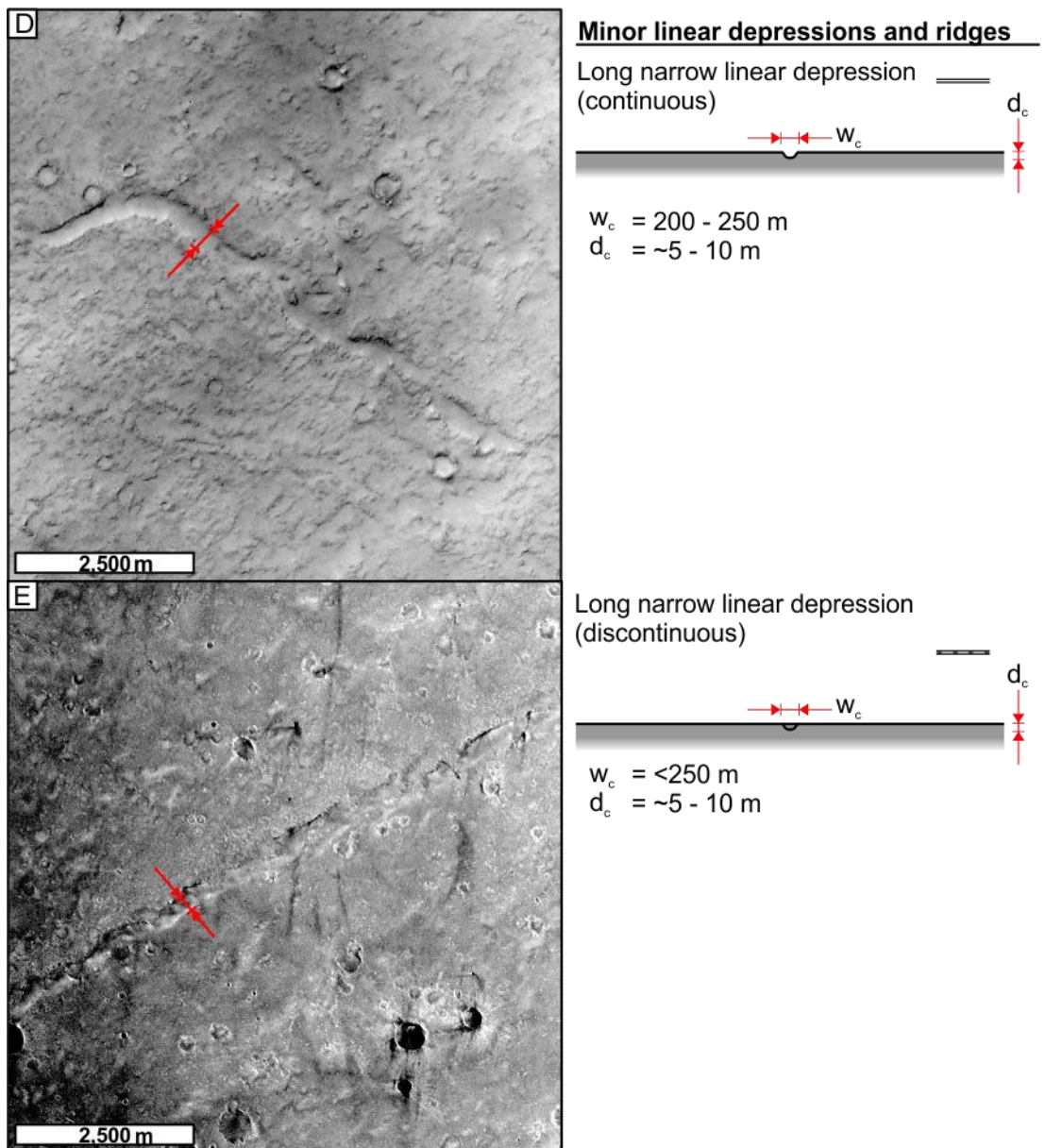
Figure 4.5 (d) and (e)

 (d) Long narrow linear depressions (continuous), too narrow to be easy identifiable in THEMIS (100 m/pixel) data seen here in CTX D20_034878_1831_XN_03N297W. E. Long narrow linear depressions (discontinuous), too narrow to be easily identifiable in THEMIS (100 m/pixel) data seen here in CTX P13_006119_1936_XN_13N290W.
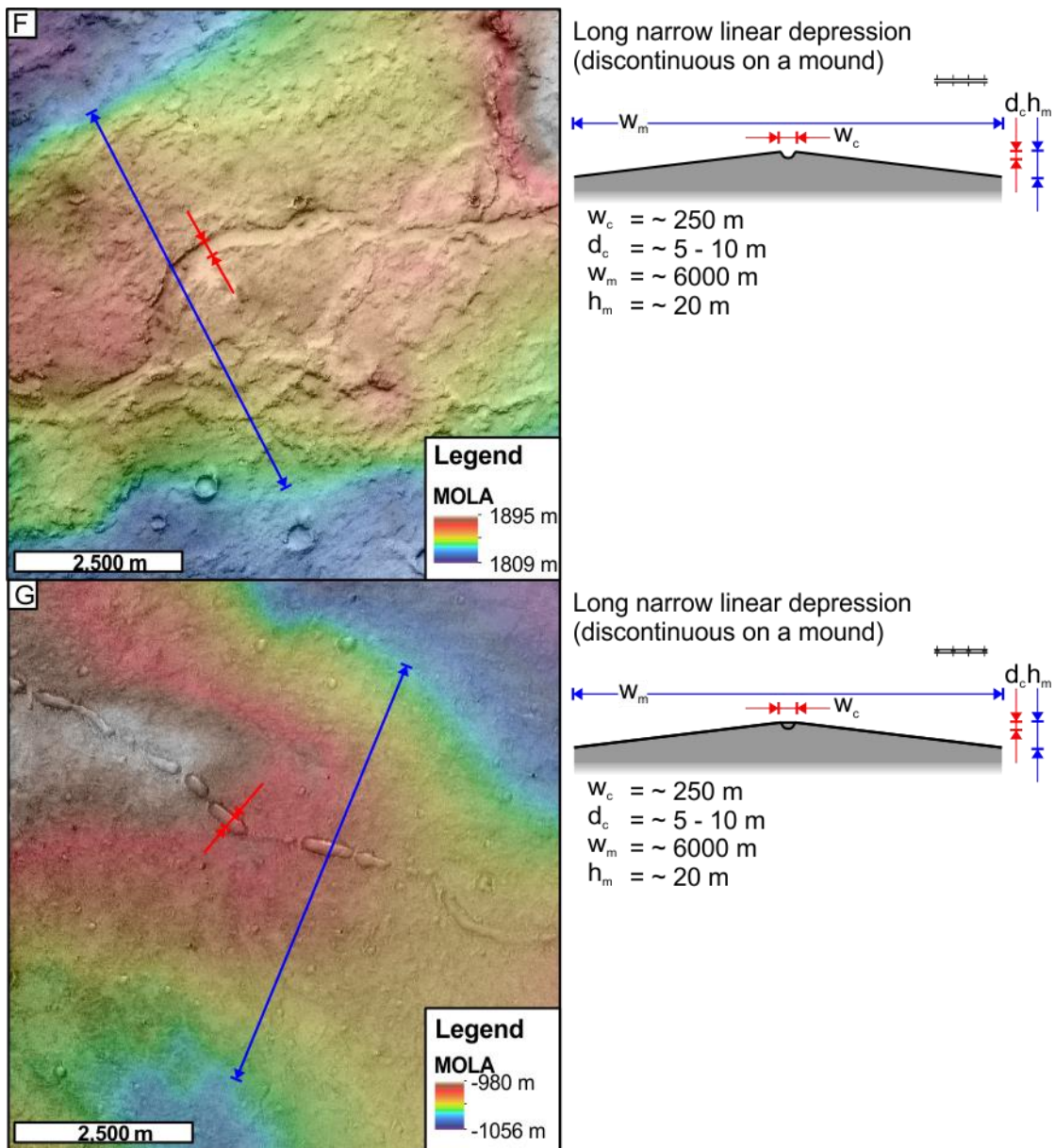
F. Long narrow linear depressions (continuous on a mound), on the axis of a mound, seen here in CTX G20_025885_1841_XN_04N297W overlain with gridded MOLA data. G. Long narrow linear depressions (discontinuous on a mound), running along the axis of a low mound, seen in CTX G14_023801_1970_XN_17N285W and gridded MOLA data.

Long narrow ridge (continuous)

w_r = < 100 m
h_r = ~5 - 10 m

Long narrow ridge (discontinuous)

w_r = < 100 m
h_r = ~ 5 - 10 m
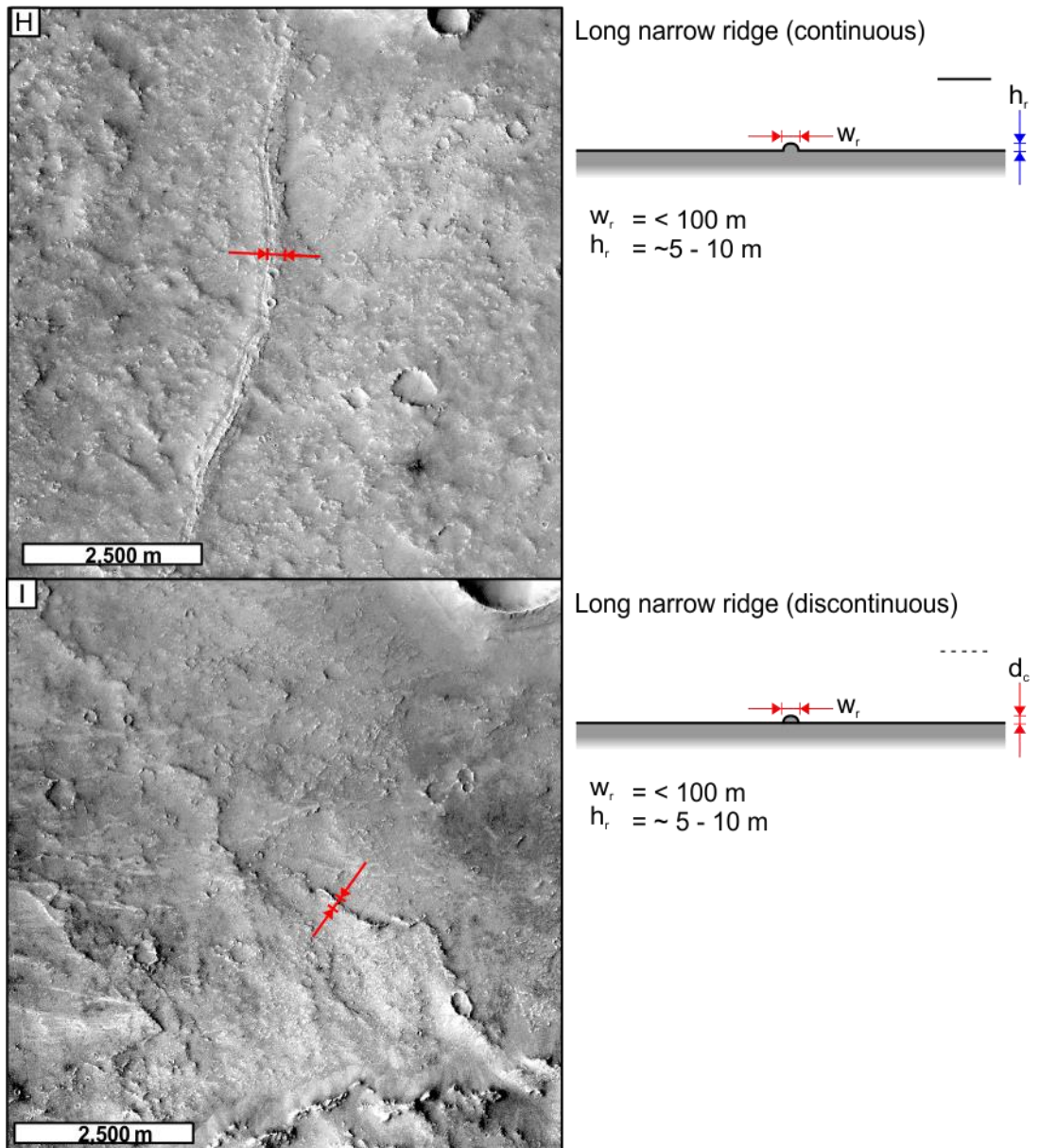
Figure 4.5 (h) and (i)

H. Long linear ridges (continuous), features too narrow to be easilyy identifiable in THEMIS (100 m/pixel) data but seen here in CTX D04_028786_1947_XN_14N295W. I. Long narrow ridges (discontinuous), too narrow to be easily identifiable in THEMIS (100 m/pixel) data seen in CTX image F04_037225_1965_XN_16N294W.
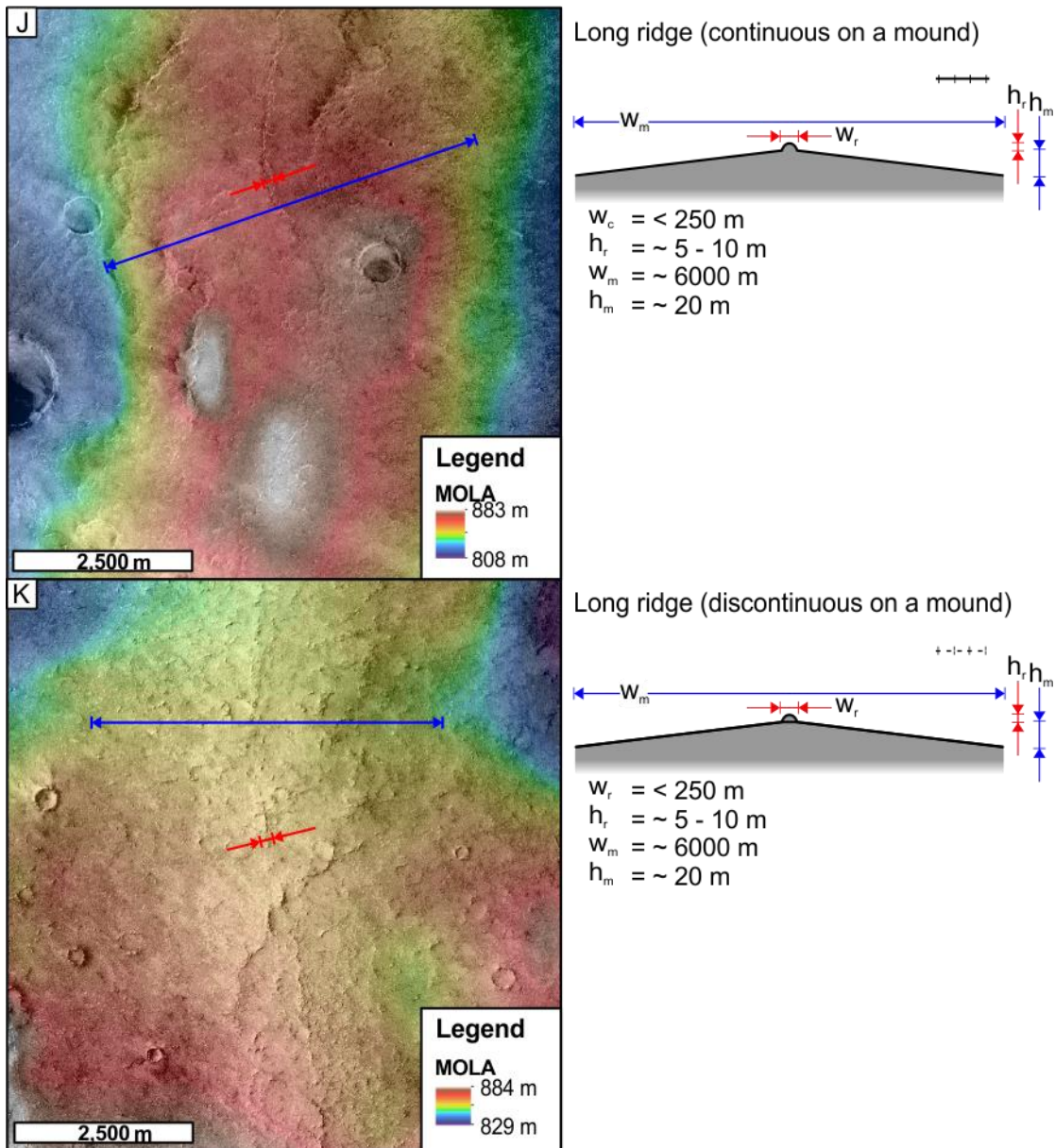
Figure 4.5 (j) and (k)

(j) Long narrow ridges (continuous on a mound) running along the axis of a low mound (CTX P12_005618_1952_XI_15N292W with gridded MOLA overlay). (k) Long narrow ridges (discontinuous on a mound) running along the axis of a low mound (CTX G21_026610_1969_XN_16N292W and gridded MOLA overlay).

4.2.2.3 Wide medial channels

The largest linear features of this type are very wide flows with compression or festoon ridges [*Theilig and Greeley*, 1986] (Figure 4.5l). There are only two locations where flows of this morphology are observed (Figure 4.2b) and in both cases the flows are many kilometres wide and formed of a channel and levee structure. The levees are formed of hummocky material with

hummocks orientated parallel to the flow directions (Figure 4.5l). The channel fill material has the same mean elevation as the levees and is again formed of hummocky material. However, in the case of the channel fill, this is arranged into parallel ridges perpendicular to the flow direction. Between the channel fill and levee material there is a ~50 m wide region of long linear ridges and groves which, given the context of the perpendicular hummock orientations I suggest is a shear zone formed from narrow ridges (Figure 4.5l).

The other type of wide channel is the narrow flow **medial channels** that form lava flows in the Late Hesperian volcanic flow unit (*lHvf*; Figure 4.5m). These channels are the key identification feature of the Late Hesperian volcanic flow unit.

Lava flows with medial channels are emplaced in a radial distribution north of the SMCCC and in flows emplaced to the east impinging into the Isidis basin (see Map Sheet 1). The flows have a channel and levee structure common in martian and terrestrial lava flows [*Baloga and Glaze*, 2008]. The channels occur as the central 1/3 to 2/3 of the width of lava flows in this group. The levees are formed of hummocky material separated from the channel fill by linear shear zone ridges. The channel fill is either at the same elevation as the levees or a few meters below the elevation of the levees and made of a similar hummocky material.

There is one example of a streamlining around an impact crater which may indicate laminer flow within the channel during this stage of the lava flow emplacement. This is proposed because as the surface of the flow has been dragged around the obstacle the blocks and hummocks of the flow surface have remained in position relative to other blocks and hummocks in the flow surface.

Wide and medial channels

Wide channel

w_c = ~ 5000 - 10000 m
h_f = ~ 50 m

Medial channel

w_c = ~ 1500 m
h_r = ~ 5 - 10 m
w_f = ~ 2-6000 m
h_f = ~ 20 m
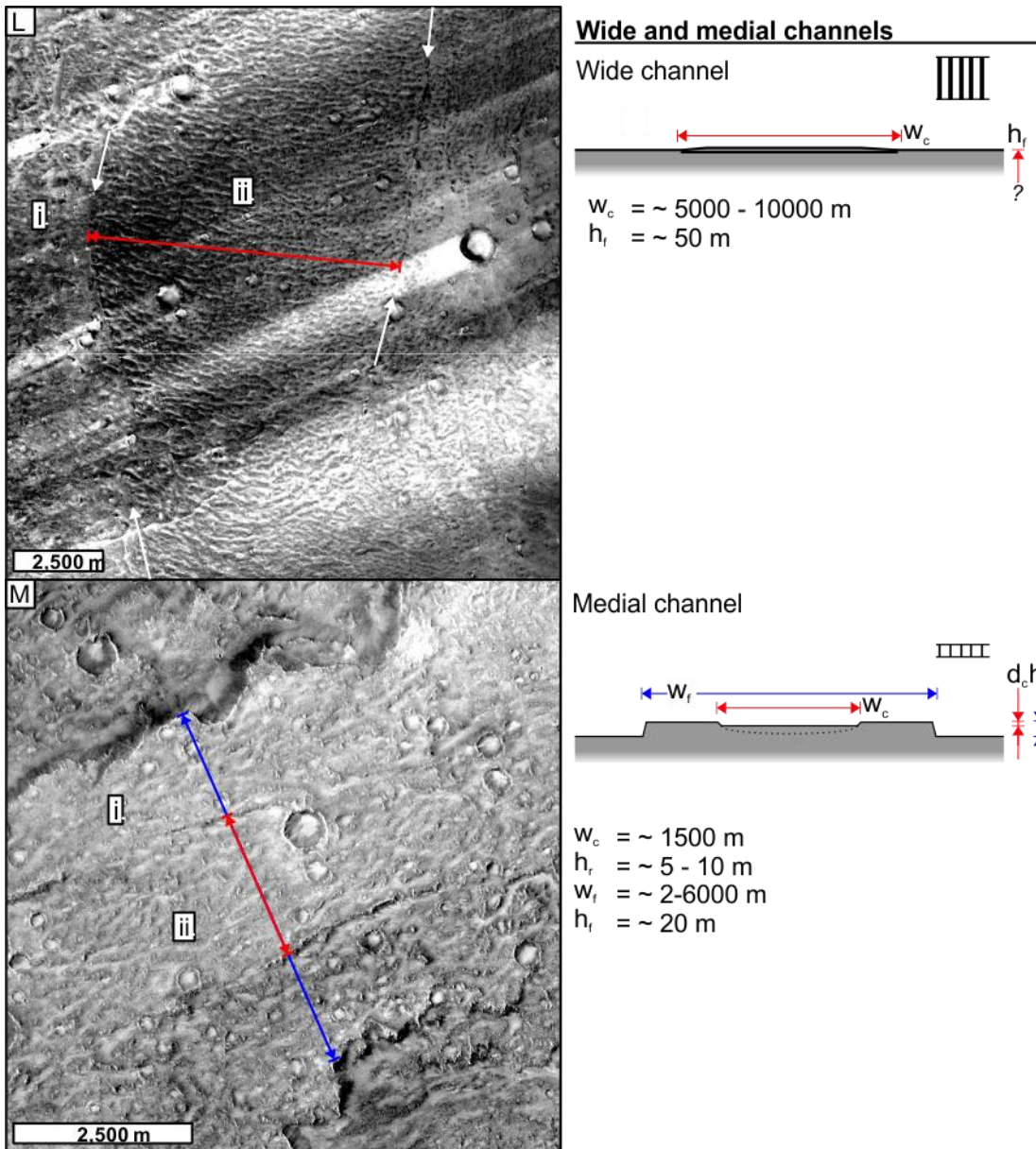
Figure 4.5 (l) and (m)

Wide and medial channels. *L. **Wide channels;** Compression flow ridges (CTX G12_022852_1806_XN_00N294W) in a very wide lava flow (i) hummocky levee material, (ii) channel fill with ridges perpendicular to flow direction (iii) shear zone ridge shown in white. M. **Medial channels;** Channels in the narrow lava flow unit (CTX B19_016852_1959_XN_15N286W) (i) hummocky levee (ii) channel fill (iii) sheer zone.*

	Count	%	Mean length (m)	%
Major channel/rill	145	*7.2*	11858.90	*7.4*
Long narrow linear depression	1440	*71.6*	26361.25	*16.5*
Long narrow ridges	246	*12.2*	39770.21	*24.8*
Mega channel/Rectangular section ridge	20	*1.0*	42783.97	*26.7*
Medial and wide channels	160	*8.0*	39423.18	*24.6*

Table 4.2

Number and length statistics for the different classes of Linear volcanic features (Figure 4.5).

	Count	%	Mean length (m)	%
Continuous linear depressions	178.00	*12.4*	14485.75	*55.0*
Discontinuous linear depressions	592.00	*41.1*	450.78	*1.7*
Continuous linear depressions on a mound	474.00	*32.9*	2536.36	*9.6*
Discontinuous linear depressions on a mound	196.00	*13.6*	8888.36	*33.7*

Table 4.3

Number and Length statistics for long narrow linear depression features.

	Count	%	Mean length (m)	%
Continuous ridge	102.00	*41.5*	8998.62	*22.6*
Discontinuous ridge	51.00	*20.7*	8584.78	*21.6*
Continuous ridge on a mound	48.00	*19.5*	12270.41	*30.9*
Discontinuous ridge on a mound	45.00	*18.3*	9916.39	*24.9*

Table 4.4

Number and Length statistics for long narrow ridge features.

4.3 Volcanic groups

These were mapped as areas that have (i) similar morphology as observed in the THEMIS day-time data base layer, (ii) similar thermal properties in THEMIS night-time data, and (iii) have thermal signatures that are consistent with structures or textures seen in CTX data. This tripartite analysis (THEMIS day, THEMIS night, and CTX) provides confidence in the interpretation that defined spatial areas can be linked into specific flow groups.

4.3.1 Early Hesperian volcanic plains unit (eHvp)

The Early Hesperian volcanic plains unit (eHvp) is the mapped group that incorporates low-relief surfaces with no specific flow features observable in the THEMIS base layer dataset within which evidence and associations can be found to support a volcanic origin. Surfaces in this group occur around the outer portion of the Syrtis Major Planum volcanic edifice. The eHvp on-laps cratered highland terrain (Cht) and Syrtis Major Basement groups (Figures 4.7b, d and e). There are a large number of instances where the group surrounds outcrops of older, underling highland material (Figure 4.7b). These are distributed around the edge of the planum but are most numerous in the region of the south eastern contact with the Noachian highland massifs (Nhm). In MOLA data, the group hosts numerous wrinkle ridges (Chapter 6). Notably, the numerous circular wrinkle ridges are interpreted to be 'ghost craters' (Figure 4.7a).
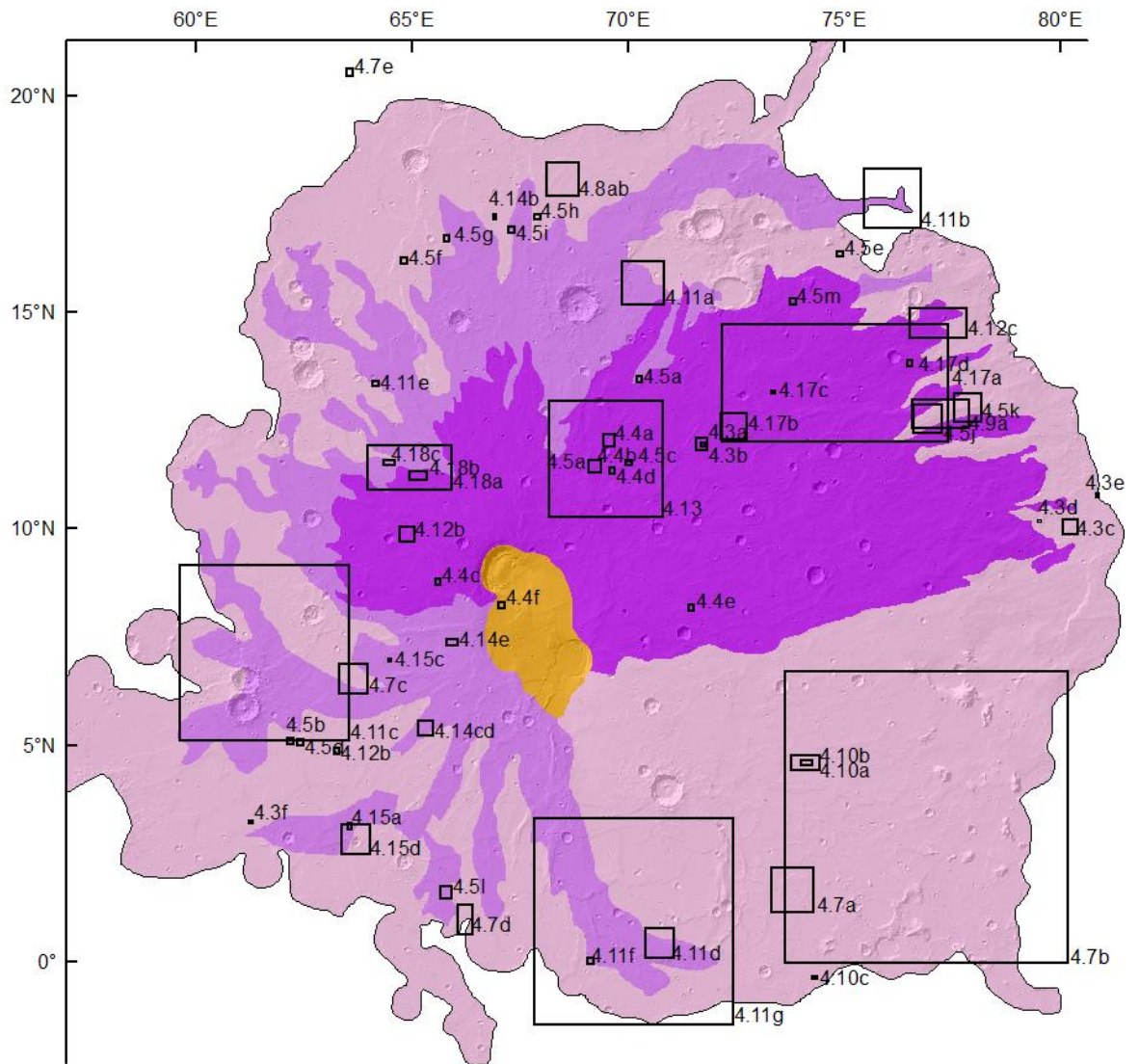
Figure 4.6

Summary map of the major planum building volcanic units. The locations of figures are also marked.

In the THEMIS day-time base layer data, this group is generally darker than the other planum building groups and also more variable, appearing somewhat mottled in tone. When viewed using THEMIS night-time data this group is brighter than the broad and late Hesperian volcanic flow unit materials, but again has a mottled tone (Figure 4.7c). Small impacts into this material produce ejecta that are very bright in THEMIS night-time data.
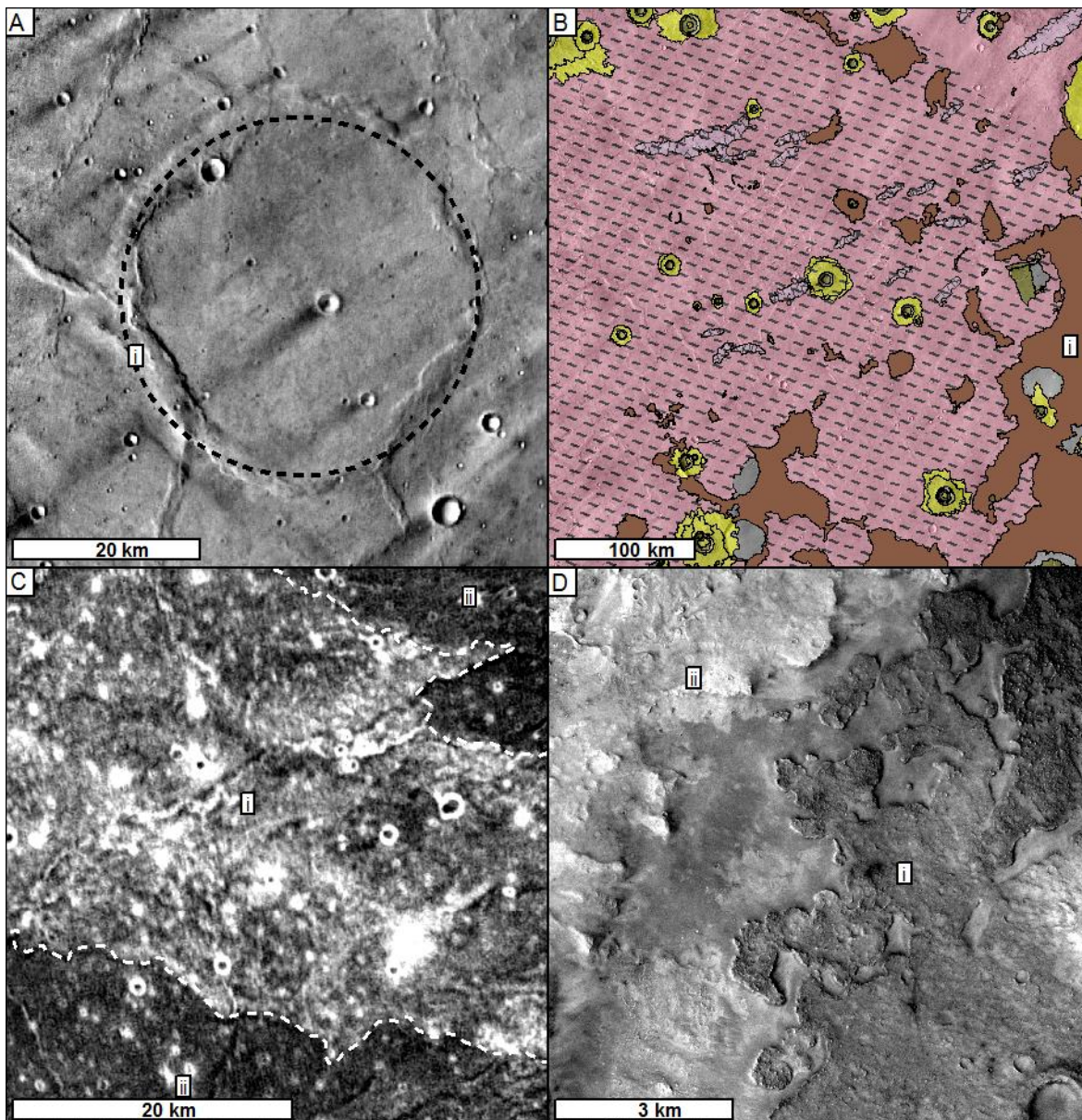
Figure 4.7 (a-d)

Surfaces found in the eHvp. (a) A circular wrinkle ridge (i) forming a 'ghost crater'. (b) Outliers of (i) Highland material in the south east of Syrtis Major. (c) Night time Themis data showing (i) the mottled character of the (eHvp) relative to elements of the superposing (ii) Hesperian volcanic plateau unit (Hvp). (d). The contact between (i) early Hesperian volcanic plains unit material (dark) and (ii) Noachian highland (bright) in the north west of Syrtis Major showing a lobate margin 15-25 m high on-lapping the highlands in CTX P05_003060_2012_XN_21N296W.

In CTX and HRSC visible data, this group is darker than the underlying basal and highland units (Figure 4.7; d, e). It is dark grey in tone and dark blue-grey in HRSC colour data, consistent with terrestrial and martian basaltic volcanic material [*Williams et al.*, 2009a]. The eHvp is also distinguished from overlying broad and late Hesperian volcanic flow units by the lack of structures such as steep sided lobes, lobate flow fronts and wide medial channels.
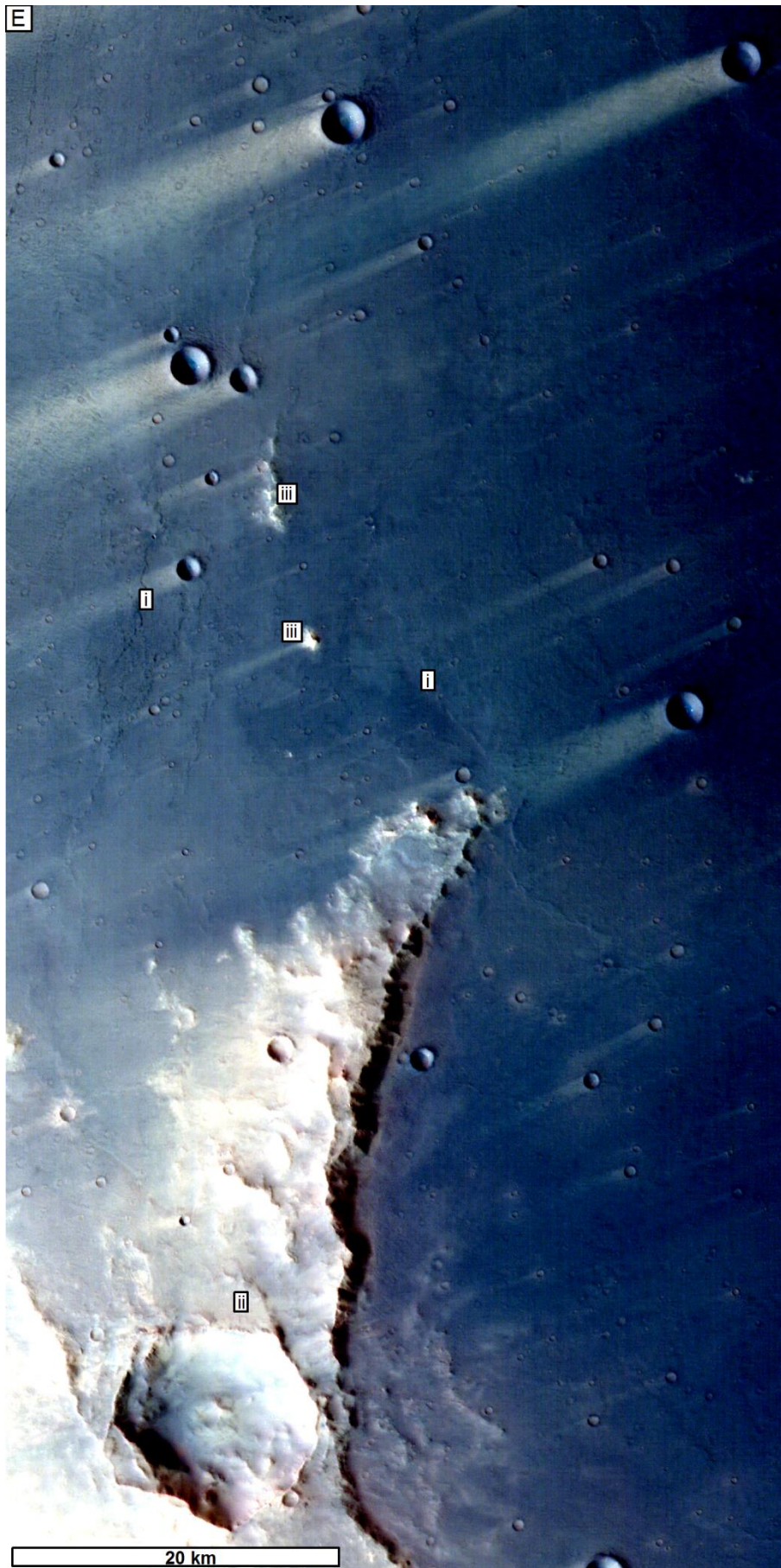
Figure 4.7 (e)

(e) HRSC RGB product H1990_0000 showing the dark blue grey lava plain of Syrtis Major, (i) structure seen within this area represents different areas of lava flow surface texture. Bright (ii) high relief material in the image is the edge of the Noachian Highlands and (iii) small outliers of highland material.

4.3.2 Early Hesperian volcanic ridge unit (eHvr).

The surface of this group is closely related to, but distinct from the Early Hesperian volcanic plains unit (eHvp). The flanks of these mounds are less 'mottled' than the eHvp, being darker overall (in THEMIS night time data). The bottoms of the mounds are often superposed by eHvp in other cases the contact is either gradational or indeterminable.

The linear mounds which make up the eHvr are between 5 and 15 km wide, and extend for tens of kilometres in a trend predominantly radial to the centre of the planum. The relief of the mounds is variable, both within a single mound, and between different mounds. The relief ranges from 20 – 100 m, but is typically between 30 – 50 m.

The ridges were identified in MOLA hill shade model (Figure 4.8b, c) and in the night-time THEMIS data (Figure 4.8a). In the THEMIS night-time data, the linear ridges are darker than the surrounding early Hesperian volcanic plains unit. Often, there is a bright line along the axis of the linear mound, with streaks perpendicular to the axis of the rise. These linear mounds predominantly occur in the north and south west of Syrtis Major Planum.

Towards the eastern margin, where Syrtis Major Planum impinges on the Isidis basin, the linear rises have two alternate forms. In the middle of the eastern edge of Syrtis Major Planum the linear rises are between 20 and 40 km wide and have 100 – 200 m of relief, increasing to up to 400 m closer to the Isidis basin (Figure 4.9b). This is ~three times wider and ~four times taller than typical examples of the mounds associated with the eHvr (Figure 4.9). These two much larger examples have mega channels along there apices which trend into and rectangular section ridges; (Figures 4.9 and 4.5a and b). These two channels are parallel with the long axes orientated running perpendicular to the Isidis basin.
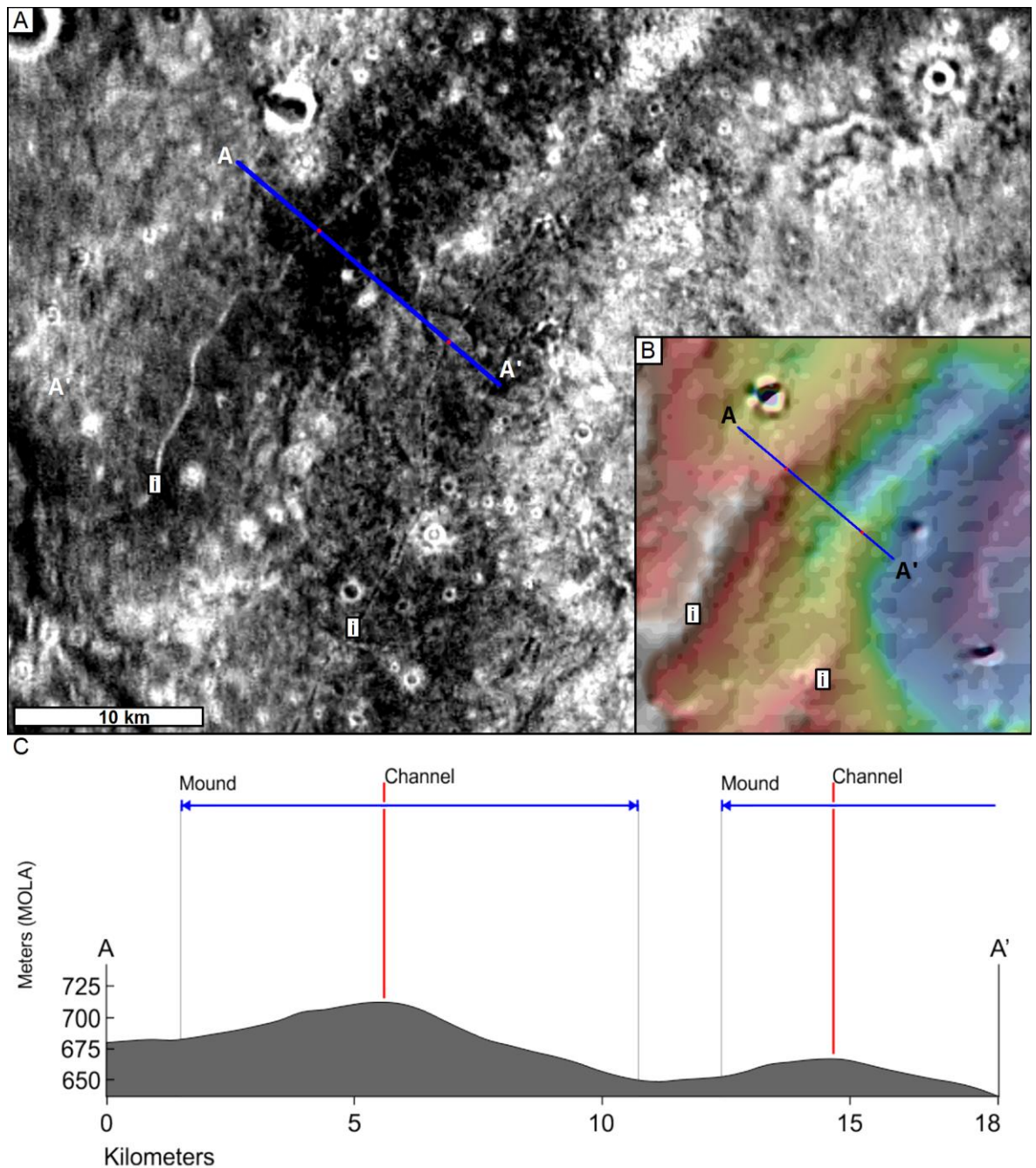
Figure 4.8

Early Hesperian volcanic ridge unit (eHvr); A pair of parallel linear mounds (i) in the northern part of Syrtis Major Planum. (a) night time Themis data and (b) MOLA elevation (c), the cross-section A to A' cross-section of the channel is belwo the resolution of the gridded MOLA data.

These channels (Figure 4.5a 4.9) are ~1500 m wide with a rectangular cross section 50 m deep. The 'upstream' end of the mega channels are buried by the Late Hesperian volcanic flow unit (lHvf; Figure 4.5f and j). The 'downstream' ends either change into flat topped ridges, become minor linear depressions, or are buried by overbanking lavas that appear to have flowed down the channel. These are also instances of lHvf-style flows which have flowed along the mega

channel and have overflowed where the channel changes to a rectangular section ridge. Additionally, it is noted that a flow (in the style of the late Hesperian volcanic flow unit, which on-laps the base of the mounds and buries their upstream end) appears to have inhabited the apex-occupying channel after the last levee-building event. Therefore, the contemporary channel depth of 50 m is a minimum depth.
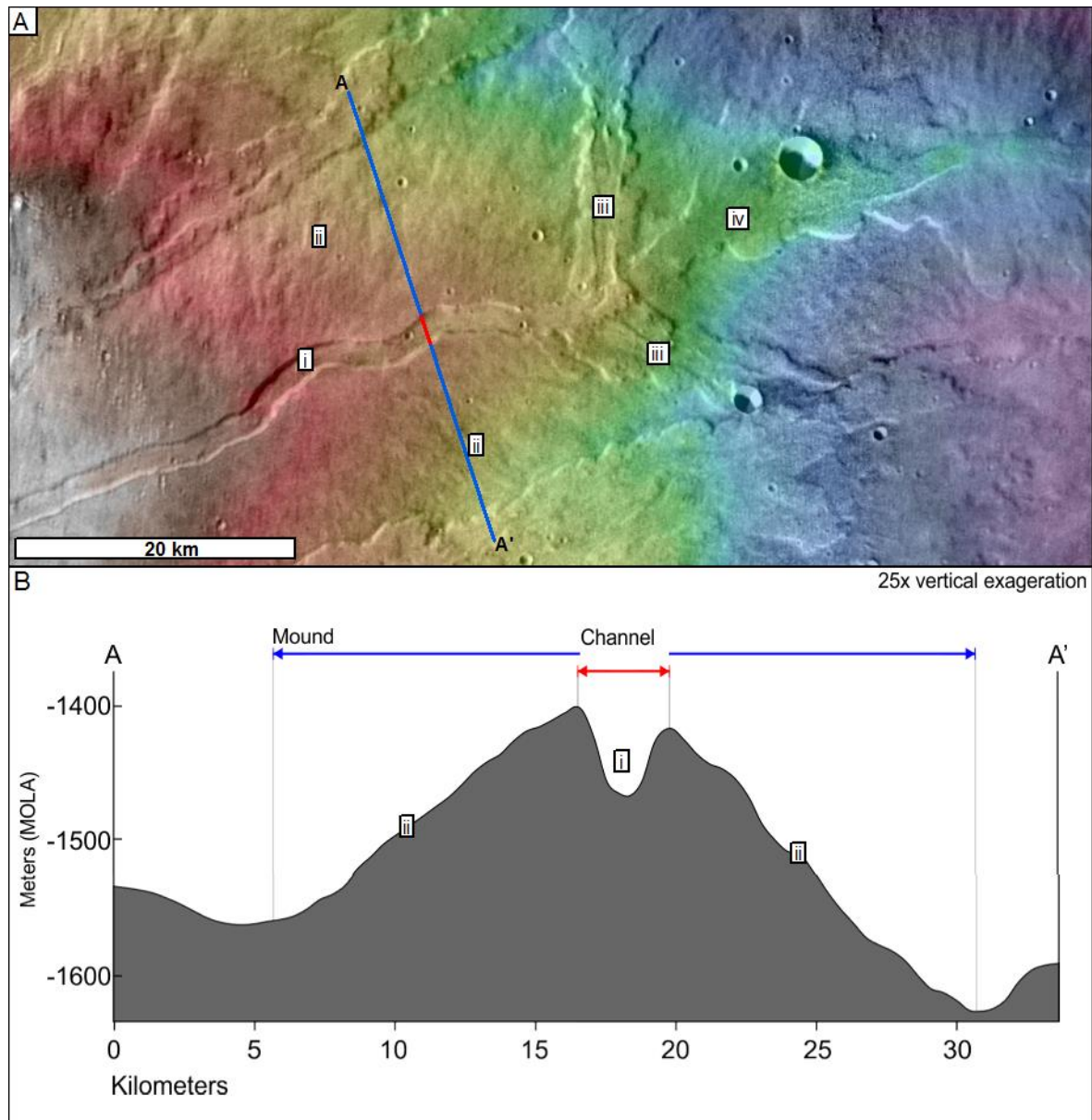
Figure 4.9

Mega channels perched on a large linear ridge striking east into the Isidis basin. (A) Themis day with MOLA elevation shows the channel (i) mound flanks (ii) mound flank overflows (iii) and the 'inverted' flat topped ridge section (iv) Also shown are the locations of subsequent figures. (b) Showing the cross-section A to A' as marked in (a).

The second alternate forms are to the North and South of the first alternate form. Here several linear ridges on the same trend topped by a series of low shield like mounds (Figure 4.4c) rather than the continuous or discontinuous channel or ridge as commonly seen on the apex of elements of this group

4.3.3 Ridged manting field (Rmf)

The south-east quadrant of Syrtis Major Planum is dominated by volcanic plain group (eHvp) materials with a mantling cover deposit. The areas affected by these deposits are covered with an overlay hatch and labelled in the Map Sheet 1 (Rmf; Figures; 5.1, 5.10). In the lower-resolution data (MOLA THEMIS day and night) this region generally has the same colours and colour/textures as the eHvp. In THEMIS night-time data, the Rmf cannot be easily differentiated from other eHvp regions of the Planum.

CTX data, however, show the area to comprise two styles of surface material, forming darker and lighter patches (Figure 4.10b). Both are similar to eHvp material at this scale of observation, with the primary distinction being that this area is overlain by small bright linear ridges (Figure 4.10c). These ridges are discontinuous, strike between 115° - 125° and have widths of ~50 m - ~100 m. The ridges appear to be influenced by the local surface roughness on which they occur, partially following the relief of craters and other features they appear to overly. On the scale of tens of meters, they do not occur in local topographic lows, instead following local topographic highs. However, on the kilometre to tens of kilometres scale they appear to be wider, more continuous and brighter (more substantial at a sub-pixel scale) in areas that are locally lower in the MOLA gridded data.

Throughout this area there are hints of elements of volcanic architecture in both THEMIS and CTX data. These include possible lava flow fronts and numerous linear channel-like features. These structures occur as part of both the brighter and darker patches but are often overlain by the small linear ridges.
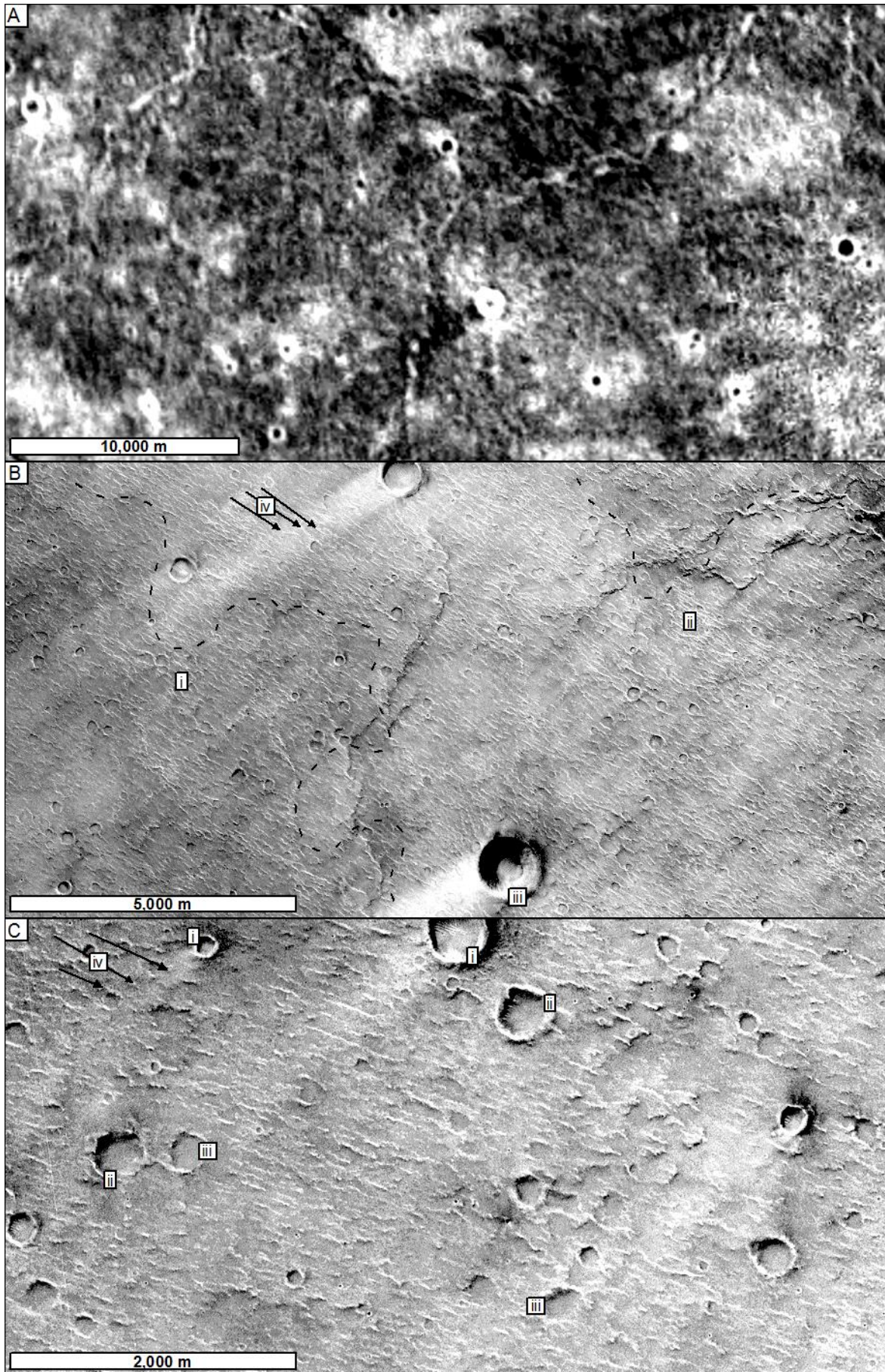
Figure 4.10

Mantled early Hesperian volcanic plains unit (Rmf) (a) Themis night-time data showing the mottled thermal character, (b) CTX image D21_035405_1834_XN_03N285W showing the darker (i) and lighter (ii) toned surface patches, and (iii) a 'normal' impact crater. Across the whole image are the bright linear ridges (iv). C. showing the two types of crater morphology exhibited in the area of this group. (i) A 'normal' crater (ii) a subdued rim crater and (iii) a subdued rim crater with a stronger influence of the bright linear ridges and (iv) small bright linear ridges.

4.3.4 Hesperian volcanic plateau unit (Hvp)

The Hesperian volcanic plateau unit (Hvp) consists of areas where there is evidence for one, or a sequence of, large flows. Stratigraphically, this group predominantly overlies the early Hesperian volcanic plains unit (eHvp). However, this is not exclusively the case because there are a few areas of eHvp overlying Flows in the Hesperian volcanic plateau unit (Hvp). Lava flow units overlying the early Hesperian volcanic plains unit (eHvp) crop out as very large flows (tens of km wide, hundreds of km long, up to 100 m high). Hvp flows partially overlain by eHvp show exposed parts that include lobate margins, characteristic relief, and contrasting night-time thermal signatures which distinguish them from the surrounding units. In the south and west of Syrtis Major there is good evidence that lava flows in this group form single flows radiating from the SMCCC. These flows are at least 350 km long. In the north and east of the planum it is not possible to determine whether the elements of this group are of similar lengths because they are overlain by the late Hesperian volcanic flow unit (lHvf).

Hvp examples are readily identifiable in the day and night-time THEMIS base layer data. In the THEMIS daytime data they have a relatively smooth surface, elevated from the surrounding eHvp and other units. They have distinct lobate flow margins (Figure 4.11a, b). In the night-time THEMIS data, the group is characteristically dark, setting it apart from the brighter or mottled eHvp (Figure 4.11c and d). MOLA point data shows that these flows typically have between 30 – 60 m of relief (Figure 4.11e) but can have up to 100 m. The edges of these flows sometimes form a series of steps, suggesting that they could be multi-stage flow or inflation packages (Figure 4.11f). In CTX data some elements of the Hvp show that the surface of these flows appear to have undulations forming an alignment of hummocks parallel to the flow direction at their edges.
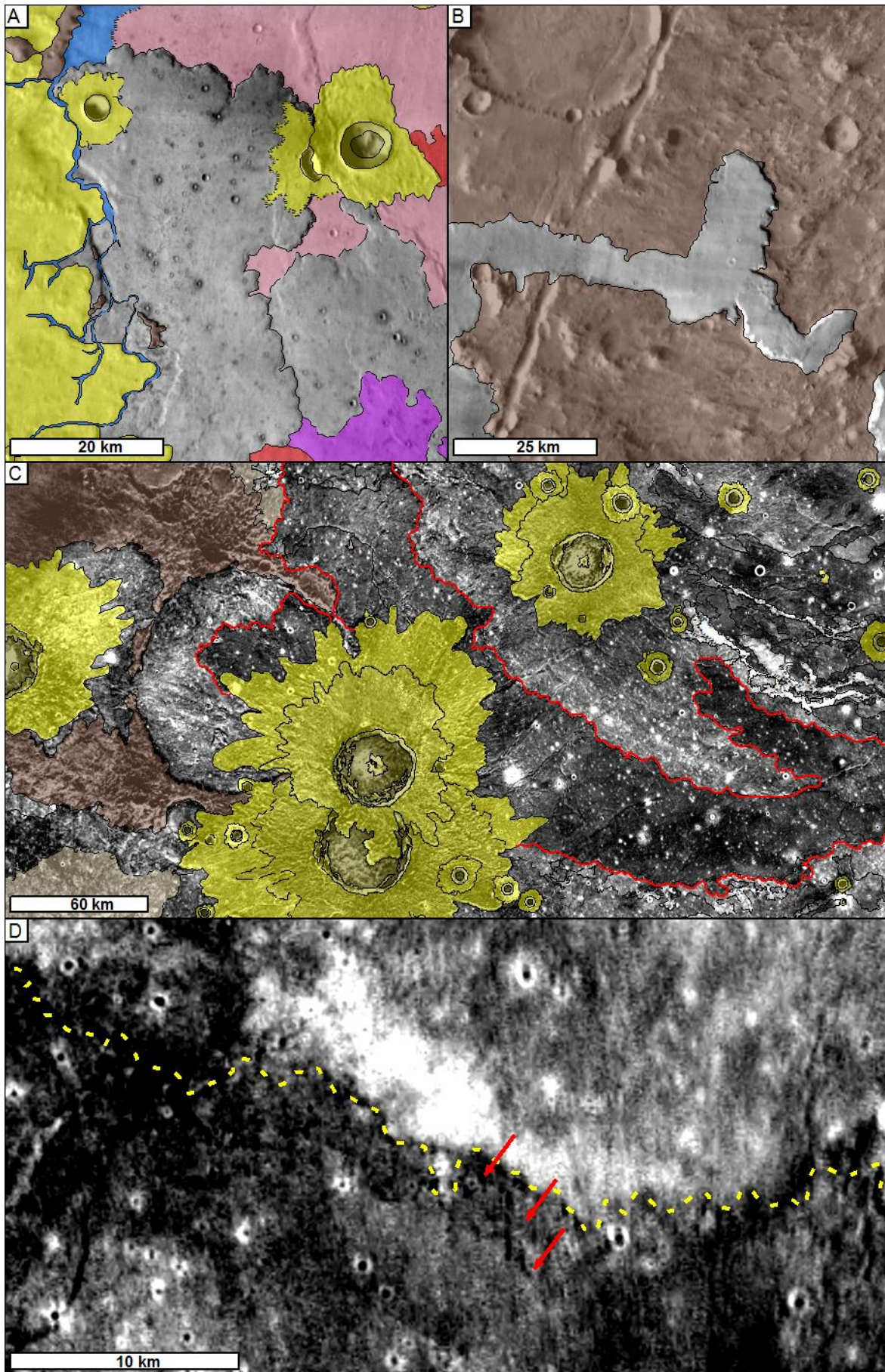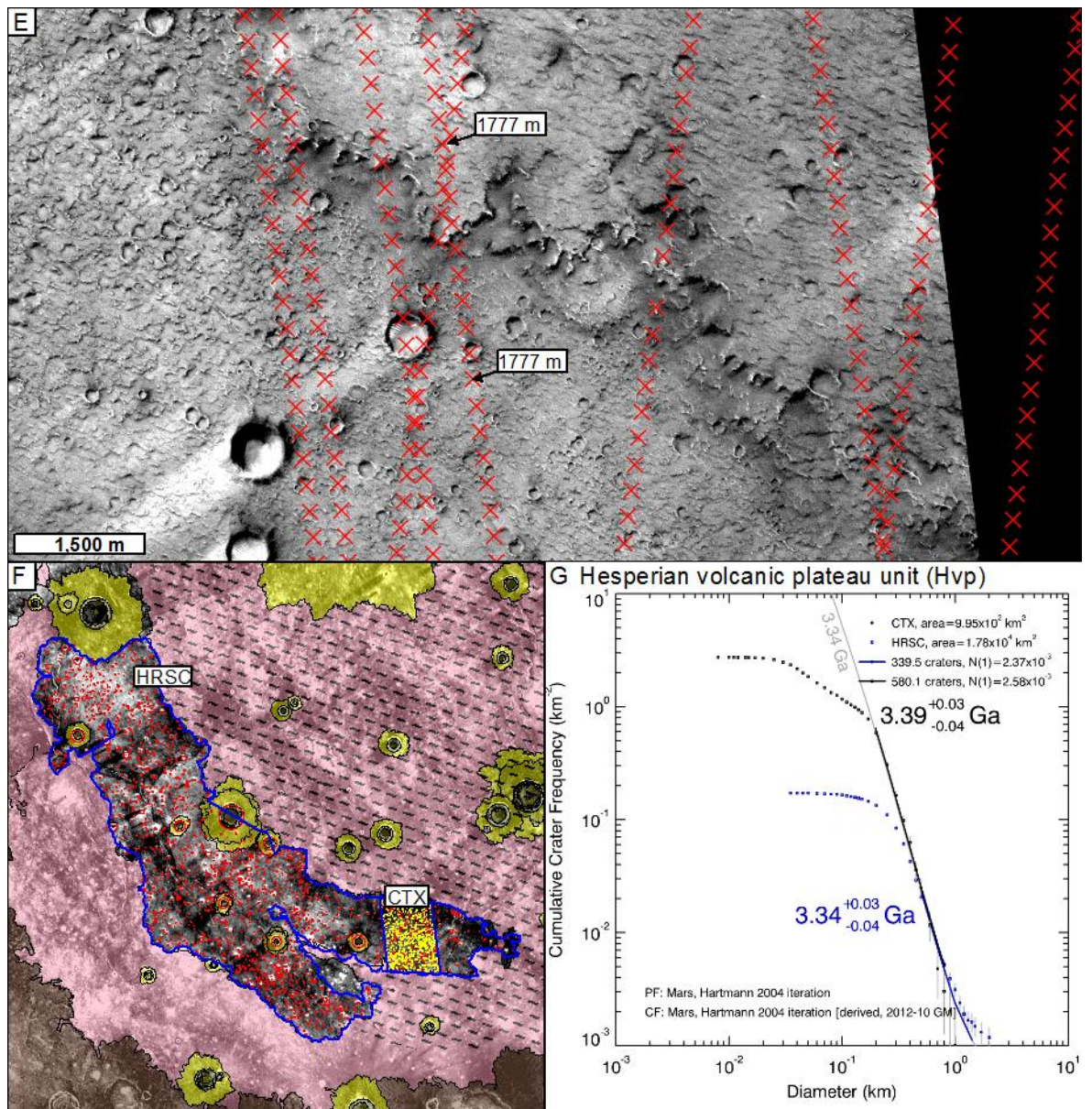
Figure 4.11

The Hesperian volcanic plateau unit (Hvp; non coloured area) identified in (a, b) Themis data showing the smooth surface and distinctive lobate flow fronts. (a), a flow from the Hesperian volcanic plateau unit overlying early Hesperian volcanic plains unit material and (b) on lapping the Noachian highland material, c, and d show the characteristically dark Night-time Themis expression of the unit. (e) Shows the relief of the Hesperian volcanic plateau unit and the stepped edges using MOLA point data.. (f). An element of the Hesperian volcanic plateau unit extending ~ 350 km south from the SMCCC showing in night time Themis with the crater count areas (blue) marked for crater HRSC craters in red and CTX in yellow (g). Crater count model ages fitted to the area of Hvp flow field from HRSC (black fit) and CTX (blue fit) crater count data. Model crater age for crater populations are summarised in Table 4.5.

Transverse ridges in the central section of the flow are perpendicular to the long axis of the flow; longitudinal ridges in the outermost parts of the flow field are parallel to the long axis of the flow. Between these trends is a narrow ~100 m ridge of upstanding material (Figure 4.5l). However, these are only seen in the stratigraphically oldest instances of this group.

4.3.5 Late Hesperian volcanic flow unit (lHvf)

The Late Hesperian volcanic flow unit (lHvf) is formed of 'narrow' lava flows a few (2-8 km) kilometres wide and tens of kilometres in length. Flows in this group have a subtle, but distinct, medial channel and levee structure (Section 4.2.1.1). These flows are orientated radially from the northern part of the central caldera complex (Figures 5.6 and 4.12a). and a set in the east of the planum, is orientated down the slope where Syrtis Major impinges on the Isidis basin.

Topographically, these Narrow flows occur in steeper regions of Nili Patera. Flows of this style are not seen in the southern part of the planum. The lHvf overlies the Early Hesperian volcanic plains unit (eHvp) and predominantly overlies the Hesperian volcanic plateau unit (Hvp). There are only a few instances where highland basement material remains protruding through the lavas in this group, and these are associated with the buried rim of the Isidis basin.

Figure 4.12 (opposite)

The Late Hesperian volcanic flow unit (lHvf). (a). The distribution of lHvf flows across Syrtis Major Planum showing; the predominant sectors of emplacement (green) lines, (Areas of Major vent systems excluded), wide medial channels (yellow), major rill like channels (black), and Large linear pits (red). (b) and (c) show the widths and (i) lobate margins of flows in the Late Hesperian volcanic flow unit (lHvf) in Themis daytime data. (d). The MOLA profile (A-A') from (b) showing the relief of the flows and the channel and levee structure MOLA profile.
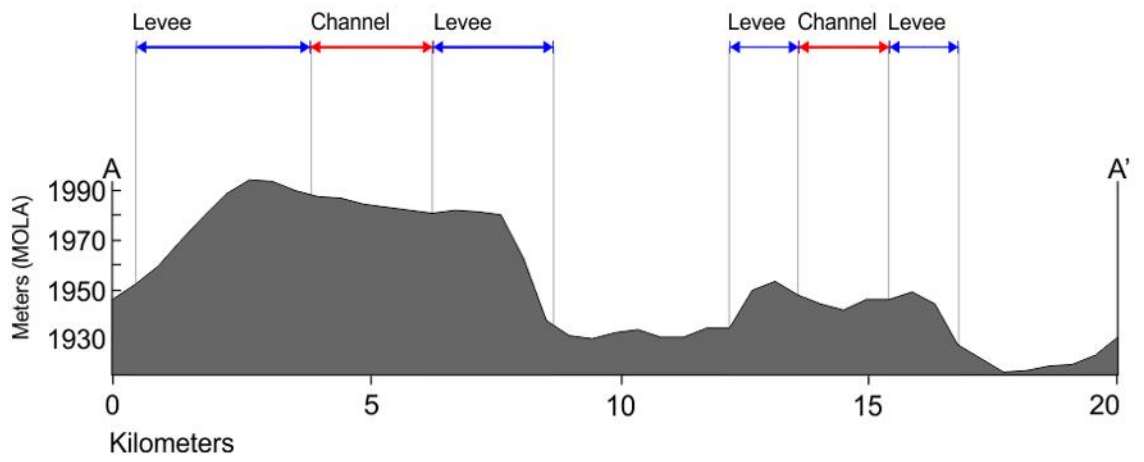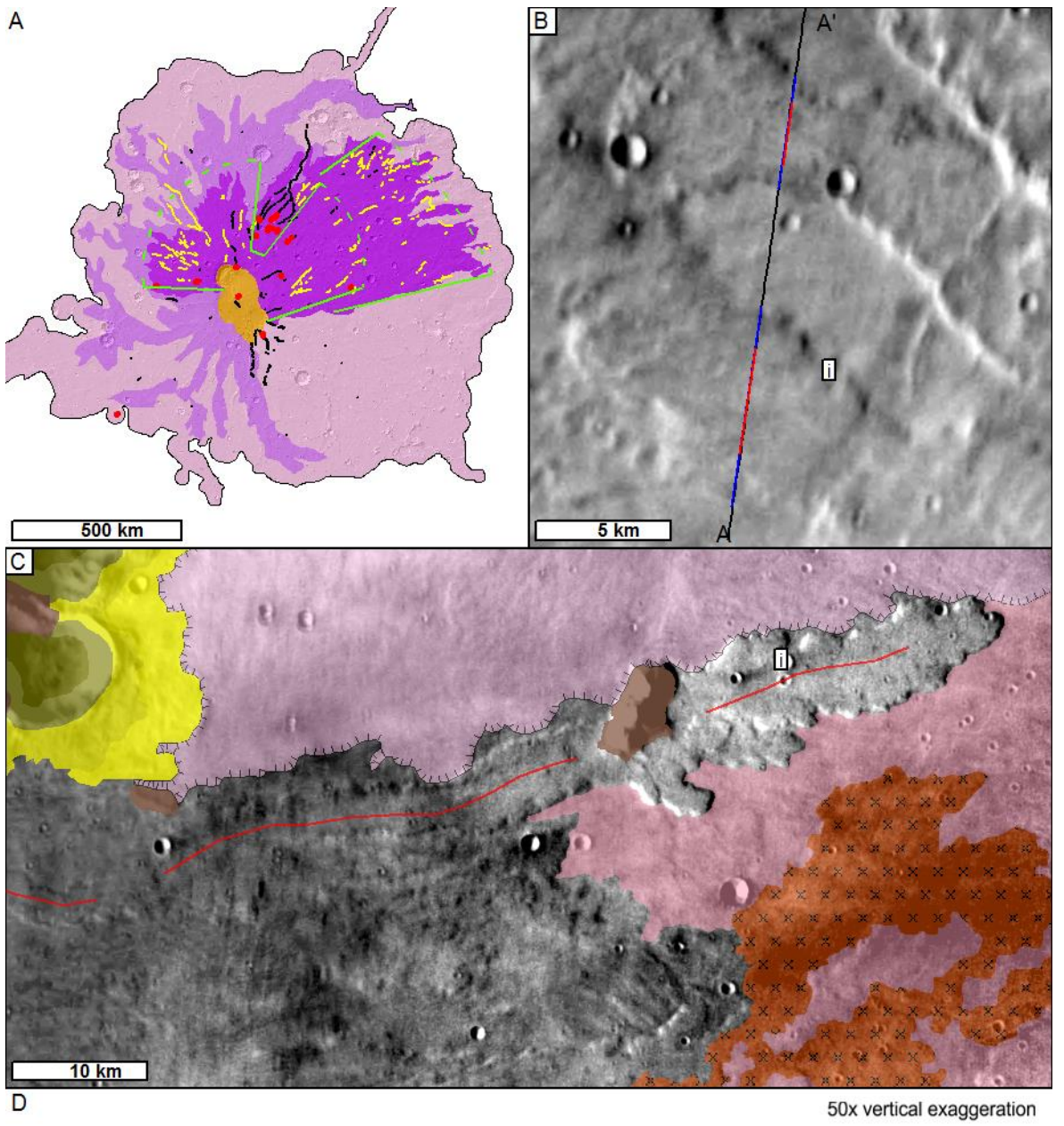
In THEMIS data, the margins of the narrow flows are easily identifiable and, in many cases, so are the medial channel structures (Figures; 4.5m, 4.12). In other instances, the medial channels are not obvious and require interrogation of the MOLA Point data (where the tracks are perpendicular to the orientation of the flows). THEMIS night-time data could not be relied upon for identification of flows in this unit. Over all, the flows in this group are similar in thermal character to the Hvp but with more variation, probably caused by the steeper slopes associated with edges of lava flows.

CTX data is useful in identifying the stratigraphical relationships between flows in this group and with the surrounding units. Although the use of CTX adds detail to measurements of flow dimensions, little morphological detail is added when using this data type, because the more detailed textures of the flow are degraded by impact cratering and surficial materials.

4.3.6 Hesperian fissure field unit (Hff)

This group contains areas where there are no clear giant or narrow flows, but where there is a relationship with areas hosting giant and narrow flows. The relationship with giant and narrow flows suggests that these areas are vent or channel proximal areas where the boundaries of giant or narrow flows are not clearly developed.

There are two main occurrences of Hff areas: Firstly, there are those associated with the SMCCC, primarily around the northern rim of Nili Patera. In this area, there are some examples of lava flow margins where the inferred flow axis points towards the centre of Nili Patera. This area has been affected by the caldera collapse, but due to the co-location with the central part of the planum and with radial lava flows it is identified as Hff.

The second occurrence of Hff areas is associated with large linear pits in the north east fissure zone (Figures 4.5 and 4.13). Here, there is a cluster of 11 large linear pits which cover an area ~100 km across and have a maximum separation of ~ 35 km. The area covered by this cluster is ~0.4% of the area of Syrtis Major Planum. The cluster is 150 km north east from Nili Patera and

wholly within the Late Hesperian volcanic flow unit (lHvf). It also forms the head area proximal to

the channel system 'Arnus Vallis' (Figures 4.2 and 4.13; [*Rampey and Harvey*, 2008].
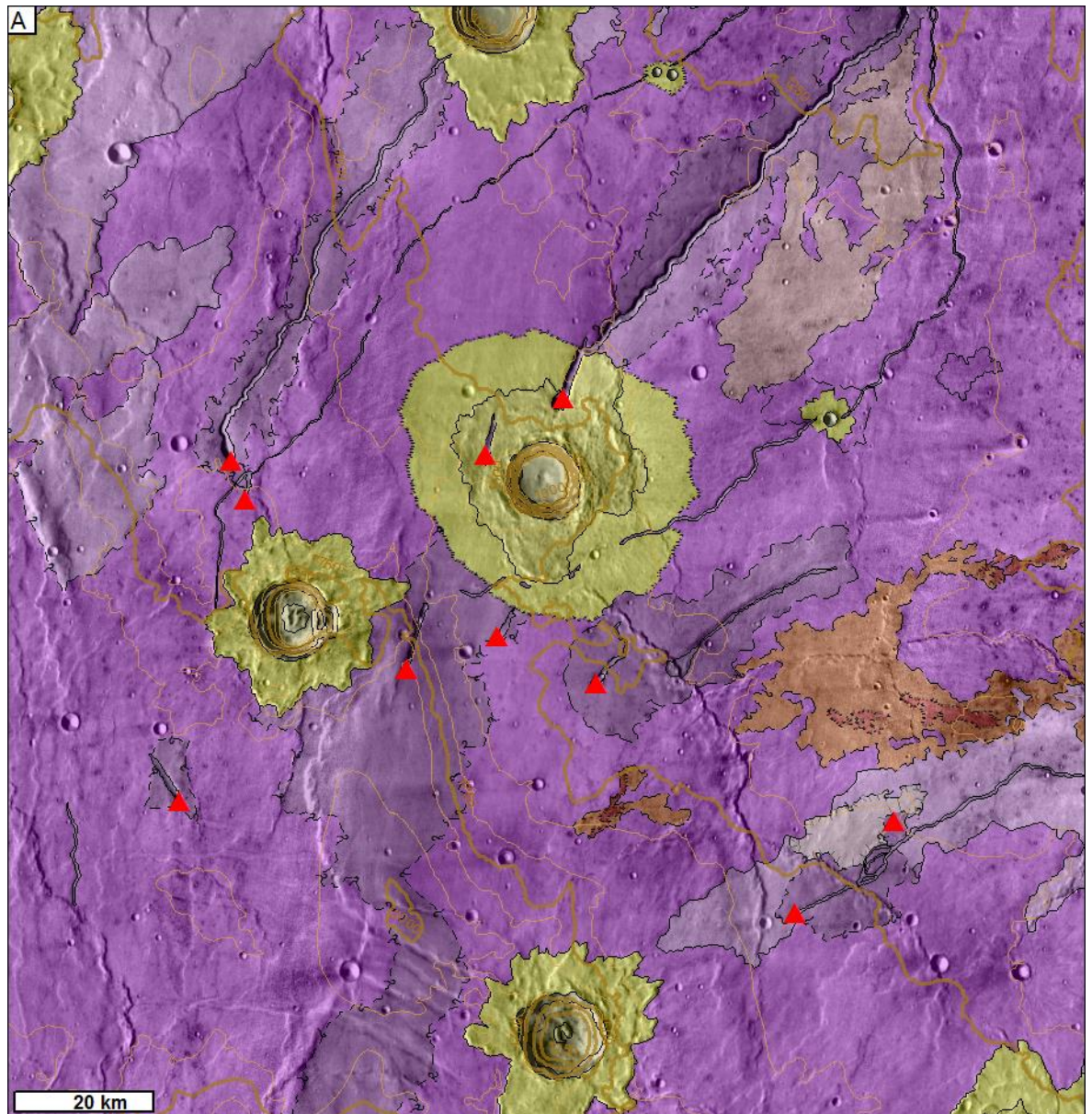
Figure 4.13

Extract from map sheet 1 showing the vent proximal regions associated with the narrow and Hesperian volcanic plateau units (Hvp, lHvf) continuous major channels (black units) and large linear pits (red triangles). Collectively this area is referred to as the north eastern fissure zone.

4.3.7 Amazonian dark ridge unit (Adr)

The Amazonian dark ridge unit group (Adr; figure 4.14) are areas on Syrtis Major Planum that are

bright in night-time THEMIS data. They have a distinctively dark appearance in THEMIS daytime

data and evidence for a different surface texture in CTX data compared to adjacent areas with a less bright response in THEMIS night-time data (Table 4.1).

The Adr are narrow in general with only a few areas greater than 5 km wide. Lineaments range in length from 2 to 100 km, but most are 10 – 30 km in length. Their long axes are generally approximately radial to the central caldera complex. The exception to this is in the northern most part of Syrtis Major, where their trend becomes sub-parallel to faults on the Nili Fossae trend. CTX data show the lineaments to have sets of narrow, 5-20 m high ridges running along their lengths. This is in contrast to the bright veneer material (Figures 4.14 b and d), discussed in 4.3.7.

Adr features are commonly seen on areas of the Early Hesperian volcanic plains unit (eHvp) and the Hesperian volcanic plateau unit (Hvp) in the north and west of Syrtis Major. They are common in both of these groups, but are also seen to be overlain by Hvp materials, for example Adr also overly the boundary between elements of both the eHvp and Hvp groups. The Adr are less common in the area of the Late Hesperian volcanic flow unit (lHvf), and examples within the area of this group are shorter and have less distinct boundaries. Adr could not be differentiated and mapped in the South-west because the covering of Ridged manting field (Rmf) material prevents identification in CTX data. Based on THEMIS data, however, the Adr group in this region follow the trend of the Early Hesperian volcanic plains unit Ridges (eHvr), striking south east close to the SMCCC and turning to strike east closer to the contact with highland materials

Figure 4.14 (oppersite)

(a) The distribution of the thermally distinct group across Syrtis Major Planum, bright lineaments (red) and bright veneer (orange). (b). Amazonian dark ridge unit (Adr) with (i) an axial ridge and (ii) Amazonian/Hesperian dark plains unit (AHdp) material in CTX D04_028720_1978_XN_17N293W coloured with Night time Themis (purple, low thermal emission, black, high thermal emission). Adr in (c) night-time and (d) daytime Themis showing the relationship between (i) the Adr and (ii) the AHdp. (e) A further example of a Adr (i) overlying material in the Hesperian volcanic plateau unit. CTX F05_037647_1858_XN_05N293W coloured with Night time Themis (purple, low thermal emission, black, high thermal emission).
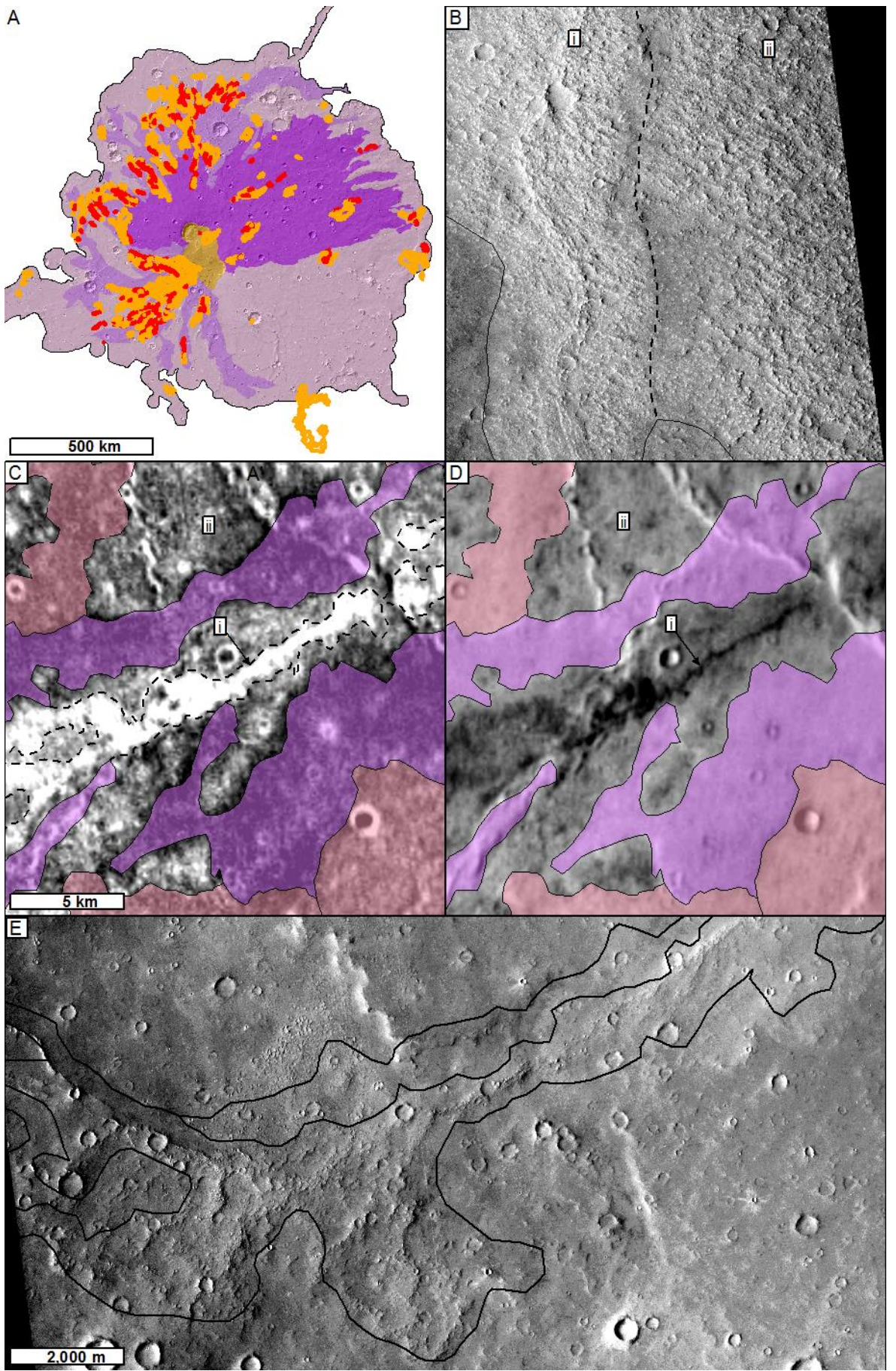
4.3.8 Amazonian/Hesperian dark plains unit (AHdp)

The Amazonian/Hesperian dark plains unit (AHdp) (Figures 4.14 and 4.15) is material that is bright in night-time THEMIS data, although less so than that of the Amazonian dark ridge unit (Adr; Table 4.1). The surface has a distinctively dark appearance in THEMIS daytime data and evidence for a hackly bright surface texture in CTX data compared to adjacent areas. This material occurs at the same stratigraphic level as the Adr. The material is predominantly on top of early Hesperian volcanic plains unit (eHvp), interlayered with the Hesperian volcanic plateau unit (Hvp), and occurs within the area of the Late Hesperian volcanic flow unit (lHvf). Where this material forms a clear stratigraphic relation with a definable area I have been able to date this element of the group (Figure 4.15d and e). In CTX data (Figure 4.15) this surface material is rougher than surfaces in the Volcanic plains and Hesperian volcanic plateau unit (eHvp, Hvp). The deposits appear to be a few meters thick, but are below the horizontal resolution of MOLA, making reliable measurement difficult (Section 3.2). The margins of the unit are irregular, but rounded, and the unit appears to be elevated relative to underlying eHvp (Figure 4.15b).

Figure 4.15

Three examples of the CTX scale texture of the Amazonian/Hesperian dark plains unit (AHdp). (a). shows the surface of (i) an area in the AHdp group abutting (ii) a flow margin of the Hesperian volcanic plateau unit (Hvp; CTX D05_029063_1811_XN_01N296W). (b) And (c) show two examples of (i) AHdp overlying the similar but more subdued (ii) Early Hesperian volcanic plains unit (eHvp) surface (CTX; B16_016048_1878_XN_07N295W and F03_036790_1856_XN_05N296W). (d). A small area of AHdp seen to have ben emplaced on top of impact ejecta. This allows the relative crater (red) density to be assessed from the areas outlined (blue; CTX D05_029063_1811_XN_01N296W). (e). crater count model ages fitted to the area of AHdp lava (Red) and the underlying impact crater (black). Model crater age for crater populations are summarised in Table 4.5.
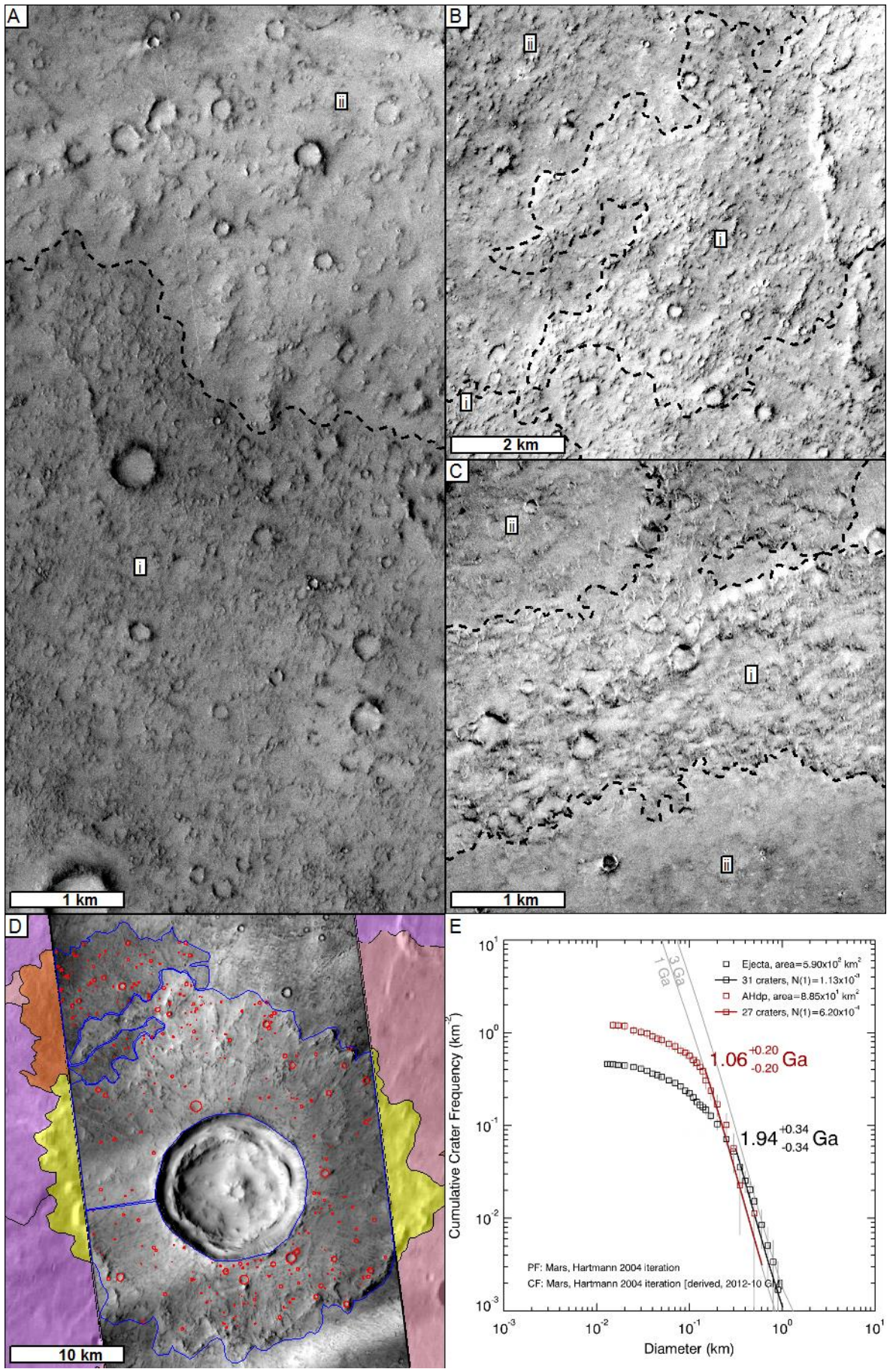
4.3.9 Amazonain volcanic field units (Avf)

In addition to the surfaces categorised as Amazonian dark ridge unit (Adr) and Amazonian/Hesperian dark plains unit (AHdp), there are three instances of unique surface areas that are also thermophysically distinct:
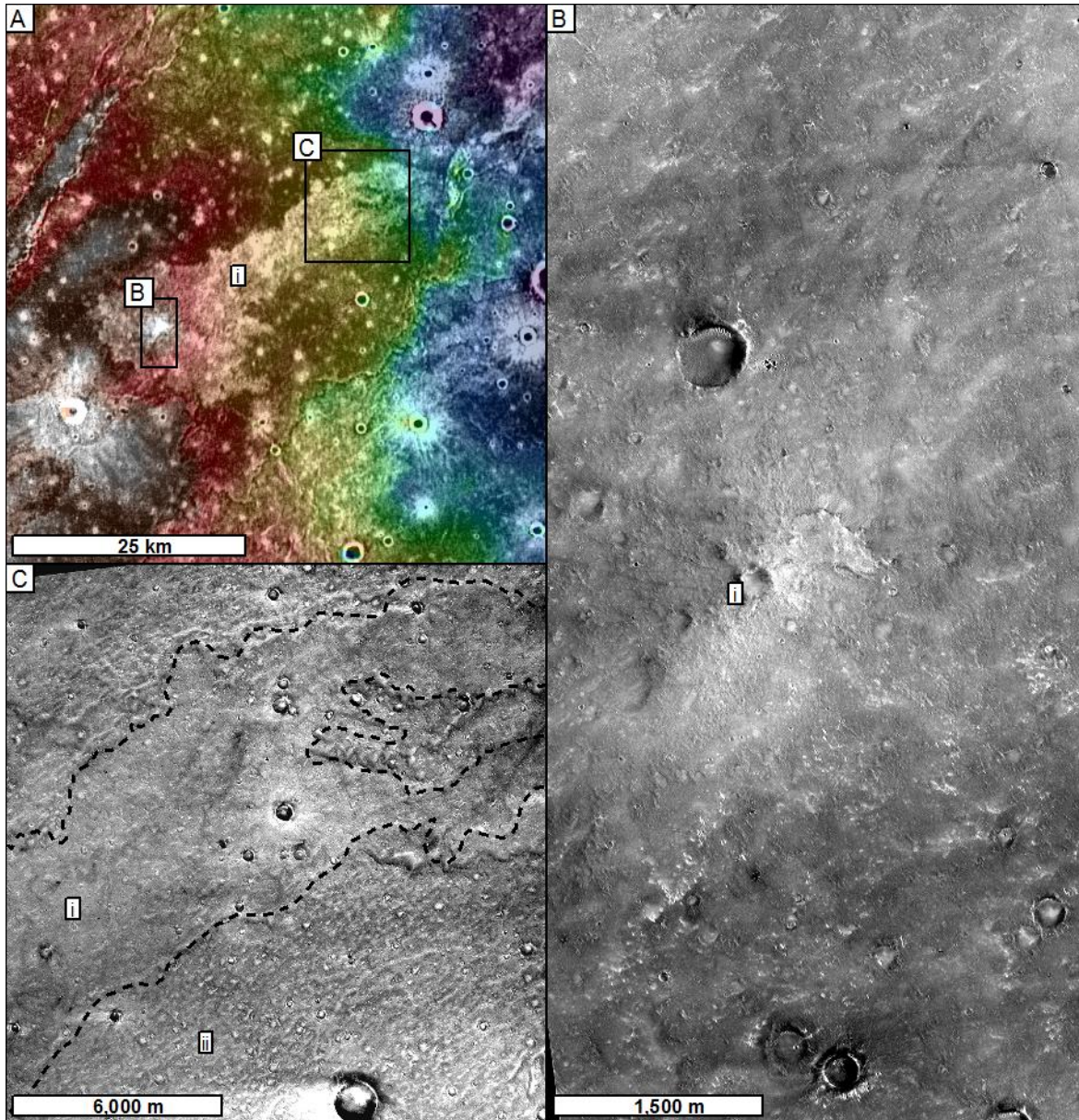
Figure 4.16

The bright cone and flow on east of the central caldera complex. (a). Night-time THEMIS showing (i) the surface of the bright flow. (b). The cone with (i) a crater at the peak at the centre of the thermally distinct area seen in HiRISE ESP_032135_1920. (c). The surface of (i) the thermally distinct region: CTX F10_039823_1915_XN_11N287W and (ii) the surrounding surface in the Late Hesperian volcanic flow unit (lHvf).

4.3.9.1 Bright cone and flow

North east of the SMCCC at (71.72 E 11.93 N; Figure 4.16) is a cone (identifiable in MOLA topography; Figure 4.3a and b) associated with a region that is bright in night-time THEMIS data it extends 33.5 km downslope (Figure 4.16). I interpret this to be a cone and lava flow. The flow is hard to distinguish in daytime THEMIS data, but CTX data show the flow margin and a surface similar to the AHdp. The flow lacks small patches of bright material, as seen on the surrounding material in the Narrow flow group (lHvf; figure 4.16c). Whilst this example is similar to AHdp in some ways, it is the only location on Syrtis Major Planum, outside of the central caldera complex, where a surface of this kind is observed to be linked to a cone of this size and morphology.

4.3.9.2 Thin bright flow

The second unique area of thermally distinct material is a 380 km long flow-like feature (originating at 71.37°E, 12.28°N). It is situated close to the termination of the cone flow (Figure 4.17a) described immediately above (Figure 4.16) where there are a series of short trench-like features (Figure 4.17b). The MOLA point data suggests that the upslope region of it is ~5-10 m thick, with additional complexity to its topography towards the centre of the flow and furthur downslope. Here it has a more complex relationship with topography possibly being up to 50 m thick in places. Clearer details of these possible structures are unavailable, as the feature is below the resolution of the topographic data available.

In CTX data, the surface texture of the flow is slightly darker than that of the surrounding terrain. In an area where discontinuous ejecta for an impact crater overlays the unit, the unit is less dark and more similar to the surrounding terrain. Also where there is discontinuous ejecta the thermal inertia on the 100 m scale of THEMIS pixels is lower. This obscurs the continuity of the feature between the up and downslope higher thermal inertia sections (Figure 4.17a).

A

50 km

B

13,000 m

C

i

ii

iii

1,500 m

D

i

ii

iii

E Thin flank flow

1 Ga 3 Ga

□ AHdp, area=3.27x10² km²
— 46 craters, N(1)=5.97x10⁻⁴
□ Ejecta, area=1.50x10³ km²
— 216 craters, N(1)=1.62x10⁻³

$2.76^{+0.16}_{-0.17}$ Ga

$1.02^{+0.19}_{-0.19}$ Ga

PF: Mars, Hartmann 2004 iteration
CF: Mars, Hartmann 2004 iteration [derived, 2012-10 GM]

Cumulative Crater Frequency (km⁻²)

Diameter (km)
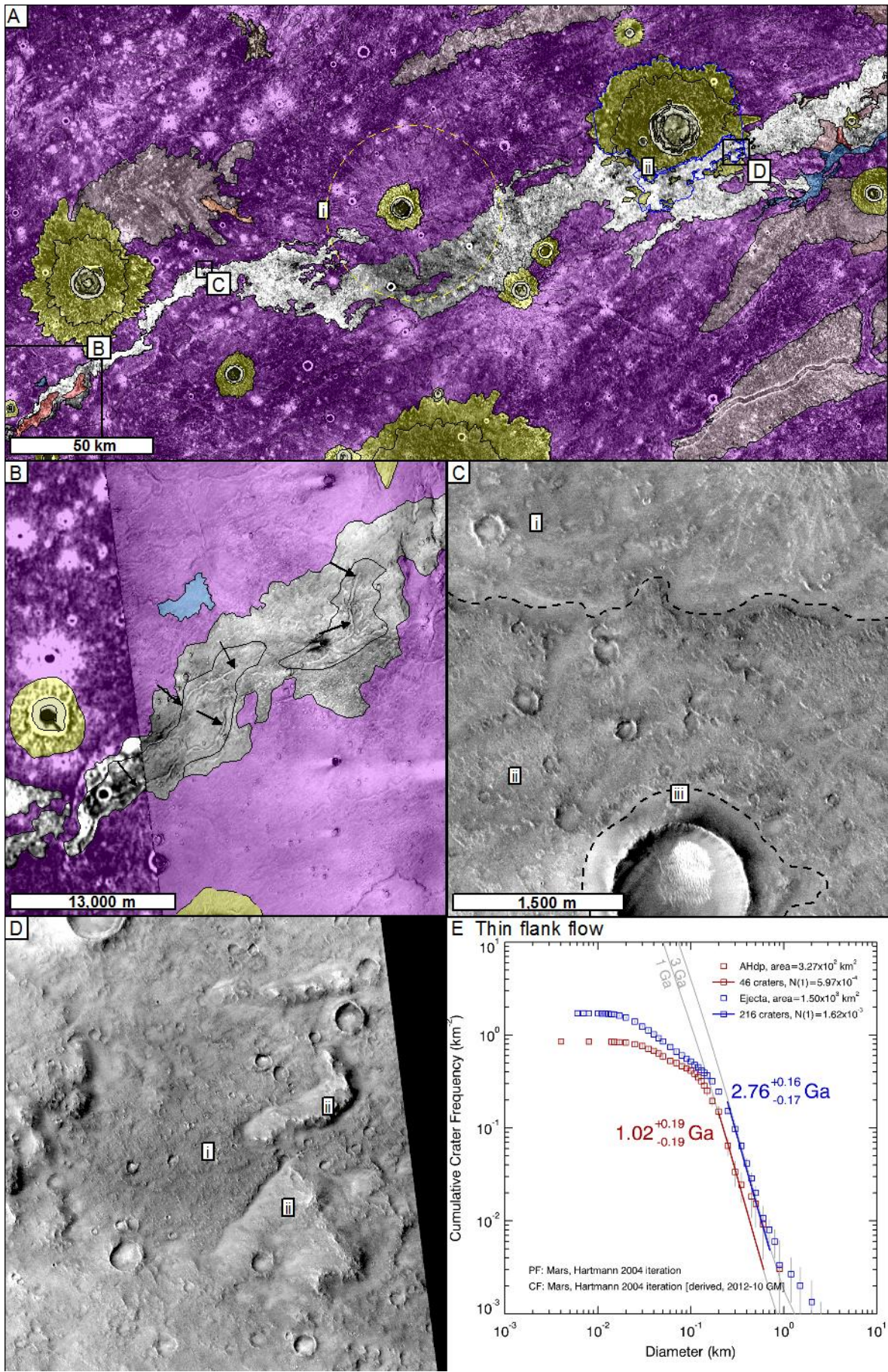
Figure 4.17

Figure showing the thin bright flow on the eastern flank of Syrtis Major Planum. (a). An extract from Map Sheet 1, excluding thermally distinct group surfaces, overlain on the Night Themis base layer. At (i) the distinct signature of the flow is partially masked by discontinuous ejecta (yellow outline). The areas outlined in blue are areas in which crater counts where conducted. (b). Close up of a group of channels and trenches at the head of the thin bright flow seen in CTX D18_034337_1927_XN_12N287W. (c). Close up of the boundary between (i), a surface in the Late Hesperian volcanic flow unit (lHvf) and (ii) Avf in CTX F04_037528_1937_XN_13N286W. Avf material has flowed around the impact crater (iii). (d). (i) the bright eastern flow infilling areas between (ii) upstanding mounds of ejecta in CTX B19_017142_1934_XN_13N283W. (e). Model crater age for crater populations the areas of which are shown in (a) and summarised in Table 4.5.

Further down flow (76.17°E, 13.64°N) the thermally bright material overlays the ejecta of an impact crater (Figure 4.17a). Here the surface of the unit can be seen abutting hummocks in the underlying ejecta (Figure 4.17d). Both the emplacement of the ejecta and thermally distinct surface (assuming it is lava) are geologically instantaneous, allowing the crater density to show the relative age (Chapter 3.3). The model age for the thermally distinct surface is ~1.1 Ga. This is ~1 Ga younger than the ejecta, which has a model age of ~2.3 Ga (Figure 4.17e). This is the place on Syrtis Major where this relationship is clearest allowing the relative dating to be established for such a distinct flow.

4.3.9.3 Western flank fissure

The third unique instance within the thermally distinct group is a short fissure vent and flow west of the SMCCC at (65.16°E 11.23°N; Figure 4.18). The flow has a maximum length of 68 km, and the main part of the flow is 10 km in maximum width. The maximum height of the flow is ~35 m. The flow appears to originate at a discontinuous linear ridge which contains small cone and crater like features. These may be associated with the volcanism or may be impact craters (Figure 4.18b). The surface of the flow has a mottled appearance in THEMIS night-time data. There is a stronger contrast between 'dark' and bright' pixels than at other thermally distinct surfaces. There is a darker region at the centre of the flow (Figure 4.18a) which correlates with the top surface of the flow as seen in MOLA point and CTX data, whereas the mottled areas correlate to the sloping sides of the flow.
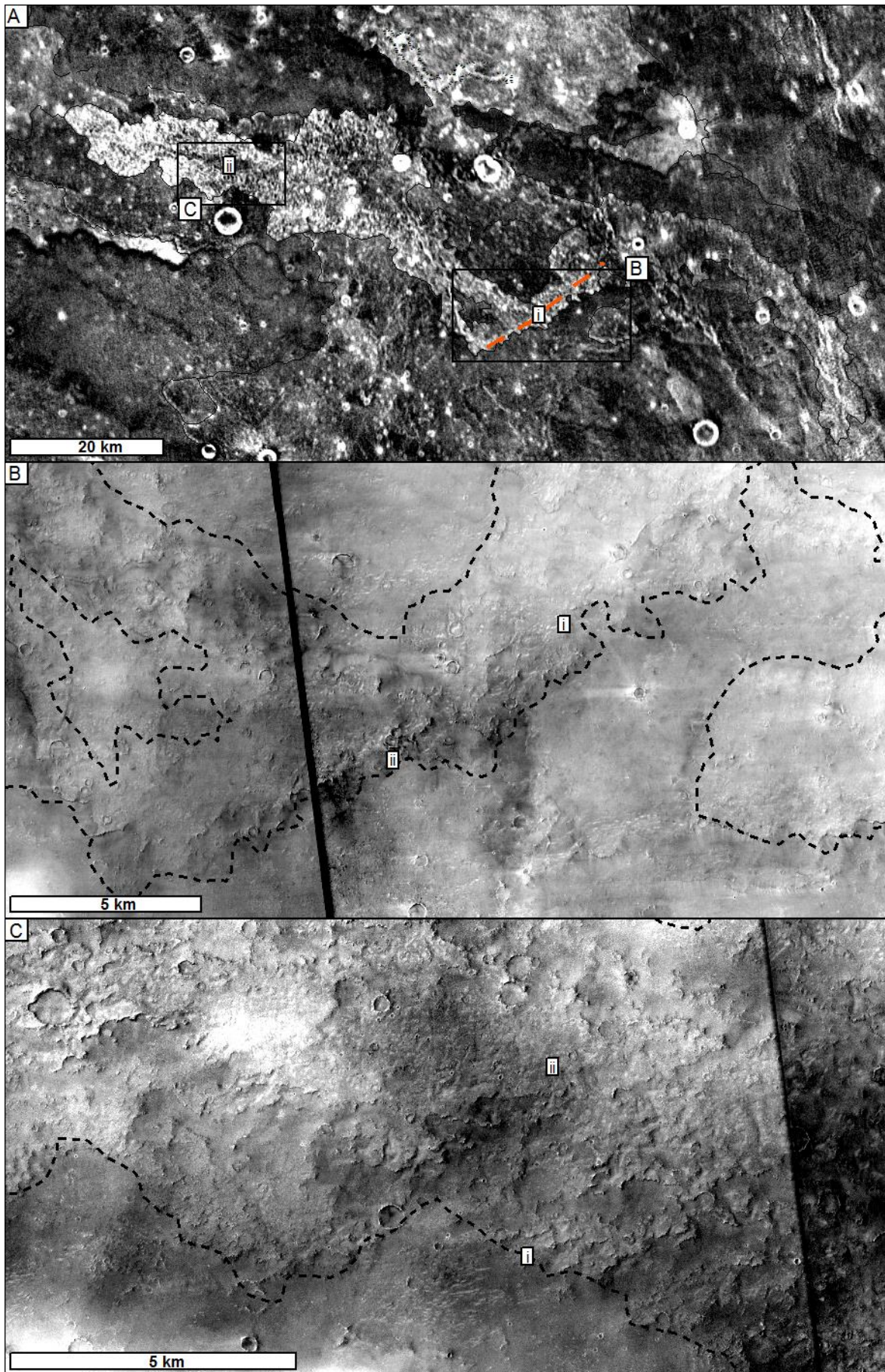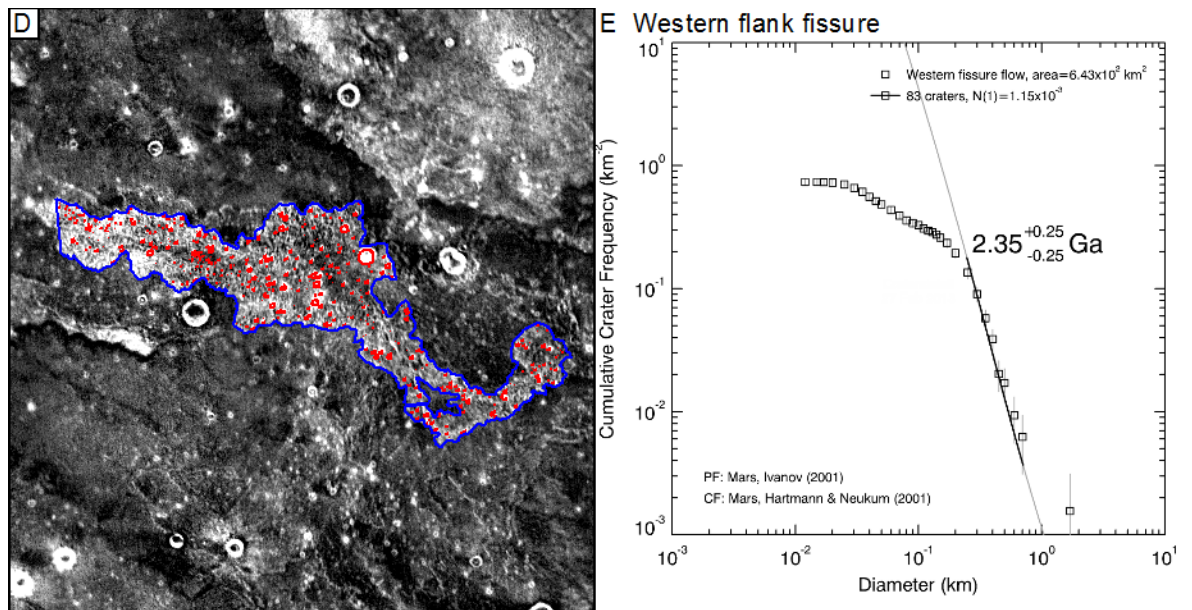
Figure 4.18

Western flank fissure shown in (a). Night-time Themis base layer showing (i) the source fissure and (ii) the darker region at the core of the flow. (b). CTX (IMAGE) of the (i) fissure vents area with (ii) possible cone like structure. (c). showing the downslope part of the flow showing the (i) complex flow margins and (ii) the rounded hummocky upper surface of the flow.(d) show the Crater count area (blue) and craters counted (red) and (e) the crater count plot for the western flank fissure summarised in Table 4.5.

This top of the lava flow associated with the western flank fissure forms a plateau, 35 m above the surrounding terrain. In CTX data the top surface of the plateau appears to undulate over length scale of 100 m – 200 m and is less rubbly than other examples of material in the group. The 'Edge' areas of the flow are rough on a 100 m – 200 m scale, with quasi-digitate promontories forming an irregular series of terraces stepping down to the surrounding terrain. The lowest 'steps' are only ~1 – 5 m in height (Figure 4.18c). This is the only place on Syrtis Major where there is such a clear relationship between a short fissure and a flow of this size and with such clear 'fresh' morphology. A crater count (Figure 4.18d) was conducted in the area of this unit using CTX data. A model age of ~2.36 Ga was fitted to these data.

4.4 The age of the planum building flows

To assess the age and longevity of volcanism at Syrtis Major Planum I conducted impact crater counts and analysed impact crater size-frequency distributions to ascertain crater retention model ages. The methods of crater counting used to investigate the Planum building volcanism of Syrtis Major are described in Section 3.3.

4.4.1 Crater counts from CTX and HRSC data

Crater size frequency distribution plots for counts counducted on CTX and HRSC data for various of the planum building lows have been are included with the relevant unit descriptions and long with figures shoing the areas in which the counts where conducted. Data pertaining to these crater counts are summarised in Table 4.5 including references to the relvent figures eg; figure 4.15d (count area) and 4.15e (CSFD plot).

4.4.2 Crater counts from the Robbins database

In addition to the local crater counts conducted on individual units presented in Sections 4.3.3, 4.3.7 I also evaluated the crater size frequency distribution for the Early Hesperian volcanic plains unit (eHvp), Hesperian volcanic plateau unit (Hvp) Late Hesperian volcanic flow unit (lHvf) and the SMCCC. This 'whole Planum' dating uses data extracted from the published crater catalogue of impact craters on Mars ≥1 km in diameter [*Robbins and Hynek*, 2012a, 2012b]. To extract these data, I used the areas of the simplified map (Figure 4.19). These boundaries were used because the area of these groups on Map Sheet 1 does not include large craters. In addition to the volcanic unit of Syrtis Major Planum, crater count data were extracted for the Isidis basin floor and the Noachian highlands surrounding Syrtis Major to provide context. The crater database has been filtered for ghost craters (Chapter 3). The results of the count for small units generally from CTX data is summarised in Table 4.5 and counts drawing on the Robbins data base [*Robbins and Hynek*, 2012a, 2012b] are summarised in Table 4.6.
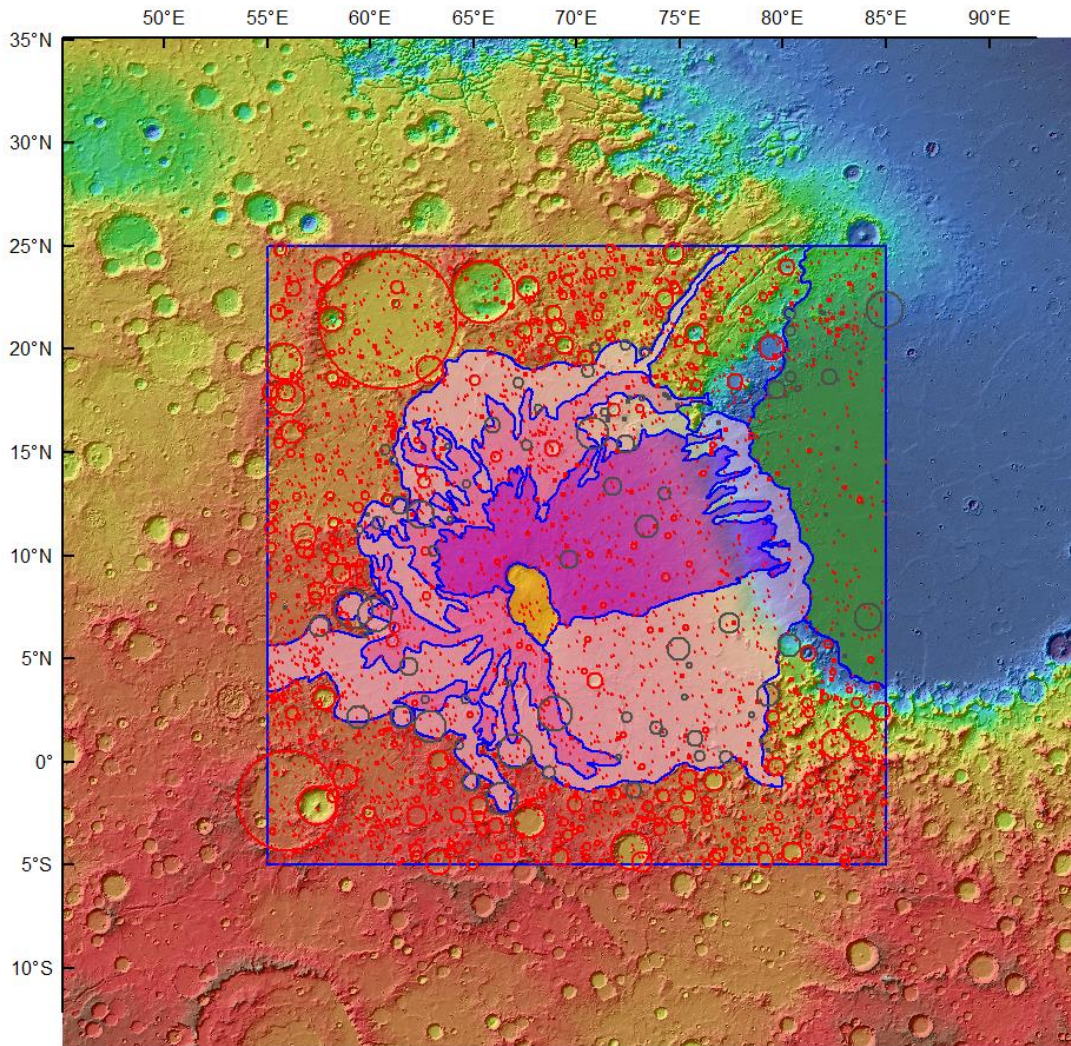
Figure 4.19

Simplified map showing the 6 areas where crater cont were conducted to support the stratigraphy of the groups of volcanic surfaces described in this chapter.

A Area of the Noachian highland massifs
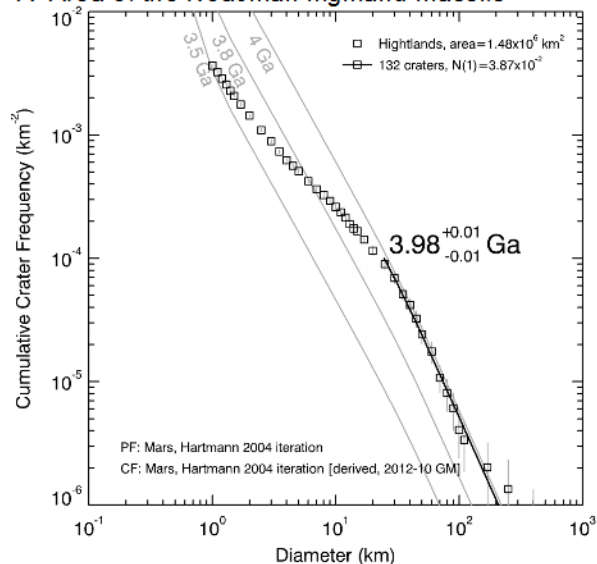
B Area of the early Hesperian volcanic plains unit
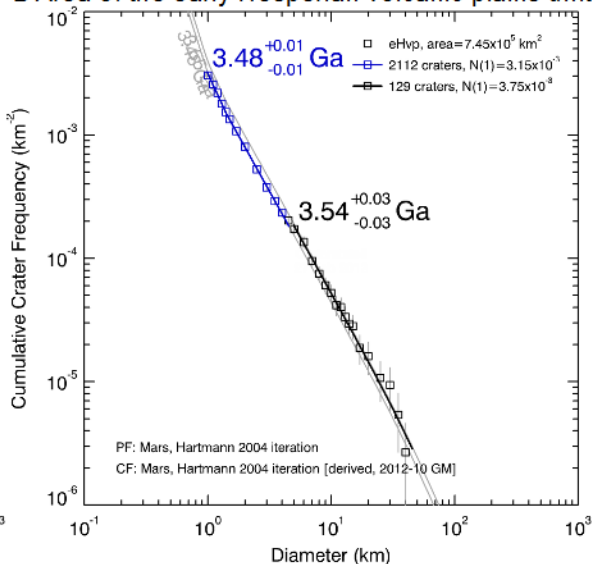
C Area of the Hesperian volcanic plateau unit
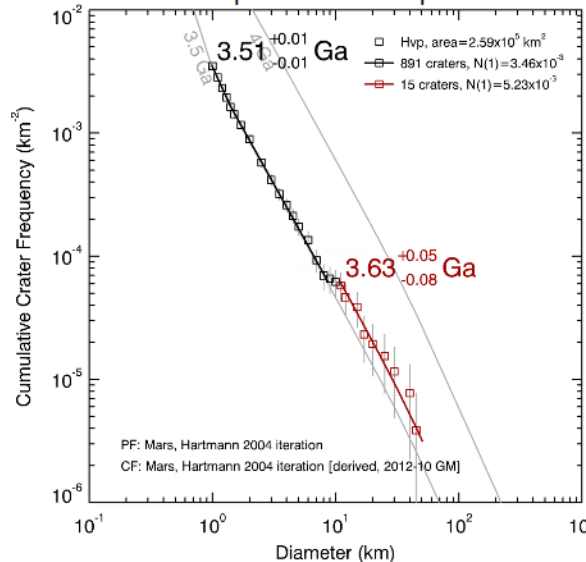
D Area of the late Hesperian volcanic flow unit
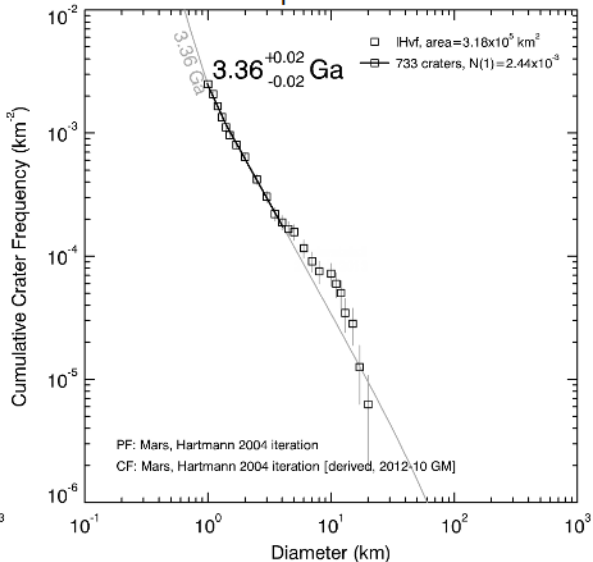
E Area of the Central caldera complex (SMCCC)
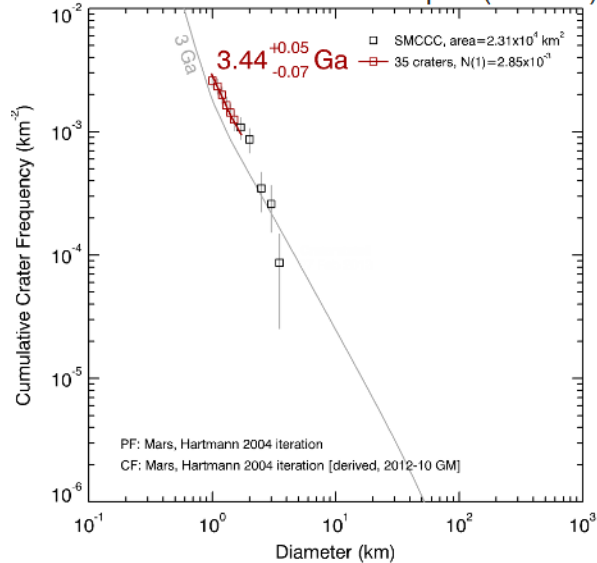
F Area of the Isidis floor
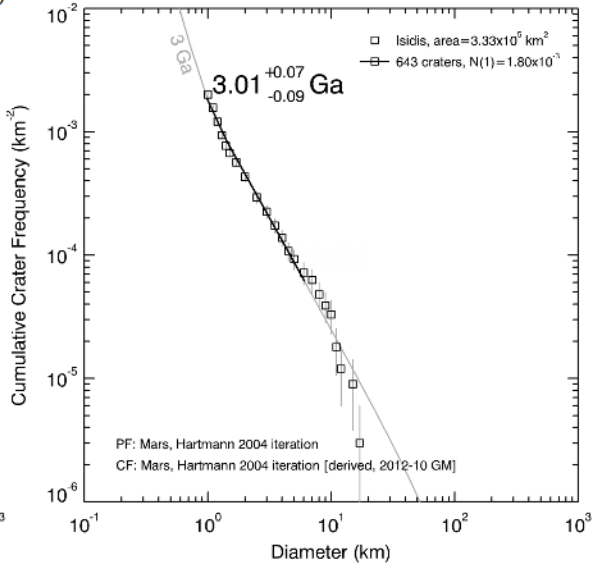
Figure 4.20

*Crater count plots showing the cumulative crater size frequency distribution for the six regions shown in Figure 4.19. (a). Count for the Noachian highland massifs (Nhm) surrounding Syrtis Major. (b). Count for the Early Hesperian volcanic plains unit (eHvp) showing the fit to two isochrones for different parts of the population, (c) Hesperian volcanic plateau unit (Hvp), (d) the Late Hesperian volcanic flow unit (lHvf) (e) the SMCCC. (f). Count for the floor of the Isidis basin. All plots use the Hartman production and chronology functions plotted in CraterstatsII [*Hartmann and Neukum*, 2001a;* Michael and Neukum*, 2010]*

Table 4.5

Surface	No. Craters	Area (km²)	Size range fitted (m)	No. Fitted	Model Age (Ge)	+	-	N(1)	Base layer	Type	Figure
Lava (*Gfg*)	3058	$1.78x10^4$	500 - 1400	580	3.34	0.03	0.04	$3.37x10^{-3}$	HRSC	Formation	4.11g
Lava (*Gfg*)	2723	$9.95x10^2$	200 - 800	339	3.39	0.03	0.04	$2.58x10^{-3}$	CTX	Formation	4.11g
Ejecta (under Avf)	2564	$1.50x10^3$	200 - 700	216	2.76	0.16	0.17	$1.62x10^{-3}$	CTX	Formation	4.15d, e
Lava (*Avf*)	279	$3.27x10^2$	200 - 600	46	1.02	0.19	0.19	$5.97x10^{-4}$	CTX	Formation	4.15d, e
Lava (*Avf*)	474	$6.43x10^2$	250 - 700	83	2.35	0.25	0.25	$6.43x10^{-2}$	CTX	Formation	4.17a, e
Crater Ejecta (Under Tdv)	272	$5.90x10^2$	300 - 1000	31	1.94	0.34	0.34	$1.13x10^{-3}$	CTX	Formation	4.17a, e
lava (*Tdv*)	107	$0.85x10^2$	150 - 600	27	1.06	0.20	0.20	$6.20x10^{-4}$	CTX	Formation	4.18d, e

Table 4.6

Surface	No. Craters	Area (km²)	Size range fitted (km)	No. Fitted	Model Age (Ge)	+	-	N(1)	Base layer	Type	Figure
Highlands	5420	$14.80x10^5$	25.0 - 300.0	132	3.98	0.01	0.01	$3.46x10^{-3}$	Robbins	Formation	4.19, 4.20a
eHvp	2263	$7.45x10^5$	5.0 - 45.0	129	3.54	0.03	0.03	$3.75x10^{-3}$	Robbins	Formation	4.19, 4.20b
		$7.45x10^5$	1.0 - 4.5	2112	3.48	0.01	0.01	$3.15x10^{-3}$	Robbins	Formation	4.19, 4.20b
Gfg	908	$2.59x10^5$	1.0 - 8.5	891	3.51	0.01	0.01	$3.46x10^{-3}$	Robbins	Formation	4.19, 4.20c
lHvf	793	$3.18x10^5$	1.0 - 4.0	733	3.36	0.02	0.02	$2.44x10^{-3}$	Robbins	Formation	4.19, 4.20d
SMCCC	60	$0.23x10^5$	1.0 - 5.0	35	3.44	0.05	0.07	$2.85x10^{-3}$	Robbins	Not used	4.19, 4.20e
Isidis	667	$3.33x10^5$	1.0 - 6.0	643	3.01	0.07	0.09	$1.80x10^{-3}$	Robbins	Resurfacing	4.19, 4.20f

Table 4.5

Summary of Crater count data and model ages for counts collected from CTX data.

Table 4.6

Summary of Crater count data and model ages for counts derived from the Robbins crater count.

4.5 Discussion

In this section the distribution of volcanic products and features on Syrtis Major Planum are discussed. Across the planum it appears that there are two areas in which volcanic vents are found. Firstly, there are volcanic events with spatially widely distributed patterns. These were lower volume eruptions from local vents distributed across the planum. This primarily includes the Early Hesperian volcanic plains unit (eHvp), the Early Hesperian volcanic plains unit Ridges (eHvr), and the Thermally distinct lineation and veneer groups (*Adr, AHdp*). Secondly, there are volcanic events that have their source region clustered towards the centre of the planum, near or in the central caldera complex (SMCCC), and in and around the north east fissure zone. This predominantly includes the Giant and Late Hesperian volcanic flow units (*Hvp,* lHvf); although there are elements of eHvp materials in these areas as well, by nature of their widespread distribution. In the following sections, the dominant styles of emplacement for each of the flow group are discussed (Section 4.3) and interpretations are made for volcanic features in these contexts (Section 4.2).

All these elements are put together in Figure 4.21 which shows the distribution of different outcrops during the major planum building phase of volcanism on Syrtis Major Planum (Phase 1, Map Sheet 1).

A

eHvp

Central zone

Plains

~3.54
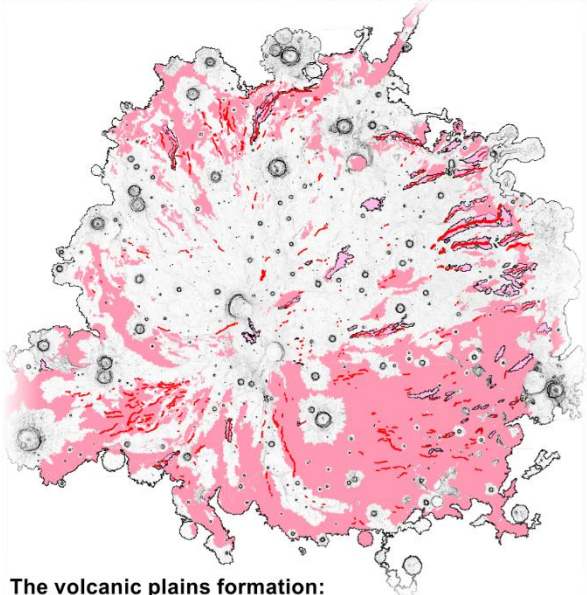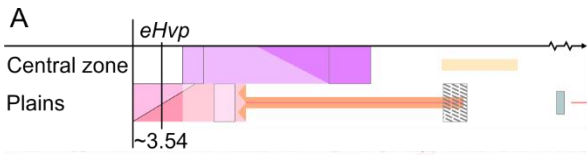
The volcanic plains formation:
- Widespread emplacement of eHvp from eHvr.
- Linear ridge structures across the Planum radial to the SMCCC.
- Minor channels are common.
- Mega levee structures formed into the Isidis rim.
- Activity at the SCFZ

B

Hvp eHvp (continued)

Central zone

Plains

~3.51
~3.48
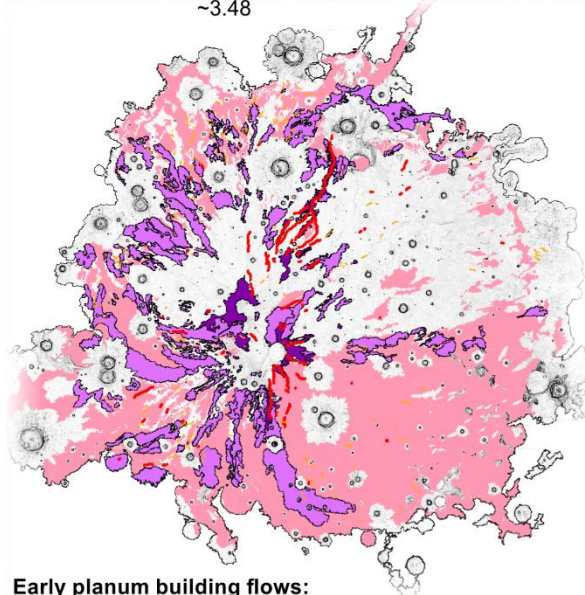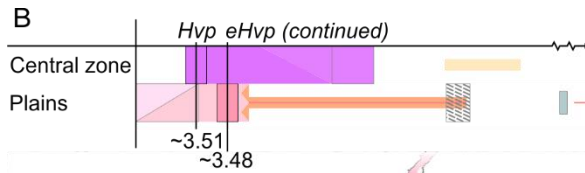
Early planum building flows:
- Emplacement of giant inflated sheet flows (The early phase of Hvp)
- Latter stages of eHvp overlie early Hvp
- Latter stages of Hvp
- Development of the NEFZ

C

lHvf

Central zone

Plains

~3.36
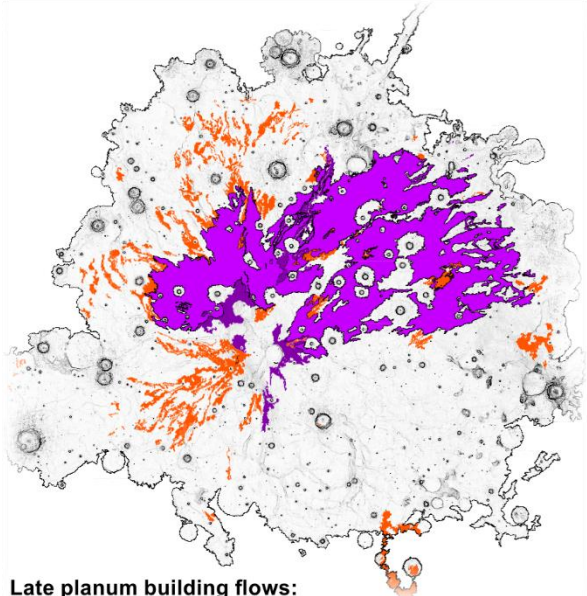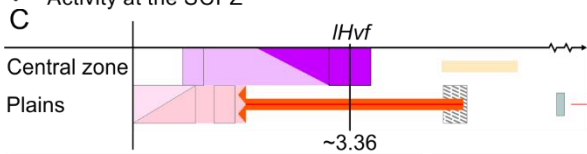
Late planum building flows:
- Effusion dominantly from the central region
- Predominant emplacement of shorter narrower lava flows with medial channels (lHvf)
- Low volume eruptions from linear fissures in the volcanic plains (Avr, AHdp)

D

Rmf   Isidis

Central zone

Plains

?   ?

~3.01
Late stage events
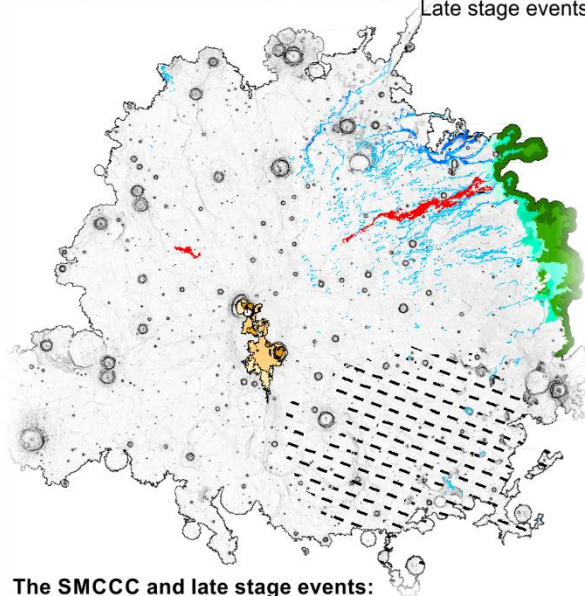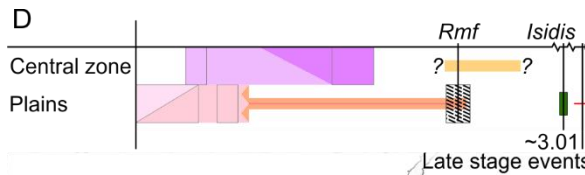
The SMCCC and late stage events:
- Volcanism in the central caldera complex (chapters 5 and 6)
- Putative widespread pyroclastic deposit
- Development of the Isidis boundary area
- Rare late stage flank volcanism
- Fluvial erosion overprints lava units

156

Figure 4.21

Extracts from Map Sheet 1 and interpretive cartoons showing the major volcanic phases of Syrtis Major Planum.

4.5.1 The Volcanic plains formation

4.5.1.1 The Early Hesperian volcanic plains unit (*eHvp*)

The early Hesperian volcanic plains unit is exposed over 48 % of Syrtis Major Planum and is also exposed around the edge of the planum. Generally, it is overlain by later volcanic groups towards the SMCCC but, where the other groups are not present this group extends right across the Planum. The Early Hesperian volcanic plains unit (eHvp) is always found below the Late Hesperian volcanic flow unit (lHvf) but it is interlayered with the Hesperian volcanic plateau unit (Hvp). This suggests that both groups formed during the same time although the eHvp covered a wider area earlier in the evolution of the planum. Because of its wide spatial distribution, and wide stratigraphic temporal range (section 4.4.2) the eHvp appears to be indicative of the most common style in which lava has been emplaced. Its location, both at the edge of the planum and at the bottom of the stratigraphy, implies that it is the oldest flow group and thus its earliest stages are demonstrative of the initial style of Syrtis Major Planum volcanism. The thickness of the planum is not known in any detail, so it is also unknown whether the eHvp represents the most voluminous main part of the planum.

The colour, surface texture and morphology of the eHvp margins implies that it is a stack of multiple lava flows (Figure 4.7). CTX data shows patterns of rubbly and hummocky terrains which appear to be degraded lobes and lava flows. However, there is only poor and indistinct evidence by which to differentiate individual flows or flow fields within the group. There are no thick lobate margins indicative of a pāhoehoe flow field that has inflated by a long sustained flow. This unit is therefore interpreted as being formed of many low volume eruptions producing relatively thin flows, building up a lava flow field over time. I attribute the 'mottled' texture in night-time thermal data to be a product of this style of emplacement.

Small low lava shields (Figure 4.4) are found commonly, although not exclusively, in this group. These structures are also found cresting the linear mounds of the Early Hesperian volcanic plains unit Ridges (eHvr) and also in the Thermally distinct lineation (Adr) group. Such structures resemble small basaltic edifices on Earth, supporting the hypothesis that the eHvp was formed by numerous widely distributed volcanic events.

4.5.1.2 The Early Hesperian volcanic plains unit with liner mounds (eHvr)

The Early Hesperian volcanic plains units ridges (eHvr) are elongate mounds with a triangular cross-section commonly hosting an axial continuous or discontinuous ridge, linear depression or series of small shields. In other respects, such as thermophysical properties, colour and texture, this group is similar to the early Hesperian volcanic plains unit (eHvp). This suggests that the eHvr is also a stack of thin pāhoehoe flows. However this group has a distinct topography and an association with continuous and discontinuous long linear ridges and long linear depressions located on the axis of the mounds. This group is always found in association the Early Hesperian volcanic plains unit (eHvp) which both gradates into it and superposes it. It is superposed by Giant and Late Hesperian volcanic flow unit (Hvp and lHvf respectively). Consequently, these elongate forms occurred early in the development of the lava plains.

The elements in this group are nearly always capped with continuous and discontinuous ridges or linear depressions (forming the continuous and discontinuous long linear ridges or long linear depressions on a mound, Map sheet 1; Figure 4.5). However, these features are also common in the eHvp (i.e. without being on a mound). There is a variety of features (pressure ridges, inverted channels, vent systems, hyaloclastic ridges, lineation of tumuli exposed dykes, raised lava levees) and processes (tectonics, lava emplacement styles, eruption styles) that could result in these landforms. The genesis of these landforms is discussed in the next section.

4.5.1.2.1 Continuous narrow linear depressions

Continuous narrow linear depressions (Figure 4.5d) have already been separated from fluvial channels (Map Sheet 1) and attributed to a volcanic origin. I interpret the majority of these features in two ways, although any individual case may have a different context dependent interpretation.

The first is the 'lava transportation' interpretation, whereby I interpret these long narrow linear depressions to be drained open lava channels. This suggests that the last eruption in this location was probably supply limited, depending on how drained the channel was [*Wilson and Head*, 1994]. In this model, magma supply stopped, and transient lava in the channel migrated through conduits to another part of the system, as opposed to the lava solidifying within the channel (in which case it is less likely that the channel would be observable).

When these features are located on mounds (Figure 4.5h), it is likely that the channel has aggraded vertically, building up a wide levee system through overflowing events and lateral flow out of the channel. The widths of the channels are consistent downslope, suggesting that while they were last active, transport was efficient and little material was left in the channel. This, and the fact that these channel are found on mounds, suggests that they are relatively long lived features. If these channels did originally form at the elevation of the bottom of the mound on which they now stand, then the eruptions feeding material into the system must have fluctuated with time, overflowing at periods of high eruption rate and transporting material to the distal reaches of the flow during periods of lower eruption rate. This is supported by the observation that channels on mounds often trend into channels with no mounds and/or discontinuous channels on and off mounds.

The second interpretation for long narrow linear depressions is that these features are short lived fissure vents that have formed where elongate conduits fed by dykes have surfaced, but where magma supply waned rapidly, draining out of the surfacing location before a ridge or other proximal deposits could form. This hypothesis is most applicable to shorter segments of narrow

linear depressions that are not found in association with other discontinuous linear depressions or ridge features. However, considering their length (many tens of km) I suggest that that this is only likely for the shorter examples not found in close linear association with other (discontinuous linear depression or ridge) landforms.

4.5.1.2.2 Discontinuous narrow linear depressions

Discontinuous narrow linear depressions (Figure 4.5e) are a series of co-aligned pits or channel-like segments. The surface between the segments appears the same as the surrounding terrain. The interpretation for narrow linear depressions is also related to lava transportation. I suggest that narrow linear depressions were initially continuous channels that have frozen over to form tubes. There has been subsequent collapse leaving 'bridges' and 'tunnels' between pits and channel sections. A slightly different interpretation would be a channel of lava in an inflated lobe which has subsequently drained, resulting in a series of skylights over a lava tube. Of these possibilities, the first is more likely, in most cases, because the well-constrained linear distribution of pits or channel segments matches that of continuous channels. Discontinuous narrow linear depressions commonly evolve from continuous channels and in some cases can evolve into continuous channels. This relationship suggests a link with the supply of magma and possibly the rate of lava flow that governs whether or not the lava channel is roofed, unroofed, or partially roofed.

There are two interpretations for discontinuous narrow linear depressions on mounds (Figure 4.5g). Again, the first is lava transportation whilst the second is eruptive. The transportation interpretation for these features draws together the interpretation of continuous open channels on mounds and the formation of a tube or roofed channel and then formation of skylights or open segments as the system matures. This interpretation fits best where these features are found immediately downslope from continuous channels or continuous channels on mounds.

The eruptive interpretation is that these are linear fissure vents above dykes. This is more plausible for instances where there is no other associated lava supply context (i.e. the ridge does

not trend out of a channel up slope). where the discontinuous channel on a mound exists in isolation, or where the morphology is particularly linear in map view and there is preservation of poorly consolidated vent-proximal deposits'.

It is difficult to differentiate between these two hypothoses. The channels do not have levees, (unless the whole mound is a levee structure, although in this case the channel floor has migrated vertically) and the pits do not have identifiable remnants of spatter ramparts [*Brown et al.*, 2015] although this would not be expected given theoretical considerations for eruptions in martian conditions [*Wilson and Head*, 1994; *Brož et al.*, 2014]. These long linear ridge features are differentiated by whether they exist on or off mounds because the feature itself would have to build or be built on the mound during their evolution. In contrast, features with no upstanding relief have either not aggraded vertically or the mound has been buried by subsequent volcanic activity. This implies that features not associated with channels are either older than examples on mounds (having had their flanks buried) or have had less material flowing through them to build topography on either side during overflows.

4.5.1.2.3 Continuous and discontinuous linear ridges

Like long linear depressions continuous and discontinuous linear ridges can be either on or off mounds (Figure 4.5f and g). These occur most commonly in the Early Hesperian volcanic plains unit (eHvp). They often occur along the axes of ridges in the eHvp or on linear mounds where there is no continuous or discontinuous channel. Also, these ridges are commonly seen along the axis of many Amazonian dark ridge unit (Adr) and rarely in the Amazonian/Hesperian dark plains unit (AHdp).

There are several possible interpretations for these ridges. They may have been formed from an erosional inversion process in which the channels originally formed in negative relief, but where weaker materials either sides of the channel were subsequently removed, leaving the channel fill and/or channel floor in positive relief. This is a common process for fluvial systems and is observed in the martian stratigraphy [e.g., *Williams et al.*, 2009]. However, the distribution of

ridges is spatially intermixed with channels that have not been eroded. Thus, such differential erosion over short distances with no other supporting evidence of localised erosive processes makes this an unlikely origin for the continuous and discontinuous ridges.

A ridge of volcanic material can result from the interaction of an eruption with environmental conditions. For example, fissure eruptions under water, ice or snow can form a hyaloclastite ridge. These features have previously been identified on Mars [*Squyres et al.*, 1987; *Chapman et al.*, 2000; *Scanlon et al.*, 2015]. However, the ridges are significantly smaller than more modern examples at Olympus Mons [*Scanlon et al.*, 2015] and no other supporting evidence has not been found in the rest of the Planum for this hypothesis. The only exception to this is a group of ridges on the boundary with Isidis Planitia. Here, the ridges are associated with later volcanic surfaces that on-lap the Isidis boundary materials. These in turn mantle Hesperian volcanic plateau unit (Hvp), Late Hesperian volcanic flow unit (lHvf) and eHvp (Map Sheet 1) materials. Here, the ridges are found in conjunction with flat topped mounds with central craters (Figure 4.3e) – possibly another indication of sub-glacial eruption [*Chapman et al.*, 2000]. Further investigation is, unfortunately, beyond the scope of this thesis (section 8.3).

The last possible interpretation again depends on the setting and detailed morphology of the individual ridge. I suggest that most of the continuous and discontinuous ridges formed from fissure eruptions where a ridge of proximal lavas or agglutinated spatter is built [*Brown et al.*, 2014]. Discontinuous ridges would be formed when either the eruption localised in its waning stages, or where a more continuous ridge was eroded. Ridges generally follow the same pattern as the distribution of channels and may well reflect the supply of lava through the planum. Thus the fissure eruption hypothesis is parsimonious for both continuous and discontinuous ridges located on both mounds (eHvr) in the eHvp or along the axes of thermally distinct lineation (Adr).

4.5.1.2.4 Special cases of channels and ridges associated with the volcanic plains

There are two cases where mounds in the early Hesperian volcanic plains unit Ridges (eHvr) go

into the Isidis basin and are significantly larger than other examples. There are several important

observations about these mega channels on mounds that must be explained by any interpretation

of their formation. Firstly, the size and shape of the mound, which is symmetrical trapezium,

three times wider and four times higher than 'typical' examples with the same cross section

(Figure 4.9). Secondly the size and depth of the channel, which at 1600 m wide and at least 50 m

deep is the largest evacuated channel on Syrtis Major (twice the width of Arnus Vallis) [*Rampey*

and Harvey, 2008]. Thirdly, elevation of the channel floor which is significantly higher (~200 m -

300 m) than the elevation of the terrain either side of the mound on which the channel is

perched. And finally the down slope development of the channel into a rectangular section ridge

perched on the same mound. The flanks of the mounds, to all along either side of the channel,

show evidence that lava flowed down them mostly likely out of the sides of the channel (Figure

4.9).

From these overspills and the straight profile of the mound flanks I propose that a significant

proportion (all that we can observe today) of the mound grew as a 'mega levee'. This evidence,

combined with the minimum channel depth being ~350 m above the minimum elevation of the

levees (Figures 4.9 and 4.5), suggests that the mound grew episodically and that there was a

hiatus in which the channel was evacuated and cooled before a subsequent phase continued to

build up the channel floor and levees. It is unlikely that this elongate channel/mound structure

could have formed in one event, as it could not then have built up vertically to such an extent.

Vertical aggradation is likely to have occurred in combination with progradation of the terminal

mega levee apron towards the Isidis basin. In the furthest reaches of these mega mounds the

channel at the apex becomes a more 'normal' major then minor linear depression in size as the

relief of the mega mound decreases. Further development of the system is not observed because

of the erosional scarp at the contact with the Isidis basin, although, it appears that these channels have transported lava into the Isidis basin at some stage [*Ivanov and Head*, 2003; *Ivanov et al.*, 2012]. The net vertical aggradation in the channel floor and progradation of the mega levee apron suggests that the lava behaved in a more 'normal' fashion, rather than the exotic high temperatures and potentially thermally eroding properties predicted behaviours for another large lava channel on Syrtis Major Planum [*Rampey and Harvey*, 2008, 2012]. The net aggradation of the channel means that this part of this channel system was not formed primarily by thermal erosion due to lava.

Further downslope, the channels invert to become flat-topped plateauxs with similar dimensions to the negative relief of the channels upslope. Like ridges associated with channels elsewhere on Syrtis Major there are number of possible explanations. It is unlikely that these features result from erosional processes because there is no evidence of suitably major erosional processes at this elevation in the vicinity. It is possible is that there was a change in the environment (e.g. presence of ice) in which the lava solidified above the elevation of the mega levees, and developed through a 'tuya like' process, whereby lava has built up because of excess cooling at the margins of the flow. Whilst there is evidence for non-volcanic mantling deposits and possible water/snow or ice along the boundary of the Isidis basin floor [*Ivanov and Head*, 2003; *Ivanov et al.*, 2012; *Skok and Mustard*, 2014], it is not currently clear how this correlates with other observations in the wider Syrtis Major region.

A more parsimonious solution is that this rectangular section ridge portion of the channel system is an inflation feature. In this case, these downstream portions of the channel system on shallower slopes solidified and subsequently inflated as a result of continued lava supply from driven by the steeper slopes of the Isidis basin margin. In places along the margin of this 'inverted' channel small lobate breakouts, can be found supporting this inflation hypothesis (Figure 4.9a iv).

4.5.2 Planum building flow formation

4.5.2.1 The Hesperian volcanic plateau unit (Hvp)

The Hesperian volcanic plateau unit (Hvp) represents lava flow fields 10's of km wide and 100's of km long, accounting for 16 % of the present day surface area of Syrtis Major Planum. They are therefore an important part of the history of Syrtis Major Planum (Figure 2.23) and occur in a variety of stratigraphic associations.

The stratigraphically oldest examples of flows in this group are towards the outer parts of the planum (Map sheet 1; Figure 4.1). These older members of the flow group are interlayered with the Early Hesperian volcanic plains unit (eHvp) but not the Early Hesperian volcanic plains unit linear mounds (eHvr). The stratigraphically youngest elements of this group can be seen stretching from the central caldera complex ~350 km to the boundary with the cratered highland terrain (figure 4.7) superposing the eHvp. In the north, toward the SMCCC, and to the east the Hvp is always overlain by the Late Hesperian volcanic flow unit (lHvf).

From this distribution I interpret that the Hvp was active after the eHvr but before the widespread activity of the Early Hesperian volcanic plains unit had ended (Figure 4.21). It also appears that the Hvp emplacement continued after the majority of the eHvp had been emplaced and that the source of the Hvp flows were within the central caldera complex region.

Within the mapped elements there is some evidence for abutting lobate margins, indicating that the Hvp formed by several related flow units which together form a compound flow. Younger examples, dominantly overlying the eHvp, have lobate margins which contain sets of topographic steps reaching a maximum height of ~60 m.
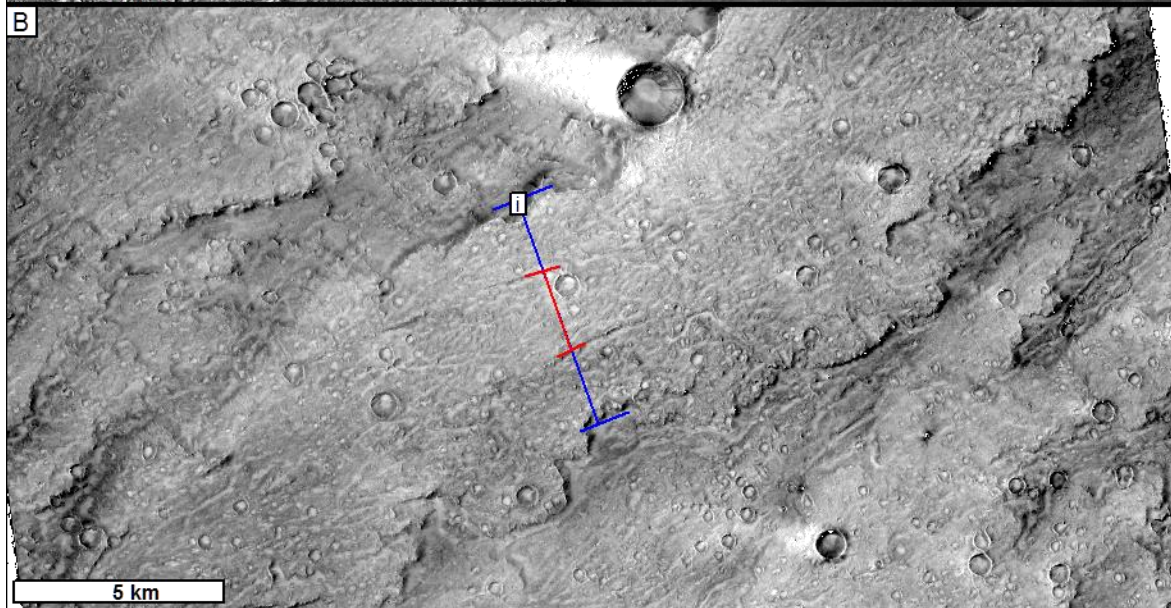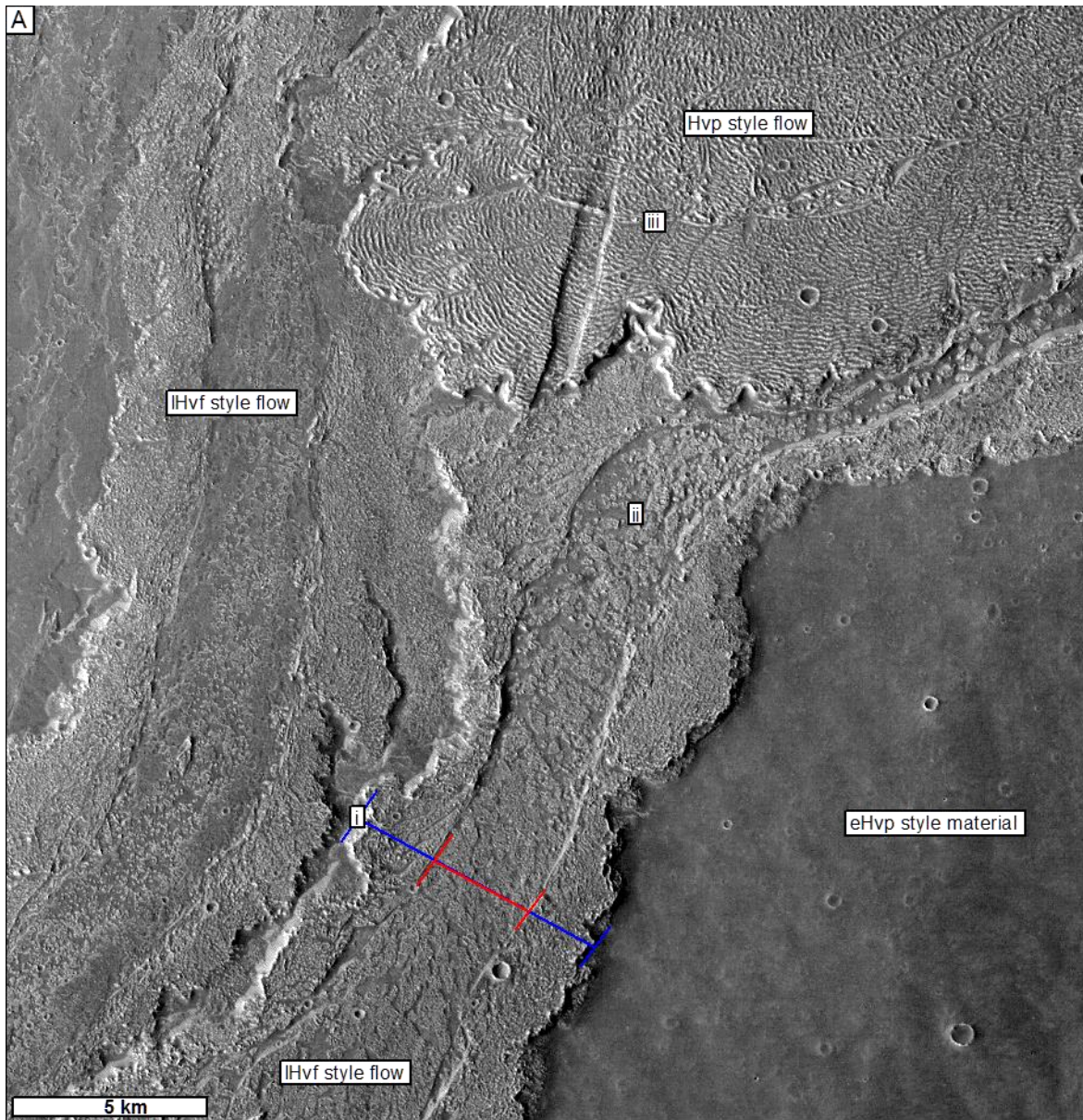
Figure 4.22

(a) An area from the eastern flank of the Arsia Mons rift apron (22°55'S 117°34'W; HRSC H4146_0000). Showing flows with similar broad scale morphology to the Late Hesperian volcanic flow unit (lHvf) Hesperian volcanic plateau unit (Hvp) and Early Hesperian volcanic plains unit (eHvp). These examples have not experienced the same duration of degradation and thickness of mantling compared to lHvf flow seen on Syrtis Major Planum shown in (b) (CTX; B19_016852_1959_XN_15N286W). This allows an analogue interrogation of the surface detail. (i) Channel and levee structures of the same scale (ii) slabby surface indicating laminar flow in the channel and (iii) festoon ridges perpendicular to the direction of flow emplacement.

The surface of the Hvp at scale of CTX data shows the surface is mantled with a layer of material, presumably wind derived deposits, which in-fill some craters and masking smaller topographic features. However, where surface texture can be seen, hummocky festoon ridges are visible [*Theilig and Greeley*, 1986; *Walker*, 1993] exhibiting two sets of orientations (Figure 4.11 and 4.25). Festoon ridges develop as a response to compression of the crust in the direction of flow. Transverse ridges result from flow along the flow axis whilst longitudinal ridges result from spreading flow pressure outward from the axis of the flow [*Theilig and Greeley*, 1986; *Cashman et al.*, 1999; *Keszthelyi et al.*, 2004; *Guilbaud et al.*, 2005].

The pattern of ridges seen in Figure 4.22a and 4.25a show that the surface of the flow has continued to develop with material moving through the middle of the flow horizontally after its initial emplacement. The ridged shear zones show that the transverse ridged central section moved down-flow relative to the longitudinally ridged lateral zones. These patterns of festoon ridges is more clearly seen in older stratigraphic members compared to the youngest upstanding member where there is a thicker layer of masking material probably associated with the Ridged mantling field (Rmf; Section 4.3.5.2).

Terrestrial festoon ridges are not supported in in basalt and require a more viscous, more evolved composition to be supported [*Walker*, 1993]. Whilst this may carry implications for the composition of the flow it may also be possible for a lower viscosity flow, such as a basalt, to support ridges because their load will be lower due to the lower gravity of Mars compared to Earth.

This surface texture, the height and morphology of the Hvp flow margins and the extreme length of flows over the low slopes of Syrtis Major Planum all suggest that the Hesperian volcanic plateau unit (Hvp) has been emplaced as compound pāhoehoe flows. This is akin to large lava flows in terrestrial large igneous provinces [*Hon et al.*, 1994; *Self et al.*, 1997, 1998; *Keszthelyi and Self*, 1998; *Thordarson and Self*, 1998; *Anderson et al.*, 1999; *Vye-Brown et al.*, 2013].

4.5.2.2 Characteristic thermal signatures

Surfaces ascribed to the Hesperian volcanic plateau unit (Hvp), and to a lesser extent the Late Hesperian volcanic flow unit (lHvf), are identified relative to the Early Hesperian volcanic plains unit (eHvp) by their characteristically consistent dark appearance in the night-time THEMIS data. Since mapping was carried out, new quantitative thermal inertia mosaics have become available [*Christensen et al.*, 2013]. Although these mosaics do not take into account all factors adding noise to the data (a necessity of producing the global mosaic), I have used the data to compare the distribution of bulk thermal inertia values within the mapped units (Figures 4.11 and 4.23; Table 4.1).

These data (Figure 4.23a) show that the Hvp and the lHvf have lower mean thermal inertia than that of the eHvp. I have interpreted both the eHvp and Hvp as pāhoehoe emplacement with the eHvp being made of from numerous small thin pāhoehoe flows from distributed sources and the Hvp representing a long lasting, thick inflated flow field. The difference in their thermal signature between the eHvp and the Hvp is attributed to different surface textures (on the scale of tens of centimetres to tens of metres) and different distribution of surface textures (on the scale of 100's of meters; Figure 22b, c). The eHvp is interpreted to be a stack of multiple thin lava flows (hummocky, irregular lobes on the scale of 10 – 100s of meters). As a result the pāhoehoe lobes will have more 'bed rock' patches interspersed with patches of sand/gravel than the Hvp. The Hesperian volcanic plateau unit is interpreted as thick inflated pāhoehoe flow fields with planar tops (on the scale of 10-100's of meters), steep sided lobes. This results in a slabby or rubbly pāhoehoe surface [*Soule et al.*, 2004; *Guilbaud et al.*, 2005] with a more uniform

distribution of sand/gravel trapped in the slabby surface, reducing the thermal inertia measured [*Zimbelman*, 1986; *Presley and Christensen*, 1997; *Fergason et al.*, 2006]. This also explains the similar thermal signature of the Hvp and the lHvf. However, in the case of the lHvf this results from the 'a'ā flow emplacement which is discussed in the next section. I also suggest that the skewed distribution of themral inertias observed for the lHvf results from the effect of slopes and scarps at the edges of the 'a'ā flows.

A

B — Plates ~30 cm high

C — Rocks ~20 cm

D — View ~5 m
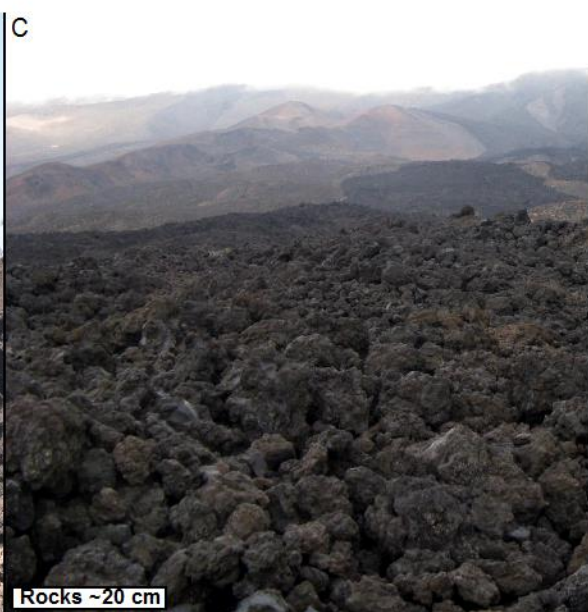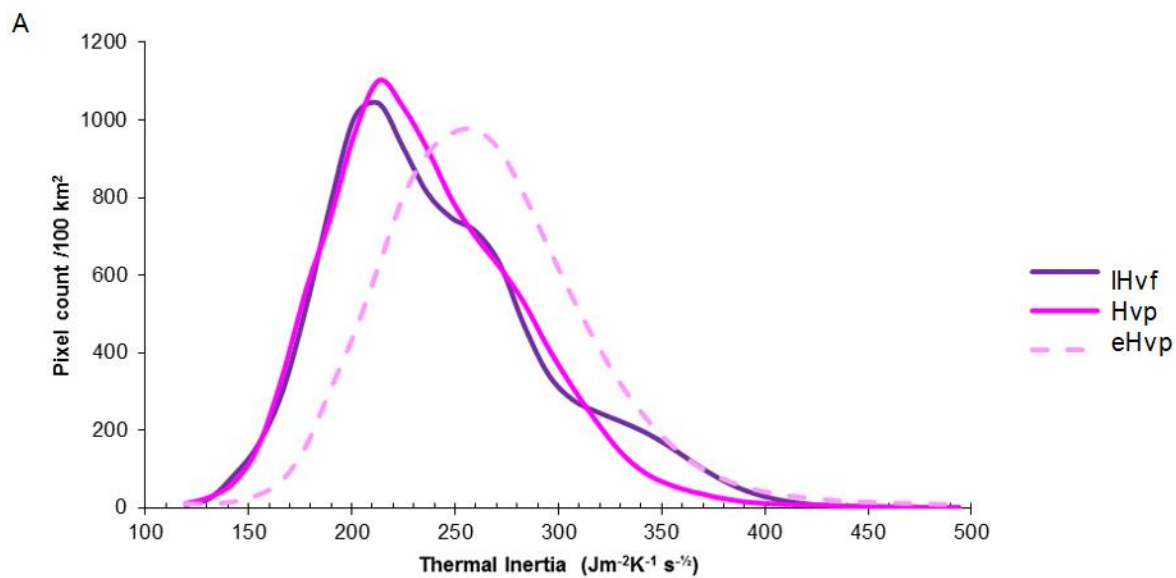
Figure 4.23

The thermal signature of the Hesperian volcanic plateau unit (Hvp) is explored using quantitate data and field relations. (a). Frequency distribution of thermal inertia pixel values for the early Hesperian volcanic plains unit (eHvp; pink, dashed), Hesperian volcanic plateau unit (Hvp; magenta) and Late Hesperian volcanic flow unit (lHvf; purple) per 100 km² (see Chapter 3.1.1) drawn from Quantitative THEMIS Thermal inertia mosaic (<ins>http://astrogeology.usgs.gov/search/details/Mars/Odyssey/THEMIS-Global-Thermal-Inertia-</ins> <ins>Mosaic/Quantitative-32-Bit/THEMIS_TI_Mosaic_Quant_00N060E_100mpp/cub</ins>*; Christensen et al., 2013]. (b). Shows a slabby/platy pāhoehoe surface from a recent (<1000 y (C.Vye-Brown pers. com.) flow in the Afar rift which is akin to the interpreted surface of the Hvp shortly after emplacement. (c). Shows the surface of an a'ā channel on the western flank of Mt Etna which may be similar to parts of the lHvf. In contrast, flow surface (d) again from the Afar region (i) shows broad areas of bedrock exposed in a pāhoehoe and sediment confined to topographic lows (ii). (Image credits: P. Fawdon 2011, 2012 and 2011 respectively).*

4.5.2.3 The Narrow flows (lHvf)

The Late Hesperian volcanic flow unit (lHvf) is differentiated from other volcanic surfaces in Syrtis

Major by the morphology of the lava flows. These lava flows are 'narrow', generally less than 10

km wide. Flows in this group nearly always have a medial channel (Figure 4.5m) at their axis and

build 10 m − 20 m of topography. These channels form a channel and levee structure, where

between 2/3 − 1/3 of the width of the flow forms the channel. These are a commonly seen

feature of terrestrial and martian lava flows [*Lopes and Kilburn*, 1990; *Kilburn and Lopes*, 1991;

Walker, 1993; *Kerr et al.*, 2006; *Hiesinger et al.*, 2007; *Baloga and Glaze*, 2008].

In terrestrial examples, channels such as this are often found in the medial reaches of flows

characterised by a platy pāhoehoe surface [*Self et al.*, 1998; *Cashman et al.*, 1999; *Soule et al.*,

2004; *Guilbaud et al.*, 2005] and as channels in 'a'ā flows, where there is sufficient shear stress to

autobrecciate the crust [*Kilburn and Lopes*, 1991; *Cashman et al.*, 1999; *Soule and Cashman*,

2005]. Flows with this cross section (Figure 4.5m) are very common on Mars [*Garry et al.*, 2007;

Hiesinger et al., 2007; *Baloga and Glaze*, 2008]. In the Amazonian Tharsis volcanic province (~2 Ga

younger than Syrtis Major Planum), the detailed surface of the channel and levee structure can be

seen (Figure 4.22). Here the levees comprise the outer ~¼ of the flow on each side and consist of

longitudinal festoon ridges [*Theilig and Greeley*, 1986; *Zimbelman*, 1998]. The central section

comprising ~½ the flow width is a few (1-5) meters lower than the levees (Figure 4.22b) and the

solidified surface of the channel shows a number of platy 'rafts' of material 100 m to 400 m wide, which appear to have been transported along the flow surface prior to flow solidification.

This level of detail is rarely visible on lHvf flows at Syrtis Major Planum. This is both because of sandy material infilling the surface texture and perhaps also due to erosion or modification, having had between two and three times longer to degrade [*Zimbelman*, 1986] and accumulate impact ejecta compared to the Tharsis examples. Despite this degradation and mantling material obscuring the surface features, flows in the lHvf are interpreted to have formed in a similar fashion to the example with a comparable cross-section from Arsia Mons (Figure 4.22) and the many other Tharsis examples of long narrow linear channelized lava flows on Mars [*Theilig and Greeley*, 1986; *Glaze and Baloga*, 2006; *Garry et al.*, 2007; *Hiesinger et al.*, 2007; *Baloga and Glaze*, 2008]. The terrestrial analogy to this would be 'a'ā flow emplacement.

4.5.2.4 Slope controls on the Late Hesperian volcanic flow unit (lHvf):

The flow morphology of the Late Hesperian volcanic flow unit (lHvf) is suggestive of higher shear stress than that of the Hesperian volcanic plateau unit (Hvp). To investigate of this, I compared the distribution of slopes between the two groups (Figure 4.24). This was calculated from slope over a baseline of 31.4 km because this is approximately the mean length of medial channels; as such this is respresentative of the length over which these channels generally formed. Because I am interested in comparing the lHvf and Hvp to evaluate the importance of slope the flows on the slope leading into the Isidis basin (where the underlying topography is known to be steep) are not included.

The results appear to show that even where the lHvf is not influenced by the topography of the Isidis basin the slopes for terrains occupied by it are ~0.5° steeper than the Hvp or eHvp (~1.5° compared to ~1°). This supports observations that the ´A´ā morphology of lava flows is related to exceeding a threshold in viscosity-strain space. For examples on Hawaii ´A´ā flows develop when effusion rate or topographic slopes are greater [*Lopes and Kilburn*, 1990; *Rowland and Walker*, 1990; *Brown et al.*, 2011], increasing the strain rate.
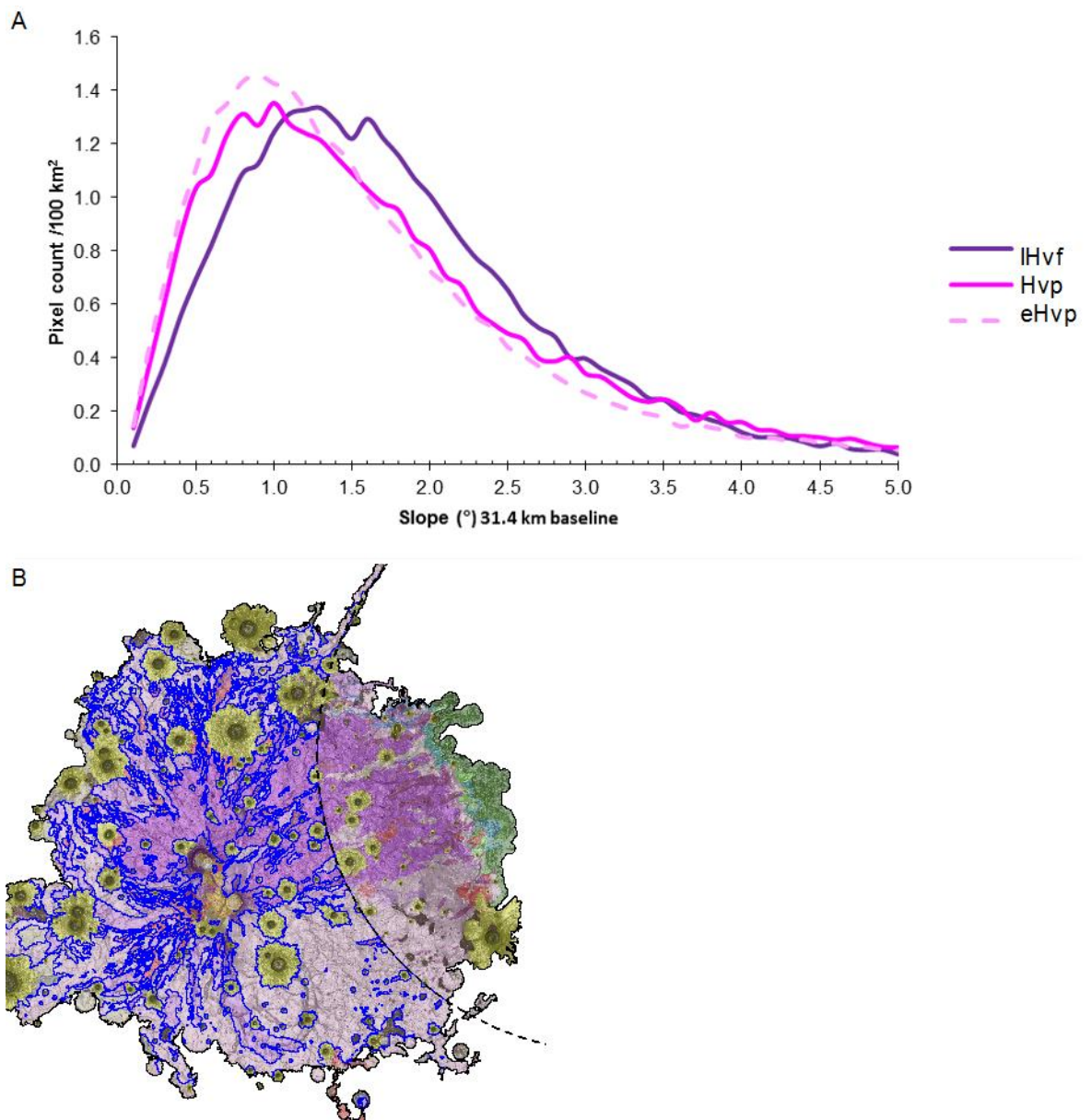
Figure 4.24

(a) The frequency distribution of slopes over a baseline of 34.1 km for the early Hesperian volcanic plains unit (eHvp, pink, dashed), Hesperian volcanic plateau unit (Hvp, magenta) and Late Hesperian volcanic flow unit (lHvf, purple) per 100 km^2 Outside the area influenced by the slope of the Isidis basin. Drawn gridded MOLA pixels aggregated to 31.4 km was chosen as the baseline length closest to the mean length of medial channels, common in the lHvf unit without introducing the topographic signature of crater rims into the area of the lHvf. (b). The area (blue outline) in which data was captured from the slope raster input and data exclusion area around the rim of the Isidis basin.

However, if the emplacement mechanism is driven by slope rather than a change with time than the following observations would be expected. (i) Narrow flows would continue to propagate in the 'A'ā fashion once lower slopes are reached as observed in terrestrial examples, although on

173

a smaller scale [*Kilburn and Lopes*, 1991; *Cashman et al.*, 1999; *Kerr et al.*, 2006]. (ii) 'Short' examples of the Hvp would be expected on areas of less steep slopes at the same age as the lHvf. (iii) If the emplacement of the flow was dominantly controlled by slope then it would not be expected that there would be numerous examples of the Hvp on slopes next to and superposed by flows emplaced in the lHvf style on the same slope close to the SMCCC. (iv) No examples of the Hvp would be expected at the bottom of the slope into the Isidis basin.

Consequently we conclude that, with the exception of specific cases (e.g. down the flank of a mega mound) slope is an important but not the single dominant control of lava flow emplacement and the change in dominant flow morphology from the tube fed inflated flows (akin to the Hvp) to progressively shorter channel fed flows (akin to the lHvf); this also mirrors trends seen on Tharsis Montes [*Bleacher et al.*, 2007a, 2007b].

4.5.2.5 Source regions of flows in the Giant and Late Hesperian volcanic flow units (Hff)

Lava flows in the Narrow and Hesperian volcanic plateau unit (lHvf and Hvp, respectively) originate from areas classified as the Hesperian fissure field unit (Hff). These are areas that resemble, and are spatially associated with, the lHvf and/or Hvp, but where there is no clear evidence for medial or distant lava flow boundaries.

There are three instances across the whole of Syrtis Major Planum which have been classified as Hff. Firstly, the Syrtis Major Central Caldera Complex (SMCCC) where there are five vents and two calderas. The SMCCC makes up 1.6 % of Syrtis Major Planum's area. Here, the remaining vents have been affected by, and thus predate, the tectonic subsidence of the SMCCC. Secondly fissure pits vents are found in the North-east fissure zone (Figure 4.35, Map Sheet 1) and a cluster of fissures at the head of major and long narrow linear depressions including Arnus Vallis [*Rampey and Harvey*, 2008]. Although, it is not possible to tell whether these predate or postdate similar vents in the SMCCC there are three instances in which wrinkle ridges cross Arnus Vallis. Whilst the channel apparently passing through the ridge has been taken as evidence that the channel

postdates the ridges [*Rampey and Harvey*, 2008], this contradicts the observation that the wrinkle ridges cross cut all the lava flows to which the channel feeds. Under close inspection it is not clear how the relationship between the channel and ridges has developed. For example, the floor of the channel may be deflected by either tectonic activity or prorogation. The upper reaches of Arnus Vallis are slightly below the surrounding flows but the lower reaches are on a raised platform. I interpret this as it predating the surrounding narrow flows which have flowed parallel to it. These built topography on either side of the low rise that it is now only visible in the lower reaches. The apparent conflict in timing between channel ridge and lava flow formation may be resolved if the wrinkle ridge formation is considered a progressive process, perhaps not interacting with the channel topography in the same way as the surrounding flatter lava flows and maybe later erosion in the channel masking the tectonic signature. Thirdly there are six additional examples distributed across the remaining >98 % of Syrtis Major Planum.

The distribution of ridges suggest that, during the later stages of planum development eruptions from these vents were the dominant origin for the lava flows of the lHvf. The distribution of vent structures also suggests that, in the later stages of planum construction, eruptions were concentrated in the central area of the planum, although the few vents distributed across the planum indicate that initial, widespread emplacement from vents may have been the norm.

Whilst there is a clear spatial connection between these major vents and the lHvf, the relationship between these vents and the Hvp is not as clear. There are no instances of lava transport structures linking the vent areas to the Hvp. However, major channels are found in the proximal reaches of the Hvp, and elsewhere on the planum large linear pits are seen to supply major and minor linear depressions (Figure 4.13)

There are two possible explanations for this. Firstly, the vent structures for the Hesperian volcanic plateau unit of this type are obscured. To the east of the SMCCC and to the south of Meroe Patera they could be buried by later Early Hesperian volcanic plains unit (eHvp) material,

whereas to the north of the central caldera complex, the proximal reaches of the Hvp are always buried by lHvf or have lHvf flows in their proximal reaches. Underlying slope, and a reduction in flow length with time if lava supply waned, could have obscured any connection to the vent concentrations in the central area of the planum. This interpretation is supported by major channels seen in the Hesperian volcanic plateau unit south of SMCCC and their similarity to Arnus Vallis. At the upslope caldera-wards end of stratigraphically young Hvp elements that flow directly south from SMCCC there is a major channel trending down the axis of the flow (Figure 4.5), implying that this feature transported material into the body of the flow.

Arnus Vallis, the largest major volcanic channel or rill [*Hulme*, 1982; *Rampey and Harvey*, 2008] on Syrtis Major Planum (excluding Mega channels; Section 4.2.2.1 and Figure 4.5) must have supplied significant volumes of lava to the North-eastern Syrtis Major area. Arnus Vallis originates in the north east vent cluster (Figure 4.13) from the largest of the large linear pits (Figure 4.4a). Down-slope, the channel narrows and shallows [*Rampey and Harvey*, 2008] and also changes from being in a very shallow local shallow topographic low, with lHvf flows on either side, to being on the apex of a low topographic rise, without the flanking late Hesperian volcanic flow unit surface.

The termination of Arnus Vallis is completely obscured by two large impact craters, 25 km and 41 km in diameter and with associated ejecta blanket ~100 km in diameter. However, beyond these is a large area of the Hesperian volcanic plateau unit material that contains several flow elements. These flows form the North-eastern boundary of Syrtis Major Planum and have been emplaced directly onto the cratered highland terrain [*Ehlmann and Mustard*, 2012]. This area of the Hvp is otherwise unconnected to any vent or any element of the lHvf, unlike all other examples of the Hvp. I conclude that the Arnus Vallis major channel supplied this area of the Hesperian volcanic plateau unit with the transition region unfortunately being obscured by the later impact craters.

Although it has been argued that Arnus Vallis crosscuts the ejecta from the earlier and smaller (at ~25 km) of these craters [*Rampey and Harvey*, 2008], no evidence is seen in THEMIS or CTX to support this as would be expected for a channel of this magnitude interpreted to host lavas capable of thermal erosion [*Rampey and Harvey*, 2008]. I suggest that the apparent observation that the channel cuts through the impact ejecta is a misinterpretation and, instead, the thin ejecta materials simply mantle the channels topography, the channel walls being sufficiently deep and steep to retain their topographic signature through the ejecta layer. I also note that, at CTX scale, this section of the channel appears shallower and less well-defined morphologically, consistent with ejecta overlying the channel. Therefore, Arnus Vallis was active before both of these impact events and it is therefore completely plausible that is connects the Hvp flows of north east Syrtis Major with source regions in the cluster of large linear pits in the north east fissure zone (NEFZ; Map Sheet 1). To summarise I think that the Hvp was sourced from large linear pits which in most cases have buried themselves, however to the north the lava has been transported further (on the steeper slope) and Arnus Vallis is the remaining example of the channel which fed the distal examples of the Hvp where they reach the Northeast Syrtis region.

An alternative explanation for the source of the Hvp flows might be that they were supplied from vents of a totally different style to the large linear pits. The inflationary development of the Hvp flows may have been fed by vents that are no longer clearly visible as source regions. It is possible that these vents could have formed as long fissures, such as those in the eHvp and the Amazonian dark ridge unit (Adr; Section 4.3.6). In this scenario the vents might be identifiable, or if the vents that buried themselves during the inflation process, they might not be visible at all.

While this second source hypothesis cannot be ruled out, there is more evidence from the association of large linear pits to channels and to the Hvp to support the first explanation. The major vent styles for both lHvf and Hvp styles are the large linear pits, the youngest of which can now be seen around the central caldera complex and in the NEFZ.

4.5.3 Later stage events (Adr, AHdp, Rmf)

In addition to the major planum-forming volcanic groups I have identified several surface types.

4.5.3.1 Amazonian/Hesperian dark plains unit and lineaments

The 'thermally distinct' veneer and lineaments (AHdp and Adr respectivly) are mapped primarily from relatively bright pixels in qualitative THEMIS Night-time data, where they correlate to 'dark' Themis daytime pixels and where there is bright rubbly material or ridges in CTX data (Figures 4.14 and 4.15). These bright angular surfaces appear to undulate irregularly on scales of 50 – 100 m, and to have irregular boundaries that follow minor variations in underlying topography. This material buries this topography within a few 10's of meters of the boundary of the area (Figure 4.25). There is also less smooth material in the areas of the thermally distinct units. When viewed at a larger scale this smooth material appears dark blue/black in colour in HRSC colour images and is almost always interpreted as dark basaltic sand [*Silvestro et al.*, 2010].

Because I identified these features from the qualitative THEMIS data I have also looked at the quantitative thermal inertia distribution for this group (Figure 4.25). These distributions show that whilst the peak of Adr is higher than Early Hesperian volcanic plains unit (eHvp) and AHdp, both Adr and AHdp are within the range of values seen across the planum for the eHvp (Figure 4.25).

This result correlates to the CTX surface texture of the AHdp and Adr groups. In these units there is a lack of sandy material and thus more bedrock (which explains the brightness) whereas for the Early Hesperian volcanic plains unit (eHvp) there is variation on a larger scale in sand coverage; as such the distribution encompases the distributions of AHdp and Adr groups but has a lower peak than those groups. The Adr are the brightest linear regions of the Themis night pixels these areas correlate with textures seen in CTX data and coincide with continuous and discontinuous ridges. The lineaments are generally orientated approximately radial to the central caldera complex and always trend in accordance with the local trend for linear volcanic features (Figure 4.2). I interpret the AHdp and Adr to be thin lava flow units emplaced in small volumes from long fissure ridge segments widely distributed across Syrtis Major Planum

The AHdp and Adr are rarely seen in the area of the lHvf group, commonly overly the Hvp and always super pose the eHvp. However, these groups occasionally are overlain by elements of the Hvp and lHvf. As such, the these groups appear to have been emplaced relatively late in the development of Syrtis Major Planum and occurred less often in the time of the Hvp and lHvf. From this I suggest that the AHdp and Adr groups are a continuation of the eHvp volcanism but represent smaller eruptions more spread out in space and time as the frequency and volume of eruptions in the eHvp/eHvr style decreased with time. These areas are distinct from the early Hesperian volcanic plains unit because their boundaries have not been degraded as much as those within the eHvp, whether or not these dispersed small eruptions with bright (in CTX data) rubbly lava from long narrow ridges reflect a change in composition is unresolved in this study.
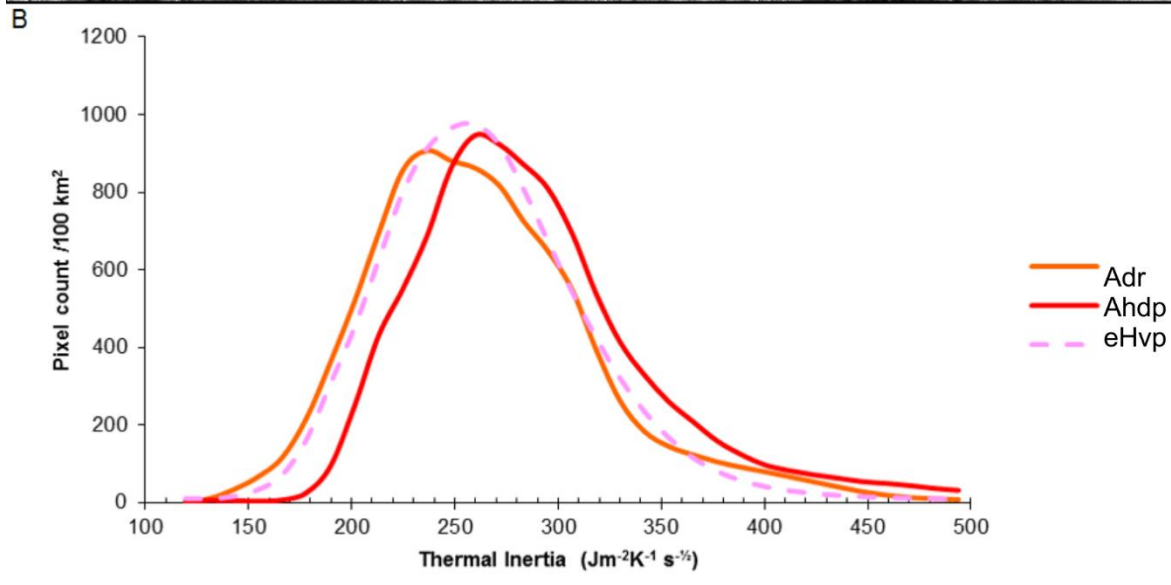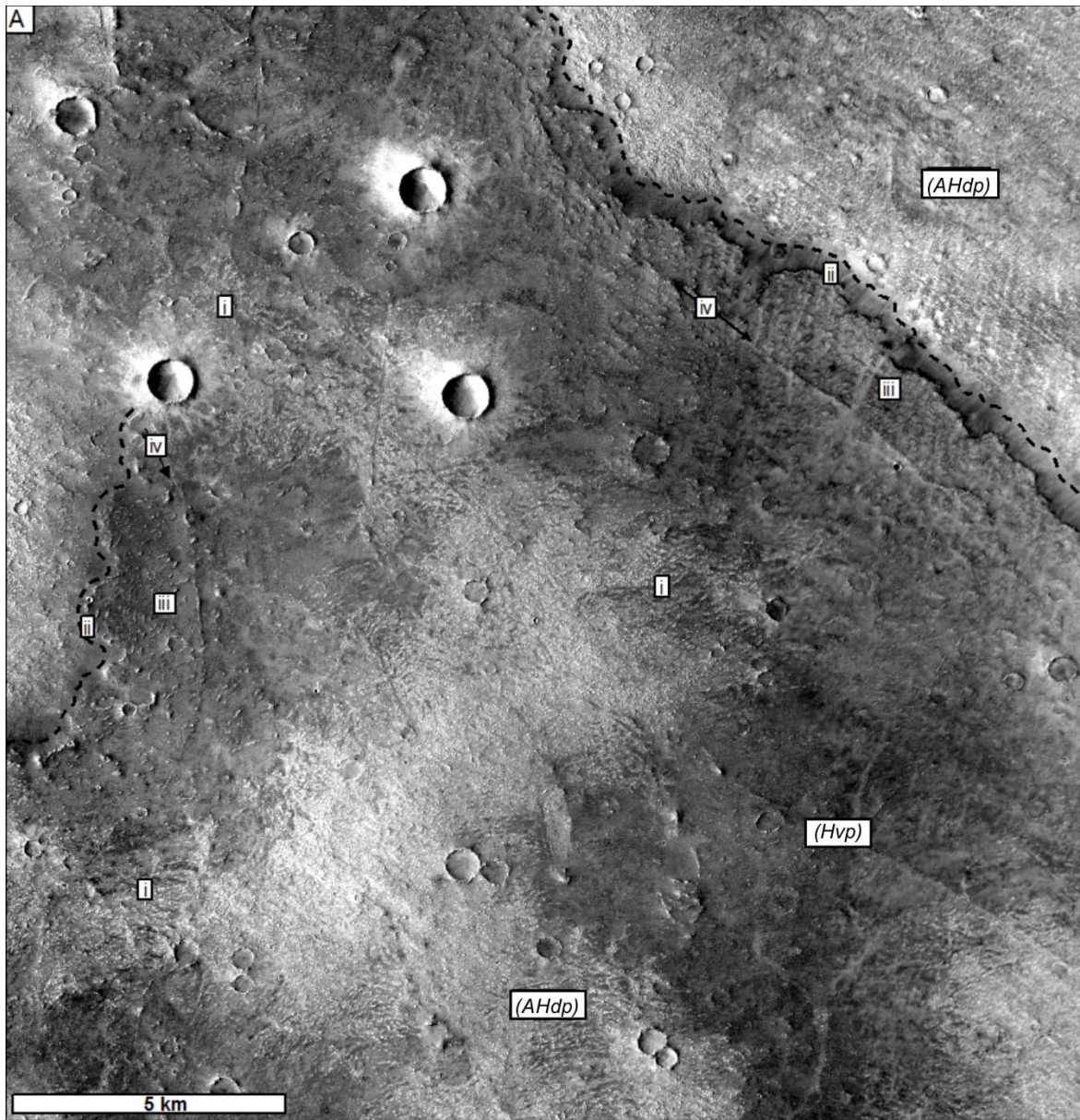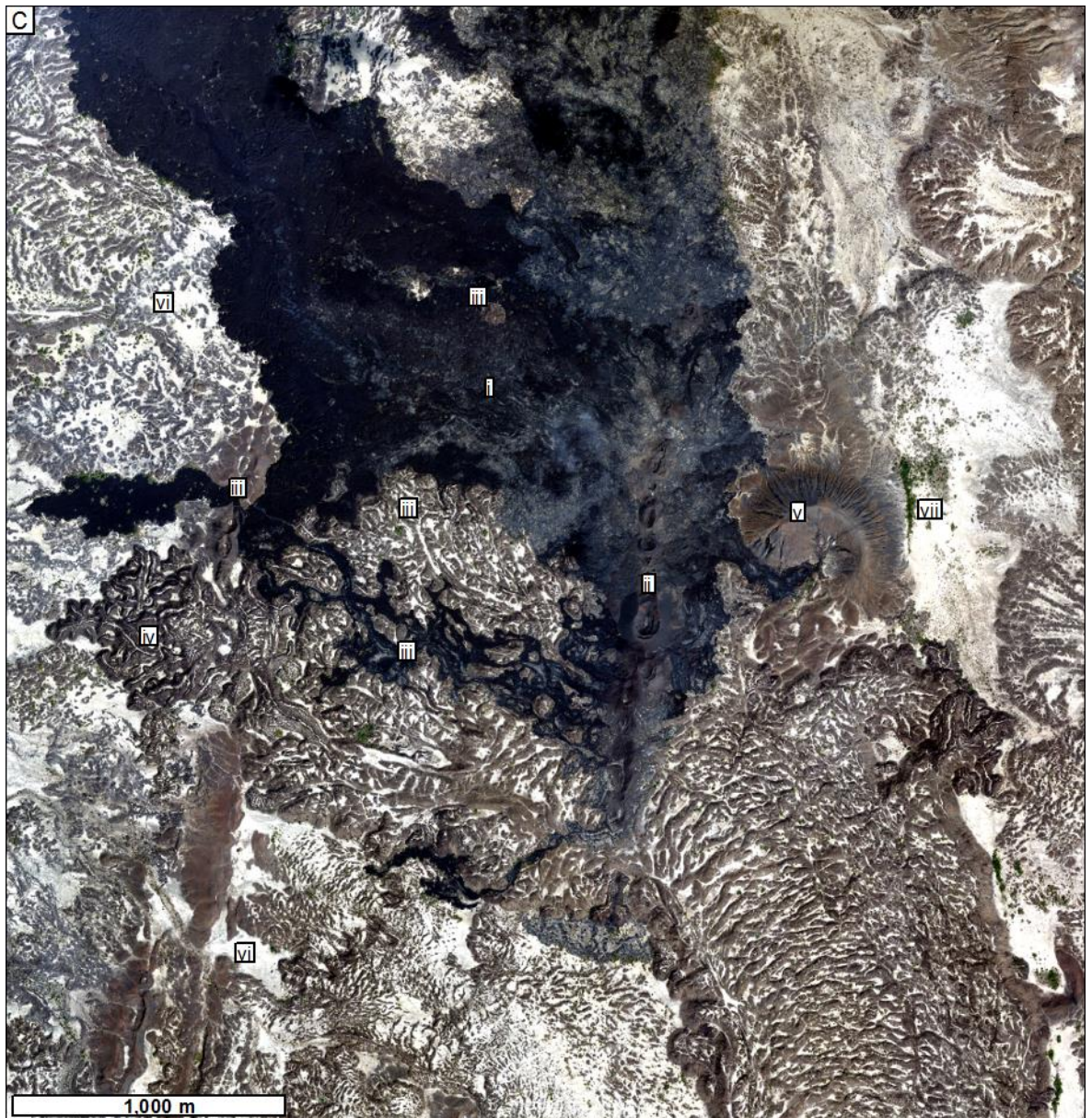
Figure 4.25

The interaction between thin lava flows and the small scale (5-10m) topography of the underlying surfaces. (a). shows the edge of the Hesperian volcanic plateau unit (Hvp) overlain by a thin Thermally distinct veneer (AHdp) unit. The interaction between the two shows (i) lobes of the AHdp unit inter-fingering with upstanding topography of the Hvp surface, (ii) lobate margin of the HVP, (iii) festoon ridges perpendicular to local flow shear stress, (iv) flow margin shear zone ridges parallel to the local flow shear stresses (mosaic of CTX; B17_016127_1963_XN_16N293W, and F04_037225_1965_XN_16N294W). (b). The frequency distribution of thermal inertia pixel values for the Early Hesperian volcanic plains unit (eHvp; pink, dashed), AHdp (orange) and Thermally distinct lineations (Adr; red) per 100 km^2 (see Chapter 3.1.1) drawn from Quantitative THEMIS Thermal inertia mosaic [Christensen et al., 2013]. This graph shows that the distribution of thermal inertias of the Adr are shifted to higher rock/sand per pixel than the AHdp but that both of these fall within the range of the eHvp. This is consistent with the interpretation that all these groups have a similar volcanic surface texture. (c). Shows the relationship between (i) a small scale lava flow from (ii) a short fissure vent and the undulating underlying topography of (iii) surface texture and (iv) inflation lobes in a pre-excising flow unit (v) older cinder cone north of the the Manda Hararo rift segment, Afar Depression, Ethiopia. Also visible is (vi) white wind derived sand and (vii) green; sparse vegetation. (Aerial photograph; NERC ARSF 2009; mosaic_299_1m)

4.5.3.2 The Ridged mantling field (Rmf)

The Southeast quadrant of Syrtis Major Planum is covered by bright linear ridges of various spatial densities (Bright ridges mantle, Rmf; Section 4.3.3 Figure 4.8). The bright ridges of the Rmf are not visible in the THEMIS base map, other than as patches of relatively bright night-time pixels. Where these bright ridges are particularly common, their presence obscures the thermal properties of the surface and prevents analysis of the wider lithology when using THEMIS data. When viewed in in CTX images, these bright ridges appear rugged and bouldery and retain even the smallest craters.

The material from which Rmf is eroding does not appear to have in-filled and erased craters 100s of m across; consequently it must have been relatively thin (<10's m) in these areas. This relationship between the ridges and craters is seen in Figure 4.10 where some small craters are merging into the ridge pattern whilst others more clearly superpose it. Additionally, where the ridges are seen overlying the edges of ejecta blankets associated with larger craters, they are not found higher up towards the crater rim or extensively in the floor of the craters themselves. Although where they do, they are found alongside Transverse Aeolian Ridges's [*Balme et al.*, 2008].

The rugged texture and qualitatively similar crater density of the Rmf underlying and/or surrounding surfaces have lead to the interpretation that the ridges are erosional features rather than depositional features. They are therefore the eroded remnants of layers indurated by partial welding, ground or meteoric water cementation or by some other other process. This overlies both the Early Hesperian volcanic plains unit (eHvp) and the Hesperian volcanic plateau unit (Hvp). The clearest boundary between those groups is south of SMCCC. This means that these features must date to after ~3.38 Ga (the approximate age of the superposed flow).

The interpretation for the formation of these ridges that I prefer is that they are Periodic bedrock ridges (PBR) [described in detail in *Montgomery et al.*, 2012] carved into an indurated mantling layer of variable thickness. Although this is not a totally satisfying explanation, the ridges

are more similar to the PBRs as described than any contemporary aeolian bed form [*Bridges et al.*, 2013]. Whilst the genesis of PBRs on Mars is not well understood [*Montgomery et al.*, 2012], similar features have been observed on Earth in a primarily bedrock environment where erosion is dominated by aeolian processes rather than water driven ones [*Hugenholtz et al.*, 2015]. In this setting, a genetic link is found whereby long wavelength mega-ripples form armoured caps, protecting bedrock against the sand blasting of saltation grains thus creating local topographic highs under the dunes. PBR's are then revealed when either sediment supply ceases or mega ripples move faster than the erosion of PBR [*Hugenholtz et al.*, 2015]. The interpretation of these forms as PBR's, formed through a mantling layer of relatively bright material, requires an origin for this mantling material.

Give the proximity to a volcanic centre (Syrtis Major Planum) previously interpreted to have produced explosive eruptions [*Fassett and Head*, 2007; *Kerber et al.*, 2012] it is reasonable to invoke some volcanoclastic fall or flow deposit to be responsible for this material. This origin for a unit with suitable grains size properties and potential degrees of internal strength is again supported by Hugenholtz et al., [2015]. The genetic evolution of PBR's could be explained by an ignimbrite deposit with varying degrees of welding. After emplacement, the deposit then became indurated by internal or external processes such as welding or cementation [*Ormö et al.*, 2004; *Gravley et al.*, 2007]. Subsequently the deposit has eroded in the genetic sequence for PBR's [*Montgomery et al.*, 2012; *Hugenholtz et al.*, 2015]. Finally, we attribute the variation in bright ridge density to different thickness of the initial deposits and varying severity of erosion, and the rugged intermittent form of the ridges to their formation over a similarly rugged, and at the time, relatively fresh textual variety of volcanic surfaces.

4.5.3.3 Late stage flank flows

In addition to the Volcanic plains formation (Early Hesperian volcanic plains unit Ridges, eHvr); Early Hesperian volcanic plains unit, eHvp) and Planum building lava flow formation (Hesperian fissure field unit, Hff; Hesperian volcanic plateau unit, Hvp and Late Hesperian volcanic flow unit,

lHvf) and late stage volcanic events associated with the early Hesperian volcanic plains unit (Amazonian dark ridge unit, Adr and Amazonian/Hesperian dark plains unit, AHdp) there have been at least three seemingly unique manifestations of magmatism outside of the SMCCC (Section 4.3.9).

4.5.3.3.1 The western flank fissure

The western flank fissure (Figure 4.18) is the oldest of the Thermally distinct (unique) group (Avf). I interpret the thickness and quasi-digitate margin to provide evidence for these flows having advanced in a pāhoehoe style and inflated to its current thickness. No other discret flow on Syrtis Major Planum, from an identifiable fissure ridge, has this inflationary development and preserves details such as marginal flow lobes and a hummocky textures on its upper surface (Figure 4.18). The interpretation of this flow with respect to the rest of the planum is that it is recent compared to the degradation and mantling of the surrounding Planum building groups. This, in combination with its small size, suggests that it is a 'last gasp' of flank volcanism. The style and size of the flow has more in common with modern terrestrial volcanism, and small scale volcanism on Mars [*Hauber et al.*, 2011; *Brož et al.*, 2015] than the flood volcanic styles and more exotic eruption conditions associated with the major stages forming Syrtis Major Planum discussed above. The CTX-based crater count model age for this flow (~2.35 Ga) places it significantly after the majority of Syrtis Major Planum had been built, and instead it is contemporary with my dating of units within the SMCCC (see Chapters 5 and 6). Also in this group of late stage flank flows are two units on the eastern flank of Syrtis Major that were initially identified by their bright night-time THEMIS signature. Closer inspection shows that they are dark flow units a few meters thick and that they are clearly two separate units.

4.5.3.3.2 Bright cone and flow

There is one example of a large conical mound (Section 4.2.1.1.1) outside the SMCCC. It is surrounded by a dark flow deposit (in CTX data; Figures 4.3a, b and 4.16). The cone is unlike any other seen on the flanks of Syrtis Major Planum. The flow around the eastern flank cone is similar

to those otherwise classified within the eHvp, or as AHdp. The cone appears to be made of a lower mound of which a plateau or terrace is partially visible on its eastern flank. I interpret this to be related to a stronger material such as lava. Superposed on this is a cone of rubbly material with a sense of streaking. In HiRISE RGB colour this cone is strikingly bright and orange compared to surrounding plains. I interpret this upper part of the feature as agglutinated spatter. The colour and morphology of this part of the cone is similar to Nili Tholus, the cone within Nili Patera. These similarities might suggest a more silica rich composition, as modeled for Nili Tholus [*Christensen et al.*, 2005] (See chapter 5). However, the flows associated with the cone have little resemblance to the bright central lava and there are other explanations for why this feature sits outside the 'normal' envelope of vent on Syrtis Major Planum. For example it might be increased volatiles in the magma at this time building up a larger agglutinated spatter rampart than seen in more 'normal' vents associated with the major phases of planum construction. Another possibility may be that the cone is built of more tephra resulting from phreatomagmatic activity. This may be possible because the cone and flow are close to the elevation of fluvial channels (See Map Sheet 1), which are common on the eastern flank of Syrtis Major Planum.

The interpretation of this cone and flow is similar to that of the western flank fissure with it representing isolated 'last gasps' of volcanism. Because of its apparent temporal (and demonstrable morphological) isolation, it may not be directly related to the plumbing associated with the major constructional phase of Syrtis Major Planum (which has been shown to concentrate in the centre of the planum [*Kiefer*, 2004; *Lillis et al.*, 2015] and have more in common with other small scale isolated volcanic activity in the martian highlands [*Hauber et al.*, 2011; *Brož et al.*, 2015]) although this leaves the source of magma an open question.

4.5.3.3.3 Thin bright flow

The youngest unique flow unit is a long flank flow on the eastern flank. This flow is over 300 km long (Figure 4.17a) and appears to originate from a cluster of pits or trenches just east and downslope of the eastern flank cone (similar to, but shallower than, the large linear pits in the

north eastern fissure zone). The upslope end of this flow is only a few meters thick (Figure 4.17c and d) with an irregular surface and there is no evidence for chains of pits that might indicate evacuated lava tubes. Towards the downslope end of the flow it over-lies the ejecta of a crater (Figure 4.17d). Firstly this shows that this flow is probably significantly younger (Figure 4.17e) than most of Syrtis Major Planum. Secondly this area reveals a more complex relationship between the flow and the underlying topography. In the vicinity of the crater ejecta MOLA tracks appear to show the thickness of the flow varying between ~5 m to 50 m thick depending on the underlying topography.

I interpret this flow to be a pāhoehoe flow that has filled in the underlying topography of the steep and rough (on the 10s of metre length scale because of the underlying late Hesperian volcanic flow unit flows) topography of the eastern flank of Syrtis Major Planum. I think that this flow is immature compared to large inflated flows in the Hvp emplaced by the same process. This flow has not been active for sufficiently long to build up a plateau like the Hvp has. It has primarily in-filled pre-existing topography before over-spilling to the next topographic low as it advanced.

4.5.4 Timing of lava flow emplacement across Syrtis Major Planum

In addition to the stratigraphic arguments, I have used crater count statistics to assess the timing of lava flow emplacement across Syrtis Major Planum. I have used data drawn from the Robbins database of craters >1 km [*Robbins and Hynek*, 2012a], as well as conducting my own counts in smaller areas (Figures 4.19 and 4.20; Tables 4.5 and 4.6). From these data, model ages have been fitted for the volcanic units of Syrtis Major Planum, as well as for some surrounding units to provide context and to test the validity of the stratigraphic deductions.

4.5.4.1 Cratered highland terrain (Cht)

The model age of ~4 Ga for Noachian highland massifs (Nhm) surrounding Syrtis Major Planum fits the Noachian ages for this unit derived to support global mapping [*Tanaka, et al.*, 2014a]. This is only an average age over a large area, though, and there is considerable diversity of crater density within it. The model age was fitted to craters over 25 km in diameter, craters smaller than this did

not fit to any isochron. I infer from this result that significant resurfacing has occurred removing or burying smaller craters, skewing the crater size-frequency plot away from any calculated isochron.

4.5.4.2 The Volcanic plains and Hesperian volcanic plateau unit (eHvp and Hvp)

Model ages fitted to the Early Hesperian volcanic plains unit (eHvp 3.54 Ga, 3.48 Ga) and the Hesperian volcanic plateau unit (Hvp; 3.51 Ga) suggest that the units formed at similar times. Close observation of the crater size frequency distribution for the Early Hesperian volcanic plains unit (Table 4.6; Figure 4.26a) shows that the population best fitted to two isochrons, one for craters above 5 km (3.54 Ga), and one for craters below 4.5 km (3.48 Ga) in diameter (Table 4.6). Theses model ages bracket the model age found for the Hvp (3.51 Ga). This is consistent with the stratigraphic observations of eHvp overlying elements of the Hvp which I therefore take to be stratigraphically older parts of the Hvp, while younger elements of the group overlie eHvp material. Therefore the derived range of dates for the eHvp represents the time span in which the Noachian highlands were resurfaced. The older age (3.54 Ga) represent the time by which craters up to 5 km would not be subsequently resurfaced by the latter stages of volcanic plains emplacement and the younger age (3.48 Ga) represents the time by which craters down to 1 km were no longer likely to be resurfaced.

The date obtained for the Hvp (3.51 Ga), draws on craters from the global database and represents the bulk age for the emplacement of this flow group. The second, and younger ages, obtained from counts performed on HRSC and CTX data (3.39 Ga, 3.34 Ga respectively) represent emplacement age for one of the stratigraphically youngest elements of this flow group. These dates and the stratigraphy of this flow show the range of times in which flows from the Hvp were emplaced and cap the age that subsidence of the southern end of the SMCCC occurred.
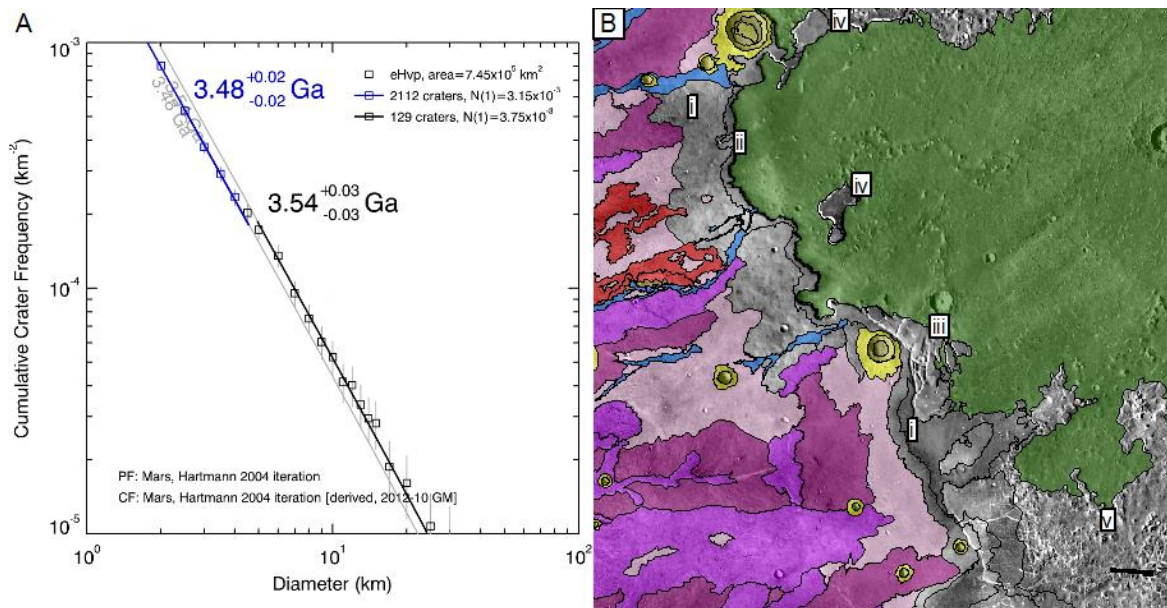
Figure 4.26

*(a). Close up of isochrons fitted to the crater count data extracted from Robbins [*Robbins and Hynek*, 2012a, b]. This shows the best fit for craters < 2.5 km in diameter (Blue) and craters > 2.5 km in diameter (black). (b) An extract of Map Sheet 1 showing the area of the contact with the Isidis basin. The extract shows the THEMIS day time data and boundaries for all surfaces but the surfaces that overly the volcanic groups (coloured). This shows; (i) Areas of post volcanic mantling, (ii) the cliffs forming the northern part of the boundary with the Isidis floor, (iii) Chaotic style terrain, (iv) outlying remnants of Syrtis Major volcanic surfaces and (v) small knobs.*

4.5.4.3 The Narrow and Hesperian volcanic plateau units (lHvf and Hvp):

The bulk model age for the Late Hesperian volcanic flow unit (lHvf; 3.36 Ga) supports the apparent stratigraphic observation that the unit is younger than the majority of the Hesperian volcanic plateau unit (Hvp). However the slope arguments (Section 4.3.2.3) suggest that it is not possible to say if the lHvf style is dependent on underlying slope or it is just younger than the Hvp. The lHvf co-exsisted with the later stages of the Hvp whilst having spatially exclusive geomorphological expressions. This date must represent the age of the surface in the area where the last flows of the lHvf took place. This means that this area is younger than the exposed areas of the Hvp. Because the area of the lHvf is younger (irrespective of the slope arguments) the extent of volcanic resurfacing diminished from the time of the Hesperian volcanic plateau unit to leave the area which now shows lHvf morphology. This diminishing of resurfacing radius from the SMCCC and thus flow length with time is supported by the observation that the last instances of the narrow flow style most commonly overly Hesperian volcanic plateau unit flows.

4.5.4.4 The Central Caldera Complex (SMCCC)

The date found for the area of the central caldera complex (3.44 Ga) is older than the Late Hesperian volcanic flow unit (lHvf) to the north and one element of the Hesperian volcanic plateau unit (Hvp) to the south (3.34 Ga, 3.36 Ga) which stratigraphically predates the collapse of the SMCCC. Although this date is apparently inconsistent with the terrain to the north and south it could suggest that the central part of the central caldera complex stabilised relative to the cratering rate before resurfacing finished on the northern flank of Syrtis Major Planum and before the subsidence of the central caldera complex. This may suggest that whilst effusion in the central portion of Syrtis Major Planum was initially evenly distributed the activity migrated to the northern vent systems and is now found in close association with the lHvf, possibly during the development of the Nili and Meroe Patera. Detailed model ages and the stratigraphic relationships of Nili Patera and Meroe Patera are explored in the next chapters. However, it is worth noting that the model age derived for the central caldera complex is fitted to only 35 craters, less than 1/3 of the any other unit from this data set and thus may be relatively less reliable.

4.5.4.5 Isidis basin floor

I have fitted a model age to the floor material of the Isidis basin (~3 Ga). This result tests the observed relationships between the surface in the Isidis basin and the emplacement of Syrtis Major Planum. The stratigraphy clearly shows that the last phase of basin floor resurfacing, including the linear patterns of small cones seen on the basin floor [*Frey and Jarosewich*, 1982; *Grizzaffi and Schultz*, 1989; *Ivanov and Head*, 2003], postdates the formation of cliffs and chaos-style terrains that demarcate the present-day edge of Syrtis Major Planum. It is therefore clear that the materials mantling the lowest elevations of Syrtis Major Planum (see Map Sheet 1), and the cliffs themselves, postdates the emplacement of the lavas making up the bulk of Syrtis Major Planum. Consequently, the model age is consistent with the stratigraphic observations. The model age for the planum-forming volcanic groups (eHvp, Hvp and lHvf; 3.51 to 3.36) represents the emplacement of the planum into Isidis and the date for the Isidis basin floor (~3 Ga). They also

probably represent the late stage of in the development of mantling units and degradation structures along what is now the edge of Syrtis Major Planum.

4.6 Conclusions

1. Lava flows associated with the major constructive phase of Syrtis Major Planum can be divided into a series of 'flow groups' and grouped into two formations (See Map Sheet 1). These are: The volcanic plains formation composed of; The Early Hesperian volcanic plains unit (eHvp) and Early Hesperian volcanic plains unit Ridges (eHvr). The Planum building flow formation comprised of the Hesperian volcanic plateau unit (Hvp), and the Late Hesperian volcanic flow unit (lHvf) and Hesperian fissure field unit (Hff).

2. The emplacement of the lavas that built the bulk of Syrtis Major Planum were erupted in a spatially bimodal distribution:

   - The volcanic plains of Syrtis Major Planum (eHvp) where emplaced from sets of long fissures distributed in an approximately radial pattern relative to the central caldera complex. The distribution of these fissures trends into regionally controlled alignments at the edge of the planum (e.g. Nili Fossae and circum-Isidis extensional features to the north).

   - The discrete lava flows of Syrtis Major Planum (Hvp, lHvf) were emplaced from the centre of the planum. These flows came from large linear pits such as those found in the North eastern fissure zone (NEFZ), and from similar vents in the area that subsequently collapsed to form the central caldera complex (SMCCC).

3. The distribution and stratigraphy of lava flows represent a development in dominant emplacement style with time (Figure 4.22).

   - The earliest stages of Syrtis Major Planum were dominated by the formation of thin pāhoehoe flows in the Volcanic plains formation (Map Sheet 1; eHvr and eHvp). Initially, the plains formed from fissures, feeding channels and tubes hosted first on and then off ridged mounds. This transport system emplaced lava radially,

presumably from the central region across the underlying highlands to form a broad volcanic plain. Consequently, the crater-count dating of the eHvp gives the oldest dates. Over time (thoughout the time of the Hvp), the number and volume of eruptions decreased. The most recent long fissures and volumetrically minor eruptions are now identifiable as Amazonian dark ridge unit (Adr)

- The later stages of eHvp emplacement were contemporaneous with the early stages of emplacement of the Hvp; evidence for this is provided by the inter-fingering stratigraphic relationships in older elements of the Hvp and the eHvp.

- Effusion had become dominantly localised to the central caldera complex (SMCCC) and the NEFZ where the Hvp was emplaced from. These flows are tube and channel fed pāhoehoe flows that have inflated to build plateaus ~ 60 m thick. Flow elements of the Hvp at the very north of the planum were supplied from the north eastern fissure zone via Arnus Vallis and other rille-like channels down the steeper northern part of the Syrtis Major Planum.

- As lava supply waned across the planum, lava flows became shorter, emplaced in the lHvf style as open channels of a'ā, lava. Eruptions that formed these flows ceased to come from the area of the central caldera complex before the caldera formation. Whilst this also appears to be true for flows from the NEFZ where the on lapping relationships suggest that, if the NEFZ werelocated on mounds (probable), activity also ceased before the collapse of the SMCCC. However there is no direct stratigraphic evidence to be certain of this.

4. The change from very long tubes in mounds (eHvr) through Giant plateau building Pāhoehoe flows (Hvp) to open channel a'ā, flows (lHvf) suggests that there was a significant change in the properties of magma and eruptions with time. Over time, apparent viscositie have increased and the volume of eruptions has decreased. Therefore it appears that, flows became smaller and less wide spread across the Planum, the

apparent viscosity, effusion rates, and volumes and by inference eruption temperatures of lava flows have decreased (This is discussed further in Chapter 7).

5. The South west quadrant of Syrtis Major Planum is covered by periodic bedrock ridges left as remnants of a bright mantling deposit. A cemented fall deposit or widespread ignimbrite with a degree of welding or cementation could be consistent with the morphology and genesis of the ridges.

Chapter 5: Nili Patera

5.1 Introduction

Nili Patera is one of two calderas located within the central caldera complex at the centre of Syrtis Major Planum. The first part of this chapter presents Fawdon et al. [2015] 'The geological History of Nili Patera, Mars', which details the sequence of events that have taken place within the Nili Patera caldera. The investigation used 6m/pixel CTX data as a base map dataset. The supplementary material for this paper is Map Sheet 2 and Section 5.3.

5.1.1 Distribution of work

In the paper [*Fawdon et al.*, 2015] presented in its entirety as Section 4.2, the following elements were contributions from the co-authors: J.R. Skok provided the CRISM data presented in Figure 5.7 as well as the first draft of the text in Section 5.2.3.1; Balme, Vye-Brown, Rothery and Jordan provided general intellectual and editorial support. The significantly larger part of the paper was my work. In addition, I acknowledge Susan Conway for ArcGIS and SocetSet assistance and Rich Brown for valuable insight into the textures and locations of terrestrial ignimbrites. The paper was reviewed by David Crown, Olivier Roche, and an anonymous reviewer. I thank them for their prompt and detailed comments which significantly improved the manuscript without changing the scientific content of the paper.

5.2 The geological history of Nili Patera, Mars

P. Fawdon[1*], J. R. Skok[2], M.R. Balme[1], C.L. Vye-Brown[3], D.A. Rothery[1] and C. J. Jordan[4]

[1]Department of Physical Sciences, The Open University, Walton Hall, Milton Keynes, UK. MK7 6AA;
[1*]peter.fawdon@open.ac.uk
[2]Department of Geology & Geophysics, Louisiana State University, Baton Rouge, LA 70803
[3]British Geological Survey, Murchison House, West Mains Road, Edinburgh, UK. EH9 3LA
[4]British Geological Survey, Nicker Hill, Keyworth, Nottingham, NG12 5GG

5.2.1 Abstract

Nili Patera is a 50 km diameter caldera at the centre of the Syrtis Major Planum volcanic province. The caldera is unique amongst martian volcanic terrains in hosting: (i) evidence of both effusive and explosive volcanism, (ii) mounds of hydrothermal silica, and (iii) compositional diversity from olivine-rich basalts to feldspathic units. We have produced a new geological map using a mosaic of three 18 m/pixel Context Camera (CTX) Digital Elevation Models (DEMs), supplemented by CRISM hyperspectral data. The map contextualises these discoveries, formulating a stratigraphy in which Nili Patera formed by trapdoor collapse into a volcano-tectonic depression. The distinctive, bright floor of Nili Patera formed either as part of a felsic pluton, exposed during caldera formation, or as remnants of welded ignimbrite(s) associated with caldera formation – both scenarios deriving from melting in the Noachian highland basement. After caldera collapse, there were five magmatic episodes: (1) a basaltic unit in the north of the caldera; (2) the Nili Tholus cone and the associated evolved unit; (3) intrusion forming a ~300 m high elliptical dome; (4) a basaltic unit emplaced from small cones in the east; and (5) an olivine-bearing unit formed on the western caldera ring fault. The mapping, together with evidence for hydrated materials, implies magmatic interaction with subsurface volatiles. This, in an area of elevated geothermal gradient, presents a possible habitable environment (sampled by the hydrothermal deposits in Nili Patera). Additionally, similarities to other highland paterae imply a similar causal mechanism and thus astrobiological potential for those edifices too.

5.2.2 Introduction

Nili Patera (Figure 5.1) is a 50 km diameter caldera within the caldera complex at the centre of the Syrtis Major Planum volcanic province. The caldera hosts a diverse range of landforms and a unique mineral assemblage, but the contextual history of these discoveries has not previously been holistically investigated. Syrtis Major Planum is a Hesperian-aged, low-angle volcanic shield located in the highlands on the rim of the Isidis basin [*Meyer and Grolier*, 1977; *Scott and Carr*, 1978; *Plescia and Saunders*, 1979; *Greeley and Guest*, 1987; *Tanaka, et al.*, 2014a, b]. It consists of a gently sloping 'shield' of lava plains 1100 km wide and estimated to have a mean thickness of 500 m [*Hiesinger and Head*, 2004]. Nili Patera is situated at the north of the 200 km × 400 km central caldera complex. Within this depression are two separate calderas: Nili Patera to the north and Meroe Patera to the south [*Hiesinger and Head*, 2004; *Plescia*, 2004]. Volcanic activity within the calderas took place after the majority of Syrtis Major's development [*Hiesinger and Head*, 2004; *Fawdon et al.*, 2013; *Platz et al.*, 2014], between 2.04 and 3.02 Ga for Nili Patera and between 2.95 and 3.03 Ga for Meroe Patera [*Robbins et al.*, 2011].

The elevation of the caldera rim around Nili Patera is asymmetrical. There is ~1800 m of relief above the floor to the highest parts of the northwestern rim, whereas the southeast rim gently slopes up into the middle of the central caldera complex (Figure 5.1) [*Hiesinger and Head*, 2004; *Plescia*, 2004]. The subsidence of the whole caldera complex has been linked to magma reservoir drainage and cooling [*Kiefer*, 2004; *Dufek et al.*, 2014].
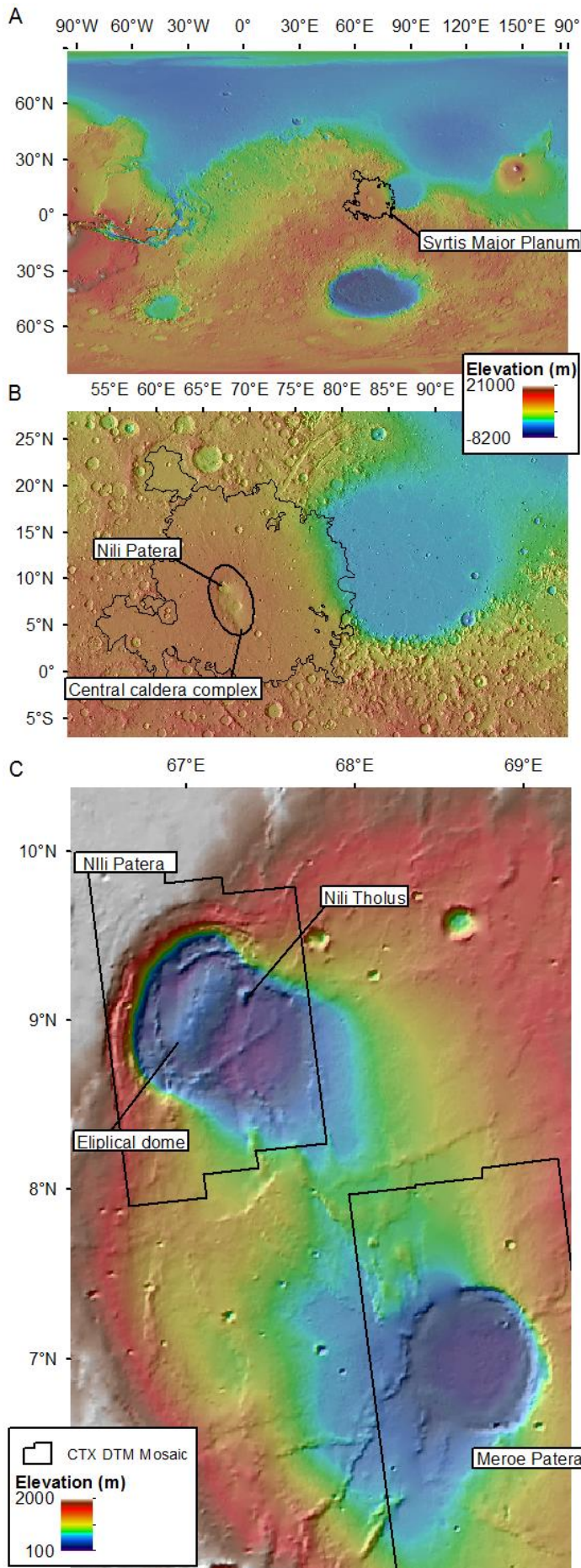
Figure 5.1:

Location of study area. (a) MOLA topography overlain on hill-shaded MOLA topography showing the extent of Syrtis Major Planum delimited by the black line within the eastern hemisphere of Mars [Tanaka, et al., 2014a]. (b) Syrtis Major Planum; the ellipse indicates the area of the central caldera complex/depression. (c) Close-up of the caldera region; the CTX mosaic study area is outlined in black. The background is MOLA topography overlain on hill-shaded MOLA topography.

Orbital spectral data support the presence of variable mineralogy across the caldera floor. These variations are interpreted to be a consequence of differing compositions of erupted materials. The caldera floor shows evidence of the magmatic evolution, evidenced by differences in the chemistry of lavas of different ages. Christiansen et al. [2005] reported THEMIS observations that suggest a region of high silica concentration correlating to a bright cone and flow in the centre of the caldera (now named Nili Tholus (http://planetarynames.wr.usgs.gov/Feature/15241?__fsk=1208884113), as well as regions of distinct thermal properties, inferred to be bedrock. These exposed bedrock parts of the caldera floor are considered by Clenet et al. [2013] to have a large olivine component. They are distinct from areas of the caldera floor identified by *Wray et a*l. [2013] as fractured bedrock enriched in feldspar relative to mafic minerals. Because different spectral units reflect various physical properties of the volcanic material, we consider these variations to be differences in the primary volcanic material. In addition to variations in primary lithology, Skok et al. [2010a] identified deposits of amorphous silica situated on Nili Tholus, leading to the suggestion that these features have a hydrothermal origin; the first, and to date only, such deposits to be discovered within a martian caldera.

The aim of this work is to understand the history of Nili Patera. We have produced a new geological and morphological map (Figure 5.2). This map compiles the spatial, structural and stratigraphic relationships between magmatic evolution, hydrothermal activity [*Christensen et al.*, 2005; *Skok et al.*, 2010a; *Wray et al.*, 2013], and new observations of the caldera's geomorphology. Using this map, we detail the history of Nili Patera. First, we investigate the formation mechanism of Nili Patera and the emplacement/exposure of caldera floor basement materials. Second, we investigate the volcano-tectonic evolution of the caldera floor, implications of intrusive activity, magma evolution, and the setting of hydrothermal deposits. Thirdly, we consider the implications of this work for calderas associated with other martian highland volcanoes.

Cross-section
A - A'
B - B'

1:500,000

Kilometers

0   5   10   20   30

198
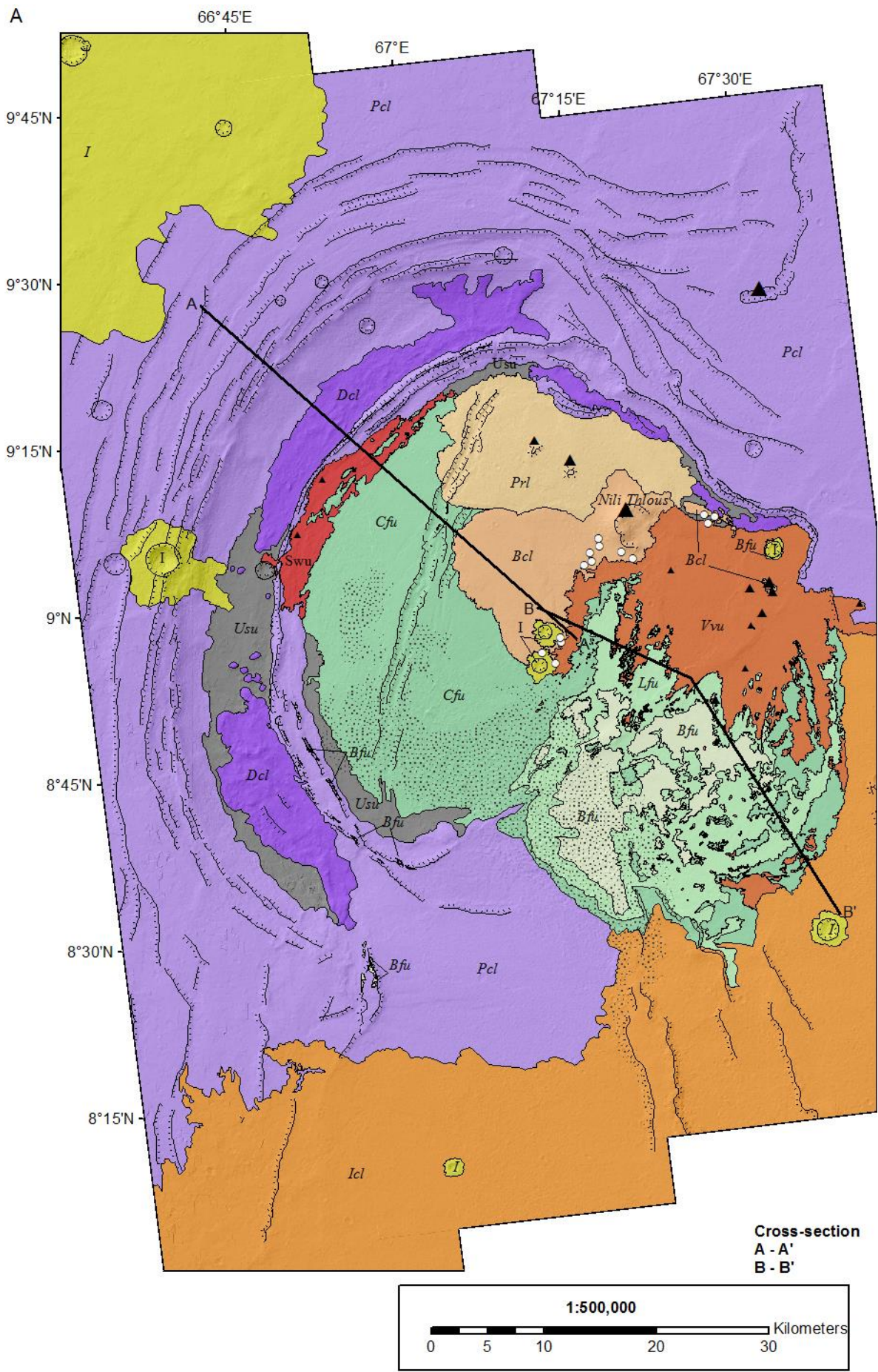
B

Map Legend

▲ Vent* (larger = more important)

○ Hydrothermal mound *(Htm)*

── Contact

╍╍╍ Scarp

Surficial units

▨ Dunes

⬜ Crater material *(I)*

⬜ Unconsolidated surficial unit *(Usu)*

Post-caldera formation volcanism

⬜ Smooth western unit *(Swu)*

⬜ Variegated volcanic unit *(Vvu)*

⬜ Intercaldera lava *(Icl)*

⬜ Bright central lava *(Bcl)*

⬜ Pre-rifting lava *(Prl)*

Caldera formation deposits

⬜ Caldera floor unit *(Cfu)*

⬜ Layered floor unit *(Lfu)*

⬜ Bright fractured unit *(Bfu)*

Pre-caldera formation lavas

⬜ Disrupted pre-caldera lava *(Dcl)*

⬜ Pre-caldera lava *(Pcl)*

*The symbol size is proportional to the size of the vent structure, the importance of the vent within the unit and our confidence in its identification.

Figure 5.2:

Geological units and surface features in and around Nili Patera. (a) Geomorphological surfaces and features and inferred geological units for Nili Patera. Geological structures are summarised in Figure 5.4. (b) Key to units and map symbols. Also, see Map Sheet 2.

5.2.3 Data and methods

Our map (Figures 5.2 and 5.3 and supplementary material presented as map sheet 1) uses three Mars Reconnaissance Obiter (MRO) [*Zurek and Smrekar*, 2007] ConTeXt camera (CTX) [*Malin et al.*, 2007] digital terrain models (DTMs) and orthorectified images from three CTX image pairs as base layers. High Resolution Imaging Science Experiment (HiRISE) [*McEwen et al.*, 2007] data have been used where available for detail, and High Resolution Stereo Camera (HRSC) [*Neukum et al.*, 2004a] data were used for colourising the other higher-resolution data products. For mapping, we used the commercially available ArcGIS 10.1 software, combined with the GeoVisionary[tm] 3D visualisation environment developed by the British Geological Survey for visualising large 3D data sets. This is fully interactive with ArcGIS 10.1, allowing unit and contact mapping to be performed in 3D.
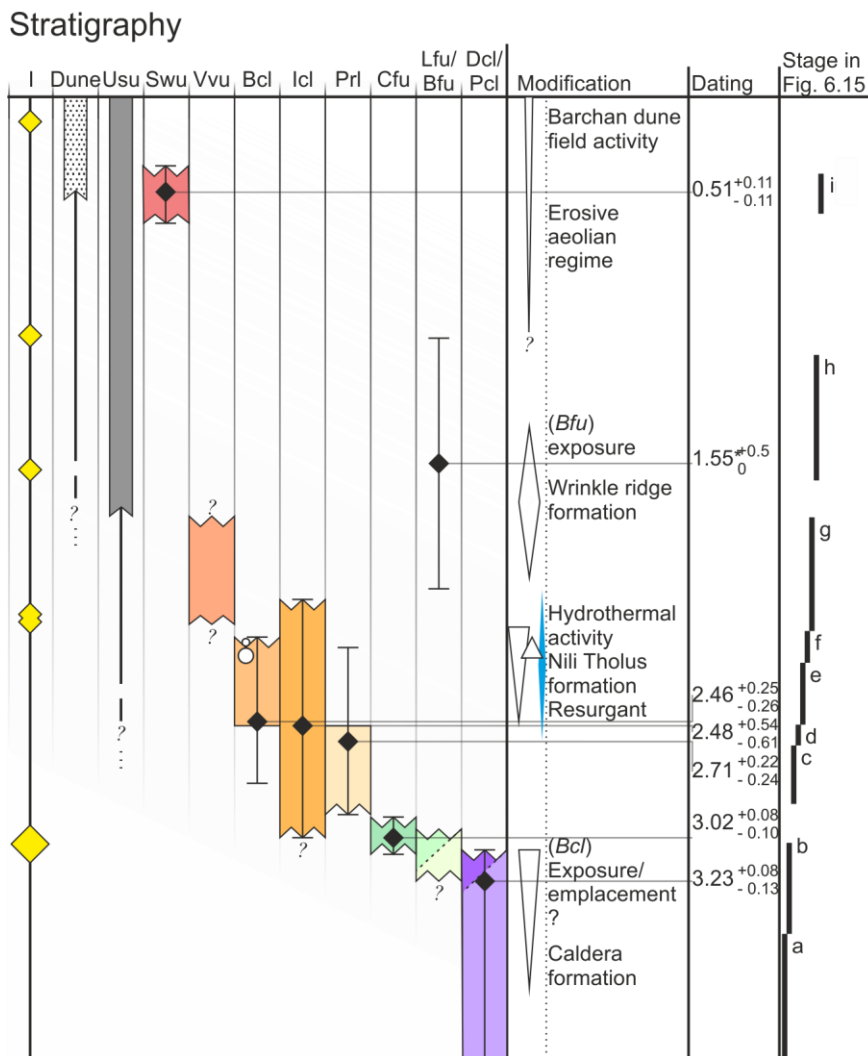
Inferred stratigraphic history of Nili Patera: Units are arranged in stratigraphic order. The size of coloured bars and modification event diamonds indicate the relative duration of the events, and the approximate time period during which they took place. Dates and error bars shown are from Table 5.1 including * taken from Robbins et al., [2011].

5.2.3.1 Topography and visual analysis

5.2.3.1.1 CTX images and DTM generation

We generated a mosaic of three digital terrain models (DTMs) from six CTX images (G04_019740_1890_XN_09N293W, G04_019595_1890_NX_09N292W, B20_017617_1891_XI_09N292W, G01_018606_1891_XI_09N292W, G01_018672_1890_XI_09N293W, and B21_017828_1890_XI_09N293W) using the method of Kirk et al. [2008]. This method uses public-domain Integrated Software for Imagers and Spectrometers (ISIS) software to pre-process the raw experimental data records (EDRs) before processing in SocetSet®, a commercially available photogrammetry suite (http://www.socetset.com). During the processing in SocetSet®, we controlled the DTMs using MOLA (Mars Orbital Laser Altimeter) track data [*Smith et al.*, 2001], thus allowing us to correlate elevations between DTMs of different scales. The output from SocetSet® was an 18 metre per pixel DTM. Additionally, the DTM was used to orthorectify three CTX images: G04_019740_1890_XN_09N293W, B20_017617_1891_XI_09N292W and G01_018672_1890_XI_09N293W. After manual geo-referencing of G04_019740_1890_XN_09N293W and B20_017617_1891_XI_09N292W to image G04_019740_1890_XN_09N293W, a mosaic of these images forms the visual and topographic base layers of the map. All other data have been geo-referenced to this layer.

5.2.3.1.2 HRSC and HiRISE images

To complement the CTX base layer, all HiRISE images publicly available at the time of writing were imported into the GIS and examined. We have also studied HiRISE DTMs DTEEC_017762_1890_018039_1890_A01 and DTEED_013582_1890_020940_1890_A01 (hirise.lpl.arizona.edu/dtm/dtm.php?ID=ESP_013582_1895, http://hirise.lpl.arizona.edu/dtm/dtm.php?ID=ESP_017762_1890) and a DTM made by ourselves

from stereo pair ESP_035247_1890 and ESP_035537_1890 using SocetSet. HiRISE data do not provide complete coverage of the mapped area, but do add detailed textural information to units mapped in CTX. We used HRSC data record H1098_0000 to provide RGB colour. The RGB colour components (h1089_0000_re3, h1098_0000_gr3 and h1089_0000_bl3) were composited using tools within ArcGIS 10.1, geo-referenced to the orthorectified CTX base map and then pan-sharpened using CTX images G04_019740_1890_XN_09N293W and B20_017617_1891_XI_09N292W. These data provide colour to help visually characterise units.

5.2.3.2 CRISM composition analysis

The primary compositional data used in this paper are observations from the CRISM VNIR hyperspectral imaging instrument [*Murchie et al.*, 2007]. CRISM acquires Full-Resolution Targeted (FRT) images at 18 m per pixel spatial resolution using 544 spectral bands ranging from 0.3–4.0 mm. CRISM observations have been corrected for instrumental artefacts and converted into I/F ratios where I is the radiance at sensor divided by the solar irradiance, F, at the top of the martian atmosphere, divided by π [*Murchie et al.*, 2007]. To use the observations for surface mineral measurements, we applied a simple multiplicative correction to remove the atmospheric contribution to the spectra. This was determined using a volcano scan method developed and tested on the Imaging Spectrometer for Mars (ISM) [*Bibring, J.-P., et al.,* 1989] and Observatoire pour la Minéralogie, l'Eau, les Glaces et l'Activité (OMEGA) [*Mustard et al.*, 2005]. A detailed description of the volcano scan method is provided in McGuire et al. [2009].

5.2.3.3 Surface age estimates

To estimate emplacement ages for some of the mapped surfaces, we employed impact crater size-frequency statistics. We identified impact craters by eye in CTX images or HiRISE images and digitised them in ArcGIS using the three-point digitisation method in the CraterTools software package [*Kneissl et al.*, 2011b] guided by the methodologies of Platz et al. [2013] and Tanaka et al. [2014a]. Units were crater-counted after they had been identified stratigraphically. Care was taken not to count craters embayed by the units being examined; craters in all states of

degradation were counted to sample formation age rather than a resurfacing age. Units with significant evidence of crater modification or ongoing erosion were not counted. To determine crater retention model ages, we used the CraterStats software package [*Michael and Neukum*, 2010]. We considered the whole cumulative population and then fitted ages using the Hartman [2004] production and chronology function to the steepest part of the slope. For consistency between units, we endeavoured to use the same crater size bins for units counted on directly comparable data for determination of model ages. Crater size frequency model ages are summarised in Table 5.1. Additionally we note the conclusions of *Warner et al. [2015] appreciating* the implications for validity consider the model ages over areas <1000 km^2.

Table 5.1   Crater count summary for units in Nili Patera

Unit	No. craters counted	Area (× 10^2 km^2)	Size range fitted (m)	No. craters in fitted range	Model age (Ga)	
Pcl	1429	18.5	350–1500	117	3.23 (+0.08, −0.13)	Formation
			20–450	522	2.54 (+0.10, −0.10)	Resurfacing[1]
Bfu[2]					1.55 (+0.50, −0.50)	Resurfacing[3]
Cfu[4]	2166	0.88	90–450[4]	495	3.02 (+0.13, −0.22)	Formation
Prl	734	1.21	150–550	116	2.71 (+0.22, −0.24)	Formation
Icl	480	1.51	480–1500	16[5]	2.48 (+0.54, −0.61)	Formation
Bcl	312	1.17	150–550	63	2.46 (+0.25, −0.26)	Formation[6]
Swu	190	0.51	110–300	22[5]	0.51 (+0.11, −0.11)	Formation

Table 5.1:

Crater count summary. Summary of input data and crater size frequency model-derived ages (full description in supplementary material). All counts used CTX data unless noted otherwise.
Notes:
[1]*Aeolian redistribution of impact ejecta and pyroclastic material.*
[2]*Data taken from Robbins (2011) for comparison.*
[3]*Determined by stratigraphy; small numbers of craters and crater remnants.*
[4]*HiRISE data were used for crater counting.*
[5]*This unit has too few craters for the model age to be considered robust.*
[6]*This unit excludes a large pair of ~750 m craters which if included produce the stratigraphically impossible result of Bcl being older than the caldera floor*

5.2.4 Observations

The primary output of our observations is a map, a summarised version of which is presented at a 1: 500,000 scale in Figure 5.2 and at a scale of 1:250,000 in the supplementary material to this article. Geologic units (Figures 5.2 and 5.3) and structure overlain on topography (Figure 5.4) are also presented. We characterised units at the highest available resolution on a geological and geomorphological basis, depending on the availability of derived mineralogy, and then mapped onto the CTX base layer.

5.2.4.1 Physiography

Nili Patera can be split topographically into four areas, as can be seen on Figure 5.4 which shows the topography of Nili Patera from the CTX DTM mosaic. The northwest area, to the left of the solid white line and external to the dashed ellipses in Figure 5.4, includes the arcuate edge of the caldera, where the terrain drops by ~1700 m to the foot of the interior scarps. The boundary with the western caldera floor is a double-ridged cliff that is ~20 m high in the middle and ~250 m high at either end. The second area, the western caldera floor (left-hand dashed ellipse in Figure 5.4), is a domed elliptical region that rises to ~400 m at its highest point. The crest, trending north-northeast to south-southwest, is split by an axial graben along the same trend. Nili Tholus lies on the boundary between the third area – the eastern caldera floor – and the western caldera floor. Nili Tholus reaches ~630 m above the surrounding caldera floor to 763 m in elevation at its peak. The eastern caldera floor, at ~200 to ~60 m MOLA elevation, is cross-cut by a conjugate pair of wrinkle ridges intersecting at 120° that are 35–50 m higher than the surrounding caldera floor. The north–south trending wrinkle ridge is poorly expressed south of the intersection (Figure 5.4) but becomes clear again nearer the margin of the eastern caldera floor. Southeast of the solid white line in Figure 4 is the fourth area, the zone between Nili and Meroe Patera. This area reaches 700 m in elevation at the southern extent of the mapped area and is demarcated by a change in surface roughness and slope outside of the caldera floor. This area also hosts ridges

longitudinally bounded by faulting with a convex cross-section, which is commonly interpreted to be indicative of compressional features [*Plescia and Golombek*, 1986]. Here, the ridges have ~125 m of relief along the axis of the central caldera complex.

5.2.4.2 Geologic units

Here we subdivide the region into units on the basis of their spectral and textural characteristics. Using this, along with stratigraphic and inferred genetic associations, we group and derive interpretation for the units. An overview of each unit's description is presented here; fuller unit descriptions can be found in the supplementary material.

We have identified 13 units (Figure 5.2) in the mapped area, and have divided these into four groups based on their geological and stratigraphic relationships (Figure 5.3 and Table 5.1). The unit and formation names are not intended to follow US Geological Survey unit names for global or regional maps of this area, but are presented in the context of this paper only. For orientation, Figure 5.5 shows the locations of subsequent figures in the Results section, as well as locations with CRISM coverage.
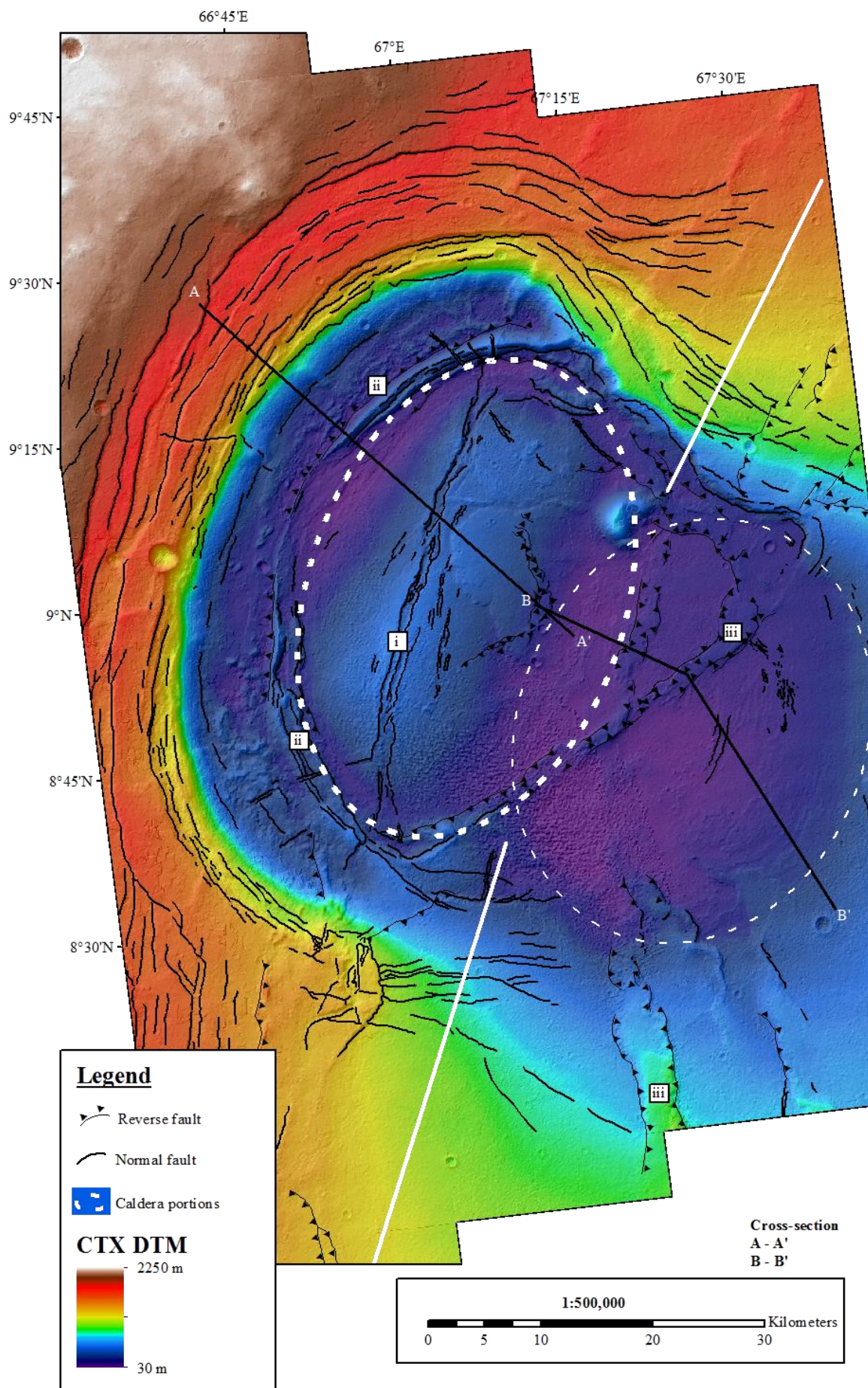
Structure and topography of Nili Patera, as shown by a mosaicked CTX colourised DTM and hill-shade. The DTM has a pixel size of 18 m. Structural mapping symbols are shown in the legend. Dashed lines show the two areas of the caldera floor, whilst solid white lines indicate approximate boundaries of different areas outside the caldera floor as described in the text. Also identified are: (i) the resurgent dome (lighter blue area), (ii) interior circumferential caldera ridges, (iii) 'wrinkle ridges' aligned along the trend of the central caldera complex floor.

5.2.4.1 Caldera external lavas

Caldera external lavas are units outside the Nili Patera floor emplaced prior to the structural development of Nili Patera (Figure 5). Vent structures, faulted flow margins, and layering exposed by caldera-centric normal faulting are observed. Pre-caldera lavas are fractured into angular to tabular blocks forming the disrupted pre-caldera lava unit (Dcl) at the base of the caldera collapse faults. The surface between these blocks is filled by unconsolidated surficial materials. Other areas are formed of rubbly mounds with occasional very bright outcrops reminiscent of the bright fractured unit (Bfu) described below. The surface between the mounds is a smooth and dusty material.
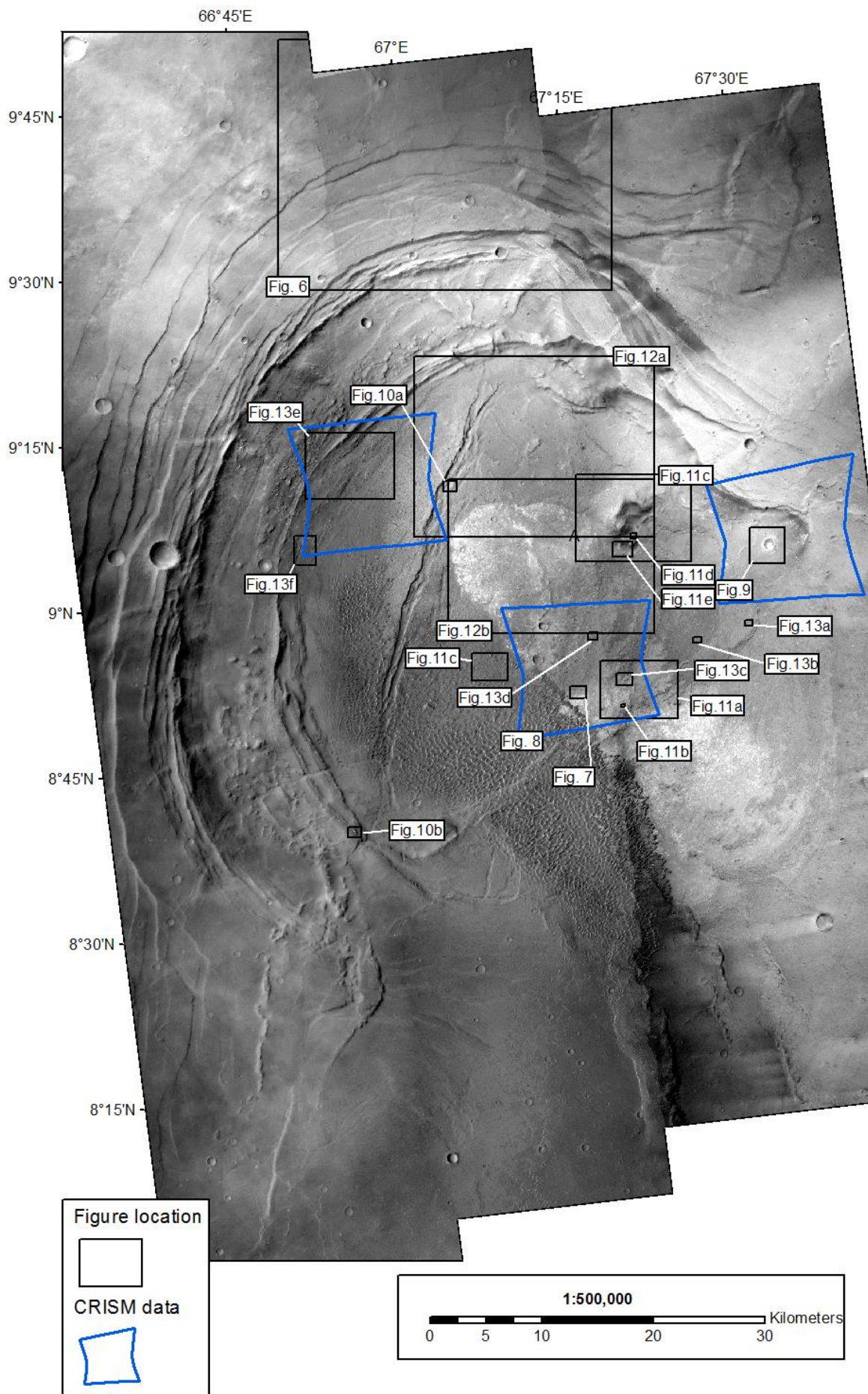
Figure 5.5:

Contextual summary of locations for Figures 5.6–11. The locations of CRISM FTR data used in this study are also shown. Background is a CTX orthoimage mosaic from (left to right); G04_019740_1890_XN_09N293W, G04_019740_1890_XN_09N293W and B20_017617_1891_XI_09N292W.

5.2.4.2 Caldera-forming deposits

Caldera-forming deposits formed contemporaneously with, to shortly after, the caldera formation event. The bright fractured unit (Bfu) at the base of this formation crops out primarily in the eastern caldera floor. It appears almost white in CTX images, and in HiRISE data it has a homogenous smooth surface with a massive internal structure comprising high- and low-centred polygonal and rectilinear fractures, 4–5 m across. Sub-horizontal, discontinuous layers exposed by erosion indicate layer-like fracture planes (Figure 5.7). Previously, Christensen et al. [2005] identified this area as bedrock. Spectrally, the bright fractured material exhibits a broad electronic absorption centred at 1.2 µm (yellow in Figure 8b). This spectroscopic signature, of a band easily masked by the spectra of other iron magnesium silicates, is consistent with a relatively pure exposure of plagioclase with ~0.1–1% FeO [*Wray et al.*, 2013]. The clarity implies <5% of the rock is made of Fe silicates and that >95% is made from plagioclase and other undetected silica-rich phases such as quartz [*Cheek et al.*, 2013]. There are three other outcrops ascribed to this unit: First, in CRISM image FRT0000B80F the key spectral signature is seen in the ejecta of a ~1100 m diameter crater (Figure 5.9), confirming that the unit is present to a minimum depth of ~100 m. Second, boulder fields of characteristically bright, 2–8 m wide boulders (Figure 5.10) can be seen eroding out from walls in the eastern caldera floor dome axial graben. Finally, high-albedo friable outcrops occur along crests of the double-ridged cliffs, within the disrupted block unit and at the edges of faulted massifs at the caldera margin (Figure 5.10). This last example could be the same material, on the basis of the very high albedo and common stratigraphic position prior to fault movement, or it could be unrelated.
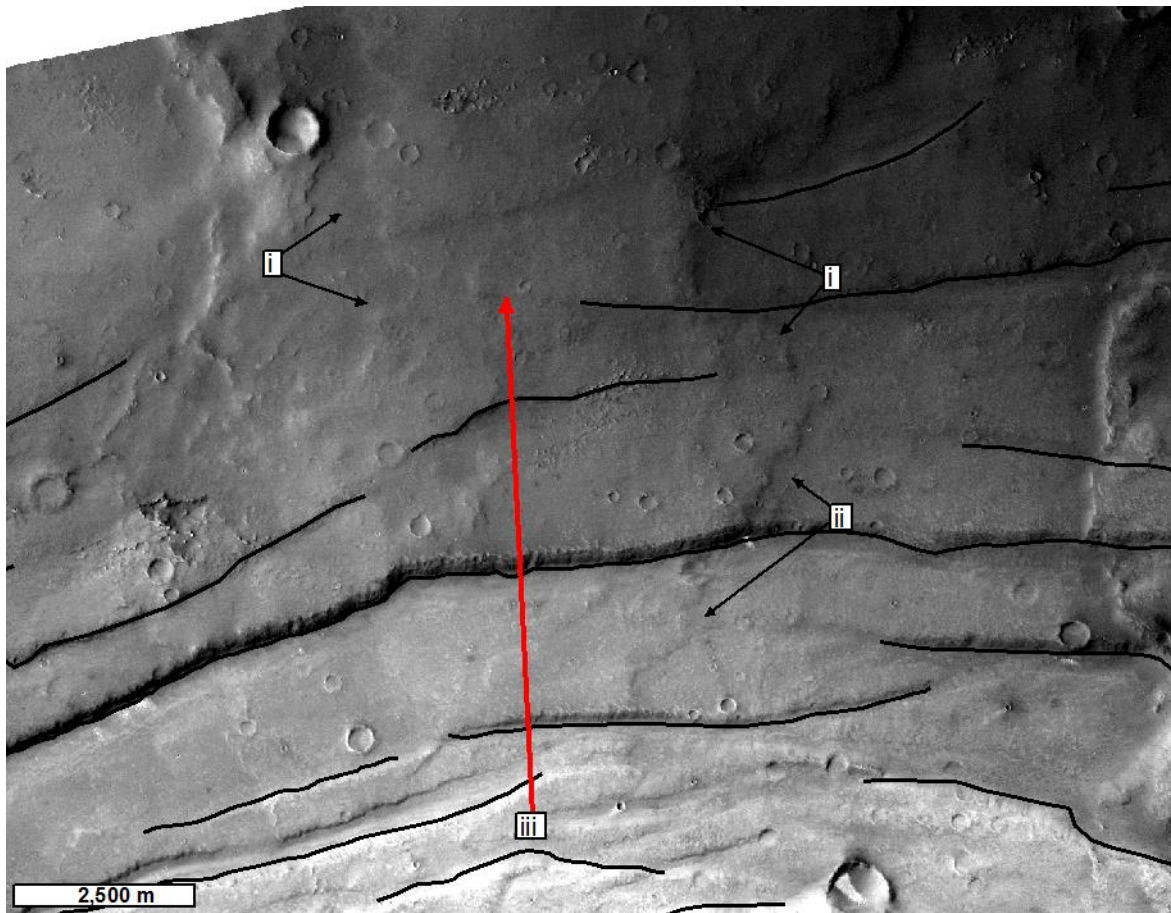
Figure 5.6:

A north–south trending lava flow that was emplaced before caldera formation-associated faulting. (i) Edges of the large lava flow (black arrows), (ii) caldera-centric normal faults (black lines), and (iii) the downhill direction of flow prior to caldera collapse (red arrow). The cross-cutting relationship shows that the flow formed before the caldera collapse faulting.

The upper contact with the layered floor unit (Lfu; see below) is gradational and poorly-defined but the units are differentiated in two key ways. Firstly, where the brightest material is covered by patchy outcrops of darker-toned material (Lfu) there is a gradual change in spectral response as this overlying material thickens, masking the spectral signature. Secondly, there is a textural progression in form from contiguous layering towards surfaces featuring regular polygonal patterns of fractures. These relationships, which often appear gradational, can be used to infer that the units could be genetically related.

Above this contact is the layered floor unit (Lfu). The layers have a smooth surface which is cross-cut by a semi-regular to rectilinear network of sub-rounded fractures (Figures 5.7 and

5.11a); and erosional windows show some fractures running through both units. Above this surface, the texture becomes rubbly. Spectral data show this unit to be characterised by more 'red' colours in the RGB image (Figure 5.8). Where the unit is patchy on a scale smaller than that of CRISM pixels (Figures 5.7b), the spectral response is evidently mixed with that of the distinctive underlying bright fractured unit.

The remainder of the caldera floor (crater floor unit, Cfu) has a rough, undulating, pitted surface made of angular boulders and rubble. Between these clasts are aeolian sediments that infill fractures (Figure 5.11c). All the unit boundaries are obscured by subsequent deposits or surficial material. In the east, the top surface of the unit is missing in the stratigraphy, except where sections are exposed on wrinkle ridges. Identification of this unit is correlated to the surface in the western region by HiRISE observations. Christensen [2005] also established that this unit occurs in both sides of the caldera.

5.2.4.3 Post-caldera formation volcanism

Post-caldera formation volcanism occurred after the emplacement of the caldera floor. The first of these units comprises lavas emplaced prior to uplift and rifting by the resurgent dome (Prl). The unit has ~20 m of relief above the caldera floor unit (Cfu), and towards the centre are several irregular flat mounds with tuya-like tops ~20 m high (Figure 5.12a). The surface is a mid-grey in tone, with smooth mantling material obscuring the detailed texture.
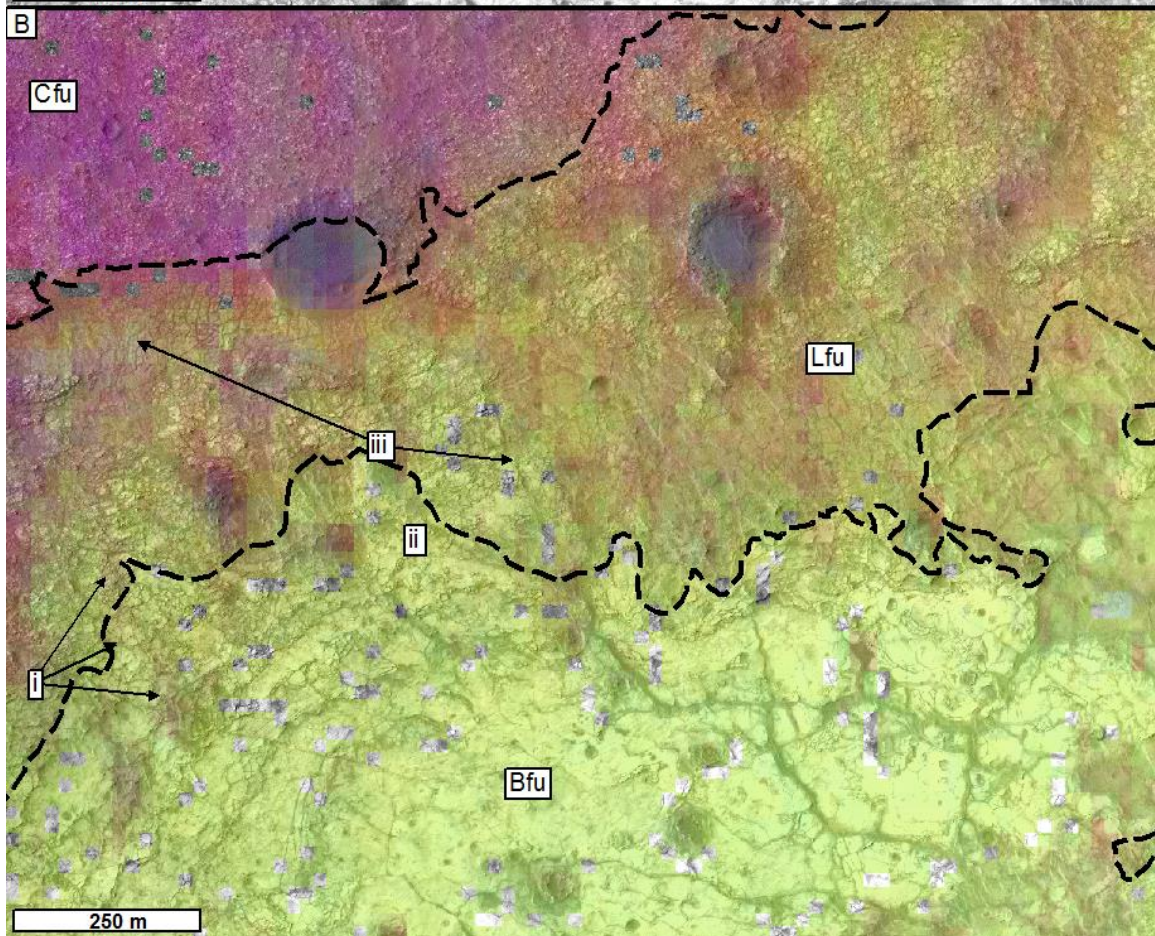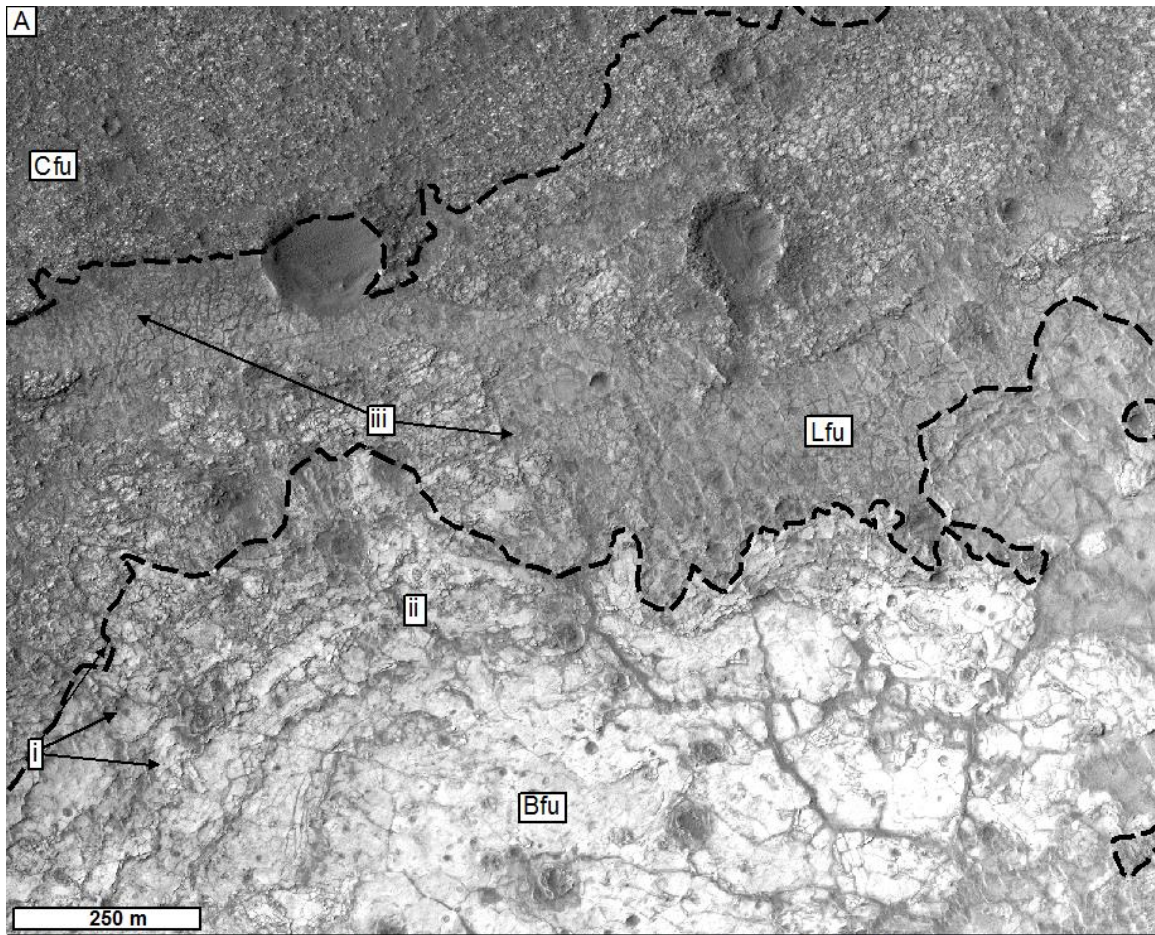
HiRISE and CRISM representation of the boundary between the bright fractured unit (Bfu), the layered floor unit (Lfu) and the caldera floor unit (Cfu). (a) HiRISE image PSP_005684_1890. Dashed lines show unit boundaries. Layers can be seen in the bright central lava (i) and it has a gradational upper boundary with Lfu (ii). The layered floor unit shows rectilinear polygonal surfaces in places (iii) but has a more distinct boundary with Cfu. (b) CRISM FRT000082EE_07_IF165L overlying the HiRISE image. Here, pink colours represent olivine and pyroxenes forming basaltic compositions and yellow represents plagioclase in the absence of iron-bearing minerals [Cheek et al., 2013]. The gradational change from the plagioclase-bearing Bfu ('yellow') to Lfu ('orange') and the contact with the overlying basaltic Cfu ('pink') can be seen. CRISM FRT000082EE_07_IF165L overlying HiRISE PSP_005684_1890.

A

Silica rich Flow (Bcl)

(Vvu)

Basalt

Dune field

Plagiclase (Bfu)

B

Silica rich Flow (Bcl)

(Vvu)

Basalt

Dune field

Plagiclase (Bfu)

3000 m

C

Nili Patera Plagioclase

FRT82EE (Bfu)

FRTB80F (crater ejecta, figure 9)

Lab Spectra

Lab Spectra Reflectance

Ratioed CRISM Reflectance

Wavelength (µm)
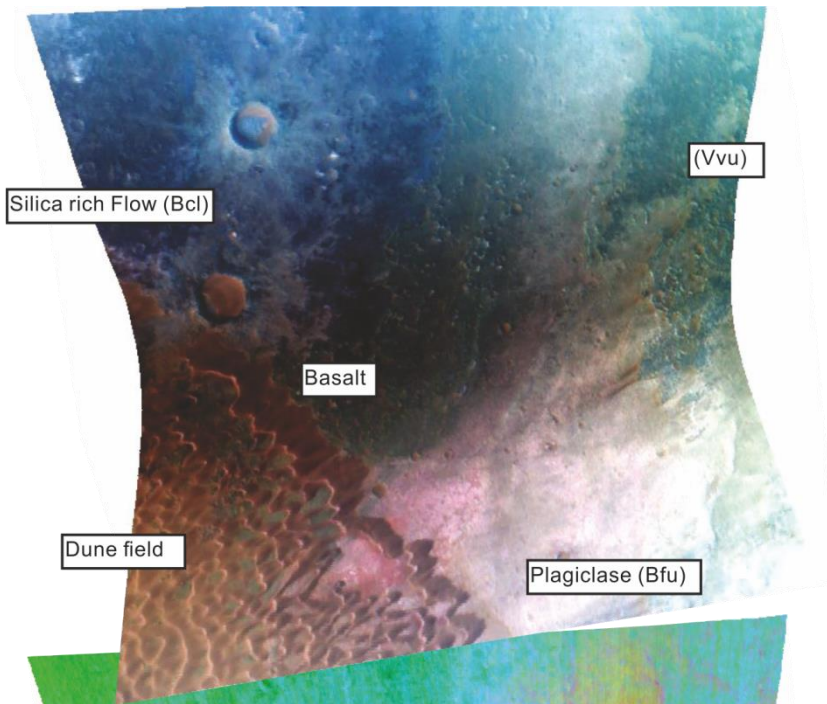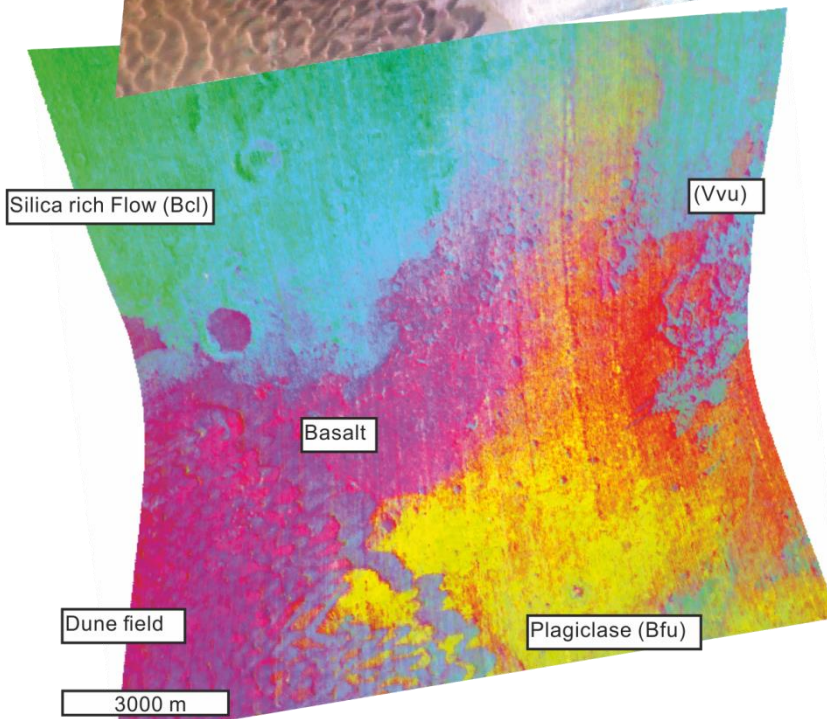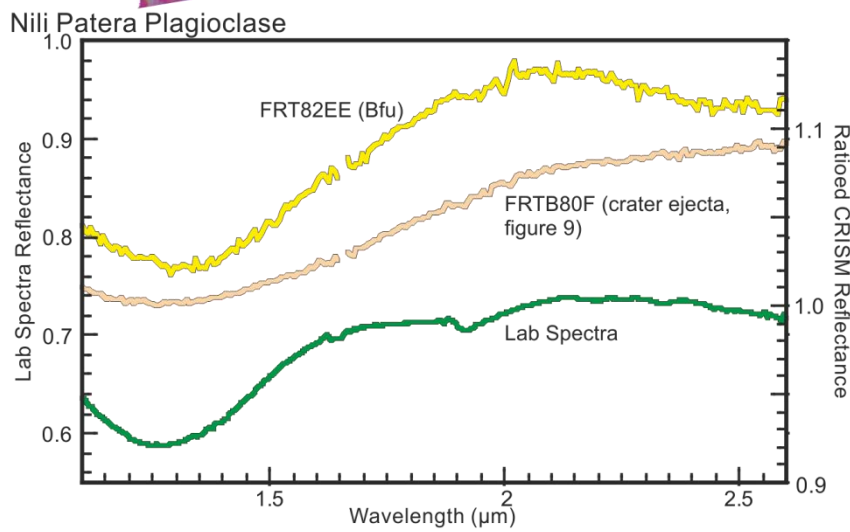
Figure 5.8: (opposite)

CRISM colour and parameter map data from CRISM FRT000082EE, in the centre of the caldera. (a) False colour, map-projected CRISM image (R: 2.4 µm, G: 1.5 µm, B: 1.08 µm). (b) CRISM false colour parameter map (R: Olindex, G: LCP index, B: HCP index; [Pelkey et al., 2007]). These images show clear spectral units: basalt (pink, some surfaces and the dune field), felsic (yellow, units low in the stratigraphy) and pyroxene-bearing materials (green and blue, probably other types of basaltic material). (c) Ratioed spectra from Nili Patera plagioclase deposits. FRT82EE is from the main deposit of the bright fractured unit (Bfu) in the centre of the caldera [Wray et al., 2013] with a spectral average of 312 pixels centred at (119,63) ratioed to a 1209-pixel region of interest centred at (361,197) (CRISM: FRT000082EE). FRTB80F is less distinct, but with a still strong 1.2 µm plagioclase absorption. It is a ratio of the 1110-pixel average of light-toned material around the 1 km wide crater in Figure 9, divided by 1177 pixels of basalt to the south of the crater (CRISM: FRT0000B80F). This indicates that the pure plagioclase material is widespread and near-surface. Lab spectrum is RELAB C1SC37, a 99% pure Bytownite from the Stillwater Complex, Montana.
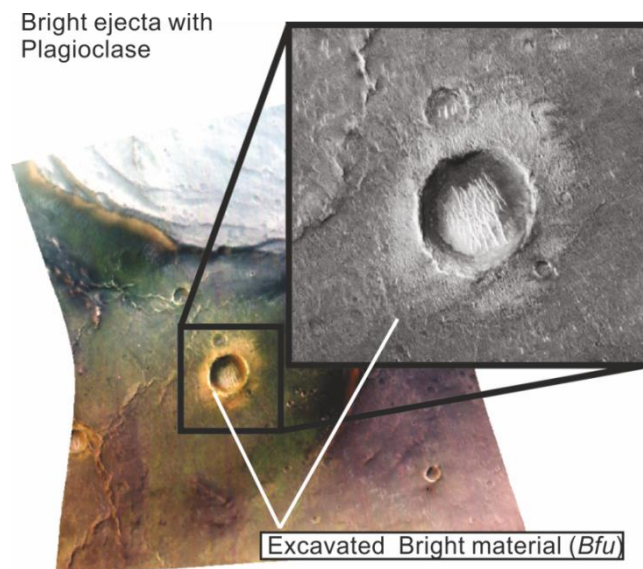
Figure 5.9: (above)

Projected CRISM (image FRT0000B80F) showing a 1 km diameter crater in eastern Nili Patera. The light-toned ejecta material strongly shows the 1.2 µm plagioclase absorption feature. Inset shows CTX view of crater and ejecta. CTX image B19_016905_1890_XN_09N292W
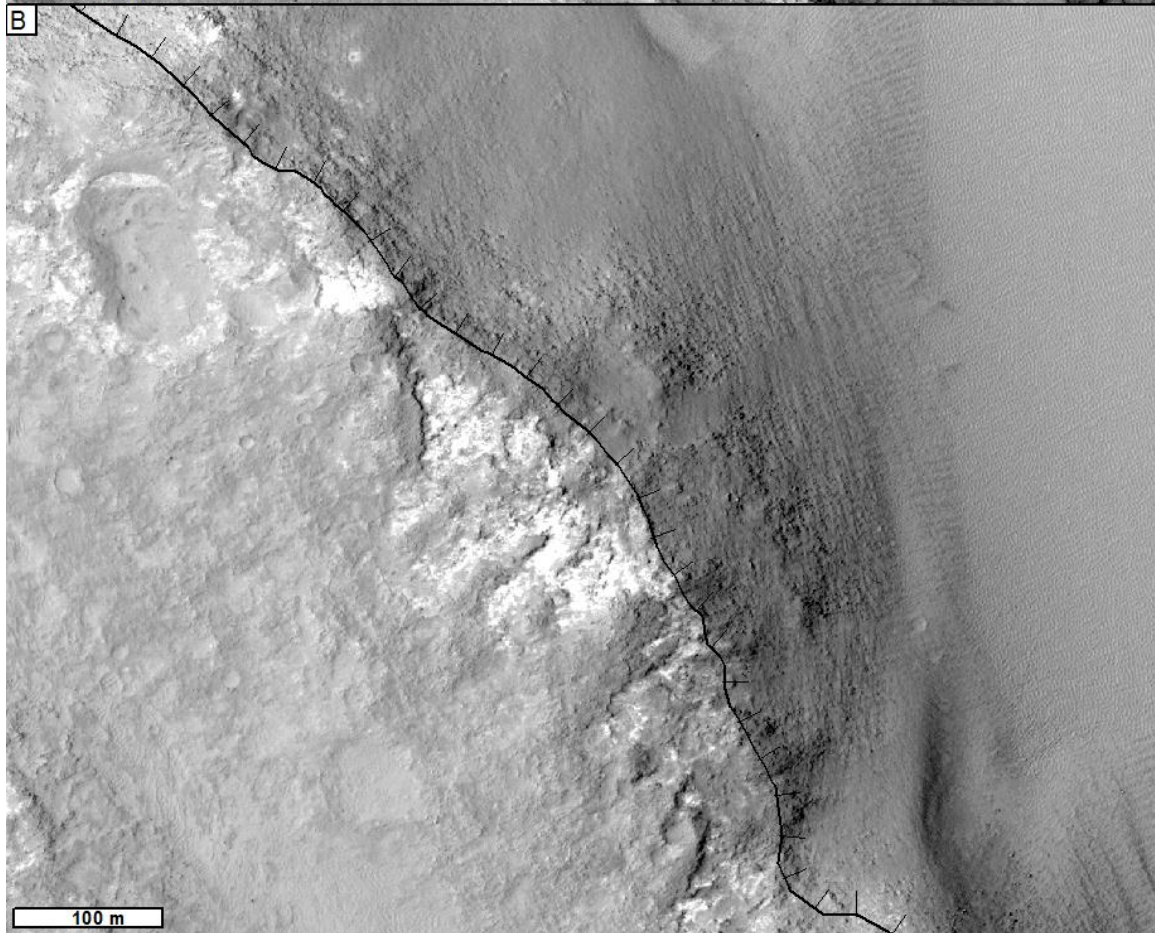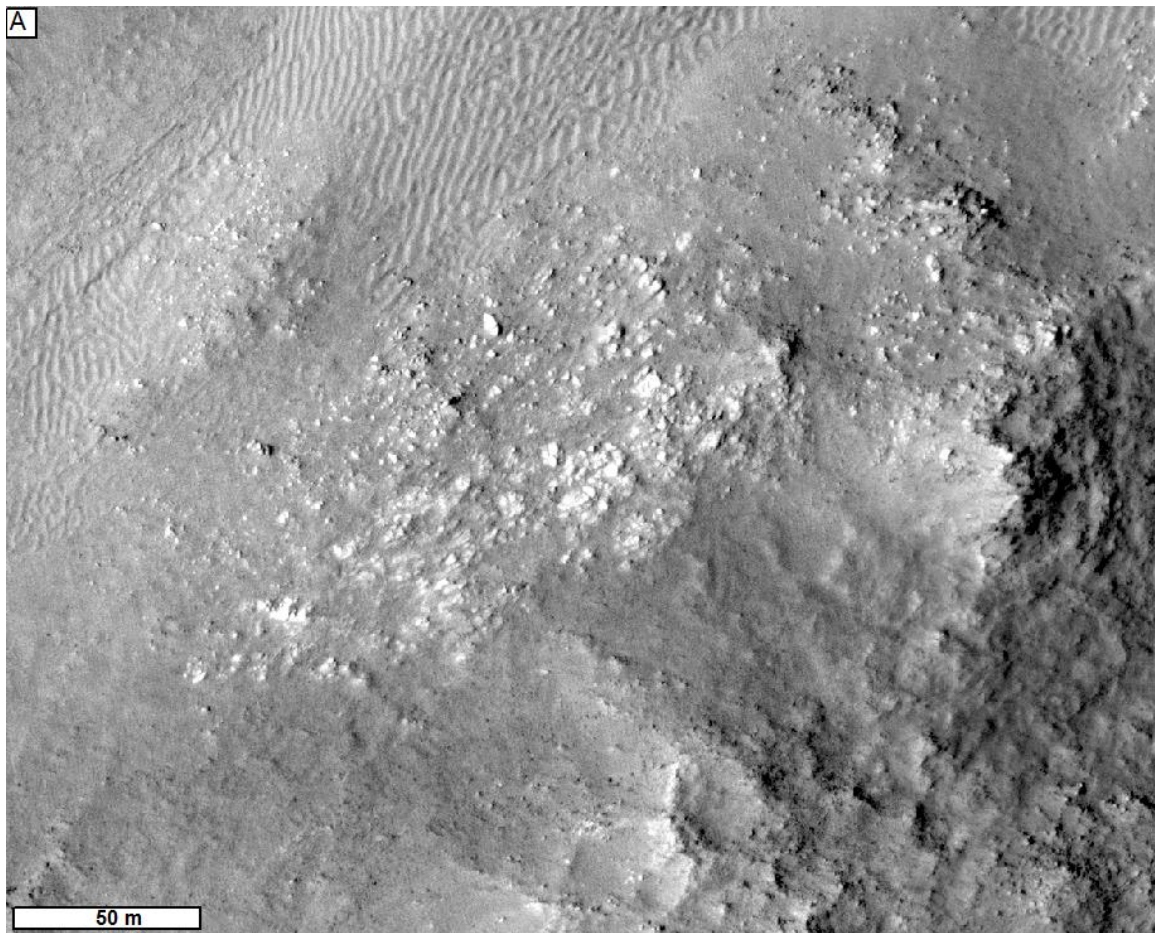
Figure 5.10:

Material inferred to be part of the bright fractured unit (Bfu) at locations around Nili Patera: (a) in the walls of the resurgent dome axial graben (HiRISE 019595_1890); (b) exposed on top of the interior circumferential caldera ridges (HiRISE ESP_027942_1890). See Figure 5 for locations.

The second volcanic unit (bright central lava, Bcl) is situated close to the centre of the caldera. The unit was emplaced contemporaneously with the initiation of faulting related to the domed portion of the western caldera floor (Figure 5.6.4), but prior to the main uplift phase of this resurgent dome (Figure 5.12b) and now dips ~1.4° east. The unit is formed of lava of an evolved composition, as inferred from its thermal characteristics and albedo [*Christensen et al.*, 2005]. This interpretation is supported by a lobate perimeter with 30-40 m of relief – observations indicative of relatively high viscosity flows, commonly associated with evolved lava compositions. The unit overlies faults parallel to the (now uplifted) resurgent dome axis. The surface is light-toned with a patchy covering of darker material. This mantling material is not seen inside the unit where excavated by two impacts. To the southeast, the unit does not have a clear topographic boundary. The edge is on-lapped by later, post-western caldera floor doming units, obscuring the topographic expression of the original extent. Two outliers share the unit's thermal characteristics [*Christensen et al.*, 2005]. The first is of unclear origin, but hosts bright mounds indicative of the hydrothermal sinter [*Skok et al.*, 2010a]. The second, with a flat top and irregular perimeter, is on-lapped by the variegated volcanic unit (*Vvu*; see below). The evolved flow unit is the only known silica-rich lava flow currently identified on Mars, and hosts all the hydrothermal silica-rich deposits mapped within Nili Patera [*Skok et al.*, 2010a].
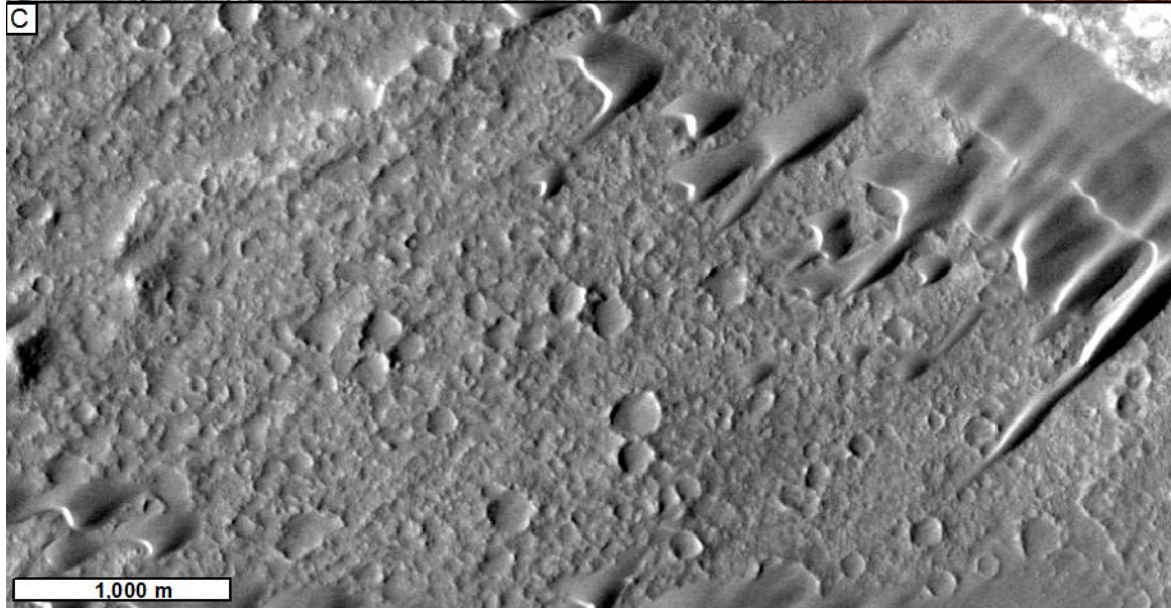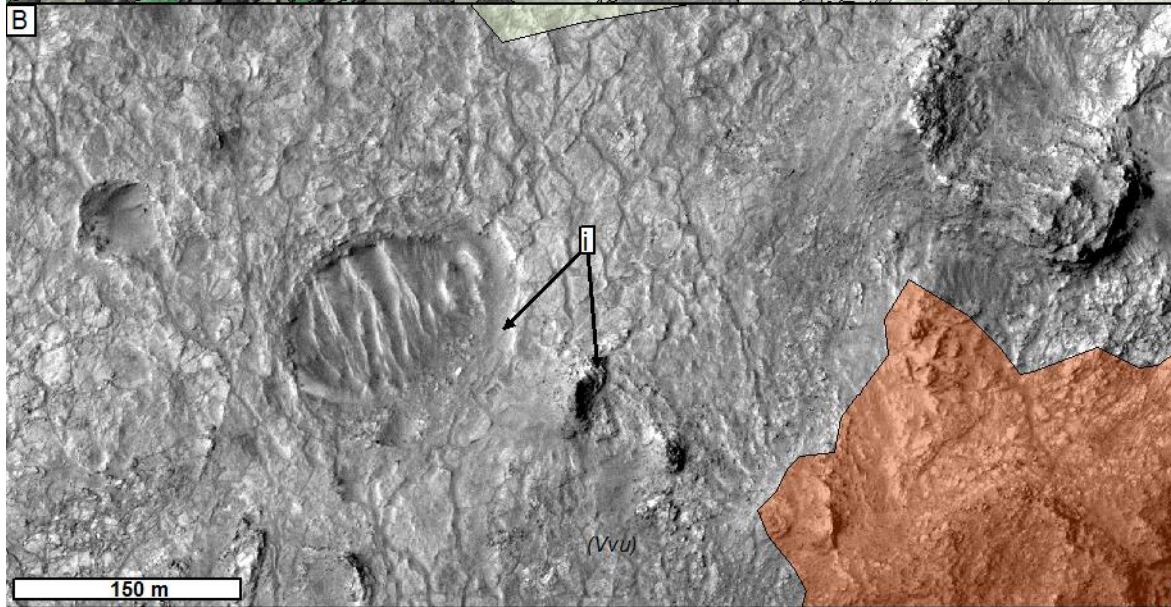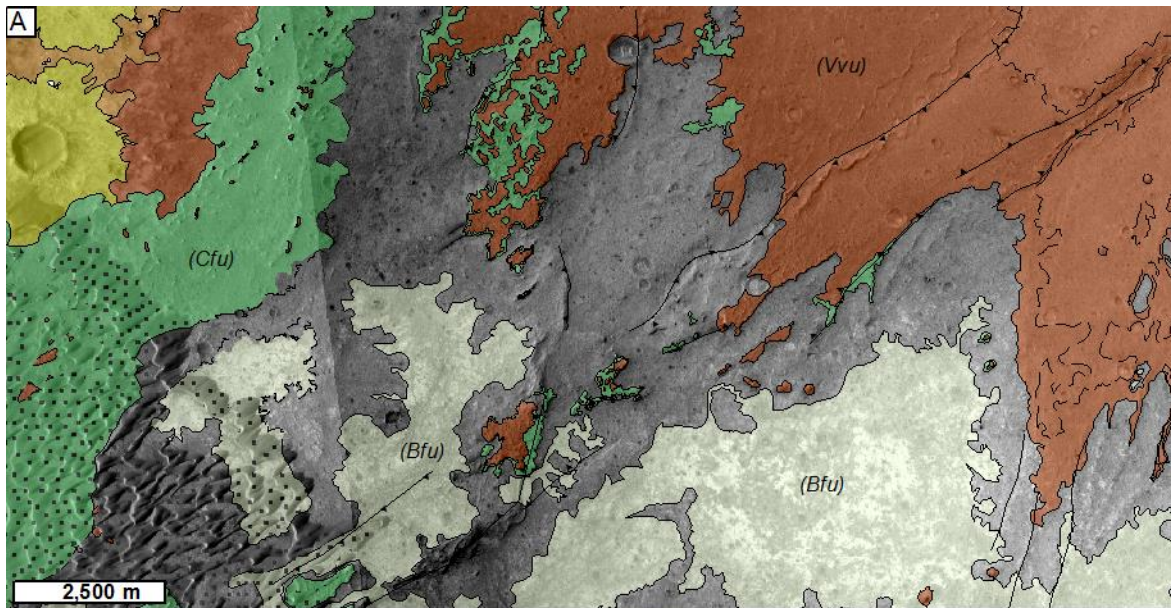
Figure 5.11:

(a) The exposed surface (non-colourised areas) of the layered floor unit (Lfu). (b) Close-up showing (i) layering in the layered floor unit (HiRISE ESP_018039_1890). (c) The heavily cratered surface of the caldera floor unit (Cfu).
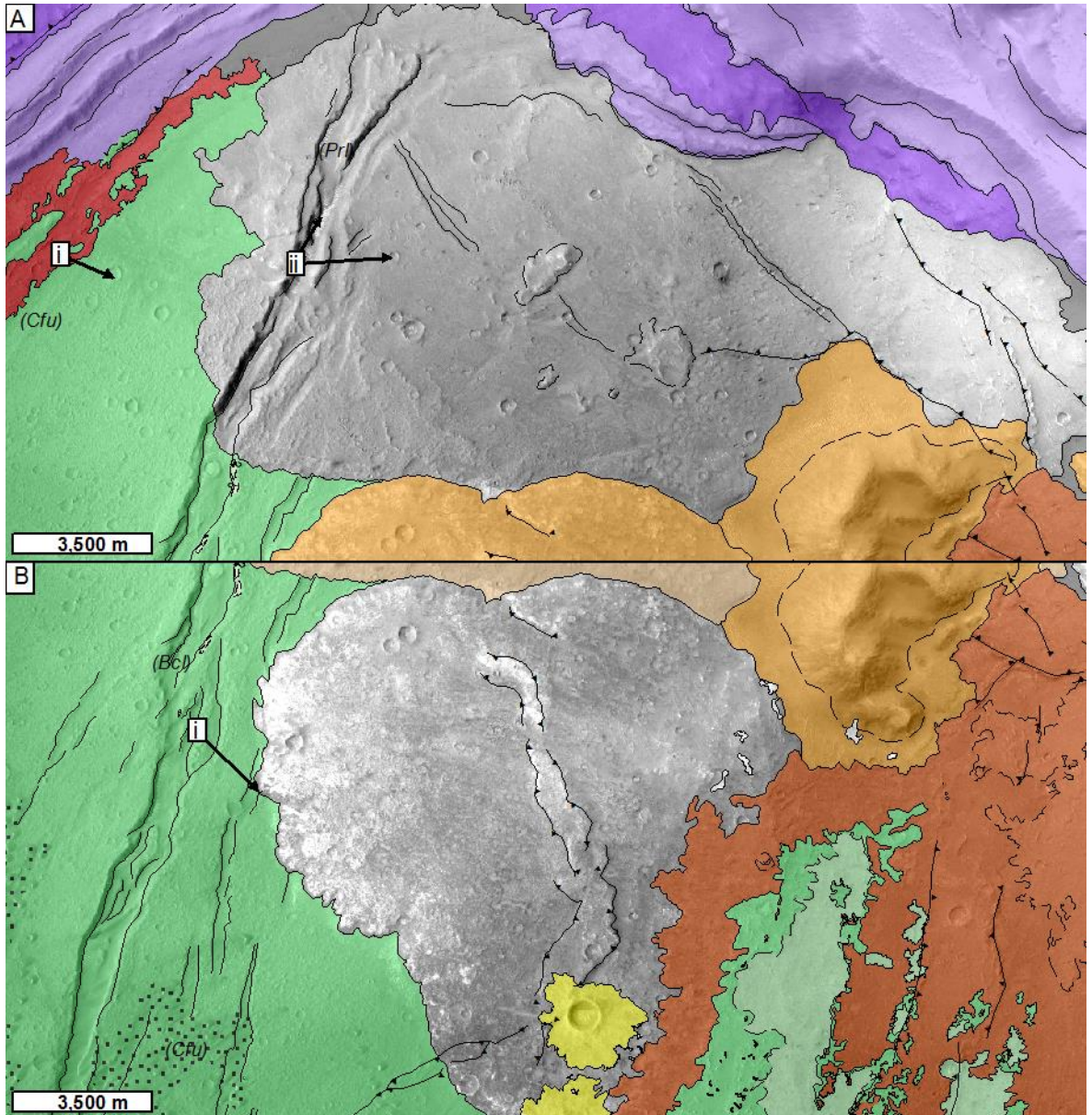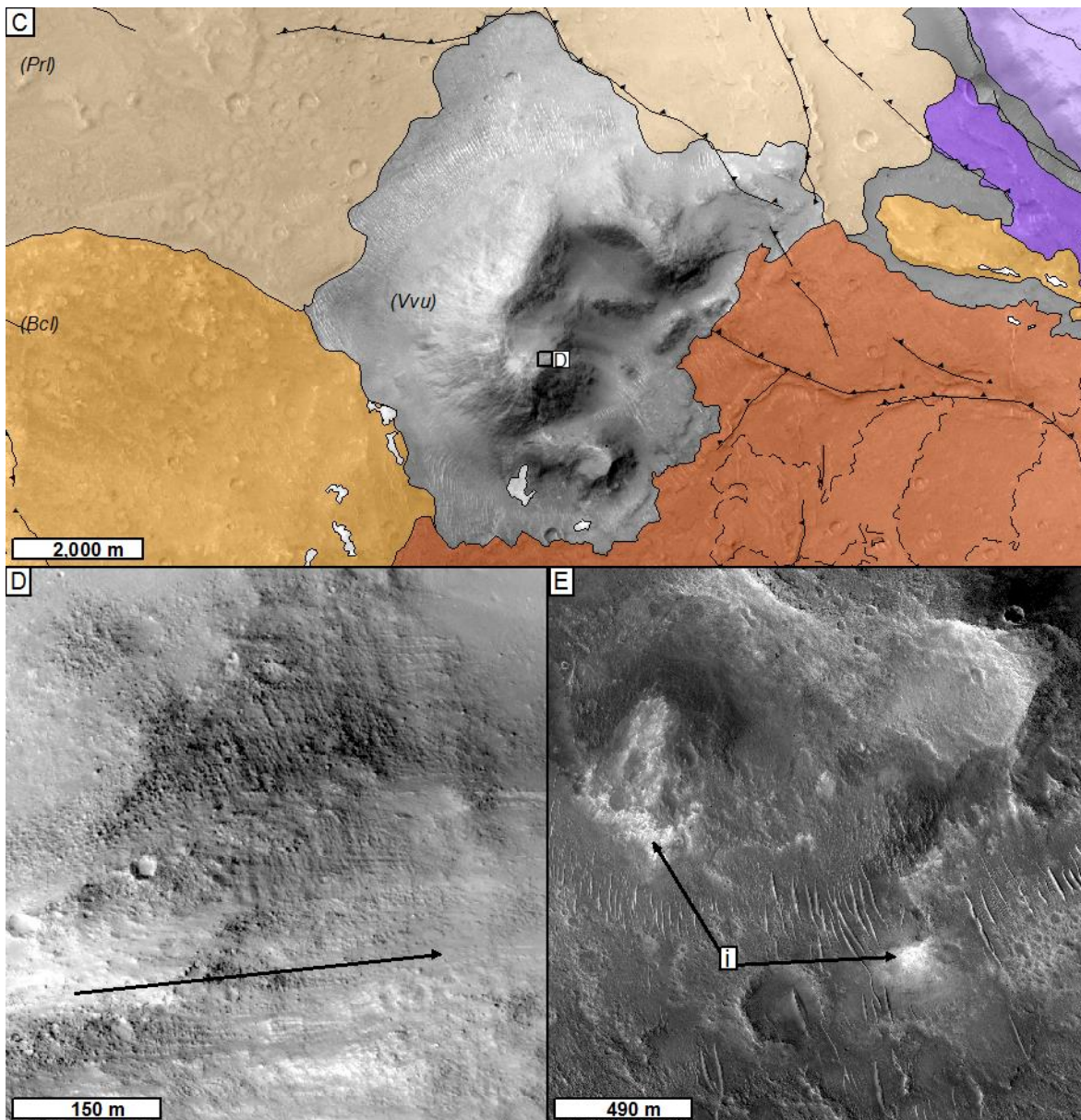
Figure 5.12:

Volcanic units emplaced on the caldera floor after caldera formation. In each case, the feature being described is the non-colourised region in the scene. (a) Pre-rifting lava (Prl): (i) normal faults of the resurgent dome axis, (ii) vent mound locations. (b) Bright central lava unit (Bcl): (i) normal faults from the first stages of doming underlying the bright central lava unit. (c) The Nili Tholus volcanic construct. (d) Close-up view showing the layered, clastic surface of Nili Tholus (arrow shows downhill direction; HiRISE ESP_020940_1895). (e) Hydrothermal mounts (arrowed) at the foot of Nili Tholus (HiRISE ESP_020940_1895; after Skok et al., [2010a]).

To the east of this unit is Nili Tholus (67° 20' E, 9° 9' N; Figure 12c) reaching 520 m above the caldera floor. Nili Tholus is broadly conical in shape with an arcuate peak ridge (Figure 5.12c). This shape is suggestive of either multiple phases of construction, or collapse of the eastern sector. Nili Tholus is light-toned in CTX images, similar to the evolved flow unit (*Bcl*) and is formed of poorly consolidated, layered clastic material with clasts <2 m in size forming on slopes of ~15°. Nili Tholus

appears to be part of the evolved flow unit (Bcl), but with a different surface texture, in agreement with the interpretation of Christiansen [2005]. These observations suggest a probable formation through the agglutination of higher-viscosity spatter. The foot of Nili Tholus and the evolved flow unit, Bcl, host mounds of amorphous silica (Htm; Figure 12d), as seen by Skok et al. [2010a], who consider the mounds to be derived from hydrothermal fluids driven by volcanic activity.

The northern part of the eastern caldera floor is covered by the variegated volcanic unit (Vvu). The unit consists of a bright, smooth surface to the south, which contains sub-circular shallow pits, and a lower-lying, dark, rubbly surface cropping out towards the northern part of the unit and formed of rounded boulders or clasts ~2 m in diameter (Figure 5.13a). Both parts of this unit have features of inflated pāhoehoe flows: several low shields, rift-crested ridges, lobate forms with marginal clefts (Figure 5.13b), and sections exposing intermittent layering of irregular thickness. In addition to low shields, there are 15 possible 'vent-like' mounds distributed across both textures of this unit. These are 3–4 m high, 60–170 m in diameter, and are composed of fine-grained material and boulders up to 2 m across (Figure 5.13a). Eight of these mounds are found within 5 km of each other. The others lie in the vicinity of reverse fault systems elsewhere in the unit. The unit has been extensively eroded, stripped back and mobilised by the prevailing winds [*Rafkin and Michaels*, 2003] in this area, which is also consistent with the slip face orientations in the active dune field [*Silvestro et al.*, 2010]. In the west, outcrops of basaltic variegated volcanic unit material cap mesas of caldera floor unit material (Figure 5.13c and d).
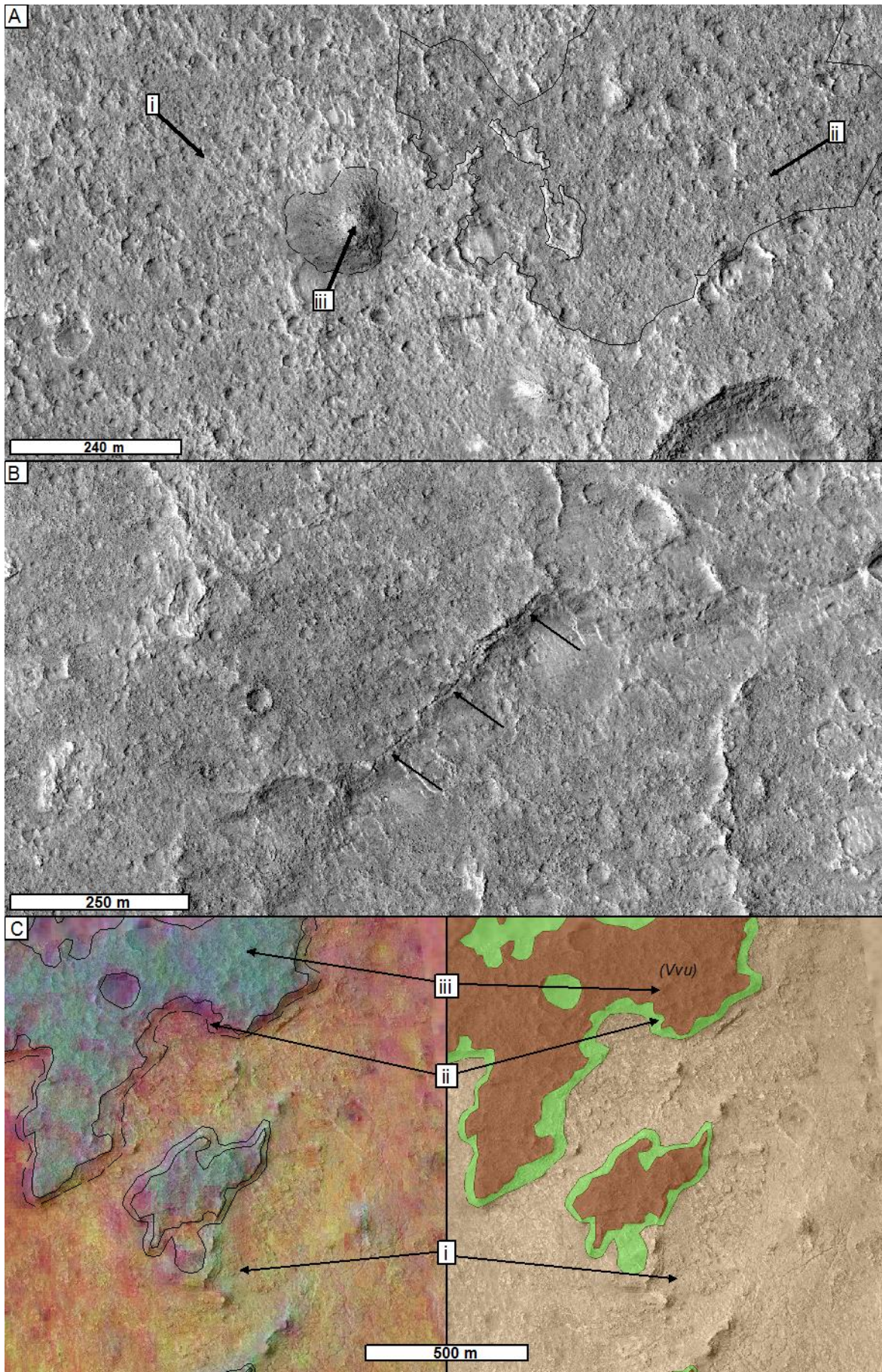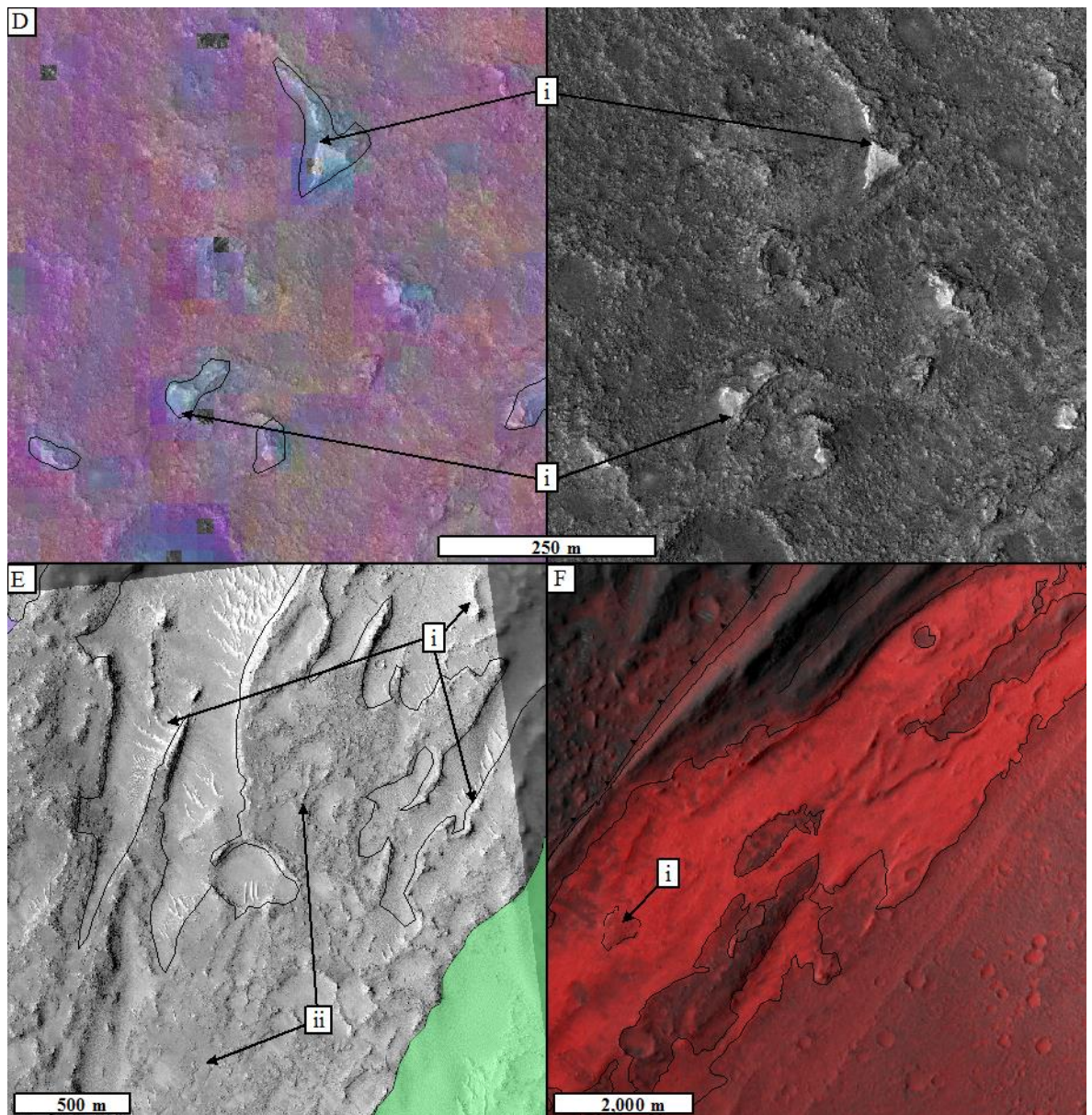
Figure 5.13:

(a) Elements from the variegated volcanic unit (Vvu) covering the eastern portion of the caldera floor: (i) bright material, commonly higher elevation; (ii) boulders, darker material, commonly lower elevation; (iii) a low mound or cone 8 m high and 140 m wide in the variegated volcanic unit. (b) Inflation cleft (arrowed) within a pāhoehoe-like lava flow axis. (c) CRISM FRT000082EE_07_IF165L overlain on HiRISE image PSP_017762_1890 (left hand panel) showing (i) the layered floor unit (Lfu; spectrally 'orange') underlying (ii) the caldera floor unit (spectrally 'pink') and (iii) the variegated volcanic unit (spectrally 'blue'). These areas, overlain with the false colour spectral response, correspond to the geomorphologically mapped units in the right-hand side of each panel. (d) CRISM FRT000082EE_07_IF165L overlain on HiRISE image PSP_005684_1890 showing (i) outliers of variegated volcanic formation (Vvu; spectrally 'blue') forming the caps on small mesas overlying surface material of basaltic composition in the cratered floor unit (Cfu). (e) The two different surface textures of the smooth western unit (Swu): (i) smooth surface and (ii) rough surface. (f) CRISM image FRT0000CB6F_07_IF165L overlying CTX mosaic showing (i) the most intense olivine parameter 'red' mapping onto the smooth surface of the olivine-rich formation. See Figure 5.5 for the location of (e) and (f) relative to each other.

223

The final post-caldera volcanism unit (the smooth western unit; Swu) is characterised by strong reflectance values in the CRISM olivine parameter map (Figure 5.13e). The unit follows the tectonic boundary of the western caldera floor. It abuts the ridged cliffs that overlie faulting in the pre-caldera lavas, and also the lowest parts of the domed, caldera floor unit (Cfu). The smooth western unit has two surface textures: smooth material making up low-lying areas, and rougher material forming high stands (Figure 5.13f). The margins of the smooth portions of the unit form linear 'high stand-like' ledges of rubbly material. These smooth areas on-lap rougher protruding knobs that are spectrally consistent with adjacent units. There is a spectrally identifiable low shield, 15 m high and 400 m in diameter, in the centre of the smooth western unit (Figure 5.13f). In addition to the volcanic units within the caldera, there is also the inter-caldera lava unit (Icl) situated to the southeast of the caldera, between Nili and Meroe Patera. Within this unit are observed channel structures and extensive lava flow fields. The unit is distinguished from pre-caldera lavas (Pcl) where it overlies normal faulting within that unit. Although this unit developed contemporaneously with the post-caldera volcanism, we do not describe it in detail because it is not on the caldera floor and not strictly part of Nili Patera.

5.2.4.4 Surficial units

Across the southwest quadrant of the caldera is an area of both inactive and active dunes [*Silvestro et al.*, 2010]. Dunes with the clearest barchan form are 300–400 m long and 25–30 m in height and show evidence of contemporaneous activity [*Silvestro et al.*, 2010]. The dune field obscures contacts between any units beneath them, although relationships can still be extrapolated by taking advantage of exposed windows between discontinuous dune-cover.

Unconsolidated surficial materials (Usu) mantle several areas of the caldera floor. In CTX images, this material has little tonal variation and few characteristic surface features. There are very few craters in this unit, with those few observed being <20 m across. The unit's boundaries are either gradational, due to mantling, or transition from extensive cover into linear and then barchan dunes.

Impact crater rim floor and ejecta materials (I) have been grouped together, and are only mapped where the boundary is distinct, or where they overlie another boundary or tectonic feature and add stratigraphic information to the map.

5.2.4.3 Tectonics

5.2.4.3.1 Normal faulting

The earliest sets of normal faults are arcuate graben structures in the pre-caldera lavas around the circumference of Nili Patera (Figure 5.4). These faults are associated with subsidence around Nili Patera and the collapse to form cliffs around the disrupted lava unit (Dcl) and caldera floor. As a group, these faults have a maximum total throw of ~1800 m and the curvature of their strikes defines the Nili Patera floor. Also part of this group of faults are two pairs of normal faults orthogonal to the caldera rim. This faulting trend appears to accommodate differential subsidence of the double-ridged cliff (Figure 5.4) around the arc of the caldera floor.

The second phase of normal faulting is uplift in the western caldera floor. Fault segments extend along the crest of the ~300 m high, -domed region of the floor, striking at ~ 017° and defining the ~90 m deep, apical graben. Activity on these faults straddles the emplacement of the evolved low unit. A set of smaller faults formed first, and these were overlain by the evolved flow unit (Figure 5.12a). A set of larger faults, which define the apical graben and accommodate resurgent dome uplift, must have been active after the emplacement of the evolved flow unit. This is because the evolved flow unit cannot have been emplaced up this slope and there is no evidence that the flow emanated from the apical graben.

5.2.4.3.2 Reverse and thrust faults

There are reverse faults inside the double-ridged cliffs (Figure 5.4), which formed from rotation of pre-caldera lava (Pcl) material. These faults define the boundary of the western caldera floor. This follows faulting trends consistent with collapse into an evacuated volume [*Acocella*, 2007].

Reverse faults bound 'wrinkle ridges' localised within the structural setting of the Nili Patera floor (Figure 5.4) to form a pair of conjugate wrinkle ridges. These ridges intersect at ~30°, close to the lowest point in the eastern caldera floor. The ridges are not continuous with axial wrinkle ridges of the central caldera complex (see below), outside of Nili Patera, although they do lie on a comparable trend.

'Wrinkle ridges' in the mapped area but outside the caldera floor cross-cut nearly all other units and tectonic features, but they are also cross-cut by normal faults related to collapse of the Syrtis Major central caldera complex (Figure 5.1b). This suggests that collapse of the Syrtis Major central caldera complex was ongoing throughout the history of tectonism associated with the formation of Nili Patera itself.

5.2.5 Discussion of Nili Patera

In this section, we consider the stratigraphic, tectonic, geomorphological and compositional observations, and discuss: (1) the formation of Nili Patera, (2) the emplacement of basement units, (3) volcanism within the caldera after its formation, and (4) the implications for the evolution of Syrtis Major Planum.

5.2.5.1 Caldera formation – Nili Patera

Brittle failure and caldera collapse are evident at Nili Patera. However, unlike many martian calderas [*Crumpler et al.*, 1996], the caldera floor is asymmetric in both plan view and cross-section, and the floor is lower than the majority of Syrtis Major Planum (Figures 5.1, 5.4 and 5.14). The caldera rim is defined by normal faulting from the southwest around to the northeast, through the highest elevation on the caldera rim. This is in stark contrast to the southeast, where a gently sloping region shows no similar fault activity. This part of the caldera rim slopes upwards towards the centre of the Syrtis Major central caldera complex. The observed pattern of interior reverse faults, and normal faulting exterior to the caldera, broadly matches the overall structural and topographic patterns characteristic of a trapdoor-style collapse (Figure 5.15c; [*Cole et al.*, 2005]) recorded in experimental studies and terrestrial caldera complexes [*Lipman*, 1984, 1997;

Marti et al., 1994; *Acocella et al.*, 2000; *Roche et al.*, 2000; *Kennedy and Stix*, 2003a, 2003b; *de Silva et al.*, 2006]. In these cases, as seen at Nili Patera, collapse is commonly driven along an outward-dipping reverse fault.

However, the collapse of Nili Patera does not appear to have been as simple as the trapdoor end-member across the whole of the present-day caldera floor. During the first phase of caldera collapse, normal faulting in the western caldera rim curved around to form an elliptical caldera floor (Figure 5.4) and, during the later phases, the whole area has also down-sagged to form the conjugate wrinkle ridges. The normal fault pattern, the topographic asymmetry, the distribution of identifiable vents, and the extent of the resurgent dome indicate that the western caldera floor is structurally distinct from the eastern caldera floor within the wider trapdoor volcano-tectonic depression. There has been at least one cycle of dome formation in the western caldera, and the resurgent dome (Figure 5.4) may be the last in a sequence of dome formation and collapse events. This is recorded by the block rotation forming the double-ridged cliffs that defined the circumference of the western caldera floor (Figures 5.4 and 5.14). Cycles of activity are common in terrestrial calderas [*Lipman*, 1984, 1997; *Marti et al.*, 1994; *Cole et al.*, 2005; *de Silva et al.*, 2006] and reflect volume changes in the magma reservoir system [*Walter and Troll*, 2001].

Cross-sections

A - A' (figure 2); 4x vertical exageration

(m) above the Mars datum

4,500
500
0
-500
0

Highland basement

Pcl

?

?

?

Dcl

Western caldera portion

Resurgant dome

Precaldera topography

Swu

Cfu

?

?

Putative dome forming intrusion

Dcl

Bfu?

Bcl

Nili Tholus

Htm

10 km

20 km

30 km

40 km

B - B' (Figure 2) 8x vertical exageration

(m) above the Mars datum

750
500
250
125
0
-250
-500

Bcl

Vvu

Bfu

?

?

Vvu

Lfu

Vvu

Bfu

Cfu

Lfu

Pcl

lcl

Highland basement

Nili Tholus   Western caldera portion Wrinkle ridge' pop up structures Precaldera topography

10 km

20 km

30 km

40 km

Note; B-B' is twice the vertical
exageration of section A-A'

228

Figure 5.14:

Cross-section of the Nili Patera (see Figure 5.2 or 5.4 for location). Topography from CTX DTM mosaic. Section A–A' shows the western portion of the caldera at four times vertical exaggeration. Section B–B' is at eight times vertical exaggeration. The cross-section shows the intra-caldera ignimbrite interpretation of the bright fractured unit.

Because the geometry of the caldera is a reflection of the size, depth and geometry of the magma reservoir, the observed pattern implies that the initial magma reservoir was large, shallow and asymmetric, with a low roof aspect ratio [*Acocella*, 2007]. The current location of the resurgent dome suggests that this elliptical portion of the caldera was where the magma reservoir roof was thinnest and the magma reservoir was closest to the surface. Here, with a thinner caldera floor, a minimum overpressure would have permitted preferential uplift by intrusion and independent volcano-tectonic development during subsequent intrusions (Figure 5.15d).

a.
(Pcl)
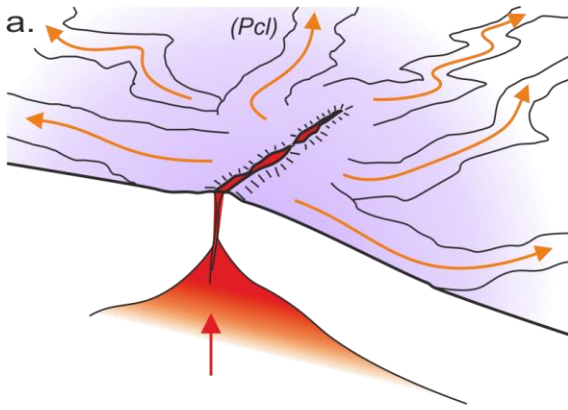
- Pre caldera topography
- Lava flows radial to a vent complex
- The magma reservoir begins to evolve

b.
N
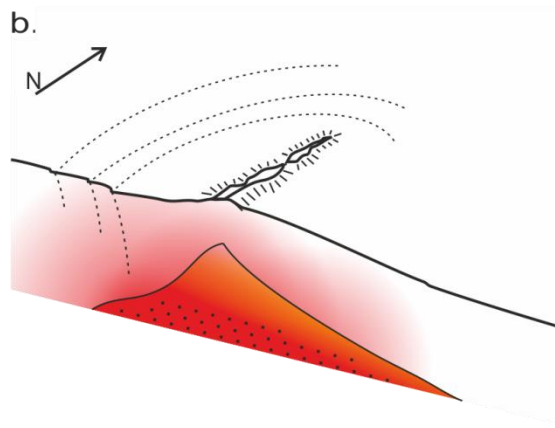
- Magma stalled in the crust
- Thermal weakening
- Initiation of a volcano-tectonic depression

d.
N
(Prl)
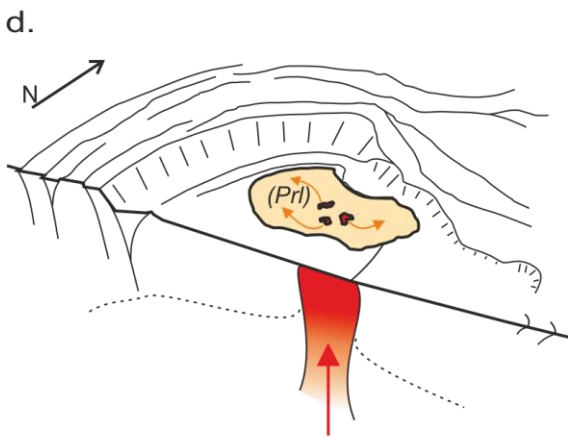
- Basalt lava flows form close to the northern caldera rim.
- Magma stalls under the caldera floor.

e.
N
(Bcl)
Nili Tholus
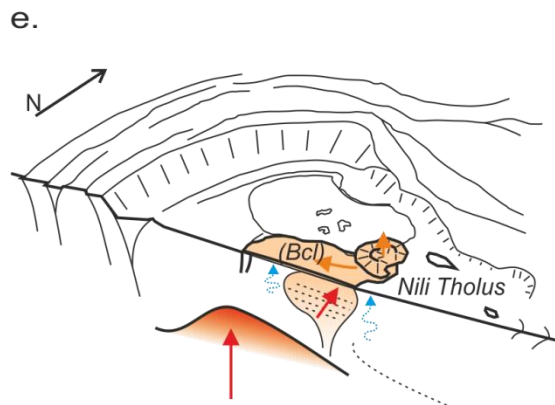
- Silica rich eruption triggered by intrusion
- Formation of Nili Tholus.
- Hydrothermal activity.

g.
N
(Vvu)
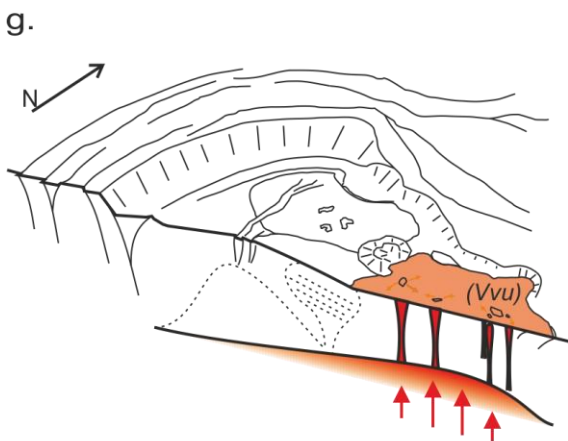
- Basaltic eruption on the eastern caldera floor.
- Rise of melt in the Syrtis Major magma reservoir.

h.
N
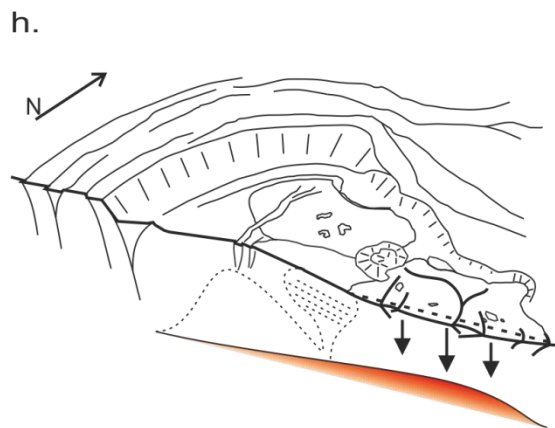
- Subsidence of the eastern caldera floor and of the central caldera complex
- Wrinkle ridge 'pop up' develop
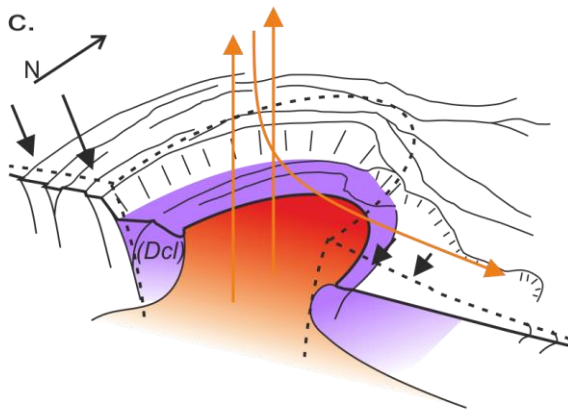
Figure 5.15:

Block diagrams (running right to left, double page spread) illustrating the volcanic history of the Nili Patera. The diagram is ~50 km wide and has 5 times vertical exaggeration. Arrows show the direction of travel for: (orange) erupted products, (red) magma, (blue) hydrothermal fluids, and (black) tectonic or structural movement.

- Trapdoor caldera collapse
- Ignimbrite emplacement or exposure or intrusive bodies

f.
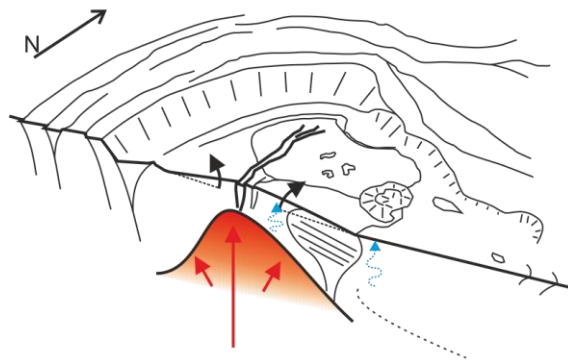
- Formation of the resurgent dome and rotation of the Bright central lava.
- Hydrothermal mounds deposited.

i.
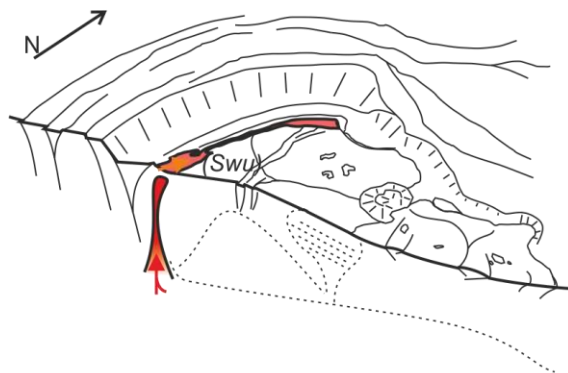
- Eruption along the western caldera rim.
- Olivene xenoliths entrained from previous crystallization events.

231

5.2.5.2 Basement emplacement

The lowest unit of the caldera floor is the bright fractured unit (Bfu). This unit appears to form the basement of the caldera floor; it apparently underlies all other volcanic products and therefore is most likely to be related to other, unseen, underlying sources, or to the formation of the caldera itself. The composition of this unit is unusual for Mars, and correlates with a characteristic 1.2 µm absorption in the reflectance spectra that indicates plagioclase in the absence of other significant mafic minerals. The spatial extent of the unit as mapped geomorphologically matches the extent mapped spectrally, lending support to the morphological mapping. Other units with similar spectral characteristics have been detected across the southern highlands of Mars, mainly in uplifted crater rims, central mounds and sedimentary deposits [*Carter and Poulet*, 2013; *Wray et al.*, 2013]. These units are considered to represent either a granitic or an anorthosite intrusive body, or sedimentary derivatives thereof. This sedimentary derivative interpretation is supported by the locations of the outcrops across the southern highlands. However, at Nili Patera this material is an *in situ* volcanic unit and has undergone no uplift nor contains other sedimentary features, and so we consider a sedimentary interpretation very unlikely. We now consider three alternative formation mechanisms for the bright fractured unit, and their implications for caldera formation:

5.2.5.2.1 An exposed plutonic basement.

The first possibility is that the unit represents an intrusive body, such as the upper regions of a fractionally crystallised magma reservoir exposed from under the caldera surface deposits. Modelling studies [*Wray et al.*, 2013] show that it is plausible to form materials with the same spectral response as Bfu through partial melting of the material that forms the evolved flow unit (Bcl). This makes the assumption that the two units are genetically related, and that the pluton crystallised after the collapse of the caldera. This co-genetic scenario requires the post-collapse caldera floor to have undergone an intrusion over the 40 km wide area under the eastern caldera floor, crystallising at a maximum of 50 m depth beneath material that has subsequently been removed through aeolian processes. There are no indicators of intrusion uplift preserved in this

half of the caldera floor, arguing against a large intrusion of such shallow depth and great lateral extent.

Alternatively, the compositionally evolved, bright fractured unit could pre-date the caldera formation but have been exposed later. In this scenario, the unit crystallised before the formation of the caldera from an earlier evolved magma pulse and is thus unrelated to the *Bcl* unit. Again, a large volume of material would have had to be removed from above the pluton. Other instances of material with this composition [*Carter and Poulet*, 2013] have been identified elsewhere suggesting uplift from depth. But the continuity of features across the caldera's peripheral fault structures suggests no substantial uplift, faulting or removal of material in this setting. A second possibility for the exposure mechanism of the unit is that the pluton was exposed during catastrophic formation of the western caldera. A catastrophic lateral blast might have removed substantial quantities of material over a 40 km wide pluton, with the unit then being re-buried to a depth of ~50 m by later eruptive products, and then re-exposed by aeolian abrasion. However, there is no other geomorphic evidence for wholesale removal of material to form the shallow eastern caldera rim, and it is hard to understand how the current topography of the caldera could fit such a model.

5.2.5.2.2 A welded ignimbrite basement.

The bright fractured unit might be an extrusive or explosive deposit lain down during such a catastrophic explosive event, and therefore might be the remnants of a welded ignimbrite or lava. Intra-caldera ignimbrites are common in terrestrial caldera complexes [Lipman, 1984, 1997]. An ignimbrite deposit might have been emplaced in association with the formation of the western part of the caldera and derived from an evolved magma reservoir similar to the pluton crystallisation hypothesis described above. If the bright fractured unit represents lavas, then these might be associated with the silica-rich [*Christensen et al.*, 2005] evolved flow unit (Bcl) to the north; this is considered in point 3, below.

The bright fractured unit hosts a complex fracture network. The type of fracturing varies with location and depth into the unit. The fractures have a crisp morphology, and layers within the unit have been eroded to form numerous metre or sub-metre scale blocks (Figure 5.7a). These blocks have eroded out from the discontinuous layering observed in the upper part of the unit, and the layering shows gradational composition change into the overlying unit (Figure 5.7b). In addition, the possible outcrops of this unit in the resurgent dome and outside of the caldera reverse faults suggest that it was once a spatially extensive unit, variable in thickness and friable in its thinnest exposures. These textural features are all seen in explosive volcanic deposits such as the Tocanao and Atana ignimbrites in Chile associated with the La Pacana Caldera [*Guest*, 1969; *de Silva and Francis*, 1989; *Lindsay et al.*, 2001] (Figure 5.16). In this analogue, the erosional exposure shows very similar sets of features as a direct consequence of its genesis. Such fabrics are all commonly seen in welded ignimbrite units, as is a transition to a more mafic (greater than 5% mafic minerals in this case) composition in the upper parts of the unit, deposited later in the eruption [*Branney and Kokelaar*, 1992, 2002]. Ignimbrites are commonly deficient in mafic minerals [*Druitt and Sparks*, 1984; *Gardeweg and Ramírez*, 1987; *Lipman*, 2000]. Eruption and emplacement mechanisms depend fundamentally on magma composition (cf. viscosity) and volatile content, although the reported composition and model partial melt from other local rocks [*Wray et al.*, 2013] are consistent with this formation mechanism. This mechanism is also supported by the implied effects of volatiles. Water within a magmatic system will not only enhance the evolution of magma from a basaltic starting point towards the observed felsic composition, but volatiles drive explosive volcanic eruptions as they are exsolved from the magma when pressure decreases. However, this hypothesis raises additional questions: was the vent (or vents) under the western part of the caldera, or along the western ring fault, and how has the observed pattern of the outcrop been emplaced with respect to the trapdoor-style caldera collapse and the ensuing interpretation of asymmetric magma chamber drainage?

If this unit is an ignimbrite, then the eruption that formed the deposits drove the initial stages of caldera collapse, but pre-dates the latter subsidence of the eastern caldera floor. The putative ignimbrite unit collected and is locally thickened in the topographic confines of the nascent central caldera complex, as well as deposited outside the caldera, but buried subsequent volcanic resurfacing. This permitted the unit contained within the early stages of caldera subsidence to be exposed after further subsidence and erosion of the caldera floor. The preservation and topographic scenario suggests that a vent would have been beneath the western caldera floor or more likely on the ring fault of the western caldera floor, and is now either auto-obliterated or located elsewhere within the central caldera complex. Because there is no evidence to support vents elsewhere, we prefer the first suggestion that one or more vents were located at the main reverse faults; these faults would have provided a pathway for ascending magma and driven subsidence.

If a violent eruption took place in the western part of Nili Patera, this part of the caldera would likely have a weaker base of the caldera roof where stress was concentrated during caldera formation. Consequently, it may be weaker than the eastern caldera portion, permitting preferential ascent of magma in this region during any subsequent magmatism. This is consistent with the location of the resurgent dome within the western half the caldera [*Lipman*, 1997]. This scenario is also tectonically consistent with the 'butterfly body' inflections in the normal faulting, dividing the caldera into two distinct regions.

The important linking implication in the two formation hypotheses presented thus far is that magmatic evolution to form differentiated intrusive or extrusive material (probably through fractional crystallisation) must have occurred in the upper part of the crust beneath Syrtis Major. The third hypothesis is different in that it explores the possibility that the bright fractured unit (Bfu) is part of the effusive volcanism that post-dates caldera formation.

150 m

150 m
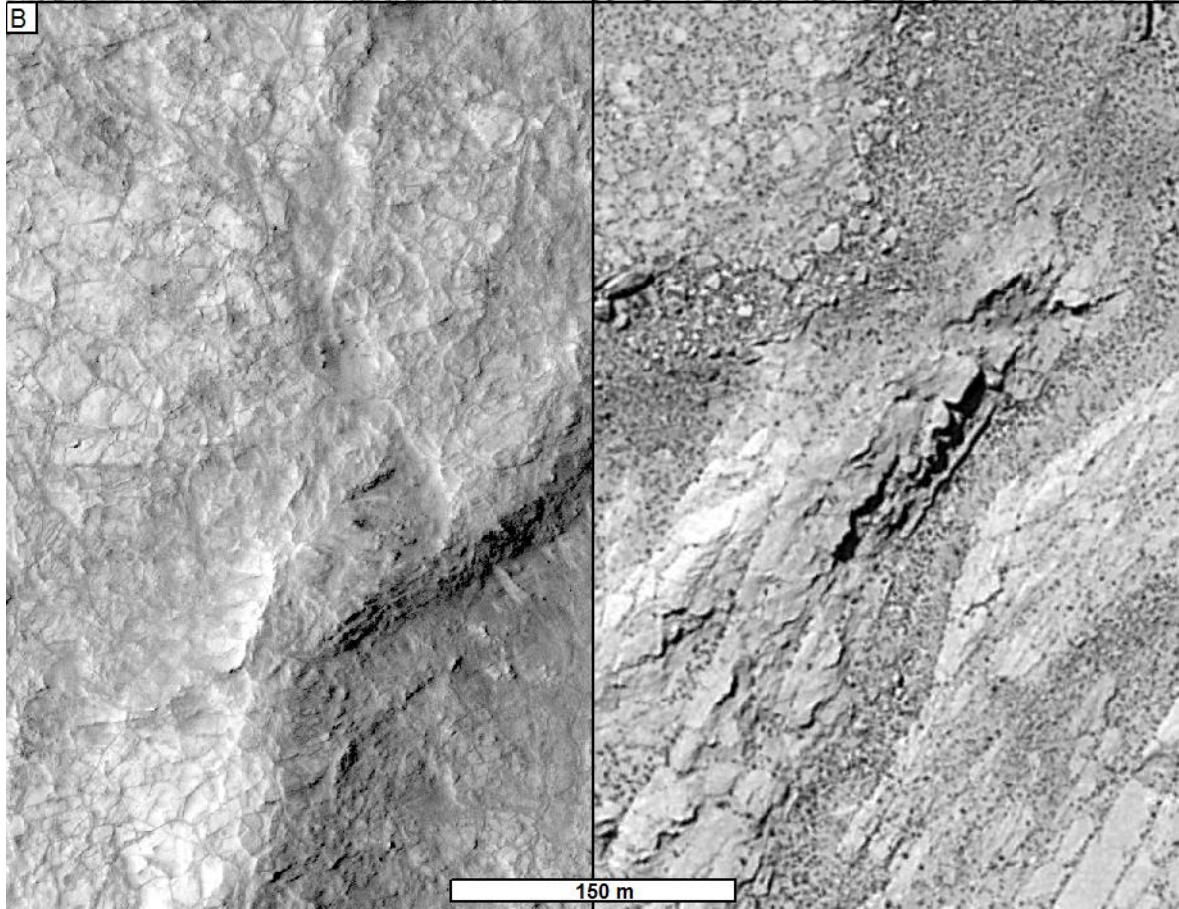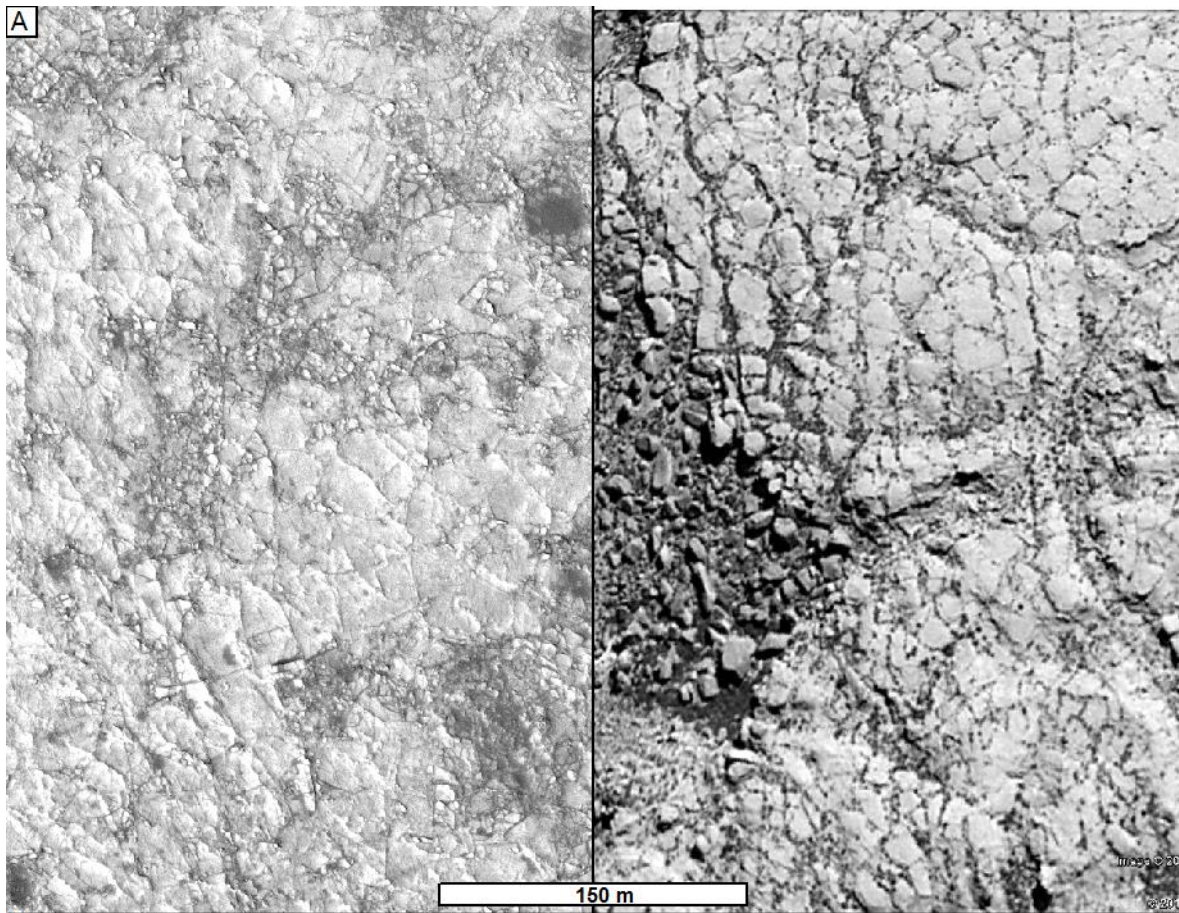
Figure 5.16:

*Two comparisons between locations in late tertiary Tocanao and Atana ignimbrites associated with the La Pacana caldera, Chile (close to 67° 52' W, 23° 07' S), right hand panels [*Gardeweg and Ramírez*, 1987;* de Silva and Francis*, 1989;* Lindsay et al*., 2001]. Locations within the bright fractured unit (Bfu) in Nili Patera, left hand panels. (a) Polygonal fracture patterns and blocky erosional fabric. (b) Undulating topography, internal layers and polygonal fracture patterns of the bright fractured unit (Bfu) and Atana ignimbrite.*

5.2.5.2.3 Exposed core of the evolved unit.

The third possibility is that the bright fractured unit is not related to caldera formation at all, and is instead the same eruptive unit as the evolved flow unit. In this scenario, when the evolved flow unit and the Nili Tholus formed, the evolved lava filled the eastern portion of the caldera. Subsequently, all but the portion of the unit uplifted by the resurgent dome became buried by the overlying variegated volcanic formation (Vvu). This model would explain the outliers of evolved composition noted by Christensen [2005], as well as their extent beneath the variegated volcanic unit. The compositional differences between the evolved flow unit and the bright fractured unit could be reconciled [*Horgan*, 2013] by considering the very different surface properties of the two areas: the lava surface will be very rough, with a high glass component, and will also contain aeolian material trapped into the rough surface; whereas the bright fractured unit is smooth and dust-free and, probably, will have a different crystal fabric. This difference can cause significant alterations in the spectral response of a surface, as measured in remote-sensing data [*Serventi et al.*, 2013; *Carli et al.*, 2014a, 2014b].

However, this idea does not appear to be consistent with the stratigraphy. Firstly, at the eastern foot of the resurgent dome, the bright fractured unit appears to underlie the cratered caldera floor unit, which in turn is seen to directly underlie the evolved flow unit; although the junction between these unit boundaries is partially obscured by dunes. Secondly, this scenario doesn't offer an explanation for the bright friable outliers on the interior ridges, pre-caldera lavas and disrupted lava unit.

Here, we have considered various mechanisms for the emplacement of the bright fractured unit, including a large explosive emplacement, the exposure of a shallow intrusion, and the differential erosion of the evolved flow unit. With the evidence available, we reject the late effusive hypothesis and consider the first two hypotheses to be more plausible; both derive from a fractionally crystallised magma reservoir. Given the structural, topographic and spatial characteristics of the bright fractured unit, the welded intra-caldera ignimbrite is our favoured hypothesis. A final differentiation between these mechanisms might, however, only be possible with rover-scale observations of texture and geochemistry.

5.2.5.3 Volcanism within Nili Patera

Since the establishment of the Nili Patera floor, it has been overprinted by several phases (both discrete and overlapping) of volcanic and tectonic events.

The first phase of events includes the formation of the northern basaltic (Prl) and bright central lava (Bcl) units with peri-contemporaneous intrusion causing resurgent dome formation (Figure 5.15c–f). Crater size-frequency statistics (Table 5.1) show the model ages for the Prl and *Bcl* units are within error of each other. Because of the small number of visible craters, and the small counting areas, strong significance cannot be placed on these absolute ages. Nevertheless, the results are consistent with these events having taken place geologically close together in time, but suggest that the northern basaltic unit may be slightly older; a result supported by the mapping and inferred stratigraphy.

Stratigraphically, the first event in this phase is the emplacement of the basaltic lavas (Prl) and the formation of small northwest–southeast striking graben-like fault systems (Figures 5.12a and 5.15d). The faults extend into the older caldera wall units, but are contemporaneous with the basalts: they cross-cut the lavas, but are also obscured by them closer to the vent structures that trend along the tectonic features at the eastern caldera floor structural bounds. Tectonic activity on this trend had ceased prior to the formation of Nili Tholus and the resurgent dome.

The second tectonic trend within this phase of activity and affecting these units is associated with the resurgent dome and the formation of its axial rift (Figure 5.15e). Resurgent dome formation has rifted the basaltic unit (Prl) and uplifted both the basaltic (Prl) and bright central lava (Bcl). However, small faults parallel to the rift axis on the flanks of the resurgent dome are flooded by the evolved flow unit (Bcl; Figures 5.12b and 5.15e). Therefore, these faults must have formed before the main resurgent dome uplift event – unless the evolved flow formed on the flank of the resurgent dome, which we consider unlikely because of the consistent slope and lack of topographically high vents. Instead there was uplift and rotation of the evolved flow unit due to the resurgent dome formation (Figure 5.15f). This implies that rifting in what was to become the resurgent dome started prior to the emplacement of the evolved lava, which, in turn, was emplaced before the final uplift of the western caldera floor that formed the resurgent dome.

The tectonic relationships, the change to a more silica-rich lava composition and the change in eruptive style (indicative of increased magma viscosity), all suggest that this part of the magma reservoir became partially crystallised. Because these events occurred within the dating measurement errors of each other, it is possible that the same magma reservoir produced both eruptive units and that after the basaltic eruption (Prl) there was a hiatus in effusive activity, during which the magma reservoir evolved due to partial crystallisation. However, it is also possible that the magma reservoir that generated the bright central lava (Bcl) was unrelated to the generation of the pre-rifting lava (Prl). Subsequently, the onset of the western caldera floor intrusion (Figure 15d and e) triggered the eruption of an evolved magma reservoir, leading to the evolved flow unit. The 300 m high evolved cone, Nili Tholus, in the eastern portion of the caldera, formed in association with the evolved flow unit. Taken together, this sequence of events implies significant activity in the magmatic plumbing beneath Nili Patera and the central caldera complex.

The second major phase of activity (Figure 5.15g–i) occurred during an extensive time window, after the formation of the evolved flow unit *(Bcl)* but before the exposure events that revealed the bright fractured unit, Bfu (Table 5.1). This phase of activity comprised two volcano-

tectonic events probably separated by a period of erosion: firstly (Vvu; Figure 5.15g), a 10–20 m thick, flow field emanated from low shields and a number of small cones in eastern Nili Patera. The flows embay the base of the resurgent dome, on-lapping the evolved flow. The unit is cross-cut by the wrinkle ridge 'pop-up' structures in the centre of eastern Nili Patera, and by the thrusts at its margins (Figure 5.15h). The temporal separation, if any, of these events is unclear, but the melting event that led to lava formation did not trigger eruption of the western caldera floor resurgent dome intrusive body, suggesting that it had cooled, stabilising the resurgent dome, before the eastern melting event that resulted in the emplacement of the variegated volcanic unit (Vvu). The variegated volcanic unit has experienced intense aeolian erosion, perhaps because of its location: prevailing winds across Syrtis Major from the northeast are topographically focused here. A maximum of 40 m depth of material has been eroded from the unit, as evidenced by the elevation change between it and the surface of the wind-scoured caldera floor units.

The second eruptive unit in this phase of activity created the smooth western unit (Swu) on the western caldera boundary (Figure 5.15i). This unit is smooth, with significantly fewer craters or crater remnants than any other surface in Nili Patera. This extrusive unit probably occurs at this location because it formed as a result of rising magma exploiting structural weakness along the caldera floor boundary faults. This positioning also supports the interpretation of the olivine-rich composition as contamination from xenoliths [*Clague*, 1987] entrained during migration, rather than representing the bulk chemistry of the lava; although this cannot be definitively demonstrated. The temporal relationship between this olivine-rich extrusive event and the final phase of wrinkle-ridge tectonics (pop-up structures [*Watters*, 2004]) in the eastern caldera floor cannot be easily assessed.

The 'pop-up' structures within the eastern caldera floor consist of two ridges, intersecting at ~60°. The ridges, and the floor between them, are uplifted relative to the topography to the west (Figures 5.14 and 5.15h). The arched ridge-profile and small peripheral ridges suggest an anticline, with thrust faults at the extent of the limb (Figure 5.4). These faults are part of a larger trend

which can be traced out of the structural bounds of Nili Patera, and is co-linear with similar structures to the south (67° 23′ E, 8° 22′ N), within the wider Syrtis Major central caldera complex. We interpret these features as providing evidence that the eastern caldera floor subsided while caldera evolution continued. The mechanism for the subsidence requires a change in pressure regime under the central caldera complex as a result of a change in volume. This late stage of local subsidence may well be a tectonic expression of contraction of a cooling cumulate body at depth after the cessation of magmatic activity. Gravity studies of the wider Syrtis Major central caldera complex suggest that contraction could account for a maximum of 300–400 m (15–20%) of subsidence [*Kiefer*, 2004].

The observations and interpretations made here, pertaining to the volcanism and tectonism expressed on the caldera floor, demonstrate several episodes of activity, including intrusion, eruption and subsidence. These suggest that there was injection of melt into, or melt migration within, the Syrtis Major plumbing system throughout the evolution of Nili Patera. Not all of this melt transport is expressed extrusively. The compositionally distinctive evolved flow unit provides evidence for this magma reservoir probably having evolved in isolation from other magmatic plumbing under the wider Syrtis Major central caldera complex. Its eruption was triggered by the injection of the melt that formed the resurgent dome below the western portion of Nili Patera (Figure 5.15e and f). The episodes of crustal melt evolution were episodic and temporally and/or spatially isolated.

5.2.5.4 Implications for the evolution of Syrtis Major Planum and highland patera-style volcanoes

5.2.5.4.1 Implications for the underlying highland crust.

The main implication is that, during the late Hesperian, the crustal conditions were suitable for at least one instance of silicic melt to occur and leading to ignimbrite emplacement. *Francis and Wood* [1982] outline mechanisms by which silica pyroclastic eruptions form. From these, we discount kimberlites [*McGetchin and Ullrich*, 1973], melting of granite crust [eg; Hawkesworth et

al., 1982] and direct magma–water interaction, on the basis of caldera morphology, evidence of basaltic composition in earlier eruptive phases [*Mustard et al.*, 1993], and on the basis of the morphological differences between the Syrtis Major flank deposits and the highland patera in east Hellas [*Greeley and Crown*, 1990; *Crown and Greeley*, 1993]. This leaves dehydration of hydrous minerals [e.g. Thorpe et al., 1979] as the primary source for volatiles, and differentiation within a large magma chamber as the driver of compositional changes in this magmatic system. Of these mechanisms, it is noted that the resulting SiO_2 content correlates to crustal thickness [*Coulon and Thorpe*, 1981], meaning that the crust was thickened and ground ice was less abundant at this latitude in the late Hesperian relative to conditions during the emplacement of the true highland patera volcanoes.

A further implication of caldera formation is that hydrated minerals are abundant in the highland crust or mega-regolith underlying Syrtis Major Planum. Nili Patera and the central caldera complex have undergone continual deformation through subsidence throughout their evolution. Most of the volume loss to erupted products happened at the beginning of the caldera's history. However, subsidence also occurred after the formation of the caldera across the wider Syrtis Major central caldera complex area (Figure 5.1). Volume has therefore been lost from the caldera system, as evidenced by subsidence, both during and after the major eruptive events. Caldera subsidence greater than the volume of erupted units can result from the deformation of a pseudo-viscous complex within the edifice [*Roche et al.*, 2000; *Merle et al.*, 2010]. In this case, Nili Patera might be considered a 'hydrothermal' caldera [*Merle et al.*, 2010]. This in turn implies that the core of Syrtis Major comprises material more ductile and deformable than the surface lavas, such as an ice-rich decollement [*Mangold et al.*, 1998]. Because the deformation was ongoing significantly after the time when thermomechanical weakening would have permitted ductile deformation associated with magmatic processes. This inference is additionally supported by (i) the required availability of crustal water to form hydrothermal deposits within Nili Patera [*Skok et al.*, 2010a] and (ii) by spectral evidence of a hydrated mineral assemblage (underlying the

peripheral lavas) recording environmental change [*Skok et al.*, 2010b; *Ehlmann and Mustard*, 2012; *Carter et al.*, 2015]. These hydrated mineral assemblages have been suggested to be forming a continuously deformable layer [*Glotch and Rogers*, 2013; *Schwegman et al.*, 2015] from which evolved compositions have been excavated [*Bandfield*, 2006]; a conclusion consistent with the style of caldera formation. We suggest that repeated intrusion, assimilation and partial melting of a ductile, hydrated Noachian highland crust, drove magmatic evolution towards the compositions observed now at Nili Patera. The same processes drove caldera formation and caused the caldera to develop its position within, or below, the edifice.

5.2.5.4.2 Implications for habitability.
The volcanic activity within Nili Patera continued longer than suggested by the formation age of Syrtis Major based on global mapping [*Tanaka, et al.*, 2014a], an observation consistent with dating of individual flows on Syrtis Major's flanks [*Platz et al.*, 2014]. This implies long-lived, intermittent magmatic processes and a supply of melt (and an associated, elevated geothermal gradient) over an interval of ~ 0.5–1 Ga. Although the duration and episodicity of volcanism are poorly constrained, in combination with the inference of a hydrous subsurface, this has important implications for subsurface habitability. Deposits within Nili Patera may provide access into a habitable enclave, formed in the Noachian crust, maintained by volcanically driven hydrothermal circulation, and protected from the surface environment by the relatively thin lava shield [*Hiesinger and Head*, 2004]. Material from such a habitat might then have found its way to the surface, as part of the hydrothermal deposits found in Nili Patera. These deposits could therefore contain evidence for biomarkers, if life ever existed within such a habitat, and as such the Nili Patera could provide an important target for future exploration.

5.2.5.4.3 Implications for highland patera-style volcanoes
Syrtis Major Planum, containing Nili and Meroe Patera, is a volcanic plain with a central caldera complex [*Carr*, 1973; *Greeley and Spudis*, 1981; *Plescia*, 2004]. Although Syrtis Major is dissimilar in its flank deposit morphology to Tyrrenus and Hadriacus Mons situated to the east of Hellas

[*Greeley and Crown*, 1990; *Crown and Greeley*, 1993; *Williams et al.*, 2007, 2008], its flank deposits are more similar to those of Amphitrities Patera, situated within Malea Planum to the south of Hellas [*Williams et al.*, 2009a] and to Hesperia Planum, northeast of Hellas.

Similarities between the patera within Syrtis Major and those within Malea Planum can also be drawn in terms of topographic and spatial characteristics. The floors of the calderas (patera) lie below the mean elevation of the volcanic plains that surround them, and the plains are cross-cut by similar networks of wrinkle ridges. Crucially, each of Hesperia Planum, Malea Planum and Syrtis Major Planum lie on the edge of giant impact structures; Hellas Planitia for Hesperia Planum and Malea Planum, and Isidis Planitia for Syrtis Major. Consequently, understanding the formation and evolution of Nili Patera has implications for the development of other volcanic edifices situated in the martian highlands. Nili Patera is a good study example, because erosion within Nili Patera provides a window into Syrtis Major, whereas similar examples in Malea Planum are overprinted by periglacial landforms [*Williams et al.*, 2009a]. We postulate that the highland paterae, and their associated volcanic plains, formed after the martian highland crust had thickened sufficiently to inhibit magma ascent, impeding melt advection in widespread areas. However, preferential pathways remained available in crustal-scale normal faults and isostatic-compensation stress-structures around giant impact basins [*Peterson*, 1978; *Schultz*, 1984; *Wichman and Schultz*, 1989]. Hence, magma ascent was favoured in zones circumferential to giant impact basins, so the highland patera-style volcanoes, along with their co-located volcanic plains, formed in these locations in the late Noachian to early Hesperian [*Williams et al.*, 2007, 2008]. This is different to other areas of the highlands, where melt would have stalled at depth, resulting in felsic intrusions now seen uplifted in impact crater rims [*Wray et al.*, 2013].

During planum-building volcanism, the raised geothermal gradient associated with the advection of hot magma to the plains-forming eruptions would have eventually resulted in conductive heating of the surrounding crust [*de Silva et al.*, 2006] and hence a reduced density-contrast between melt and crust. This would have led to magma bodies stalling, and the

consequent partial melting of the Noachian crust underlying the planums. These hot intrusions would have thermomechanically weakened the crust, allowing the development of calderas such as Nili Patera. By extension, the 'habitable enclave' arguments made for Syrtis Major Planum are also likely to be valid for the subsurface region of these other highland-patera calderas.

5.2.6 Conclusions for the history of Nili Patera

- Nili Patera formed between 3.28 (+0.80, −0.13 Ga) and 3.1 (+0.13, −0.22) Ga. The caldera formed initially by trapdoor collapse. The caldera formed in a volcano-tectonic depression caused by thermomechanical weakening of the highland crust during underlying intrusion and magma advection. Later in the caldera's history, additional subsidence occurred, probably associated with a ductile subsurface layer.

- The bright fractured unit (*Bfu*) that underlies all later volcanic units was emplaced or exposed during caldera formation. This is either exposed parts of a felsic pluton, crystallised prior to caldera collapse, or the remnants of a welded ignimbrite formed during trapdoor collapse. These processes were probably driven by volatiles. The volatiles were probably incorporated into the magma chamber by assimilation of hydrated Noachian crustal deposits, and by exsolution during fractional crystallisation of the magma body when stalled in the highland crust (which was thickening during the late Hesperian). Both scenarios derive from a felsic magma reservoir fed by partial melting of the Noachian highland basement.

- There have been five episodes of volcanic activity within Nili Patera. (1) A basaltic unit erupted from tuya-like vents in the north of the caldera. (2) Nili Tholus and the bright central lava unit (*Bcl*) were erupted from an isolated magma chamber; potentially triggered by the intrusion that resulted in the formation of a resurgent dome. (3) Intrusion under the western caldera floor that formed a ~300 m high elliptical dome. (4) In the eastern caldera floor, a basaltic unit was emplaced from a small number of small cones and shields. This unit has been eroded through aeolian abrasion and mobilised into the active dune field. (5) The youngest volcanic activity located on the western caldera ring fault has a distinct olivine-bearing

spectral signature, perhaps caused by xenoliths dredged from a crystallised magma reservoir system.

- The evidence of a ductile layer beneath Syrtis Major's lava shield, partial melting developing evolved compositions and hydrothermal deposits, imply interaction with subsurface volatiles throughout the Nili Patera's history. The convergence of evidence for water and hydrated materials in the presence of an elevated geothermal gradient over an extended period of time raises the possibility of a habitable environment. Such a subsurface enclave of crustal habitability would be sampled by hydrothermal deposits in Nili Patera and should be considered as an astrobiological target for future *in situ* exploration.

- Conclusions drawn from the exposed units at Nili Patera and the broad similarities to the topographic and spatial distribution of other highland paterae imply a similar causal mechanism and astrobiological potential for those edifices.

5.3 Supporting information

The Geological History of Nili Patera, Mars

P. Fawdon[1*], J. R. Skok[2], M.R. Balme[1], C.L. Vye-Brown[3], D.A. Rothery[1] and C. J. Jordan[4]

[1]Department of Physical Sciences, The Open University, Walton Hall, Milton Keynes, UK. MK7 6AA;

*peter.fawdon@open.ac.uk

[2]Department of Geology & Geophysics, Louisiana State University, Baton Rouge, LA 70803

[3]British Geological Survey, Murchison House, West Mains Road, Edinburgh, UK. EH9 3LA

[4]British Geological Survey, Nicker Hill, Keyworth, Nottingham, NG12 5GG

5.3.1 Introduction

This supporting information contains: (i) An additional figure showing the areas from which crater counts are taken, and, (ii) A map sheet containing: a 1:250000 version of the geological map of Nili Patera, together with a cross-section, and a summary of the description, stratigraphy, and interpretation of each unit and crater count results for those units.
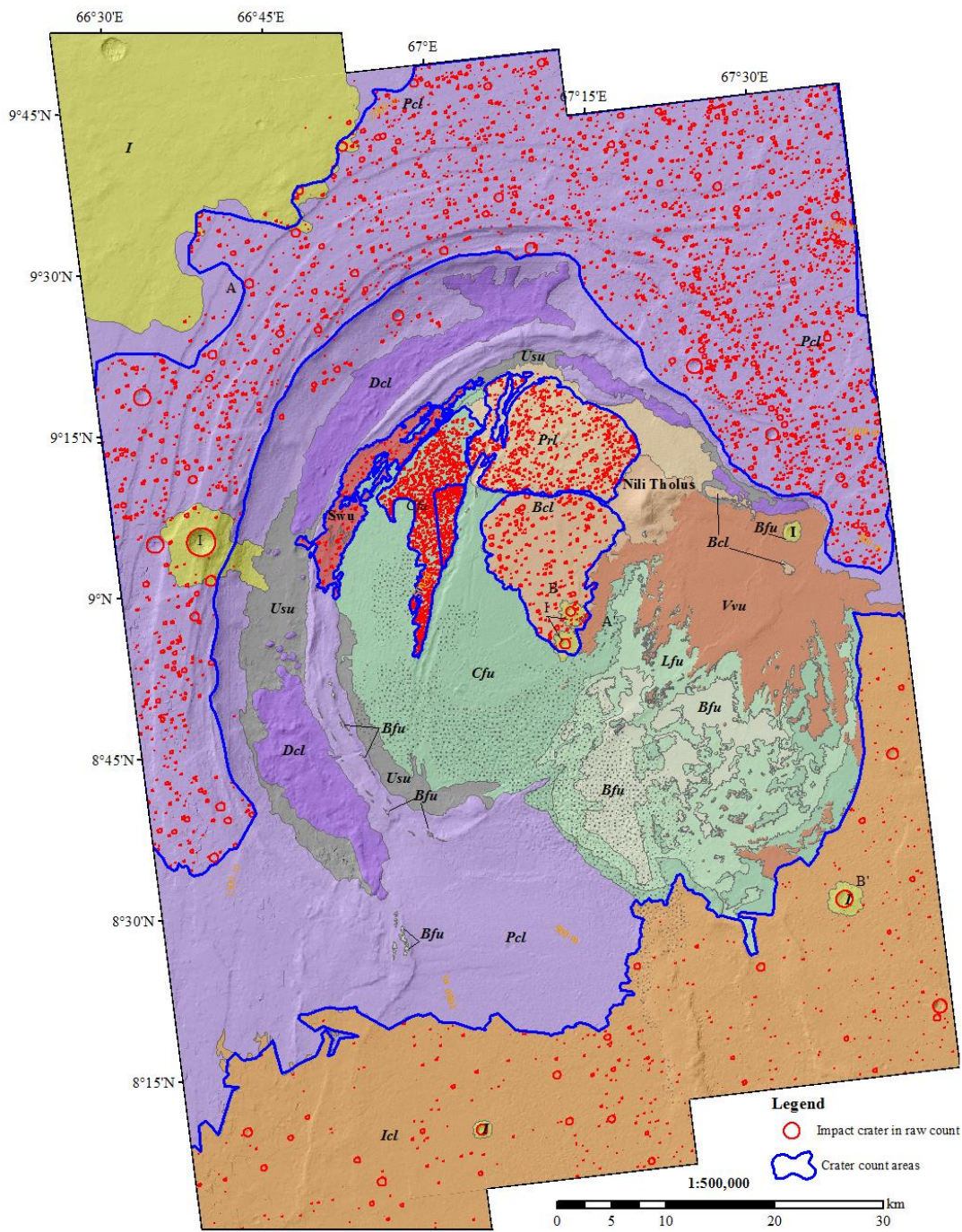
Figure 5.17 (S1)

Map showing all the craters counted in the study, and the areas from which crater size-frequency distribution samples were taken. The coloured units are the same as in figure 2 in the main text. The sampled areas do not correspond to the whole of mapped units because we wanted to consider only the formation ages, and resurfacing processes were observed to have not acted evenly across the small area of the mapped units (see Warner et al., [2015] for discussion on unit sizes).

Chapter 6: Meroe Patera

6.1 Introduction

This chapter details observation of Meroe Patera located in the south east of the Syrtis Major central caldera complex (SMCCC, Figure 6.1) and investigates evidence relevant to the discussion of Chapter 6 from the SMCCC. This includes: (i) observations that were made outside the boundary of Nili Patera map which have additional implications for the geological history of the Nili Patera caldera, (ii) a description of the units in the Meroe Patera caldera: Nili Patera's "sister caldera" within the wider SMCCC to establish a comparison between the two calderas, and (iii) an examination of instances of the materials which are either textually associated with the Bright fractured unit (Bfu; map sheet 2, late Hesperian lower Caldera floor unit; $lHlCf_{n/m}$, Map sheet 1) or compositionally comparable to the Bright central lava (Bcl, Map sheet 2; Amazonian bright caldera volcanic unit $Abcv_n$ Map sheet 1).

Meroe Patera is a circular caldera 45 km across, set into the interior slope of the central caldera complex depression (Figure 6.1). The caldera has an asymmetric rim, from 0 to 1 km above the caldera floor [*Hiesinger and Head*, 2004; *Plescia*, 2004]. Previously it had been suggested that the caldera is older than Nili Patera, possibly as old as 3.7 Ga [*Werner*, 2009; *Robbins et al.*, 2011] as opposed to ~3 Ga established for the formation of Nili Patera (Section 6.5).

This chapter uses mapping adapted from Map Sheet 1 (Figure 6.2), supplemented by three CTX DTMs and available HiRISE data. The additional observations, beyond that relevant to the scale of Map Sheet 1 are described, and units recoloured, with respect to similar units studied in more detail at Nili Patera (Map Sheet 2). The chapter then discusses the volcanology prior to the formation of the Nili and Meroe calderas, the evolution of Meroe Patera relative to the evolution of Nili Patera, and volcanism in the axis of the central caldera complex.
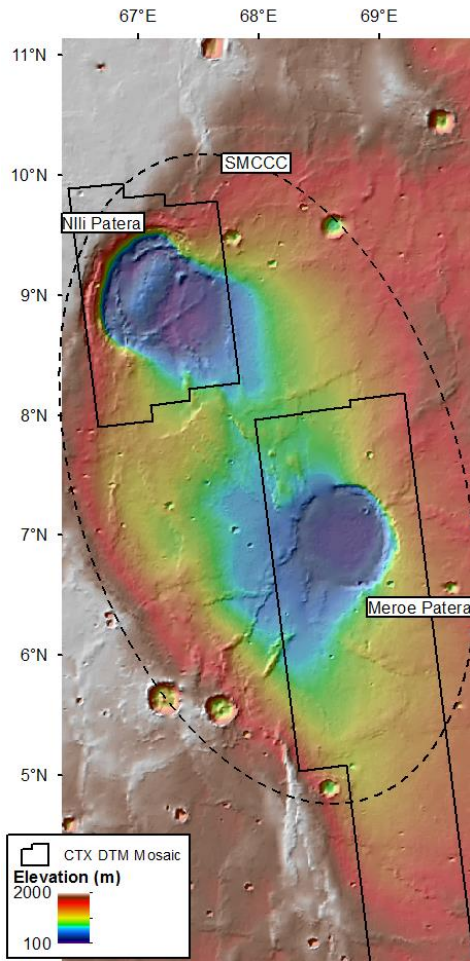
Figure 6.1:

The location of Meroe Patera within the Syrtis Major Central Caldera Complex (SMCCC). MOLA topography overlain on hill-shaded MOLA topography. The black lines indicate the areas covered by CTX DTM mosaics

6.2 Data and methods

In addition to the data types described in Chapter 3, observations for this section summarised by Figures 6.2 and 6.3 use three Mars Reconnaissance Orbiter (MRO) [*Zurek and Smrekar*, 2007] ConTeXt camera (CTX) [*Malin et al.*, 2007] digital terrain models (DTMs) and orthorectified images from three CTX image pairs as base layers. High Resolution Imaging Science Experiment (HiRISE) [*McEwen et al.*, 2007] data have been used where available for detail when appropriate.

Map Legend

Cross-sections: A - A', B - B'   1:500,000

Surficial units

- Scarps
- Contact - Confident
- Contact - Approximate
- Contact - Infered
- Contact - Gradational
- ▲ Vent* (larger = more important)

Surficial units

Ejecta *(E)*

Post-caldera formation volcanism

Amazonian late volcanic unit *(Alv_m)*

Amazonian early volcanic unit *(Acv_m)*

Caldera formation deposits

late Hesperian upper Caldera floor *(lHuCf_m)*

late Hesperian lower Caldera floor *(lHlCf_m)*

Pre-caldera formation lavas

Hesperian volcanic channel unit *(Hvc)*

Pre-caldera lava *(Pcl)*

Figure 6.2:

Extract from Map Sheet 1 modified to show the units identified in Meroe Patera and re-coloured for comparison to match Chapter 5 and Map Sheet 2. The units have been coloured to match the most similar units in the sequence of caldera evolution from Nili Patera. Divisions in the pre-caldera lavas presented in Chapter 4 and Map sheet 1 have been removed.

6.2.1 Topography and visual analysis

A mosaic of three digital elevation models (DTMs) have been generated from six CTX images (D08_030500_1866_XI_06N291W, D10_030922_1866_XI_06N291W,

D05_029142_1857_XI_05N291W, D05_029287_1857_XI_05N291W,

D06_029432_1857_XI_05N290W, and D06_029722_1857_XI_05N290W) using the method of Kirk

et al. [2008] as described in Section 5.2.3.1. The output from SocetSet® was an 18 m/pixel DTM.

In addition to the DTM, three orthorectifed images where generated;

D10_030922_1866_XI_06N291W, D05_029287_1857_XI_05N291W and

D06_029432_1857_XI_05N290W. After manual geo-referencing of

D10_030922_1866_XI_06N291W and D06_029432_1857_XI_05N290W to image

D05_029287_1857_XI_05N291W, the images and DTMs were mosaicked in ArcGis10.1. This base

layer was used in conjunction with the THEMIS base map to compile the summary map of Meroe

Patera (Figure 6.2). To complement the CTX base layer, some HiRISE images, publicly available at

the time of writing, have also been examined.
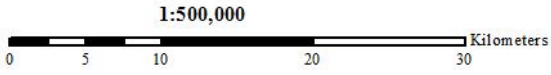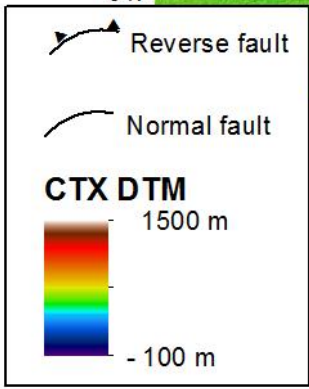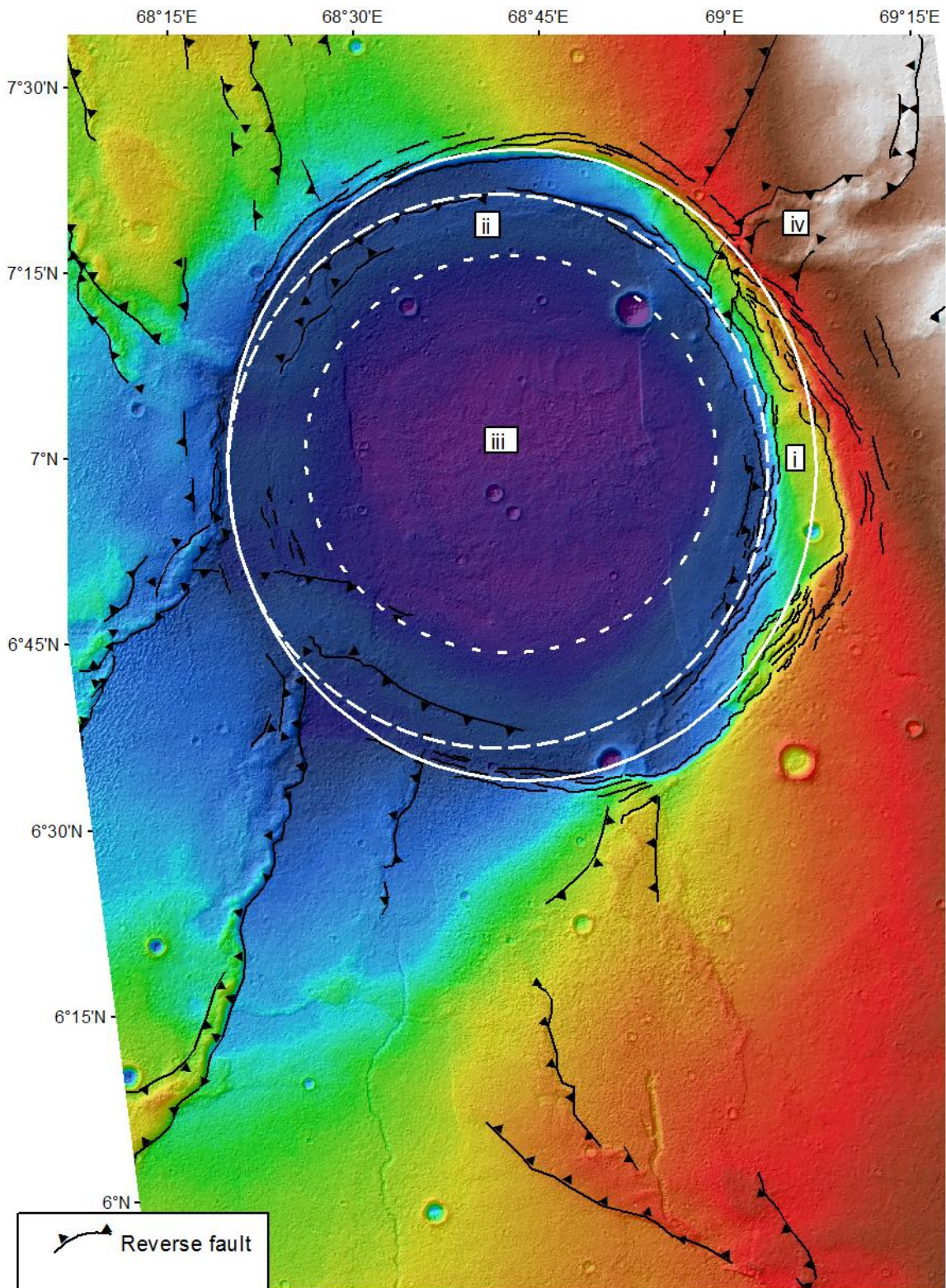
Topography of Meroe Patera. A mosaic of three CTX DTMs gridded at 18 m/pixel (image pairs: D08_030500_1866_XI_06N291W and D10_030922_1866_XI_06N291W, D05_029287_1857_XI_05N291W and D05_029142_1857_XI_05N291W, D06_029432_1857_XI_05N290W and D06_029722_1857_XI_05N290W). Normal and reverse faults are also shown. Three identified stages of caldera collapse are identified: inside the solid line, Meroe Patera caldera floor unit I (MPcfu I) (i); inside the dashed line, Meroe Patera caldera floor unit II (MPcfu II) (ii); and inside the spaced dashed line, Meroe Patera caldera floor unit III (MPcfu III) (iii). (iv) shows a wrinkle ridge, formed in the stage 1 caldera floor and truncated by subsequent normal faulting and resurfacing.

6.3 Observations of Meroe Patera

Meroe Patera is the second largest caldera within the SMCCC and is located at the southeastern end of the central caldera complex (Figure 6.1) [*Hiesinger and Head*, 2004; *Plescia*, 2004]. It is 45 km in diameter and the floor is at ~200 m elevation relative to MOLA datum. This is approximately ~1000 m below the highest point at the eastern rim of the caldera. Although the mapping (Figure 6.2) is presented only at the resolution of planum-wide mapping, three CTX DTMs and orthorectified images have been produced and mosaicked (Figures 6.3 and 6.4; sections 3.1.3.3 and 5.2.3.1). This allowed the caldera's shape to be constrained at the same scale as Nili Patera, and for a better understanding of their comparative evolution to be made.

The following sections detail units found within Meroe Patera. The map (Figure 6.2) uses the same names for the units as those in the published Nili Patera study (Section 6.2.4; Map sheet 2 and Chapter 5). This produces a stratigraphy of units 'in the style of' units found in Nili Patera. This has been done to permit comparison between the evolutions of each caldera. The locations of the unit-type-examples are shown in Figure 6.4.
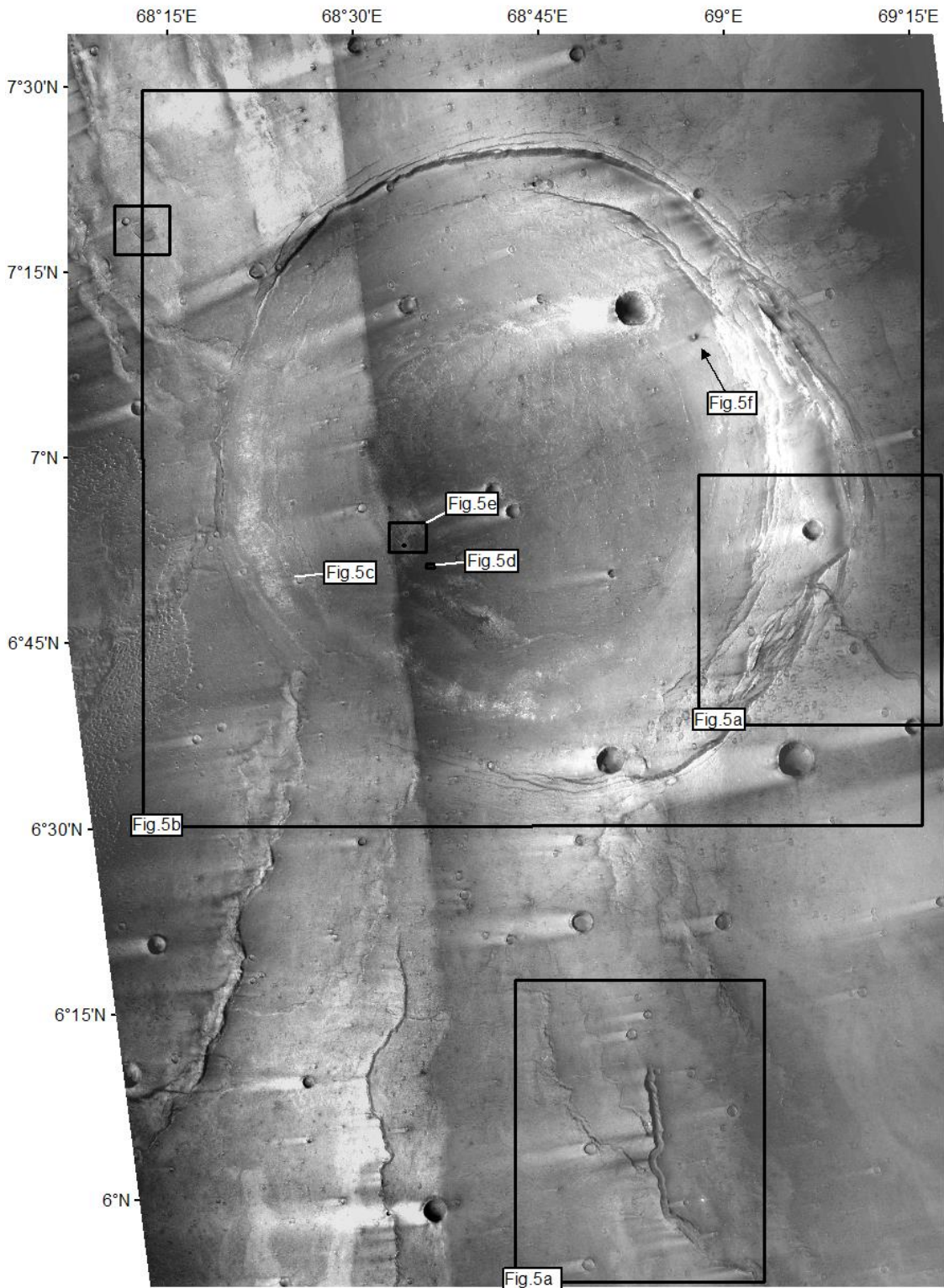
Figure 6.4:

Meroe Patera CTX mosaic and the location of subsequent figures. CTX images D10_030922_1866_XI_06N291W, D05_029287_1857_XI_05N291W and D06_029432_1857_XI_05N290W.

6.3.1 Physiography

Physiographically, Meroe Patera (Figure 6.3) comprises two components. The first is the southern part of the SMCCC elliptical depression which forms a gentle slope across the area of the caldera from 1500 m in the east to 500 m in the northwest. The otherwise uniform local slope of ~0.7° is interrupted by topographic wrinkle ridges. The ridges, which accommodate shortening of the surface associated with the formation of the depression, can be seen to the north-northwest and south-southwest of Meroe Patera. Meroe Patera is set into the slope of the central caldera complex depression. This regional slope forms the rim of the caldera with a relief of ~1000 m from the caldera floor in the east, decreasing to the west where the caldera rim has only ~100 m of topographic expression and associated faults have been masked by later deposits.

The second component is the caldera floor. The floor is approximately circular and formed of three tectonic sections. The oldest is at the eastern margin of the caldera floor and is a sloping circumferential bench ~3 km across. This has a maximum relief of ~400 m in the east, sloping down to the north to match the elevation of the local caldera floor (Figure 6.3iii). The second tectonic section is an aureole ~5–10 km wide (Figure 6.3i) and the third is an inner circular depression, ~25 km across, cross-cut by numerous small ridges in a quasi-polygonal pattern (Figure 6.3ii).
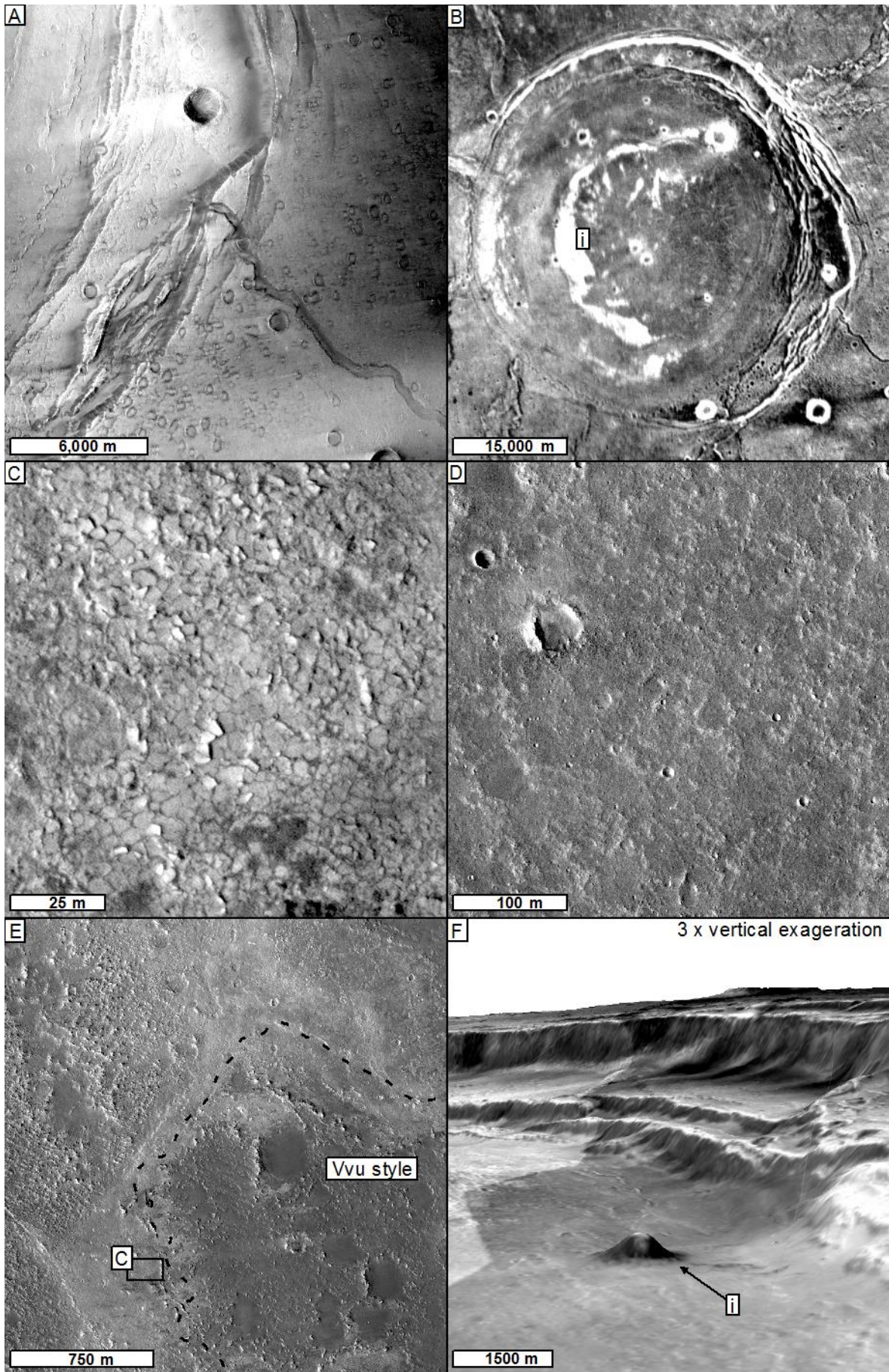
Figure 6.5:

Units in Meroe Patera. (a) The Pre-caldera lava unit and lava rill/trench cross-cut by normal faulting at the edge of Meroe Patera. (b) THEMIS night-time mosaic showing (i) very bright partial annulus at the boundary between the sections of Meroe Patera caldera floor corresponding to the CTX and HiRISE observations of bright fractured unit (Bfu) style material (lHlCf; Figure 6.3). (c) HiRISE image PSP_003917_1870 showing a polygonised exposure of the Bfu the location of which is marked (i) in (b). These polygons (c) are 3–5 m in across. The most recent, unit in Mero Patera is a thin, covering material which has a rubbly undulating surface formed of irregular blocky shapes ~2-5 m in size. This appears similar to the Variegated volcanic unit (Vvu) in Nili Patera although here there is more red sand, bright in CTX data. (e) Part of HiRISE image PSP_003917_1870. Dashed line shows later resurfacing units (in the Style of the Vvu) on-lapping the outcrop of polygonised bright fractured unit (Bfu) material. (f) Perspective view of the 1500 m x 100 m cone close to the eastern wall of Meroe Patera with three times vertical exaggeration. The chevron-shaped brightness contrast at the left of the image is an artefact of the CTX mosaic. Locations of all figure parts are given in Figure 6.4.

6.3.2 Geologic units

In this section the geological units of Meroe Patera and the surrounding area are described. The units and stratigraphic sequence found within Meroe Patera are very similar to that found within Nili Patera and described in chapter 5. As such, the Nili Patera units are used as a conceptual framework from which to draw a comparative investigation. I have used the same unit names for similar instances of units found within Mero Patera. These units are labels the same as on Map sheet 1 with a subscript '*m*' denoting are identified in Meroe Patera rather than Nili Patera (subscript 'n' on Map sheet 1). In doing this no connection is made about timing, only similarities in appearance and local stratigraphy.
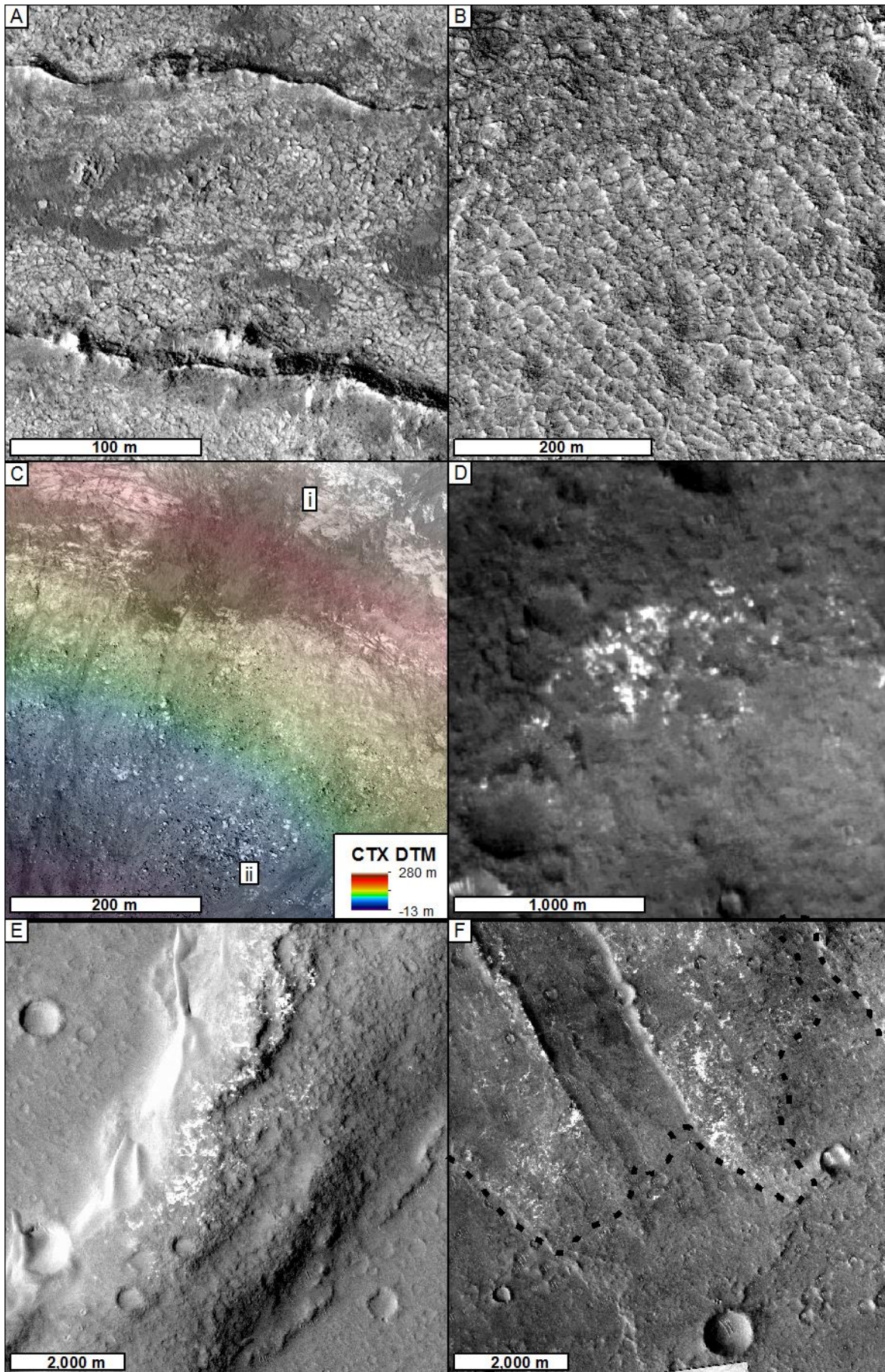
Figure 6.6:

Examples of anomalously bright material. (a) Bright, polygonally-fractured material inside the Meroe Patera (HiRISE image PSP_003917_1870). (b) Part of the bright fractured unit (Bfu) in Nili Patera (HiRISE image ESP_030843_1890). (c) Distinctive bright layers exposed in the wall of a crater within Meroe Patera where the bright material appears in discrete layers, all with a massive internal fracture fabric (i) and in boulders on the crater floor (ii) (HiRISE image PSP_003917_1870). (d) A small anomalously bright patch not associated with any impact crater, south of the central caldera complex (CTX image D10_030922_XI_06N291W). (e) Anomalous steep bright material exposed along the break in slope of a wrinkle ridge to the south-western margin of the central caldera complex; typical for exposures of this material in this setting (CTX image F05_037581_1849_XN_04N292W). (f) Anomalously bright patches on faulted blocks of volcanic basement subsequently overlain in the south by resurfacing units (CTX image P05_003139_1887_XI_08N292W).

6.3.2.1 Caldera external lavas

The volcanic units included in Map Sheet 1 are grouped into a single unit called Pre-Caldera Lavas (Pcl). These are the same units as in Chapter 5 (volcanic materials emplaced before the tectonic development of the Meroe or Nili calderas; Figures 5.6, 6.7b and c). Unlike the expression of this unit at Nili Patera, here there are no examples of individual lava flows being cross-cut by ring faults but there are features that could be individual flows close to the caldera and other structures also interpreted to be of volcanic origin are cross-cut by those faults (Figures 6.5a and 6.7b). There is also abundant evidence for large linear pits (Section 4.2.1.2.1) being cross cut by the caldera ring faults, thus predating them. These structures, although not included on Map Sheet 2, are included here (Figure 6.2) to illustrate the key stratigraphic relationships with caldera faulting and the inter-caldera lava-style material. There is no evidence for a 'disrupted caldera lava' Dcl-style unit at Meroe Patera. The circumferential faulting has down-dropped a contiguous arcuate block of pre-caldera lavas and there is no zone of disruption forming a hummocky surface as seen in Nili Patera.

6.3.2.2 Bright fractured unit (Bfu) and caldera floor unit (Cfu) style material

Bright fractured unit (Bfu) and caldera floor unit (Cfu) style materials are found exposed together in four windows on the Meroe Patera caldera floor (Figures 6.2 and 6.5b) marked as late Hesperian upper and lower Caldera floor (lHlCf$_m$ lHuCf$_m$) respectively on Map sheet 1. These units are very bright in THEMIS night-time data and this is the criterion by which these units are

261

mapped in Map Sheet 2. The units outcrop in two arcuate patches. The outer arc is just within the rim of Meroe Patera and the inner arc is at the approximate boundary between the inner and outer caldera floor sections (Figures 6.2, 6.3 and 6.5b). Within each of these very bright areas CTX data allow the differentiation of the surface material. Areas of Bfu style material are very light-toned, lying at the lowest point in the stratigraphy. They have a blocky fracture pattern with parts of the unit exhibiting a rectilinear to polygonal surface fracture pattern (Figures 6.6a and 6.5c). This unit is also found as a bright group of layers in the interior wall of an impact crater and in the ejecta from that impact where it has sampled the layer below the surface of the caldera floor (Figure 6.6c). This is similar to the crater found in the north-eastern region of Nili Patera (Figure 5.9). This material is also found in anomalously bright outcrops in the vicinity of Meroe Patera (Figure 6.6c). The poorer exposures and lack of image coverage in Meroe Patera prevent a clear assessment of whether this unit grades up into a 'layered caldera floor' (*Lcf*)-style unit as it does in Nili Patera on Map sheet 2. On Map sheet 1 it grouped with the late Hesperian upper Caldera floor (lHuCf$_n$). The night-time, thermally-bright, arcuate patches in Meroe Patera are very similar in appearance, with the same contact relationships, as this material in Nili Patera (Figures 5.11 and 6.5d).

6.3.2.3 Meroe Patera caldera floor sections

The floor of Meroe Patera has been divided into three sections: Meroe Patera caldera floor units I, II, and III (MPcfu I, II and III respectively; Figure 6.3).

6.3.2.3.1 MPcfu I.

This is the oldest tectonic section and is found in the eastern caldera floor area. This material covers the topographic step in this area. It overlies volcanic architecture that would crop out on this shelf if there had not been resurfacing after the initial collapse. The unit does not appear to extend outside the outermost normal faults, suggesting that it was confined to the previous extent of the caldera floor (Figures 6.2 and 6.3i).

6.3.2.3.1 MPcfu II.

The second oldest tectonic section of the caldera floor appears to be a continuation of the inter-caldera lava (Icl) found in the vicinity of the Nili Patera (a continuation of the unit outlined in Section 5.2.4.2; Map sheet 1; Amazonian early volcanic units Acv and Acv_n). This material partially overlies the region where caldera ring faults would outcrop if they were not overlain by this material and also overlies Cfu- and Bfu- style material (the late Hesperian upper and lower caldera floor units). However, the material covering the floor of Meroe Patera is not easily differentiable, thus preventing a confident assignment of the boundary between this and MPcfu III (Figures 6.2 and 6.3ii).

6.3.2.3.1 MPcfu III.

The youngest section occupies the centre and east of the caldera floor (Figures 6.2 and 6.3iii). This area is down-warped and cross-cut by numerous small ridges making differentiation of the primary surface textures difficult. However, there is a clear topographic edge where this area overlies the bright fractured unit (Bfu) / late Hesperian lower Caldera floor (Meroe) $lHlCf_m$ material (Figure 6.5e). This area is associated with a conical vent structure in the northeast (Figure 6.5f). It has a diameter of 1500 m with 100 m of relief. The cone appears similar in morphology to small cones in the variegated volcanic unit (Vvu) in Nili Patera (Section 5.2.4.2; Map sheet 1; Amazonian late volcanic unit (Nili) Alv_n) but it is ~ten times larger. Unfortunately, there are no HIRISE data available to investigate the detail of its structure. The relief in some areas, and the numerous partially infilled craters, suggest that this area was filled with material (probably volcanic) from within the caldera before the central area subsided forming the network of small ridges.

6.3.3 Tectonics

6.3.2.3.1 Normal faulting

There is only one family of normal faults in Meroe Patera, as defined by their trend. Normal faults occur in arcuate segments, trending around the circumference of the caldera (Figure 6.3). This set of faults appears to result from the collapse of the caldera floor. The throw of the normal faults

increases progressively inwards through the normally faulted aureole, and hanging walls become progressively more similar in morphology to landslip-like structures towards the centre of the caldera. Fault segments where the western part of the caldera rim would be being overlain by later deposits.

6.3.2.3.2 Reverse faulting

There are two sets of reverse faults in the area of Meroe Patera. The first set of faults is associated with collapse of the caldera. These faults are found in arcuate segments in a circumferential trend inside the caldera rim area of the caldera floor (Figure 6.3). These faults cross-cut the crater floor units but appear to be overlain by later lavas flows in the resurfaced areas in the east of the caldera floor. The second trend of reverse faults controls the topographic wrinkle ridges striking out of Meroe Patera north-northwest and south-southwest into the SMCCC axis. This system of faults is truncated by the caldera floor collapse faulting. There is no evidence for SMCCC axial wrinkle ridges cross-cutting the floor of Meroe Patera. However, this type of wrinkle ridge is present on the topographic step in the east of the caldera (Figure 6.3i) meaning it formed before the ring fault in that area.

6.4 Observations concerning the wider Syrtis Major central caldera complex

6.4.1 Volcanic structures in the central caldera complex

There are several vent structures within the SMCCC, some of which appear to have formed before, and some after, the Nili and Meroe calderas.. Four large linear pits (as described in 4.2.1.1) are found proximal to Meroe and Nili Patera (Figure 6.7a–c). In three cases associated channels appear to trend up-slope, away from the fissure pit vents, but the profile of the whole long linear depression (as described in Section 4.2.2.2) trends downhill away from the central caldera complex. The channels are overlain by Amazonian early volcanic units (Aev)deposits and the apparently anomalous channel slopes are all in the area affected by caldera subsidence. Other examples of the channels are cross-cut by wrinkle ridges. One channel connected to a large linear

pit (Figure 6.7b) is also directly connected to Meroe Patera means that where it is cross-cut by the associated normal faulting. This and the anomalous slopes of the channels and fissure pit vents must predate the outermost collapse of the caldera floor.

In addition to the large linear pits, there is a quasi-circular, flat-bottomed pit close to Meroe Patera (Figure 6.7e) described in in section 4.2.1.1. The pit is a 50–70 m deep depression, 1000 m x 1700 m across, located on the axis of a wrinkle ridge to the northwest of Meroe Patera. This pit crater has no elevated rim, but has straight steep sides and a flat floor, in contrast to impact structures of a similar diameter.

Lastly, there is a long fissure vent with proximal lava flows (Figure 6.7f; section 4.2.1.2). This vent system strikes northwest–southeast forming a shallow ridge, the minimum dimensions of which are 15 km wide and 60 m high. These are minimum dimensions because MOLA points are sparse perpendicular to the ridge axis, and the ridge has been later deformed by two wrinkle ridges. Lava flows are perpendicular to the trend of the ridge, which is contrary to the southeast slope of the vent axis, implying that the lava flows formed before rotation or tilting of the whole vent-flow system. The system is onlapped by units conforming to the present-day topography. This corroborates its formation before the majority of subsidence in the central caldera complex.

6.4.2 Extent of the bright fractured unit

In chapter 5 and *Fawdon et al.* [*2015*], the 'bright fractured unit' (Bfu) on the floor of Nili Patera (Figures 5.7, 5.8, 5.9 and 5.16) is described and the unit is inferred to be an ignimbrite deposit. The morphology and setting of the Bfu includes: very bright friable outcrops on uplifted ridges (late Hesperian light-toned outliers, lHLto), bright blocky outcrops in the axis of the resurgent dome (Figure 5.9) and spectrally bright ejecta in the north of the caldera (Figure 5.8). In addition to the main exposure of this unit, the analysis of the wider SMCC shows that several small outcrops of this material occur; it is inferred that these have the same origin.
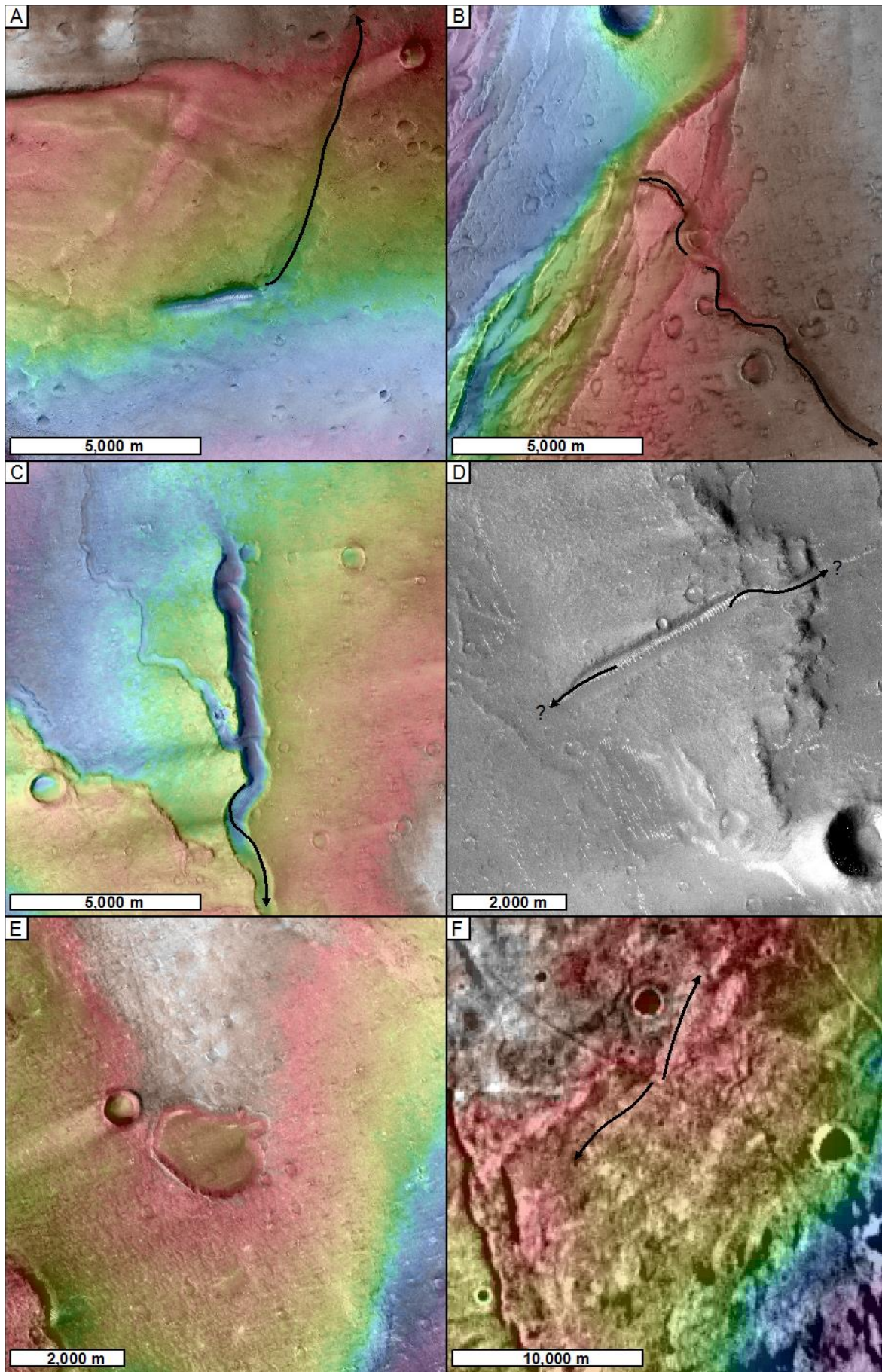
Figure 6.7:

Vent structures in the Pre-caldera lava unit close to the central caldera complex. Black arrows indicate the direction of associated rill or flow thus demonstrating examples which must have formed prior to the caldera collapse events in Nili and Meroe Patera or SMCCC. (a) Fissure pit vents and associated sinuous rilles northeast of Nili Patera (CTX image B20_017617_1891_XI_09N292W, with Nili Patera CTX DTM mosaic overlain, Figure 5.4) (b) southeast of Meroe Patera where they are dissected by caldera rim normal faulting (CTX image D06_029432_1857_XI_05N290W with Meroe Patera CTX DTM overlain) and (c) south of Meroe Patera (CTX image CTX D05_029287_1857_XI_05N291W with Meroe Patera CTX DTM overlain) (d) is transverse to the axis of the central caldera complex preserved on the topographic high of a wrinkle ridge where evidence for an associated rill has been inundated by subsequent intra-caldera units (CTX image P05_003139_1887_XI_08N292W). (e) Oval flat-bottomed pit on an upstanding wrinkle ridge northwest of Meroe Patera (CTX image D05_029287_1857_XI_05N291W with CTX DTM overlain). (f) A fissure vent forming a low ridge with perpendicular lava flows (night-time THEMIS Mosaic and MOLA Gridded DTM).

Minor outcrops of such anomalously bright material are found over a wide area, throughout the central caldera complex and to the south of Meroe Patera (Figure 6.8). All the available CTM and HiRISE images covering SMCCC were inspected (black and red outlines in Figure 6.8). These outcrops can be identified in CTX data only when it is not too noisy (Figure 6.8 shows the data coverage). HiRISE data are required for detailed characterisation of the material, without which reasonable comparison with the outcrops in Nili Patera cannot be made.

All these newly discovered bright outcrops are in locations where they have been exposed by tectonic activity or some other denudation process, providing a window to shallowly-buried, earlier units. Additionally, similar, very bright material often occurs in ejecta from very small impact craters (<50 m diameter), however, these occurrences have not been mapped because the brightness may actually be because of the albedo of the small crater, and similar scale topography only a few pixels across, rather than a specific high albedo component to the ejector.
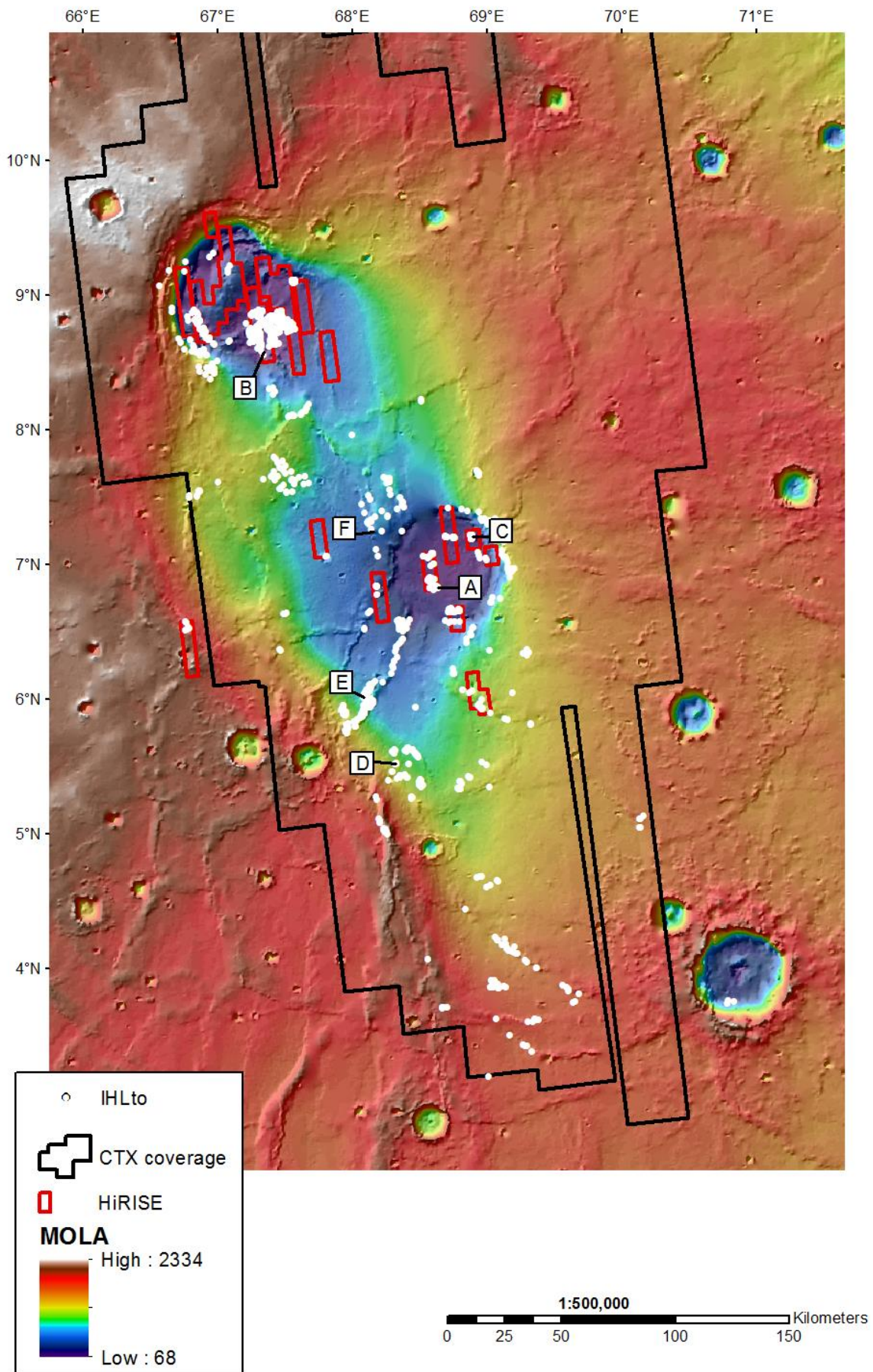
Figure 6.8:

The extent of outlined examples of the bright fractured unit style (late Hesperian Light toned outliers, lHLto; Map Sheet 1). White dots indicate an outcrop of anomalously bright material similar to outcrops in Nili Patera discussed in Section 5.2.5.3 and Figure 5.12b. The outlines show the extent of the available CTX (black) and HiRISE (red) data to date. Labels indicate the location of examples presented in Figure 6.6 overlain on gridded MOLA elevation over MOLA hill shade.

Six examples of outcrops of the bright material are shown in Figure 6.6. The first is exposed on the floor of Meroe Patera and exhibits a polygonal fracture network with bright polygons ~5 m across (Figure 6.6a). These are comparable in appearance, texture and fracture fabric to the smaller examples of polygons from Nili Patera (Figure 6.6b). The second example is also from Meroe Patera and shows distinct bright layers with a massive polygonal fabric found within the walls of a 2.8 km impact crater (Figure 6.6c). The elevation of these outcrops in the crater wall suggests that they would be at, or just below, the surface prior to the impact. The third and fourth examples are outside Meroe Patera (Figure 6.9d and e). Figure 6.6d is at the edge of the Amazonian early volcanic unit (Aev) and Figure 6.6e is an outcrop at the break in slope close to the southernmost margin of the SMCCC and along the steepest point of wrinkle ridges. Both 6.6d and e typify the majority of outcrops documented in Figure 6.8. The final example (Figure 6.6f) illustrates the relationship between exposures of this anomalously bright material and tectonic deformation within the central caldera complex and subsequent resurfacing materials. The anomalously bright outcrops located within tectonically perturbed terrain have been onlapped by the resurfacing material in the south-east of the image.
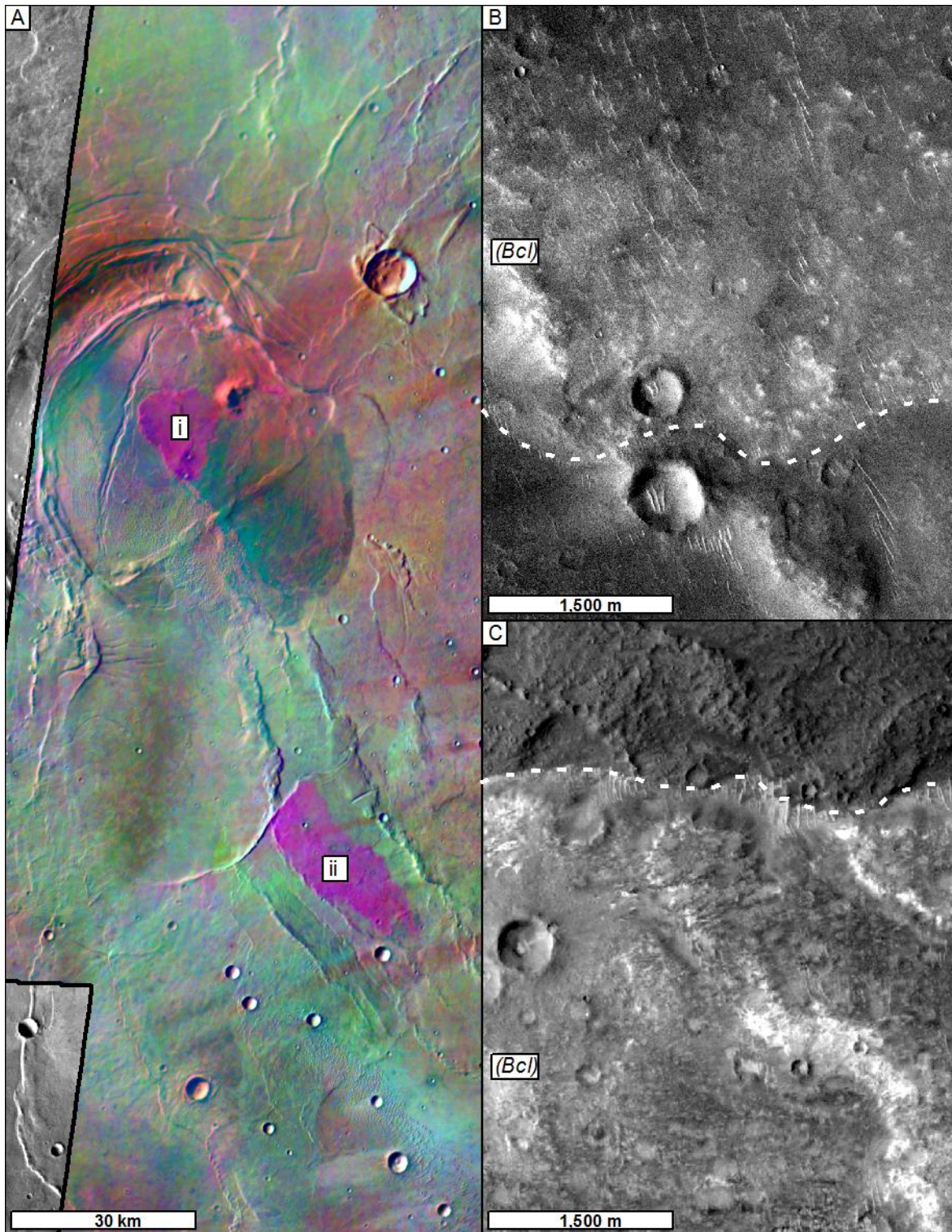
Figure 6.9:

The extent of the Amazonian bright caldera volcanic unit (Abcv), a bright central lava (Bcl)-like material. (a) THEMIS de-correlation stretch of bands 6, 4, and 2 [Christensen et al., 2004], after Christensen et al. [2005]: (i) bright central lava (Bcl) in Nili Patera ($Abcv_n$ on Map sheet 1); (ii) bright central lava composition material at the axis of the central caldera complex (Abcv). Mosaicked THEMIS data (black outlined areas): I02569002D642, I03293003D642, I03655002D642, I03680006D642 and I03318006D642. (b) Bcl-like unit (ii, in a) in CTX P05_003139_1887_XI_08N292W. (c) Bright central lava in Nili Patera for comparison ($Abcv_n$).

6.4.3 Bright central lava-like material

In addition to the outcrops identified in Nili Patera, there is an outcrop of material with the same thermal signature as the bright central lava (*Bcl*) unit in the central caldera complex. This material is identified in both THEMIS data CTX and Colour HRSC (Figure 6.9). THEMIS data (I02569002D642 and I03680006D642) showing the De-Correlation Stretched (DCS) of bands 9, 6 and 4 (Section 3.2.3) produce images with regions that show a distinctive 'pink' colour, in Nili Patera. These areas correspond to the mapped extent of the bright central lava unit. This pink signature can also be seen in an outcrop to the south and outside of Nili Patera but within the SMCCC (Figure 6.9). In visible and RGB false colour data, this unit has a bright surface with a dark lag-like material on the surface, similar to the bright central lava. On the basis of this identification this unit is mapped as the same type of material, in accordance with the mapping protocol developed for this project (Section 3.1) and named the Amazonian bright caldera volcanic unit (Abcv) outside Nili Patea and ($Abcv_n$) within. No connection other than the similarity in thermal and visible appearance is made, so the similarity in lithology and composition is an inference only.

6.5 Surface age estimates

Crater size frequency distribution measurements (CSFD) have been conducted in four areas to assess ages of units within in Meroe Patera and the SMCCC. These connect the stratigraphy to the timelines established for Nili Patera. Crater counts have been conducted using the same criteria described in Sections 3.3 and 5.2.3.3. Figure 6.10 shows the areas from which CSFD measurements were collected for this chapter. Figure 6.11 shows crater count plots and fitted model ages whilst, these results are summarised in Table 6.1.

Labels visible on map A: PcI_m, AIv_m, $IHuCf_m$, Aev_m

Scale: Kilometers — 0 4 8 16 24
1:500,000

Crater count areas
Red circle — (crater symbols)
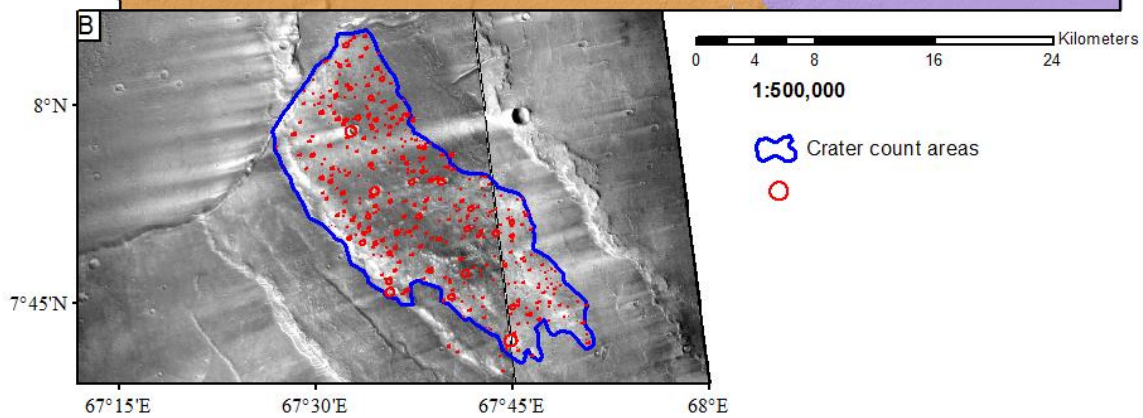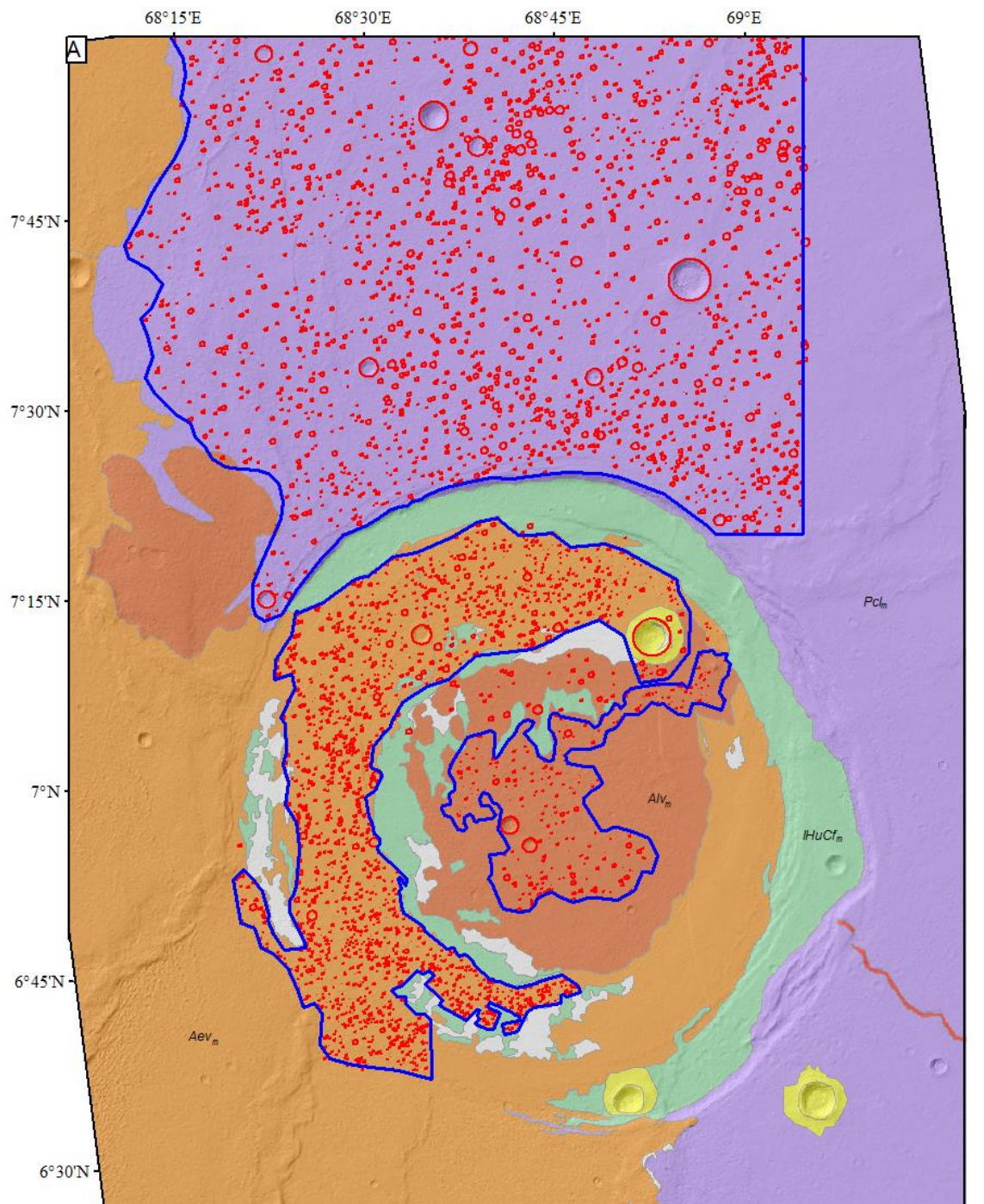
Figure 6.10 (opposite):

The area and raw crater count data for (a) areas at Meroe Patera and (b) the bright central lava (Bcl)-like units (Abcv) in the axial depression of the central caldera complex. The figure shows a THEMIS DCS mosaic slightly misaligned relative to the CTX data on which the count was performed.
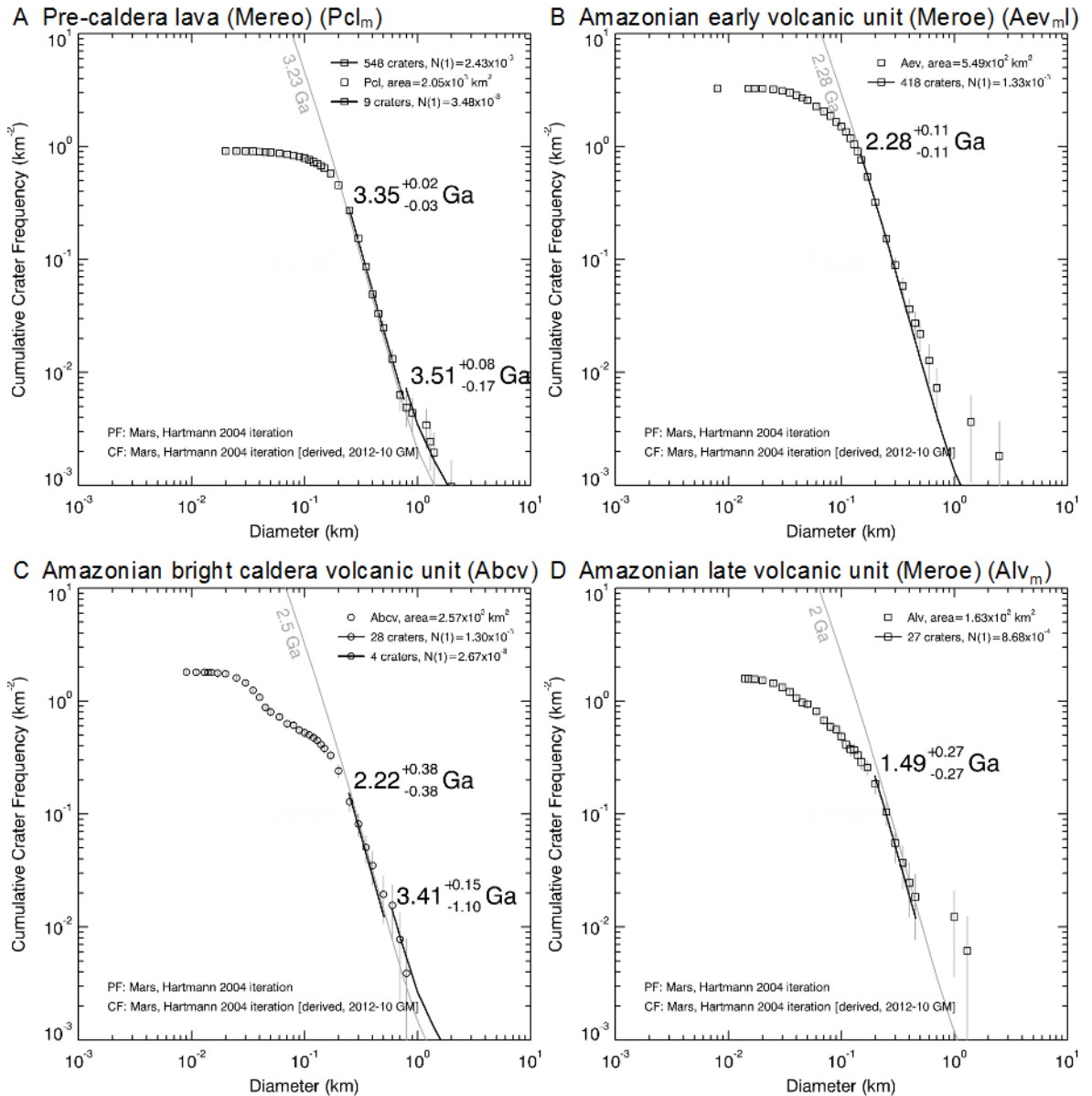
Figure 6.11 (above):

Crater count plots for the areas close to Meroe Patera. All plots are cumulative size frequency distributions using the Hartman production function and Hartman isochrons as defined within CraterStats II [Michael and Neukum, 2010] and consistent with those detailed in Fawdon et at. [2015]. Crater counts of areas in: (a) undifferentiated pre-caldera lavas, (b) caldera floor filling materials in the eastern half of Meroe Patera (c) the 'bright central lava-style unit' in the central caldera complex and (d) the putative region implied to be Vvu-style material in the centre of Meroe Patera. This last count, (d), avoided partially filled craters and most probably represents the minimum resurfacing age of the central part of Meroe Patera with a thin volcanic unit.

Table 6.1 Crater count summary for units related to Meroe Patera

Unit	No. craters counted	Area ($\times 10^2$ km^2)	Size range fitted (m)	No. craters in fitted range	Model age (Ga)	
Pcl	1869	20.1	250–750	548	3.35 (+0.02, −0.03)	Formation
						Possiblely
						older
Pcl			750-3500	9	3.51 (+0.08, -0.17)	volcanism[1]
Aev*	1791	5.5	150–3000	418	2.28 (+0.11, -0.11)	Formation
Abcv*	464	2.6	200–600	62	2.22 (+0.38, -0.38)	Formation
			600 - 900	4	3.4 (+0.15, -1.10)	Basement[1]
Alv$_m$*	257	1.6	150–1400	47	1.49 (+0.27, −0.27)	Formation

All counts used CTX data.

1These dates reflect underlying volcanic units not the most recent volcanism of the units being counted

6.6 Discussion of Meroe Patera and the central caldera complex

6.6.1 The formation of Meroe Patera

Meroe Patera appears to be less complex than Nili Patera. Like other martian calderas [*Crumpler et al.*, 1996] there is no obvious evidence for any resurgent phase. However, there is some complexity, as there appears to have been at least two stages of caldera collapse.

Similar to Nili Patera, Meroe Patera has an asymmetrical caldera rim however; this asymmetry is not reflected in the second stage (present-day) floor of the caldera (Figure 6.3). This suggests that the topographic asymmetry, into which the caldera rim is set, formed before the collapse that resulted in the flat, gravitationally stable, majority of the contemporary caldera floor. This sequence of events is supported by the observation that wrinkle ridges (trending sub-parallel to the axis of the central caldera complex) do not crop out on the second-stage caldera floor, but do cross-cut the hemi-circumferential stage remnant of the original caldera floor (Figure 6.3i).

This interpretation is also supported by caldera floor (*MPcfu II*) crater count data that give a crater retention age of ~2.28 Ga. This is substantially after the floor of Nili Patera was established and also after the dates of volcanic units on the Nili Patera caldera floor which are clustered at ~2.5 Ga. It remains unknown how this compares with the age of later volcanism on the Nili Patera

floor (either the Variegated volcanic unit (*Vvu; Alv$_n$*) or the smooth western unit as satisfactory ages were not established for these units).

The observations of two sets of ring faults and the topographic step to the east imply that there were two stages of collapse at Meroe Patera. The first stage (Figure 6.3i) is delineated by the outer normal faults to the east and southeast of the caldera (Figure 6.8). Here, material is retained which resurfaced the pre-caldera lava unit hosting large linear pits (Figure 6.7b). It is cross-cut by at least one wrinkle ridge (Figure 6.3iv). The arcuate part of the caldera floor slopes to the east, maintaining approximately the same depth relative to today's, asymmetric caldera rim above. These relationships imply that this stage of collapse occurred after the pre-caldera lavas at ~3.35 Ga (Figures 6.10 and 6.11 and Table 6.1), but before the major phase of subsidence in the wider SMCCC.

Caldera ring faults at Meroe Patera follow nearly circular arcs, although there is a slight degree of elongation in the north-northwest to south-southeast direction, matching the trend of the wider SMCCC. The topographic patterns of normal- and reverse-faulting in Meroe Patera closely resemble those of piston/plate-style collapse [*Cole et al.*, 2005] recorded in experimental studies and terrestrial caldera complexes [*Lipman*, 1984, 1997; *Marti et al.*, 1994; *Acocella et al.*, 2000; *Roche et al.*, 2000; *Kennedy and Stix*, 2003a, 2003b].
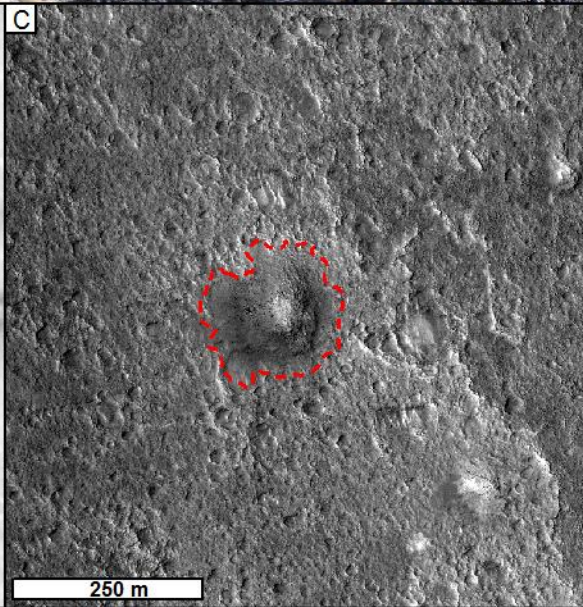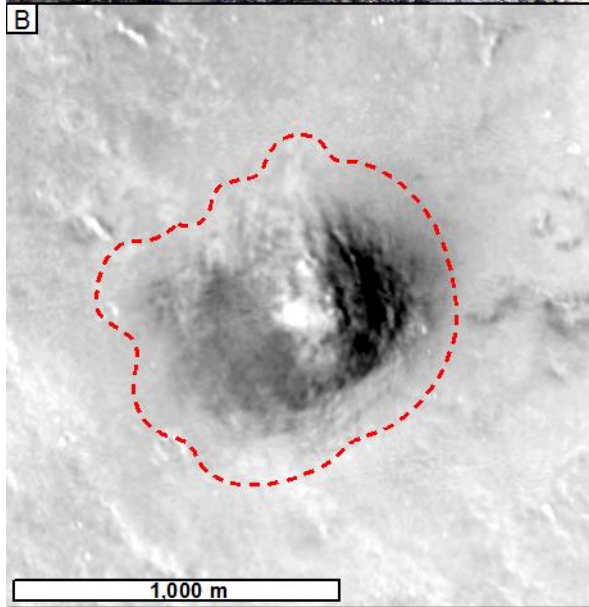
Figure 6.12:

Comparison of small lava mounds. (a) Perspective view of a small lava mound in Afar, Ethiopia (b) Cone/lava mound in Mero Patera which is very similar to (c) the small cones in Nili Patera (Chapter 5, Figure 5.12a HiRISE ESP_034891_1890), (d) small lava mound on Mt Etna. Mound (b) is ~1/5 of the size of that in (c) and (d). (Images (a) and (d) credit: Peter Fawdon, 2011).

6.6.2 Post-caldera floor volcanism in Meroe Patera

There is evidence that the floor of the Meroe Patera caldera was resurfaced after each of the two stages discussed in Section 6.6.1, and has been resurfaced again since.

It is evident that the caldera floor was resurfaced following the first stage of collapse because it lacks any surface expression of the long linear depression (interpreted to be a lava channel) that is seen running up the caldera rim and on to one of the faulted blocks in the interior of the Meroe Patera rim. Its position in the stratigraphy relative to the development of the Meroe Patera Caldera allows it to be classified as late Hesperian upper Caldera floor (Meroe) ($lHuCf_m$)). This area does not have the same appearance in night-time THEMIS as similar caldera floor units in Nili Patera ($lHuCf_n$). However, it should be noted that the surface of Meroe Patera contains more loose material than Nili Patera where there is significant wind activity leading to a small amount of sediment on the surface of this unit. This is evidenced by the barchan dunes in Nili Patera which are indicative of low sand supply and consistent wind direction [*Wasson and Hyde*, 1983]. The larger amount of loose material in Meroe Patera relative to Nili Patera is likely to have substantially changed the thermal conductivity on the 100 m scale of a THEMIS pixel (See Section 3.1.1 for more information).

The second resurfacing of Meroe Patera took place after the caldera had collapsed to the present-day floor level (Figure 6.3). After this floor level was established, material associated with the Amazonian early volcanic unit (Aev) buried evidence for faulting at the lowest western-most part of the caldera rim. This Aev unit advanced as far as the windows to the late Hesperian upper Caldera floor (Meroe) ($lHuCf_m$) and late Hesperian lower Caldera floor (Meroe) ($lHlCf_m$), however, it is not clear which processes caused the windows to form in their arcuate shape. Impact crater

size frequency data suggests that this part of the Aev unit has an age of ~2.28 Ga (Table 6.1) and therefore is younger than the ~2.41 Ga age obtained for the Amazonian early volcanic units close to Nili Patera (Table 5.1, Icl)). However, the error bars on the latter date do not rule out these being of the same age. This could indicate that resurfacing in the central caldera complex was not a single event or that there was some level of resurfacing of the caldera floor shortly after the Aev unit was emplaced thus making the model age from the crater count appear younger than the emplacement of the unit.

The final resurfacing event of the floor of Meroe Patera appears to have covered the eastern part of the caldera floor where it onlaps the eastern edge of the windows to the late Hesperian lower Caldera floor (Meroe) ($lHlCf_m$) below (Figure 6.5e). This resurfacing appears to be associated with the small cone in the northeast of the caldera (Figure 6.5f).

Currently, there are no HIRISE data available to investigate the detailed surface texture of this structure. It is possible that this cone is similar to Nili Tholus in Nili Patera; a suggestion possibly backed up by the 'pink' area in the Themis decorrelation stretch data (Figure 6.9), although this is not clear enough to be certain. Additionally, the cone in Meroe Patera is only one-fifth of the size of Nili Tholus, lacks the distinctive light tone colour, and shows negligible evidence for any associated bright central lava-style unit. The Meroe Patera cone therefore appears most similar to, although an order of magnitude larger than, cones associated with the variegated volcanic unit (Vvu) unit of Nili Patera (Alv_n on Map sheet 1) which are located in areas associated with faulting in the caldera floor (Chapter 5, Figure 6.12a). *Fawdon et al. (2015)* interpreted these to be small domical vent structures without apical pits, similar to, although larger than, terrestrial examples seen in Afar, Ethiopia and Mt. Etna, Sicily (Figure 6.12). The size and singular occurrence of the cone implies a less spatially dispersed transport system of magma to the surface (an implication supported by the observation of small-scale faulting in the floor of Nili Patera).

Unfortunately, the materials covering the floor of Meroe Patera prevent confident discrimination of boundaries between the Amazonian early volcanic unit (Aev) and material

thought to be similar in style to the Nili Patera variegated volcanic unit (vvu/ Alv_n). This may be because these units are composed of similar materials, and formed through a similar mechanism at about the same time. Hence, any usefully differentiatable characteristics might have been obliterated by aeolian deposition, tectonic modification and ongoing impact gardening. However, tentative units are still identifiable, based on the structural and physiographic relationships. These units have then been grouped with the other units to complete Map Sheet 2 and to reflect the similar sequence of formation.

The final major process that occurred in Meroe Patera was the down-warping of the central caldera floor section (Figure 6.3). The subsidence of this section is accommodated for by numerous small ridges which cross-cut this circular area. This deformation further masks differentiation of any possible Vvu/Alv -style unit from Icl unit (Aev on Map sheet 1) material and from remnants of the original Meroe Patera cratered caldera floor (MPcfu I).

6.7 Conclusions

- Prior to the formation of Nili and Meroe Patera and the Syrtis Major central caldera complex (SMCCC), the last pre-caldera lavas (*Pcl*) were emplaced near the centre of Syrtis Major. These were volume-limited eruptions from fissure vents (large linear pits) feeding channels similar to lunar rilles, that radiated from the present central location of the Nili and Meroe calderas.

- Meroe Patera formed through a piston-like collapse in two stages, later than previously reported and contemporaneous with the early development of Nili Patera. Meroe Patera started to collapse after ~3.2 Ga but before the majority of subsidence in the SMCCC had taken place. The second stage occurred after the wrinkle ridge-forming event, but before ~2.3 Ga. Between then and ~1.2 Ga there has been volcanic resurfacing within the caldera, probably related to a small cone. However, it is not currently possible to satisfactorily differentiate units in the caldera.

- Outcrops of Bright fractured unit-style material (Bfu) are exposed on the floor of Meroe Patera (lHlCf$_m$). No evidence supports an endogenic origin for these materials. Outliers of Bfu material (late Hesperian light-toned outliers, lHLto) extend throughout the wider SMCCC, exposed by later tectonic activity. This supports the ignimbrite hypothesis for the origin of the Bfu in Nili Patera.

- Heterogeneities in the distribution of widespread, low-strength, volatile-rich deposits, older than Syrtis Major, help to explain the different evolutionary pathways of Nili and Meroe Patera. At Nili Patera, the magma reservoir was affected by these deposits, resulting in eruptions of the shallow magma chamber and late-stage subsurface ductile deformation. Neither of these events was experienced by Meroe Patera, so it is unlikely that it formed over the same crustal structure that has been inferred for Nili Patera.

- The unit of evolved composition [*Christensen et al.*, 2005] is not unique to Nili Patera. There is a second, younger, unit with this composition in the axis of the SMCCC.

Chapter 7: Understanding the Evolution of Syrtis Major Planum

In this chapter the evolution of Syrtis Major Planum is discussed drawing on the results and discussions presented in the three previous thematic chapters (Chapter 4, 5 and 6). First, I discuss the volcanic history of Syrtis Major. Particular emphasis is placed on the spatial and temporal evolution of lava flows and effusive eruptions across Syrtis Major Planum and within the central caldera complex. I also discuss evidence for major explosive episodes associated with the formation of the Syrtis Major Central Caldera Complex (SMCCC) (Figure 1.1 and Map Sheet 1).

Secondly, I review the model ages for surfaces at Syrtis Major Planum and use these to collate a sequence of events. This generates a single timeline comprising all the observed and inferred events tied to the local and global stratigraphy.

Finally, I discuss the magmatic evolution of Syrtis Major Planum as evidenced by the volcanic history, magmatic has evolution though time and the implications of the evolution of other volcanoes on Mars in terms of the observations and inferences made at Syrtis Major Planum.

7.1 Eruption styles

Detailed geological mapping of Syrtis Major Planum has identified abundant evidence for different phases of volcanism, both before and after caldera formation and the subsidence that formed the SMCCC. In Chapter 4 I discussed the lava flows in the major constructional phase of Syrtis Major Planum and the timing of those events (Section 4.5). I also discussed the effusion associated with the second phase of volcanism, after caldera formation.

7.1.1 Effusive eruptions prior to caldera formation

Eruptive vents and lava flows produced by effusive eruptions are distributed across the Syrtis Major Planum. In Chapters 4 and 6, both large linear pits and wide flat bottomed pits were identified as primary vent features associated with the planum building lava flows (Figures 4.4 and 6.7, Section 4.2.1.2). Here, I discuss the eruption styles at various putative vents, and what these imply about the volcanic history of Syrtis Major Planum.

7.1.1.1 Large linear pits

Large linear pits interpreted to be vent structures for the planum building lava flows occur around the central caldera complex and in the Hesperian fissure field unit (Hff) (Map sheet 1, Figures 4.4 and 4.13). Morphologically, large linear pits on Syrtis Major Planum are between 2 km and 10 km in length and 40 m – 150 m deep (Figures 4.4 and 6.7). They are often spatially associated with both major channels and long linear depressions.

Large linear pits appear to be similar to two distinct vent morphologies seen on Earth. Some are similar to fissure vents, such as the vent at Holuhraun in the Nornahraun lava field, which erupted from August 2014 to January 2015 [*Icelandic Meteorological Office*, 2014; *Lavallee et al.*, 2015]. Large linear pits in Figures 4.4b, d and, 6.7d and 7.1a share the most characteristics with the Holuhraun vent (Figure 7.1b). For example, they have similar proportions to, but are on a much larger scale than, the Holuhraun vent; they have channels coming out of them which connect lava flow fields and a convex outward rim which suggests formation by a coalesced series of circular collapse pits. In the case of Holuhraun, the eruptions began with fire fountains along a segment of a fracture that was associated with seismically-detected dyke propagation in the weeks beforehand [*Icelandic Meteorological Office*, 2014; *Sigmundsson et al.*, 2015]. These fire fountains rapidly localised to a series of small, aligned cones, creating a lava-filled crater (Figure 7.1b). This ponded lava over-spilled at both ends and flowed into channels which then fed the lava flow field [*Icelandic Meteorological Office*, 2014; *Lavallee et al.*, 2015]. Few of the large linear pits on Syrtis Major Planum have distinct spatter ramparts or any cone-like morphology that could

have held an upstanding lava lake (Section 4.3.2.5). Such features may not be preserved, due to either post-eruption erosion or syn-eruption disruption of the spatter mounds by lava flows [*Brown et al.*, 2015]. Large linear pits are generally an order of magnitude larger than the Holuhraun vent, which is only 1.6 km long [*Icelandic Meteorological Office*, 2014; *Lavallee et al.*, 2015]. This may reflect the large volume of lava erupted at Syrtis Major Planum, although this should not rule out a fissure vent [*Brown et al.*, 2014].

Large linear pits also share many features in common with 'lava trenches' seen close to Hawaiian summit craters, in particular Mauna Ulu [*Cruikshank and Wood*, 1972; *Greeley*, 1972, 1974] (Figure 7.1d). Like these "lava trenches" [*Greeley*, 1974] the large linear pits of Syrtis Major Planum also appear to have formed from a series of coalesced pits. For example, Figure 4.4c appears to fit six pits into the main trench with an additional unattached, although possibly impact-related, crater to the Northeast. Figure 4.4d shows a large linear pit that contains at least seven superposed circular craters and what appears to be a shallow terrace at the Southwestern end. The Mauna Ulu [*Swanson et al.*, 1979] lava trench formed when a linear series of small craters coalesced as they expanded laterally [*Greeley*, 1972]. In the case of Mauna Ulu, this trench was downslope of a lava-filled crater which subsequently overflowed, pouring though the trench into a tube system beyond. It finally re-emerged as a pāhoehoe lava field downslope [*Cruikshank and Wood*, 1972; *Rowland and Walker*, 1990]. This formation satisfies the morphology of some large linear pits, but it does not address their common association with open channels and the lack of association with a vent upslope. However, it is also noted that lava trench features bear a striking resemblance [*Cruikshank and Wood*, 1972] to short straight sections of Lunar rilles (Figure 7.1c).
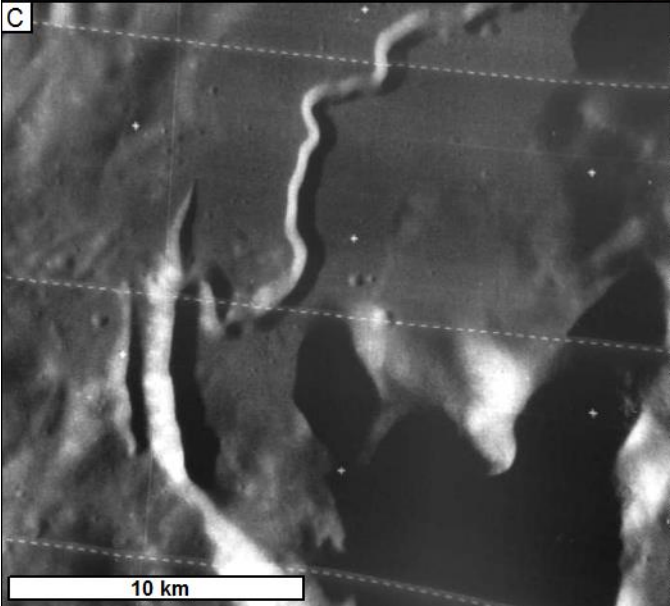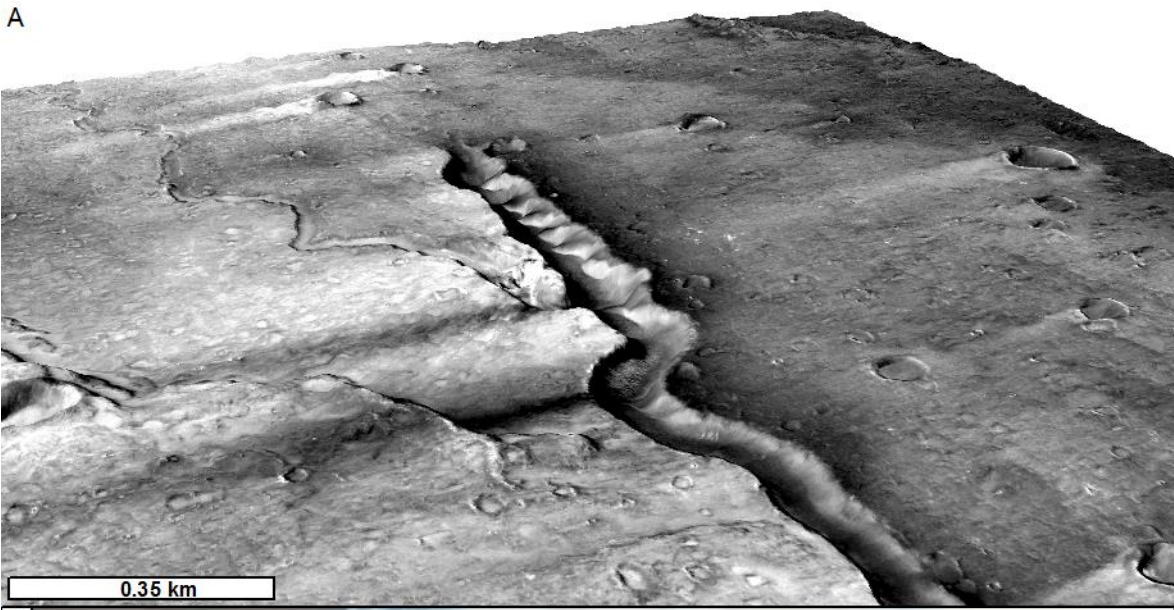
Figure 7.1:

Fissure vents in the pre-caldera lavas. (a) Perspective view of vents in Syrtis Major Planum visualised in Geovisionary™. The straight section of the vent is ~6 km in length, with a maximum width of ~500 m. (b) The fissure vent at Holuhraun in the Nornahraun lava field (64° 51' N, 16° 50' W) that erupted from August 2014 to January 2015. The fissure length was estimated to be ~1.6 km [Icelandic Meteorological Office, 2014; Lavallee et al., 2015] (Image credit; Einar Gudmann, www.Gudmann.is). (c) Head region of Hadley Rille a lunar sinuous rille from Lunar Orbiter data which shows a similar plan view morphology and association with a sinuous rill. (d) Southwestward view along the trench towards the summit crater of Mauna Ulu. From Greeley [1974] (Photo W.A. Duffield, USGS September 14th 1972).

If the large linear pits are vents, and the eruption that formed them supplied lava to the associated channels, then they have been drained of lava, collapsed after the end of the eruption, or have been subjected to erosion since the eruption ceased. Any combination of these processes satisfies the observation that channel depth at the connection to the large linear pit is often shallower than the depth to floor of the large linear pit. Both drain-back and post-eruptive collapse suggest that the last stages of effusion was limited by the volume of lava available, as opposed to solidification in a cooling-limited scenario [*Wilson and Head*, 1994; *Cashman and Sparks*, 2013]. It is possible that that the martian equivalents of these features did form, but were then obliterated by widening and collapse of the large linear pits due to either post-eruption erosion or syn-eruption disruption of the spatter mounds by lava flows [*Brown et al.*, 2015]. However, it seems unlikely that such diagnostic features would be erased totally in each of the 26 large linear pits I have catalogued (Figure 4.2).

The lack of substantial spatter ramparts may also be explained by enhanced fragmentation [*Wilson and Head*, 1994] and dispersal of magma erupting into the martian environment [*Brož et al.*, 2014] compared to Earth (Section 2.1.3). The volatile content, composition and the temperature of an eruption are important factors that influence the morphology of vent landforms [*Walker*, 1993; *Wilson and Head*, 1994; *Cashman and Sparks*, 2013; *Brown et al.*, 2014]. For the Holuhraun fissure, the composition of the erupted lava was olivine tholeiite with sufficient volatiles to drive fire fountain activity 40 m high, and a lava eruption temperature of ~850 °C (Figure 7.1b) [*Haddadi et al.*, 2015]. Large-volume eruptions of basalt from fissure vents

have not been observed on Earth, but 800-1400 m high fire fountains have been reconstructed for the eruption of the 14.7 km^3 Laki eruption, Iceland [*Thordarson and Self*, 1993]. It is inferred that eruptions such as the 1300 km^3 Roza flow field in the Columbia River Basalt Province may have been more intense [*Brown et al.*, 2014] with fire fountains of up to 6 km high being suggested [*Self et al.*, 1997]. The 1969-1971 Mauna Ulu eruption [*Swanson et al.*, 1979] was also basaltic and associated with the development of a lava lake [*Cruikshank and Wood*, 1972; *Greeley*, 1972]. The development of lava lakes suppresses the explosivity of eruptions by persistently degassing the magma, removing the volatiles [*Oppenheimer and Francis*, 1998].

The composition, viscosity and thermal conductivity of Lunar rille lavas [*Hulme*, 1982], such as at the head region of Hadley Rille (Figure 7.1c), bear a striking resemblance to terrestrial lava trenches [*Cruikshank and Wood*, 1972]. These large linear pits on the Moon have been measured experimentally [*Murase and McBirney*, 1970a, 1970b]. Result show that the lavas associated with rilles have a higher iron content and density compared to terrestrial basalt (2.95 g/cm^3 and ~2.6 g/cm^3, respectively). They are also very low in volatiles, have half the thermal conductivity, and a higher liquidus temperature of ~1370 °C, and a viscosity a tenth of terrestrial flood basalt at this temperature [*Murase and McBirney*, 1970a, 1970b].

The implications of these properties on lava flows are that the velocity of the laminar flow of lavas in the lunar rilles will be twice as fast and will take twice as long to cool compared to basalt lavas on Earth, due to their lower thermal conductivity [*Murase and McBirney*, 1970a]. Thus, lavas in open channels on the Moon will take longer to roof over and form a tube than on Earth [*Cruikshank and Wood*, 1972; *Greeley*, 1972; *Favre*, 1993; *Byrnes and Crown*, 2001]. The effect of a lunar rille-like composition for martian lavas will also affect the total length of lava flows because once lava enters an insulated tube where, effectively, radiative cooling cannot occur. Together with the lower thermal conductivity, the lava will remain at a higher temperature for longer, leading to longer total flow lengths [*Cruikshank and Wood*, 1972; *Wilson and Head*, 1994].

Taking into account the morphological similarities between lunar rilles, large linear pits on Syrtis Major Planum, and their associated major channels/long linear depressions, the envelope of possibilities can be enlarged from simple basaltic flows to consider more exotic compositions for the erupted lava. This is supported by morphological analysis of Arnus Vallis, a major channel connected to the largest large linear pit, suggested to have low-viscosity lava with a sufficiently high eruption temperature and flow rate to slowly erode the base and walls of the channel Vallis [*Rampey and Harvey*, 2008]. Furthermore, model compositions drawn from spectral data [*Mustard et al.*, 1990, 1993; *Bibring et al.*, 2005; *Clenet et al.*, 2013] also suggest a composition more like komatiite, for which terrestrial analogues are known to have high melting temperatures and correspondingly low viscosity lavas.

Hesperian fissure field unit (Hff)

Hesperian volcanic plateau unit (Gfg)

Morphology

(I) (II) (III) (IV) (V)

Festoon ridges

layered lobate margins

discontinuous linear depressions/pits

Landform

Major channel/ Long linear depression

Long linear depressionon a mound

Processes

Downwearing open channel

Aggrading channel building levees from overspill

Progression of tube development

Development of skylights over empty/partially empty tubes

freezing

Conduction cooling dominant

Radiation/convective cooling dominant

topographic slope

Fissure initation

Vent development

late Hesperian volcanic flow unit (lHvf)

Morphology

(I) (II) (III)

Medial channel lobate magins

End of channel morphology, Lobate flow front breakout

Landform

Process

Pahoehoe to Aá transition

Aa flow front freezing

Radiation/convective cooling dominant

topographic slope

Vent widening and

Vent collapse after magma withdral

288

Figure 7.2:

A series of block diagrams showing an interpreted sequence of events that form the large linear pits in the Hesperian fissure field unit (Hff) and their relationship to the formation mechanism for the Hesperian volcanic plateau unit (Hvp) and Late Hesperian volcanic flow unit (lHvf). For the Hff this shows the initiation of a fissure vent, its development with fire fountains and a pond of lava though local collapse and widening to draining and the formation of the large linear pits seen on Syrtis Major Planum. For the Hvp this shows the progression though the flow. This starts with the rille-like major channels which subsequently build mounds and are then roofed over and form a network in the inflating Hvp flow lobe. Finally, when lava reaches the margin of the flow it is emplaced as a fresh pāhoehoe toe. For the lHvf this shows the progression from poorly formed discontinuous channels to the slabby surface of rafted blocks which float downstream where they form new levees in the advancing flow front.

Taking into account terrestrial and lunar analogues and the theoretical physical properties of lavas the formation mechanism of typical large linear pits can be constrained (Figure 7.2):

(i) There was propagation of a dyke to the surface and the formation of fire fountains producing a lava lake draining out into a channel.

(ii) The rate of the eruptions was sufficiently high to sustain long open lava channels. The eruptions created short linear pits (mean 5.4 km fissure length).

(iii) Eruptions continued for long enough to build lava flow fields such as the Hesperian volcanic plateau unit (Hvp) flow to the south of Meroe Patera (with a volume of ~500 km^3). During this time, the erupting lavas eroded the neck of the vent, deepening the large linear pit. Linear pit vents without obvious channels may be more closely associated with feeding Late Hesperian volcanic flow unit (lHvf) style flows while continuing to feed the open channels (Figure 7.2, Section 7.3). These in turn fed the lava flow fields.

(iv) Eruptions ceased when magma drained out of the vent structure back down into the conduit or through supply to a lava flow front as the eruption waned. After this, collapse into the void vacated by the withdrawing magma formed a deeper pit.

7.1.1.2 Wide flat bottomed pits on the flanks and in the central caldera complex

In addition to the large linear pits, there are several wide, flat bottomed pits in the central caldera complex. Two of these are found in the central caldera complex (Figures 4.4f, 6.7e and 7.3). There is one other possible example in the North East Fissure Zone (NEFZ).

Northwest of Meroe Patera is a 'deep example' of a wide flat bottomed pit (Figure 6.7e). This quasi-circular, steep-walled depression is located on a SMCCC axial wrinkle ridge. The pit is morphologically dissimilar to impact craters of a similar diameter, and is therefore probably volcanic in origin. Shallower examples are found south east of Nili Patera and in the west of the NEFZ. These examples both have long linear depressions associated with them, interpreted as lava channels and indicating that they have hosted vents (Section 4.2.2.). None of the floors of wide flat bottomed pits are totally flat, and they have some structures within them, although with the image resolution available it is not possible to resolve what these might be. In one example, there appear to be terraces deepening towards the centre of one side of the pit floor (Figure 6.7e and 7.3a and b).

I consider three terrestrial analogues to help understand the formation of the wide, flat bottomed pits. The first is a vent in the Mando-Hararo rift segment, Afar, Ethiopia (Figure 7.3c and d) which is similar to the wide flat bottom pit example of Figure 7.3a, b and g. This Ethiopian example is a single monogenetic vent in an extensional tectonic setting. It is similar to the examples on Syrtis major Planum in its irregular shape and depth. However, the wide flat bottomed pits of Syrtis Major Planum are larger, and their flat bottoms have more in common with the second analogue, Hawaiian pit craters [*Wilkes*, 1845; *Okubo and Martel*, 1998]. These are almost rimless with steep walls, much like those on Syrtis Major. The Hawaiian pit craters are, however, very much smaller and are considered to be collapse pits over subsurface voids associated with a fault zone and are therefore not directly associated with the eruption of lava. In contrast, wide flat bottomed pits on Syrtis Major are associated with channels and lava flows.

The third possibility is that the wide flat bottomed pits are more similar to pit craters that have held lava lakes, such as Kilauea Iki, Big Island Hawaii (Figure 7.3e and f) or calderas with persistent lava lakes such as Erta 'Ale in Ethiopia [*Barberi and Varet*, 1970; *Field et al.*, 2012] (Figure 7.3h) or Halemaumau Crater, Big Island Hawaii [*Richter et al.*, 1970] (Figure 7.3f). The possible floor terraces within wide flat bottomed pits, and their direct connection to lava channels, both support the interpretation that these features are vents that have hosted persistent lava lakes, allowing the margins and floor of the pit to develop over time.

This interpretation suggests that, whilst both the wide flat bottomed pits and large linear pits are the foci of large eruptions, and therefore associated with the planum building lava flows, they are also interpreted to be long-lived structures. These are associated with persistent degassing of magma in a convection cycle through the conduit between the vent and a magma reservoir [*Oppenheimer and Francis*, 1998; *Field et al.*, 2012].

Figure 7.3: (Overleaf)

Earth analogues of vents for the Syrtis Major Planum wide bottomed pits. (a) Perspective ((visualised in Geovisionary™) and (b) a hill shade model of the flat-bottomed pit close to Meroe Patera from 18 mpp CTX DTM data. (c) Hill shade model from SRTM data of the rift axial pit crater at Alo Alé (11° 21' 19" N, 40° 45' 40" E) in the Afar Rift. (d) Perspective view of the same pit crater taken from its Northeastern rim. (e) Perspective view across Kilauea Iki pit crater, Big Island Hawaii. (f) Hill shade model of 18 m DTM of Kilauea caldera, Halemaumau Crater and Kilauea Iki, Big Island Hawaii (view (e) marked; Source USGS). (g) Repeat of panel b. (h) Hill shade of Erta 'Ale lava lake and caldera, Afar rift Ethiopia Landsat 2010 RGB 30m/pixel. (Perspective view image credits: Peter Fawdon, 2011, 2015).
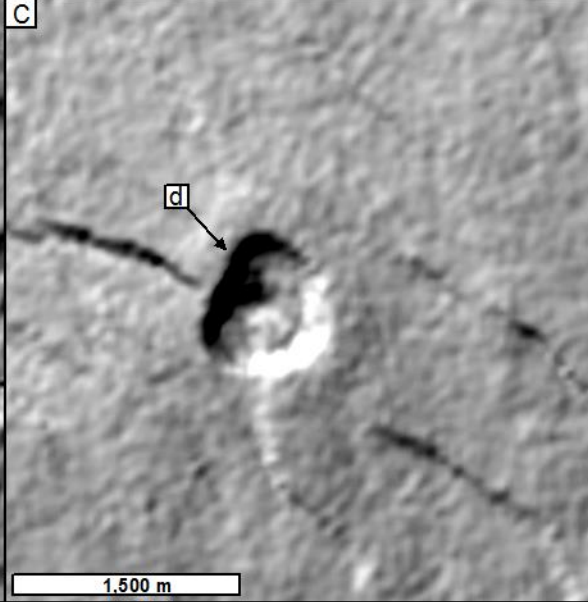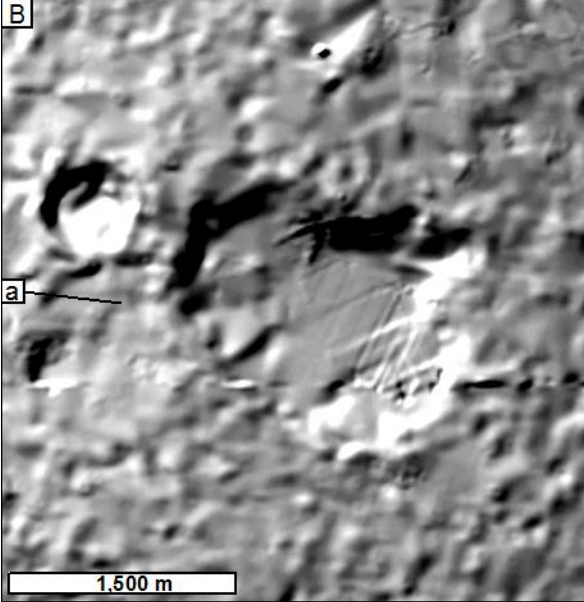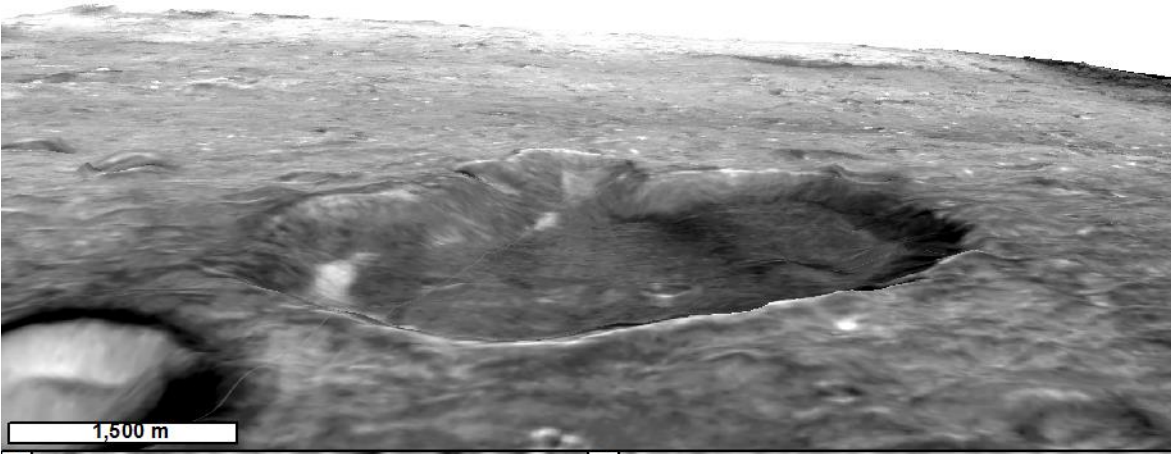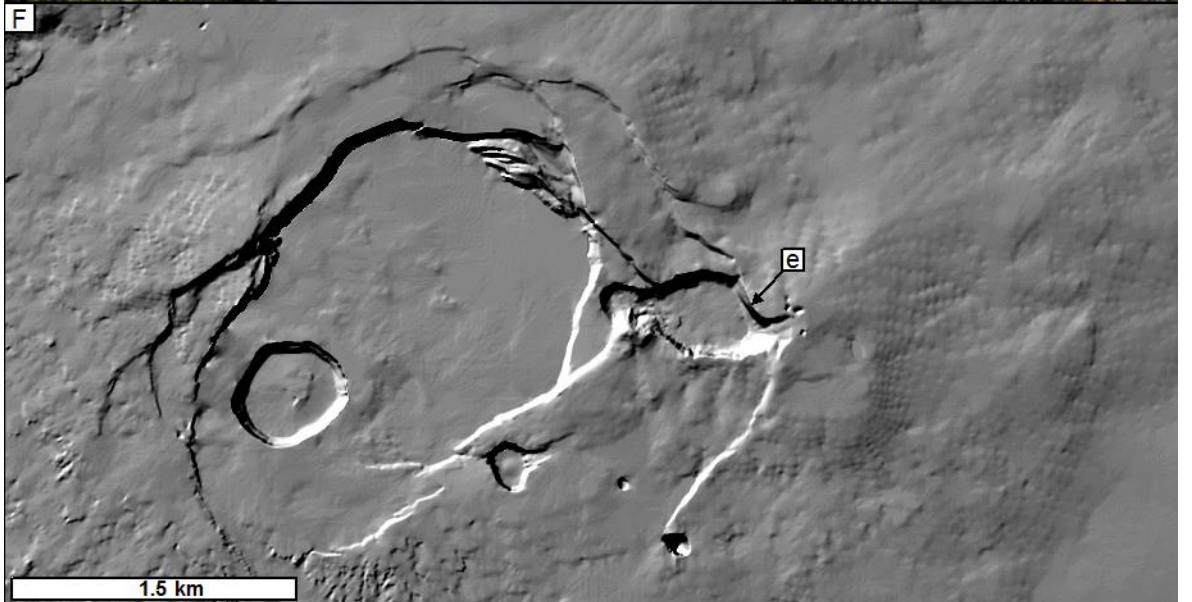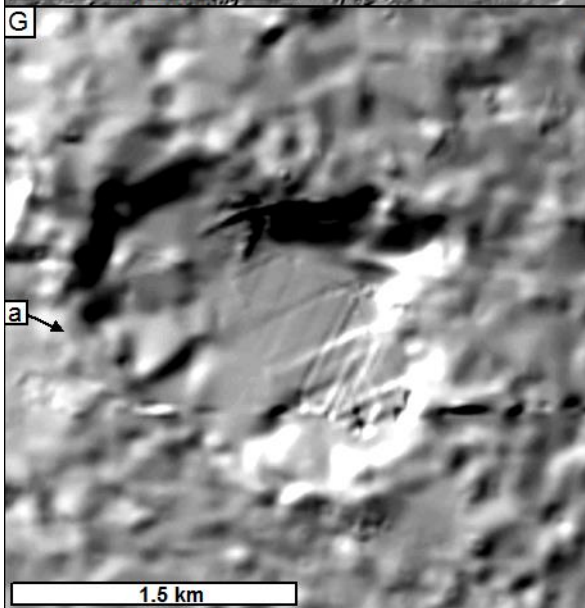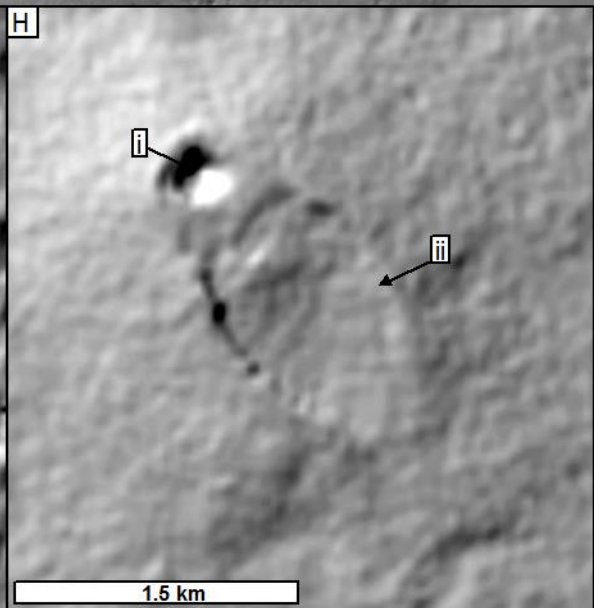
7.1.2 Explosive eruptions associated with caldera formation

In Chapter 5 I conclude that the parsimonious explanation for the formation of the Bright fractured unit (Bfu) is an ignimbrite which formed during the caldera collapse and formation of Nili Patera. Meroe Patera is located at the Southeastern corner of the central caldera complex. In Chapter 6 I identify outcrops of Bfu-style material in the caldera floor (Figure 6.6 and 6.8). However, the structure of the caldera rim (which is made of coherent subsided blocks) and the lack of proximal deposits do not support a large eruption close to here. The following subsections will discuss the explosive volcanic phases associated with the formation of the SMCCC, the timescale of subsidence, and the distribution of preserved deposits which are unique on Mars.

7.1.2.1 Implications of the extent of the Bright fractured unit (Bfu)

Of the volcanic deposits on the Syrtis Major Planum which represent compositionally evolved magma, and are likely to be products of explosive eruptions, the Bright fractured unit (Bfu) is the most areally extensive. In Nili Patera there are four different modes of expression of the Bfu and associated outlying material. These are: (i) the bright polygonised basal unit, (ii) ejecta from an impact crater in the Northeast of the caldera, (iii) very light-toned blocks eroding from the interior fault scarp in the resurgent dome axial ridge and (iv) the very light-toned outlier outcrops (Chapter 5). Expression modes (i) and (ii) are corroborated with CRISM data (Figure 5.9), (iii) is a stratigraphic inference, and (iv) is a mutually supportive genetic association with the Bfu in exposure style (e.g. (i)).

For the formation mechanism proposed in Chapter 5 (an ignimbrite associated with caldera collapse) each of these four modes of expression are satisfied and, if they were to be considered independently of each other, each would predict the others. That is, if the late Hesperian light-toned outliers (lHLto) are a light-toned fall deposit, exposed by tectonic activity, they would predict a thicker, light-toned deposit at the same stratigraphic level closer to the vent. Conversely, if the Bfu is a welded explosive deposit a thinner, more friable deposit would be predicted on local topographic highs at the same stratigraphic level. Alternatively, if the Bfu is an exposed

intrusive body, no prediction is made. In this case, however, the observation of the lHLto also remains with no satisfactory explanation – arguing against this hypothesis.

In Meroe Patera (Chapter 6) examples of all four of these modes of expression can be seen. The first mode (i) is seen in windows to the caldera floor through the Caldera floor units (lHuCf$_m$). The second (ii) is probably seen in ejecta in two craters in the North-northeast and South of the crater floor. In these instances, this is a somewhat ambiguous observation as there has been no spectral investigation of these surfaces, unlike the impact crater in Nili Patera. The third (iii) has a clearer stratigraphic connection than in Nili Patera. In Meroe Patera, at least one light-toned layer with an apparently massive internal fabric (on the scale of HiRISE) clearly crops out. Lastly, lHLto are observed in several locations in the wider SMCCC, and in many instances at the top of fault scarps around the rim of Meroe Patera.

In the SMCCC, only the fourth (iv) mode of expression is clearly observed in the CTX data (Figure 6.6 and 6.8). However, (ii) and (iii) are possibly observed, but (ii) is unconstrained by spectral data, and (iii) is possibly demonstrated by observations of bright material in a fault scarp to the northwest of the bright central lava-style unit in the central caldera complex. Regrettably, the lack of CRISM or HiRISE data (at time of writing) precludes observation of the surface composition or internal fabric in the SMCCC.

Given these observations, it is possible to test the competing hypotheses for the origin of the Bfu presented in Section 5.2. It is also possible to reconsider the conclusions and implications of Fawdon et al. [2015] (Section 5.2.5) in light of new modelling of the THEMIS and CRISM data [*Rogers and Nekvasil*, 2015]. There are therefore three possible hypotheses; the exposed pluton hypothesis, the ignimbrite hypothesis and the exposed effusive unit hypothesis.

7.1.2.1.1 The exposed pluton hypothesis

In this scenario, plutons have been intruded into the area of both Meroe Patera and Nili Patera. These intrusive bodies have then both been exposed by a period of erosion. This hypothesis

requires that the exposed plutons have similar properties so as to satisfy the very similar appearance on their exposed tops. The hypothesis is weakened by several lines of evidence (or lack thereof): (i) there is no evidence for significant erosion to expose the pluton, (ii) the pluton would have had to be spatially restricted so as not to crop out in the walls of the Meroe Petera caldera and thus could only be a thin (metres thick) sill within 10 m or less of the surface in the Northeast region of the caldera. Although small intrusions can occur close to the surface, the outcrops in Meroe Patera have a maximum overburden of 10 m and no associated tectonic signatures of intrusion on this scale (that could explain the observed polygonal fractures) [*Gilbert*, 1877; *Pollard and Johnson*, 1973; *Roman-Berdiel et al.*, 1995]. (iii) In addition, this hypothesis provides no explanation or account for the lHLto seen across the wider SMCCC.

7.1.2.1.2 The ignimbrite hypothesis

In this scenario, all the types of bright outcrop described in Section 7.1.2 have a common pyroclastic origin. The simplest scenario for this is one source event, i.e. the formation of Nili Patera between 3.28 (+ 0.08 or −0.13 Ga) and 3.1 (+0.13 or −0.22) Ga. I argue that if this material is an ignimbrite then it is consistent with the observations that the material is thickest in the topographic low of the incipient eastern portion of Nili Patera, forming the Bfu. There are further outcrops of this style of bright fractured material in Meroe Patera, meaning that either Meroe Patera produced similar eruptive materials or that this is part of the same deposit.

The first possibility lacks supporting evidence. On Earth ignimbrite forming eruptions are nearly always associated with caldera collapse events. However, there is less obvious structural evidence that Meroe Patera formed during any sort of cataclysmic event compared to Nili Patera. Instead the evidence points to two stages of subsidence.

Despite a distance of ~110 km between Nili Patera and Meroe Patera, it is plausible that the bright fractured material in both calderas originated from the same eruption. Similar runout distances are seen for terrestrial deposits associated with comparably sized calderas, for example, La Pacana (Andes of northern Chile), the Nevsehir plateau (central Turkey), the Currabubula

formation (Australia), and the Campanian ignimbrite (Italy) [*McPhie*, 1983; *Gardeweg and Ramírez*, 1987; *Fisher et al.*, 1993; *Le Pennec et al.*, 1994; *Branney and Kokelaar*, 2002]. This also implies that the incipient Meroe Patera formed a sufficiently deep depression in the landscape for the deposit to pond. This would allow thickening during deposition enabling the polygonal fracture network to form [*Soden and Shipton*, 2013].

The timeline suggested by this model of formation means that this material was deposited before the majority of SMCCC subsidence, after the start of Meroe Patera's formation but before subsidence associated with the formation of the wrinkle ridge in the Eastern floor of Nili Patera. These ridges are the same tectonic structures that expose the late Hesperian light toned outliers (lHLto) in the central caldera complex. This stratigraphic interval is supported by the distribution of lHLto in the central caldera complex (Map Sheet 1, Figure 6.8). The lHLto are observed in an elliptical pattern, matching the shape of the central caldera complex. They are predominantly exposed on the crests and in the foot walls of wrinkle ridge bounding faults and other tectonic structures. This supports the proposed timeline in two ways. Firstly, if the unit was deposited in this area before there had been any subsidence of the SMCCC, it is likely that the area would have been a high-stand relative to the developing floor of the caldera, and the deposit would not have been confined to the area at all. Secondly, the ignimbrite would have to have been deposited before the tectonic movement that exposed it. Additionally, local thickening in the incipient Meroe Patera also fits into this timeline.

The third type (iii) of material are very light-toned blocks eroding from the interior fault scarp in the resurgent dome axial ridge in Nili Patera (Section 7.1.2.1). In Meroe Patera, a similar unit is a thin (~10 m) layer of material in the North-Northeastern crater wall (Figure 6.6b). This supports a shallow, ponded layer in the incipient Meroe Patera (Section 7.2.2). In the SMCCC, there is also a similar outcrop, exposed in a fault wall northwest of the bright central lava-style unit (Figure 6.7) suggesting that ponding also occurred in the axis of the early-stage SMCCC.

7.1.2.1.3 Eroded evolved effusive unit

The third hypothesis discussed (Section 5.2.5.2) explored the possibility that the Bright fractured unit (Bfu) was the eroded core of an effusive unit such as an evolved lava flow [*Horgan*, 2013] in which the surface textures caused differing spectral responses [*Horgan*, 2013; *Carli et al.*, 2014a; *Rogers and Nekvasil*, 2015]. This scenario was unsatisfactory in Nili Patera because the stratigraphic relationship means that the Bright central lava (Bcl) and Bright fractured unit (Bfu) are not connected. The hypothesis is also unsatisfactory in the case of Meroe Patera, where there is negligible evidence of any Bcl material. Furthermore, in the central caldera complex, where there is very strong evidence for a spatially well-defined unit with the THEMIS DCS (Section 3.1.1) properties of the Bcl, there is no stratigraphic connection with any local outcrop of any type of Bfu. This hypothesis therefore fails to offer any explanation for the late Hesperian light-toned outliers (lHLto).

7.1.2.1.4 Formation of the late Hesperian lower Caldera floor (Bright fractured unit)

In light of this additional evidence and pre-existing modelling [*Rogers and Nekvasil*, 2015], magma genesis could be the same for a magma body that is subsequently emplaced either intrusively (pluton) or extrusively (ignimbrite). Therefore, I conclude that the ignimbrite hypothesis for the formation of the Bfu is the most consistent with all the available lines of independent evidence. The most important steps to further test this hypothesis would be: (i) interrogation of CRISM data available within Meroe Patera, (ii) investigation of the Southeast segment of Syrtis Major Planum for distal fall deposits, and (iii) rover-scale observations of outcrops in either of the two calderas. Unfortunately, there are currently no full resolution CRISM data within Meroe Patera, and the other possibilities are well beyond the scope of this thesis.

7.1.2.2 Distribution of vents and products of explosive volcanism

I have identified two or possibly three deposits associated with explosive volcanism. The Bright fractured units (Bfu)/late Hesperian lower Caldera floor units in both Nili Patera (Figure 5.7, Bfu on Map Sheet 2, lHlCf$_n$ on Map sheet 1) and Meroe Patera (Figures 6.2, 6.5 and 6.6, lHlCf$_m$ on Map sheet 1). The late Hesperian Light toned outliers (lHLto on Map Sheet 1, Figures 6.6 and 6.8) and

the Ridged mantling field (Rmf on Map Sheet 1, Section 4.3.3, Figure 4.10). These deposits are found to overlay the planum-building lava flows and volcanic plains formation but are contemporaneous with the initial collapse of Nili Patera (the source of the ignimbrite). Spatially, they are thickest in the floors of Nili Patera and Meroe Patera, also cropping out as thin layers in the uplifted folds of wrinkles ridges in the central caldera complex (Figure 6.8). Additionally, the area overlain by remnant Ridged mantling field covers at least 200,000 km^2 in the Southeast of Syrtis Major Planum (the extent of these ridges in the highlands was not mapped).

The composition identified for the Bright fractured unit (Bfu) is unique in an eruptive volcanic setting. Other examples of units with this composition are in sediments derived from uplifted crater rims or in uplifted crater rims themselves [*Carter and Poulet*, 2013; *Wray et al.*, 2013]. Whilst the identification of martian explosive deposits is not unique [*Greeley and Crown*, 1990; *Crown and Greeley*, 1993; *Gregg and Farley*, 2006](Section 2.2.2.1), this composition reported in association with a caldera-forming event is. Although violent calderaforming eruptions have been suggested for some other caldera-like features on Mars [*Michalski and Bleacher*, 2013] these are not associated with any recognised volcanic province.

This process had previously been considered on Mars, however, no evidence was found [*Francis and Wood*, 1982] making Syrtis Major Planum a currently unique location on Mars. Three factors have been identified which could have led to this explosive volcanism: (i) its emplacement during a Hesperian environment, (ii) its location on the rim of a giant impact crater known to host hydrated sedimentary materials (Section 2.3.5.1) and/or (iii) its location at the edge of a gravity anomaly [*Kiefer*, 2004; *Lillis et al.*, 2015], perhaps indicating the presence of an underlying large fractionated magma chamber. These possible influences are discussed in Section 7.2.2.2, while the prediction and implications for other Noachian/Hesperian plains volcanism is discussed in Section 7.6.

7.2 The age of Syrtis Major Planum

In this section I bring together all the observed events and processes discussed in Chapters 4, 5 and 6, and compile them in chronological order, along with additional observations reported from the literature (Section 2.3). This sequence of events and processes is presented alongside both crater count model ages performed as part of this thesis, and crater count results from the literature. The model ages I have incorporated from the literature are those that make sense within their stratigraphic context. I have chosen to do this, rather than attempt to incorporate all of the available dates due to the uncertainties associated with compiling model ages. These are reported by many authors. Different authors have different approaches to crater counting, fitting model ages, and choices of production and chronology functions. Furthermore, due to the variety of model ages possible for adjacent areas (as shown in Warner et al., [*Warner et al.*, 2015] and illustrated in Figure 2.13a), I have given more interpretative weight to model age dates that fit a clear stratigraphic context and have sensible superposition relationships with other datable areas.

7.2.1 The stratigraphy of Syrtis Major Planum

The tabulated sequence of events (Table 7.1) allows events in different parts of the planum (as reported and discussed in Chapters 4, 5 and 6) to be correlated. Chapter 4 draws on names and colours presented in Map sheet 1 (compiled at 1:2,000,000), Chapter 5 used the names and colours from Map Sheet 2 (compiled at 1:250,000) whilst Chapter 6 considered the units mapped on Map Sheet 1, but primarily drew on the CTX base layer data, with a scale of 1:250,000, and often compares these to unit shown on Map Sheet 2.

Table 7.1 summarises the sequence of events across Syrtis Major Planum, Nili Patera and Meroe Patera. To facilitate understanding I have tried to ensure consistency in terminology across the Planum and across time. Alongside the groups/units, listed in bold, are geological events (in plain text) and interpretation of processes (in italics) based on my observations from Chapters 4, 5 and 6. Some other events that are recorded on Map Sheet 1, but not discussed in the text, are also shown, as are events associated with Syrtis Major Planum drawn from the literature.

Phase 3

Volcanic plains and Planum building lava flows	Nili Patera	Meroe Patera/ SMCCC	Peripheral events	Date (Ga)	References

PHASE 3: LATE STAGE FLANK ACTIVITY/POSTCALDERA DEVELOPMENT VOLCANICS

Volcanic plains and Planum building lava flows	Nili Patera	Meroe Patera/ SMCCC	Peripheral events	Date (Ga)	References
	Olivene rich unit (Oru) *Late stage ring fault eruption dredging mafic cumulates from the frozen magma reservoir*			**0.51** (+0.11/-0.11)	**Map sheet 2** **Figure 5.15i**
AHdp / Adr *Thin pahoehoe flows from small fissures across the flanks*				**1.02** (+0.19/-0.19)	
Avf / AHdp (Estern long flow) *Thin pahoehoe flows from small fissures across the flanks*				**1.06** (+0.20/-0.20)	
Amazonian late volcanic units (Alv)		**(Alv$_m$)** *Thin pahoehoe flow*		**1.20** (+0.17/-0.17)	**Map sheet 1** **Figure 7.9i**

PHASE 2: MAGMATISM IN THE CENTRAL CALDERA COMPLEX

Volcanic plains and Planum building lava flows	Nili Patera	Meroe Patera/ SMCCC	Peripheral events	Date (Ga)	References
Erosion of the Rmf	Exposure of bright fractured unit (Bfu) / lateHesperian lower Caldera floor (Nili) (lHlCf$_n$)			1.55 (+0.50/-0.50)	[Robbins et al., 2011]
		Amazonian bright caldera volcanic unit (Abcv)		**2.22** (+0.26/-0.26)	**Table 4.5**
		Amazonian early volcanic unit (Aev$_m$)		**2.28** (+0.11/-0.11)	**Map sheets; 1, 2**
Western flank fissure (Avf)		Caldera floor flooding		**2.35** (+0.25/-0.25)	**Table 4.5** **Figure 7.9i**
Small pāhoehoe flow, inflated to 30m thick from a short fissure			Lipany crater floor fill	2.42 (non given)	[Bamberg et al., 2014]
	Wrinkle ridge cross cutting eastern caldera floor and walls	Subsidence of the Central caldera complex			**Figure 5.15h** [Kiefer, 2004; Lillis et al., 2015]
	SMCCC magma body	*Subsidence of the Meroe Patera*			
	Variegated volcanic unit (Vvu)/ Amazonain late volcanic unit (Nili) (Alv$_n$)				**Map sheet 2** **Figure 5.15g**
	Thin pāhoehoe from small mound like vents				
	Dome in the western caldera floor				
	Intrusion under the caldera floor				

Volcanic plains and Planum building lava flows	Nili Patera	Meroe Patera/ SMCCC	Peripheral events	Date (Ga)	References
	Bright central lava (Bcl) / Amazonian bright caldera volcanic units (Nili) (Abcv$_n$) *Eruption triggered by melt injection into Nili Patera magma reservoir*			2.46 (+0.25/-0.26)	Map sheet 2 Figures; 5.15e, 5.17g
Amazonian/Hesperian dark plains unit (AHdp) *Thin pāhoehoe flows from small fissures across the flanks*	**Inter-caldera lava (Icl) / Amazonian early volcanic units (Aev)** *Thin pāhoehoe flows from small fissures in the central caldera complex*			2.48 (+0.54/-0.61)	Map sheets; 1, 2 Figure 7.9g
	Pre-rifting lava (Prl) / Amazonian early volcanic units (Nili) (Aev$_n$) *Small scale eruption of basaltic material from the SMCCC magma reservoir*			2.71 (+0.22/-0.24)	Map sheets; 1, 2 Figures; 5.15e, 7.9g

Volcanic plains and Planum building lava flows	Nili Patera	Meroe Patera/ SMCCC	Peripheral events	Date (Ga)	References

PHASE 1: SYRTIS MAJOR CENTRAL CALDERA COMPLEX FORMATION/ START OF NILI AND MEROE PATERA MAPS

Volcanic plains and Planum building lava flows	Nili Patera	Meroe Patera/ SMCCC	Peripheral events	Date (Ga)	References
	Caldera floor unit (Cfu) / late Hesperian upper Caldera floor (nili) (lHuCf$_n$)			3.08 (+0.08/-0.10)	
	Volcanic units covering the bright parts of the Bfu/lHICf, possibly deposits form explosive eruptions?	Volcanic units covering the bright parts of the Bfu/lHICf$_n$, possibly deposits form explosive eruptions?			
Deposition of **Ridged mantling field (Rmf)** material	Caldera-forming eruption				
Possible widespread fall deposit in south east Syrtis Major Planum	Ignimbrite; **Bright Fractured unit (Bfu) / late Hesperian lower Caldera floor (nili) (lHICf$_n$)**	Ignimbrite; **Bright Fractured unit (Bfu) / late Hesperian lower Caldera floor (nili) (lHICf$_m$) and late Hesperian Light toned outers Bright outliers (lHLto)**			
	Stage 1 collapse of Nili Patera	Stage 1 collapse of Meroe Patera			**Map sheets; 1, 2 Figures; 5.15b, 7.9f**
	Development of a volcano-tectonic depression by thermo-mechanical weakening of the crust during the SMCCC magma reservoirs development	Development of a volcano-tectonic depression by thermo-mechanical weakening of the crust during the SMCCC magma reservoirs developmentrs			

PHASE 1: FORMATION OF THE BOUNDARY BETWEEN SMP AND ISIDIS/ISIDIS BASIN FORMATION EMPLACEMENT

Volcanic plains and Planum building lava flows	Nili Patera	Meroe Patera/ SMCCC	Peripheral events	Date (Ga)	References
			Emplacement of Isidis floor unit and Deuteronilus contact	3.01 (+0.07/-0.09)	**Map sheet 2 Figure 4.19, 4.20**
				3.01 (minimum)	[*Erkeling et al., 2014*]

Volcanic plains and Planum building lava flows	Nili Patera	Meroe Patera/ SMCCC	Peripheral events	Date (Ga)	References
			Late Hesperian Hummocky field unit (IHhf)		
			Deposition mantling remnant blocks of Syrtis Major Planum lava		
			late Hesperian Lower Planum dark unit (IHLPd)		
			deposition		
			late Hesperian Lower Planum dark unit (IHLPb)		
			Deposition		
			late Hesperian Lower Planum transitional unit (IHLPt)		
Flat topped mounds and ridges close to the Isidis boundary			*Collapse and brake up of Syrtis Major Planum lavas overlying Isidis floor units*	3.23 (+0.08/-0.13)	**Figures; 5.15a, 7.9e**
Volcanism close to the Isidis boundary associated with the brake up of Syrtis Major Planum lavas			**late Hesperian Lower Planum hummocky unit (IHLPh)**	3.23 (+0.05/-0.06)	

PHASE 1: PLANUM BUILDING FLOW FORMATION/CONTINUATION OF VOLCANIC PLAINS EMPLACEMENT

Volcanic plains and Planum building lava flows	Nili Patera	Meroe Patera/ SMCCC	Peripheral events	Date (Ga)	References
late Hesperian volcanic flow unit (IHvf): *'A'ā emplacement from SMCCC to the North of Nili Patera and to the North-east of Meroe Patera*	**Pre-caldera lavas (Pcl):** *topography and vent system*	**Pre-caldera lavas (Pcl):** *topography and vent system*		3.34 (+0.03/-0.04)	**Figures; 5.15a, 7.9e**
Last volcanic plateau unit (Hvp) flows Start of the observable Narrow Flow group (**IHvf**):		Last long duration volcanic plains group eruption from large linear pits		3.39 (+0.03/-0.04) 3.36 (+0.02/-0.02)	**Figure 7.9d**

Volcanic plains and Planum building lava flows	Nili Patera	Meroe Patera/ SMCCC	Peripheral events	Date (Ga)	References
Volcanic plains older than the Isidis boundary				3.46	[Ivanov et al., 2012]
lHvf/Hvp					
early Hesperian Volcanic plains unit (eHvp):				**3.48** (+0.01/-0.01)	**Figure 7.9d**
Continued emplacement of thin Pāhoehoe flows from distributed sources					
Eastern Syrtis Major Planum				3.50	[Hiesinger and Head, 2004]
Gfg/Nfg (into Isidis rim)					
Hesperian volcanic plateau unit (Hvp):				**3.51** (+0.01/-0.01)	**Figure 7.9c**
Giant flows which have inflated to build ~50 m of topography					
early Hesperian volcanic plains (eHvp):				**3.54** (+0.03/-0.03)	**Figure 7.9d**
Very long tube systems distributing lava to numerous thin Pāhoehoe flows					

PHASE 1: EARLIEST SYRTIS MAJOR PLANUM PLUME ACTIVITY/ VOLCANIC PLAINS FORMATION

Volcanic plains and Planum building lava flows	Nili Patera	Meroe Patera/ SMCCC	Peripheral events	Date (Ga)	References
				Figures; 5.15a, 7.9e	
Western Syrtis Major Planum, eHvp/Hvp				3.60	[Hiesinger and Head, 2004]
early Hesperain volcanic ridge unit (eHvr): Earliest activity from the Syrtis Major Planum vent systems.					**Map sheet 1** **Figure 7.9a** [Lillis et al., 2015]
Very long tube systems distributing lava to numerous thin Pāhoehoe flows and emplacement of thin Pāhoehoe flows from distributed sources					
Probable activity in the Southern Crypto Fissure Zone **(SCCFZ)**					

306

Volcanic plains and Planum building lava flows	Nili Patera	Meroe Patera/ SMCCC	Peripheral events	Date (Ga)	References

EVENTS BEFORE SYRTIS MAJOR PLANUM/ PRE-PLANUM BASAL MATERIALS

Volcanic plains and Planum building lava flows	Nili Patera	Meroe Patera/ SMCCC	Peripheral events	Date (Ga)	References
			Antoniadi crater floor fill	3.70	[Hiesinger and Head, 2004]
			Noachian Hesperian flat topped ridges (NHfr): *Inverted fluvial landforms*		
			Low calcium pyroxene volcanic units exposed in NE Syrtis region		[Ehlmann and Mustard, 2004]
Noachian/Hesperian bright plains unit (NHbp): *Volcanic material below the Volcanic plains group*			**Noachian crater fill unit (Ncf):** Floor fractured craters;	3.95	[Bamberg et al., 2004]
Noachian upper plains unit (Nup): *Volcanic and sedimentary materials*			*Intrusions under the southern highlands. Fractional crystallisation produces granitic compositions exposed in crater central peaks*		
Noachian lower plains unit (Nlp): *Volcanic and sedimentary materials*			**Noachian highland massif unit (Nhm)**	3.98 (+0.01/-0.001)	**Map sheet 1**

Table 7.1

The timing of events and processes in the history of Syrtis Major Planum divided into the geographic area in which they occur. Bold text refers to unit's dates from Map Sheets 1, 2 and Chapter 6 whilst italic text refers to interpretations and inferred processes. Further description can be found in the chapters relevant to the event columns.

7.2.1.1 Phases in the development of Syrtis Major Planum

In summary, I have divided the entire stratigraphy of Syrtis Major Planum into four phases.

Phase 0 (> ~3.6 Ga) occurred before the emplacement of the earliest volcanic units that are associated with the rest of Syrtis Major Planum. This phase includes units emplaced before the opening of the Nili Fossae and contain high levels of olivine [*Ody et al.*, 2013]. In this part of the stratigraphy there are three examples of inverted channel-like features, similar to those found in terrain of comparable age in Arabia Terra [*Davis et al.*, 2016]. This period of time also includes the last resurfacing of Antoniadi crater floor [*Hiesinger and Head*, 2004], although this area is not included in Map Sheet 1 because it does not appear to be part of the Syrtis Major Planum lava shield. (See section 8.3)

Phase 1 (~3.6 Ga to ~3.2 Ga) is the major constructional phase of Syrtis Major Planum. During this phase, a mantle plume initiated the emplacement of the Early Hesperian volcanic plains unit (Ridges) (eHvr), contemporary with the emplacement of the Early Hesperian volcanic plains unit (eHvp). The first focus of magma emplacement into the crust was the Southern Crypto Fissure Zone (SCFZ, Section 7.3.1.1) section, demagnetizing the crust in this area until the plumehead moved to the North (or the focus of the magma pathways rising in the crust switched). The vents in this first area were buried by lava flows emplaced subsequently from the central caldera complex.

During this time, the magma reservoir in the central caldera complex developed, and there is evidence that the most recent vents in this area may have hosted persistent lava lakes connected to the shallow fractionating magma reservoir below. Throughout this time, the Early Hesperian volcanic plains unit was emplaced via tube-fed pāhoehoe flows which inflated to build huge (~ 30

km x ~ 300 km, 50m thick) flow fields. The Hesperian volcanic plateau unit was also emplaced at this time.

Towards the end of this phase the focus of magmatism switched to the North East Fissure Zone (NEFZ) and the influence or presence of the mantle plume started to reduce. Smaller volume eruptions resulted in progressively shorter lava flows and that lava flow emplacement style changed from predominantly pāhoehoe to predominately 'a'ā flows on the increasingly steep northern part of the volcanic plain. This phase of stratigraphy ends with the catastrophic eruption and formation of Nili Patera caldera.

Erosional structures along the boundary between Syrtis Major Planum and the Isidis basin also developed towards the end of this phase. During this time the topographically lowest parts of the Planum (below ~-3 km) were mantled by 'hummocky' material. Then, the lava flows which descend to the floor of Isidis broke up to form 'chaos style terrain' [*Ivanov and Head*, 2003] and a 600 m high scarp. Penultimately, the area below ~3.3 km elevation was mantled again by 'bright' and 'dark' units. Finally, the floor of Isidis basin was deposited, forming the 'Deuteronilus contact' [*Ivanov and Head*, 2003; *Ivanov et al.*, 2012; *Erkeling et al.*, 2014] and chains of linear mounds [*Grizzaffi and Schultz*, 1989; *Farrand et al.*, 2005]. Any connections between these and volcanism on Syrtis Major are beyond the scope of this study (see section 8.3).

Phase 2 consists of the development of the SMCCC and its associated volcanism (~2.7 Ga to 2.2 Ga). During this phase, there were numerous spatially and temporally isolated volcanic eruptions across the planum, although most instances of such eruptions occurred in and around the SMCCC. Two of these isolated volcanic units, one in Nili Patera [*Christensen et al.*, 2005] and another, younger one in the central caldera complex, have high silica composition (Figures 5.11 and 6.9). This suggests that considerable magma evolution and/or partial melting of higher silica components took place within the magma reservoir associated with the central caldera complex.

There is also evidence for hydrothermal activity in Nili Patera during this phase [*Skok et al.*, 2010a]. This is alongside the peri-contemperaneous formation of Meroe Patera, the central caldera complex and the continued collapse of Nili Patera.

Phase 3, the development of Syrtis Major Planum was predominantly characterised by aeolian erosion punctuated by emplacement of a few isolated, thin volcanic units. During this time some fluvial activity occurred in the Northeast of the planum [*Mangold et al.*, 2008], carving channels into the martian surface as recently as ~1 Ga.

7.2.1.2 Confidence in dating

These phases summarise the history of events through which Syrtis Major Planum developed over the last ~4 Ga. The relative timing of events is dictated by their stratigraphic relationships while the absolute timing and durations of events are inferred based on crater count model ages. Although I am confident that these data indicate that the majority of Syrtis Major Planum was emplaced in the Hesperian, I have less confidence in the duration of events inferred from the crater count data for phase 1 volcanism, and even less confidence for the durations of activity in phase 2. There are two reasons for this:

Firstly, these data imply that the emplacement of Syrtis Major Planum took ~ 500 million years. This is 1-2 orders of magnitude longer than comparable large igneous provinces on Earth. Whilst this is consistent with thermal evolution models of dwindling numbers of long lived plumes though the history of Mars (*Harder and Christensen*, 1996). However, I think it is more likely that Syrtis Major Planum was emplaced in a shorter period of time, a theory supported by the lack of partially-embayed impact craters across the planum. This implies that there was insufficient time to accumulate a high number of impacts between volcanic resurfacing episodes and suggests a short overall period of emplacement.

Secondly, dating of the 2nd phase of volcanism is based on relatively small areas, all of which have large margins for error. Although the model ages suggest sporadic volcanism in the early

Amazonian, it is also possible that this late stage volcanism, like terrestrial large igneous provinces or plumedriven oceanic islands, is actually older, occurring in this case in the late Hesperian. Thus it could have been associated with the same source of mantle heat as the rest of Syrtis Major Planum. The length of time it took for Syrtis Major Planum to be emplaced is therefore still an open question, and one which might not be resolved until a series of igneous samples from Syrtis Major can be radiometrically dated and crystallisation ages determined.

7.2.2 The structural evolution of Nili and Meroe Patera

Here, I consider what the impact of my observations in the SMCCC and Meroe Patera has on the conclusions made about Nili Patera, and on the understanding of the evolution of the whole of Syrtis Major. I consider the stratigraphic, tectonic, geomorphological and compositional observations and discuss (i) the style of Meroe Patera caldera collapse, and the timing of this event relative to other tectonic events in the central caldera complex, (ii) the implications of the seemingly large extent of the bright fractured unit material, and (iii) volcanism within the central caldera complex after its formation.

I have found that Nili and Meroe Patera developed through the same period of time. Crater size-frequency data (Tables 5.1, 6.1 and 7.1) suggest that the pre-caldera lavas at both calderas are ~3.2 Ga old, with the floor of Nili Patera (prior to post-caldera volcanic units) established by 3 Ga. Meroe Patera appears to have had a two-stage development prior to the limited endogenic volcanic activity (Figure 6.12). This is younger than the oft-cited ages of Meroe Patera which are 3.8 ± 1.0 Ga [*Robbins et al.*, 2011] and 3.75 Ga [*Werner*, 2009] (although no errors are stated and no count area is identified in the latter). Werner's [2009] age is older than that of Nili Patera from my work and that of Robbins et al. [*Robbins et al.*, 2011]. However, this older age estimate is not supported in the details of the count areas shown in Robbins et al. [*Robbins et al.*, 2011]. In Robbins et al. [*Robbins et al.*, 2011], consistent with the interpreted history from my work, the majority of the caldera floor within Meroe Patera is dated to ~2.9 Ga. The areas towards the western rim of Meroe Pater that have the oldest date in Robbins et al. [*Robbins et al.*, 2011] do

not fit with the history. However, these are, in fact, two small areas which I have identified as the first resurfaced caldera floor, and an area that has been demonstrably resurfaced after caldera normal faulting. No dating in the pre-caldera lavas is presented in Robbins et al. [2011] or Werner [2009] to compare with my counts at Nili and Meroe Patera.

My dating and stratigraphical analysis suggest that Nili and Meroe Patera formed during the same time period and that they began to form before the subsidence of the SMCCC depression had finished down-warping. However, these events did not happen simultaneously, and neither Nili nor Meroe Patera formed in a single event. The distribution of the late Hesperian light-toned outliers (lHLto), exposed by the earliest faults at Meroe Patera, suggests that Nili Patera began forming first. In Meroe Patera, the floor of the first stage of collapse formed before the axial wrinkle ridge formation in the central caldera complex. The second stage formed after this wrinkle ridge-forming phase, when the SMCCC depression had already formed. At Nili Patera, wrinkle ridges originating outside the caldera are cross-cut by normal faulting, and these faults, in turn, are offset by other local wrinkle ridges. This relationship suggests ongoing collapse of the central caldera complex during the formation of Nili Patera. This is consistent with the contemporary, but interrupted, collapse of Meroe Patera.

The eastern caldera floor of Nili Patera is cross-cut by a conjugate pair of fault-bounded ridges which post-date the most recent volcanic caldera floor unit; although this contradicts evidence of the caldera forming at the same time, and presumes that the wrinkle ridge-associated subsidence in the central caldera complex took place during the same phase. The late-stage ridge-forming subsidence in Nili Patera is compensated for by normal faulting transverse to the axis of the central caldera complex. These faults are northeast of the bright, central lava-style unit (Figures 5.12 and 6.9) and in the Amazonian early volcanic unit (Aev) south of Nili Patera. These fault systems disconnected the eastern floor of Nili Patera, allowing it to subside later than any other activity in the central caldera complex.

Both Nili and Meroe Patera host post caldera-formation volcanic units. In Nili Patera, these are extensive, including three major eruptive phases and one sizable intrusion (Figure 5.15) over the lifetime of its evolution. In contrast to this, Meroe Patera has evidence for only one endogenic volcanic event (Figure 6.6f). This appears to be in the style of the variegated volcanic unit (Vvu) in Nili Patera. There is no evidence for either an earlier stage of basaltic lava (Aev$_n$-style) or any bright central lava (Bcl) composition material, intrusive or otherwise. Furthermore, there is no evidence supporting hydrothermal activity in the Meroe caldera. An explanation for the difference in morphology and interpreted geological evolution between Meroe Patera and Nili Patera is that heterogeneities in the crust under the Syrtis Major lava shield influenced the magma reservoirs in different ways.

7.2.3 The distribution of compositions derived from spectral data

In section 2.3.2 I reviewed the compositional observations of Syrtis Major Planum. Because the composition is crucial to the magmatic evolution, I now examine the published distributions of compositions and discuss them in terms of any correlations with geomorphic features. The overall conclusion of these studies is that Syrtis Major Planum has a basaltic to basaltic komatiitic composition and the mineralogy is dominated by pyroxene with a minor amount of olivine [*Mustard et al.*, 1993; *Reyes and Christensen*, 1994; *Poulet et al.*, 2003; *Clenet et al.*, 2013]. These studies show a distribution of pyroxene minerals [*Poulet et al.*, 2003; *Baratoux et al.*, 2013; *Clenet et al.*, 2013], or what is known as "type 1 and type 2" basaltic terrains [*Bandfield et al.*, 2000; *Hiesinger and Head*, 2004] across Syrtis Major Planum. These works show that the central part of Syrtis Major Planum is characterised by high calcium pyroxene (HCP) and that this is different to the western and eastern parts of the planum. These peripheral regions are characterised by a low calcium pyroxene (LCP) – high calcium pyroxene (HCP) mixture. Finally, the highland terrain surrounding and underlying Syrtis Major Planum is characterised by the signatures of low calcium pyroxene (LCP). Some authors (e.g. Baratoux et al. [2013] and Clenet et al. [2013]) go on to contend that this shows an evolution in volcanism (and, by inference, the temperature of melting

in the mantle) between the Noachian highlands and Syrtis Major Planum and then a continued evolution within Syrtis Major Planum. Although the variation between the Highland terrain (our understanding of which is developing rapidly; e.g. Sautter et al. [2016]) and Syrtis Major Planum is clear, there are no compelling correlations between the distribution of minerals on Syrtis Major Planum (summarised above) and any geomorphological features directly relating to volcanism on Syrtis Major Planum. However, there is a relationship between the distribution of wind streaks, 'dust' and the variation in pyroxene composition/type 1 and 2 terrain [*Bandfield et al.*, 2000].

Since the first observations and description of Syrtis Major Planum as a 'low albedo feature' it has been recognised as having very low levels of surface dust. This 'surface dust' is nano-phase iron oxide which coats surfaces and gives Mars its characteristic red/orange colour. Figure 7.4 shows the distribution of nano-phase iron oxide across Syrtis Major Planum. The distribution of nano-phase iron oxide is found to correlate with the population of wind streaks across the planum (Figure 7.4a), with individual wind streaks (Figure 7.4b) and is anti-correlated with abundance of high calcium pyroxene (HCP; Figure 7.5). A 'wind streak' (Figure 7.4c) is defined as a region on the leeward side of an impact crater which is bright (in RGB HRSC data) or dark (in daytime THEMIS data) and has diffuse margins. The presence of wind streaks means that the wind regime in the area is sufficiently strong to either (i) remove previously deposited dust, or (ii) transport (not deposit) dust except downwind of a crater (or other topographic obstacle) where dust is either (i) protected by the topographic obstacle or (ii) airflow is disrupted and dust is deposited [*Greeley et al.*, 1974; *Thomas et al.*, 1981]. In either case, the presence of wind streaks is indicative of strong unidirectional surface winds and minimal dust. Because wind streaks correlate to the HCP central areas of Syrtis Major Planum, these areas better represent the composition of the planum than LCP mixtures. Furthermore, individual flows from the Hesperian volcanic plateau unit (Hvp) can be seen crossing the gradational boundary from high to low levels of HCP (Figure 7.5). However, despite the lack of correlation between the central region and the peripheral regions, there are important correlations within the central region. Clenet et al., [2013] report higher levels of

olivine in the central part of the planum than previous studies. This distribution of olivine can be correlated to several geomorphological structures.

In the north of Syrtis Major Planum, the olivine signature correlates to the ejecta of craters. In this area of the planum, there are many instances of highland terrain protruding though the thin Syrtis Major lavas. Consequently, I suggest that these olivine signatures represent excavated material that predates Syrtis Major Planum, and is probably associated with the olivine signature found to the north of Syrtis Major Planum in the Nili Syrtis regions which are stratigraphically older than the Syrtis Major Planum lavas [*Mustard et al.*, 2005; *Ehlmann and Mustard*, 2012; *Ody et al.*, 2013].

Olivine is also detected in a large area of the central caldera complex [*Clenet et al.*, 2013; *Ody et al.*, 2013]. Whilst Clenet et al., [2013] attribute this to a "late stage, high temperature eruptive episode", geomorphologically it is found to correlate with windward facing escarpments with bright night-time THEMIS signatures, very little evidence of mantling surface sands and gravels (barchan dune field), and lower zones of nanophase iron oxide signature. Whilst the spectral data show olivine in the rocks, it is the wind regime, rather than a volcanic event, that controls the distribution. Also, this region does correlate to part of a volcanic unit emplaced after the subsidence of the central caldera complex (part of the Amazonian/Hesperian dark plains unit, AHdp). It may be the case, as with the interpretation of the late stage olivine rich unit in Nili Patera (Figure 5.15i), that this flow has entrained olivine-rich xenoliths from the Central caldera complex magma reservoir (which would have solidified by this time) and that this, combined with the fortuitous wind conditions that have "cleaned off" the dust, has permitted the olivine detection.
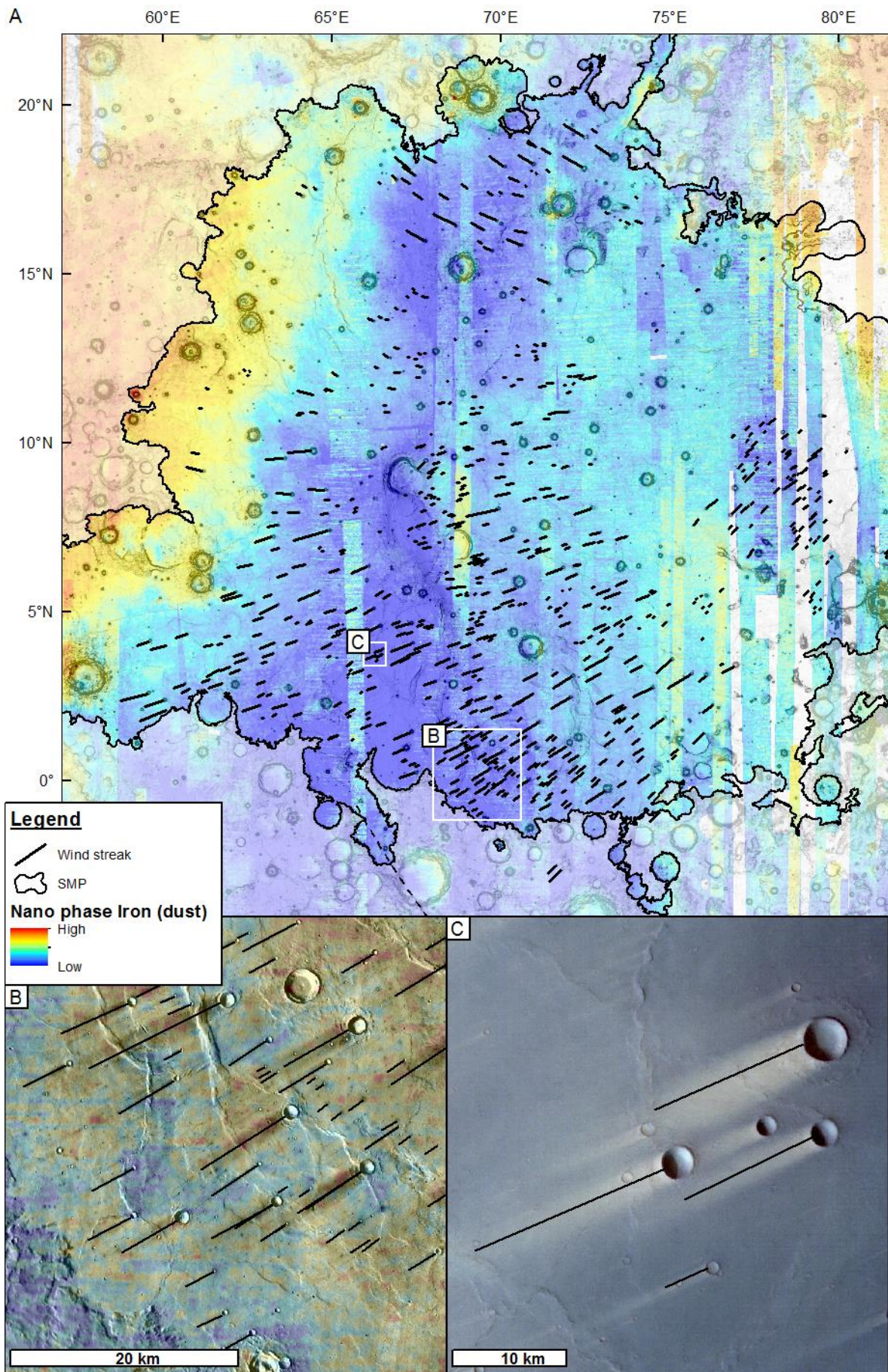
Figure 7.4: Wind streaks and dust

The distributions of (a) nano-phase iron oxide (dust) and wind streaks across Syrtis Major Planum using OMEGA data from Ody et al., [2012]. *(b) the local correlation between wind streaks (black lines) and dust (red) in OMEGA data* [*Ody et al.*, 2012] *and false colour HRSC data showing streaks as defuse bright orange patches relative to the dark blue/grey lavas (HRSC image H1990_0000).*

Interestingly, a small olivine rich region is also detected in correlation with outcrops of material in the AHdp and Thermally distinct lineation groups (Adr), and also in the area where the first fissure zone of Syrtis Major Planum (the SCFZ) is inferred to be located (Figure 7.5a iii). I interpret this to have the same explanation as olivine detections on the western escarpment of the central caldera complex, and in Nili Patera (Figure 5.15i): i.e., the olivine signature represents mafic cumulates dredged from the solidified plumbing system. Olivine is not detected in any other instances of the AHdp or Adr groups.

The final sets of olivine detections are clearest in the south of the planum (Figure 7.5a). Here, there is a clear correlation between olivine and the Noachian bright plains unit (Nbp) group. This material, very bright in night time THEMIS data, predates the Early Hesperian volcanic plains unit and Hesperian volcanic plateau unit, and appears to correlate with the pre-Syrtis Major Planum terrain north of the Planum which also has a strong olivine signature. It is presumed that these are volcanic materials that predate Syrtis Major Planum because outcrops of Npb material are seen to predate the opening of Nili Fossae.

The conclusion from examining the spectrally-determined composition of Syrtis Major Planum is that although there has been an evolution from LCP in the Noachian highland to Syrtis Major Planum, the composition of Syrtis Major Planum is dominantly HCP. Olivine detections can be associated with either the pre-Syrtis Major Planum materials, which are presumed to be volcanic in origin, or with xenoliths dredged up in late-stage effusive activity and sourced from the frozen or near-frozen magma reservoir left after the major phase of planum construction.
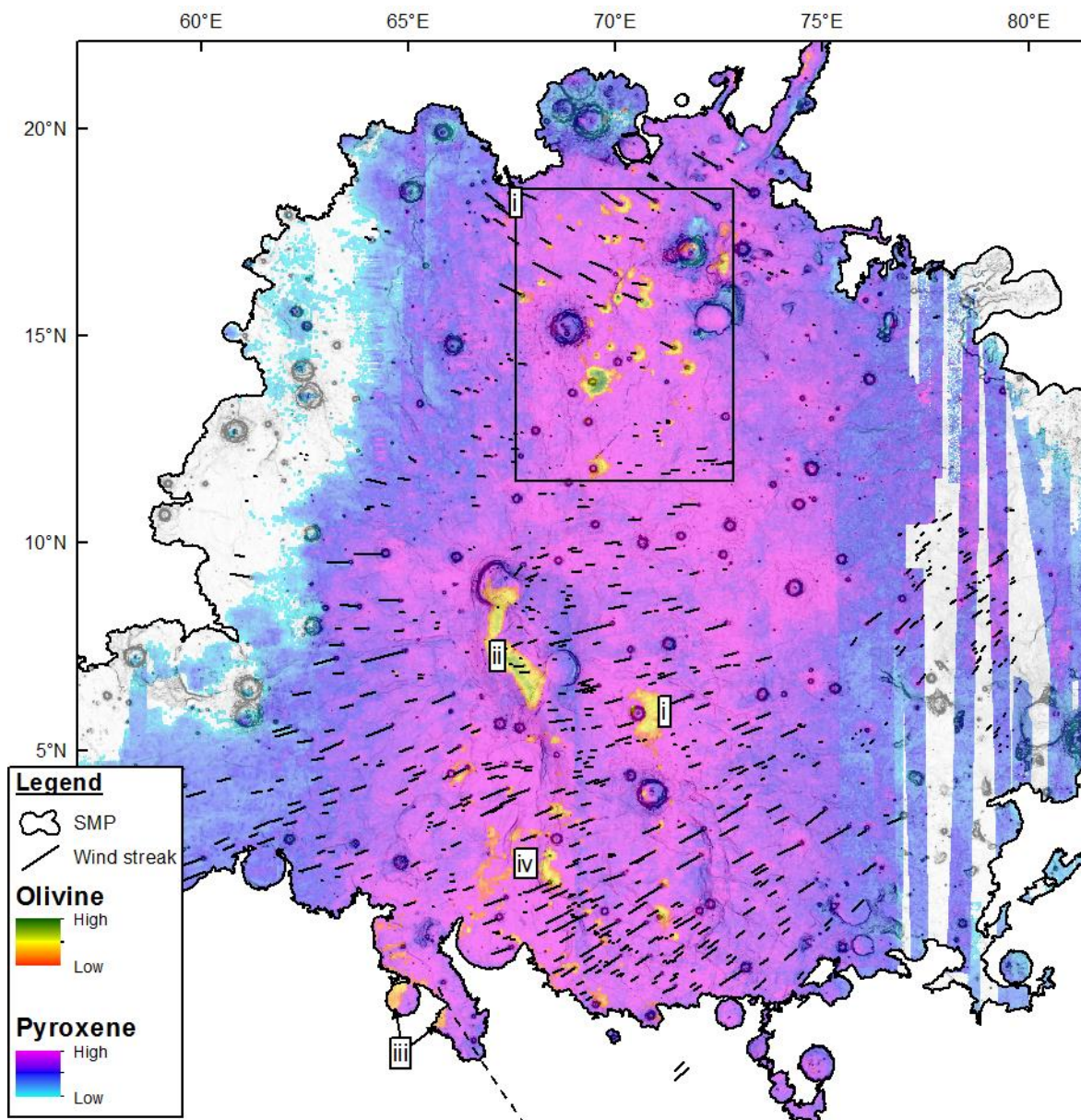
Figure 7.5

The distribution of high calcium pyroxene (HCP) (cyan though blue to purple) and olivine (red though yellow to green) from the global maps from OMEGA data made by Ody et al. [2012]. Olivine outcrops in (i) the ejecta of impact craters, (ii) in the central caldera complex and (iii) in the area of the Noachian bright plains unit and (iv) associated with the SCFZ. Also shown is the distribution of wind streaks.

7.3 Magmatic history

Chapters 4, 5 and 6 established the variety and stratigraphic relationships of the volcanic features

and surfaces found both across the whole planum (Map Sheet 1, Phase 1; Chapter 4) and the

central caldera complex (Map sheet 1, Phase 2/3; Map Sheet 2; Chapters 5 and 6). This section

discusses what the spatial and temporal distribution of these features can tell us about the

magma genesis processes, magma transport and the influence of subsurface structures of Syrtis Major Planum.

7.3.1 Phase 1 magmatism

7.3.1.1 Distribution of vents and the most recent magmatic system for Syrtis Major Planum

The distribution of major vent like features (discussed in sections 4.2.1 and 7.1 and shown on Map Sheet 1, Figures 4.2 and 7.6) shows two loose clusters of landforms that might indicate where magma has reached the surface in the centre of the planum. One of these is the central caldera complex (SMCCC) and the other is the North East Fissure Zone (NEFZ). Whilst both these areas share large linear pits and associations with all the planum building flow groups (Early Hesperian volcanic plains unit, eHvp; Hesperian volcanic plateau unit, Hvp; and Late Hesperian volcanic flow unit, lHvf), the SMCCC has developed two major calderas and a substantial post caldera volcanic sequence, whereas the NEFZ has not. Here, I discuss what might control this distribution and refer especially to recent geophysical results.

This disparity, the distribution of vent structures (a cluster of Large linear pits in the NEFZ and a low density of large linear pits, wide flat bottomed pits and calderas in the SMCCC) is reflected in the observations of remnant magnetism (Figure 7.6) and the gravity anomaly (Figure 7.7) over Syrtis Major Planum [*Kiefer*, 2004; *Lillis et al.*, 2015]. The northern zone of demagnetisation occurs to the north of the central caldera complex and is associated with the south west of the NEFZ. This location is beneath the present day topographic high point of Syrtis Major Planum. The northern zone of demagnetisation was caused by the intrusion of many dikes and sills into the area (Figure 7.6) [*Lillis et al.*, 2015]. In comparison, the free air gravity anomaly lies beneath the SMCCC (Figure 7.7). As discussed in section 2.3.4.2, [2004] and Lillis et al. [2015], the model that best fit to this gravity and magnetic data is a north-south orientated 'dog bone' shaped load beneath the SMCCC. Lillis et al. [2015] infer this to be composed of dense minerals that accumulate in fractionating magma reservoirs. Lillis et al. [2015] show two zones over Syrtis Major

Planum where the Noachian crust underlying Syrtis Major Planum has been demagnetised by emplacement of dykes in the subsurface, raising the temperature of magnetic minerals in the Noachian crust above their Curie temperature and wiping the record of the magnetic field they experienced when they last cooled below the Curie temperature. The second zone of demagnetisation is 250 km to the south of the central caldera complex. Based on the relationship between the northern zone of demagnetisation and the NEFZ (and to a lesser extent SMCCC) I infer that the demagnetisation in this southern area was also associated with a fissure vent zone in this area. The only geomorphic feature that correlates with the southern total demagnetisation is a large (95 km) 'ghost' crater [*Cruikshank et al.*, 1973], the southern part of which is identified by a circumferential wrinkle ridges (Figure 7.8a). Because of the correlation between this crater and zone of demagnetisation, I suggest that the earliest demagnetising intrusions and eruptions in this part of Syrtis Major Planum occurred in the "the Southern Crypto Fissure Zone" (SCFZ). This initial stage of volcanism filled the 95 km crater, which may have had a depth of up to 1.6 km (based on the depth of comparable diameter craters, Figure 7.8b). In the process of flooding this crater, the vent systems probably buried themselves, because erupted lava was spatially confined within the crater walls.
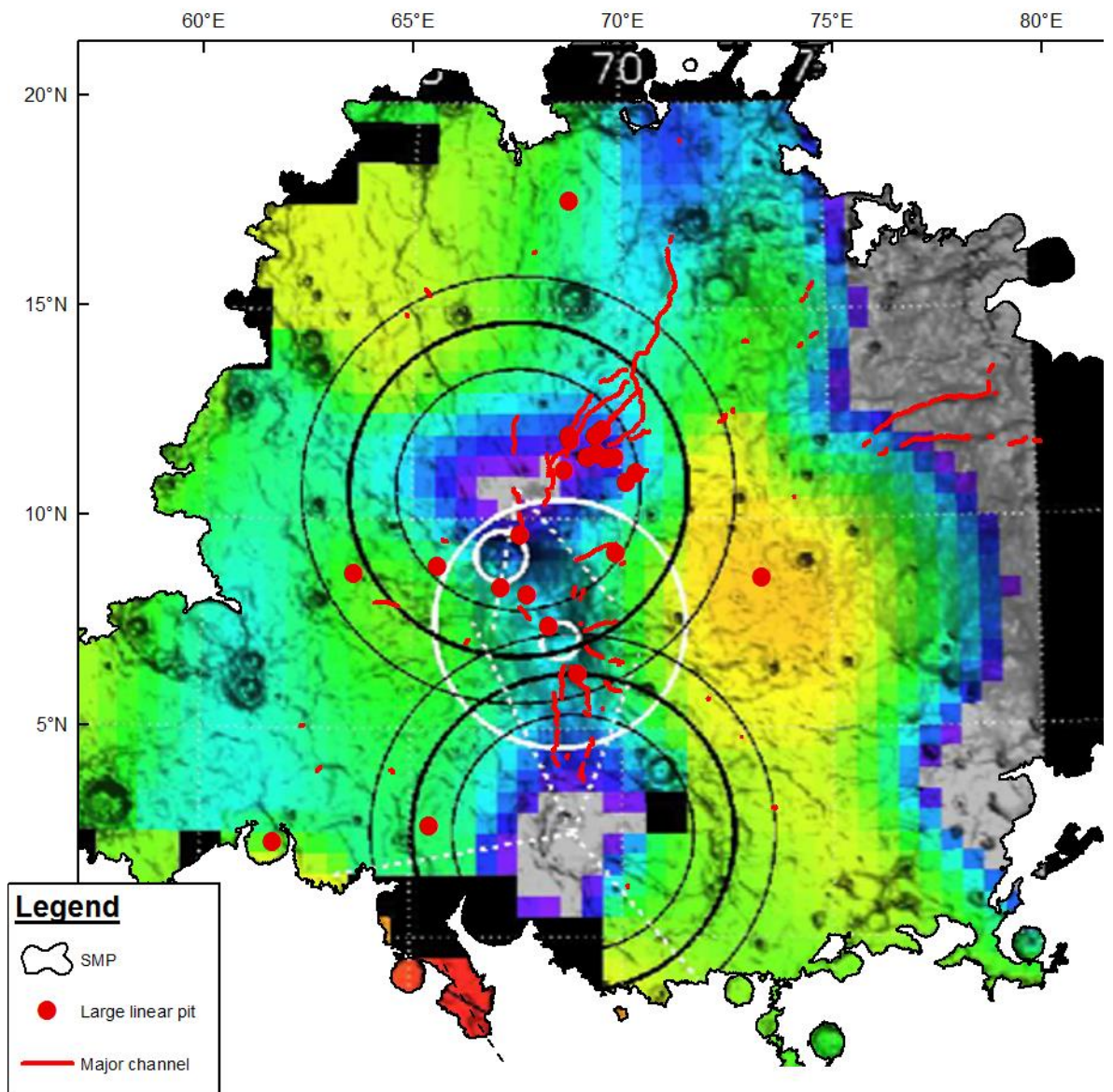
Figure 7.6:

Map of the major volcanic features on Syrtis Major Planum (this study) and the free crustal magnetisation at 200 km from Lillis et al. [Lillis et al., 2015]. Orange = high crustal magnetisation, purple/white = low/no remnant crustal magnetisation. The small white circles are Nili (to the north) and Meroe (to the south) Paterae; the larger white circle represents a high density cylindrical intrusive body modelled to fit the gravity data. The large black circles represent the cylindrical areas of magmatic intrusion causing demagnetisation; these are 234 ± 66 km in the north and 225 ± 57 km in the south (thinner lines represent the 1 sigma uncertainties).
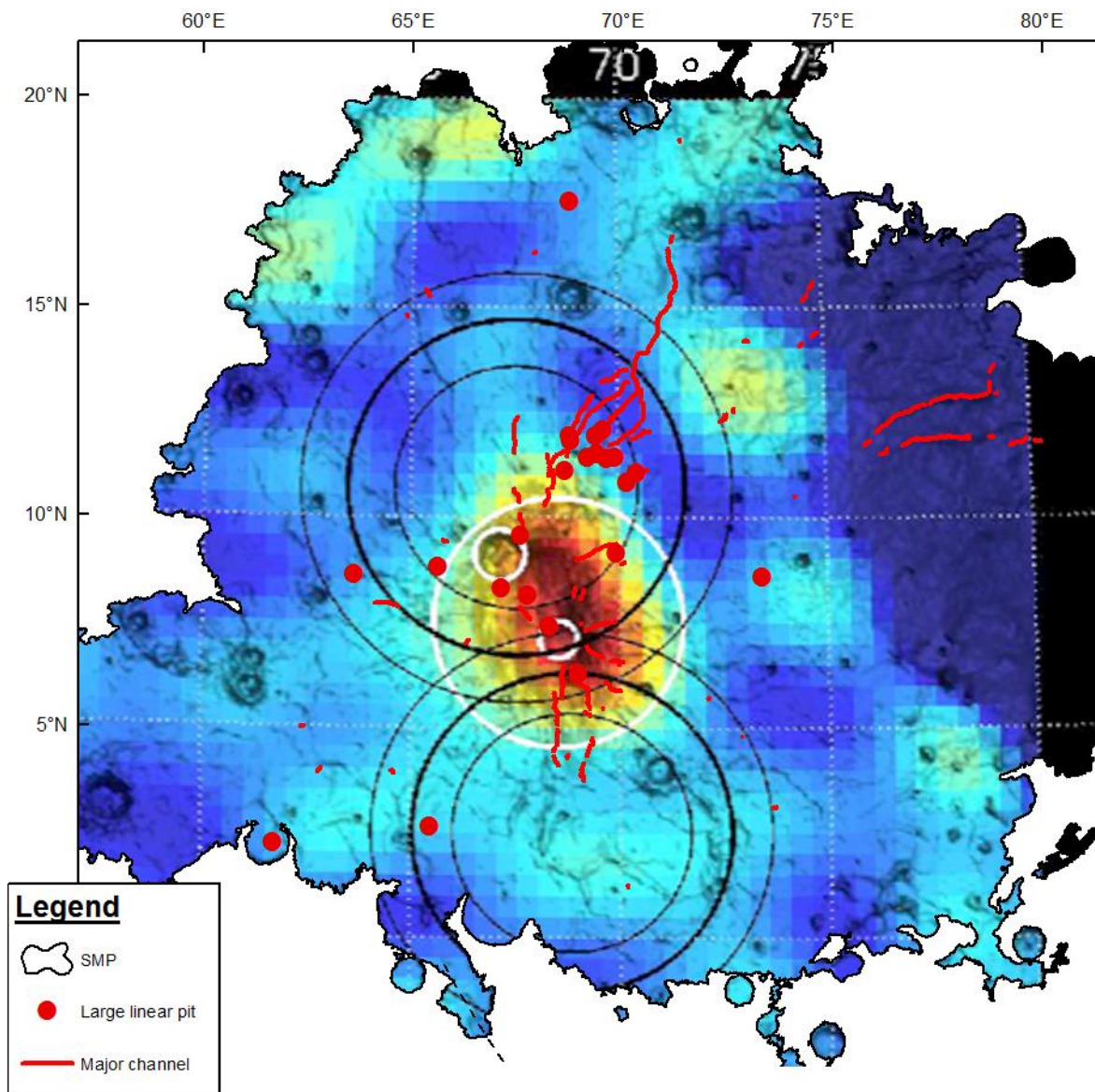
Figure 7.7:

Map of the major volcanic features on Syrtis Major Planum (this study) and the free air gravity data from Lillis et al. [Lillis et al., 2015]. Red = positive gravity anomaly. The small white circles are Nili (to the north) and Meroe (to the south) Paterae; the larger white circle represents a high density cylindrical intrusive body modelled to fit the gravity data. The large black circles represent the cylindrical areas of magmatic intrusion causing demagnetisation; these are 234 ± 66 km in the north and 225 ± 57 km in the south (thinner lines represent the 1 sigma uncertainties).
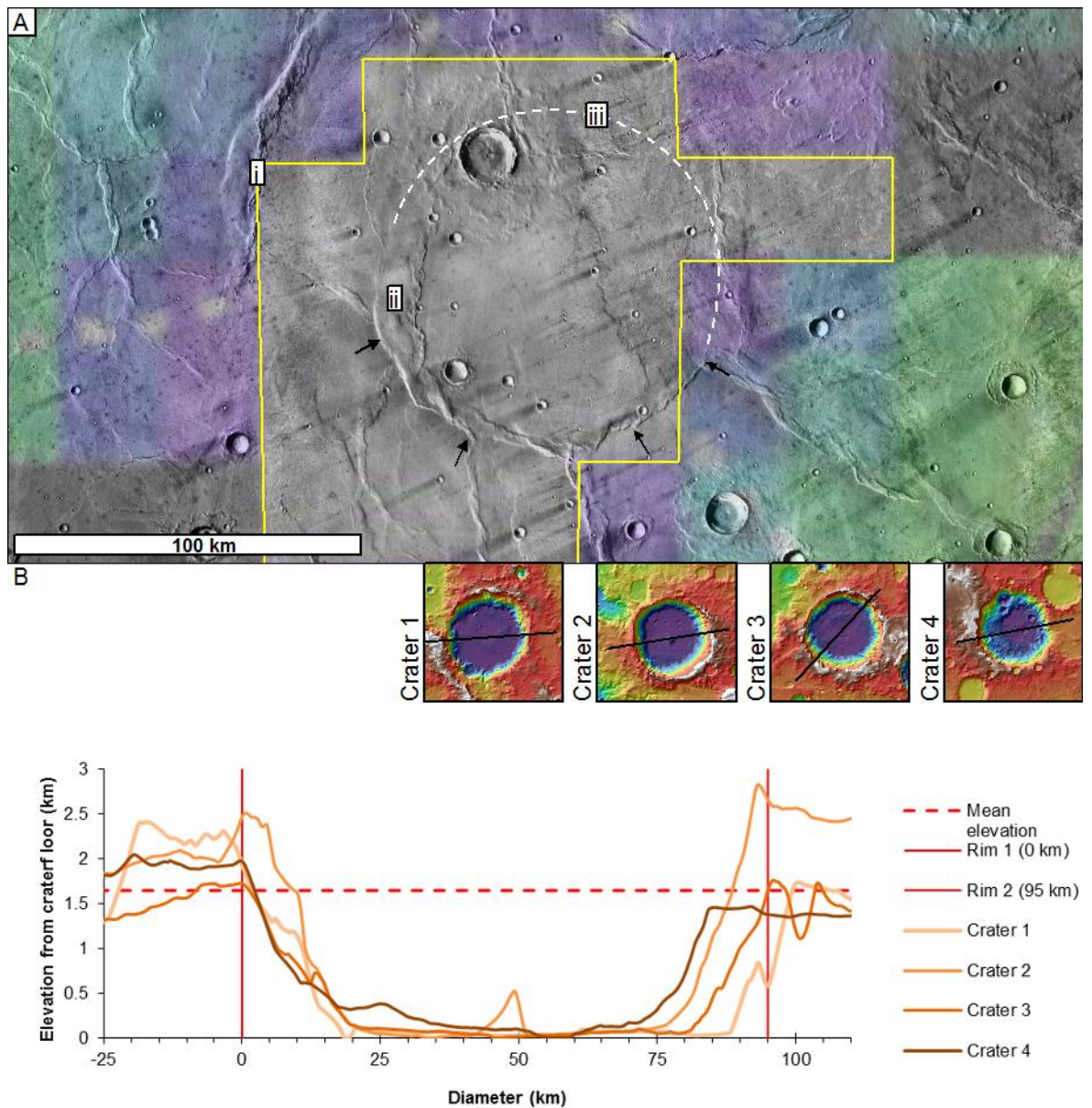
Figure 7.8:

The geomorphology of the southern zone of demagnetised crust. (a) (i) The outline (yellow) of the pixels where there is no remnant crustal magnetisation. It is in this area that the Southern Crypto Fissure Zone is located roughly correlating to a ghost crater ~ 95 km in diameter identified by (ii) a circumferential wrinkle ridge outlining the southern buried rim. The northern rim (iii) is completely buried. (b) Diameter depth relationships for four ~ 95 km diameter craters in the highland surrounding Syrtis Major Planum, showing a mean depth of 1.6 km.

The interpretation of Lillis et al. [2015] for these geophysical signatures is that Syrtis Major Planum is the surface expression of a longlived mantle plume and that the mineralogical diversity (basaltic to basaltic komatiite plains [*Reyes and Christensen*, 1994; *Rampey and Harvey*, 2008, 2012] to isolated high silica units [*Christensen et al.*, 2005; *Bandfield*, 2006]) at the surface is a result of fractional crystallisation within an extensive magma reservoir system and/or limited

partial melting of the crust. This interpretation is consistent with the geomorphology I have observed and my derived interpretations of volcanic history. Furthermore, using these results I conclude that magmatism in the main planum-building phase of Syrtis Major (Map Sheet 1, Phase 1) took place in the following steps (Figure 7.9a, f):

7.3.1.1.1 Phase 1 magmatism (step i).

Initially (Figure 7.9a), a magmatic plumbing system developed as a consequence of heat advection from the crust to the surface that was equal to or greater than advection from the mantle to the crust, likely the result of a mantle plume. This caused demagnetisation in the crust and volcanism was most probably focussed in the lowest elevation point in the region. This is most likely to have been the base of an impact crater which has now been completely buried within the body of the planum. It is also possible this 'low point' was a caldera in the opening stages of Syrtis Major Planum formation. This could be comparable to Noachian calderas proposed in Arabia terra [*Michalski and Bleacher*, 2013].

7.3.1.1.2 Phase 1 magmatism (step ii).

During this time (Figure 7.9b), while the SCFZ was still active, magmatism migrated north, influenced by the geometry of circum-Isidis faulting [*Schultz*, 1984], with dyke emplacement resulting in the development of the vent systems in the central area of Syrtis Major Planum. Vents in this area are more spread out than the cluster in the NEFZ and the crust has not been totally demagnetised (Figure 7.6). This suggests that magmatic activity was less intense, with fewer dykes reaching the surface per unit area. The lower intensity (smaller/more dispersed dykes) failed to achieve the same rate of advection from the crust to the surface and this area has developed a magma reservoir where heat advection from the crust to the surface was less than advection from the mantle to the crust, thereby building up a subsurface magma body in this region.
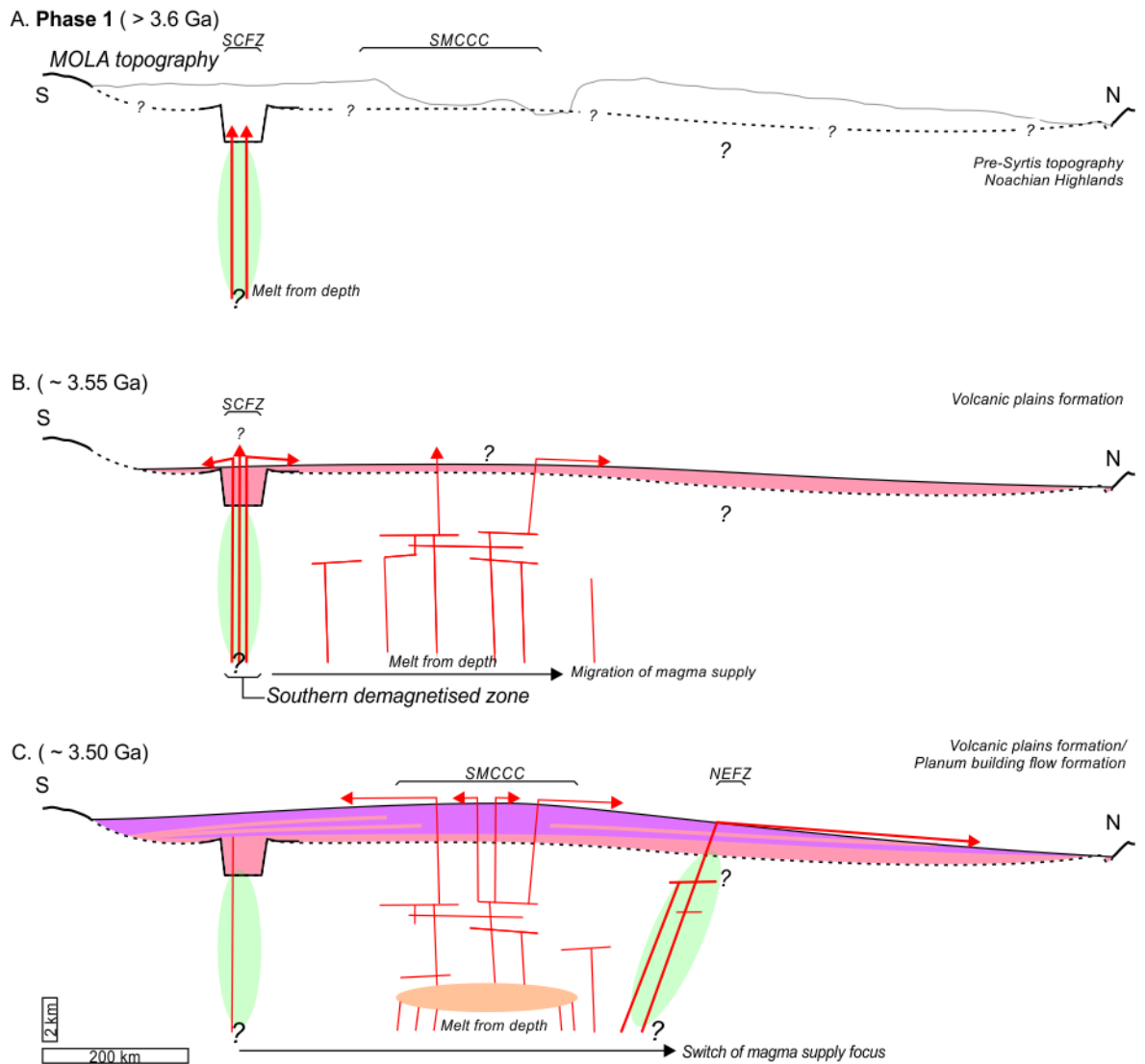
Figure 7.9:

A series of cartoon cross-sections though the pre- and post-eruption of the planum-building (but pre-caldera formation) topography of Syrtis Major Planum. This illustrates how the magmatic plumbing system of Syrtis Major Planum may have evolved though the history of the planum. Grey line in (a) shows current Syrtis Major Planum topography. (a) – (f) cover Phase 1 volcanism and the major construction of the planum. (g) and (h) cover the Phase 2 volcanism focussed on the central caldera complex discussed in chapters 5 and 6, but including the late stage volcanic formation. (i) covers isolated Phase 3 volcanism. In all sections red lines indicate dyke and sill emplacement, red arrows indicate where there have been eruptions. The orange zone indicates the magma reservoir, whilst the grey zone indicates a solidified magma reservoir. Yellow zones and lines indicate 'evolved compositions' e.g. Christensen et al. [2005] and Wray et al. [2013]. Blue lines indicate hydrothermal and/or surface run-off activity in the area of the planum. Black lines indicate tectonic activity. Lines indicate faulting and arrows show the direction of movement (primarily subsidence). Green zones indicate areas where the mean temperature of the crust has been raised over the Curie temperature of magnetic minerals, as in Lillis [2015].

D. (~3.36 Ga)
S
SMCCC   NEFZ   Planum building flow formation
N
Melt from depth   ?   Northern demagnetised zone

E. (> 3.23$_{0.13}^{0.08}$ Ga)
S
SMCCC   NEFZ   Planum Building Lava Flow Formation
Initial volcano tectonic depression
(Figure 5.15a/b)
N
Melt from depth
Initial gravity anomaly

F. (< 3.23$_{0.13}^{0.08}$ Ga)
S
SMCCC   Nili Patera caldera collapse   SMCCC Formation
late Hesperian lower caldera floor (IHICf)
(Bfu Figure 5.15c)
N
?   ?   ?
Initial subsidence of the central caldera complex
2 km
200 km

7.3.1.1.3 Phase 1 magmatism (step iii).

While low-volume eruptions continued in the area of the SMCCC, the foci of high intensity magmatism switched to the north (Figure 7.9c). Hence, the second open magmatic system, which may or may not be related, developed at the Northern zone of demagnetisation as magmatism in the SCFZ shut down. It is possible that this was guided by circum-Isidis faulting Nili fossae [e.g Schultz [1984]) and/or the Oenotria Scopuli trend [e.g. Raitala and Kauhanen [1989]. However, there is considerable debate around the tectonic influence of the emplacement of dykes and the distribution of surface volcanism [*Nakamura*, 1977; *Rowland and Sibson*, 2001; *Geoffroy*, 2005; *Kiyosugi et al.*, 2009]. However, understanding of this debate in terms of martian volcanism is hindered by the lack of comparable tectonic settings between Earth and Mars [e.g. Sleep [1994].

G. **Phase 2** (< ~2.71 Ga)

S

Meroe Patera   *Nili Patera*

Late stage volcanic formation
SMCCC formation,
(Figure 5.15d-f)

N

Hydrothermal activity
in Nili Patera and impact craters

Melt from depth

Evolving closed magma systems

H. (> ~2.09 Ga)

S

Meroe Patera   *Nili Patera*

Furthur subsidence of SMCCC
(Figure 5.15h)

N

Wrikle ridge formation and
continued subsidence of the planum

Development of the gravity anomaly

I. **Phase 3** (< ~2 Ga)

S

SMCCC

Late stage volcanism
Fluvial like channel formation
(Figure 5.15i)

N

2 km

200 km   *Contemporary the gravity anomaly*   Late stage volcanism dredges Olivine xenoliths

7.3.1.1.4 Phase 1 magmatism (step iv).

The penultimate stage of magmatism (Figure 7.9d) was the continued development of the magmatic system in the area of the SMCCC. In this stage, the wide, flat-bottomed pit craters, which possibly hosted long-lived lava lakes, formed, during which time there was degassing and convection within the magma reservoir.

7.3.1.1.5 Phase 1 magmatism (step v).

In the final stage of planum building (Figure 7.9e), volcanism in the SMCCC ceased and it is likely that the supply of magma from deep in the mantle into the crustal magma reservoir waned. Subsidence in the area of the SMCCC then began to develop (chapter 5). At this time, volcanism

also ceased in the NEFZ. Following this, caldera collapse occurred to form Nili Patera (Figures 5.15a-b and 7.9f)

Hence, by drawing on the geophysical interpretations of Lillis et al. [2015], and considering the relationship to geomorphological observations and stratigraphical correlations, an understanding of the most recent volcanic plumbing system and magmatic history of Syrtis Major Planum can be derived. This is because these geophysical data are an expression of the most recent magma reservoir, and melt in the crust beneath the Syrtis Major Planum is likely to have varied throughout the time in which Syrtis Major was active. Consequently, the combination of sub-surface information and geomorphological observations is needed to gain insight into the development of the complex as a whole. These conclusions are consistent with volcanism associated with a mantle plume.

7.3.1.2 Magma supplying the volcanic plains formation and Planum-building flow formation

Chapter 4 (Map sheet 1) identified the stratigraphic progression from (i) thin, widespread, tubefed flows to (ii) thick, giant, tabular flows (Hvp), being emplaced contemporaneously with numerous thin tube fed flows (eHvp), to (iii) narrow, channel-fed a'a flows, in which the channelized part of the flows have a distinctive slabby/rubbly surface. Overall, this trend appears to be comparable to the trends observed in the Tharsis Montes [*Bleacher et al.*, 2007a, 2007b], although they are quite different classes of martian volcano, (Amazonian central shield volcanoes compared to Hesperian plains volcanism, see section 2.2). The diameter of Syrtis Major planum is larger than any individual 'mons' in Tharsis, but it has several kilometres less relief [*Plescia*, 2004] and yet Syrtis Major Planum is considerably smaller than the overall lava plain around Tharsis.

Bleacher et al. [2007b] compared these Tharsis trends to the development of Hawaiian Islands. In this analogue, the magma chamber acts as buffer between the source of melt and dykes reaching the surface. It experiences the highest magma production rates in the early stages of development and hence produces longer duration, and more stable, tube-fed flows with a

higher total volume. This is followed by a transition to shorter-lived, buffered eruptions of more evolved alkali lavas, associated with fractional crystallisation of the melt and a decrease in the rate of production of magma [*Greeley*, 1972; *Lockwood et al.*, 1987; *Kallianpur and Mouginis-Mark*, 2001].

At Hawaii, these trends are understood in terms of the migration of the Pacific plate over a stationary hotspot. Watson and Mckenzie [1991] (and references herein,) model this and derive the following sequence of events: In the first phase there is a low degree of partial melting in a shallow, decompressed mantle on the edge of the plume. In the second phase, there are higher degrees of partial melting in the hotter plume head. This is the major constructional phase for the edifice, and consists of repeated cycles of storage and fractionation above the Mohorovicic Discontinuity, followed by recharge of more primitive melt from depth. The third phase sees a return to the low degree of partial melting as the plume moves away; during this period there is further fractionation of melts. Finally, the fourth stage involves the lowest degrees of partial melt. Metasomatism reaches critical levels, facilitating low degrees of partial melting that form alkali magmas. In these latter stages of development, isolated small bodies of magma occur, producing late stage parasitic eruptions [*Watson and McKenzie*, 1991; *Wolfe et al.*, 1997].

Similarities in the sequence of volcanism between the Tharsis region and Syrtis Major Planum [*Bleacher et al.*, 2007a, 2007b] suggest that it may be valid to extend the plume melting model to Syrtis Major Planum, although there are some differences that need to be explained. The most important is that the Hawaiian melting sequence is driven by the relative motion of the plate and plume, and a similar sequential model has been proposed for the Tharsis Mons (e.g. Figure 12 from Bleacher et al. [2007b]). Syrtis Major, however, is an isolated volcano and there is no evidence of a mobile lithosphere on Mars in the Hesperian [*Banerdt et al.*, 1982].

Consequently, it is more instructive to consider Syrtis Major Planum as reflecting the complete evolution of the lifetime of a mantle plume. On Earth, an example of this might be the Columbia River Basalt Group (northwest USA), where the mantle plume arrived quickly, emplacing

most of the extrusive igneous rocks [*Hooper*, 1988; *Tolan et al.*, 1989; *Camp et al.*, 2003; *Camp*, 2013], and then migrated several hundred kilometres, to a position beneath the Yellowstone area (e.g. Nash et al. [2006]). The initiation of volcanism was associated with a dyke swarm [*Ernst et al.*, 1995; *Ernst and Buchan*, 1997]; lithospheric rifting to the south, in Nevada, has been associated with the same plume [*Glen and Ponce*, 2002].

Such tectonic activity and dyke swarm emplacement could be comparable to the opening of the Nili fossa graben systems, and the subsequent emplacement of the Early Hesperian volcanic plains unit Ridges (eHvr), the earliest parts of the volcanic plains formation in Syrtis Major Planum. eHvr outcrops are at the bottom of the stratigraphy. If they reflect the planum-wide magmatic plumbing and dyke distribution at this time, they are consistent with the longest dykes associated with a plume head forming during dyke swarm initiation in a continuously pressurised magma reservoir [*Parfitt and Head*, 1993]. On Earth, the distribution of dykes reflects the regional stress field [*Ernst et al.*, 1995; *Tibaldi*, 2015]. The distribution of these outcrops (Map sheet 1; Figure 4.1), and the linear volcanic features associated with them (Figure 4.2), follow a radiating pattern. This is similar to terrestrial examples where there is only a limited stress field, such as the Spanish Peaks dyke swarm [*Smith*, 1987; *Ernst and Buchan*, 1997], or examples from Venus, where dykes often radiate though 360° [*Ernst et al.*, 1995]. In the case of Syrtis Major Planum, however, there is a sense that they were also affected by the regional circum-Isidis tectonics and crustal structure. Drawing on the observations of eHvr in the opening phase of planum development, through to relatively shorter flows which are more likely to form a brittle and disrupted a'a surface, and by comparison to sequences of melting induced by the onset and withdrawal of a mantle plume heat source, I suggest the following sequence for melting at Syrtis Major Planum (Figure 7.9a, b):

7.3.1.2.1 Plume history (step i)

The initial stages of magmatism at Syrtis Major Planum were associated with dykes radiating from the central area (the areas of the SCFZ and SMCCC). This was driven by the onset of a mantle

plume. It is presumed that impingement of the plume-derived melt would have seen low degrees of partial melting, but would have evolved towards higher temperatures, producing a higher degree of partial melting when associated with the head of the mantle plume. This predicts that the earliest phases of volcanism were hotter, and associated with higher degrees of partial melting, so the result would be an increased proportion of low-calcium pyroxene when the melt crystallises, relative to later stages of the magmatic evolution, higher in the stratigraphy. This prediction is apparently borne out in spectral data [*Clenet et al.*, 2013], as discussed in section 7.2.1.2.

7.3.1.2.2 Plume history (step ii)

Subsequently, magma supply stabilised to develop the major constructional phase of Syrtis Major Planum. Very large volume, long duration, sustained eruptions occurred, which emplaced the Early Hesperian volcanic plains unit (eHvp) and Hesperian volcanic plateau unit (Hvp). This reflects the "middle-age" period of the plume.

7.3.1.2.3 Plume history (step iii)

As the plume began to die out, the mantle potential temperature dropped and there was time to fractionate melts between eruptions, and reduced buffering in the magma reservoir. During this waning phase of volcanism, eruptions would have been shorter-lived and less stable, and the magma possibly more alkali in nature. During this time, the Late Hesperian volcanic flow unit (lHvf) was emplaced, and the properties of the magma led to an enhanced tendency to form channel-fed a'a flows on the increasingly steep northern flank of Syrtis Major Planum.

7.3.1.2.4 Plume history (step iv)

Finally, small parasitic eruptions would be expected towards the end of the active period in a similar manner to the small, late stage shields in Tharsis [*Bleacher et al.*, 2007b; *Hauber et al.*, 2009] and cones on the Hawaiian Islands [*Wolfe et al.*, 1997]. However, there is little evidence to connect the small peripheral eruption sites I have observed in Syrtis Major to this time period. The late stage eruptions that are seen on Syrtis Major, associated with the Amazonian/Hesperian dark

plains unit (AHdp), Amazonian dark ridge unit (Adr), and the lava units in the central caldera complex, were emplaced after caldera formation and are found to be at least 0.5 Ga later and clustered in the early Amazonian. If the crater model ages that show this time gap are robust, then it is unlikely these late stage groups are a direct result of the plume driving the major constructional phase (Map sheet 1, Phase 1) of Syrtis major Planum. However, if the crater count dates for these units are not robust, then they are likely to be older than I report (see Warner et al. [2015], section 2.3.6). Hence, it is possible that they are associated with the final phase of plume-related magmatism and the waning of the major constructional phase of Syrtis Major Planum (Figure 7.9).

7.3.1.3 Magmatic development of the central caldera complex

The evolution of the whole central caldera complex is discussed in section 5.2.5.4, based upon the observations from Nili Patera [*Fawdon et al.*, 2015]. Fawdon et al. [*Fawdon et al.*, 2015] postulated that there was a subsurface layer with low internal strength and hydrated minerals [*Skok et al.*, 2010b; *Ehlmann and Mustard*, 2012; *Glotch and Rogers*, 2013; *Schwegman et al.*, 2015] below Syrtis Major. It was further postulated that partial melting and assimilation of this country rock would explain: (i) the composition of the bright fractured material, (ii) the associated large-volume explosive eruptions, (iii) ductile deformation in the subsurface, facilitating wrinkle ridge formation and, (iv) the presence of hydrothermal deposits during the latter phase of volcanism. It has also been demonstrated that the composition of the bright fractured material, and possibly associated deposits, is consistent with fractional crystallisation in a low-pressure, shallow, magma chamber [*Rogers and Nekvasil*, 2015]. Although these are satisfying explanations for Nili Patera, consistent with the geomorphological and geophysical evidence (section 7.1.2), they do not explain the differences in expression (section 7.2.2) of such low-pressure magma reservoirs between the two calderas [*Rogers and Nekvasil*, 2015]. However, there are two mutually exclusive explanations that may explain the difference between the Nili and Meroe Patera.

The first possible explanation is that if these modelled magma bodies were emplaced and developed in different country rock with different chemistry (e.g. more volatiles) and strength, then this could account for an ignimbrite-forming eruption in one location, not the other (although it should be noted that while there is no specific evidence of such an eruption in Meroe Patera, it is not impossible and even likely given that on Earth calderas are nearly always associated with ignimbrites and caldera forming eruptions). Although it is not possible to directly observe the structure and composition of the Noachian crust that existed prior to the emplacement of Syrtis Major Planum, there is evidence in addition to that previously described [*Skok et al.*, 2010b; *Ehlmann and Mustard*, 2012; *Glotch and Rogers*, 2013; *Schwegman et al.*, 2015] for numerous outcrops of hydrated material around Syrtis Major Planum (Figure 7.10) [*Carter et al.*, 2015]. These outcrops are dated to between the late Noachian and early Hesperian; immediately before the emplacement of Syrtis Major Planum. The outcrops are located in all the terrains onto which Syrtis Major Planum was emplaced and, in some cases, they reach over a kilometre in inferred pre-erosional thickness [*Carter et al.*, 2015]. Additionally, many of these deposits are associated with Noachian paleo-lakes [*Fassett and Head III*, 2008]. Therefore, it is possible that the heterogeneity in the distribution of these materials is similar under Syrtis Major Planum to that in the surrounding terrains, and that it is the concomitant spatial differences in the county rock beneath Syrtis Major Planum that explain the differing volcanic and tectonic expressions of maturing magma chambers.

The second explanation is that that there is a close association between the northern zone of demagnetisation and Nili Patera, compared with the lack of an association between Meroe Patera and either zone of demagnetisation. In the zones of demagnetisation, there must have been a sufficient heat flux from dykes propagating from depth to a minimum of 50% replacement by volume by dykes. The exact percentage required to cause the demagnetisation depends on the model composition of minerals hosting remnant magnetism [*Lillis et al.*, 2015] but a 50% minimum is close to the ~60% observed where exposed in the Hawaiian Islands [*Macdonald et al.*,

1983; *Bohrson*, 2007]. Because of this spatial association I infer that there was a higher spatial density of dykes close to Nili Patera, compared to Meroe Patera. Therefore, it is likely that the magma reservoir under Nili Patera was larger (by volume) and, consequently, the region surrounding the magma reservoir will have been hotter. This in turn means that there will have been more partial melting and assimilation of the country rock (including any volatile bearing phases) into the fractionating magma. It also means that there could have been an enhanced rate of convective flow within the network of dykes and sills that make up the magma reservoir [*Cashman and Sparks*, 2013]. Both these factors enable the fractionation invoked to produce the composition of the bright fractured unit (Bfu) e.g. Rogers and Nekvasil [2015] and Wray et al., [2013] (Section 5.2.5.2) and compositional stratification for eruption at a later date (e.g. Wray et al., [2013]; Section 7.2.4).
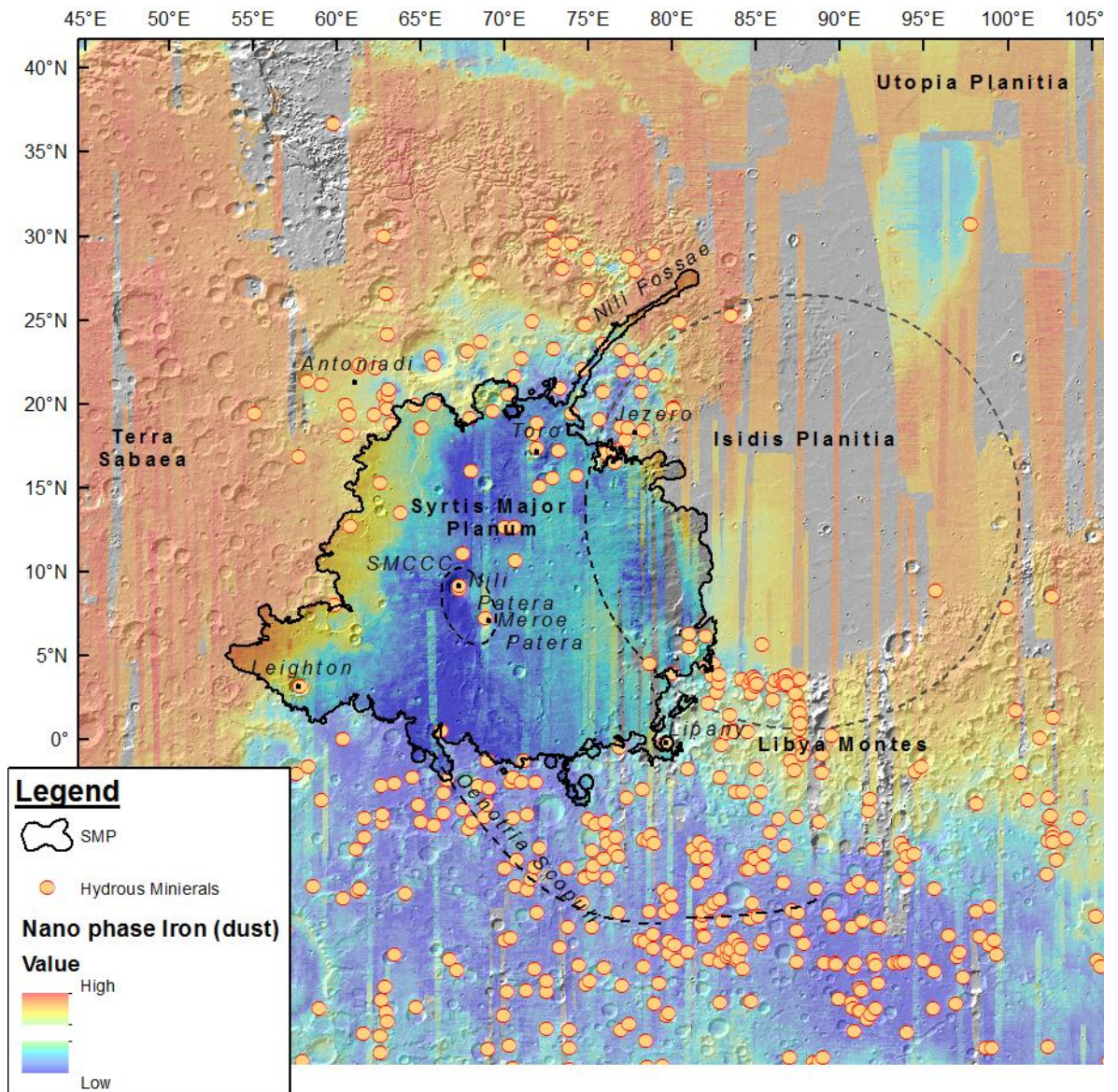
Figure 7.10

The distribution of detections of hydrous bearing phases as identified by Caret et al. [2015] *(tan circles) in the region around Syrtis Major Planum. The overlay is the nano-phase iron (dust) Map of Ody et al.* [2012]*. This shows that hydrated minerals are found in the Noachian highland massifs (Nhm) all around Syrtis major Planum, but to the west, where there is more dust, the hydrated spectra are masked.*

In summary, magmatism in the central caldera complex has developed into a volatile rich magma reservoir by incorporation of volatile-bearing species from the highland terrains underlying Syrtis Major Planum. This allowed the otherwise dry magma [*Mustard et al.*, 1993; *Filiberto and Treiman*, 2009; *Rampey and Harvey*, 2012] to erupt in a predominantly explosive manner. A combination of the differences in magma supply/density of dykes in the crust and/or the composition/structure of the underlying Noachian crust caused the differences between the

more intense activities at Nili Patera (deeper caldera, evidence of ignimbrite emplacement) and the simpler, shallower Meroe Patera. The fractionally-crystallised remnant of this magma reservoir caused (i) the gravitational collapse of the Syrtis Major central caldera complex and (ii) a reservoir of evolved material for small-volume eruptions of evolved dacitic magma [*Christensen et al.*, 2005; *Wray et al.*, 2013].

7.3.2 Phase 2 magmatism

The second phase of volcanism in the history of Syrtis Major Planum was focused on the central caldera complex (Map sheet 1, Phase 2; Table 7.1), although there are a few examples of eruption elsewhere on the planum in this time (e.g. section 4.3.9). The model ages for this phase of volcanism range from ~2.7 to ~2.2Ga. This volcanism occurred after the major planum-building phase of Syrtis Major Planum (Phase 1 Map Sheet 1,) and after the initial formation of Nili Patera. Magmatism across the planum in this phase is discussed in section 4.5.3 and magmatism in Nili Patera during this phase is discussed in section 5.2.5.3. Here, I discuss the outcrops of magmas with silica-rich compositions [*Christensen et al.*, 2005] in the central caldera complex, and the implication for those latter-stage volcanic units which have a composition not observably distinct from the rest of Syrtis Major Planum basaltic composition.

7.3.2.1 Evolved-composition lavas in the central caldera complex

Nili Patera contains a lava flow unit with an evolved composition, interpreted as dacite [*Christensen et al.*, 2005]. This is mapped as the bright central lava (Bcl) in Nili Patera and as 'bright central lava (*Bcl*)-style' material where an area has similar visual and geomorphic properties (Figures 5.2, 5.12 and 6.9). Although the outcrop in the central caldera complex is alluded to in Christensen et al., [2005] they do not make a direct comparison between the outcrop seen in the central caldera complex and the unit of similar composition in Nili Patera. Both surfaces share the THEMIS DCS signal, as well as colour, surface texture, apparent thickness,

area, lobate margins and gradational boundary with overlying material (in this case, inter-caldera lava (Icl); Map sheet 2, north of a normal fault). The age of this unit can be only loosely constrained by stratigraphy. It formed after SMCCC subsidence, but before the normal faulting associated with the further subsidence of Nili Patera (Figure 5.15i). The impact crater dating age of the unit should be considered a minimum, due to material mantling the surface. Nevertheless, those data do suggest that the unit is significantly younger than the comparable unit in Nili Patera (although this is open to speculation given the uncertainties encountered when small units are counted on CTX; see Warner et al. [2015] and Section 2.3.6).

The importance of this outcrop is that magma of this composition (dacite [*Christensen et al.*, 2005]) is not unique to Nili Patera and is not uniquely related to magmatic and/or volcanic processes associated with that caldera. Therefore, magmas of this composition were erupted on at least two different occasions. Therefore, melt has been generated with this composition in the shallow crust in the region of the SMCCC at least twice in this time. This could occur when either (i) melt ascends from depth, stalls, fractionally crystalizes and then an eruption is triggered (the mechanism invoked in chapter 5), or (ii) when melt ascends from depth, stalls at a position of neutral buoyancy (such as above high density mafic cumulates and below lower density felsic layers), melts the existing, crystalized magma chamber, which then goes on to erupt, emplacing a more silica-rich felsic magma. Although it is not possible to tell between these two mechanisms from remote sensing data, I note that the outcrops with the evolved composition only occur in the region of the central caldera complex. This matches the region where there is geophysical evidence for a crystallised magma reservoir [*Lillis et al.*, 2015]. The association of these two factors supports the second mechanism: outcrops of this composition are only seen where there is a pre-existing crystallised magma reservoir that provides a more felsic country rock that can then be partially melted to produce the compositions that we observe on the surface. However, this scenario could be indistinguishable from there being a higher number of intrusions and thus an increased likelihood that later intrusions would disrupt older, crystallising ones, as observed on

Earth [*de Silva et al.*, 1994; *Cashman and Sparks*, 2013] and suggested for the outcrop in Nili Patera (Figure 5.15e-f)

7.3.2.1 Phase 2 magmatism

In addition to these two compositionally-distinct examples, there are many other volcanic units which are either dated (Tables 4.6, 5.1 and 6.1) or are stratigraphically located in the second phase of volcanism (Map sheet 1, Phase 2; Figure 7.9g, h,). The distribution (Table 7.1) of these units is primarily within the two calderas and the central caldera complex, with few examples outside this area. This is also the time period in which there was continued subsidence of the central caldera complex (Figures 5.15d-h, 7.9g; Sections 6.4 and 7.2.2), suggesting an increasing load in the subsurface. In addition, there is evidence of intrusive emplacement (Figures 5.15e-f, 7.9g; Section 5.2.5.3). Because the gravity anomaly observed over Syrtis Major Planum (Figure 7.6) [*Kiefer*, 2004; *Dufek et al.*, 2014] represents the cumulative and most recent emplacement of load into the crust, I suggest that, during this phase, continued subsidence in the central caldera complex was driven by the further intrusion of melt into the shallow subsurface from the deeper origin of melting.

7.3.3 Phase 3 magmatism

Phase 3 is the final stage of volcanic activity on Syrtis Major Planum. This history of Syrtis Major Planum in this phase is dominated by erosion processes and final wrinkle ridge development in Nili Patera (Figures 5.15i and 7.9i). There are four outcrops that have been dated to fit into this phase (Table 7.1); however, there may be numerous others grouped within the Amazonian/Hesperian dark plains unit (AHdp) and Amazonian dark ridge unit (Adr).

The model ages for these units suggest they are late Amazonian, and these dates are consistent with the stratigraphic relationship to impact ejecta underlying these lava flows (Figures

4.15, 4.17). This sporadic and dispersed distribution of volcanism suggests that magmatism at this time had dwindled, and then consisted only of isolated melt pockets reaching the surface and some continued loading in the subsurface under the central caldera complex. This is consistent with a global pattern in which the volume of volcanic materials erupted decayed exponentially over time as the planet has cooled over the last 4 Ga [*Grott et al.*, 2012].

7.4 Implications for martian volcanism

The findings of this research for the magmatism, evolution and styles of volcanism on Syrtis Major may throw light on the interpretation of features at other Martian volcanoes. I discuss the formation of Nili Patera and implications for other volcanoes on Mars in section 5.2.5.4. Here, I discuss additional observations relating to other Hesperian-age volcanoes.

In determining a geological history for Syrtis Major Planum, I have explained the magmatic diversity from low-silica, high-magnesium basaltic komatiites [*Mustard et al.*, 1993; *Reyes and Christensen*, 1994; *Rampey and Harvey*, 2012] to high-silica dacite [*Christensen et al.*, 2005], and the variety of eruptions styles, including fissure-fed fire fountains producing lava flows, an explosive caldera-forming ignimbrite, and effusion of dacitic lava flows and domes [*Christensen et al.*, 2005]. To reconcile the volcanic history, I observe with geophysical data [*Kiefer*, 2004; *Lillis et al.*, 2015] I invoke a waxing and waning mantle plume that drove melting at the base of the crust to generate the early Syrtis Major Planum volcanism, similar to the interpretation of some terrestrial large igneous provinces, [*Griffiths and Campbell*, 1991; *Coffin and Eldholm*, 1994; *Courtillot and Renne*, 2003], followed by a second phase of volcanism, 0.5 Ga later. To explain all the observations I suggest that these phases of melting, possibly controlled by deep crustal faults associated with the Isidis basin [*Schultz*, 1984], have at times variously (i) fractionally crystallised (section 7.3.1.4), (ii) assimilated (section 7.3.1.4) and/or (iii) demagnetised (by heating over the Curie temperature by hot dyke emplacement; section 7.3.1.1) the heterogeneous Noachian crust (section 2.3.5.1) underlying Syrtis Major Planum.

7.4.1 Comparison with Hesperian volcanism

Syrtis Major Planum is morphologically similar to, but younger than, Malea Planum (Werner, [2009]; Figures 2.5 and 2.6a) which hosts the caldera-like structures Peneus Patera and Pityusa Patera [*Williams et al.*, 2009a]. These morphological similarities suggest a genesis similar to that of Syrtis Major Planum. This could be tested if a comparable investigation was conducted at Malea Planum. Such similarities may also be true for the Hesperian plains of Hesperia Planum, and Hesperian-aged plains in the Tharsis area. However, there are no comparable caldera-bearing regions for these volcanic plains. Hesperia Planum is overlain by Tyrrhena Mons (Figure 2.6b), and the Hesperian-aged plains in the Tharsis region are overlain by the Amazonian-aged Tharsis Mons (Figure 2.7a). Therefore, it seems very likely that younger volcanism has obscured the older volcanic features.

The Highland Pateras volcanoes (section 2.2.2.1) differ from Syrtis Major in that they form edifices several kilometres high that have deeply incised flanks. They are interpreted to form from pyroclastic material [*Greeley and Crown*, 1990; *Gregg and Farley*, 2006], which modelling has shown to be driven by interaction with ground water, rather than by the presence of magmatic volatiles [*Greeley and Crown*, 1990; *Crown and Greeley*, 1993; *Gregg and Farley*, 2006].

These similarities and differences suggest that both 1) the volcanic plains, and 2) volcanic plains with associated caldera-like depressions, may have formed in a similar way to Syrtis Major Planum. However, the Highland Patera-style volcanoes which are associated with them represent a further step in the primary construction phase of their volcanic history that has not taken place at Syrtis Major Planum. It has been suggested [*Werner*, 2009] that there is an overall evolution in martian volcanism with time and in space from the plains with caldera-like constructs to Highland Patera volcanoes. This study disagrees with this concept in terms of the detail during the Noachian/Hesperian but does not comment on changes in volcanism between the Hesperian to present day.

7.4.2 Compositional uniqueness

At present, Syrtis Major Planum appears to be unique on Mars: it has evidence of a caldera-forming eruption from an evolved magma chamber and two separate instances of volcanic deposits that have high silica compositions. Neither of these has been similarly observed in any other major volcanic setting on Mars which are 'normally' characterised by basaltic central volcanoes. Recent research does identify similar anomalies: For example, morphologies best-explained by 'very high viscosity lava', parsimoniously explained by high silica content, have been inferred in one minor volcanic feature in the southern highlands [*Brož et al.*, 2015], and also 'super volcano' calderas have been attributed to some structures in Arabia terra [*Michalski and Bleacher*, 2013]. Both of these examples are similar to parts of the evolution of Syrtis Major Planum; however, Syrtis Major Planum shows a more complete evolution of a magmatic system.

Terrestrial eruptions of dacitic compositions are associated with subduction zones [*Druitt and Sparks*, 1984; *de Silva et al.*, 1994; *Cashman and Sparks*, 2013]. In these cases, magmatism is associated with a dehydrating subducting slab at depth and is consequently enriched in volatiles. This is expressed at the surface when eruptions are triggered by younger magma (with a lower silica content) advecting up into a fractionally crystallising magma body higher in the crust, causing it to erupt. Furthermore, the confining pressure fails to contain the overpressure of evolving volatiles [*Cashman and Sparks*, 2013] driving explosive volcanism. It seems likely that Syrtis Major Planum developed apparently-unique volcanic features because of its relationship with the underlying Noachian highlands. This possibility is further supported by the increasing evidence of magmatic diversity in the early Noachian/early Hesperian [*Sautter et al.*, 2016]. The recent review of *Sautter et al.* [2016] reports that orbital [*McSween et al.*, 2003; *Taylor et al.*, 2006; *Mustard et al.*, 2009; *Gasnault et al.*, 2010; *Quantin et al.*, 2012], *in-situ* [*Foley et al.*, 2003; *McSween et al.*, 2006], and meteorite data [*Agee et al.*, 2013] suggest that magma emplacement in the crust of Mars during the Noachian was widespread and consisted of a range of compositions associated with low degrees of partial melting. The development of magma in the martian crust at this time may have been more similar to the terrestrial continental crust than has

previously been considered [*Sautter et al.*, 2016]. Other plains-style volcanoes in the circum-Hellas volcanic province [*Williams et al.*, 2009a], which are both morphologically similar (flat plains with down-set calderas-like depressions), and located in a similar structural setting (on the rim of a giant impact basin), may well have a similar range of magma compositions due to interaction with the southern highland crust. However, it is hard to obtain information about these areas as they are overlain by younger ice and dust rich mantling materials.

7.5 Conclusions

In addition to the conclusions presented in the three previous thematic chapters, I draw further conclusions based on the discussion presented in this chapter:

- There have been three phases of volcanism in Syrtis Major Planum. The first phase, from ~3.6 -3.2 Ga in the Hesperian, was volumetrically the most significant. During this time the majority of the planum was emplaced. The second phase of volcanism was from 2.7-2.1 Ga in the early Amazonian. This phase consisted of spatially isolated, low-volume eruptions across the planum, two instances of dacitic eruptions in the central caldera complex, and continued subsidence of the central caldera complex. The third phase of volcanism was a continuation of sporadic spatially isolated, low-volume eruptions both within the caldera complex, and on the flanks of the planum.

- The Phase 1 volcanism was associated with large linear pits, interpreted to be collapse pits following intense fissure eruptions, and wide flat bottomed pits, interpreted to have hosted lava lakes long enough to develop quasi-circularity. This means that there was a stable and convecting magma reservoir in the central caldera complex but not in the NEFZ, and that the eruptions forming the large linear pits were intense and supply limited.

- The evolution of magma being supplied to Syrtis Major Planum during the first phase of volcanism can be inferred using the distribution of large linear pits and wide flat bottomed pits along with the tectonic development of the central caldera complex,

and maps of the gravity and demagnetisation anomalies over Syrtis Major Planum [*Lillis et al.*, 2015]. Magma supply to Syrtis Major Planum can be divided into high and low spatial densities of dyke events. There was a sufficiently high density of dykes to demagnetise the crust whilst feeding the Southern Crypto Fissure Zone (SCFZ), whilst at the same time the low spatial density population of dykes migrated north. The high spatial density of dikes then switched to the North, to develop the northern demagnetized zone and North East Fissure Zone (NEFZ). Meanwhile, the low spatial density population of dykes continued to feed the growing magma reservoir in the central caldera complex.

- The stratigraphic development of Syrtis Major Planum, from tube fed volcanic plains and Hesperian volcanic plateau unit (Hvp) through to shorter channel fed a'a flows, shows a similar trend to that observed for Olympus Mons and the Tharsis volcanoes (section 7.3.1.2) [*Bleacher et al.*, 2007a, 2007b]. To understand these trends, I compare Syrtis Major to other plume-fed volcanic provinces, where similar patterns reflect an increase in magma viscosity from a progressively cooling of the source of melt over time. Examples include the big Island of Hawaii, moving over a long-standing plume, and large igneous provinces experiencing a full cycle of plume initiation and decay. I conclude that Syrtis Major has formed through a similar scenario. The eHvr ridges reflect an initial giant dyke swam, and the volcanic plains and Hesperian volcanic plateau unit are long-lived, voluminous eruptions of tholeiitic lavas, mechanically buffered from below the magma chamber. These represent the highest magma production rates. This activity transitioned to shorter-lived eruptions of more alkali lavas with an increased tendency to form channel-fed a'a flows on the increasingly steep northern flank of Syrtis Major Planum. Finally, if the reported crater counting is not robust, the last, more sporadic elements of Syrtis Major volcanism (phase 2) may be related to the final dwindling stages of the plume tail melting the

metasomatised crust. However, if the reported crater counting is robust, then this latter phase is related to a later, temporally disconnected source of heat.

- The planum-wide distribution of high-calcium pyroxene correlates with the distribution of nano-phase iron oxide and wind streaks, rather than any geomorphological features. The distribution of olivine, though, can be associated with one of two options: (i) outcrops or impact crater ejecta which sample pre-Syrtis Major basement materials. These are stratigraphically comparable to olivine units in Nili Syrtis [*Bibring et al.*, 2005; *Mustard et al.*, 2005]. (ii) Phase 2 outcrops associated with materials dredged up from magma chamber cumulates or the demagnetised zones. With current datasets, it is not possible to discriminate between the two options.

- Bright outliers exposed by tectonic activity in the central caldera complex support the timing and distribution of an ignimbrite sourced form Nili Patera. It is possible, but not certain, that the Ridged mantling field is also associated with this event.

- During the second phase of volcanism there were two separate examples of the emplacement of dacitic composition materials, both within the central caldera complex. Therefore, the eruption of this composition was not a unique event, and the process leading to these eruptions are spatially associated with central caldera complex. I suggest that this occurred due to the partial melting of a pre-existing, fractionally-crystallised magma reservoir.

Chapter 8: Conclusions and further work

8.1 Summary

I have compiled new interpretations of the geomorphology, composition and texture of Syrtis Major Planum to produce two new maps. The first map uses the 100 m/pixel THEMIS data as the base layer and draws on the 6 m/pixel CTX data to provide additional data to help understand the geomorphology and textures seen in the study area, and to group features and regions on the map. Map sheet 1 is presented at a scale of 1:2,000,000. Map sheet 2 is 1:250,000 scale map of the Nili Patera caldera. This map uses base layer mosaics of CTX data and a CTX Digital Terrain Models (DTM). Using these maps, I have identified various sub-groups within the volcanic plains of Syrtis Major Planum, and recorded the distribution of different types of volcanic geomorphology. I have combined observations with relative dates, based on my mapping, to build a stratigraphy. I have also used crater counting to add more quantitative age data. I have synthesised these strands of evidence to understand the volcanic history of the planum and the development of the Central Caldera Complex.

8.2 Conclusions

My research has revealed that:

- It is possible to meaningfully interpret the geomorphology and differentiate the volcanic deposits of a Hesperian aged volcanic plain style volcano using a combination of THEMIS and CTX data imaging.

- Syrtis Major Planum developed through three phases of volcanic activity, excluding a pre-emplacement "Phase 0". Phase 1 was the major planum-building phase. Phase 2 saw the development of the Central Caldera Complex and sparse late-stage volcanism distributed

across the planum. Phase 3 was primarily erosional, with a few isolated volcanic eruptions.

- Phase 1, the major constructional phase of Syrtis Major Planum, occurred in the Hesperian, from ~3.6 Ga to ~3.2 Ga. During this time, the lava plains were emplaced primarily from three fissure zones (SCFZ, SMCCC and NEFZ; Map sheet 1) towards the centre of the planum on a north-south alignment. The lava plains consist of thin lava flows erupted from long fissures. Over time these became interleaved with an increasing proportion of giant pāhoehoe flows emplaced from the central vent zones. At the end of volcanism, lava flows became shorter, with channel and levee 'A´ā structures.

- At the end of the first phase of volcanism, an eruption was triggered in the maturing magma reservoir at the northern end of what is now the Central Caldera Complex. The result of this was the formation of Nili Patera and the emplacement of the Nili Patera ignimbrite.

- The second phase of volcanism occurred during the early Amazonian, between ~2.7 Ga and ~2.2 Ga. In the Central Caldera Complex, basaltic lava flows were erupted and two eruptions produced deposits that have a high silica composition. In the lava plains, there were a dwindling number of eruptions.

- During this time, progressive subsidence and collapse of the central caldera complex and the calderas within it occurred. Meroe patera subsided during this time, although this was most likely preceded by a caldera forming eruption similar to Nili Patera.

- High-silica composition lava flows were produced on two occasions in Syrtis Major. These occurred at different places and at different times, but both were within the central caldera complex. The eruption of such evolved compositions suggests either a stratified, fractionated magma reservoir, and/or a partial melt derived from the upper crust (i.e. hydrated materials in the Noachian highlands).

- Evidence from other data sources, including spectral, gravity and remnant crustal magnetism can be explained by progressive development of the crust under Syrtis Major

Planum. This process likely involved the development of one or more fractionally crystallising magma reservoirs, possibly assimilating the county rock (Figure 7.9).

- The spatial differences in the county rock beneath Syrtis Major Planum, interacting with a migrating mantle plume, and maturing magma reservoir, explain the differing volcanic and tectonic expressions seen across the Planum. The areas in which melt ascended from depth migrated north over time, whilst the foci of magmatic activity switched from a southern fissure zone to a northern fissure zone (Figure 7.9). The country rock heterogeneity is a combination of the diversity of the Noachian crust and the heterogeneity in the distribution of Noachian surface materials that surround Syrtis Major Planum, many of which are associated with Noachian paleo-lakes [*Fassett and Head III*, 2008].

- The subsurface under Syrtis Major Planum may be an enclave of crustal habitability where water and hydrated materials from the Noachian have existed in an elevated geothermal gradient over an extended period (until at least ~2.5Ga. Although these would be hard to reach for any surface mission, minerals from this zone might be found in the hydrothermal deposits in Nili Patera, and hence sampled by a targeted mission.

- Caldera-forming eruptions depositing ignimbrites, not previously observed, are seen across the Syrtis Major Central Caldera Complex. Thus, ignimbrite formation is possible on Mars.

- I have documented the geological history of Syrtis Major Planum. Other volcanoes on Mars share physiographic similarities with Syrtis Major Planum, and I predict a similar history for these Noachian/Hesperian highland plains volcanoes.

8.3 Further work

In addition to the work that I have done so far on Syrtis Major Planum the process of mapping Syrtis Major Planum has identified new questions and areas for future research. These include:

The rheological properties of lava flows on Syrtis Major Planum. Using observed relationships between rate (Q) and final flow dimensions (i.e., flow volume) [*Moore et al.*, 1978; *Wilson and Head*, 1983; *Lopes and Kilburn*, 1990; *Sakimoto and Gregg*, 2001] it is possible to calculate model eruption and rheological parameters. These techniques have been widely employed on Mars to determine model eruption and rheological parameters (e.g. Moore et al. [1978], [1990] Hiesinger et al. [2007], Vaucher et al. [2009], Pasckert et al. [2012], and Chevrel et al. [2013]). These techniques could be employed for flows in the Late Hesperian volcanic flow unit, where cooling-limited channelized 'A'á emplacement means that modelling these flows as Bingham fluids [*Moore et al.*, 1978] is appropriate. These parameters could be used to compare to other, younger martian volcanoes, and hence to explore long term-trends in the evolution of volcanism on Mars. They could also be used to investigate possible differences between lava flows emplaced to the north of the central caldera complex, and those on the slopes of the Isidis basin rim (e.g. Fawdon et al., [2013]).

The genetic relationship between Syrtis Major Planum and the Isidis basin is poorly understood. Whilst this has been explored before, concluding that the products of volcanism filled Isidis Planitia, followed then by glacial/lacustrine episodes [*Ivanov and Head*, 2003; *Hiesinger and Head*, 2004; *Ivanov et al.*, 2012], many new details could be gleaned from the CTX data which is now available in the area. It would be possible to investigate the timings and origins of the different units I have identified in this region. Being a relatively erosion-resistant lava shield, Syrtis Major Planum preserves a better record of the degradation processes that must have affected the whole of the Isidis rim area, so environmental information can be extracted that is relevant to the understanding of how Isidis evolved. This is important for understanding the role, timing and interplay between volcanic, lacustrine and glacial processes in the Isidis basin (e.g. Bridges et al.

[2003] and Erkeling et al. [2014]). The history of this region is important, also, because it is closely associated with the North East Syrtis region, which includes three proposed landing sites for the NASA 2020 Rover mission [*Golombek et al.*, 2015].

Antoniadi crater and the Nili fossae, located on the north west corner of Syrtis Major Planum, have not been specifically investigated in this research, although they are included as part of Syrtis Major Planum in some global maps [*Meyer and Grolier*, 1977b; *Greeley and Guest*, 1987b; *Tanaka et al.*, 2014b]. My reconnaissance mapping of Antoniadi crater failed to identify good evidence to directly associate Atonidai crater with Syrtis Major Planum, in agreement with some other previous studies [*Hiesinger and Head*, 2004]. Antoniadi crater, and areas around Nili Fossae, contain layered units and inverted branching channel networks which may be indicative of lacustrine and fluvial features. This explanation is notable, as Atoniadi crater has also been included in the database of martian crater lakes [*Fassett and Head III*, 2008]. Further investigation of this area would help us to understand the early Hesperian geography of the northern Syrtis Major Planum region. This is important because it could serve as a type-example of the sort of craters that were buried by Syrtis Major Planum as it evolved, and hence provide information about the types of minerals that would likely have been available in the country rock for alteration and entrainment by the magmas that went on to erupt to form Syrtis Major Planum. Antoniadi and Nili Fossae are also of interest due to their association with minerals indicative of potentially habitable environments. Studies of these regions can tell us about possible ancient habitable environments that may now be buried and preserved beneath Syrtis Major Planum.

References

Acocella, V. (2007), Understanding caldera structure and development: An overview of analogue models compared to natural calderas, *Earth-Science Reviews*, *85*(3–4), 125–160, doi:10.1016/j.earscirev.2007.08.004.

Acocella, V., F. Cifelli, and R. Funiciello (2000), Analogue models of collapse calderas and resurgent domes, *Journal of Volcanology and Geothermal Research*, *104*(1–4), 81–96, doi:10.1016/S0377-0273(00)00201-8.

Agee, C. B. et al. (2013), Unique Meteorite from Early Amazonian Mars: Water-Rich Basaltic Breccia Northwest Africa 7034, *Science*, *339*(6121), 780–785, doi:10.1126/science.1228858.

Albee, A. L., R. E. Arvidson, F. Palluconi, and T. Thorpe (2001), Overview of the Mars Global Surveyor mission, *J. Geophys. Res.*, *106*(E10), 23291–23316, doi:10.1029/2000JE001306.

Anderson, R. C., J. M. Dohm, A. F. C. Haldemann, E. Pounders, M. Golombek, and A. Castano (2008), Centers of tectonic activity in the eastern hemisphere of Mars, *Icarus*, *195*(2), 537–546, doi:10.1016/j.icarus.2007.12.027.

Anderson, S. W., E. R. Stofan, S. E. Smrekar, J. E. Guest, and B. Wood (1999), Pulsed inflation of pāhoehoe lava flows: implications for flood basalt emplacement, *Earth and Planetary Science Letters*, *168*(1–2), 7–18, doi:10.1016/S0012-821X(99)00044-8.

Andrews-Hanna, J. C., M. T. Zuber, and W. B. Banerdt (2008), The Borealis basin and the origin of the martian crustal dichotomy, *Nature*, *453*(7199), 1212–1215, doi:10.1038/nature07011.

Arvidson, R., J. Boyce, C. Chapman, M. Cintala, M. Fulchignoni, H. Moore, L. Soderblom, G. Neukum, P. Schultz, and R. Strom (1979), Standard techniques for presentation and analysis of crater size-frequency data.[on moon and planetary surfaces,

Balme, M., D. C. Berman, M. C. Bourke, and J. R. Zimbelman (2008), Transverse Aeolian Ridges (TARs) on Mars, *Geomorphology*, *101*(4), 703–720, doi:10.1016/j.geomorph.2008.03.011.

Baloga, S. M., and L. S. Glaze (2008), A self-replication model for long channelized lava flows on the Mars plains, *Journal of Geophysical Research: Planets*, *113*(E5), doi:10.1029/2007je002954.

Bamberg, M., R. Jaumann, H. Asche, T. Kneissl, and G. G. Michael (2014), Floor-Fractured Craters on Mars – Observations and Origin, *Planetary and Space Science*, *98*, 146–162, doi:10.1016/j.pss.2013.09.017.

Bandfield, J. L. (2006), Extended surface exposures of granitoid compositions in Syrtis Major, Mars, *Geophys. Res. Lett.*, *33*(6), L06203, doi:10.1029/2005gl025559.

Bandfield, J. L., V. E. Hamilton, and P. R. Christensen (2000), A Global View of Martian Surface Compositions from MGS-TES, *Science*, *287*(5458), 1626–1630.

Banerdt, W., R. Phillips, N. Sleep, and R. Saunders (1982), Thick shell tectonics on one-plate planets: Applications to Mars, *Journal of Geophysical Research: Solid Earth*, *87*(B12), 9723–9733.

Baratoux, D., N. Mangold, P. Pinet, and F. Costard (2005), Thermal properties of lobate ejecta in Syrtis Major, Mars: Implications for the mechanisms of formation, *Journal of Geophysical Research: Planets*, *110*(E4), n/a–n/a, doi:10.1029/2004je002314.

Baratoux, D., P. Pinet, A. Gendrin, L. Kanner, J. Mustard, Y. Daydou, J. Vaucher, and J.-P. Bibring (2007), Mineralogical structure of the subsurface of Syrtis Major from OMEGA observations of lobate ejecta blankets, *J. Geophys. Res.*, *112*(E8), doi:10.1029/2007JE002890.

Baratoux, D., M. J. Toplis, M. Monnereau, and V. Sautter (2013), The petrological expression of early Mars volcanism, *J. Geophys. Res. Planets*, *118*(1), 59–64, doi:10.1029/2012JE004234.

Barberi, F., and J. Varet (1970), The Erta Ale volcanic range (Danakil depression, northern afar, ethiopia), *Bulletin Volcanologique*, *34*(4), 848–917, doi:10.1007/BF02596805.

Bargar, K., and E. Jackson (1974), Calculated volumes of individual shield volcanoes along the Hawaiian-Emperor chain, *J. Res. US Geol. Surv*, *2*(5), 545–550.

Barlow, N. G., J. M. Boyce, F. M. Costard, R. A. Craddock, J. B. Garvin, S. E. H. Sakimoto, R. O. Kuzmin, D. J. Roddy, and L. A. Soderblom (2000), Standardizing the nomenclature of Martian impact crater ejecta morphologies, *J. Geophys. Res.*, *105*(E11), 26733–26738, doi:10.1029/2000je001258.

Basilevsky, A. T., S. C. Werner, G. Neukum, J. W. Head, S. van Gasselt, K. Gwinner, and B. A. Ivanov (2006), Geologically recent tectonic, volcanic and fluvial activity on the eastern flank of the Olympus Mons volcano, Mars, *Geophys. Res. Lett.*, *33*(13), doi:10.1029/2006GL026396.

Berman, D. C., and W. K. Hartmann (2002), Recent Fluvial, Volcanic, and Tectonic Activity on the Cerberus Plains of Mars, *Icarus*, *159*(1), 1–17, doi:10.1006/icar.2002.6920.

Bibring, J. P. et al. (2005), Mars Surface Diversity as Revealed by the OMEGA/Mars Express Observations, *Science*, *307*(5715), 1576–1581.

Bibring, J. P. et al. (2006), Global Mineralogical and Aqueous Mars History Derived from OMEGA/Mars Express Data, *Science*, *312*(5772), 400–404, doi:10.2307/3845879.

Bibring, J. P., et al., (1989), Results from the ISM experiment, *Nature, 341*, 591–592.

Bishop, J. L. et al. (2013), Mineralogy and morphology of geologic units at Libya Montes, Mars: Ancient aqueously derived outcrops, mafic flows, fluvial features, and impacts, *Journal of Geophysical Research: Planets*, *118*(3), 487–513, doi:10.1029/2012je004151.

Bleacher, J. E., R. Greeley, D. A. Williams, S. C. Werner, E. Hauber, and G. Neukum (2007a), Olympus Mons, Mars: Inferred changes in late Amazonian aged effusive activity from lava flow mapping of Mars Express High Resolution Stereo Camera data, *J. Geophys. Res.*, *112*(E4), E04003, doi:10.1029/2006je002826.

Bleacher, J. E., R. Greeley, D. A. Williams, S. R. Cave, and G. Neukum (2007b), Trends in effusive style at the Tharsis Montes, Mars, and implications for the development of the Tharsis province, *J. Geophys. Res.*, *112*(E9), E09005, doi:10.1029/2006je002873.

Bohrson, W. A. (2007), Insight into subvolcanic magma plumbing systems, *Geology, 35*(8), 767–768, doi:10.1130/focus082007.1.

Branney, M., and P. Kokelaar (1992), A reappraisal of ignimbrite emplacement: progressive aggradation and changes from particulate to non-particulate flow during emplacement of high-grade ignimbrite, *Bull Volcanol*, *54*(6), 504–520, doi:10.1007/BF00301396.

Branney, M. J., and B. P. Kokelaar (2002), *Pyroclastic density currents and the sedimentation of ignimbrites*, Geological Society of London.

Branney, M. J., and P. Kokelaar (1994), Volcanotectonic faulting, soft-state deformation, and rheomorphism of tuffs during development of a piecemeal caldera, English Lake District, *Geological Society of America Bulletin*, *106*(4), 507–530.

Breuer, D., and T. Spohn (2003), Early plate tectonics versus single-plate tectonics on Mars: Evidence from magnetic field history and crust evolution, *J. Geophys. Res.*, *108*(E7), doi:10.1029/2002JE001999.

Bridges, J. C. et al. (2003), Selection of the landing site in Isidis Planitia of Mars probe Beagle 2, *J.-Geophys.-Res.*, *108*(E1), 1–1, doi:10.1029/2001JE001820.

Bridges, N., P. Geissler, S. Silvestro, and M. Banks (2013), Bedform migration on Mars: Current results and future plans, *Aeolian Research*, *9*, 133–151, doi:10.1016/j.aeolia.2013.02.004.

Brown, A. J., S. J. Hook, A. M. Baldridge, J. K. Crowley, N. T. Bridges, B. J. Thomson, G. M. Marion, C. R. de Souza Filho, and J. L. Bishop (2010), Hydrothermal formation of Clay-Carbonate alteration assemblages in the Nili Fossae region of Mars, *Earth and Planetary Science Letters*, *297*(1–2), 174–182, doi:10.1016/j.epsl.2010.06.018.

Brown, R. J., S. Blake, N. R. Bondre, V. M. Phadnis, and S. Self (2011), ´A´ā lava flows in the Deccan Volcanic Province, India, and their significance for the nature of continental flood basalt eruptions, *Bulletin of Volcanology*, *73*(6), 737–752, doi:10.1007/s00445-011-0450-7.

Brown, R. J., S. Blake, T. Thordarson, and S. Self (2014), Pyroclastic edifices record vigorous lava fountains during the emplacement of a flood basalt flow field, Roza Member, Columbia River Basalt Province, USA, *Geological Society of America Bulletin*, *126*(7-8), 875–891, doi:10.1130/B30857.1.

Brown, R. J., T. Thordarson, S. Self, and S. Blake (2015), Disruption of tephra fall deposits caused by lava flows during basaltic eruptions, *Bulletin of Volcanology*, *77*(10), 1–15, doi:10.1007/s00445-015-0974-3.

Brož, P., O. Čadek, E. Hauber, and A. P. Rossi (2014), Shape of scoria cones on Mars: Insights from numerical modeling of ballistic pathways, *Earth and Planetary Science Letters*, *406*, 14–23, doi:10.1016/j.epsl.2014.09.002.

Brož, P., E. Hauber, T. Platz, and M. Balme (2015), Evidence for Amazonian highly viscous lavas in the southern highlands on Mars, *Earth and Planetary Science Letters*, *415*, 200–212.

Byrnes, J. M., and D. A. Crown (2001), Relationships between pāhoehoe surface units, topography, and lava tubes at Mauna Ulu, Kilauea Volcano, Hawaii, *J. Geophys. Res.*, *106*(B2), 2139–2151, doi:10.1029/2000jb900369.

Camp, V. E. (2013), Origin of Columbia River Basalt: Passive rise of shallow mantle, or active upwelling of a deep-mantle plume?, *Geological Society of America Special Papers*, *497*, 181–199, doi:10.1130/2013.2497(07).

Camp, V. E., M. E. Ross, and W. E. Hanson (2003), Genesis of flood basalts and Basin and Range volcanic rocks from Steens Mountain to the Malheur River Gorge, Oregon, *Geological Society of America Bulletin*, *115*(1), 105–128, doi:10.1130/0016-7606(2003)115<0105:GOFBAB>2.0.CO;2.

Carli, C., M. Ciarniello, F. Capaccioni, G. Serventi, and M. Sgavetti (2014a), Spectral variability of plagioclase–mafic mixtures (2): Investigation of the optical constant and retrieved mineral abundance dependence on particle size distribution, *Icarus*, *235*(0), 207–219, doi:10.1016/j.icarus.2014.03.022.

Carli, C., G. Serventi, and M. Sgavetti (2014b), VNIR spectral characteristics of terrestrial igneous effusive rocks: mineralogical composition and the influence of texture, *Geological Society, London, Special Publications*, *401*, doi:10.1144/SP401.19.

Carr, M. H. (1973), Volcanism on Mars, *Journal of Geophysical Research*, *78*(20), 4049–4062, doi:10.1029/JB078i020p04049.

Carr, M. H., and J. W. Head (2010), Geologic history of Mars, *Earth and Planetary Science Letters*, *294*(3–4), 185–203, doi:10.1016/j.epsl.2009.06.042.

Carr, M. H. et al. (1976), Preliminary Results from the Viking Orbiter Imaging Experiment, *Science*, *193*(4255), 766–776.

Carr, M. H., R. Greeley, K. R. Blasius, J. E. Guest, and J. B. Murray (1977), Some Martian volcanic features as viewed from the Viking orbiters, *J. Geophys. Res.*, *82*(28), 3985–4015, doi:10.1029/JS082i028p03985.

Carter, J., and F. Poulet (2013), Ancient plutonic processes on Mars inferred from the detection of possible anorthositic terrains, *Nature Geosci*, *6*(12), 1008–1012, doi:10.1038/ngeo1995.

Carter, J., D. Loizeau, N. Mangold, F. Poulet, and J.-P. Bibring (2015), Widespread surface weathering on early Mars: A case for a warmer and wetter climate, *Icarus*, *248*(0), 373 – 382, doi:http://dx.doi.org/10.1016/j.icarus.2014.11.011.

Cashman, K. V., and R. S. J. Sparks (2013), How volcanoes work: A 25 year perspective, *Geological Society of America Bulletin*, *125*(5-6), 664–690, doi:10.1130/B30720.1.

Cashman, K. V., C. Thornber, and J. P. Kauahikaua (1999), Cooling and crystallization of lava in open channels, and the transition of Pāhoehoe Lava to "A"ā, *Bulletin of Volcanology*, *61*(5), 306–323, doi:10.1007/s004450050299.

Chapman, M., C. Allen, M. Gudmundsson, V. Gulick, S. Jakobsson, B. Lucchitta, I. Skilling, and R. Waitt (2000), Volcanism and Ice Interactions on Earth and Mars, in *Environmental Effects on Volcanic Eruptions*, edited by J. Zimbelman and T. P. Gregg, pp. 39–73, Springer US.

Cheek, L. C., K. L. Donaldson Hanna, C. M. Pieters, J. W. Head, and J. L. Whitten (2013), The distribution and purity of anorthosite across the Orientale basin: New perspectives from Moon Mineralogy Mapper data, *J. Geophys. Res. Planets*, *118*(9), 1805–1820, doi:10.1002/jgre.20126.

Chevrel, M. O., T. Platz, E. Hauber, D. Baratoux, Y. Lavallée, and D. B. Dingwell (2013), Lava flow rheology: A comparison of morphological and petrological methods, *Earth and Planetary Science Letters*, *384*, 109–120, doi:10.1016/j.epsl.2013.09.022.

Christensen, P. et al. (2004), The Thermal Emission Imaging System (THEMIS) for the Mars 2001 Odyssey Mission, *Space Science Reviews*, *110*(1), 85–130, doi:10.1023/b:spac.0000021008.16305.94.

Christensen, P., R. Fergason, C. Edwards, and J. Hill (2013), THEMIS-derived thermal inertia mosaic of Mars: Product description and science results, vol. 44, p. 2822.

Christensen, P. R. et al. (2001), Mars Global Surveyor Thermal Emission Spectrometer experiment: Investigation description and surface science results, *J. Geophys. Res.*, *106*(E10), 23823–23871, doi:10.1029/2000JE001370.

Christensen, P. R. et al. (2005), Evidence for magmatic evolution and diversity on Mars from infrared observations, *Nature*, *436*(7050), 504–509, doi:10.1038/nature03639.

Clague, D. (1987), Hawaiian xenolith populations, magma supply rates, and development of magma chambers, *Bulletin of Volcanology*, *49*(4), 577–587, doi:10.1007/BF01079963.

Clenet, H., P. Pinet, G. Ceuleneer, Y. Daydou, F. Heuripeau, C. Rosemberg, J.-P. Bibring, G. Bellucci, F. Altieri, and B. Gondet (2013), A systematic mapping procedure based on the Modified Gaussian Model to characterize magmatic units from olivine/pyroxenes mixtures: Application to the Syrtis Major volcanic shield on Mars, *Journal of Geophysical Research: Planets*, n/a–n/a, doi:10.1002/jgre.20112.

Coffin, M. F., and O. Eldholm (1994), Large igneous provinces: Crustal structure, dimensions, and external consequences, *Reviews of Geophysics*, *32*(1), 1–36, doi:10.1029/93rg02508.

Cole, J. W., D. M. Milner, and K. D. Spinks (2005), Calderas and caldera structures: a review, *Earth-Science Reviews*, *69*(1–2), 1–26, doi:10.1016/j.earscirev.2004.06.004.

Condit, C. D. (1978), Distribution and relations of 4- to 10-km-diameter craters to global geologic units of Mars, *Icarus*, *34*(3), 465–478, doi:10.1016/0019-1035(78)90038-6.

Coulon, C., and R. S. Thorpe (1981), Role of continental crust in petrogenesis of orogenic volcanic associations, *Tectonophysics*, *77*(1–2), 79 – 93, doi:http://dx.doi.org/10.1016/0040-1951(81)90162-1.

Courtillot, V. E., and P. R. Renne (2003), On the ages of flood basalt events, *Comptes Rendus Geoscience*, *335*(1), 113–140, doi:10.1016/s1631-0713(03)00006-3.

Craddock, R. (1994), Geologic History of Isidis Planitia and Syrtis Major Planum, Mars, vol. 25, p. 291.

Crown, D. A., and R. Greeley (1993), Volcanic geology of Hadriaca Patera and the eastern Hellas region of Mars, *Journal of Geophysical Research: Planets*, *98*(E2), 3431–3451, doi:10.1029/92je02804.

Crown, D. A., K. H. Price, and R. Greeley (1992), Geologic evolution of the east rim of the Hellas basin Mars, *Icarus*, *100*(1), 1 – 25, doi:http://dx.doi.org/10.1016/0019-1035(92)90014-X.

Cruikshank, D., and C. Wood (1972), Lunar rilles and Hawaiian volcanic features: Possible analogues, *The Moon*, *3*(4), 412–447.

Cruikshank, D., W. Hartmann, and C. Wood (1973), Moon:"ghost"craters formed during mare filling, *The moon*, *7*(3-4), 440–452.

Crumpler, L. S., J. W. Head, and J. C. Aubele (1996), Calderas on Mars: characteristics, structure, and associated flank deformation, *Geological Society, London, Special Publications*, *110*(1), 307–348.

Davis, J. M., M. R. Balme, P. M. Grindrod, R. M. E. Williams, and S. Gupta (2016), Inverted Channels in Arabia Terra, Mars: Remnants of and Ancients Drainge Network, p. #1982, 47th Lunar and Planetary Science Conference, The Woodlands, Texas.

DeHon, R., and J. Waskom (1976), Geologic structure of the eastern mare basins, vol. 7, pp. 2729–2746.

Di Achille, G., and B. M. Hynek (2010), Ancient ocean on Mars supported by global distribution of deltas and valleys, *Nature Geosci*, *3*(7), 459–463.

Druitt, T. H., and R. S. J. Sparks (1984), On the formation of calderas during ignimbrite eruptions, *Nature*, *310*(5979), 679–681, doi:10.1038/310679a0.

Dufek, J., W. S. Kiefer, M. Manga, J. E. Bleacher, and R. J. Lillis (2014), Mystery of intrusion history at syrtis major: clues from multiple data sets., in *45th Lunar and Planetary Science Conference, Abstract# 2135*.

Ehlmann, B. L., and J. F. Mustard (2012), An in-situ record of major environmental transitions on early Mars at Northeast Syrtis Major, *Geophys. Res. Lett.*, *39*(11), L11202, doi:10.1029/2012gl051594.

Ehlmann, B. L., J. F. Mustard, C. I. Fassett, S. C. Schon, J. W. Head Iii, D. J. Des Marais, J. A. Grant, and S. L. Murchie (2008), Clay minerals in delta deposits and organic preservation potential on Mars, *Nature Geosci*, *1*(6), 355–358.

Ehlmann, B. L., J. F. Mustard, and S. L. Murchie (2010), Geologic setting of serpentine deposits on Mars, *Geophys. Res. Lett.*, *37*(6), n/a–n/a, doi:10.1029/2010GL042596.

Erkeling, G., D. Reiss, H. Hiesinger, M. A. Ivanov, E. Hauber, and H. Bernhardt (2014), Landscape formation at the Deuteronilus contact in southern Isidis Planitia, Mars: Implications for an Isidis Sea?, *Icarus*, *242*, 329–351, doi:10.1016/j.icarus.2014.08.015.

Ernst, R. E., and K. L. Buchan (1997), Giant Radiating Dyke Swarms: Their Use in Identifying Pre-Mesozoic Large Igneous Provinces and Mantle Plumes, in *Large Igneous Provinces: Continental, Oceanic, and Planetary Flood Volcanism*, pp. 297–333, American Geophysical Union.

Ernst, R. E., J. W. Head, E. Parfitt, E. Grosfils, and L. Wilson (1995), Giant radiating dyke swarms on Earth and Venus, *Earth-Science Reviews*, *39*(1–2), 1–58, doi:10.1016/0012-8252(95)00017-5.

ESRI (2011). ArcGIS Desktop: Release 10. Redlands, CA: Environmental Systems Research Institute

Fagents, S., P. Lanagan, and R. Greeley (2002), Rootless cones on Mars: a consequence of lava-ground ice interaction, *Geological Society, London, Special Publications*, *202*(1), 295–317.

Farrand, W. H., L. R. Gaddis, and L. Keszthelyi (2005), Pitted cones and domes on Mars: Observations in Acidalia Planitia and Cydonia Mensae using MOC, THEMIS, and TES data, *J. Geophys. Res.*, *110*(E5), n/a–n/a, doi:10.1029/2004JE002297.

Fassett, C. I., and J. W. Head III (2008), Valley network-fed, open-basin lakes on Mars: Distribution and implications for Noachian surface and subsurface hydrology, *Icarus*, *198*(1), 37–56, doi:10.1016/j.icarus.2008.06.016.

Fassett, C. I., and J. W. Head (2007), Layered mantling deposits in northeast Arabia Terra, Mars: Noachian-Hesperian sedimentation, erosion, and terrain inversion, *J. Geophys. Res.*, *112*(E8), n/a–n/a, doi:10.1029/2006JE002875.

Fastook, J. L., and J. W. Head (2015), Glaciation in the Late Noachian Icy Highlands: Ice accumulation, distribution, flow rates, basal melting, and top-down melting rates and patterns, *Planetary and Space Science*, *106*, 82–98, doi:10.1016/j.pss.2014.11.028.

Favre, G. (1993), Some observations on Hawaiian pit craters and relations with lava tubes, pp. 37–41.

Fawdon, P., M. R. Balme, C. L. Vye-Brown, D. A. Rothery, and C. J. Jordan (2013), The Evolution of Volcanism in Syrtis Major Planum (Mars): Drawing Insight from Terrestrial Analogues, p. #2135, 44th Lunar and Planetary Science Conference, The Woodlands, Texas.

Fawdon, P., J. R. Skok, M. R. Balme, C. L. Vye-Brown, D. A. Rothery, and C. J. Jordan (2015), The Geological History of Nili Patera, Mars, *J. Geophys. Res. Planets*, doi:10.1002/2015JE004795.

Fergason, R. L., P. R. Christensen, and H. H. Kieffer (2006), High-resolution thermal inertia derived from the Thermal Emission Imaging System (THEMIS): Thermal model and applications, *J. Geophys. Res.*, *111*(E12), n/a–n/a, doi:10.1029/2006JE002735.

Field, L., T. Barnie, J. Blundy, R. A. Brooker, D. Keir, E. Lewi, and K. Saunders (2012), Integrated field, satellite and petrological observations of the November 2010 eruption of Erta Ale, *Bulletin of Volcanology*, *74*(10), 2251–2271, doi:10.1007/s00445-012-0660-7.

Filiberto, J., and A. H. Treiman (2009), Martian magmas contained abundant chlorine, but little water, *Geology*, *37*(12), 1087–1090, doi:10.1130/G30488A.1.

Fisher, R. V., G. Orsi, M. Ort, and G. Heiken (1993), Mobility of a large-volume pyroclastic flow — emplacement of the Campanian ignimbrite, Italy, *Journal of Volcanology and Geothermal Research*, *56*(3), 205–220, doi:10.1016/0377-0273(93)90017-L.

Foley, C. N., T. E. Economou, R. N. Clayton, and W. Dietrich (2003), Calibration of the Mars Pathfinder alpha proton X-ray spectrometer, *J.-Geophys.-Res.*, *108*(E12), doi:10.1029/2002JE002018.

Francis, P. W., and G. Wadge (1983), The Olympus Mons Aureole: Formation by gravitational spreading, *J. Geophys. Res.*, *88*(B10), 8333–8344, doi:10.1029/JB088iB10p08333.

Francis, P. W., and C. A. Wood (1982), Absence of silicic volcanism on Mars: Implications for crustal composition and volatile abundance, *Journal of Geophysical Research: Solid Earth*, *87*(B12), 9881–9889, doi:10.1029/JB087iB12p09881.

Frey, H., and M. Jarosewich (1982), Subkilometer Martian volcanoes: Properties and possible terrestrial analogs, *J. Geophys. Res.*, *87*(B12), 9867–9879, doi:10.1029/JB087iB12p09867.

Frey, H., and R. A. Schultz (1988), Large impact basins and the mega-impact origin for the crustal dichotomy on Mars, *Geophys. Res. Lett.*, *15*(3), 229–232, doi:10.1029/GL015i003p00229.

Frey, H., B. L. Lowry, and S. A. Chase (1979), Pseudocraters on Mars, *J. Geophys. Res.*, *84*(B14), 8075–8086, doi:10.1029/JB084iB14p08075.

Frey, H., S. E. Sakimoto, and J. Roark (1998), The MOLA Topographic signature at the crustal dichotomy boundary zone on Mars, *Geophys. Res. Lett.*, *25*(24), 4409–4412, doi:10.1029/1998GL900095.

Gardeweg, M., and C. Ramírez (1987), La Pacana caldera and the Atana Ignimbrite — a major ash-flow and resurgent caldera complex in the Andes of northern Chile, *Bull Volcanol*, *49*(3), 547–566, doi:10.1007/bf01080449.

Garry, W. B., J. R. Zimbelman, and T. K. P. Gregg (2007), Morphology and emplacement of a long channeled lava flow near Ascraeus Mons Volcano, Mars, *J. Geophys. Res.*, *112*(E8), E08007, doi:10.1029/2006je002803.

Garvin, J., S. Sakimoto, J. Frawley, and C. Schnetzler (2002), Global geometric properties of martian impact craters, vol. 33, p. 1255.

Gasnault, O., G. Jeffrey Taylor, S. Karunatillake, J. Dohm, H. Newsom, O. Forni, P. Pinet, and W. V. Boynton (2010), Quantitative geochemical mapping of martian elemental provinces, *Icarus*, *207*(1), 226–247, doi:10.1016/j.icarus.2009.11.010.

van Gasselt, S., and G. Neukum (2011), Chronology, Cratering and Stratography, in *Encyclopedia of Astrobiology*, edited by M. Gargaud, R. Amils, J. C. Quintanilla, H. (Jim) J. Cleaves, W. M. Irvine, D. L. Pinti, and M. Viso, pp. 304–313, Springer Berlin Heidelberg, Berlin, Heidelberg.

Geoffroy, L. (2005), Volcanic passive margins, *Comptes Rendus Geoscience*, *337*(16), 1395–1408, doi:10.1016/j.crte.2005.10.006.

Gilbert, G. K. (1877), *Report on the Geology of the Henry Mountains*, US Government Printing Office.

Glaze, L. S., and S. M. Baloga (2006), Rheologic inferences from the levees of lava flows on Mars, *J. Geophys. Res.*, *111*(E9), E09006, doi:10.1029/2005je002585.

Glen, J. M. G., and D. A. Ponce (2002), Large-scale fractures related to inception of the Yellowstone hotspot, *Geology*, *30*(7), 647–650, doi:10.1130/0091-7613(2002)030<0647:LSFRTI>2.0.CO;2.

Glotch, T. D., and A. D. Rogers (2013), Evidence for magma-carbonate interaction beneath Syrtis Major, Mars, *Journal of Geophysical Research: Planets*, *118*(1), 126–137, doi:10.1029/2012je004230.

Golombek, M., J. Grant, K. Farley, and A. Chen (2015), Science Objectives, Engineering Constraints, and Landing Sites Proposed for the Mars 2020 Rover Mission, vol. 46, p. 1653.

Golombek, M. P. (1985), Fault type predictions from stress distributions on planetary surfaces: Importance of fault initiation depth, *J. Geophys. Res.*, *90*(B4), 3065–3074, doi:10.1029/JB090iB04p03065.

Golombek, M. P., F. S. Anderson, and M. T. Zuber (2001), Martian wrinkle ridge topography: Evidence for subsurface faults from MOLA, *J. Geophys. Res.*, *106*(E10), 23811–23821, doi:10.1029/2000je001308.

Gravley, D. M., C. J. N. Wilson, G. S. Leonard, and J. W. Cole (2007), Double trouble: Paired ignimbrite eruptions and collateral subsidence in the Taupo Volcanic Zone, New Zealand, *Geological Society of America Bulletin*, *119*(1-2), 18–30.

Greeley, R. (1972), Additional observations of actively forming lava tubes and associated structures, Hawaii,

Greeley, R. (1974), Geologic guide to the island of Hawaii: A field guide for comparative planetary geology,

Greeley, R., and D. A. Crown (1990), Volcanic geology of Tyrrhena Patera, Mars, *Journal of Geophysical Research: Solid Earth*, *95*(B5), 7133–7149, doi:10.1029/JB095iB05p07133.

Greeley, R., and J. E. Guest (1987a), Geologic map of the eastern eastern equatorial region of Mars,

Greeley, R., and J. E. Guest (1987b), *Geologic map of the eastern equatorial region of Mars*, IMAP, Report.

Greeley, R., and P. D. Spudis (1981), Volcanism on Mars, *Rev. Geophys.*, *19*(1), 13–41, doi:10.1029/RG019i001p00013.

Greeley, R., J. D. Iversen, J. B. Pollack, N. Udovich, and B. White (1974), Wind Tunnel Simulations of Light and Dark Streaks on Mars, *Science*, *183*(4127), 847–849.

Gregg, T., and S. de Silva (2009), Tyrrhena Patera and Hesperia Planum, Mars: New Insights (and Old Interpretations) from High-Resolution Imagery, vol. 40, p. 1700.

Gregg, T. K. P., and M. A. Farley (2006), Mafic pyroclastic flows at Tyrrhena Patera, Mars: Constraints from observations and models, *Journal of Volcanology and Geothermal Research*, *155*(1–2), 81–89, doi:10.1016/j.jvolgeores.2006.02.008.

Griffiths, R. W., and I. H. Campbell (1991), Interaction of mantle plume heads with the Earth's surface and onset of small-scale convection, *J. Geophys. Res.*, *96*(B11), 18295–18310, doi:10.1029/91JB01897.

Grizzaffi, P., and P. H. Schultz (1989), Isidis basin: Site of ancient volatile-rich debris layer, *Icarus*, *77*(2), 358–381, doi:10.1016/0019-1035(89)90094-8.

Grott, M. et al. (2012), Long-Term Evolution of the Martian Crust-Mantle System, *Space Science Reviews*, *174*(1), 49–111, doi:10.1007/s11214-012-9948-3.

Guest, J. E. (1969), Upper Tertiary Ignimbrites in the Andean Cordillera of Part of the Antofagasta Province, Northern Chile, *Geological Society of America Bulletin*, *80*(3), 337–362, doi:10.1130/0016-7606(1969)80[337:UTIITA]2.0.CO;2.

Guilbaud, M.-N., S. Self, T. Thordarson, and S. Blake (2005), Morphology, surface structures, and emplacement of lavas produced by Laki, A.D. 1783–1784, *Geological Society of America Special Papers*, *396*, 81–102, doi:10.1130/0-8137-2396-5.81.

Haddadi, B., S. Moune, O. Sigmarsson, P.-J. Gauthier, and M. Gouhier (2015), Pre-eruptive volatile and erupted gas phase characterization of the 2014 basalt of Bárðarbunga volcanic system, Iceland., vol. 17, p. 9572.

Harder, H. and U. Christensen (1996), A one-plume model of Martian mantle convection, Nature, 380, 507-509.

Harris, A. J. L., J. B. Murray, S. E. Aries, M. A. Davies, L. P. Flynn, M. J. Wooster, R. Wright, and D. A. Rothery (2000), Effusion rate trends at Etna and Krafla and their implications for eruptive mechanisms, *Journal of Volcanology and Geothermal Research*, *102*(3–4), 237–269, doi:10.1016/s0377-0273(00)00190-6.

Hartmann, W. K. (1973), Martian Cratering, 4, Mariner 9 initial analysis of cratering chronology, *J. Geophys. Res.*, *78*(20), 4096–4116, doi:10.1029/JB078i020p04096.

Hartmann, W. K. (1977), Relative crater production rates on planets, *Icarus*, *31*(2), 260–276.

Hartmann, W. K. (1999), Martian cratering VI: Crater count isochrons and evidence for recent volcanism from Mars Global Surveyor, *Meteoritics & Planetary Science*, *34*(2), 167–177.

Hartmann, W. K. (2005), Martian cratering 8: Isochron refinement and the chronology of Mars, *Icarus*, *174*(2), 294–320.

Hartmann, W. K., and G. Neukum (2001a), Cratering Chronology and the Evolution of Mars, *Space Science Reviews*, *96*(1), 165–194, doi:10.1023/a:1011945222010.

Hartmann, W. K., and G. Neukum (2001b), Cratering Chronology and the Evolution of Mars, *Space Science Reviews*, *96*(1), 165–194, doi:10.1023/a:1011945222010.

Hartmann, W. K., and S. C. Werner (2010), Martian Cratering 10. Progress in use of crater counts to interpret geological processes: Examples from two debris aprons, *Earth and Planetary Science Letters*, *294*(3–4), 230–237, doi:10.1016/j.epsl.2009.10.001.

Hauber, E., J. Bleacher, K. Gwinner, D. Williams, and R. Greeley (2009), The topography and morphology of low shields and associated landforms of plains volcanism in the Tharsis region of Mars, *Journal of Volcanology and Geothermal Research*, *185*(1–2), 69–95, doi:10.1016/j.jvolgeores.2009.04.015.

Hauber, E., P. Brož, F. Jagert, P. Jodłowski, and T. Platz (2011), Very recent and wide-spread basaltic volcanism on Mars, *Geophysical Research Letters*, *38*(10), doi:10.1029/2011gl047310.

Hawkesworth, C. J., M. Hammill, A. R. Gledhill, P. van Calsteren, and G. Rogers (1982), Isotope and trace element evidence for late-stage intra-crustal melting in the High Andes, *Earth and Planetary Science Letters*, *58*(2), 240 – 254, doi:http://dx.doi.org/10.1016/0012-821X(82)90197-2.

Head, J. W. I., and S. Pratt (2001), Malea Planum Hesperian Volcanic Province: Characterization Using MOLA Data, p. #1627, Lunar and Planetary Institute, Houston.

Hiesinger, H., and J. W. Head III (2004), The Syrtis Major volcanic province, Mars: Synthesis from Mars Global Surveyor data, *J. Geophys. Res.*, *109*(E1), E01004, doi:10.1029/2003je002143.

Hiesinger, H., J. W. Head, U. Wolf, R. Jaumann, and G. Neukum (2002), Lunar mare basalt flow units: Thicknesses determined from crater size-frequency distributions, *Geophys. Res. Lett.*, *29*(8), 89–1, doi:10.1029/2002GL014847.

Hiesinger, H., J. W. Head III, and G. Neukum (2007), Young lava flows on the eastern flank of Ascraeus Mons: Rheological properties derived from High Resolution Stereo Camera

(HRSC) images and Mars Orbiter Laser Altimeter (MOLA) data, *J. Geophys. Res.*, *112*(E5), E05011, doi:10.1029/2006je002717.

Hodges, C., and H. Moore (1994), Atlas of volcanic features on Mars, *US Geol. Survey Professional Paper*, *1534*.

Hon, K., J. Kauahikua, R. P. Denlinger, and K. Mackay (1994), Emplacement and inflation of pāhoehoe sheet flows: Observations and measurements of active lava flows on Kilauea Volcano, Hawaii, *Geological Society of America Bulletin*, *106*(3), 351–370, doi:10.1130/0016-7606(1994)106<0351:eaiops>2.3.co;2.

Hooper, P. (1988), The Columbia river basalt, *Continental Flood Basalts*, 1–33.

Horgan, B. (2013), Planetary science: Evolved magma on Mars, *Nature Geosci*, *6*(12), 991–992, doi:10.1038/ngeo2010.

Howington-Kraus, E., R. Kirk, L. Soderblom, B. Giese, and J. Oberst (2002), USGS and DLR topographic mapping of Comet Borrelly, *International Archives Of Photogrammetry Remote Sensing And Spatial Information Sciences*, *34*(4), 723–727.

Hugenholtz, C. H., T. E. Barchyn, and E. A. Favaro (2015), Formation of periodic bedrock ridges on Earth, *Aeolian Research*, *18*, 135–144, doi:10.1016/j.aeolia.2015.07.002.

Hulme, G. (1982), A review of lava flow processes related to the formation of lunar sinuous rilles, *Geophysical Surveys*, *5*(3), 245–279, doi:10.1007/BF01454018.

Icelandic Meteorological Office (2014), *Bárðarbunga and Holuhraun - overview*, Icelandic Meteorological Office.

Ivanov, M. A., and J. W. Head III (2003), Syrtis Major and Isidis Basin contact: Morphological and topographic characteristics of Syrtis Major lava flows and material of the Vastitas Borealis Formation, *J. Geophys. Res.*, *108*(E6), 5063, doi:10.1029/2002je001994.

Ivanov, M. A., J. Korteniemi, V.-P. Kostama, M. Aittola, J. Raitala, M. Glamoclija, L. Marinangeli, and G. Neukum (2005), Major episodes of the hydrologic history in the region of Hesperia Planum, Mars, *J. Geophys. Res.*, *110*(E12), doi:10.1029/2005JE002420.

Ivanov, M. A., H. Hiesinger, G. Erkeling, F. J. Hielscher, and D. Reiss (2012), Major episodes of geologic history of Isidis Planitia on Mars, *Icarus*, *218*(1), 24–46, doi:10.1016/j.icarus.2011.11.029.

Kallianpur, K., and P. Mouginis-Mark (2001), Slopes of Martian volcanoes, vol. 32, p. 1258.

Kennedy, B., and J. Stix (2003a), Igneous Rock Associations 1. Styles and Mechanisms of Caldera Collapse, *Geoscience Canada; Volume 30, Number 2 (2003)*, doi:10.12789/gs.v30i2.4144.

Kennedy, B., and J. Stix (2003b), Igneous Rock Associations of Canada 2. Stages in the Temporal Evolution of Calderas, *Geoscience Canada; Volume 30, Number 3 (2003)*, doi:10.12789/gs.v30i3.4151.

Kerber, L., J. W. Head, J.-B. Madeleine, F. Forget, and L. Wilson (2012), The dispersal of pyroclasts from ancient explosive volcanoes on Mars: Implications for the friable layered deposits, *Icarus*, *219*(1), 358–381, doi:10.1016/j.icarus.2012.03.016.

Kerr, R. C., R. W. Griffiths, and K. V. Cashman (2006), Formation of channelized lava flows on an unconfined slope, *J. Geophys. Res.*, *111*(B10), B10206, doi:10.1029/2005jb004225.

Keszthelyi, L., and S. Self (1998), Some physical requirements for the emplacement of long basaltic lava flows, *J. Geophys. Res.*, *103*(B11), 27447–27464, doi:10.1029/98jb00606.

Keszthelyi, L., T. Thordarson, A. McEwen, H. Haack, M.-N. Guilbaud, S. Self, and M. J. Rossi (2004), Icelandic analogs to Martian flood lavas, *Geochem. Geophys. Geosyst.*, *5*(11), Q11014, doi:10.1029/2004gc000758.

Kiefer, W. S. (2004), Gravity evidence for an extinct magma chamber beneath Syrtis Major, Mars: a look at the magmatic plumbing system, *Earth and Planetary Science Letters*, *222*(2), 349–361, doi:10.1016/j.epsl.2004.03.009.

Kilburn, C. R. J., and R. M. C. Lopes (1991), General Patterns of Flow Field Growth: Aa and Blocky Lavas, *J. Geophys. Res.*, *96*(B12), 19721–19732, doi:10.1029/91jb01924.

Kirk, R. L. et al. (1999), Digital photogrammetric analysis of the IMP camera images: Mapping the Mars Pathfinder landing site in three dimensions, *J. Geophys. Res.*, *104*(E4), 8869–8887, doi:10.1029/1998JE900012.

Kirk, R. L., E. Howington-Kraus, B. Redding, D. Galuszka, T. M. Hare, B. A. Archinal, L. A. Soderblom, and J. M. Barrett (2003), High-resolution topomapping of candidate MER landing sites with Mars Orbiter Camera narrow-angle images, *Journal of Geophysical Research: Planets*, *108*(E12), doi:10.1029/2003JE002131.

Kirk, R. L. et al. (2008), Ultrahigh resolution topographic mapping of Mars with MRO HiRISE stereo images: Meter-scale slopes of candidate Phoenix landing sites, *J. Geophys. Res.*, *113*(E3), E00A24, doi:10.1029/2007JE003000.

Kiyosugi, K., C. B. Connor, D. Zhao, L. J. Connor, and K. Tanaka (2009), Relationships between volcano distribution, crustal structure, and P-wave tomography: an example from the Abu Monogenetic Volcano Group, SW Japan, *Bulletin of Volcanology*, *72*(3), 331–340, doi:10.1007/s00445-009-0316-4.

K.L. Tanaka, J. A. S. Jr., and T.M. Hare (2010), *Planetary Geologic Mapping Handbook*.

Kneissl, T., S. van Gasselt, and G. Neukum (2011a), Map-projection-independent crater size-frequency determination in GIS environments—New software tool for ArcGIS, *Planetary and Space Science*, *59*(11–12), 1243–1254, doi:10.1016/j.pss.2010.03.015.

Kneissl, T., S. van Gasselt, and G. Neukum (2011b), Map-projection-independent crater size-frequency determination in GIS environments—New software tool for ArcGIS, *Planetary and Space Science*, *59*(11–12), 1243–1254, doi:10.1016/j.pss.2010.03.015.

Kreslavsky, M. A., and J. W. Head (2000), Kilometer-scale roughness of Mars: Results from MOLA data analysis, *J. Geophys. Res.*, *105*(E11), 26695–26711, doi:10.1029/2000JE001259.

Lanagan, P. D., A. S. McEwen, L. P. Keszthelyi, and T. Thordarson (2001), Rootless cones on Mars indicating the presence of shallow equatorial ground ice in recent times, *Geophys. Res. Lett.*, *28*(12), 2365–2367, doi:10.1029/2001GL012932.

Lane, N. (2010), *Life ascending: the ten great inventions of evolution*, Profile books.

Lanz, J. K., R. Wagner, U. Wolf, J. Kröchert, and G. Neukum (2010), Rift zone volcanism and associated cinder cone field in Utopia Planitia, Mars, *Journal of Geophysical Research: Planets*, *115*(E12), n/a–n/a, doi:10.1029/2010je003578.

Lavallee, Y., J. Kendrick, R. Wall, F. von Aulock, B. Kennedy, and F. Sigmundsson (2015), Experimental constraints on the rheology and mechanical properties of lava erupted in the Holuhraun area during the 2014 rifting event at Bárðarbunga, Iceland, vol. 17, p. 11544.

Lemoine, F., G. Neumann, D. Chinn, D. Smith, M. Zuber, D. Rowlands, D. Rubincam, and D. Pavlis (2001), Solutions for Mars geophysical parameters from Mars global surveyor tracking data, vol. 1, p. 0545.

Le Pennec, J-L., J-L. Bourdier, J.-L. Froger, A. Temel, G. Camus, and A. Gourgaud (1994), Neogene ignimbrites of the Nevsehir plateau (Central Turkey): stratigraphy, distribution and source constraints, *Journal of Volcanology and Geothermal Research*, *63*(1–2), 59–87, doi:10.1016/0377-0273(94)90018-3.

Lillis, R. J., J. Dufek, W. S. Kiefer, B. A. Black, M. Manga, J. A. Richardson, and J. E. Bleacher (2015), The Syrtis Major volcano, Mars: A multidisciplinary approach to interpreting its magmatic evolution and structural development, *J. Geophys. Res. Planets*, *120*(9), 1476–1496, doi:10.1002/2014JE004774.

Lindsay, J. M., A. K. Schmitt, R. B. Trumball, S. De Silva, W. Siebell, and R. Emmermann (2001), Magmatic Evolution of the La Pacana Caldera System, Central Andes, Chile: Compositional Variation of Two Cogenetic, Large-Volume Felsic Ignimbrites, *Journal of Petrology*, *42*(3), 459–486, doi:10.1093/petrology/42.3.459.

Lipman, P. W. (1984), The roots of ash flow calderas in western North America: windows into the tops of granitic batholiths, *Journal of Geophysical Research: Solid Earth (1978–2012)*, *89*(B10), 8801–8841.

Lipman, P. W. (1997), Subsidence of ash-flow calderas: relation to caldera size and magma-chamber geometry, *Bulletin of Volcanology*, *59*(3), 198–218.

Lipman, P. W. (2000), Central San Juan caldera cluster: Regional volcanic framework, *Special Papers-Geological Society Of America*, 9–70.

Lockwood, J., J. Dvorak, T. English, R. Koyanagi, A. Okamura, M. Summers, and W. Tanigawa (1987), Mauna Loa 1974–1984: A decade of intrusive and extrusive activity, *Volcanism in Hawaii*, *2*, 537–570.

Loizeau, D. et al. (2007), Phyllosilicates in the Mawrth Vallis region of Mars, *Journal of Geophysical Research: Planets*, *112*(E8), n/a–n/a, doi:10.1029/2006JE002877.

Lopes, R. M. C., and C. R. J. Kilburn (1990), Emplacement of Lava Flow Fields: Application of Terrestrial Studies to Alba Patera, Mars, *J. Geophys. Res.*, *95*(B9), 14383–14397, doi:10.1029/JB095iB09p14383.

Lucchitta, B. K. (1981), Mars and Earth: Comparison of cold-climate features, *Icarus*, *45*(2), 264–303, doi:10.1016/0019-1035(81)90035-X.

Macdonald, G. A., A. T. Abbott, and F. L. Peterson (1983), *Volcanoes in the sea: the geology of Hawaii*, University of Hawaii Press.

Malin, M. C. (1977), Comparison of volcanic features of Elysium (Mars) and Tibesti (Earth), *Geological Society of America Bulletin*, *88*(7), 908–919.

Malin, M. C. et al. (2007), Context Camera Investigation on board the Mars Reconnaissance Orbiter, *J. Geophys. Res.*, *112*(E5), E05S04, doi:10.1029/2006je002808.

Mangold, N., P. Allemand, and P. G. Thomas (1998), Wrinkle ridges of Mars: structural analysis and evidence for shallow deformation controlled by ice-rich décollements, *Planetary and Space Science*, *46*(4), 345–356, doi:10.1016/s0032-0633(97)00195-5.

Mangold, N., V. Ansan, D. Baratoux, F. Costard, L. Dupeyrat, H. Hiesinger, P. Masson, G. Neukum, and P. Pinet (2008), Identification of a new outflow channel on Mars in Syrtis Major Planum using HRSC/MEx data, *Planetary and Space Science*, *56*(7), 1030–1042, doi:10.1016/j.pss.2008.01.011.

Marti, J., G. J. Ablay, L. T. Redshaw, and R. S. J. Sparks (1994), Experimental studies of collapse calderas, *Journal of the Geological Society*, *151*(6), 919–929, doi:10.1144/gsjgs.151.6.0919.

Marzo, G. A., A. F. Davila, L. L. Tornabene, J. M. Dohm, A. G. Fairén, C. Gross, T. Kneissl, J. L. Bishop, T. L. Roush, and C. P. McKay (2010), Evidence for Hesperian impact-induced hydrothermalism on Mars, *Icarus*, *208*(2), 667–683, doi:10.1016/j.icarus.2010.03.013.

McEwen, A. S. et al. (2007), Mars Reconnaissance Orbiter's High Resolution Imaging Science Experiment (HiRISE), *J. Geophys. Res.*, *112*(E5), E05S02, doi:10.1029/2005je002605.

McGetchin, T. R., and G. W. Ullrich (1973), Xenoliths in Maars and Diatremes with inferences for the Moon, Mars, and Venus, *Journal of Geophysical Research*, *78*(11), 1833–1853, doi:10.1029/JB078i011p01833.

McGill, G. E. (2000), Crustal history of north central Arabia Terra, Mars, *Journal of geophysical research*, *105*, 6945–6959.

McGill, G. E., and A. M. Dimitriou (1990), Origin of the Martian global dichotomy by crustal thinning in the Late Noachian or Early Hesperian, *J. Geophys. Res.*, *95*(B8), 12595–12605, doi:10.1029/JB095iB08p12595.

McGovern, P. J., J. R. Smith, J. K. Morgan, and M. H. Bulmer (2004), Olympus Mons aureole deposits: New evidence for a flank failure origin, *J. Geophys. Res.*, *109*(E8), doi:10.1029/2004JE002258.

McGuire, P. C. et al. (2009), An improvement to the volcano-scan algorithm for atmospheric correction of CRISM and OMEGA spectral data, *Planetary and Space Science*, *57*(7), 809–815, doi:10.1016/j.pss.2009.03.007.

McPhie, J. (1983), Outflow ignimbrite sheets from Late Carboniferous calderas, Currabubula Formation, New South Wales, Australia, *Geological Magazine*, *120*(05), 487–503, doi:10.1017/S0016756800027485.

McSween, H. Y., T. L. Grove, and M. B. Wyatt (2003), Constraints on the composition and petrogenesis of the Martian crust, *J.-Geophys.-Res.*, *108*(E12),, doi:10.1029/2003JE002175.

McSween, H. Y. et al. (2006), Alkaline volcanic rocks from the Columbia Hills, Gusev crater, Mars, *J. Geophys. Res.*, *111*(E9), n/a–n/a, doi:10.1029/2006JE002698.

Merle, O., S. Barde-Cabusson, and B. Wyk de Vries (2010), Hydrothermal calderas, *Bull Volcanol*, *72*(2), 131–147, doi:10.1007/s00445-009-0314-6.

Meyer, J. D., and M. J. Grolier (1977a), Geological Map of the Syrtis Major Quadrangle,

Meyer, J. D., and M. J. Grolier (1977b), *Geologic map of the Syrtis Major Quadrangle of Mars*, IMAP, Report.

Michael, G. G., and G. Neukum (2010), Planetary surface dating from crater size–frequency distribution measurements: Partial resurfacing events and statistical age uncertainty, *Earth and Planetary Science Letters*, *294*(3–4), 223–229, doi:10.1016/j.epsl.2009.12.041.

Michalski, J. R., and J. E. Bleacher (2013), Supervolcanoes within an ancient volcanic province in Arabia Terra, Mars, *Nature*, *502*(7469), 47–52.

Michalski, J. R., and P. B. Niles (2010), Deep crustal carbonate rocks exposed by meteor impact on Mars, *Nature Geosci*, *3*(11), 751–755.

Michalski, J. R., and E. Z. Noe Dobrea (2007), Evidence for a sedimentary origin of clay minerals in the Mawrth Vallis region, Mars, *Geology*, *35*(10), 951–954.

Montési, L. G. J., and M. T. Zuber (2003), Clues to the lithospheric structure of Mars from wrinkle ridge sets and localization instability, *J. Geophys. Res.*, *108*(E6), 5048, doi:10.1029/2002je001974.

Montgomery, D. R., J. L. Bandfield, and S. K. Becker (2012), Periodic bedrock ridges on Mars, *J. Geophys. Res.*, *117*(E3), n/a–n/a, doi:10.1029/2011JE003970.

Moore, H. J., D. W. G. Arthur, and G. G. Schaber (1978), Yield strengths of flows on the earth, Mars, and moon, *Lunar and Planetary Science Conference, 9th, Houston, Tex., March 13-17, 1978, Proceedings*, *3*, 3351–3378.

Moore, J. G., W. R. Normark, and R. T. Holcomb (1994), Giant hawaiian landslides, *Annual Review of Earth and Planetary Sciences*, *22*, 119–144.

Mouginis-Mark, P. J., and P. R. Christensen (2005), New observations of volcanic features on Mars from the THEMIS instrument, *J. Geophys. Res.*, *110*(E8), doi:10.1029/2005JE002421.

Mouginis-Mark, P. J., L. Wilson, J. W. Head, S. H. Brown, J. L. Hall, and K. D. Sullivan (1984), Elysium Planitia, Mars: Regional geology, volcanology, and evidence for volcano-ground ice interactions, *Earth, Moon, and Planets*, *30*(2), 149–173.

Murase, T., and A. R. McBirney (1970a), Thermal Conductivity of Lunar and Terrestrial Igneous Rocks in Their Melting Range, *Science*, *170*(3954), 165–167.

Murase, T., and A. R. McBirney (1970b), Viscosity of Lunar Lavas, *Science*, *167*(3924), 1491–1493.

Murchie, S. et al. (2007), Compact Reconnaissance Imaging Spectrometer for Mars (CRISM) on Mars Reconnaissance Orbiter (MRO), *J. Geophys. Res.*, *112*(E5), E05S03, doi:10.1029/2006je002682.

Murray, J. B. (2013), John Guest's legacy on Mt Etna: a spreading volcano with no magma chamber, in *Volcanic and magmaic Studies Group Annual Meeting 2013*, p. 46, School of Earth Sciences, University of Bristol.

Mustard, J., J.-P. Bibring, S. Erard, E. Fischer, J. Head, S. Hurtrez, Y. Langevin, C. Pieters, and C. Sotin (1990), Interpretation of spectral units of Isidis-Syrtis Major from ISM-Phobos-2 observations, vol. 1, p. 227.

Mustard, J. F., S. Erard, J. P. Bibring, J. W. Head, S. Hurtrez, Y. Langevin, C. M. Pieters, and C. J. Sotin (1993), The Surface of Syrtis Major: Composition of the Volcanic Substrate and Mixing With Altered Dust and Soil, *J. Geophys. Res.*, *98*(E2), 3387–3400, doi:10.1029/92je02682.

Mustard, J. F., S. Murchie, S. Erard, and J. Sunshine (1997), In situ compositions of Martian volcanics: Implications for the mantle, *J. Geophys. Res.*, *102*(E11), 25605–25615, doi:10.1029/97JE02354.

Mustard, J. F., F. Poulet, A. Gendrin, J.-P. Bibring, Y. Langevin, B. Gondet, N. Mangold, G. Bellucci, and F. Altieri (2005), Olivine and Pyroxene Diversity in the Crust of Mars, *Science*, *307*(5715), 1594–1597.

Mustard, J. F., B. L. Ehlmann, S. L. Murchie, F. Poulet, N. Mangold, J. W. Head, J.-P. Bibring, and L. H. Roach (2009), Composition, Morphology, and Stratigraphy of Noachian Crust around the Isidis basin, *J. Geophys. Res.*, *114*(E2), n/a–n/a, doi:10.1029/2009JE003349.

Nakamura, K. (1977), Volcanoes as possible indicators of tectonic stress orientation—principle and proposal, *Journal of Volcanology and Geothermal Research*, *2*(1), 1–16.

Nash, B. P., M. E. Perkins, J. N. Christensen, D.-C. Lee, and A. N. Halliday (2006), The Yellowstone hotspot in space and time: Nd and Hf isotopes in silicic magmas, *Earth and Planetary Science Letters*, *247*(1–2), 143–156, doi:10.1016/j.epsl.2006.04.030.

Neukum, G., and K. Hiller (1981), Martian ages, *J. Geophys. Res.*, *86*(B4), 3097–3121, doi:10.1029/JB086iB04p03097.

Neukum, G. et al. (2004a), HRSC: the high resolution stereo camera of Mars Express, *ESA special publication*, *1240*, 1–19.

Neukum, G. et al. (2004b), Recent and episodic volcanic and glacial activity on Mars revealed by the High Resolution Stereo Camera, *Nature*, *432*(7020), 971–979.

Neumann, G. A., M. T. Zuber, M. A. Wieczorek, P. J. McGovern, F. G. Lemoine, and D. E. Smith (2004), Crustal structure of Mars from gravity and topography, *J. Geophys. Res.*, *109*(E8), E08002, doi:10.1029/2004je002262.

Noble, S., and C. Pieters (2001), Type 2 terrain: Compositional constraints on the Martian lowlands, vol. 32, p. 1230.

Ody, A., F. Poulet, Y. Langevin, J.-P. Bibring, G. Bellucci, F. Altieri, B. Gondet, M. Vincendon, J. Carter, and N. Manaud (2012), Global maps of anhydrous minerals at the surface of Mars from OMEGA/MEx, *J. Geophys. Res.*, *117*(E11), n/a–n/a, doi:10.1029/2012JE004117.

Ody, A., F. Poulet, J. P. Bibring, D. Loizeau, J. Carter, B. Gondet, and Y. Langevin (2013), Global investigation of olivine on Mars: Insights into crust and mantle compositions, *Journal of Geophysical Research: Planets*, n/a–n/a, doi:10.1029/2012je004149.

Okubo, C. H., and S. J. Martel (1998), Pit crater formation on Kilauea volcano, Hawaii., *Journal of Volcanology and Geothermal Research*, *86*(1–4), 1–18, doi:10.1016/S0377-0273(98)00070-5.

Opheim, J. A., and A. Gudmundsson (1989), Formation and geometry of fractures, and related volcanism, of the Krafla fissure swarm, northeast Iceland, *Geological Society of America Bulletin*, *101*(12), 1608–1622, doi:10.1130/0016-7606(1989)101<1608:FAGOFA>2.3.CO;2.

Oppenheimer, C., and P. Francis (1998), Implications of longeval lava lakes for geomorphological and plutonic processes at Erta 'Ale volcano, Afar, *Journal of Volcanology and Geothermal Research*, *80*(1–2), 101–111, doi:10.1016/S0377-0273(97)00041-3.

Ormö, J., G. Komatsu, M. A. Chan, B. Beitler, and W. T. Parry (2004), Geological features indicative of processes related to the hematite formation in Meridiani Planum and Aram Chaos, Mars: a comparison with diagenetic hematite deposits in southern Utah, USA, *Icarus*, *171*(2), 295–316, doi:10.1016/j.icarus.2004.06.001.

Parfitt, E. A., and J. W. Head (1993), Buffered and unbuffered dike emplacement on Earth and Venus: implications for magma reservoir size, depth, and rate of magma replenishment, *Earth, Moon, and Planets*, *61*(3), 249–281, doi:10.1007/BF00572247.

Pasckert, J. H., H. Hiesinger, and D. Reiss (2012), Rheologies and ages of lava flows on Elysium Mons, Mars, *Icarus*, *219*(1), 443–457, doi:10.1016/j.icarus.2012.03.014.

Pelkey, S. M. et al. (2007), CRISM multispectral summary products: Parameterizing mineral diversity on Mars from reflectance, *J. Geophys. Res.*, *112*(E8), E08S14, doi:10.1029/2006JE002831.

Peterson, J. (1978), Volcanism in the Noachis-Hellas region of Mars, 2, in *Lunar and Planetary Science Conference Proceedings*, vol. 9, pp. 3411–3432.

Platz, T., and G. Michael (2011), Eruption history of the Elysium Volcanic Province, Mars, *Earth and Planetary Science Letters*, *312*(1–2), 140–151, doi:10.1016/j.epsl.2011.10.001.

Platz, T., S. Münn, T. R. Walter, J. N. Procter, P. C. McGuire, A. Dumke, and G. Neukum (2011), Vertical and lateral collapse of Tharsis Tholus, Mars, *Earth and Planetary Science Letters*, *305*(3–4), 445–455, doi:10.1016/j.epsl.2011.03.012.

Platz, T., G. Michael, K. L. Tanaka, J. A. S. Jr, and C. M. Fortezzo (2013a), Crater-based dating of geological units on Mars: Methods and application for the new global geological map, *Icarus*, *225*(1), 806 – 827, doi:http://dx.doi.org/10.1016/j.icarus.2013.04.021.

Platz, T., G. Michael, K. L. Tanaka, J. A. S. Jr, and C. M. Fortezzo (2013b), Crater-based dating of geological units on Mars: Methods and application for the new global geological map, *Icarus*, *225*(1), 806 – 827, doi:http://dx.doi.org/10.1016/j.icarus.2013.04.021.

Platz, T., P. Jodlowski, P. Fawdon, G. G. Michael, and K. L. Tanaka (2014), Amazonian Volcanic Activity at the Syrtis Major Volcanic Province, Mars, p. #2524, 46th Lunar and Planetary Science Conference, The Woodlands, Texas.

Plescia, J., (2003), Tharsis Tholus: an unusual martian volcano, *Icarus*, *165*(2), 223–241, doi:10.1016/S0019-1035(03)00199-4.

Plescia, J., and R. Saunders (1979), The chronology of the Martian volcanoes, in *Lunar and Planetary Science Conference Proceedings*, vol. 10, pp. 2841–2859.

Plescia, J. B. (1994), Geology of the Small Tharsis Volcanoes: Jovis Tholus, Ulysses Patera, Biblis Patera, Mars, *Icarus*, *111*(1), 246–269, doi:10.1006/icar.1994.1144.

Plescia, J. B. (2004), Morphometric properties of Martian volcanoes, *J. Geophys. Res.*, *109*(E3), E03003, doi:10.1029/2002je002031.

Plescia, J. B., and M. P. Golombek (1986), Origin of planetary wrinkle ridges based on the study of terrestrial analogs, *Geological Society of America Bulletin*, *97*(11), 1289–1299, doi:10.1130/0016-7606(1986)97<1289:OOPWRB>2.0.CO;2.

Pollard, D. D., and A. M. Johnson (1973), Mechanics of growth of some laccolithic intrusions in the Henry mountains, Utah, II: Bending and failure of overburden layers and sill formation, *Tectonophysics*, *18*(3–4), 311–354, doi:10.1016/0040-1951(73)90051-6.

Poulet, F., N. Mangold, and S. Erard (2003), A new view of dark Martian regions from geomorphic and spectroscopic analysis of Syrtis Major, *A&A*, *412*(2), L19–L23, doi:10.1051/0004-6361:20031661.

Presley, M. A., and P. R. Christensen (1997), Thermal conductivity measurements of particulate materials 2. Results, *J. Geophys. Res.*, *102*(E3), 6551–6566, doi:10.1029/96JE03303.

Quantin, C., J. Flahaut, H. Clenet, P. Allemand, and P. Thomas (2012), Composition and structures of the subsurface in the vicinity of Valles Marineris as revealed by central uplifts of impact craters, *Icarus*, *221*(1), 436–452, doi:10.1016/j.icarus.2012.07.031.

Rafkin, S. C. R., and T. I. Michaels (2003), Meteorological predictions for 2003 Mars Exploration Rover high-priority landing sites, *J.-Geophys.-Res.*, *108*(E12), 8091, doi:10.1029/2002JE002027.

Raitala, J. (1988), Superposed ridges of the Hesperia Planum area on Mars, *Earth, Moon, and Planets*, *40*(1), 71–99.

Raitala, J., and K. Kauhanen (1989), Tectonics of Syrtis Major Planum on Mars, *Earth Moon Planet*, *46*(3), 243–260, doi:10.1007/BF00117193.

Rampey, M., and R. Harvey (2012), Mars Hesperian Magmatism as Revealed by Syrtis Major and the Circum-Hellas Volcanic Province, *Earth Moon Planets*, *109*(1-4), 61–75, doi:10.1007/s11038-012-9404-0.

Rampey, M. L., and R. P. Harvey (2008), Volcanology of Arnus Vallis, Mars, *Icarus*, *196*(1), 49–62, doi:10.1016/j.icarus.2008.03.004.

Reimers, C. E., and P. D. Komar (1979), Evidence for explosive volcanic density currents on certain Martian volcanoes, *Icarus*, *39*(1), 88–110, doi:10.1016/0019-1035(79)90103-9.

Reyes, D. P., and P. R. Christensen (1994), Evidence for Komatiite-type lavas on Mars from Phobos ISM data and other observations, *Geophys. Res. Lett.*, *21*(10), 887–890, doi:10.1029/94GL01002.

Richter, D. H., J. P. Eaton, K. J. Murata, W. U. Ault, and H. L. Krivoy (1970), *Chronological narrative of the 1959-60 eruption of Kilauea Volcano, Hawaii*, Professional Paper, Report.

Robbins, S. J., and B. M. Hynek (2012a), A new global database of Mars impact craters ≥1 km: 1. Database creation, properties, and parameters, *J. Geophys. Res.*, *117*(E5), E05004, doi:10.1029/2011je003966.

Robbins, S. J., and B. M. Hynek (2012b), A new global database of Mars impact craters ≥1 km: 2. Global crater properties and regional variations of the simple-to-complex transition diameter, *J. Geophys. Res.*, *117*(E6), E06001, doi:10.1029/2011je003967.

Robbins, S. J., G. D. Achille, and B. M. Hynek (2011), The volcanic history of Mars: High-resolution crater-based studies of the calderas of 20 volcanoes, *Icarus*, *211*(2), 1179–1203, doi:10.1016/j.icarus.2010.11.012.

Roche, O., T. H. Druitt, and O. Merle (2000), Experimental study of caldera formation, *J. Geophys. Res.*, *105*(B1), 395–416, doi:10.1029/1999JB900298.

Rogers, A. D., and A. H. Nazarian (2013), Evidence for Noachian flood volcanism in Noachis Terra, Mars, and the possible role of Hellas impact basin tectonics, *J. Geophys. Res. Planets*, *118*(5), 1094–1113, doi:10.1002/jgre.20083.

Rogers, A. D., and H. Nekvasil (2015), Feldspathic rocks on Mars: Compositional constraints from infrared spectroscopy and possible formation mechanisms, *Geophys. Res. Lett.*, 2015GL063501, doi:10.1002/2015GL063501.

Roman-Berdiel, T., D. Gapais, and J. P. Brun (1995), Analogue models of laccolith formation, *Journal of Structural Geology*, *17*(9), 1337–1346, doi:10.1016/0191-8141(95)00012-3.

Rowland, J. V., and R. H. Sibson (2001), Extensional fault kinematics within the Taupo Volcanic Zone, New Zealand: Soft-linked segmentation of a continental rift system, *New Zealand Journal of Geology and Geophysics*, *44*(2), 271–283, doi:10.1080/00288306.2001.9514938.

Rowland, S. K., and G. P. Walker (1990), Pāhoehoe and aa in Hawaii: volumetric flow rate controls the lava structure, *Bulletin of Volcanology*, *52*(8), 615–628, doi:10.1007/BF00301212.

Sakimoto, S. E. H., and T. K. P. Gregg (2001), Channeled flow: Analytic solutions, laboratory experiments, and applications to lava flows, *J. Geophys. Res.*, *106*(B5), 8629–8644, doi:10.1029/2000jb900384.

Saunders, R., T. G. Bills, and L. Johanson (1981), The ridged plains of Mars, vol. 12, pp. 924–925.

Saunders, R., R. Arvidson, G. Badhwar, W. Boynton, P. Christensen, F. Cucinotta, W. Feldman, R. Gibbs, C. Kloss Jr, and M. Landano (2004), 2001 Mars Odyssey mission summary, in *2001 Mars Odyssey*, pp. 1–36, Springer.

Sautter, V. et al. (2016), Magmatic complexity on early Mars as seen through a combination of orbital, in-situ and meteorite data, *Lithos*, doi:10.1016/j.lithos.2016.02.023.

Scanlon, K. E., J. W. Head, and D. R. Marchant (2015), Volcanism-induced, local wet-based glacial conditions recorded in the Late Amazonian Arsia Mons tropical mountain glacier deposits, *Icarus*, *250*, 18–31, doi:10.1016/j.icarus.2014.11.016.

Schaber, G. G. (1982), Syrtis Major: A Low-Relief Volcanic Shield, *J. Geophys. Res.*, *87*(B12), 9852–9866, doi:10.1029/JB087iB12p09852.

Schmidt, R. (2001), Mars Express- ESA'S first mission to planet Mars, *Space Technology*, *20*(5), 219–224.

Schulte, M., D. Blake, T. Hoehler, and T. McCollom (2006), Serpentinization and Its Implications for Life on the Early Earth and Mars, *Astrobiology*, *6*(2), 364–376, doi:10.1089/ast.2006.6.364.

Schultz, P. H. (1984), Impact basin control of volcanic and tectonic provinces on Mars, in *Lunar and Planetary Science Conference*, vol. 15, pp. 728–729.

Schultz, P. H., and P. D. Spudis (1983), Beginning and end of lunar mare volcanism, *Nature*, *302*(5905), 233–236, doi:10.1038/302233a0.

Schultz, R. A. (2000), Localization of bedding plane slip and backthrust faults above blind thrust faults: Keys to wrinkle ridge structure, *J. Geophys. Res.*, *105*(E5), 12035–12052, doi:10.1029/1999JE001212.

Schultz, R. A., and H. V. Frey (1990), A new survey of multiring impact basins on Mars, *J. Geophys. Res.*, *95*(B9), 14175–14189, doi:10.1029/JB095iB09p14175.

Schumacher, S., and D. Breuer (2007), An alternative mechanism for recent volcanism on Mars, *Geophys. Res. Lett.*, *34*(14), n/a–n/a, doi:10.1029/2007GL030083.

Schwegman, R. D., G. R. Osinski, and L. L. Tornabene (2015), Layered ejecta morphologies on Syrtis Major and implications for regional geology., p. #2645, 46th Lunar and Planetary Science Conference, The Woodlands, Texas.

Scott, D. H., and M. J. Carr (1978), *Geologic map of Mars*, Misc. Invest. Ser. Map I-1083, IMAP, U.S. Geol. Surv,.

Scott, D. H., K. L. Tanaka, and P. Geology (1986), *Geologic map of the western equatorial region of Mars*, Geological Survey (US).

Self, S., T. Thordarson, and L. Keszthelyi (1997), Emplacement of continental flood basalt lava flows, *Large Igneous Provinces: continental, oceanic, and planetary flood volcanism*, 381–410.

Self, S., L. Keszthelyi, and T. Thordarson (1998), The Importance of Pāhoehoe, *Annu. Rev. Earth Planet. Sci.*, *26*(1), 81–110, doi:10.1146/annurev.earth.26.1.81.

Serventi, G., C. Carli, M. Sgavetti, M. Ciarniello, F. Capaccioni, and G. Pedrazzi (2013), Spectral variability of plagioclase–mafic mixtures (1): Effects of chemistry and modal abundance in reflectance spectra of rocks and mineral mixtures, *Icarus*, *226*(1), 282–298, doi:10.1016/j.icarus.2013.05.041.

Sheehan, W. (1996a), *The planet Mars: a history of observation & discovery, Chapter 2*, University of Arizona Press.

Sheehan, W. (1996b), *The planet Mars: a history of observation & discovery, Chapter 4*, University of Arizona Press.

Sigmundsson, F. et al. (2015), Segmented lateral dyke growth in a rifting event at Bar[eth]arbunga volcanic system, Iceland, *Nature*, *517*(7533), 191–195.

de Silva, S., and P. W. Francis (1989), Correlation of large ignimbrites — Two case studies from the Central Andes of northern Chile, *Journal of Volcanology and Geothermal Research*, *37*(2), 133–149, doi:10.1016/0377-0273(89)90066-8.

de Silva, S., G. Zandt, R. Trumbull, J. G. Viramonte, G. Salas, and N. Jiménez (2006), Large ignimbrite eruptions and volcano-tectonic depressions in the Central Andes: a thermomechanical perspective, *Geological Society, London, Special Publications*, *269*(1), 47–63.

de Silva, S. L., S. Self, P. W. Francis, R. E. Drake, and R. R. Carlos (1994), Effusive silicic volcanism in the Central Andes: The Chao dacite and other young lavas of the Altiplano-Puna Volcanic Complex, *J. Geophys. Res.*, *99*(B9), 17805–17825, doi:10.1029/94JB00652.

Silvestro, S., L. K. Fenton, D. A. Vaz, N. T. Bridges, and G. G. Ori (2010), Ripple migration and dune activity on Mars: Evidence for dynamic wind processes, *Geophysical Research Letters*, *37*(20), L20203, doi:10.1029/2010gl044743.

Skok, J., and J. Mustard (2014), Glaciation and Volcanic Interaction to form the Modern Northeast Syrtis Region of Mars, vol. 45, p. 1924.

Skok, J. R., J. F. Mustard, B. L. Ehlmann, R. E. Milliken, and S. L. Murchie (2010a), Silica deposits in the Nili Patera caldera on the Syrtis Major volcanic complex on Mars, *Nature Geosci*, *3*(12), 838–841, doi:10.1038/ngeo990.

Skok, J. R., J. F. Mustard, S. L. Murchie, M. B. Wyatt, and B. L. Ehlmann (2010b), Spectrally distinct ejecta in Syrtis Major, Mars: Evidence for environmental change at the Hesperian-Amazonian boundary, *J. Geophys. Res.*, *115*(E2), E00D14, doi:10.1029/2009je003338.

Sleep, N. H. (1994), Martian plate tectonics, *J. Geophys. Res.*, *99*(E3), 5639–5655, doi:10.1029/94JE00216.

Smith, D. E., and M. T. Zuber (1996), The shape of Mars and the topographic signature of the hemispheric dichotomy, vol. 27, p. 1221.

Smith, D. E. et al. (2001), Mars Orbiter Laser Altimeter: Experiment summary after the first year of global mapping of Mars, *J. Geophys. Res.*, *106*(E10), 23689–23722, doi:10.1029/2000je001364.

Smith, M. R., and J. L. Bandfield (2012), Geology of quartz and hydrated silica-bearing deposits near Antoniadi Crater, Mars, *Journal of Geophysical Research: Planets*, *117*(E6), n/a–n/a, doi:10.1029/2011je004038.

Smith, R. (1987), Dyke emplacement at Spanish Peaks, Colorado, in *Mafic dyke swarms*, vol. 34, pp. 47–54, Geol. Assoc. Canada.

Snyder, C. W. (1977), The missions of the Viking orbiters, *J. Geophys. Res.*, *82*(28), 3971–3983, doi:10.1029/JS082i028p03971.

Soden, A. M., and Z. K. Shipton (2013), Dilational fault zone architecture in a welded ignimbrite: The importance of mechanical stratigraphy, *Journal of Structural Geology*, *51*, 156–166, doi:10.1016/j.jsg.2013.02.001.

Solana, M. C., C. R. J. Kilburn, E. Rodriguez Badiola, and A. Aparicio (2004), Fast emplacement of extensive pāhoehoe flow-fields: the case of the 1736 flows from Montaña de las Nueces, Lanzarote, *Journal of Volcanology and Geothermal Research*, *132*(2–3), 189–207, doi:10.1016/S0377-0273(03)00345-7.

Solomatov, V. S., and L.-N. Moresi (1997), Three regimes of mantle convection with non-Newtonian viscosity and stagnant lid convection on the terrestrial planets, *Geophys. Res. Lett.*, *24*(15), 1907–1910, doi:10.1029/97GL01682.

Solomon, S. C., and J. W. Head (1980), Lunar Mascon Basins: Lava filling, tectonics, and evolution of the lithosphere, *Rev. Geophys.*, *18*(1), 107–141, doi:10.1029/RG018i001p00107.

Soule, S. A., and K. V. Cashman (2005), Shear rate dependence of the pāhoehoe-to-ʻaʻā transition: Analog experiments, *Geology*, *33*(5), 361–364, doi:10.1130/g21269.1.

Soule, S. A., K. V. Cashman, and J. P. Kauahikaua (2004), Examining flow emplacement through the surface morphology of three rapidly emplaced, solidified lava flows, Kīlauea Volcano, Hawaiʻi, *Bull Volcanol*, *66*(1), 1–14, doi:10.1007/s00445-003-0291-0.

Spohn, T., and G. Schubert (1983), Convective thinning of the lithosphere: A mechanism for rifting and mid-plate volcanism on Earth, Venus, and Mars, *Tectonophysics*, *94*(1–4), 67–90, doi:10.1016/0040-1951(83)90010-0.

Squyres, S. W., D. E. Wilhelms, and A. C. Moosman (1987), Large-scale volcano-ground ice interactions on Mars, *Icarus*, *70*(3), 385–408, doi:10.1016/0019-1035(87)90085-6.

Stone, D. S. (1993), Basement-involved thrust-generated folds as seismically imaged in the subsurface of the central Rocky Mountain foreland, *Geological Society of America Special Papers*, *280*, 271–318, doi:10.1130/SPE280-p271.

Strom, R. G., S. K. Croft, and N. G. Barlow (1992), The Martian impact cratering record, *Mars*, *1*, 383–423.

Strom, R. G., G. G. Schaber, and D. D. Dawson (1994), The global resurfacing of Venus, *J. Geophys. Res.*, *99*(E5), 10899–10926, doi:10.1029/94JE00388.

Swanson, D. A., W. A. Duffield, D. B. Jackson, and D. W. Peterson (1979), *Chronological narrative of the 1969-71 Mauna Ulu eruption of Kilauea Volcano, Hawaii*, Professional Paper, Report.

Szwast, M. A., M. I. Richardson, and A. R. Vasavada (2006), Surface dust redistribution on Mars as observed by the Mars Global Surveyor and Viking orbiters, J. Geophys. Res., 111(E11), doi:10.1029/2005JE002485.Tanaka, K., N. Hoffman, T. Hare, D. MacKinnon, and J. Kargel (2001), Magmatically driven catastrophic erosion on Mars, vol. 1.

Tanaka, K. L. (1985), Ice-lubricated gravity spreading of the Olympus Mons aureole deposits, *Icarus*, *62*(2), 191–206, doi:10.1016/0019-1035(85)90117-4.

Tanaka, K. L. (1986), The stratigraphy of Mars, vol. 17, p. 139.

Tanaka, K. L. (1997), Sedimentary history and mass flow structures of Chryse and Acidalia Planitiae, Mars, *J. Geophys. Res.*, *102*(E2), 4131–4149, doi:10.1029/96JE02862.

Tanaka, K. L., D. H. Scott, and R. Greeley (1992), Global stratigraphy, *Mars*, *1*, 345–382.

Tanaka, K. L., J. S. Kargel, D. J. MacKinnon, T. M. Hare, and N. Hoffman (2002), Catastrophic erosion of Hellas basin rim on Mars induced by magmatic intrusion into volatile-rich rocks, *Geophys. Res. Lett.*, *29*(8), 37–1, doi:10.1029/2001GL013885.

Tanaka, K. L., J. A. Skinner, T. M. Hare, T. Joyal, and A. Wenker (2003), Resurfacing history of the northern plains of Mars based on geologic mapping of Mars Global Surveyor data, *J. Geophys. Res.*, *108*(E4), n/a–n/a, doi:10.1029/2002JE001908.

Tanaka, K. L., J. A. Skinner Jr, L. S. Crumpler, and J. M. Dohm (2009), Assessment of planetary geologic mapping techniques for Mars using terrestrial analogs: The SP Mountain area of the San Francisco Volcanic Field, Arizona, *Planetary and Space Science*, *57*(5–6), 510–532, doi:10.1016/j.pss.2008.06.012.

Tanaka, K. L., J. A. Skinner, J. . Dohm, R. P. Irwin III, E. J. Kolb, C. M. Fortezzo, T. Platz, G. G. Michael, and T. M. Hare (2014a), Geologic map of Mars: U.S. Geological Survey Scientific Investigations Map 3292, scale 1:20,000,000, pamphlet 43 p.,

Tanaka, K. L., S. J. Robbins, C. M. Fortezzo, J. A. S. Jr, and T. M. Hare (2014b), The digital global geologic map of Mars: Chronostratigraphic ages, topographic and crater morphologic characteristics, and updated resurfacing history, *Planetary and Space Science*, *95*(0), 11 – 24, doi:http://dx.doi.org/10.1016/j.pss.2013.03.006.

Taylor, G. J. et al. (2006), Bulk composition and early differentiation of Mars, *J. Geophys. Res.*, *111*(E3), n/a–n/a, doi:10.1029/2005JE002645.

Theilig, E., and R. Greeley (1986), Lava flows on Mars: Analysis of small surface features and comparisons with terrestrial analogs, *Journal of Geophysical Research: Solid Earth (1978–2012)*, *91*(B13), E193–E206.

Thomas, P., J. Veverka, S. Lee, and A. Bloom (1981), Classification of wind streaks on Mars, *Icarus*, *45*(1), 124–153, doi:10.1016/0019-1035(81)90010-5.

Thomas, R. J., D. A. Rothery, S. J. Conway, and M. Anand (2014), Long-lived explosive volcanism on Mercury, *Geophys. Res. Lett.*, *41*(17), 6084–6092, doi:10.1002/2014GL061224.

Thorarinsson, S. (1953), The crater groups in Iceland, *Bull Volcanol*, *14*(1), 3–44, doi:10.1007/BF02596003.

Thordarson, T., and S. Self (1993), The Laki (Skaftár Fires) and Grímsvötn eruptions in 1783–1785, *Bulletin of Volcanology*, *55*(4), 233–263.

Thordarson, T., and S. Self (1998), The Roza Member, Columbia River Basalt Group: A gigantic pāhoehoe lava flow field formed by endogenous processes?, *J. Geophys. Res.*, *103*(B11), 27411–27445, doi:10.1029/98JB01355.

Thorpe, R. S., P. W. Francis, and S. Moorbath (1979), Rare earth and strontium isotope evidence concerning the petrogenesis of North Chilean ignimbrites, *Earth and Planetary Science Letters*, *42*(3), 359 – 367, doi:http://dx.doi.org/10.1016/0012-821X(79)90044-X.

Tibaldi, A. (2015), Structure of volcano plumbing systems: A review of multi-parametric effects, *Journal of Volcanology and Geothermal Research*, *298*, 85–135, doi:10.1016/j.jvolgeores.2015.03.023.

Tolan, T. L., S. P. Reidel, M. H. Beeson, J. L. Anderson, K. R. Fecht, and D. A. Swanson (1989), Revisions to the estimates of the areal extent and volume of the Columbia River Basalt Group, *Geological Society of America Special Papers*, *239*, 1–20.

Tuzo Wilson, J. (1963), Hypothesis of Earth's Behaviour, *Nature*, *198*(4884), 925–929, doi:10.1038/198925a0.

Vaucher, J., D. Baratoux, M. J. Toplis, P. Pinet, N. Mangold, and K. Kurita (2009), The morphologies of volcanic landforms at Central Elysium Planitia: Evidence for recent and fluid lavas on Mars, *Icarus*, *200*(1), 39–51, doi:10.1016/j.icarus.2008.11.005.

Vye-Brown, C., S. Self, and T. L. Barry (2013), Architecture and emplacement of flood basalt flow fields: case studies from the Columbia River Basalt Group, NW USA, *Bulletin of Volcanology*, *75*(3), 1–21, doi:10.1007/s00445-013-0697-2.

Walker, G. P. L. (1993), Basaltic-volcano systems, *Geological Society, London, Special Publications*, *76*(1), 3–38.

Walter, T., and V. Troll (2001), Formation of caldera periphery faults: an experimental study, *Bull Volcanol*, *63*(2-3), 191–203, doi:10.1007/s004450100135.

Warner, N. H., S. Gupta, F. Calef, P. Grindrod, N. Boll, and K. Goddard (2015), Minimum effective area for high resolution crater counting of martian terrains, *Icarus*, *245*, 198–240.

Wasson, R. J., and R. Hyde (1983), Factors determining desert dune type, *Nature*, *304*(5924), 337–339, doi:10.1038/304337a0.

Watson, S., and D. McKenzie (1991), Melt Generation by Plumes: A Study of Hawaiian Volcanism, *Journal of Petrology*, *32*(3), 501–537, doi:10.1093/petrology/32.3.501.

Watters, T. R. (1988), Wrinkle ridge assemblages on the terrestrial planets, *J. Geophys. Res.*, *93*(B9), 10236–10254, doi:10.1029/JB093iB09p10236.

Watters, T. R. (1993), Compressional Tectonism on Mars, *J. Geophys. Res.*, *98*(E9), 17049–17060, doi:10.1029/93je01138.

Watters, T. R. (2004), Elastic dislocation modeling of wrinkle ridges on Mars, *Icarus*, *171*(2), 284–294, doi:10.1016/j.icarus.2004.05.024.

Werner, S. C. (2005), Major aspects of the chronostratigraphy and geologic evolutionary history of Mars,

Werner, S. C. (2009), The global martian volcanic evolutionary history, *Icarus*, *201*(1), 44–68, doi:10.1016/j.icarus.2008.12.019.

Werner, S. C., and K. L. Tanaka (2011), Redefinition of the crater-density and absolute-age boundaries for the chronostratigraphic system of Mars, *Icarus*, *215*(2), 603–607, doi:10.1016/j.icarus.2011.07.024.

Wichman, R., and P. Schultz (1988), Ridged plains units on the margins of martian impact basins, vol. 19, p. 1266.

Wichman, R., and P. Schultz (1989), Sequence and mechanisms of deformation around the Hellas and Isidis impact basins on Mars, *Journal of Geophysical Research: Solid Earth (1978–2012)*, *94*(B12), 17333–17357.

Wieczorek, M. A., and M. T. Zuber (2004), Thickness of the Martian crust: Improved constraints from geoid-to-topography ratios, *J. Geophys. Res.*, *109*(E1), n/a–n/a, doi:10.1029/2003JE002153.

Wilhelms, D. E., and S. W. Squyres (1984), The martian hemispheric dichotomy may be due to a giant impact, *Nature*, *309*(5964), 138–140, doi:10.1038/309138a0.

Wilkes, C. (1845), *Narrative of the United States' Exploring Expedition: During the Years 1838, 1839, 1840, 1841, 1842*, Whittaker.

Williams, D. (2001), Chronology of Mars Exploration, *Webpage. URL http://nssdc. gsfc. nasa. gov/planetary/chronology_mars. html*.

Williams, D. A., R. Greeley, W. Zuschneid, S. C. Werner, G. Neukum, D. A. Crown, T. K. P. Gregg, K. Gwinner, and J. Raitala (2007), Hadriaca Patera: Insights into its volcanic history from Mars Express High Resolution Stereo Camera, *Journal of Geophysical Research: Planets*, *112*(E10), n/a–n/a, doi:10.1029/2007JE002924.

Williams, D. A., R. Greeley, S. C. Werner, G. Michael, D. A. Crown, G. Neukum, and J. Raitala (2008), Tyrrhena Patera: Geologic history derived from Mars Express High Resolution Stereo Camera, *Journal of Geophysical Research: Planets*, *113*(E11), doi:10.1029/2008JE003104.

Williams, D. A. et al. (2009a), The Circum-Hellas Volcanic Province, Mars: Overview, *Planetary and Space Science*, *57*(8–9), 895 – 916, doi:http://dx.doi.org/10.1016/j.pss.2008.08.010.

Williams, D. A. et al. (2010a), Surface-compositional properties of the Malea Planum region of the Circum-Hellas Volcanic Province, Mars, *Earth and Planetary Science Letters*, *294*(3–4), 451–465, doi:10.1016/j.epsl.2009.11.019.

Williams, D. A., R. Greeley, L. Manfredi, J. Raitala, and G. Neukum (2010b), The Circum-Hellas Volcanic Province, Mars: Assessment of wrinkle-ridged plains, *Earth and Planetary Science Letters*, *294*(3–4), 492–505, doi:10.1016/j.epsl.2009.10.007.

Williams, R. M. E., R. P. Irwin III, and J. R. Zimbelman (2009b), Evaluation of paleohydrologic models for terrestrial inverted channels: Implications for application to martian sinuous ridges, *Geomorphology*, *107*(3–4), 300–315, doi:10.1016/j.geomorph.2008.12.015.

Wilson, L. (2009), Volcanism in the Solar System, *Nature Geosci*, *2*(6), 389–397, doi:10.1038/ngeo529.

Wilson, L., and J. W. Head (1983), A comparison of volcanic eruption processes on Earth, Moon, Mars, Io and Venus, *Nature*, *302*(5910), 663–669, doi:10.1038/302663a0.

Wilson, L., and J. W. Head (1994), Mars: Review and analysis of volcanic eruption theory and relationships to observed landforms, *Rev. Geophys.*, *32*(3), 221–263, doi:10.1029/94rg01113.

Wilson, L., and P. J. Mouginis-Mark (2001), Estimation of volcanic eruption conditions for a large flank event on Elysium Mons, Mars, *Journal of Geophysical Research: Planets*, *106*(E9), 20621–20628, doi:10.1029/2000je001420.

Wilson, L., E. D. Scott, and J. W. Head III (2001), Evidence for episodicity in the magma supply to the large Tharsis volcanoes, *J. Geophys. Res.*, *106*(E1), 1423–1433, doi:10.1029/2000je001280.

Wolfe, E. W., W. S. Wise, and G. B. Dalrymple (1997), *The geology and petrology of Mauna Kea Volcano, Hawaii; a study of postshield volcanism*, Professional Paper, Report.

Wood, C. A. (1979), Monogenetic volcanoes of the terrestrial planets, vol. 10, pp. 2815–2840.

Wray, J. J., S. W. Squyres, L. H. Roach, J. L. Bishop, J. F. Mustard, and E. Z. Noe Dobrea (2010), Identification of the Ca-sulfate bassanite in Mawrth Vallis, Mars, *Icarus*, *209*(2), 416–421, doi:10.1016/j.icarus.2010.06.001.

Wray, J. J., S. T. Hansen, J. Dufek, G. A. Swayze, S. L. Murchie, F. P. Seelos, J. R. Skok, R. P. Irwin Iii, and M. S. Ghiorso (2013), Prolonged magmatic activity on Mars inferred from the detection of felsic rocks, *Nature Geosci*, *6*(12), 1013–1017, doi:10.1038/ngeo1994.

Xiao, L., J. Huang, P. R. Christensen, R. Greeley, D. A. Williams, J. Zhao, and Q. He (2012), Ancient volcanism and its implication for thermal evolution of Mars, *Earth and Planetary Science Letters*, *323–324*, 9–18, doi:10.1016/j.epsl.2012.01.027.

Zhong, S., and M. T. Zuber (2001), Degree-1 mantle convection and the crustal dichotomy on Mars, *Earth and Planetary Science Letters*, *189*(1–2), 75–84, doi:10.1016/S0012-821X(01)00345-4.

Zimbelman, J. R. (1986), The role of porosity in thermal inertia variations on basaltic lavas, *Icarus*, *68*(2), 366–369, doi:10.1016/0019-1035(86)90028-X.

Zimbelman, J. R. (1998), Emplacement of long lava flows on planetary surfaces, *J. Geophys. Res.*, *103*(B11), 27503–27516, doi:10.1029/98jb01123.

Zuber, M. T. et al. (2000), Internal Structure and Early Thermal Evolution of Mars from Mars Global Surveyor Topography and Gravity, *Science*, *287*(5459), 1788–1793.

Zurek, R. W., and S. E. Smrekar (2007), An overview of the Mars Reconnaissance Orbiter (MRO) science mission, *J. Geophys. Res.*, *112*(E5), E05S01, doi:10.1029/2006JE002701.